R. Mayes · D. Rixen · D.T. Griffith · D. De Klerk · S. Chauhan · S.N. Voormeeren · M.S. Allen   *Editors*

Topics in Experimental Dynamics Substructuring and Wind Turbine Dynamics, Volume 2

Proceedings of the 30th IMAC,
A Conference on Structural Dynamics, 2012

SEM

Springer

Conference Proceedings of the Society for Experimental Mechanics Series

R. Mayes • D. Rixen • D.T. Griffith • D. De Klerk
S. Chauhan • S.N. Voormeeren • M.S. Allen
Editors

Topics in Experimental Dynamics Substructuring and Wind Turbine Dynamics, Volume 2

Proceedings of the 30th IMAC, A Conference on Structural Dynamics, 2012

Springer

Editors
R. Mayes
Sandia National Laboratories
Albuquerque, NM, USA

D.T. Griffith
Sandia National Laboratories
Albuquerque, NM, USA

S. Chauhan
Brüel and Kjær
Skodsborgvej, Denmark

M.S. Allen
University of Wisconsin
Madison, WI, USA

D. Rixen
Delft University of Technology
The Netherlands

D. De Klerk
Delft University of Technology
The Netherlands

S.N. Voormeeren
Delft University of Technology
The Netherlands

Printed on acid-free paper

Preface

Topics in Experimental Dynamics Substructuring and Wind Turbine Dynamics represents one of six volumes of technical papers presented at the 30th IMAC, A Conference and Exposition on Structural Dynamics, 2012 organized by the Society for Experimental Mechanics, and held in Jacksonville, Florida, January 30 – February 2, 2012. The full proceedings also include volumes on Dynamics of Civil Structures; Nonlinear Dynamics; Model Validation and Uncertainty Quantification; and Modal Analysis, I & II.

Each collection presents early findings from experimental and computational investigations on an important area within Structural Dynamics. The current volume on *Topics in Experimental Dynamics Substructuring and Wind Turbine Dynamics* presents research in two areas of great importance. Recent advances in experimental techniques, sensor/actuator technologies, novel numerical methods, and parallel computing have rekindled interest in substructuring in recent years leading to new insights and improved experimental and analytical techniques.

Governments around the world have set ambitious goals of meeting 20% of energy requirements by 2020 through renewable energy sources including wind energy. This presents challenges, including the growing size and complexity of the wind turbine structure, necessitating the need for designers to better understand and characterize the dynamics of the wind turbine. Despite well-established techniques (Experimental and Operational Modal Analysis) for dynamic characterization of structures, their application to wind turbines is not straight forward due to the complexities involved on account of considerable aeroelastic interaction and time-varying nature of wind turbines, when in operation. This volume showcases research activities with regards to application of modal analysis to wind turbines, preparing and updating numerical models, instrumentation and sensing on wind turbine blades, and structural health monitoring as applied to wind turbines.

The organizers would like to thank the authors, presenters, session organizers, and session chairs for their participation in this track.

Albuquerque, NM, USA	R. Mayes
The Netherlands	D. Rixen
Albuquerque, NM, USA	D.T. Griffith
The Netherlands	D. De Klerk
Skodsborgvej, Denmark	S. Chauhan
The Netherlands	S.N. Voormeeren
Madison, WI, USA	M.S. Allen

Contents

Chapter 1
Tutorial on Experimental Dynamic Substructuring Using the Transmission Simulator Method*

Randy L. Mayes

Abstract Although analytical substructures have been used successfully for years, practical experimental substructures have been limited to special cases until recently. Many of the historical practical applications were based on a single point attachment. Since substructures have to be connected, theoretically, in both translation and rotation degrees of freedom, measurement translation responses and forces around the single point attachment could be used to estimate the rotational responses and moments. For multiple attachment points, often the rotations and moments have been neglected entirely. In addition, often the effect of the joint stiffness and damping is neglected. The translation simulator approach developed by Allen and Mayes captures the interface forces and motions through a fixture called the transmission simulator, overcoming the historical difficulties. The experimental free modes of the experimental substructure mounted to the transmission simulator and the finite element model of the transmission simulator are used to couple the experimental substructure to another substructure and subtract the transmission simulator. This captures the effects of the joint stiffness and damping. The experimental method and mathematics will be explained with examples. The tutorial assumes a basic understanding of the linear multi-degree of freedom equations of motion and the modal approximation.

1.1 Introduction

The modal constraint for fixture and subsystem (MCFS) method was introduced at IMAC in 2007 for the component mode synthesis approach (Allen and Mayes [1]) and the Frequency Based Substructuring approach (Mayes and Stasiunas [2]). It uses a fixture in the experimental dynamic substructure called the transmission simulator, so is also called the transmission simulator method. An analytical model of the transmission simulator is always required with this method.

Physically, the transmission simulator is mounted to the experimental substructure with exactly the same joint geometry and material as that to which the experimental substructure will ultimately be connected. Because of this, the resulting experimental substructure inherently includes the linearized stiffness and damping in the joint, which classical methods neglect, to their peril. The fixture is also designed to provide accessible locations to mount response sensors and to apply input forces. Often the actual connection points are poor locations to mount sensors. For example, the connection point may be at a bolt or a threaded screw interface. Special features can also be included to provide good driving point measurements, which are extremely important to obtain accurate modal mass for scaling the mode shapes.

The analytical model of the transmission simulator is used in multiple ways. It is generally mounted with an assumed welded connection to the analytical substructure (often a finite element model) to which the experimental substructure is to be connected. By constraining the transmission simulator on the experimental substructure to have the same motion as the transmission simulator on the analytical substructure, the systems are joined. Then the mass and stiffness of the analytical and experimental transmission simulators are subtracted from the assembled system. The analytical model of the transmission simulator can also be thought of as an aid to interpolate from the measurement sensor locations back to the actual

R.L. Mayes (✉)
Experimental Mechanics, NDE and Model Validation Department, Sandia National Laboratories,
5800 – MS0557, Albuquerque, NM 87185, USA
e-mail: rlmayes@sandia.gov
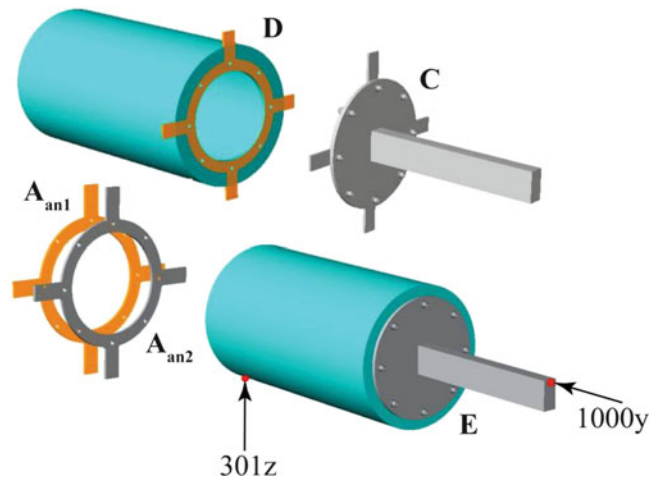
Fig. 1.1 Coupling of experimental substructure C with analytical substructure D to generate full system E after transmission simulators (A_{an1} and A_{an2}) are subtracted

connection degrees of freedom (dof). A truncated set of the mode shapes of the transmission simulator is used that spans the frequency bandwidth of interest. The sensor set can be chosen to provide a set of sensor locations for which all chosen transmission shapes are linearly independent. These sensors can all be translational – no rotations are required. The rotations at the connection points are inherently carried in the modal coordinates of the transmission simulator. The connections can actually be continuous, not just discrete, as long as the transmission simulator mode shape set spans the space of the connection motion reasonably well. In addition the transmission simulator mass stresses the joint. This stress across the joint provides a much better Ritz vector shape basis than simple free modes where there is no stress at the joint. It provides enough improvement in the basis vectors that residuals, which are difficult to measure, do not need to be added to the basis set.

Although this method requires fabrication of a fixture and generation of its associated analytical model, it provides extensive benefits for the investment. One does not have to measure exactly at the connection points. One does not have to measure rotations because they are inherently included in the analytical model modal coordinates (so they are not just being neglected). The stiffness and damping of the joint are inherently included. No residual measurements are required.

One problem that can result in this method is that the mass matrix can be indefinite when the transmission simulator is subtracted. However, methods to correct the mass matrix have been developed recently [3]. This has cleared the way so that in practice, refinements can be made without theoretical road blocks.

An example from [3] shows conceptually how the method was implemented for one actual hardware case in Fig. 1.1. The transmission simulator hardware, which is a ring with tabs, is mounted to the experimental substructure with eight bolts, just as it will be attached in the real system to the cylinder substructure, so it contains the joint. An analytical model of the transmission simulator is welded in to the flange of the cylinder analytical model. The transmission simulator and the cylinder flange actually occupy the same space, which can be done with an analytical model. Then transmission simulators for each substructure are forced to have the same motion, which connects them. Finally the stiffness and mass of the two transmission simulators are analytically subtracted.

The free-free experimental modal test setup is shown in Fig. 1.2 with 12 triaxial accels on the transmission simulator and 2 triaxial accels at points of interest on the beam. Twenty five rigid body and elastic modes were extracted out to 4 kHz. This structure had eight discrete bolted attachments, which would require 48 discrete constraints for the three rotations and three translations at each connection. Figure 1.3 shows the 12 triax locations, which are not at the eight connection points. 18 modes of the transmission simulator analytical model were used to span the connection space motion, using 36 measured dof to describe the mode shapes. The method thus reduces the number of constraints down from the classic 48 connections to 18. The 18 modes covered a frequency bandwidth of 2 kHz.

Fig. 1.2 Experimental substructure free modal test setup with 36 sensors on the transmission simulator ring and a few sensors at points of interest on the substructure
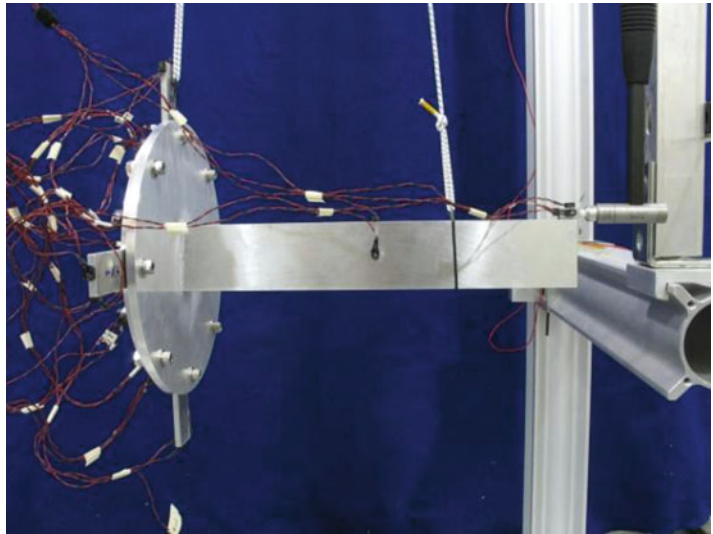
Fig. 1.3 Transmission simulator with 12 triaxial accelerometers at blue nodes for sensing
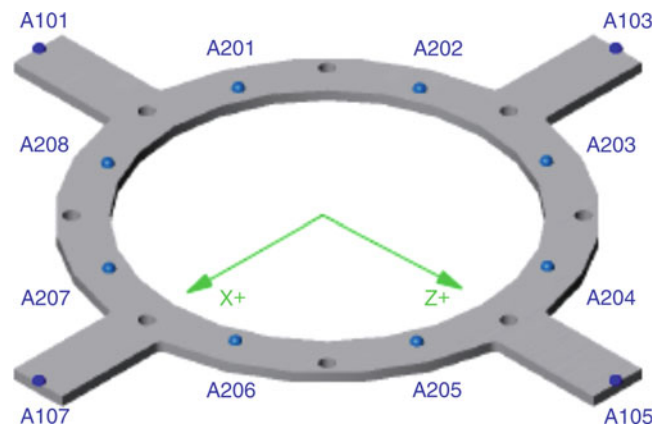
1.2 Component Mode Synthesis Theory Using Primal Formulation in a Generalized Framework

The generalized framework of deKlerk, Rixen and Voormeeren [4] for dynamic substructuring is utilized. Here assume that each substructure has been approximated with a reduced model, whether experimental or analytical. Then the displacements are approximated with the modal substitution as

$$\bar{\mathbf{u}} \cong \mathbf{R}\bar{\boldsymbol{\eta}} \tag{1.1}$$

where $\bar{\mathbf{u}}$ is the vector of physical displacements, $\bar{\boldsymbol{\eta}}$ is the vector of generalized coordinates from a modal test or eigenvector analysis and $\mathbf{R}$ is the truncated mode shape matrix relating the generalized coordinates to the physical coordinates. Then the equations of motion for the substructure can be written as

$$\mathbf{M}^{(s)}\mathbf{R}\ddot{\bar{\boldsymbol{\eta}}}^{(s)} + \mathbf{C}^{(s)}\mathbf{R}\dot{\bar{\boldsymbol{\eta}}}^{(s)} + \mathbf{K}^{(s)}\mathbf{R}\bar{\boldsymbol{\eta}}^{(s)} = \bar{\mathbf{f}}^{(s)} + \bar{\mathbf{g}}^{(s)} + \bar{\mathbf{r}}^{(s)} \tag{1.2}$$

Where $\mathbf{M}$, $\mathbf{C}$ and $\mathbf{K}$ are mass stiffness and damping matrices, the superscript *(s)* denotes the particular substructure, $\bar{\mathbf{f}}^{(s)}$ denotes the external forces applied to the substructure, $\bar{\mathbf{g}}^{(s)}$ represents the equilibrium joining forces from another substructure

that will be applied to the substructure, and $\bar{\mathbf{r}}^{(s)}$ is the residual force due to the mismatch caused by the approximation of the displacements in (1.1). Premultiplying by $\mathbf{R}^T$ yields

$$\mathbf{R}^T\mathbf{M}^{(s)}\mathbf{R}\ddot{\bar{\boldsymbol{\eta}}}^{(s)} + \mathbf{R}^T\mathbf{C}^{(s)}\mathbf{R}\dot{\bar{\boldsymbol{\eta}}}^{(s)} + \mathbf{R}^T\mathbf{K}^{(s)}\mathbf{R}\bar{\boldsymbol{\eta}}^{(s)} = \mathbf{R}^T\bar{\mathbf{f}}^{(s)} + \mathbf{R}^T\bar{\mathbf{g}}^{(s)} + \mathbf{R}^T\bar{\mathbf{r}}^{(s)}. \tag{1.3}$$

It can be shown that, because of orthogonality of the mode shapes with respect to $\mathbf{M}$, $\mathbf{C}$ and $\mathbf{K}$,

$$\mathbf{R}^T\bar{\mathbf{r}}^{(s)} = \bar{\mathbf{0}} \tag{1.4}$$

which leaves

$$\mathbf{R}^T\mathbf{M}^{(s)}\mathbf{R}\ddot{\bar{\boldsymbol{\eta}}}^{(s)} + \mathbf{R}^T\mathbf{C}^{(s)}\mathbf{R}\dot{\bar{\boldsymbol{\eta}}}^{(s)} + \mathbf{R}^T\mathbf{K}^{(s)}\mathbf{R}\bar{\boldsymbol{\eta}}^{(s)} = \mathbf{R}^T\bar{\mathbf{f}}^{(s)} + \mathbf{R}^T\bar{\mathbf{g}}^{(s)}, \tag{1.5}$$

or in a renamed form

$$\mathbf{M}_m^{(s)}\ddot{\bar{\boldsymbol{\eta}}}^{(s)} + \mathbf{C}_m^{(s)}\dot{\bar{\boldsymbol{\eta}}}^{(s)} + \mathbf{K}_m^{(s)}\bar{\boldsymbol{\eta}}^{(s)} = \bar{\mathbf{f}}_m^{(s)} + \bar{\mathbf{g}}_m^{(s)} \tag{1.6}$$

where subscript m denotes modal quantities. The matrices are, if the mode shapes are mass normalized,

$$\begin{aligned} \mathbf{M}_m^{(s)} &= \mathbf{R}^T\mathbf{M}^{(s)}\mathbf{R} = \mathbf{I} \\ \mathbf{C}_m^{(s)} &= \mathbf{R}^T\mathbf{C}^{(s)}\mathbf{R} = diag(2^*\bar{\boldsymbol{\zeta}}.^*\bar{\boldsymbol{\omega}}) \\ \mathbf{K}_m^{(s)} &= \mathbf{R}^T\mathbf{K}^{(s)}\mathbf{R} = diag(\bar{\boldsymbol{\omega}}.^\wedge 2) \\ \bar{\mathbf{f}}_m^{(s)} &= \mathbf{R}^T\mathbf{f}^{(s)} \\ \bar{\mathbf{g}}_m^{(s)} &= \mathbf{R}^T\mathbf{g}^{(s)}. \end{aligned} \tag{1.7}$$

At this point, let us concatenate the various substructures together in the uncoupled form as

$$\mathbf{M}_m\ddot{\bar{\boldsymbol{\eta}}} + \mathbf{C}_m\dot{\bar{\boldsymbol{\eta}}} + \mathbf{K}_m\bar{\boldsymbol{\eta}} = \bar{\mathbf{f}}_m + \bar{\mathbf{g}}_m. \tag{1.8}$$

Compatibility is now enforced with a constraint equation from

$$\mathbf{B}\bar{\mathbf{u}}_c = \bar{\mathbf{0}} \tag{1.9}$$

Where $\mathbf{B}$ is a Boolean matrix of ones, zeros and negative ones, and for convenience we will include only connection dof in the displacement vector. Take the partition of (1.1) for only the connection dof and again make the modal substitution

$$\mathbf{B}\mathbf{R}_c\bar{\boldsymbol{\eta}} \cong \bar{\mathbf{0}} \tag{1.10}$$

where the subscript c indicates taking only the partition of R necessary for the connection dof.

Up to this point we have followed the generalized framework rather strictly, but at this point, the transmission simulator method affects the rest of the development. It is assumed that there is an analytical model of the transmission simulator, one uses a truncated set of its mode shapes, Ψ_c, as a basis to span the space of the connection motion for each substructure. Now we use the pseudo-inverse (denoted with a superscript +) to project the constraint on the space of the transmission simulator vector space by premultiplying both sides by the block diagonal pseudo-inverse as

$$\Psi_c^{BD+}\mathbf{B}\mathbf{R}_c\bar{\boldsymbol{\eta}} \cong \Psi_c^{BD+}\bar{\mathbf{0}} \tag{1.11}$$

where

$$\Psi_c^{BD+} = \begin{bmatrix} \Psi_c^+ & 0 & 0 \\ 0 & ... & 0 \\ 0 & 0 & \Psi_c^+ \end{bmatrix} \tag{1.12}$$

will have as many block rows as there are substructures. The right hand side of (1.11) is still a vector of zeros, although the number of constraints (rows) is reduced since the matrix $\boldsymbol{\Psi}_c$ is selected so that it always has more dof than modes. The final constraint is

$$\tilde{\mathbf{B}}\bar{\boldsymbol{\eta}} = \bar{\mathbf{0}} \tag{1.13}$$

where

$$\tilde{\mathbf{B}} = \boldsymbol{\Psi}_c^{BD+}\mathbf{B}\mathbf{R}_c \tag{1.14}$$

There are multiple reasons for premultiplying by $\boldsymbol{\Psi}_c^{BD+}$. First it softens the constraint (reduces the number of constraints). The advantage of this is that it gives a least squares fit through the measured motions of the transmission simulator at the dof to which the constraints will be applied. The mode shapes of the transmission simulator provide a smoothing effect through the measured motions, which always have experimental error. The modified matrix greatly improves the conditioning of the problem. Also, one does not HAVE to use motions measured directly at the attachment points and also does not HAVE to measure rotations, which are inherently carried along in the generalized dof of the transmission simulator. The generalized modal dof of the transmission simulator are $\bar{\boldsymbol{\gamma}}$ in the following

$$\boldsymbol{\Psi}_c\bar{\boldsymbol{\gamma}} \cong \mathbf{R}_c^{(s)}\bar{\boldsymbol{\eta}}^{(s)} \tag{1.15}$$

but can be expressed as

$$\bar{\boldsymbol{\gamma}} \cong \boldsymbol{\Psi}_c^+\mathbf{R}_c^{(s)}\bar{\boldsymbol{\eta}}^{(s)} \tag{1.16}$$

which can be seen in the left hand side of (1.11) as converting the constraint to the transmission simulator modal coordinates.

Now continue the development in the general framework from (1.13). We perform another modal-like substitution with

$$\bar{\boldsymbol{\eta}} = \tilde{\mathbf{L}}\bar{\boldsymbol{\varepsilon}}. \tag{1.17}$$

Substitute (1.17) into (1.13) to give

$$\tilde{\mathbf{B}}\tilde{\mathbf{L}}\bar{\boldsymbol{\varepsilon}} = \bar{\mathbf{0}}. \tag{1.18}$$

If one chooses $\tilde{\mathbf{L}}$ such that it is in the null space of $\tilde{\mathbf{B}}$, then (1.18) is guaranteed to be satisfied because

$$\tilde{\mathbf{B}}\tilde{\mathbf{L}} = [zeros]. \tag{1.19}$$

All the rows of $\tilde{\mathbf{B}}$ are orthogonal to all the columns of $\tilde{\mathbf{L}}$. Since $\tilde{\mathbf{B}}$ is known, a one line command in matlab can provide $\tilde{\mathbf{L}}$. Substituting (1.17) back into the uncoupled equations of motion in (1.8) and premultiplying by $\tilde{\mathbf{L}}^T$ gives

$$\tilde{\mathbf{L}}^T\mathbf{M}_m\tilde{\mathbf{L}}\ddot{\bar{\boldsymbol{\varepsilon}}} + \tilde{\mathbf{L}}^T\mathbf{C}_m\tilde{\mathbf{L}}\dot{\bar{\boldsymbol{\varepsilon}}} + \tilde{\mathbf{L}}^T\mathbf{K}_m\tilde{\mathbf{L}}\bar{\boldsymbol{\varepsilon}} = \tilde{\mathbf{L}}^T\bar{\mathbf{f}}_m + \tilde{\mathbf{L}}^T\bar{\mathbf{g}}_m, \tag{1.20}$$

which couples the equations of motion, reducing the number of rows in (1.8) by the number of constraints (rows) in (1.13). This leads to the primal coupling formulation in this framework. In this formulation $\tilde{\mathbf{L}}^T\bar{\mathbf{g}}_m = \tilde{\mathbf{L}}^T\mathbf{R}^T\bar{\mathbf{g}} = \bar{0}$, since the rows of $\tilde{\mathbf{L}}^T$ are orthogonal to a linear combination of the columns of $\mathbf{R}^T$, leaving

$$\tilde{\mathbf{M}}_m\ddot{\bar{\boldsymbol{\varepsilon}}} + \tilde{\mathbf{C}}_m\dot{\bar{\boldsymbol{\varepsilon}}} + \tilde{\mathbf{K}}_m\bar{\boldsymbol{\varepsilon}} = \tilde{\bar{\mathbf{f}}}_m \tag{1.21}$$

where

$$\begin{aligned} \tilde{\mathbf{M}}_m &= \tilde{\mathbf{L}}^T\mathbf{M}_m\tilde{\mathbf{L}} \\ \tilde{\mathbf{C}}_m &= \tilde{\mathbf{L}}^T\mathbf{C}_m\tilde{\mathbf{L}} \\ \tilde{\mathbf{K}}_m &= \tilde{\mathbf{L}}^T\mathbf{K}_m\tilde{\mathbf{L}} \\ \tilde{\bar{\mathbf{f}}}_m &= \tilde{\mathbf{L}}^T\bar{\mathbf{f}}_m. \end{aligned} \tag{1.22}$$

1.3   Frequency Based Substructuring Dual Formulation in the General Framework

Again following [4], for the physical dof, the uncoupled equations of motion, the compatibility and the equilibrium are written as

$$\mathbf{M\ddot{\bar{u}}} + \mathbf{C\dot{\bar{u}}} + \mathbf{K\bar{u}} = \mathbf{\bar{f}} + \mathbf{\bar{g}} \tag{1.23}$$

$$\mathbf{B\bar{u}} = \mathbf{\bar{0}} \tag{1.24}$$

$$\mathbf{L}^T\mathbf{g} = \mathbf{\bar{0}} \tag{1.25}$$

where $\mathbf{M}$, $\mathbf{C}$ and $\mathbf{K}$ are block diagonal with as many blocks as substructures. The constraint forces $\mathbf{\bar{g}}$ between the substructures can be written as

$$\mathbf{g} = -\mathbf{B}^T\mathbf{\bar{\lambda}} \tag{1.26}$$

where $\mathbf{\bar{\lambda}}$ are Lagrange multipliers corresponding physically to the interface forces. Equations (1.23) and (1.24) can now be written in matrix form as

$$\begin{bmatrix} \mathbf{M} & \mathbf{0} \\ \mathbf{0} & \mathbf{0} \end{bmatrix} \begin{bmatrix} \mathbf{\ddot{u}} \\ \mathbf{\lambda} \end{bmatrix} + \begin{bmatrix} \mathbf{C} & \mathbf{0} \\ \mathbf{0} & \mathbf{0} \end{bmatrix} \begin{bmatrix} \mathbf{\dot{u}} \\ \mathbf{\lambda} \end{bmatrix} + \begin{bmatrix} \mathbf{K} & \mathbf{B}^T \\ \mathbf{B} & \mathbf{0} \end{bmatrix} \begin{bmatrix} \mathbf{u} \\ \mathbf{\lambda} \end{bmatrix} = \begin{bmatrix} \mathbf{f} \\ \mathbf{0} \end{bmatrix}. \tag{1.27}$$

Taking the Fourier transform to put into the frequency domain, where each quantity is a function of frequency, gives

$$\begin{bmatrix} \mathbf{Z} & \mathbf{B}^T \\ \mathbf{B} & \mathbf{0} \end{bmatrix} \begin{bmatrix} \mathbf{u} \\ \mathbf{\lambda} \end{bmatrix} = \begin{bmatrix} \mathbf{f} \\ \mathbf{0} \end{bmatrix} \tag{1.28}$$

where $\mathbf{Z}$ is the block diagonal impedance matrix resulting from the mass, stiffness and damping. The frequency response function matrix, $\mathbf{H}$, which is often measured experimentally is the inverse of $\mathbf{Z}$. The dual formulation coupled formulation in terms of $\mathbf{H}$ is derived from (1.28) by eliminating $\mathbf{\lambda}$, yielding

$$\mathbf{\bar{u}} = \mathbf{H\bar{f}} - \mathbf{HB}^T(\mathbf{BHB}^T)^{-1}\mathbf{BH\bar{f}}. \tag{1.29}$$

The transmission simulator method modifies the $\mathbf{B}$ matrix in (1.24) as

$$\mathbf{\Psi}^{BD+}\mathbf{B\bar{u}} \cong \mathbf{\bar{0}} \tag{1.30}$$

So one has

$$\mathbf{\hat{B}\bar{u}} = \mathbf{\bar{0}} \tag{1.31}$$

where

$$\mathbf{\hat{B}} = \mathbf{\Psi}^{BD+}\mathbf{B}. \tag{1.32}$$

Now simply substitute (1.32) into (1.29) to give the frequency based transmission simulator equation as

$$\mathbf{\bar{u}} = \mathbf{H\bar{f}} - \mathbf{H\hat{B}}^T(\mathbf{\hat{B}H\hat{B}}^T)^{-1}\mathbf{\hat{B}H\bar{f}}. \tag{1.33}$$

The $\mathbf{\hat{B}}$ matrix transforms the physical connection dof frequency response functions (FRFs) into generalized dof FRFs cast on the space of the transmission simulator mode shapes. This collapses the size of the physical connection dof FRFs down to the size of the number of modes of the transmission simulator, providing some least squares smoothing, and makes the matrix inversion in (1.33) much better conditioned.

1.4 Example Combining Experimental Plate/Beam Substructure with Analytical Cylinder Substructure Using the CMS Approach

The example is based on the hardware and analytical finite element models depicted in the first three figures. In the equations below, the finite element (FE) substructure is considered to have the analytical model of the transmission simulator attached, and the experimental (EXP) substructure has the physical transmission simulator attached. Two transmission simulators must be subtracted. In this example, 100 modes were utilized from the finite element substructure, 25 modes from the experimental substructure, and 18 modes from the transmission simulator giving 143 uncoupled equations of motion. Consider only the eigenvalue equations of motion, and then the final coupled modal parameters can be used to analytically form any desired full system response FRF. Damping will be predicted in a simplified method later. The undamped frequency domain equations of motion using modal coordinates when forces are removed are

$$\begin{bmatrix} \boldsymbol{\omega}_{\mathbf{FE}}^2 & \mathbf{0} & \mathbf{0} \\ \mathbf{0} & \boldsymbol{\omega}_{\mathbf{EXP}}^2 & \mathbf{0} \\ \mathbf{0} & \mathbf{0} & -2\boldsymbol{\omega}_{\mathbf{TS}}^2 \end{bmatrix} \begin{Bmatrix} \boldsymbol{\eta}_{\mathbf{FE}} \\ \boldsymbol{\eta}_{\mathbf{EXP}} \\ \boldsymbol{\eta}_{\mathbf{TS}} \end{Bmatrix} - \boldsymbol{\omega}^2 \begin{bmatrix} \mathbf{I}_{\mathbf{FE}} & \mathbf{0} & \mathbf{0} \\ \mathbf{0} & \mathbf{I}_{\mathbf{EXP}} & \mathbf{0} \\ \mathbf{0} & \mathbf{0} & -2\mathbf{I}_{\mathbf{TS}} \end{bmatrix} \begin{Bmatrix} \ddot{\boldsymbol{\eta}}_{\mathbf{FE}} \\ \ddot{\boldsymbol{\eta}}_{\mathbf{EXP}} \\ \ddot{\boldsymbol{\eta}}_{\mathbf{TS}} \end{Bmatrix} = \begin{Bmatrix} 0 \\ 0 \\ 0 \end{Bmatrix} \tag{1.34}$$

and the physical displacements, $\mathbf{y}$, on each substructures are

$$\begin{Bmatrix} \mathbf{y}_{\mathbf{FE}} \\ \mathbf{y}_{\mathbf{EXP}} \\ \mathbf{y}_{\mathbf{TS}} \end{Bmatrix} = \begin{bmatrix} \mathbf{R}_{\mathbf{FE}} & \mathbf{0} & \mathbf{0} \\ \mathbf{0} & \mathbf{R}_{\mathbf{EXP}} & \mathbf{0} \\ \mathbf{0} & \mathbf{0} & \mathbf{R}_{\mathbf{TS}} \end{bmatrix} \begin{Bmatrix} \boldsymbol{\eta}_{\mathbf{FE}} \\ \boldsymbol{\eta}_{\mathbf{EXP}} \\ \boldsymbol{\eta}_{\mathbf{TS}} \end{Bmatrix} \tag{1.35}$$

where $\mathbf{R}$ are a truncated set of the mass normalized mode shapes of each substructure coming from experiment or analysis. The motion of the transmission simulator in all three substructures should be the same when all the substructures are coupled, so two sets of physical constraints can be written

$$\mathbf{y}_{\mathrm{FEmeas}} = \mathbf{y}_{\mathrm{EXPmeas}} \text{ and } \mathbf{y}_{\mathrm{EXPmeas}} = \mathbf{y}_{\mathrm{TSmeas}} \tag{1.36}$$

Just consider the first of these constraints, invoke the modal substitution from (1.35) and premultiply by the pseudo-inverse of transmission simulator mode shapes, $\mathbf{R}_{\mathbf{TS}}^+$ to give

$$\mathbf{R}_{\mathbf{TS}}^+ \mathbf{R}_{\mathbf{FEmeas}} \bar{\boldsymbol{\eta}}_{\mathbf{FE}} = \mathbf{R}_{\mathbf{TS}}^+ \mathbf{R}_{\mathbf{EXPmeas}} \bar{\boldsymbol{\eta}}_{\mathbf{EXP}} \tag{1.37}$$

Or moving everything to the left had side gives

$$\mathbf{R}_{\mathbf{TS}}^+ \mathbf{R}_{\mathbf{FEmeas}} \bar{\boldsymbol{\eta}}_{\mathbf{FE}} - \mathbf{R}_{\mathbf{TS}}^+ \mathbf{R}_{\mathbf{EXPmeas}} \bar{\boldsymbol{\eta}}_{\mathbf{EXP}} = \mathbf{0}. \tag{1.38}$$

A similar process can be applied to the second constraint of (1.36). The constraints can now be written in the form given in (1.12)–(1.14) as

$$\begin{bmatrix} \mathbf{R}_{\mathbf{TS}}^+ & \mathbf{0} \\ \mathbf{0} & \mathbf{R}_{\mathbf{TS}}^+ \end{bmatrix} \begin{bmatrix} \mathbf{I} & -\mathbf{I} & \mathbf{0} \\ \mathbf{0} & \mathbf{I} & -\mathbf{I} \end{bmatrix} \begin{bmatrix} \mathbf{R}_{\mathbf{FEmeas}} & \mathbf{0} & \mathbf{0} \\ \mathbf{0} & \mathbf{R}_{\mathbf{EXPmeas}} & \mathbf{0} \\ \mathbf{0} & \mathbf{0} & \mathbf{R}_{\mathbf{TS}} \end{bmatrix} \begin{Bmatrix} \boldsymbol{\eta}_{\mathbf{FE}} \\ \boldsymbol{\eta}_{\mathbf{EXP}} \\ \boldsymbol{\eta}_{\mathbf{TS}} \end{Bmatrix} = \begin{Bmatrix} 0 \\ 0 \end{Bmatrix} \tag{1.39}$$

Where $\boldsymbol{\Psi}_c^{BD+}$ in (1.11) is $\mathbf{R}_{TS}^{BD+}$ and $\mathbf{B}$ is the Boolean matrix here, thus

$$\tilde{\mathbf{B}} = \begin{bmatrix} \mathbf{R}_{\mathbf{TS}}^+ & \mathbf{0} \\ \mathbf{0} & \mathbf{R}_{\mathbf{TS}}^+ \end{bmatrix} \begin{bmatrix} \mathbf{I} & -\mathbf{I} & \mathbf{0} \\ \mathbf{0} & \mathbf{I} & -\mathbf{I} \end{bmatrix} \begin{bmatrix} \mathbf{R}_{\mathbf{FEmeas}} & \mathbf{0} & \mathbf{0} \\ \mathbf{0} & \mathbf{R}_{\mathbf{EXPmeas}} & \mathbf{0} \\ \mathbf{0} & \mathbf{0} & \mathbf{R}_{\mathbf{TS}} \end{bmatrix}. \tag{1.40}$$

Repeating (1.17) and (1.18) here for clarity gives

$$\bar{\boldsymbol{\eta}} = \tilde{\mathbf{L}}\bar{\boldsymbol{\varepsilon}} \tag{1.41}$$

and

$$\tilde{\mathbf{B}}\tilde{\mathbf{L}}\bar{\boldsymbol{\varepsilon}} = \bar{\mathbf{0}} \tag{1.42}$$

and $\tilde{\mathbf{L}}$ is the null space of $\tilde{\mathbf{B}}$, which is known. Substitute (1.41) into (1.34) and premultiply by $\tilde{\mathbf{L}}^T$ to give

$$\mathbf{L}^T \begin{bmatrix} \boldsymbol{\omega}_{\mathbf{FE}}^2 & \mathbf{0} & \mathbf{0} \\ \mathbf{0} & \boldsymbol{\omega}_{\mathbf{EXP}}^2 & \mathbf{0} \\ \mathbf{0} & \mathbf{0} & -2\boldsymbol{\omega}_{\mathbf{TS}}^2 \end{bmatrix} \mathbf{L}\bar{\boldsymbol{\varepsilon}} - \boldsymbol{\omega}^2 \mathbf{L}^T \begin{bmatrix} \mathbf{I}_{\mathbf{FE}} & \mathbf{0} & \mathbf{0} \\ \mathbf{0} & \mathbf{I}_{\mathbf{EXP}} & \mathbf{0} \\ \mathbf{0} & \mathbf{0} & -2\mathbf{I}_{\mathbf{TS}} \end{bmatrix} \mathbf{L}\ddot{\bar{\boldsymbol{\varepsilon}}} = \bar{\mathbf{0}} \tag{1.43}$$

providing the coupled equations from which the eigenvalue problem can be solved yielding. The solution will provide a set of eigenvectors, Φ, frequencies, $\boldsymbol{\omega}^2$, and modal coordinates, $\bar{\boldsymbol{\beta}}$. Now the coupled displacements will be

$$\bar{\mathbf{y}} = \mathbf{RL}\Phi\bar{\boldsymbol{\beta}}. \tag{1.44}$$

The resulting new damping matrix is formed by

$$\Phi^T \mathbf{L}^T \begin{bmatrix} \boldsymbol{\omega}_{\mathbf{FE}}^2 & \mathbf{0} & \mathbf{0} \\ \mathbf{0} & \boldsymbol{\omega}_{\mathbf{EXP}}^2 & \mathbf{0} \\ \mathbf{0} & \mathbf{0} & -2\boldsymbol{\omega}_{\mathbf{TS}}^2 \end{bmatrix} \mathbf{L}\Phi \tag{1.45}$$

From which we usually just take the diagonal values to give $2\bar{\boldsymbol{\zeta}}_{new}. * \bar{\boldsymbol{\omega}}_{new}$.

1.5 Example Combining Experimental Plate/Beam Substructure with Analytical Cylinder Substructure Using the CMS Approach

Generally, the author does not execute (1.33) in a single step, since it makes the matrices very large and the resulting inversions are computationally too intensive. For this example, assume we have one step where systems C and D in the figure are too be joined. (Another step can be taken to subtract the transmission simulators, which will not be done here). Define **HC** and **HD** as the frequency response function matrices for substructures C and D respectively. **HT** is the FRF matrix of the total system after C and D are coupled. Each substructure has a two dimensional FRF matrix for every frequency line of the FRFs. The first subscript on any of these matrices represents the output response dof and the second subscript represents the input force dof. Perhaps the two most useful equations from partitions of the classical method in (1.29) are

$$\mathbf{HT}_{ri} = \mathbf{HD}_{rc}(\mathbf{HD}_{cc} + \mathbf{HC}_{cc})^{-1}\mathbf{HC}_{ci} \tag{1.46}$$

where the force input is on substructure C and the response output is on substructure D, and

$$\mathbf{HT}_{ri} = \mathbf{HC}_{ri} - \mathbf{HC}_{rc}(\mathbf{HD}_{cc} + \mathbf{HC}_{cc})^{-1}\mathbf{HC}_{ci} \tag{1.47}$$

where the force input is on substructure C and the response output is also on substructure C. Here the subscript r represents the output response and the subscript i represents the input force, and the subscript c represents the connection dof between

Fig. 1.4 Transmission simulator method FRF of coupled system (*red*) versus truth model (*blue*) – Driving point response at tip of beam in Fig. 1.1 (color figure online)
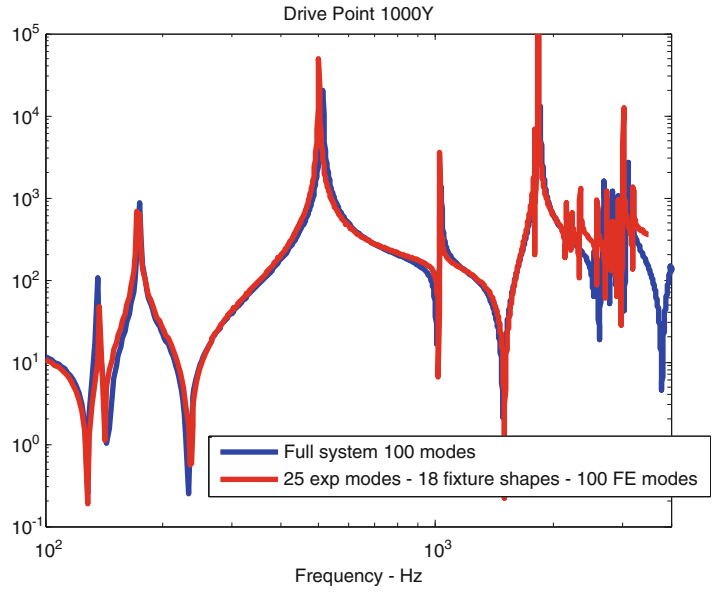
the two substructures. With the transmission simulator method, the Boolean matrix $\mathbf{B}$ is replaced with $\hat{\mathbf{B}}$ to convert all the connection dof to modal dof of the transmission simulator in (1.33), so that

$$\mathbf{HD}_{rc} = \mathbf{HD}_{rp}\mathbf{R}_{TS}^{T+} \tag{1.48}$$

$$\mathbf{HD}_{cc} = \mathbf{R}_{TS}^{+}\mathbf{HD}_{pp}\mathbf{R}_{TS}^{T+} \tag{1.49}$$

$$\mathbf{HC}_{cc} = \mathbf{R}_{TS}^{+}\mathbf{HC}_{pp}\mathbf{R}_{TS}^{T+} \tag{1.50}$$

$$\mathbf{HC}_{ci} = \mathbf{R}_{TS}^{+}\mathbf{HC}_{pi} \tag{1.51}$$

$$\mathbf{HC}_{rc} = \mathbf{HC}_{rp}\mathbf{R}_{TS}^{T+} \tag{1.52}$$

in (1.46) and (1.47). The subscript p represents the dof at the transmission simulator measurement locations on either substructure. The pseudo-inverse of the mode shape matrix $\mathbf{R}_{TS}$ of the transmission simulator reduces the size of the physical measurement FRF matrices down to the number of modes kept for the transmission simulator at all the connection dof.

In Fig. 1.4 one can see the axial FRF at the tip of the beam (see Fig. 1.1 for location). The red FRF was constructed from the modal parameters of the coupled system mode shapes, frequencies and damping using the transmission simulator method with the CMS approach. The blue FRF represents the truth data constructed from the modal parameters of a highly validated finite element model of the full system.

References

1. Allen MS, Mayes RL (2007) Comparison of FRF and modal methods for combining experimental and analytical substructures. In: Proceedings of the 25th IMAC conference on structural dynamics, Paper #269, Orlando
2. Mayes RL, Stasiunas EC (2007) Combining lightly damped experimental substructures with analytical substructures. In: Proceedings of the 25th IMAC conference on structural dynamics, Paper #207, Orlando
3. Mayes RL, Allen MS, Kammer DC (2012) Eliminating indefinite mass matrices with the transmission simulator method of substructuring. In: Proceedings of the 30th IMAC Conference on Structural Dynamics, Paper #163, Jacksonville, FL
4. de Klerk D, Rixen DJ, Voormeeren SN (2008) General framework for dynamic substructuring: history, review, and classification of techniques. AIAA J 46(5):1169–1181

Chapter 2
Experimental–Analytical Substructure Model Sensitivity Analysis for Cutting Machine Chatter Prediction

Anders Liljerehn and Thomas Abrahamsson

Abstract Process reliability and dynamic stability is a growing customer demand in the metal machining industry. A limiting factor in process stability is regenerative vibrations which may damage the machined component, the cutting tool and even the machine tool. Spindle speed optimization to ensure process stability and enable larger cutting depths is based on the machine tool and cutting tool assembly's frequency response at the tool-tip. The traditional procedure to retrieve the tool-tip frequency response is to conduct dynamic testing of each machine tool mounted cutting tool. This methodology is normally very time-consuming. In an attempt to reduce testing time, receptance coupling substructure analysis (RCSA) has been proposed by a number of researchers. The objective with this approach is to measure the machine tool structure once and then couple a finite element based substructure representation of the cutting tool of interest. The accuracy of the predicted tool-tip frequency response is then dependent on the quality of measured data. This paper details the state-space based sub-structure coupling technique that is used and presents a sensitivity analysis. This analysis distinguishes key considerations for the machine tool component test and it quantifies the parameter influence on the process stability predictions of the coupled system.

2.1 Introduction

In metal cutting, spindle speed optimization for process stability is one example of action that may reduce production time and increase process reliability. For process stability, it is crucial to avoid regenerative vibrations due to feedback of the cutting forces and thereby enable larger cutting depth, with higher material removal rate as benefit. An analytical spindle speed optimization is based on the real part of frequency response functions, FRFs, in two orthogonal transversal directions at the tool tip of a machine tool and cutting tool assembly. Based on the real part of the tool tip FRFs a chart of what is known as stability lobes can be constructed see Fig. 2.1. The stability lobe chart indicates optimal spindle speeds where regenerative vibrations can be avoided for larger depths of cut. The chart, Fig. 2.1, should be read as follows. A stable machining process can be expected if the spindle speed and axial depth of cut is in a combined state in the stable region of the chart. In the unstable state, however, regenerative vibrations also known as chatter do occur. From the stability chart one can see that some spindle speeds are more beneficial than others where greater cutting depths, and thus a better production, are allowed without encountering chatter.

The stability chart is only constructed out of the negative values of the real FRF in two orthogonal main directions at the tool tip of the cutting tool. The creation of the whole set of stability lobes to create the complete stability chart is based on the phase shifts between the vibration marks left on the machined surface made from one cutting tooth to the next tooth that comes in to cut, see [1].

Stability lobe predictions have been a vast research area since the early 1960s, [2, 3]. One of the limitations of FRF-based chatter predictions is that the FRF at the tool tip of a machine tool and cutting tool assembly only yields for a specific setup.

A. Liljerehn (✉)
AB Sandvik Coromant, R & D Metal Cutting Research, Sandviken SE-811 81, Sweden
e-mail: anders.c.liljerehn@sandvik.com

T. Abrahamsson
Dept Applied Mechanics, Chalmers University of Technology, Gothenburg SE-41296, Sweden
e-mail: thomas.abrahamsson@chalmers.se
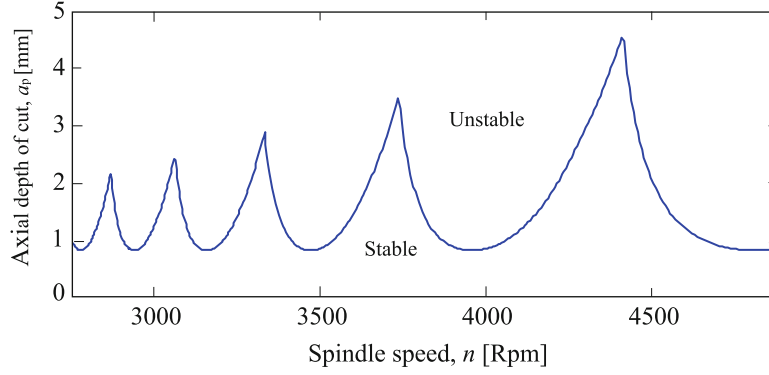
Fig. 2.1 Stability lobe chart

Larger production plants are usually equipped with a substantial amount of cutting tools in their machine tools. To measure each cutting tool combination is not only time consuming but it also requires that the machine tool is taken out of operation during measurements. This results in productivity losses which in many cases are regarded as unacceptable by the plant company. To reduce testing time receptance coupling substructure analysis (RCSA) has been utilized by a number of researchers. The objective with this approach is to only measure the machine tool structure once and then couple a substructure representation of the cutting tool of interest into an assembly.

To use a receptance coupling technique by synthesizing the frequency response displacement function of the system is indeed very appealing but is not without obstacles. This paper is a factor relevance investigation, trying to answer questions that aroused after the writing of [4]. One of the conclusions drawn in [4] was that a slight overestimation of the first bending mode of the coupled system's spindle/cutting tool assembly, compared to verification measurements, can have a large impact on the stability chart. The question of which parameters effects the result of the substructured system is one of the key understandings that need to be in place in order to conduct relevant measurements and stability lobe predictions.

The factor relevance investigation in this paper is strictly restricted to FRFs generated from FEM of the assembly components. The models are described in [4] and the coupling routines used are fully described in [5]. The approach of using synthetic data has been chosen in order to avoid the complexity and uncertainties that follows with measurements in terms of noise, misalignment of force and output sensors, etc. The necessity of further sensitivity analyses to the measurement problem is evident but excluded from this paper.

2.2 Component Synthesis

Component substructuring is usually divided in to two main categories. The first is direct frequency response function coupling [6–11]. The direct FRF coupling method has the advantage that it is fast in that sense that it can be applied directly on measured FRFs and don't require a system identification data processing. The absence of data processing is also its biggest disadvantage since it makes this type of coupling techniques sensitive to noise. The other type of coupling methods often found in literature is component mode synthesis [12–15]. This method has the advantage that it diminishes the noise problems but on the other hand requires that the mode shapes are captured well and it may also suffer from errors that can come from mode truncation. The mode truncation issue for the modal synthesis coupling technique is not a problem in the direct FRF coupling methods since the influences of higher frequency modes are accounted for in the measurement data. The component synthesis used in this sensitivity analysis is based on the state-space coupling method proposed in [5]. This coupling method utilizes the benefits of noise suppression introduced by modal analysis. This is done by coupling of identified first-order state-space substructure component models. The coupling method is used to couple two subsystems ($i = 1, 2$) on state-space form with displacement or velocities as output. A state-space model with external force inputs $\mathbf{u}$ and displacement outputs $\mathbf{y}$ can be written as follows

$$\begin{cases} \dot{\mathbf{x}}^i = \mathbf{A}^i \mathbf{x}^i + \mathbf{B}^i \mathbf{u}^i \\ \mathbf{y}^i = \mathbf{C}^i \mathbf{x}^i \end{cases} \tag{2.1}$$

The state vector is $\mathbf{x}$, and $\mathbf{A}$, $\mathbf{B}$ and $\mathbf{C}$ are constant coefficient matrices. Both subsystems are partitioned with respect to coupling degrees of freedom (DOFs), subscript c, and other DOFs, subscript o, according to the partition of response and loading

$$\mathbf{y}^i = \left\{ \begin{array}{c} \mathbf{y}_c^{\ i} \\ \mathbf{y}_o^{\ i} \end{array} \right\} \quad \mathbf{u}^i = \left\{ \begin{array}{c} \mathbf{u}_c^{\ i} \\ \mathbf{u}_o^{\ i} \end{array} \right\} \tag{2.2}$$

Using the non-uniqueness of state-space representations, the system might be transformed with similarity transformation without approximation. A similarity transform $\mathbf{T}$ with certain properties transforms the states as

$$\tilde{\mathbf{x}}^i = \mathbf{T}^i \mathbf{x}^i = \left\{ \begin{array}{c} \dot{\mathbf{y}}_c^{\ i} \\ \mathbf{y}_c^{\ i} \\ \mathbf{x}_o^{\ i} \end{array} \right\} \tag{2.3}$$

it can be shown, see [5], that the state-space matrices in this case turn into the particular coupling form as

$$\tilde{\mathbf{A}}^i = \begin{bmatrix} \mathbf{A}_{vv}^i & \mathbf{A}_{vd}^i & \mathbf{A}_{vo}^i \\ \mathbf{I} & \mathbf{0} & \mathbf{0} \\ \mathbf{0} & \mathbf{A}_{od}^i & \mathbf{A}_{oo}^i \end{bmatrix} \quad \tilde{\mathbf{B}}^i = \begin{bmatrix} \mathbf{B}_{vv}^i & \mathbf{B}_{vo}^i \\ \mathbf{0} & \mathbf{0} \\ \mathbf{0} & \mathbf{B}_{oo}^i \end{bmatrix} \quad \tilde{\mathbf{C}}^i = \begin{bmatrix} \mathbf{0} & \mathbf{I} & \mathbf{0} \\ \mathbf{C}_{ov}^i & \mathbf{C}_{od}^i & \mathbf{C}_{oo}^i \end{bmatrix} \tag{2.4}$$

The partition subscripts indicate velocity outputs (v), displacement outputs (d) and other states (o), all in accordance with (2.3). The next stage in order to couple the models together, equilibrium and compatibility conditions has to be taken in to account at the coupling DOFs. For response and excitation of two subsystems that are co-oriented and numbered in the same order we can write the relation between the response and the excitation quantities between the uncoupled subsystem models and the synthesized models as

$$\left\{ \begin{array}{c} \mathbf{y}_c^I \\ \mathbf{y}_c^{II} \end{array} \right\} = \begin{bmatrix} \mathbf{I} \\ \mathbf{I} \end{bmatrix} \bar{\mathbf{y}}_c \quad \bar{\mathbf{u}}_c = [\mathbf{I} \quad \mathbf{I}] \left\{ \begin{array}{c} \mathbf{u}_c^I \\ \mathbf{u}_c^{II} \end{array} \right\} \tag{2.5}$$

and from here on considering coupling responses only in displacement, $\mathbf{y}_c^i$ for simplicity. We can now write the state-space realization on coupled form using (2.4) and (2.5), which is defined as

$$\left\{ \begin{array}{c} \ddot{\bar{\mathbf{y}}}_c \\ \dot{\bar{\mathbf{y}}}_c \\ \dot{\mathbf{x}}_o \end{array} \right\} = \begin{bmatrix} \mathbf{A}_{vv}^i & \mathbf{A}_{vd}^i & \mathbf{A}_{vo}^i \\ \mathbf{I} & \mathbf{0} & \mathbf{0} \\ \mathbf{0} & \mathbf{A}_{od}^i & \mathbf{A}_{oo}^i \end{bmatrix} \left\{ \begin{array}{c} \dot{\bar{\mathbf{y}}}_c \\ \bar{\mathbf{y}}_c \\ \mathbf{x}_o \end{array} \right\} + \begin{bmatrix} \mathbf{B}_{vv}^i & \mathbf{B}_{vo}^i \\ \mathbf{0} & \mathbf{0} \\ \mathbf{0} & \mathbf{B}_{oo}^i \end{bmatrix} \left\{ \begin{array}{c} \bar{\mathbf{u}}_c \\ \mathbf{u}_o \end{array} \right\} \tag{2.6a}$$

$$\left\{ \begin{array}{c} \bar{\mathbf{y}}_c \\ \mathbf{y}_o \end{array} \right\} = \begin{bmatrix} \mathbf{0} & \mathbf{I} & \mathbf{0} \\ \mathbf{C}_{ov}^i & \mathbf{C}_{od}^i & \mathbf{C}_{oo}^i \end{bmatrix} \left\{ \begin{array}{c} \dot{\bar{\mathbf{y}}}_c \\ \bar{\mathbf{y}}_c \\ \mathbf{x}_o \end{array} \right\} \tag{2.6b}$$

The advantage of using first-order state-space models in lieu to a second-order modal model is that the state-space model has lesser restriction which enables this model to better reproduce the measured data. However, some physical properties, introduced as constraints in the system identification phase, have been found to enhance the first-order state-space model, [5]. To enforce these kinematic and equilibrium constraints we first need to transform the two subcomponents, subsystem I and subsystem II, in to coupling form in accordance with (2.6a) and (2.6b). The first kinematic constraint to enforce is that the interface velocities and displacements should be equal. This is done by considering the first row of equation (2.6a) from which we have that the acceleration output for substructure I, 2.7a and II, 2.7b can be formulated as

$$\ddot{\bar{\mathbf{y}}}_c^I = \mathbf{A}_{vv}^I \dot{\bar{\mathbf{y}}}_c^I + \mathbf{A}_{vd}^I \bar{\mathbf{y}}_c^I + \mathbf{A}_{vo}^I \mathbf{x}_o^I + \mathbf{B}_{vv}^I \bar{\mathbf{u}}_c^I + \mathbf{B}_{vo}^I \mathbf{u}_o^I \tag{2.7a}$$

$$\ddot{\bar{\mathbf{y}}}_c^{II} = \mathbf{A}_{vv}^{II} \dot{\bar{\mathbf{y}}}_c^{II} + \mathbf{A}_{vd}^{II} \bar{\mathbf{y}}_c^{II} + \mathbf{A}_{vo}^{II} \mathbf{x}_o^{II} + \mathbf{B}_{vv}^{II} \bar{\mathbf{u}}_c^{II} + \mathbf{B}_{vo}^{II} \mathbf{u}_o^{II} \tag{2.7b}$$

and to fulfill the stated kinematic constraints it follows that the velocity output at the coupling DOFs, 2.8a, satisfies

$$\dot{\bar{\mathbf{y}}}_c^I = \dot{\bar{\mathbf{y}}}_c^{II} \overset{def}{=} \dot{\bar{\mathbf{y}}}_c \tag{2.8a}$$

and the displacement output at the coupling DOFs 2.8b, satisfies

$$\bar{\mathbf{y}}_c^I = \bar{\mathbf{y}}_c^{II} \overset{def}{=} \bar{\mathbf{y}}_c \tag{2.8b}$$

and the equilibrium conditions are met for substructure I, 2.9a and II, 2.9b respectively

$$\bar{\mathbf{u}}_c^I = \bar{\mathbf{u}}_c^{I,II} + \bar{\mathbf{u}}_{c,e}^I \tag{2.9a}$$

$$\bar{\mathbf{u}}_c^{II} = -\bar{\mathbf{u}}_c^{I,II} + \bar{\mathbf{u}}_{c,e}^{II} \tag{2.9b}$$

Where $\bar{\mathbf{u}}_c^{I,II}$ denotes the cross-sectional force between the two subsystems and $\bar{\mathbf{u}}_{c,e}$ denotes the externally applied force to the interface DOFs. By introducing (2.8a,b) and (2.9a,b) into (2.7a,b) we get

$$\ddot{\bar{\mathbf{y}}}_c = \mathbf{A}_{vv}^I \dot{\bar{\mathbf{y}}}_c + \mathbf{A}_{vd}^I \bar{\mathbf{y}}_c + \mathbf{A}_{vo}^I \mathbf{x}_o^I + \mathbf{B}_{vv}^I \bar{\mathbf{u}}_c^{I,II} + \mathbf{B}_{vv}^I \bar{\mathbf{u}}_{c,e}^I + \mathbf{B}_{vo}^I \mathbf{u}_o^I \tag{2.10a}$$

$$\ddot{\bar{\mathbf{y}}}_c = \mathbf{A}_{vv}^{II} \dot{\bar{\mathbf{y}}}_c + \mathbf{A}_{vd}^{II} \bar{\mathbf{y}}_c + \mathbf{A}_{vo}^{II} \mathbf{x}_o^{II} - \mathbf{B}_{vv}^{II} \bar{\mathbf{u}}_c^{I,II} + \mathbf{B}_{vv}^{II} \bar{\mathbf{u}}_{c,e}^{II} + \mathbf{B}_{vo}^{II} \mathbf{u}_o^{II} \tag{2.10b}$$

The mass inertial of the interface DOFs correspond to the inverse of $\mathbf{B}_{vv}^I$ and $\mathbf{B}_{vv}^{II}$. To introduce these kinematic constraints the first step is to multiply (2.10a) with $\left(\mathbf{B}_{vv}^I\right)^{-1}$ from the left and (2.10b) with $\left(\mathbf{B}_{vv}^{II}\right)^{-1}$ also from the left and add them together.

$$\begin{aligned}
\left(\left(\mathbf{B}_{vv}^I\right)^{-1} + \left(\mathbf{B}_{vv}^{II}\right)^{-1}\right)\ddot{\bar{\mathbf{y}}}_c = {}& \left(\left(\mathbf{B}_{vv}^I\right)^{-1}\mathbf{A}_{vv}^I + \left(\mathbf{B}_{vv}^{II}\right)^{-1}\mathbf{A}_{vv}^{II}\right)\dot{\bar{\mathbf{y}}}_c \\
& + \left(\left(\mathbf{B}_{vv}^I\right)^{-1}\mathbf{A}_{vd}^I + \left(\mathbf{B}_{vv}^{II}\right)^{-1}\mathbf{A}_{vd}^{II}\right)\bar{\mathbf{y}}_c \\
& + \left(\mathbf{B}_{vv}^I\right)^{-1}\mathbf{A}_{vo}^I\mathbf{x}_o^I + \left(\mathbf{B}_{vv}^{II}\right)^{-1}\mathbf{A}_{vo}^{II}\mathbf{x}_o^{II} + \bar{\mathbf{u}}_c \\
& + \left(\mathbf{B}_{vv}^I\right)^{-1}\mathbf{B}_{vo}^{II}\mathbf{u}_o^{II} + \left(\mathbf{B}_{vv}^{II}\right)^{-1}\mathbf{B}_{vo}^{II}\mathbf{u}_o^{II}
\end{aligned} \tag{2.11}$$

were $\bar{\mathbf{u}}_c$ is the total external load applied to assembled components interface DOFs and is defined as

$$\bar{\mathbf{u}}_c \overset{def}{=} \bar{\mathbf{u}}_c^I + \bar{\mathbf{u}}_c^{II} = \bar{\mathbf{u}}_c^{I,II} + \bar{\mathbf{u}}_{c,e}^I - \bar{\mathbf{u}}_c^{I,II} + \bar{\mathbf{u}}_{c,e}^{II} = \bar{\mathbf{u}}_{c,e}^I + \bar{\mathbf{u}}_{c,e}^{II} \tag{2.12}$$

rearranging (2.11) slightly we can write it in the following structure

$$\ddot{\bar{\mathbf{y}}}_c = \bar{\mathbf{A}}_{vv}\dot{\bar{\mathbf{y}}}_c + \bar{\mathbf{A}}_{vd}\bar{\mathbf{y}}_c + \bar{\mathbf{A}}_{vo}^I\mathbf{x}_o^I + \bar{\mathbf{A}}_{vo}^{II}\mathbf{x}_o^{II} + \bar{\mathbf{B}}_{vv}\bar{\mathbf{u}}_c^{II} + \mathbf{B}_{vo}^I\bar{\mathbf{u}}_o^I + \mathbf{B}_{vo}^{II}\bar{\mathbf{u}}_o^{II} \tag{2.13}$$

where

$$\bar{\mathbf{A}}_{vv} = \mathbf{B}_{vv}^{II}\left(\mathbf{B}_{vv}^I + \mathbf{B}_{vv}^{II}\right)^{-1}\mathbf{A}_{vv}^I + \mathbf{B}_{vv}^I\left(\mathbf{B}_{vv}^I + \mathbf{B}_{vv}^{II}\right)^{-1}\mathbf{A}_{vv}^{II} \tag{2.14}$$

$$\bar{\mathbf{A}}_{vd} = \mathbf{B}_{vv}^{II}\left(\mathbf{B}_{vv}^I + \mathbf{B}_{vv}^{II}\right)^{-1}\mathbf{A}_{vd}^I + \mathbf{B}_{vv}^I\left(\mathbf{B}_{vv}^I + \mathbf{B}_{vv}^{II}\right)^{-1}\mathbf{A}_{vd}^{II} \tag{2.15}$$

$$\bar{\mathbf{A}}_{vo}^I = \mathbf{B}_{vv}^{II}\left(\mathbf{B}_{vv}^I + \mathbf{B}_{vv}^{II}\right)^{-1}\mathbf{A}_{vo}^I \tag{2.16}$$

$$\bar{\mathbf{A}}_{vo}^{II} = \mathbf{B}_{vv}^I\left(\mathbf{B}_{vv}^I + \mathbf{B}_{vv}^{II}\right)^{-1}\mathbf{A}_{vo}^{II} \tag{2.17}$$

$$\bar{\mathbf{B}}_{vv} = \mathbf{B}_{vv}^I\left(\mathbf{B}_{vv}^I + \mathbf{B}_{vv}^{II}\right)^{-1}\mathbf{B}_{vv}^{II} \tag{2.18}$$

$$\bar{\mathbf{B}}_{vo}^{I} = \mathbf{B}_{vv}^{II} \left(\mathbf{B}_{vv}^{I} + \mathbf{B}_{vv}^{II} \right)^{-1} \mathbf{B}_{vv}^{I} \tag{2.19}$$

$$\bar{\mathbf{B}}_{vo}^{II} = \mathbf{B}_{vv}^{I} \left(\mathbf{B}_{vv}^{I} + \mathbf{B}_{vv}^{II} \right)^{-1} \mathbf{B}_{vv}^{II} \tag{2.20}$$

the assembled systems on state-space form can now be written as

$$
\begin{Bmatrix} \ddot{\bar{\mathbf{y}}}_c \\ \dot{\bar{\mathbf{y}}}_c \\ \dot{\mathbf{x}}_o^I \\ \dot{\mathbf{x}}_o^{II} \end{Bmatrix} =
\begin{bmatrix} \bar{\mathbf{A}}_{vv} & \bar{\mathbf{A}}_{vd} & \bar{\mathbf{A}}_{vo}^I & \bar{\mathbf{A}}_{vo}^{II} \\ \mathbf{I} & 0 & 0 & 0 \\ 0 & \mathbf{A}_{od}^I & \mathbf{A}_{oo}^I & 0 \\ 0 & \mathbf{A}_{od}^{II} & 0 & \mathbf{A}_{oo}^{II} \end{bmatrix}
\begin{Bmatrix} \dot{\bar{\mathbf{y}}}_c \\ \bar{\mathbf{y}}_c \\ \mathbf{x}_o^I \\ \mathbf{x}_o^{II} \end{Bmatrix} +
\begin{bmatrix} \bar{\mathbf{B}}_{vv} & \bar{\mathbf{B}}_{vo}^I & \bar{\mathbf{B}}_{vo}^{II} \\ 0 & 0 & 0 \\ 0 & \bar{\mathbf{B}}_{oo}^I & 0 \\ 0 & 0 & \bar{\mathbf{B}}_{oo}^{II} \end{bmatrix}
\begin{Bmatrix} \bar{\mathbf{u}}_c \\ \bar{\mathbf{u}}_o^I \\ \bar{\mathbf{u}}_o^{II} \end{Bmatrix} \tag{2.21}
$$

$$
\begin{Bmatrix} \bar{\mathbf{y}}_c \\ \mathbf{y}_o^I \\ \mathbf{y}_o^{II} \end{Bmatrix} =
\begin{bmatrix} 0 & \mathbf{I} & 0 & 0 \\ \mathbf{C}_{ov}^I & \mathbf{C}_{od}^I & \mathbf{C}_{oo}^I & 0 \\ \mathbf{C}_{ov}^{II} & \mathbf{C}_{od}^{II} & 0 & \mathbf{C}_{oo}^{II} \end{bmatrix}
\begin{Bmatrix} \dot{\bar{\mathbf{y}}}_c \\ \bar{\mathbf{y}}_c \\ \mathbf{x}_o^I \\ \mathbf{x}_o^{II} \end{Bmatrix} \tag{2.22}
$$

For the system studied in this paper which is a non-gyroscopic, non-circulatory and passive mechanical system it is expected that Betti's reciprocity principle should apply. To ensure reciprocity the condition $\mathbf{C}^i \mathbf{B}^i = \mathbf{0}$ has been enforced, in order for the system to be self-adjoint. The state-space models used have also been forced to be stable and passive, see [5].

2.3 System Setup

The purpose of the investigation is to investigate the causal effects different factors have on the tool tip FRF which is the foundation for the stability lobe chart. This approach requires a system which is free from errors, such as noise and model order uncertainties. The system chosen for this investigation is a simplified FE-model of a test rig used in [4], see Fig. 2.2.

The FE-model of the test rig consists of two substructures, Fig. 2.3. The spring suspended metal block with the clamping unit along with the coupling and the tool family generic part of the cutting tool, referred to as the blank, constitutes subsystem I. The tool tip, with a geometry that may vary within the tool family, is considered to be substructure II. Figure 2.4 shows the DOF numbering of the interface. In this study we are particularly interested in motion in the y- and z-directions, DOFs 2 and 3.

Before proceeding with sensitivity analysis we made a validation of the coupling technique. As a reference we obtained frequency response functions of the total system coupled to an entity by ordinary FEM assembly procedures. We see one example in Fig. 2.5. To mimic the system identification procedures for test data we made a system identification of FRFs given by FEM analysis of substructure I. In the frequency range from 0 to 5 kHz it was found that 30 states were sufficient to capture data. In the FE representation 0.5% damping was introduced to all modes.
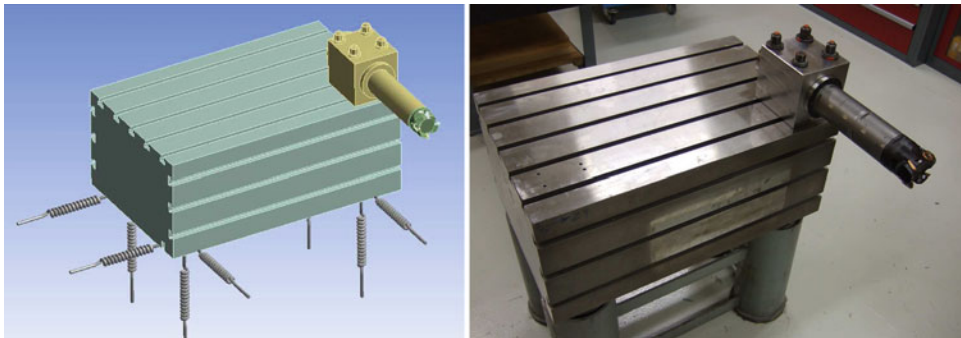
Fig. 2.2 Left; FE-model of test rig. Right; real test rig
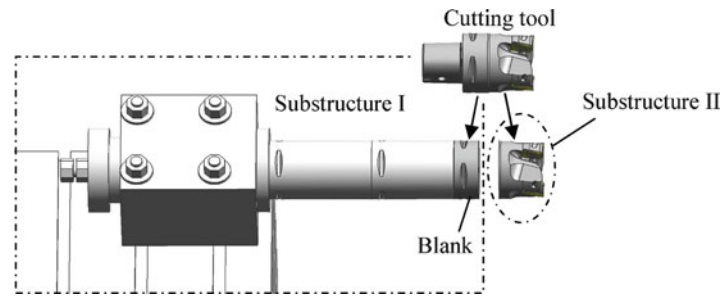
Fig. 2.3 Substructures I and II
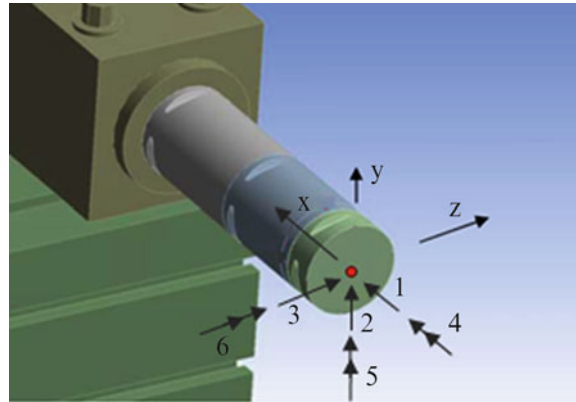
Fig. 2.4 Reference coordinate system and degree of freedom notations
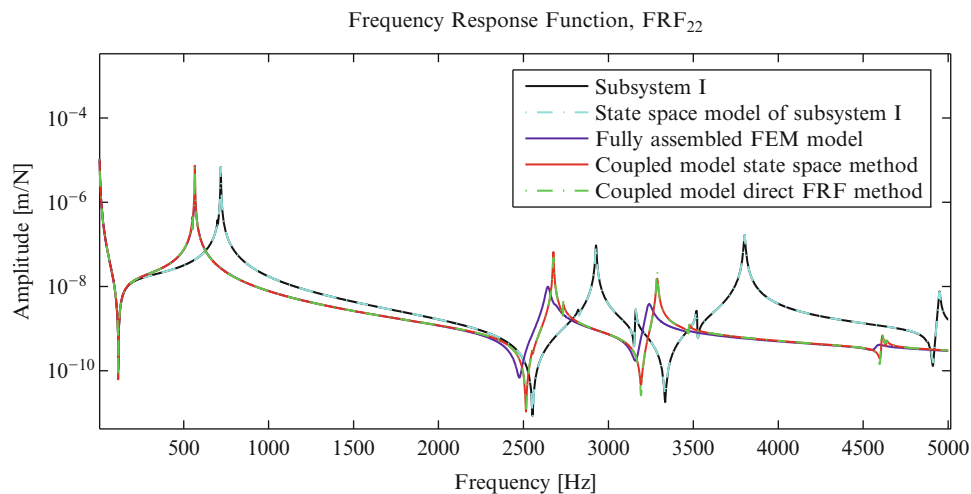
Fig. 2.5 Frequency response function comparison between uncoupled subsystem I and the state space identification of subsystem I as well as the fully assembled FEM model and the assembled substructures using state space and direct FRF coupling technique of the y-direction direct FRF, the FRF_{22}

2.3.1 Results of Validation and Substructuring Method

The result of the state-space coupling of the identified model can be seen in Fig. 2.5. It is seen that it compares favorable to the FEM results and validates the coupling technique. Figure 2.5 also shows the FRF of Subsystem I from FEM and system identification can be seen to match very well. Figure 2.5 also contains and an additional comparison using a direct FRF

coupling method, [6], of the two substructures using generalized frequency domain substructure synthesis. The coupled FRFs using this method match the re-estimated assembled parallel model perfectly which is a good indication that the state space coupling routines works properly. It can be seen in Fig. 2.5 that the FRFs of these three systems matches the fully assembled FEM model very well up and over the first bending mode which is at about 500 Hz. The slight deviation at higher frequencies Is due to model truncation in the synthesis of FRFs of component I.

2.4 Sensitivity Analysis and Evaluation Method

With a reliable identification process in place the next step is the sensitivity analysis based on perturbation of the state space model from modal data and model estimation of that system.

2.4.1 *Problem Formulation*

The evaluation is limited to investigate the factors governing the accuracy of the predicted spindle speed and depth of cut and *quantify* the impact they have on the predicted stability lobes. A criterion function based on the stability lobe chart is required. The sensitivity analysis is performed through a screening process where each parameter can vary within a certain interval. Each test combination resulted in a perturbed FRF from which a stability lobe chart were obtained. The lobes from the perturbed test were evaluated against a stability lobe chart based on the solution of the unperturbed coupled state space model presented in Fig. 2.5 system based on two criteria.

A first criterion is an evaluation of the angle between stability lobe data vectors of the nominal and perturbed systems. These data vectors are stability lobe functions at discrete spindle speeds. The good thing about this approach is that amplitude of the vectors is disregarded. The angle ranges between 0 and $\pi/2$ were 0 means that the two data vectors are completely parallel and an angle of $\pi/2$ means that the two data vectors are orthogonal. In this evaluation the angle is normalized by taking cosine of the angle resulting in a number ranging from 0 to 1 were 1 means that the two data vectors are perfectly parallel and in that sense equal and 0 means completely orthogonal which is not desirable. We call this normalized angle the co-linearity index

A second evaluation criterion is the minimum axial depth of cut, a_p^{lim}, were the cutting process is stable for all spindle speeds, see Fig. 2.6. This criterion was selected since this depth of cut is the local minimum value of all lobes. This is not the case with the stability peaks which grows with higher spindle speeds. The minimum depth of cut is also the parameter that is especially important when machining at low spindle speeds.

2.4.2 *Screening*

A traditional screening set up, see [16], is an essential first step of the objective evaluation method that will be used to answer the question of which factors has the largest impact on the criterion function and if there are any interaction between these factors. The aim is to assign all factors the same possibility to influence the criteria and then, if possible, reduce the number
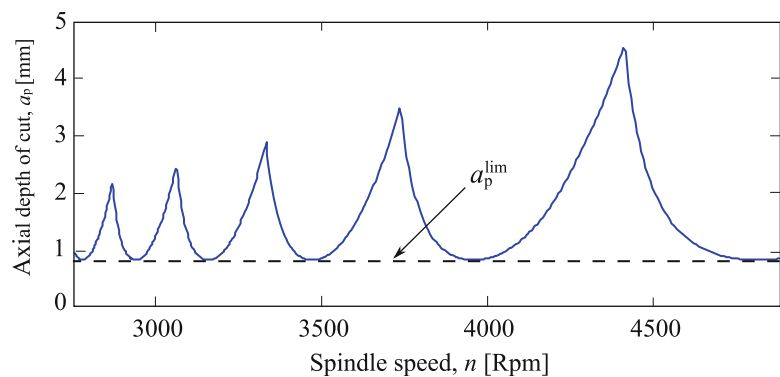
Fig. 2.6 Description of minimum axial depth of cut, a_p^{lim}

Table 2.1 Factors subjected to perturbation in identification of subsystem I

Test nr.	Factor	Change
N1	Number of states that describe first bending mode	Add 2
N2	Number of states that describe first bending mode	Subtract 2
N3	Damping estimation of first bending mode	Add 20%
N4	Damping estimation of first bending mode	Subtract 20%
N5	FRF level	Add 10%
N6	FRF level	Subtract 10%
N7	Cut off frequency for system identification	2 kHz instead of 5 kHz

factors for further investigations. Some of the factors subjected to investigation in this paper have been found to have a strong nonlinear behavior within their range of variation. This makes them unsuitable for the coupled analysis, proposed in [16], which would make it hard to determine their separate impact on the coupled system. A much simpler approach was taken regarding the sensitivity analysis based on the insight that the attempt to investigate the full design space was much to complicate. The approach was instead of changing many parameters all at once to simply change one parameter at the time and keep all others at their reference values. The screening procedure starts with listing, categorizing and determine a relevant range that each factor can vary within. Table 2.1 presents the factors chosen to be investigated in this investigation along with their category and variation span. The screening procedure has multiple objectives. The first is to get an insight of which factors have most influence on the result of the coupled model. If a factor is found to have no influence on the criteria then that result is also useful information. The exclusion of a factor can be proven to be very beneficial from a time or economical perspective. The screening also ranks each factor and therefore gives an indication of which of the factors to put additional focus on.

The chosen factors all contribute differently to the identified models. The number of states included in the state-space model is an interesting parameter to investigate. Previous tests conducted in [17] showed that too few states could influence the coupled systems of but no investigation of the impact of too many states was made. Damping is another parameter of interest since it can normally not be precisely determined from measurements. To see how much amplitude error influences the coupled system is also of interest. This parameter can be influenced from ill calibrated accelerometers, errors in force input measurements and test setup errors. The cut-off frequency will determine how many modes that are taken into account by the state-space substructures and this should influence the coupled system.

2.5 Results

The stability lobe chart is constructed from the real part of FRF_{22} and FRF_{33}, the FRFs associated to transversal motion. Both these directions are important for the final evaluation of the stability lobe chart. The results of a comparison between the real part of the FRF_{22} of the reference and the perturbed systems show how the different parameter influences the location of the bending eigenfrequency and the amplitude of the FRF_{22}, see Fig. 2.7.

Stability lobes for comparison were constructed based on the results of the perturbed FRFs for evaluation. The ingoing cutting parameters used to obtain the stability lobe charts presented in tabled in Table 2.2.

Figure 2.8 shows how the different parameter settings affect the stability lobe chart. It should be noted that the perturbed system with a reduced number of states is not seen in the chosen plot interval. The amplitude of the stability lobes for this setting is much too high to be included in the plot. The drastic impact of this setting is seen in Fig. 2.7.

The plotted stability lobe chart comparison gives a good indication of the influence of different perturbations to the system but it makes it hard to quantify its meaning. The results of the comparisons of the angle between stability lobe data vectors and the minimum value of the depth of cut for each perturbed system compared to the reference system makes it easier to interpret the results. Such results are presented in Table 2.3.

From the results in Table 2.3 it can be seen that the factor with the smallest impact on the system is the one were two additional states has been introduced to add a resonance frequency close to that of the first bending mode. This factor has a very small influence on the angle between the real FRF vectors and almost no influence on the minimum amplitude value compared to the reference. The perturbed system were the state order had been underestimated by neglecting a bending mode showed a significant impact on both evaluation criterions. The damping perturbation proved to have a very small influence on the subspace angle criterion and minimum amplitude seemed to be proportional to the magnitude of the
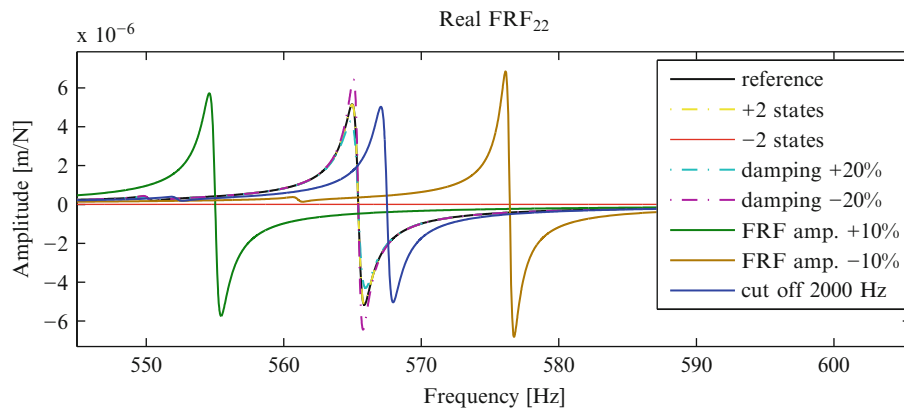
Fig. 2.7 Real part of FRF$_{22}$ of unperturbed (reference) and the perturbed systems

Table 2.2 Cutting parameters used in stability lobe predictions

Cutting parameters	Quantity	Unit
Number of teeth, z	1	–
Tool diameter, D_c	80	[mm]
Radial width of cut, a_e	80	[mm]
Cutting force coefficient in tangential direction, K_t	1319	[MPa]
Cutting force coefficient in radial direction, K_r	789	[MPa]
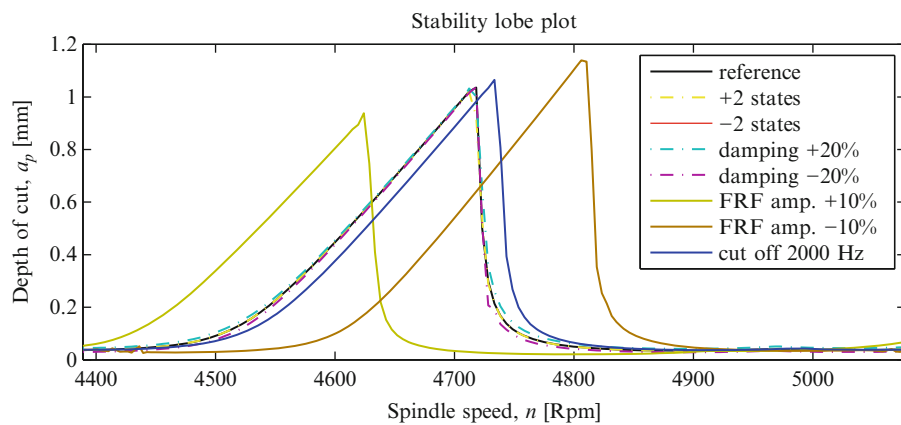
Fig. 2.8 Stability lobe comparisons between unperturbed (reference) and the perturbed systems

Table 2.3 Comparison between the influences of the different perturbation factors minimum axial depth of cut and co-linearity index relative to that of reference configuration

Test nr.	Type of perturbation	Co-linearity index	Minimum axial depth of cut
N1	Number of states +2	0.985	0.99
N2	Number of states −2	0.410	1335.33
N3	Damping estimation of first bending mode +20%	0.975	1.21
N4	Damping estimation of first bending mode −20%	0.976	0.83
N5	FRF amplitude +10%	0.484	0.60
N6	FRF amplitude −10%	0.427	0.81
N7	Cut-off frequency	0.825	1.06

damping. A factor that influenced the coupled system much was the FRF amplitude. The system that had its amplitude increased by 10% underestimated the eigenfrequency with 12 Hz and overestimated the eigenfrequency with 12 Hz with a similar underestimation for an amplitude decrees. Both these errors then propagated to the stability lobe chart resulting in an optimum spindle speed error of 90 rpm. The lowered cut-off frequency perturbation was the fourth least influential perturbation when it comes to the subspace angle criterion. The lowered cut-off frequency also had a small minimum amplitude error.

2.6 Conclusions

The methodology and workflow used to conduct these analyses make up a good foundation for designing the measurement set up. The approach with the two evaluation criteria based on subspace angle and minimum amplitude, makes the evaluation of the perturbed systems much clearer and the two evaluation criteria makes good indications on the comparison to the reference system. This method allows several factors to be evaluated against each other even though they can play a very different role in the identification process. Regarding the results the sensitivity analysis definitely distinguishes the important from the less important parameters. The parameter that influenced the coupled system the most was an error in the estimation of the FRF amplitude. Such significant impact points towards that great care must be taken during the measurement procedure. Accelerometer imprecision of 5% is not uncommon for accelerometers used in these types of measurements. Large accelerometer errors can be expected from temperature transients, calibration errors, linearity errors, frequency and phase response errors, aging errors, cable motion, and electromagnetic interference in cables. Load cell errors affect the FRF estimation similarly. It is seen that the number of states may be very important. This is much in line with the conclusions drawn in [17]. It seems that an excessive state order not necessarily causes bad coupling results as long as the identified modes fit is also shown in the stability chart. The damping perturbation seems to practically only influence the amplitude error in the stability chart. This is good from an application standpoint were the accurate spindle speed is considered much more important than the amplitude of the stability chart. To find the stability limit is fairly easy compared to finding the optimum spindle speed. Regarding the cut-off frequency it is shown that it influences the coupled model but it should not have a large impact as long as no states are disregarded.

References

1. Altintas Y (2000) Manufacturing automation: metal cutting mechanics, machine tool vibrations and CNC design. Cambridge University Press, Cambridge
2. Tlustly J, Polacek M (1963) The Stability of machine tools against self excited vibrations in machining. Int Res Prod Eng ASME 1:465–474
3. Tobias SA (1965) Machine tool vibrations. Blackie and Sons, Glasgow
4. Liljerehn A, Johansson A, Abrahamsson T (2010) Dynamic substructuring in metal cutting machine chatter. In: Proceedings of ISMA2010 international conference on noise and vibration engineering including USD2010, Leuven, 20–22 Sept 2010, ISBN/ISSN: 9789073802872
5. Sjövall P, Abrahamsson T (2007) Component system identification and state-space model synthesis. Mech Syst Signal Process 21(7):2697–2714
6. Jetmundsen B, Bielawa RL, Flanelly G (1988) Generalized frequency domain substructure synthesis. J Am Helicopter Soc 33:55–64
7. Park S, Altintas Y, Movahhedy M (2003) Receptance coupling for end mills. Int J Mach Tools Manu 43:889–896
8. Gordis JH, Bielawa RL, Flannelly WG (1998) A general theory for frequency domain structural synthesis. J Sound Vib 150(1):139–158
9. Liu W, Ewins DJ (2002) Substructure synthesis via elastic media. J Sound Vib 257(2):361–379
10. Lim TC, Li J (2000) A theoretical and computational study of the FRF-based Substructuring technique applying enhanced least square and TSVD approaches. J Sound Vib 231(4):1135–1157
11. Ren Y, Beards CF (1995) On substructure synthesis with FRF data. J Sound Vib 185(5):845–866
12. Craig RR, Bampton MCC (1968) Coupling of substructures for dynamic analysis. AIAA J 6(7):1313–1319
13. Rixen DJ (2004) A dual craig-bampton method for dynamic substructuring. J Comput Appl Math 168:383–391
14. Jen CW, Johanson DA, Dubois F (1995) Numerical modal analysis of structures based on a revised substructure synthesis approach. J Sound Vib 180(2):185–203
15. Balmès E (1996) Use of generalized interface degrees of freedom in component mode synthesis. In: Proceedings of 14th international modal analysis conference, Dearborn
16. Eriksson L, Johansson E, Kettaneh-Wold N, Wikström C, Wold S (2008) Design of experiments: principles and applications. MKS Umetrics AB, Umea 2008
17. Sjövall P, McKelvey T, Abrahamsson T (2006) Constrained state-space system identification with application to structural dynamics. Automatica 42:1539–1546

Chapter 3
Eliminating Indefinite Mass Matrices with the Transmission Simulator Method of Substructuring*

Randy L. Mayes, Mathew S. Allen, and Daniel C. Kammer

Abstract The transmission simulator method of experimental dynamic substructuring captures the interface forces and motions through a fixture called a transmission simulator. The transmission simulator method avoids the need to measure connection point rotations and enriches the modal basis of the substructure model. The free modes of the experimental substructure mounted to the transmission simulator are measured. The finite element model of the transmission simulator is used to couple the experimental substructure to another substructure and to subtract the transmission simulator. However, in several cases the process of subtracting the transmission simulator has introduced an indefinite mass matrix for the experimental substructure. The authors previously developed metrics that could be used to identify which modes of the experimental model led to the indefinite mass matrix. A method is developed that utilizes those metrics with a sensitivity analysis to adjust the transmission simulator mass matrix so that the subtraction does not produce an indefinite mass matrix. A second method produces a positive definite mass matrix by adding a small amount of mass to the indefinite mass matrix. Both analytical and experimental examples are described.

3.1 Introduction

Experimental-analytical substructuring has been a topic of interest since modal testing was first introduced several decades ago. It is appealing because it has the potential to allow one to replace complicated subcomponents with experimental models that may be much less expensive to derive. It also allows the experimentalist to re-use the experimental model, predicting its response in a multitude of other configurations without repeating the test. One can also think of structural modification [1] as a special case of substructuring, where the modification is a special substructure that one wishes to determine in order to produce a desired response, (although the terms "substructuring" and "structural modification" are often used interchangeably [2]).

The authors recently presented a new substructuring methodology, called Modal Constraints for Fixture and Subsystem (MCFS), that has proven quite effective at subtracting one structure from another [3]. Typically one has experimentally measured the modes of a built-up structure and one wishes to remove one subcomponent from that assembly. The subtraction is accomplished by creating a model of the subcomponent that is to be removed, making its mass, stiffness, and damping negative and then coupling the negative subcomponent to the assembly. Whereas, in conventional substructuring one enforces constraints between the points where the substructures are joined, the MCFS method estimates a set of modal

R.L. Mayes (✉)
Experimental Structural Dynamics, Sandia National Laboratories, Albuquerque, NM, USA
e-mail: rlmayes@sandia.gov

M.S. Allen • D.C. Kammer
Department of Engineering Physics, University of Wisconsin, Madison, WI 53706, USA
e-mail: msallen@engr.wisc.edu; kammer@engr.wisc.edu

coordinates on the substructure and enforces constraints on those coordinates. This reduces the sensitivity of the method to experimental errors and assures that an appropriate number of constraints is enforced.

The MCFS method is primarily used to estimate a modal model that can be used for substructuring predictions. The substructure is connected to a fixture or transmission simulator [4] and the assembly is tested in free-free conditions. This is equivalent to the well-known method where rigid masses are attached to the structure and used to create a mass-loaded interface, except that the proposed methodology is valid even if the transmission simulator is flexible. The transmission simulator serves to mass-load the interface of the subcomponent, enriching the modal basis and circumventing the need to measure displacements and rotations at the connection point. A model of the transmission simulator is then created and used to subtract its effects from the measured modal model in order to obtain a model for the substructure of interest in isolation, but with an improved modal basis. However, because a system with negative mass has been introduced in order to remove the transmission simulator, the substructure model may not necessarily have a positive definite mass matrix. Similar problems were encountered by other researchers when removing rigid masses from a structure [5]. This paper presents two methods that can be used to assure that the mass matrix of the subcomponent has positive mass.

3.2 Theory

3.2.1 Review of Subtraction of Modal Substructures

Suppose that the natural frequencies, ω_r, damping ratios, ζ_r, and matrix of mass-normalized mode shapes, $\mathbf{\Phi}_C$, of an assembly consisting of the subcomponent of interest and the transmission simulator have been measured. The modal parameters of the transmission simulator are also known. (Here we shall refer to the substructure that is being removed as the transmission simulator, but in a general problem it could be any subcomponent that one wishes to subtract from the assembly). The assembly shall be referred to as system C and the transmission simulator as system A, as in [3], so the uncoupling procedure estimates the modes of B, the component of interest, since $C - A = (A + B) - A = B$. First the equations of motion of C and (-A) are concatenated as follows

$$\begin{bmatrix} \mathbf{I}_C & 0 \\ 0 & -\mathbf{I}_A \end{bmatrix} \left\{ \begin{matrix} \ddot{\mathbf{q}}_C \\ \ddot{\mathbf{q}}_A \end{matrix} \right\} + \begin{bmatrix} [\backslash 2\zeta_r\omega_r\backslash]_C & 0 \\ 0 & -[\backslash 2\zeta_r\omega_r\backslash]_A \end{bmatrix} \left\{ \begin{matrix} \dot{\mathbf{q}}_C \\ \dot{\mathbf{q}}_A \end{matrix} \right\} + \begin{bmatrix} [\backslash \omega_r^2\backslash]_C & 0 \\ 0 & -[\backslash \omega_r^2\backslash]_A \end{bmatrix} \left\{ \begin{matrix} \mathbf{q}_C \\ \mathbf{q}_A \end{matrix} \right\} = \left\{ \begin{matrix} \mathbf{\Phi}_C^T\mathbf{F}_C \\ \mathbf{\Phi}_A^T\mathbf{F}_A \end{matrix} \right\}$$

$$\left\{ \begin{matrix} \mathbf{y}_C \\ \mathbf{y}_A \end{matrix} \right\} = \begin{bmatrix} \mathbf{\Phi}_C & 0 \\ 0 & \mathbf{\Phi}_A \end{bmatrix} \left\{ \begin{matrix} \mathbf{q}_C \\ \mathbf{q}_A \end{matrix} \right\}$$

(3.1)

where the q dof are the generalized modal coordinates of each substructure, and then constraints are enforced as

$$\begin{bmatrix} \mathbf{\Phi}_{A,m}^\dagger \mathbf{\Phi}_{C,m} - \mathbf{I}_A \end{bmatrix} \left\{ \begin{matrix} \mathbf{q}_C \\ \mathbf{q}_A \end{matrix} \right\} = 0$$

(3.2)

Where the superscript, $\dagger$, denotes the pseudo-inverse of the matrix, and subscript m represents degrees of freedom common to both system C and system A that have been measured.

This is done by finding a matrix $\mathbf{B}$ that transforms the concatenated coordinates into a set of unconstrained coordinates. The coordinates of C are typically a suitable set [6], so one can choose

$$\left\{ \begin{matrix} \mathbf{q}_C \\ \mathbf{q}_A \end{matrix} \right\} = \mathbf{B}\mathbf{q}_C$$

$$\mathbf{B} = \begin{bmatrix} \mathbf{I}_C \\ \boldsymbol{\tau} \end{bmatrix}$$

(3.3)

where $\boldsymbol{\tau} = \mathbf{\Phi}_{A,m}^\dagger \mathbf{\Phi}_{C,m}$. The number of modal coordinates in A and C are denoted N_A and N_C respectively. One can verify that $\mathbf{B}$ is in the null space of the matrix on the left in (3.2), so these coordinates always satisfy the constraints. As discussed in [3], if the model for the transmission simulator is accurate then the negative transmission simulator model completely

cancels the forces that the transmission simulator would exert on system B. The equations of motion of the system after applying constraints are

$$\mathbf{M}_B \ddot{\mathbf{q}}_c + \mathbf{C}_B \dot{\mathbf{q}}_c + \mathbf{K}_B \mathbf{q}_c = \mathbf{B}^T \left\{ \begin{array}{c} \mathbf{\Phi}_C{}^T \mathbf{F}_C \\ \mathbf{\Phi}_A{}^T \mathbf{F}_A \end{array} \right\}$$

$$\left\{ \begin{array}{c} \mathbf{y}_C \\ \mathbf{y}_A \end{array} \right\} = \left[\begin{array}{cc} \mathbf{\Phi}_C & \mathbf{0} \\ \mathbf{0} & \mathbf{\Phi}_A \end{array} \right] \mathbf{B} \mathbf{q}_c \qquad (3.4)$$

where the mass matrix of the constrained system is

$$\mathbf{M}_B = \mathbf{B}^T \left[\begin{array}{cc} \mathbf{I}_C & 0 \\ 0 & -\mathbf{I}_A \end{array} \right] \mathbf{B} = \mathbf{I}_C - \boldsymbol{\tau}^T \mathbf{I}_A \boldsymbol{\tau} \qquad (3.5)$$

and similarly for the damping and stiffness matrices.

The equation above shows that the eigenvalues of $\mathbf{M}_B$ can become negative if any of the terms that are subtracted are too large. This might be the case, for example if the density value used in the transmission simulator model was higher than the true density. In that case one would simply need to adjust the modal mass of each the transmission simulator modes to alleviate the problem. In practice the situation is more complicated; negative mass is typically encountered due to a mismatch in the modal bases of A and C, causing the modal mass of A to be assigned incorrectly to the modes of C. Two approaches to adjust $\mathbf{M}_B$ to make it positive definite are given in Sect. 3.2.2 and 3.2.3, the modal scale factor method and the added mass method. First the modal scale factor method is discussed.

3.2.2 Modal Scale Factor Method

The matrix $\boldsymbol{\tau}$ is related to an orthogonal projector that projects the motion of C onto the space spanned by the modes of the transmission simulator, A, as explained in [3]. One might be able to create a model for B that has a positive definite mass matrix by decreasing certain values along the diagonal in $\mathbf{I}_A$ (or equivalently, by increasing the mode shape values on some of the modes of the transmission simulator by multiplying by a scale factor). With this approach, revise the name of the transmission simulator mass matrix from $\mathbf{I}_A$ to $\mathbf{M}_A$. $\mathbf{M}_A$ begins as the identity matrix, but individual elements will be reduced as described below. The eigenvalues of the mass matrix, $\mathbf{M}_B$, are found by solving the eigenvalue problem,

$$\mathbf{M}_B \mathbf{\Psi}_k = \lambda_k \mathbf{\Psi}_k \qquad (3.6)$$

There are typically only a few negative eigenvalues $\lambda_k < 0 \quad k = 0...N_{neg}$ and several modal masses, so this can be cast as an under-constrained optimization problem where one seeks values for the modal masses of the transmission simulator, $M_{TS,j}$, in $\mathbf{M}_A = diag[M_{TS,1} \quad ... \quad M_{TS,N_A}]$ that cause all of the eigenvalues of $\mathbf{M}_B$ to be positive. An equivalent approach is to reduce the diagonals of $\mathbf{M}_A$ until all of the eigenvalues of $\boldsymbol{\tau}^T \mathbf{M}_A \boldsymbol{\tau}$ are *less* than one (see (3.5)). A simplified Newton-Raphson algorithm can be devised to accomplish this. First calculate the Jacobian (sensitivity matrix) of the eigenvalues which are greater than one in $\boldsymbol{\tau}^T \mathbf{M}_A \boldsymbol{\tau}$ with respect to each diagonal member of $\mathbf{M}_A$. Let $\mathbf{f}(M_{TS,j}) = [\lambda_k ... \lambda_{N>1}]^T$. A first order Taylor series expansion of this function is

$$\mathbf{f}_{desired}(M_{TS,j}) = \mathbf{f}(M_{TS,j}) + [\nabla \mathbf{f}(M_{TS,j})]_{M_{TS,j}} \Delta M_{TS,j} \qquad (3.7)$$

where $\mathbf{f}_{desired}(M_{TS,j})$ is chosen as a new eigenvalue slightly below one (.9999) for this work. Instead of proceeding in the usual way with the full matrices, one chooses the worst (largest) eigenvalue of $\boldsymbol{\tau}^T \mathbf{M}_A \boldsymbol{\tau}$ and only the mass value of $\mathbf{M}_A$ which is most sensitive to the worst eigenvalue. This reduces the matrices down to scalars, which alleviates some problems if the matrices have high condition numbers. Then one solves for the reduction in a single diagonal member of $\mathbf{M}_A$ as

$$\Delta M_{TS,j} = [\nabla \mathbf{f}(M_{TS,j})]^{-1}{}_{M_{TS,j}} [\mathbf{f}_{desired}(M_{TS,j}) - \mathbf{f}(M_{TS,j})] \qquad (3.8)$$

where there is only one member in the Jacobian and one eigenvalue to change. The eigenvalues are a nonlinear function, so the process is iterative. On each iteration, the mass that is most sensitive to the largest eigenvalue above one is adjusted, until all eigenvalues of $\boldsymbol{\tau}^T \mathbf{M}_A \boldsymbol{\tau}$ are below one. Then $\mathbf{M}_B$ will have no negative eigenvalues.

The modal scale factors found using this approach will be optimum only in the sense that they are the smallest perturbations to the transmission simulator mass matrix that produce a positive definite $\mathbf{M}_B$.

3.2.3 Added Mass Method

The procedure in Sect. 3.2.2 seeks to find a positive definite mass matrix by adjusting the modal scale factors (or the modal mass) of the transmission simulator. An alternative is to simply compute $\mathbf{M}_B$ in (3.5) and then to add mass to the system to cause the negative eigenvalues of the mass matrix to become slightly greater than zero. Physically, this is identical to attaching point masses to the system at various locations, which are governed by equations of motion $\mathbf{m}\ddot{\mathbf{y}}_C = 0$, where $\mathbf{m}$ is a diagonal matrix of point masses. One can use the same procedure described in (3.1) through (3.4) to compute the equations of motion for the system with these additional masses, and the resulting equations are identical to those in (3.4) only with $\mathbf{M}_B$ replaced with $\mathbf{M}_B + \Delta\mathbf{m}$, where $\Delta\mathbf{m} = \boldsymbol{\Phi}_C{}^T \mathbf{m} \boldsymbol{\Phi}_C$.

Typically there are more physical nodes than there are modes, so $\boldsymbol{\Phi}_C$ has more rows than columns and one can determine a pattern for the applied masses that would create an arbitrary increase, $\Delta\mathbf{m}$, in the mass of the system. The smallest change to $\mathbf{M}_B$ will cause the negative eigenvalues to increase to just above zero while leaving the remaining eigenvalues unchanged, and can be obtained by adding the following to each eigenvalue.

$$\Delta\lambda_k = \begin{cases} 0 & \lambda_k > 0 \\ -\lambda_k + \varepsilon & \lambda_k \leq 0 \end{cases} \tag{3.9}$$

One can then find $\Delta\mathbf{m}$ using,

$$\Delta\mathbf{m} = \boldsymbol{\Psi}\hat{\Lambda}\boldsymbol{\Psi}^T \tag{3.10}$$

where $\hat{\Lambda} = diag[\,(\lambda_1 + \Delta\lambda_1) \quad \cdots \quad (\lambda_{Nc} + \Delta\lambda_{Nc})\,]$ and $\boldsymbol{\Psi} = [\,\boldsymbol{\Psi}_k \quad \cdots \quad \boldsymbol{\Psi}_{Nc}\,]$. The eigenvalues of $\mathbf{M}_B + \Delta\mathbf{m}$ will then be the strictly positive values that are on the diagonal of $\hat{\Lambda}$. One would hope that very little mass would need to be added to the structure to make the eigenvalues positive. One can measure the amount of mass added using the ratio of the norms: $n_{\text{rat}} = \frac{\|\Delta\mathbf{m}\|}{\|\mathbf{M}_B\|}$.

3.3 Applications

3.3.1 Analytical T-Beam System

The first system considered is a 12-in. long steel beam with a 0.75 by 1.0 in. cross section. This is the same system that was considered in [6]. A 6.0-in. long transmission simulator with the same cross section is attached to the beam and the modes of the assembly (the C system) are computed; in the usual practice these modes would be found experimentally with a modal test, but here the analytically computed modes are used in order to simulate perfect measurements (Fig. 3.1).
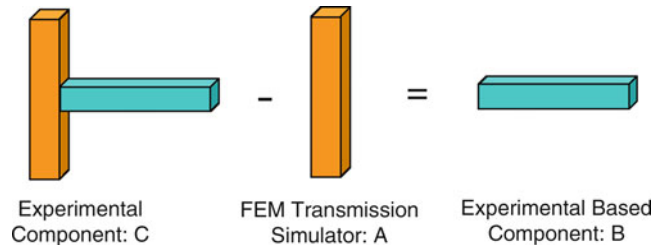

Fig. 3.1 T-Beam System. The substructure of interest is the (*blue*) horizontal beam. It is tested while connected to the (*orange*) vertical beam, or transmission simulator. The proposed procedures will be used to obtain a positive definite mass matrix after removing the transmission simulator (color figure online)

As discussed in [6], it is important to assure that enough modes of the transmission simulator are used to span the space of the motions of C in the frequency band of interest. Using the best practice identified in that work, seven modes are used for the transmission simulator and 15 modes for C, which corresponds to all modes below 20 kHz for C and below 24 kHz for A. The resulting model for B has two negative eigenvalues: $\lambda_1 = -0.00050468$, $\lambda_2 = -2.4058\text{e-}16$, although λ_2 is essentially zero. We desire to make these eigenvalues positive using the methods presented in Sect. 3.2.

3.3.1.1 Mode Scale Factor Method

The mode scale method was applied to this system using the scalar Newton-Raphson algorithm. The Jacobian was used to identify the two modes of the transmission simulator that most strongly influenced the negative eigenvalues, revealing that the first and sixth modes had the largest influence. These were the same modes that were identified by the metrics in [6] as having the largest contribution to the negative eigenvalues. The Newton-Raphson algorithm converged to values of $M_{TS,1} = 0.9984$ and $M_{TS,6} = 0.9999$, which correspond to multiplying the first and sixth mode shapes of the transmission simulator by 1.0008and 1.000050 respectively. The smallest two eigenvalues of $\mathbf{M_B}$ were positive values on the order of 1e-5.

It is important to mention that some difficulty was encountered in selecting a value of $\mathbf{f}_{desired}(M_{TS,j})$ for these calculations. Initially $\mathbf{f}_{desired}(M_{TS,j}) = 0.99$ was used in which case the Newton-Raphson algorithm gave results in which the FRFs had extra zeros in the response. When more significant figures were used (0.9999) the results converged to analytical up to 20 kHz.

3.3.1.2 Added Mass Method

The added mass method was also applied to this system. An addition to the mass matrix, $\Delta\mathbf{m}$, was computed using (3.9) and (3.10) with $\varepsilon = 2.2\text{e-}14$ (one hundred times larger than the estimated machine precision) and added to $\mathbf{M_B}$. As expected, the smallest eigenvalues of $\mathbf{M_B}$ became 2.2e-14. The amount of mass that has been added can be quantified using the ratio between the norm of the added mass and the total mass of $\mathbf{M_B}$, which was found to be $n_{rat} = 0.000505$, indicating that a minuscule amount of mass has been added to the system in order to make $\mathbf{M_B}$ positive definite.

Now that the model has positive mass, it is important to check that it still represents the system accurately. In previous works the authors have found that very small changes to the modal scale factors can sometimes introduce errors causing significant changes to the model. These are easiest to assess by reconstructing the frequency responses (FRFs) of the model, since they give a visual indication of whether both the frequency and amplitude of each mode is correct. Figures 3.2 and 3.3 show the FRFs of the system that were obtained after using each of the proposed methods to correct for the negative eigenvalues in the mass matrix.

Figures 3.2 and 3.3 reveal that the substructure models accurately reproduce all of the modes of the system out to almost 20 kHz, which is not too surprising since the set of modes used to derive them spanned this same range. (According to the traditional rule of thumb, one would only expect the model to be accurate out to about half the bandwidth of the modes used to derive it). Both the Added Mass and Modal Scale Factor approaches produce nearly identical results in this bandwidth, accurately reproducing the first five bending and two axial modes. This is significant, since, as described in [6], the authors previously tried many different adjustments to the substructure model and were unable to obtain a model that reproduced the FRFs accurately. For example, Sect. A.1 in the Appendix shows the result obtained when using an ad-hoc approach to eliminate the negative mass, where there are fairly significant errors in the FRFs predicted by the substructure model.

3.3.2 Three Dimensional Beam-Plate System

In this section the proposed methods are applied to the system studied in [3], a schematic of which is repeated in Fig. 3.4. The experimental subcomponent, C, consists of a beam connected to a plate at its center. A transmission simulator, A, is attached and a modal test is performed, as shown in the photograph. System C is attached to the transmission simulator with eight bolts around the circumference of the plate. The finite element model consists of the cylinder plus a second copy of the transmission simulator. Modal substructuring is used to assemble C and D and to remove two copies of the transmission simulator, resulting in the built-up structure, E.
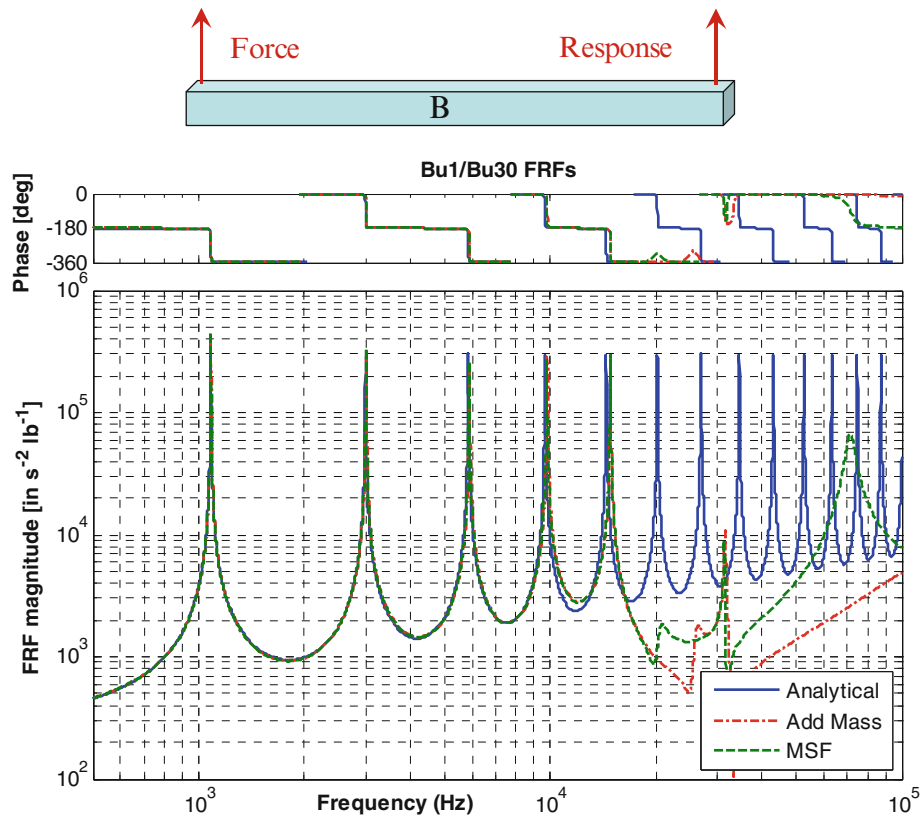
Fig. 3.2 Frequency response function of beam in bending direction after removing the transmission simulator. The *blue* line shows the analytical FRF computed from the FEA model of the beam alone, while the *red* and *green* lines show those of the substructure model estimated after removing the transmission simulator and after adjusting the mass matrix using the Added Mass and Modal Scale Factor approaches (color figure online)
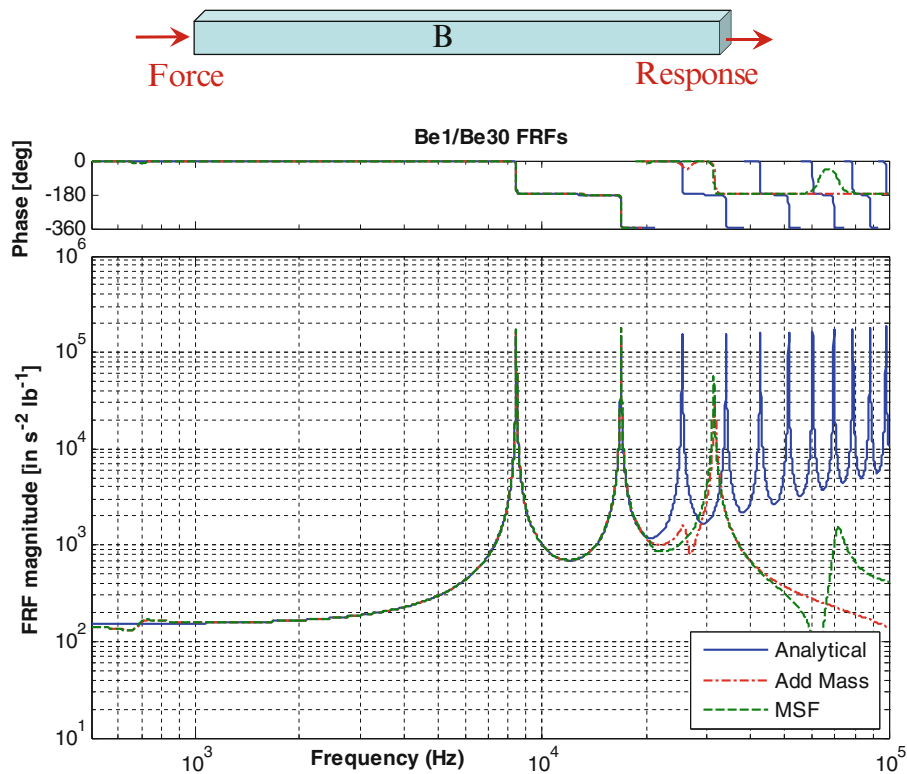
Fig. 3.3 Frequency response function in the axial direction (See description for Fig. 3.2)
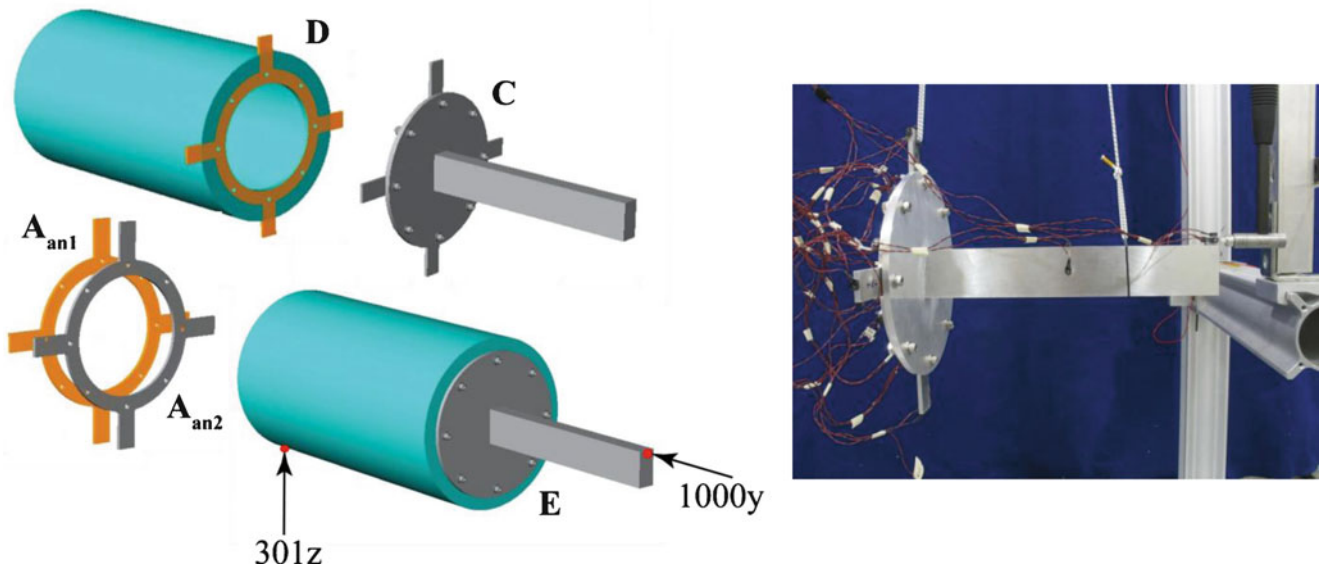
Fig. 3.4 Schematic of Cylinder-Plate System and photograph of the hardware that was tested to obtain an experimental model for substructure C. Labels are shown indicating the names of the substructures, as well as two drive points where FRFs were later reconstructed

As explained in [3], two copies of the transmission simulator were used in this problem to simplify the coupling between D and C. Using this approach, the same modal constraints that are used to connect C or D to the negative transmission simulator model are also used to connect C to D. Since the transmission simulator is welded to D, this results in an effective, continuous constraint between the two systems. Furthermore, because the bolted joints are part of system C, their effect is captured experimentally as it is manifest in the coupling between C and the transmission simulator.

Because there are two transmission simulator models in this problem, the methods proposed in this work must be implemented differently. The C system could be treated in the usual way, but one must also treat subcomponent D as if it were an experimental subcomponent (although with a large number of perfectly measured modes, since they can be readily extracted from the FEA model). Then one could remove A from D, assure that the mass is positive and return the resulting model to the FEA package. On the other hand, either of the methods proposed here could potentially be implemented within FEA, eliminating the negative mass after the subcomponents had been assembled but before computing the modes or response of the assembly. Both of these approaches will be explored briefly.

The experimental test identified 25 modes of the C system, the highest having a natural frequency of 3,835 Hz. Eighteen modes were used to model the transmission simulator spanning 0 to 1,850 Hz. To facilitate the implementation, the D system was reduced to a 100-mode model spanning 0 to 6,165 Hz. When all of these components are assembled, the resulting system has four negative eigenvalues: $\lambda_1 = -0.197$, $\lambda_2 = -0.0764$, $\lambda_3 = -0.134$, $\lambda_4 = -0.118$. The negative mass causes the system to have four spurious natural frequencies that are purely imaginary $f_1 = 2144i$, $f_2 = 2636i$, $f_3 = 2813.3i$, $f_4 = 3453.3i$ Hz. Plots of the reconstructed FRFs are shown in [3], revealing that these spurious natural frequencies apparently do not contaminate the FRFs noticeably, but a positive definite mass matrix is still desired, so the methods presented here will be employed.

3.3.2.1 Case 1: Assemble All Substructures then Correct the Mass Matrix

First consider the case where all of the substructures are assembled before correcting the mass matrix. (In the applications of interest, this would require one to embed the mass correction algorithm within the FEA code). The added mass method was used to compute a matrix $\Delta \mathbf{m}$ that would make the mass matrix positive definite. The resulting mass addition was relatively large compared to the original mass matrix, with a norm ratio of $n_{\mathrm{rat}} = 0.197$. The frequency response functions were reconstructed at two points in order to determine whether the added mass had changed the nature of the response. Figures 3.5 and 3.6 show the frequency responses before and after applying the mass addition algorithm, as well as the finite element truth model described in [3].
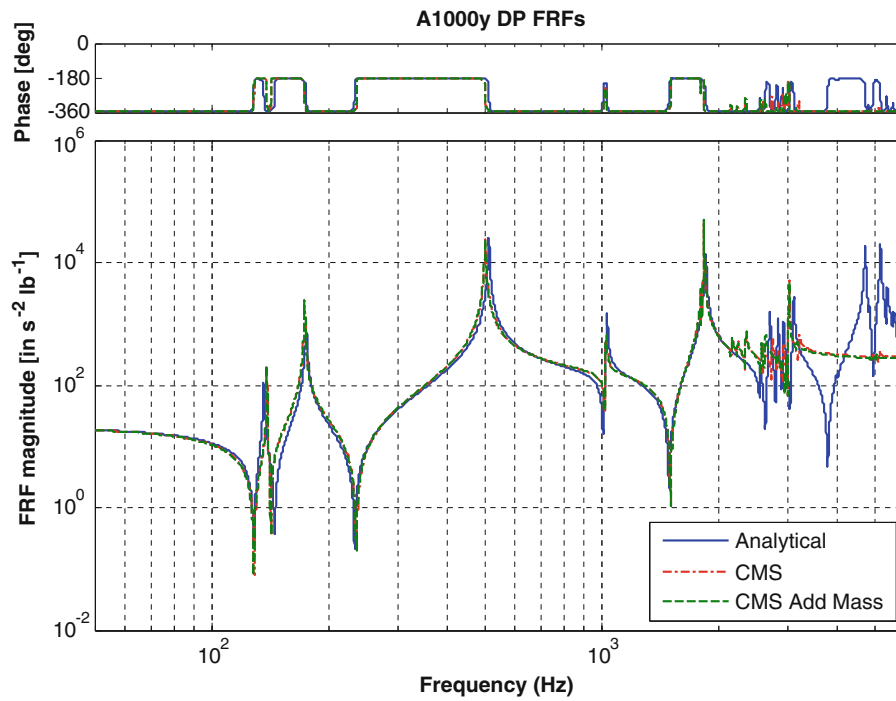
Fig. 3.5 Frequency response function of the assembled system at the drive point labeled 1,000y (axial direction). The *blue* line shows the analytical FRF of a finite element truth model. The other lines show the FRFs estimated by modal substructuring, the *red* is the baseline model that has negative mass while the *green* is from a model that was corrected using the added mass algorithm in Sect. 3.3.1.2 (color figure online)
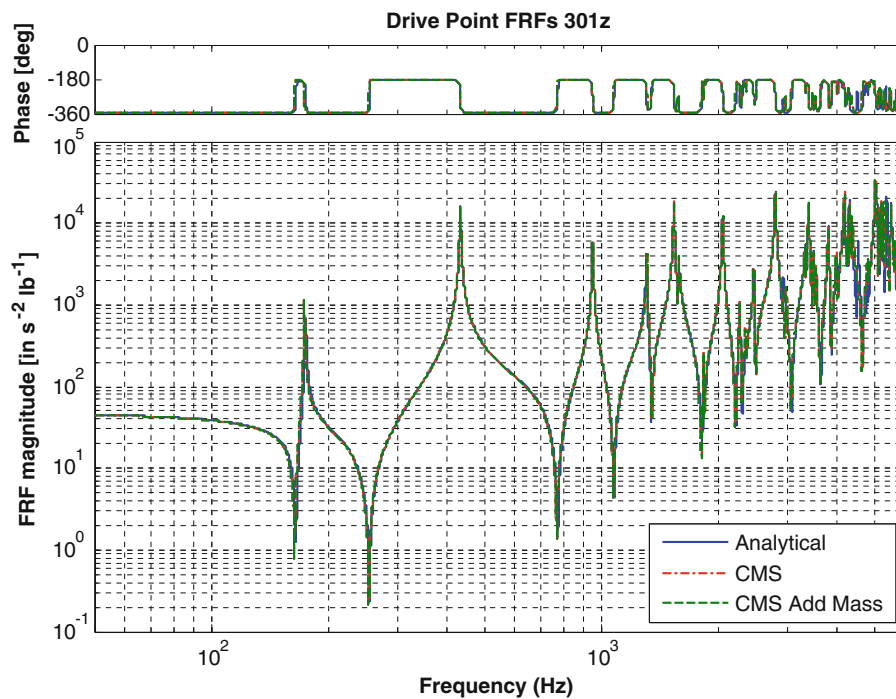
Fig. 3.6 Frequency response function of the assembled system at the drive point labeled 301z (radial direction) (See description for Fig. 3.5)
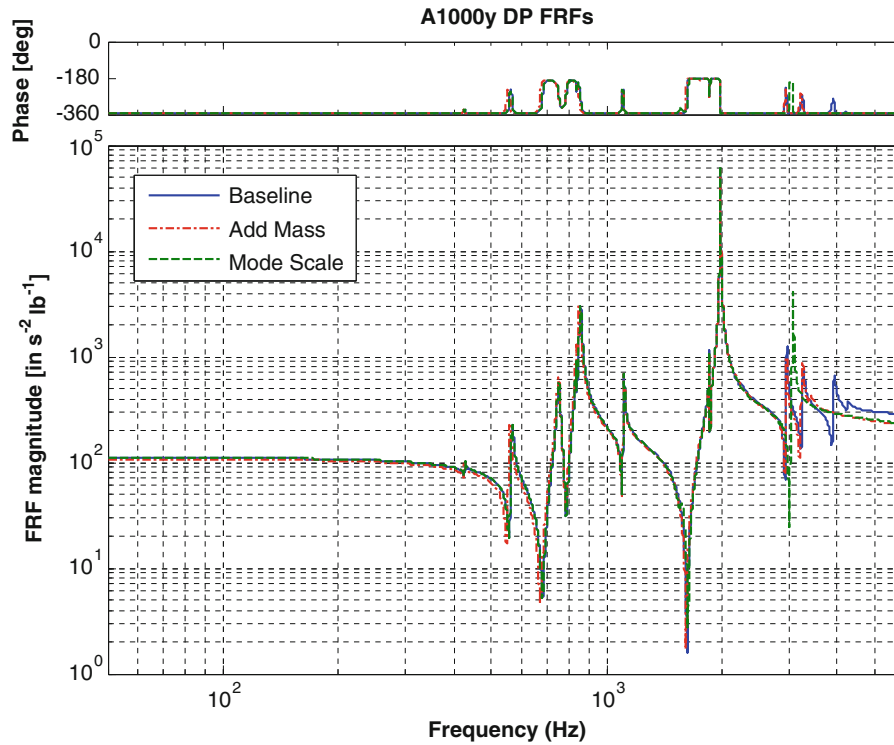
Fig. 3.7 *Blue* curve provides the analytical axial C-A plate/beam FRF, *red* is the added mass method and *green* is the mode scale factor method for generating positive definite mass matrix after subtraction

3.3.2.2 Case 2: Correct the Mass Matrix for C-A

Next consider the case where we wish to create a model for subcomponent C that has positive definite mass after removing the transmission simulator A. Coupling C-A directly one finds that the resulting system's mass matrix has two negative eigenvalues: $\lambda_1 = -0.116$ and $\lambda_2 = -0.0865$. There are eight imaginary natural frequencies, although three of them are above 100 kHz and three are below 1 Hz. The other two are at 0 + 2304.4i and 0 + 2532.1i Hz, within the range of the modes of C.

First the added mass method was used to correct the mass matrix for this system. It computed a mass addition whose norm was $n_{rat} = 0.116$. The resulting system no longer had the two imaginary natural frequencies in the band of interest.

Next the mode scale factor method was employed. This algorithm reduced five of the 18 modal masses of the transmission simulator as follows: mass 1 = .9931; mass 9 = .5783; mass10 = .9488; mass 11 = .8224; and mass 13 = .4942. This achieved a positive definite mass matrix. The resulting axial FRF of the axial response of the plate and beam is shown in Fig. 3.7. The mode scale method has slightly more degradation than the mass added method as compared with the analytical result.

3.3.3 Observations on the Transmission Simulator Mass Corrections Based on the Applications

In the T beam studies, only a small amount of mass had to be subtracted from the transmission simulator using the modal scale factor method, and only a small amount had to be added with the added mass approach. With the cylinder/plate/beam system, the amount of mass subtracted by the modal scale factor method or added by the added mass method was much larger. It was also observed that the FRF quality of the final result for the modal scale factor method degraded when larger mass changes were required to make the constrained mass matrix positive definite. The authors believe that the severity of the correction is related to adequacy with which the mode shapes of the transmission simulator span the space of the actual motion of the substructures when they are constrained together. The transmission simulator mode shapes probably never span the constrained connection motion perfectly. If the transmission simulator mode shapes span the space well, only small corrections are needed, but larger corrections are required when they do not span the space as well. Therefore the amount of mass change required may provide a metric on the quality of the transmission simulator mode shapes for use in the specific application.

3.4 Conclusions

This work presented two methods that can be used to obtain a positive definite mass matrix from the indefinite result that is often obtained when removing one structure from another using modal substructuring. The first method, called the mode scale factor method, used a nonlinear optimization algorithm to vary the modal masses (or equivalently mode scale factors) of the modes of the transmission simulator. This approach was found to work well in cases where the required transmission simulator modal mass changes were small, and it has the advantage that it is physically justifiable whenever the mode scale factors found are reasonable considering the uncertainty in the transmission simulator model. When large changes in the mode scale factors were required, the resulting response FRFs degraded slightly in the applications investigated here.

The second method corrects the system of interest by adding mass to the structure. A simple equation is available to compute the amount of mass required to make the mass matrix positive definite. This approach appears to be more robust than the modal scale factor method. However, one disadvantage of this approach is that one cannot readily relate the mass added to the transmission simulator modes, which are the cause of the negative mass in the first place.

Appendix

Results Using Ad-hoc Approach to Eliminate Negative Mass for T-Beam System

The following Figures show the FRFs that were obtained using an ad-hoc approach to eliminate the negative mass. The modal mass of all of the transmission simulator modes was decreased (simulating a uniform decrease in density of that model) until the negative eigenvalues disappeared. Trial and error revealed that the modal scale factors had to be multiplied by 1.011 to eliminate all of the negative eigenvalues.
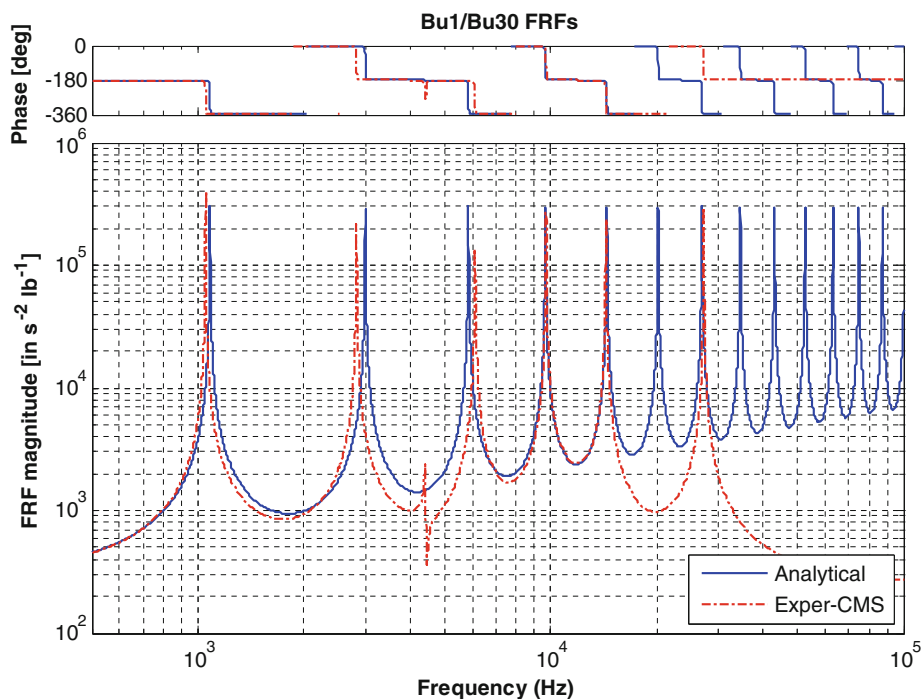
Fig. 3.8 Frequency response function of beam in bending direction after removing the transmission simulator. The *blue line* shows the analytical FRF computed from the FEA model of the beam alone, while the *red line* shows that of the substructure model after eliminating the negative eigenvalues using the ad-hoc approach (color figure online)
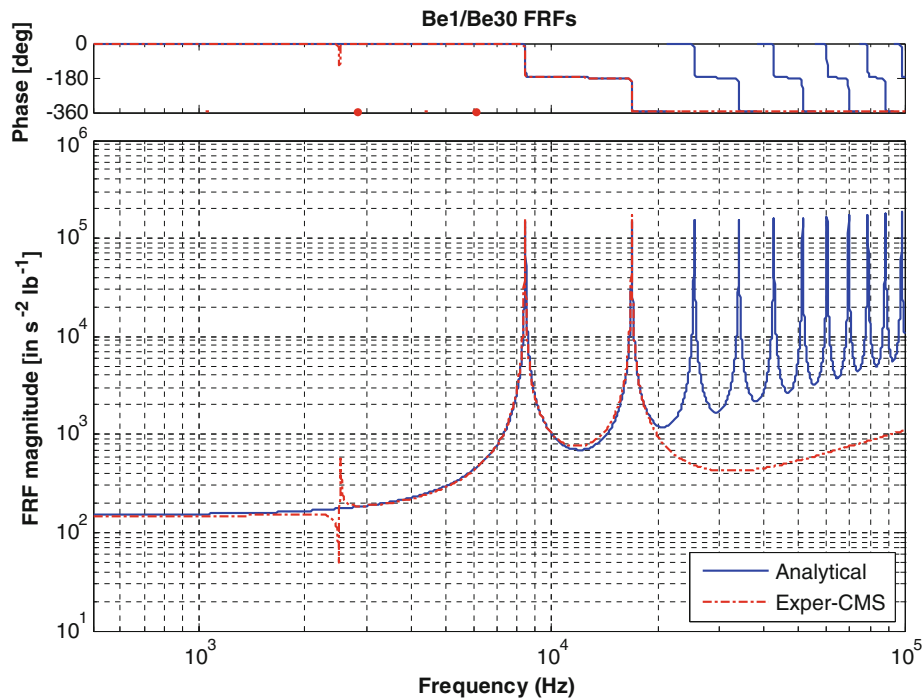
Fig. 3.9 Frequency response function in the axial direction (See description for Fig. 3.8)

References

1. Mottershead JE, Kyprianou A, Ouyang H (2005) Structural modification. Part 1: rotational receptances. J Sound Vib 284:249–65
2. Imregun M, Robb DA, Ewins DJ (1987) Structural modification and coupling dynamic analysis using measured FRF data. In: 5th international modal analysis conference (IMAC V), London
3. Allen MS, Mayes RL, Bergman EJ (2010) Experimental modal substructuring to couple and uncouple substructures with flexible fixtures and multi-point connections. J Sound Vib 329:4891–4906
4. Mayes RL, Arviso M (2010) Design studies for the transmission simulator method of experimental dynamic substructuring. In: International seminar on modal analysis 2010 (ISMA2010), Lueven
5. Yasuda C, Riehle PJ, Brown DL, Allemang RJ (1984) Estimation method for rotational degrees of freedom using a mass additive technique. In: 2nd international modal analysis conference (IMAC II), Orlando
6. Allen MS, Kammer DC, Mayes RL (2011) Metrics for diagnosing negative mass and stiffness when uncoupling experimental and analytical substructures. In: 29th international modal analysis conference (IMAC XXIX), Jacksonville

Chapter 4
Using Substructuring to Predict the Human Hand Influence on a Mechanical Structure

Sébastien Perrier, Yvan Champoux, and Jean-Marc Drouet

Abstract Substructuring methods have been widely used on mechanical structures to study and improve the dynamic behavior of complex assemblies by analyzing the behavior of each substructure separately. Substructuring methods can potentially be used to create a functional link between the dynamic behavior of the human body and mechanical structures in order to enhance the interactions between the body and these same structures. Keeping in mind that significant amounts of vibrations are transmitted to the body from contact with vibrating structures – human-structure coupling interactions could be used as a way to study components of comfort during vibration exposure, and even with the goal of preventing injuries caused by transmitted vibration.

This paper investigates a coupling between a straight beam and the hand-arm system which is a non-linear structure. Each structure is characterized by experimentally obtained mechanical mobility Frequency Response Function (FRF) data over a frequency range between [5, 300] Hz. The FRF Based Substructuring method (FBS) allows coupling through the interface set of substructures. This links mechanical structures with the human body where only interface measurements are gathered. The FBS method is used to predict the dynamic behavior of the assembly.

4.1 Introduction

Knowledge of the interactions between structure assemblies is a major concern in mechanical engineering. Since the 1960s, substructuring methods have become a focus of research in structural dynamics [1–11]. These methods have been used on mechanical structures to study and improve the dynamic behavior of complex assemblies. Human-structure interactions are also an important issue for persons exposed to vibrating structure. The mechanical behavior of the human body has been characterized and studied mainly in the context of health and safety, as well as in the context of dynamic comfort evaluation [12–28]. Furthermore, a compliant structure's dynamic behavior is strongly influenced by contact with the human body [19]. For future studies, developments, and product designs, a clear understanding must be established of all the dynamics involved in the coupling between a mechanical structure and a human subject. While these previous research efforts have provided valuable insight into the dynamic characterization of assemblies through the use of substructuring methods and the characterization of the human body's dynamic behavior, no attempts have yet been made to study a substructuring coupling that involves both the human body and a mechanical structure. Therefore, in this study we propose to assemble the dynamic characteristics of the hand-arm system with a mechanical structure using the Frequency Response Function Based Substructuring (FBS) method in order to predict the mechanical influence of the hand-arm system on the structure.

FBS coupling between a straight beam and the hand-arm system is investigated in this study. To our knowledge, no coupling has been performed with a structure and the human body using the FBS method. Mechanical coupling using the FBS method is an important research tool to study vibration transmission. In human applications, transmissibility is a viable means of studying the subject's health, safety, and dynamic comfort. Also, specific FBS coupling with the human body allows us to assess both the mechanical behavior of the human body alone by the mechanical impedance, as well as the

S. Perrier (✉) • Y. Champoux • J.-M. Drouet
Department of mechanical engineering, VélUS, Université de Sherbrooke,
2500 boul. de l'université, Sherbrooke, QC J1K 2R1, Canada
e-mail: sebastien.perrier@usherbrooke.ca

human influence on a structure as predicted by the FBS model. These results will be beneficial to further enhance interactions between humans and structures. Finally, during the developing process of a mechanical structure, it is valuable to be able to predict the human impact on newly developed structures. The FBS method allows coupling between substructures through consideration of their interface set only [6]. This is a major advantage in linking a mechanical structure with the human body where only interface measurements can be gathered. One of the main conditions when using the FBS method is the linearity of the structures involved [6]. Although the human body is not linear, including the hand-arm system, mechanical coupling using the FBS method can be used with the hand-arm system by controlling various parameters. The dynamic behavior of the hand-arm system varies according to several parameters such as posture, hand position, type of excitation, excitation direction, amplitude, push and grip force [20–23].

In this paper, each structure is characterized in the frequency range [5, 300] Hz. The beam is characterized by the mechanical mobility Frequency Response Function (FRF) and the hand-arm system by mechanical impedance FRF. Impedance measurement is typical when studying the dynamic behavior of the hand-arm system [24–27]. Two of the main parameters that must be controlled when performing measurements on the hand-arm system are the person's posture and the push force applied by the hand. In this paper we present the influence of these two factors on the mechanical impedance of the hand-arm system and the resulting FBS prediction for the hand on the beam.

4.2 Methods

The methods used in this paper to predict the influence of the human hand on a mechanical structure include the generalized frequency domain substructure synthesis presented in [6]. This well-known method, also referred to as FBS (Frequency Based Substructuring), combines the response FRF data of each substructure to analyze the dynamics of a complex assembled structure. This method is based on an implicit statement of the force and velocity continuity considerations at the connection nodes. It enables substructures to be coupled by taking into account the characteristics of the interface nodes only [6] Fig. 4.1.

The mathematical expression for the FRF coupling of two substructures using the FBS method in terms of mobility $\mathbf{Y}$ is shown in (4.1) where: a and b identify the two substructures involved; A is the set of internal degrees of freedom in substructure a; I is the set of interface contact points between substructures a and b; and B is the set of internal degrees of freedom in substructure b.

$$\begin{bmatrix} \mathbf{Y}_{AA} & \mathbf{Y}_{AI} & \mathbf{Y}_{AB} \\ \mathbf{Y}_{IA} & \mathbf{Y}_{II} & \mathbf{Y}_{IB} \\ \mathbf{Y}_{BA} & \mathbf{Y}_{BI} & \mathbf{Y}_{BB} \end{bmatrix}^{ab} = \begin{bmatrix} \mathbf{Y}_{AA}^a & \mathbf{Y}_{AI}^a & 0 \\ \mathbf{Y}_{IA}^a & \mathbf{Y}_{II}^a & 0 \\ 0 & 0 & \mathbf{Y}_{BB}^b \end{bmatrix} - \left\{ \begin{matrix} \mathbf{Y}_{AI}^a \\ \mathbf{Y}_{II}^a \\ -\mathbf{Y}_{BI}^b \end{matrix} \right\} \left[\mathbf{Y}_{II}^a + \mathbf{Y}_{II}^b \right]^{-1} \left\{ \begin{matrix} \mathbf{Y}_{IA}^a \\ \mathbf{Y}_{II}^a \\ -\mathbf{Y}_{IB}^b \end{matrix} \right\}^{\mathrm{T}} \tag{4.1}$$

Substructures a and b represent the beam (mechanical structure) and the hand-arm system respectively. The coupling process using the FBS method is achieved by measuring the beam mobility characteristics and the hand mobility characteristics separately. These characteristics are assembled through (4.1) to predict the influence of the hand on the beam. The mobility characteristics of the assembly are then compared with the measured mobility characteristics of the beam in contact with the hand. For this study, only interface data can be gathered for the hand-arm system, and therefore only the equation for the interface set will be considered in (4.2) where $\mathbf{Y}_{\mathrm{II}}^{\mathrm{Beam}}$ corresponds to the mechanical mobility of
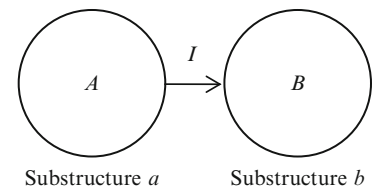
Fig. 4.1 Diagram of two coupled substructures a and b with interface set I

Substructure a Substructure b
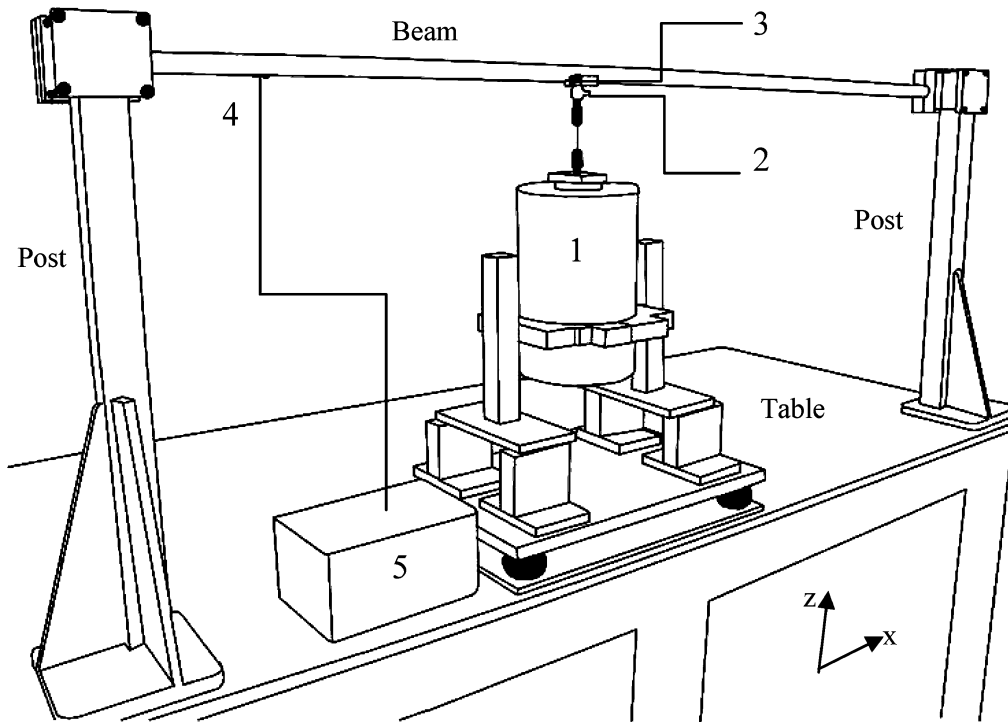
Fig. 4.2 Experimental setup to measure the dynamic behavior of the beam at the I point ((**1**) Vibration exciter (shaker), (**2**) Force sensor 208C03 type ICP from PCB Piezotronics at the I point, (**3**) Accelerometer 356B20 type ICP from PCB Piezotronics, (**4**) Strain gauge, (**5**) Signal conditioner type P-3500 from Vishay for the strain gauge)

the beam determined by an excitation force applied at the interface point (N°2 on Fig. 4.2) and a velocity response also at the interface point (N°3 on Fig. 4.2).

$$\mathbf{Y}_{\text{II}}^{\text{Beam}\_Hand} = \mathbf{Y}_{\text{II}}^{\text{Beam}} - \mathbf{Y}_{\text{II}}^{\text{Beam}} \left[\mathbf{Y}_{\text{II}}^{\text{Beam}} + \mathbf{Y}_{\text{II}}^{\text{Hand}} \right]^{-1} \mathbf{Y}_{\text{II}}^{\text{Beam}} \tag{4.2}$$

An assumption is made where only vertical z-axis is considered, resulting in (4.3).

$$Y_{\text{IzIz}}^{\text{Beam}\_Hand} = Y_{\text{IzIz}}^{\text{Beam}} - Y_{\text{IzIz}}^{\text{Beam}} \left[Y_{\text{IzIz}}^{\text{Beam}} + Y_{\text{IzIz}}^{\text{Hand}} \right]^{-1} Y_{\text{IzIz}}^{\text{Beam}} \tag{4.3}$$

4.2.1 Beam Mobility

Figure 4.2 shows the beam that was used to perform an FBS coupling. The beam is straight with a 1 in diameter through a hollow circular section, a wall thickness of 1/8 in., and a total length of 5.5 ft. The beam configuration is clamped at both ends on two rigid steel posts which are firmly screwed onto a rigid steel table. This structure was chosen to reveal multiple modes in the frequency range of interest 5–300 Hz. In this configuration there is a strong modification of the dynamic behavior of the beam when in contact with the hand. Beam mobility is measured (velocity/force) using an accelerometer (integrated in the frequency domain) and a force transducer installed on an adaptor which is fixed to the beam and linked to the shaker by a stringer (N°2 and 3 on Fig. 4.2). A random vibration signal is provided to the shaker within the frequency range of 5–300 Hz. The acquisition system is Test.Lab 11B software from LMS. A strain gauge is installed on the beam (N°4 on Fig. 4.2) to control the force applied by the hand when performing measurements on the beam coupled with the hand. This strain gauge is calibrated prior to measuring the corresponding force.

Fig. 4.3 Diagram of the hand-arm impedance measurement system ((**1**) LMS Test.Lab 11b software, (**2**) Power amplifier SS250VCF from MB Dynamics for the shaker, (**3**) Vibration exciter (shaker), (**4**) 6 DOFs force sensor model MC3-6-500 from AMTI, (**5**) Accelerometer 356B20 type ICP from PCB Piezotronics, (**6**) Handle)
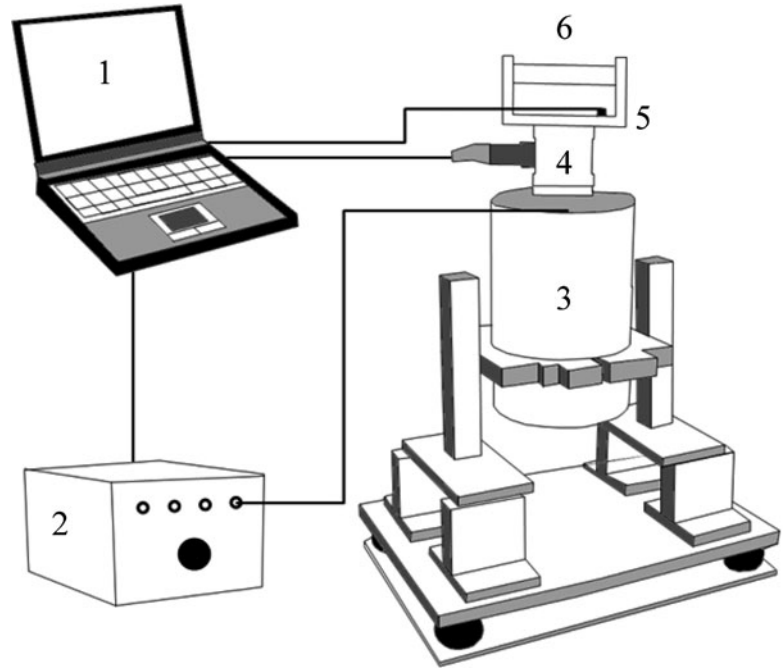
4.2.2 Hand-Arm System Mechanical Impedance

In (4.3), $Y_{IzIz}{}^{Beam}$ corresponds to the mobility of the beam at point I under the vertical z-axis and $Y_{IzIz}{}^{Hand}$ corresponds to the mobility of the hand-arm system at point I under the vertical z-axis.

Typically, the dynamic characteristics of the hand-arm system are in the form of mechanical impedances. Several investigators have conducted impedance measurements on the Hand-Arm system. However, the results from these studies have not resulted in a consensus [24, 28]. For these reasons and in this paper, the hand-arm system is characterized in terms of measured impedance.

Theoretically, the mobility also known as Admittance is the inverse of Impedance $\left([\mathbf{Y}] = [\mathbf{Z}]^{-1} \right)$.

The mechanical impedance of the hand-arm system is obtained using a specially designed handle equipped with an accelerometer and mounted on a force sensor installed on a shaker for mobility measurements (Fig. 4.3). The same LMS system is used as a signal generator to provide a random vibration signal to the shaker within the frequency range of 5–300 Hz.

Measurements are performed with and without a hand on the handle. Because the handle is sufficiently rigid in the frequency range of interest, the handle impedance can then be subtracted from the total impedance (hand + handle) to obtain the hand-arm system mechanical impedance [16, 23]:

$$Z_{Hand}(\omega) = Z_{Total}(\omega) - Z_{Handle}(\omega) \tag{4.4}$$

The impedance data can be inverted to get the mobility of the hand-arm system and used directly in (4.3).

The study is carried out on one subject to avoid inter-subjects variability. Two different hand-arm postures are used for impedance measurements in the vertical and transverse directions. In accordance with ISO-5349 [27], these directions refer to an excitation of the hand and arm in the X_h and Z_h directions (Fig. 4.4). A total of four push forces are tested at 20, 30, 40, and 50 N. The angle between the upper arm and forearm is a 180° elbow extension (arm fully extended). In the X_h direction, the angle between the upper body and shoulder is 90°, and in the Z_h direction, the angle is 0° (Fig. 4.5).

For each configuration, the subject is asked to hold the handle without applying any grip force. After the correct posture and push force are established, the vibration data are measured. The subject is requested to maintain a constant push force during the test using the DC force displayed by the force sensor. A total of 10 measurements are performed for each configuration to evaluate intra-subject variability. The measurements are carried out over several days to avoid subject fatigue.
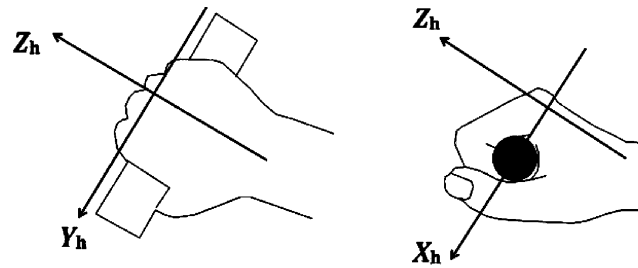
Fig. 4.4 The biodynamic co-ordinates of the hand-arm system according to ISO/DIS 5349 [27]
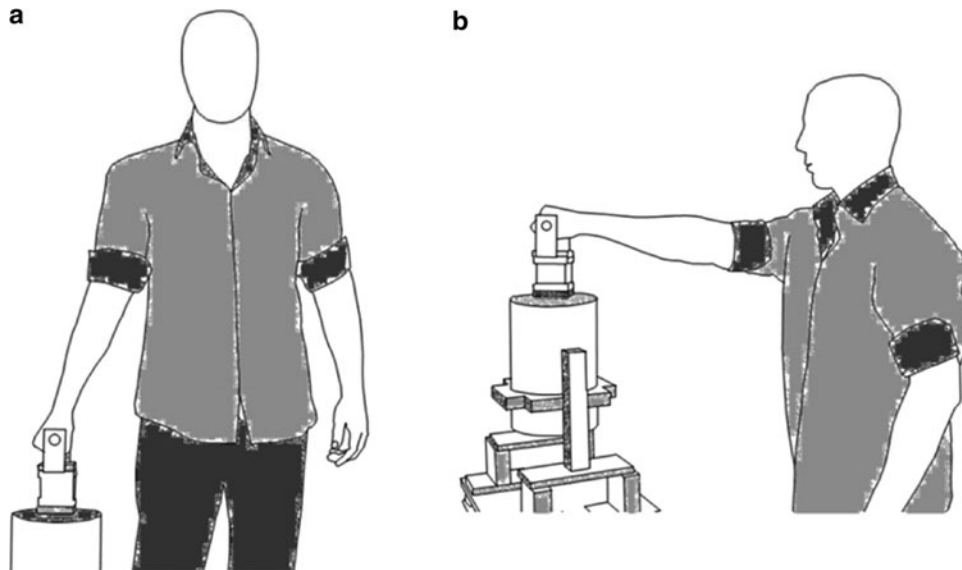
Fig. 4.5 Postures for excitations of the hand (**a**) along the Z_h-axis and (**b**) along the X_h-axis

4.2.3 Target Measurements

These measurements are used to evaluate the accuracy of the FBS prediction for the circular hollow beam coupled with a hand (4.3). Using the same procedure as for the hand-arm system mechanical impedance section above, the subject is requested to grasp the beam and maintain a constant push force during the exposure by looking at the force level displayed through a strain gauge signal conditioner (N°5 on Fig. 4.2).

4.3 Results

4.3.1 Hand-Arm System Mechanical Impedance

The results for the four push forces are illustrated in Fig. 4.6 for the hand-arm system under the Z_h-axis and in Fig. 4.8 for the hand-arm system under the X_h-axis. Each curve represents the mean of the measured frequency spectrums for each configuration. One important thing to mention is that the measured impedances for the hand-arm system under the Z_h and X_h-axes have the same trend and the same magnitude as those published in the literature.

For the Z_h-axis posture and each push force (Fig. 4.6), the results mainly show two damped peaks in the frequency range of 5–75 Hz and higher amplitude for this range of frequencies. Between 75 and 300 Hz, the amplitude decreases for any push force. This reveals a more important influence of the dynamic behavior of the hand-arm system under Z_h-axis vibration for
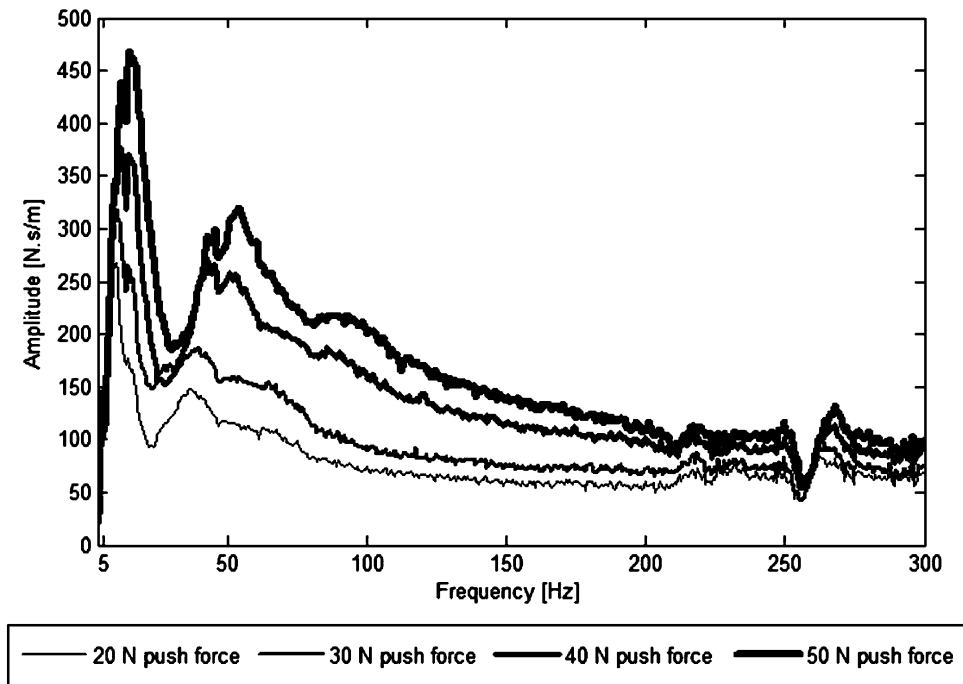
Fig. 4.6 Mechanical impedance of the hand-arm system under Z_h-axis Vibration
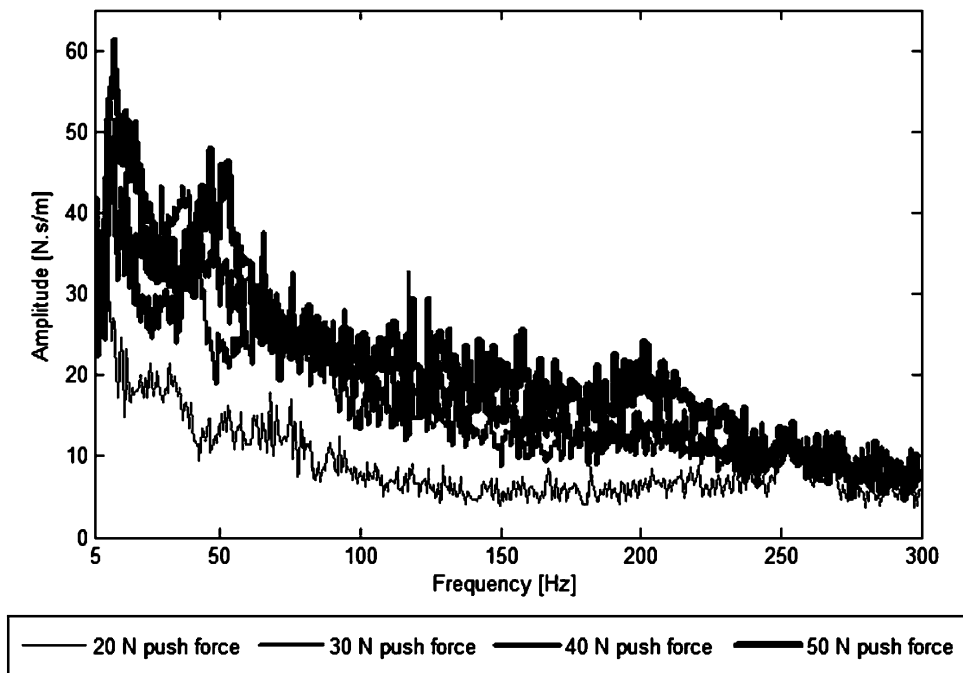
Fig. 4.7 Standard deviation for the hand-arm system impedance under Z_h-axis Vibration

frequencies between 5 and 75 Hz. By looking at the standard deviation (Fig. 4.7) and the impedance results (Fig. 4.6) for different push forces, a $\pm$ 10 N difference in the push force can be differentiated on the resulting hand-arm impedances. By taking a close look at the two peaks in Fig.4.6, it is possible to identify that these peaks are shifting as a function of the applied push force. This is a clear display of the non-linear behavior of the hand-arm system. Between 250 and 270 Hz,

a small bump in the results is noticeable in Fig. 4.6. This is due to the subtraction of the handle impedance in (4.4) whose dynamic behavior is not strictly rigid around 250 Hz. This is associated with the handle dynamic behavior, and not with the hand impedance response.

For the X_h-axis posture and each push force (Fig. 4.8), results mainly show one damped peak in the frequency range of 50–175 Hz and higher amplitude for this range of frequencies. Between 175 and 300 Hz, the amplitude decreases for any
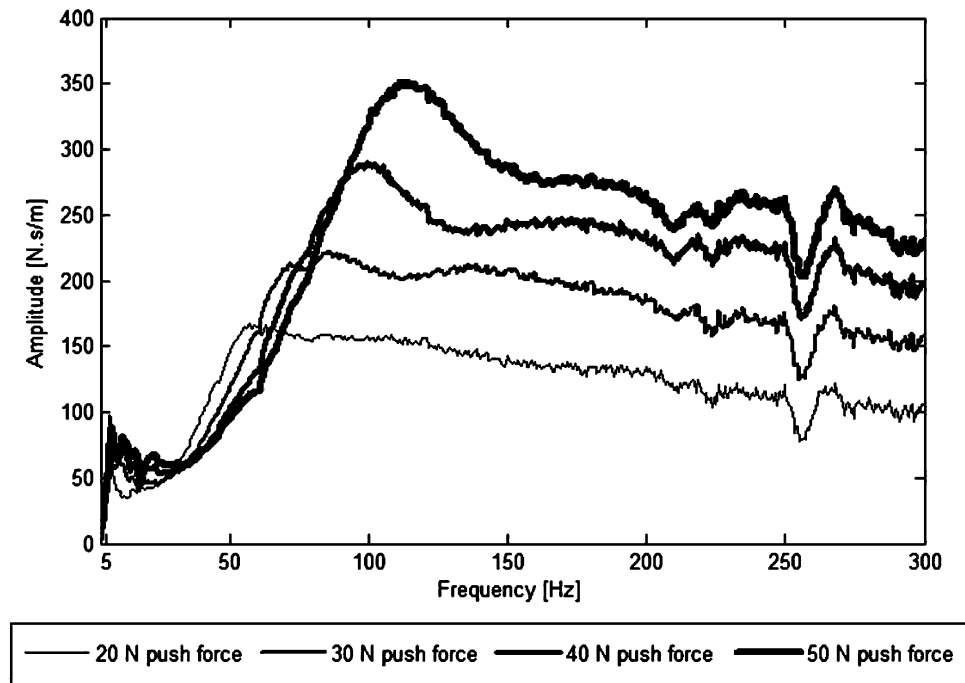
Fig. 4.8 Mechanical impedance of the hand-arm system under X_h-axis Vibration
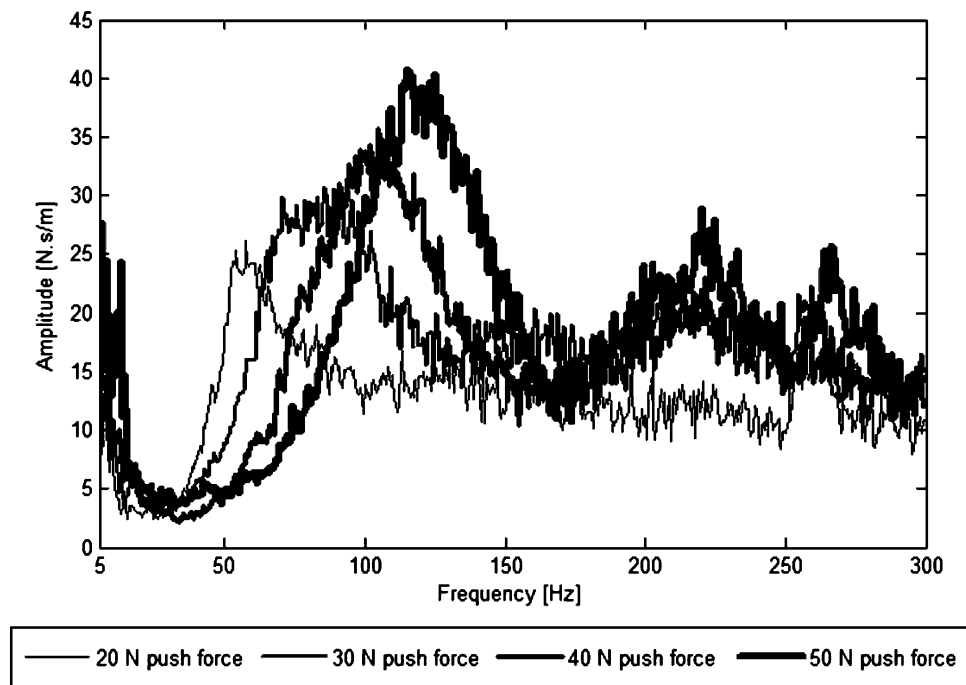
Fig. 4.9 Standard deviation for hand-arm system impedance under X_h-axis vibration
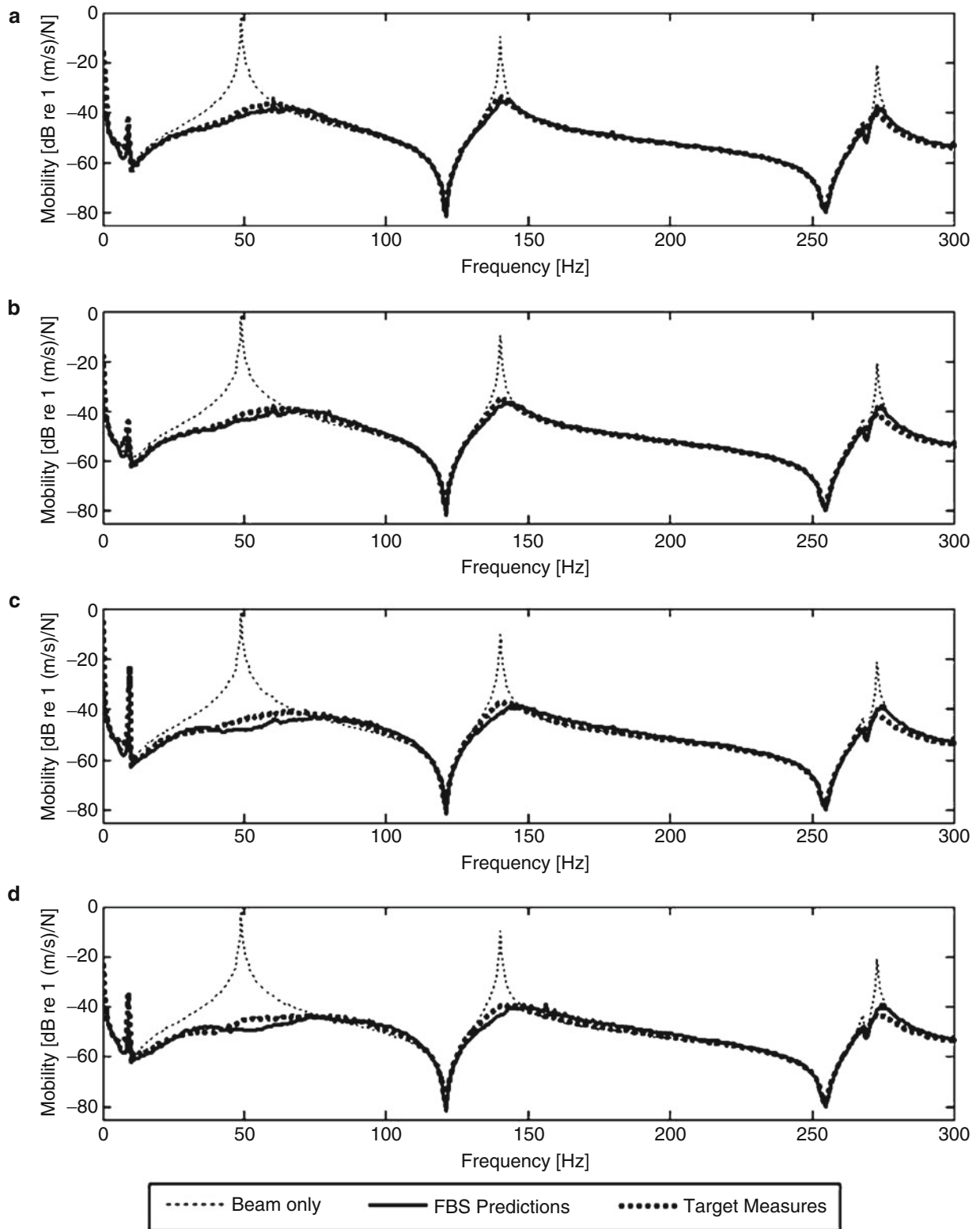
Fig. 4.10 FBS mobility predictions of the hand coupled to the beam in the Z_h-axis posture compared to the target mobility measurements for the four push forces ((**a**) 20 N, (**b**) 30 N, (**c**) 40 N, (**d**) 50 N)
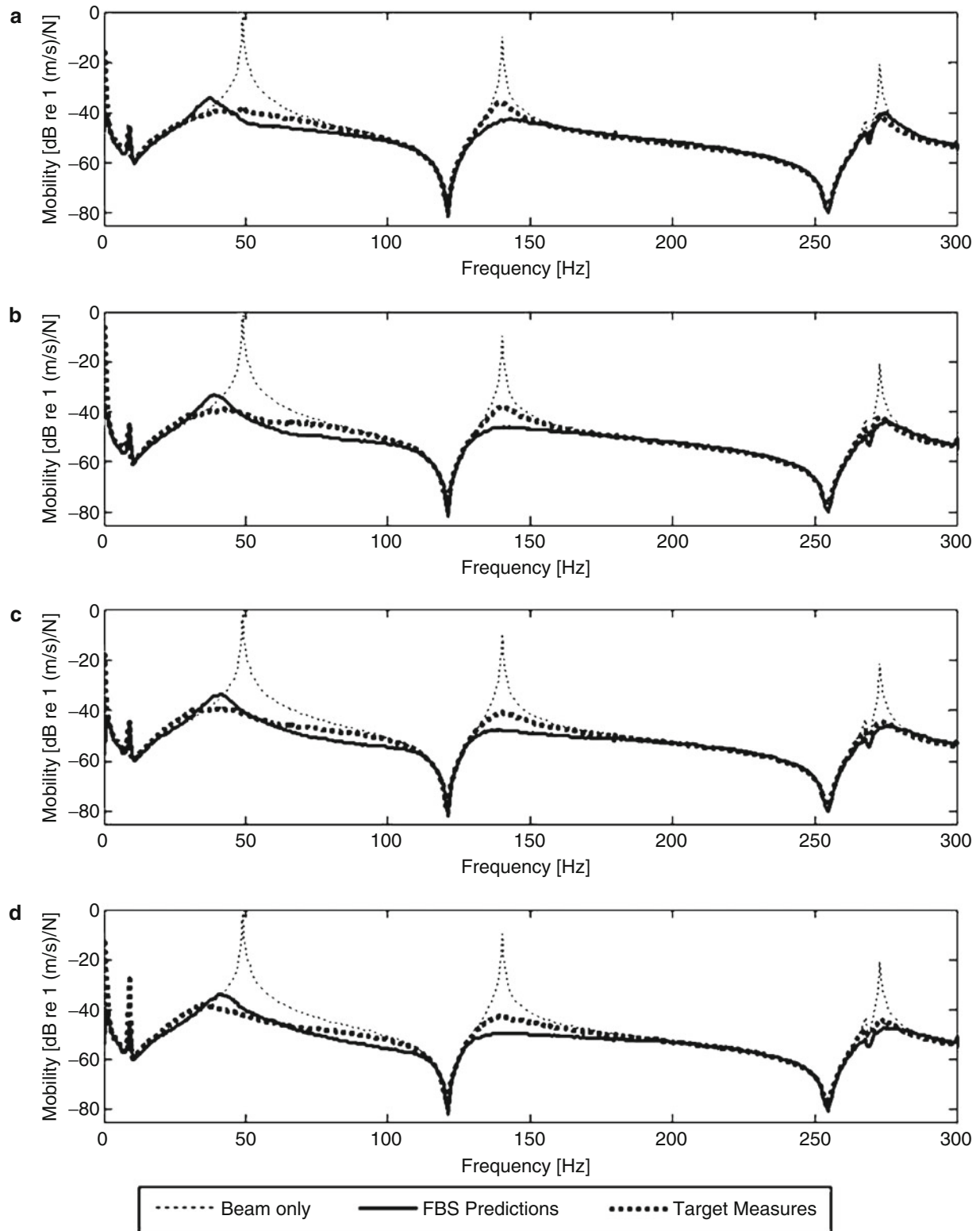
Fig. 4.11 FBS mobility predictions of the hand coupled to the beam in the X_h-axis posture compared to the target mobility measurements for the four push forces ((**a**) 20 N, (**b**) 30 N, (**c**) 40 N, (**d**) 50 N)
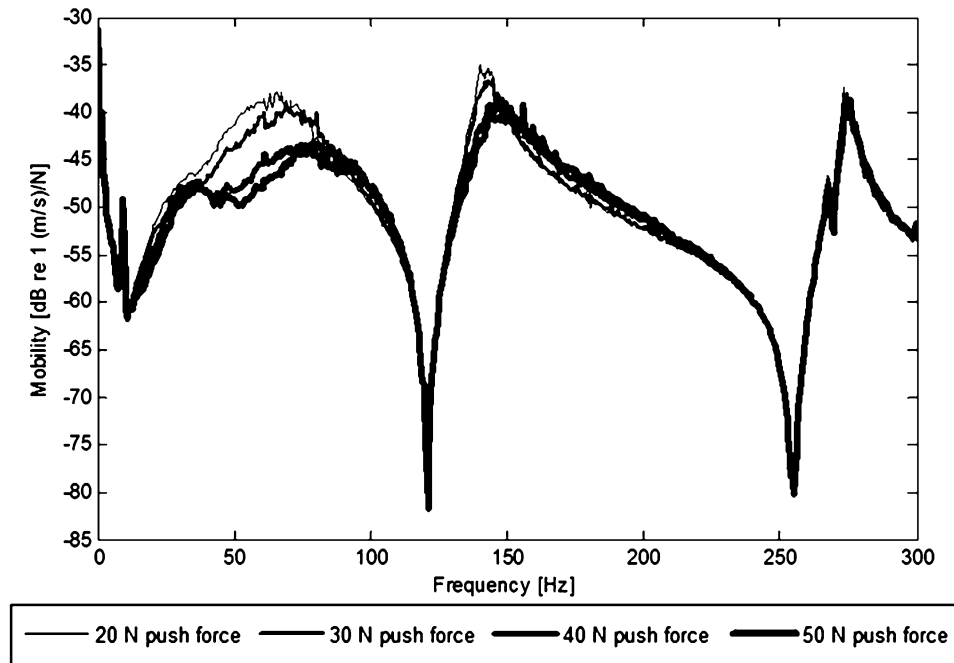
Fig. 4.12 Comparison of the four FBS predictions for the hand coupled to the beam in the Z_h-axis posture and with the four push forces

push force. This reveals a more important influence of the dynamic behavior of the hand-arm system under X_h-axis vibration for frequencies from 50 to 175 Hz. By looking at the standard deviation (Fig. 4.9) and the impedance results (Fig. 4.8) for the different push forces, a $\pm$ 10 N difference in the push force can be differentiated on the resulting hand-arm impedances as for Z_h-axis. By taking a close look at this damped peak in Fig. 4.8, it is possible to detect the shift of this peak as function of the applied push force, displaying the non-linear behavior of the hand-arm system. Between 250 and 270 Hz in Fig. 4.8, a small bump in the results is also noticeable. This is again associated with the handle dynamic behavior, and not with the hand impedance response.

4.3.2 FBS Model

The FBS predictions for the hand coupled with the beam at the four different push forces in the Z_h-axis posture (Fig. 4.10) and the X_h-axis posture (Fig. 4.11) are compared to the target measurements corresponding to the hand holding the beam with the same posture and push forces. In order to observe the influence of the hand on the beam, the dynamic behavior of the beam only is added (dotted line). The influence of the hand on the beam is also presented with the four different push forces for the Z_h-axis posture to highlight the importance of controlling the push forces when performing FBS predictions involving the hand-arm system (Fig. 4.12).

4.4 Discussion and Conclusion

The results for the Z_h-axis posture (Fig. 4.10) demonstrate that the FBS model succeeds in providing reliable predictions for the influence of the hand on a beam with four different push forces. This gives a strong indication that coupling between the hand-arm system and a mechanical structure is possible using this method.

The impedances for the Z_h-axis posture reveal a strong influence of the hand-arm system for frequencies up to 75 Hz. The FBS predictions also show that the hand with this posture has an influence on the beam up to around 75 Hz for the first mode of the beam. For the second and third modes of the beam, the hand adds damping. Furthermore, by looking at the differences on the first mode of the beam, FBS predictions for the four push forces (Fig. 4.12) show that it is really important

to control the push force while performing measurements in order to obtain accurate predictions. Finally, inaccuracies in the impedance measurements between 250 and 270 Hz are due to the dynamics of the handle and do not appear in the FBS coupling between the hand-arm system and the beam.

According to the results for the X_h-axis posture (Fig. 4.11), the FBS model failed to provide reliable predictions for the influence of the hand on a beam with the four different push forces. This indicates that coupling between the hand-arm system and the beam is not simple with this posture. The discrepancy between the FBS predictions and the target measurements can be explained by the fact that only the vertical z-axis is considered in this work and that this assumption is too restrictive for the coupling of the hand-arm system with the beam in this X_h-axis posture.

This work shows that reliable predictions can be obtained using the FBS method even with a non-linear structure such as the hand-arm system. Mechanical coupling predictions between the human body and a mechanical structure are thus possible using this method. Results show that it is important to control several parameters when performing the FBS coupling with a human body part because the mechanical behavior of the human body is sensitive to several factors such as position, orientation, and forces. This work also highlights the following merits of the FBS method: (1) Direct use of shaker test data, (2) Combination of substructures when only the data interfaces are known.

However, a lack of information regarding degrees of freedom in some specific cases can lead to the failure of mechanical coupling prediction. Despite this limitation and the need to process a large amount of data when several substructures are coupled through several contact points, the results revealed in this study indicate that the FBS method is a promising approach to study vibration interaction mechanisms between a mechanical structure and the human body.

References

1. Hurty WC (1960) Vibrations of structural systems by component mode synthesis. J Eng Mech/Am Soc Civil Eng 86(4):51–69
2. Craig R, Bampton M (1968) Coupling of substructures for dynamic analysis. AIAA J 6(7):1313–1319
3. MacNeal R (1971) Hybrid method of component mode synthesis. Comput Struct 1(4):581–601
4. Klosterman A (1971) On the experimental determination and use of modal representations of dynamic characteristics. Ph.D. thesis, University of Cincinnati, Department of Mechanical Engineering
5. Rubin S (1975) Improved component-mode representation for structural dynamic analysis. AIAA J 13(8):995–1006
6. Jetmundsen B (1986) On frequency domain methodologies for prescribed structural modification and subsystem synthesis. Ph.D. thesis, Rensselaer Polytechnic Institute, New York
7. Jetmundsen B, Bielawa R, Flanelly W (1988) Generalized frequency domain substructure synthesis. J Am Helicopter Soc 33(1):55–65
8. Ewins DJ (2000) Modal testing: theory, practice and application, 2nd edn. Research Studies Press, Philadelphia
9. Avitabile P (2003) Twenty years of structural dynamic modification: a review. J Sound Vib 37:14–25
10. De Klerk D, Rixen D, De Jong J (2006) Frequency based substructuring (FBS) method reformulated according to the dual domain decomposition method. In: Proceedings of the fifteenth international modal analysis conference, society for experimental mechanics, Paper 136
11. De Klerk D, Rixen DJ, Voormeeren SN (2008) General framework for dynamic substructuring: history, review, and classification of techniques. AIAA J 46(5):1169–1181
12. Griffin MJ (1990) Handbook of human vibration. Academic, London
13. Mansfield NJ (2005) Human response to vibration. CRC Press, Boca Raton
14. International Standard Organization, ISO 2631 (1997) Mechanical vibration and shock – evaluation of human exposure to whole-body vibration. International Standard Organization, Geneva
15. Reynolds DD, Angevine EN (1977) Hand-arm vibration, Part II: vibration transmission characteristics of the hand and arm. J sound vib 51 (2):255–265
16. Dong RG, Welcome DE, McDowell TW, Wu JZ (2006) Measurement of biodynamic response of human hand-arm system. J Sound Vib 294:807–827
17. Griffin MJ, Whitham EM, Parsons KC (1982) Vibration and comfort, I. Translational seat vibration. Ergonomics 25(7):603–630
18. Richard S, Champoux Y (2006) Development of a metric related to the dynamic comfort of a road bike. In: Proceedings of the international modal analysis conference XXIV (IMAC XXIV), St. Louis
19. Richard S (2005) Etude du comportement dynamique d'un vélo de route en lien avec le confort du cycliste. M.ScA thesis, Université de Sherbrooke
20. Burström L (1997) The influence of biodynamic factors on the mechanical impedance of the hand and arm. Int Arch Occup Environ Health 69:437–446
21. Aldien Y, Marcotte P, Rakheja S, Boileau P-E (2005) Mechanical impedance and absorbed power of hand-arm under x_h-axis vibration and role of hand forces and posture. Ind Health 43:495–508
22. Aldien Y, Marcotte P, Rakheja S, Boileau P-E (2006) Influence of hand-arm posture on biodynamic response of the human hand-arm exposed to z_h-axis vibration. Int J Ind Ergon 36:45–59
23. Besa AJ, Valero FJ, Suñer JL, Carballeira J (2007) Characterization of the mechanical impedance of the human hand-arm system: the influence of vibration direction, hand-arm posture and muscle tension. Int J Ind Ergon 37:225–231
24. Lundström R, Burström L (1989) Mechanical impedance of the human hand-arm system. Int J Ind Ergon 3:235–242
25. Burström L (1990) Measurements of the impedance of the hand and arm. Int Arch Occup Environ Health 62:431–439

26. Dong RG, Rakheja S, Schopper AW, Han B, Smutz WP (2001) Hand-transmitted vibration and biodynamic response of the human hand-arm: a critical review. Crit Rev Biomed Eng 29(4):391–441
27. International Standard Organization, ISO/DIS 5349 (2001) Mechanical vibration – measurement and evaluation of human exposure to hand-transmitted vibration. International Standard Organization, Geneva
28. Adewusi SA, Rakheja S, Marcotte P, Boileau P-E (2008) On the discrepancies in the reported human hand-arm impedance at higher frequencies. Int J Ind Ergon 38:703–714

Chapter 5
Simple Experiments to Validate Modal Substructure Models

Mathew S. Allen and Daniel C. Kammer

Abstract While significant strides have been made in recent years, experimental/analytical substructuring methods can be quite sensitive to seemingly small measurement errors, to modal truncation (for modal methods), small residual terms (for frequency based methods), etc. . . As a result, one tends to have less confidence in a substructuring prediction than, for example, a finite element model, even though both may have similar accuracy in some situations. This work explores ways of estimating the uncertainty in modal substructure models, seeking to provide the experimentalist with an approach that could be used to evaluate the fidelity of a substructure model. This would allow one to detect cases where the substructuring problem is very sensitive to uncertainty, so a remedy can be sought, and perhaps even provide a measure of the expected scatter in the predictions. Simple experiments are proposed, for example obtaining the natural frequencies of the subcomponent after attaching a well characterized subcomponent at a point, in order to verify the subcomponent model and to estimate the sensitivity of the substructuring predictions to uncertainties. Special attention is paid to the adequacy of the modal basis of the substructure.

5.1 Introduction

Experimental-analytical substructuring is a procedure in which an experimental model for a subcomponent is obtained, e.g. using modal testing techniques, and then coupled with an analytical model (typically a finite element model) of another subsystem in order to predict the response of the assembled system. By replacing part of the system with a test based model one saves the difficulty and expense required to create a computational model; hence the method is most often desirable when the subcomponent of interest is poorly known (e.g. its material properties, interface stiffnesses, etc. . .) or difficult to model (intricate geometric features, etc. . .). On the other hand, although the tests required to create the experimental model are straightforward and have existed for over 40 years, there are several issues that must be addressed in order to obtain an accurate subcomponent model. Specifically, one must assure that an adequate number of subcomponent modes are captured to describe the substructure adequately in the assembly of interest (modal truncation), rotational motions may need to be measured, which are generally difficult to obtain and susceptible to noise. As a result of these issues, seemingly insignificant experimental errors can cause dramatic errors in the substructuring predictions in some situations (see, e.g. [1, 2]). Some of these issues are summarized in recent review papers [3, 4]. Because of these and other factors, experimental-analytical substructuring seems to be quite under-utilized today, although there has been a resurgence of interest in recent years and recent studies have shown better success in several situations [5–9].

Because substructuring predictions can sometimes be extremely sensitive to experimental errors, one may be hesitant to rely on them and this inhibits more widespread use of the techniques. (One could, perhaps, argue that a finite element model of a complicated substructure is just as likely to be plagued with severe errors, but that is a discussion for another paper. . .) This paper takes initial steps towards addressing this lack of confidence by exploring whether some small number of additional measurements can be taken when creating the experimental substructure model in order to assess its accuracy. Specifically, after creating the subcomponent model, a second test is proposed where a known fixture is attached to the subcomponent and its natural frequencies are measured. Those results are then compared with predictions of the natural

M.S. Allen (✉) • D.C. Kammer
Department of Engineering Physics, University of Wisconsin, Madison, WI 53706, USA
e-mail: msallen@engr.wisc.edu; kammer@wisc.edu

frequencies of the assembly, obtained using substructuring techniques in order to assess the quality of the subcomponent model. Mode shapes could also be measured but here we presume that those would not be available since they might increase the cost of the test. (If a large channel count system is used with fixed sensors then the mode shapes might be easily obtained and used in this validation as well; this will not be explored here).

Substructuring predictions can be obtained using modal models for the subcomponents (Modal Substructuring) or the frequency response functions directly (Frequency Based Substructuring). This work focuses on the modal substructuring approach; some of the similarities and differences between these approaches are discussed in [3, 4]. The authors are not aware of any other works where model validation has been applied to substructure models, but the work by Kanda, Wei, Brown & Allemang [10] is closely related. In that work they attached rigid blocks with known properties to a structure in order to verify that the mode shape scale factors had been identified accurately. Several studies have compared substructuring predictions with analytical models and/or experiments on the actual assembly (see, e.g. [1, 8, 11, 12]), but here we treat a more realistic case where the modes of the assembly of interest are not known so one must infer whether the subcomponent model is adequate using some other test.

The following section describes the proposed technique using a simple beam system as an example. Simulated results for this system are then presented in Sect. 5.3 followed by the conclusions in Sect. 5.4.

5.2 Theory

Suppose that an experimental model of a certain system is desired. The system of interest might be as complicated as an automotive engine, a rocket payload with exotic, difficult to characterize materials, or it might be as simple as a truss or a basic electronic component. In any event, experiments would be performed to find the modes of the subcomponent and those would constitute a modal model for the substructure. One of two basic approaches are typically used, both of which are illustrated in Fig. 5.1. In the free-free modes approach, the structure of interest (the cyan colored beam in the figure) is suspended from negligibly soft supports [13] and a modal test is performed to extract its modes. This method is known to produce quite inaccurate substructure models since all of the modes in the substructure's modal basis have zero shear and moment at the connection point (the left end of the beam in this example). This can often be remedied by including residual effects of out of band modes [14–16], although additional tests are often required to obtain the residual flexibilities and even then they tend to be weakly represented in the measurements and difficult to accurately extract.

An attractive alternative is the mass-loaded interface approach, where a well characterized fixture or a transmission simulator (TS) is attached to the subcomponent of interest and the free-free modes of the assembly are measured. The effects of the transmission simulator are then removed from the substructure model in order to estimate the desired modal model for the system of interest. Traditionally the fixture was designed to be rigid in the frequency band of interest so it could be treated as a point mass [10, 17], but the authors recently showed that flexible fixtures could be readily accommodated so long as the proper constraints were applied between the fixture and its analytical model when removing its effects [6]. They introduced the name "transmission simulator" in [18] a few years after their initial work [6]. This method produces a model whose modal basis is enriched with mode shapes that involve nonzero shear and moment at the interface, so it tends to serve as an accurate, efficient basis for the substructure. This approach can also simplify substructure testing when the components of interest are connected at many points. On the other hand, one disadvantage of this approach is that one must subtract one subcomponent from another to estimate the substructure model, and this may introduce negative mass (or stiffness) causing the results to be nonphysical. The authors recent works present some very promising remedies to these difficulties [19, 20].

5.2.1 Substructure Validation Experiments

Once a substructure model has been obtained, this work proposes to validate it by performing an additional experiment. A well characterized fixture or structure is attached to the system and its natural frequencies are measured. The natural frequencies of the assembly are then predicted using modal substructuring and the frequencies are compared with the measured frequencies. (The details of the substructuring method are reviewed in [6], or also in Chap. 9 of the text by Ginsberg [21]).

The implicit assumption is that the error in the natural frequencies found when connecting the subcomponent to a fixture in the validation experiment will be representative of the errors that will be obtained when the substructure model is assembled in the system of interest. This issue should be considered very carefully, as it will determine whether the

Free-Free Modes   **Mass-Loaded Modes**
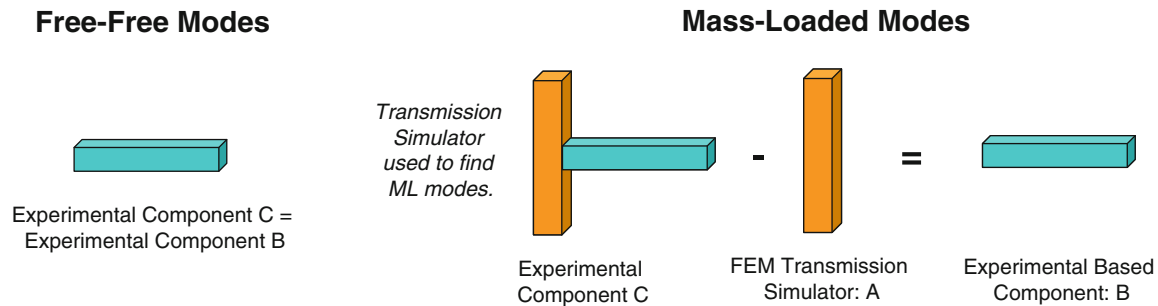
Fig. 5.1 Two common methods for obtaining a modal model of a subcomponent of interest (the cyan colored beam is the substructure of interest in this example) (color figure online)

validation experiment is useful. If the validation experiment is well designed, then good correlation between the test results and the natural frequencies predicted with the substructure model will provide a strong indication of how accurate the substructure model.

Eventually, one might be able to rigorously quantify the accuracy of the substructure model using an approach such as this, but that would probably require more tests than are likely to be practical. On the other hand, if one is willing to make a strong assumption, for example that the errors in the natural frequencies are normally distributed and that each natural frequency has the same standard deviation, then one could estimate bounds on the substructuring predictions. There is no evidence yet to support such an assumption so for the moment this method should be expected to give only a qualitative measure of the accuracy of the substructure model.

5.3   Results

The proposed validation methodology will be explored using the system pictured in Fig. 5.1, where the substructure of interest is a 12-in. long beam with 0.75-in. height and 1.0-in. length (similar to the system studied in [6]). The transmission simulator for the mass-loaded modes method is a 6.0-in. long beam with the same cross section. (The transmission simulator used here differs significantly from that used in [6].) The frequency range of interest for this very stiff structure is 0–20 kHz. All of the components were modeled using one dimensional finite element models (three degrees of freedom per node) with 30 nodes for the system of interest and 21 nodes for the transmission simulator.

Two different models were then obtained, one using the Free-Free modes method, denoted FF, and the other using the mass-loaded interface method, denoted ML. The natural frequencies of these two models are shown in Table 5.1 below. In practice the FF model would have been obtained by performing a modal test on the 12.0-in. beam with soft supports simulating free-free boundary conditions. Here such a test was simulated by simply taking the FF model to be a modal model with all of the modes of the beam that were within the testable bandwidth (e.g. assuming that a perfect test was performed). Here the testable bandwidth was taken to be 0–20 kHz, so ten modes were obtained, three of which are rigid body modes. As discussed previously, a FF model such as this without residual terms is known to be a poor model for a substructure. In the following the goal is to see whether the results of the validation experiment can be used to discriminate between this poor model and the more accurate ML model.

To obtain the ML model for the beam, a test on the T-beam system was simulated by coupling the transmission simulator to the beam (resulting in a 30*3 + 21*3-3 = 150 DOF system). Then all of the modes of the system below 20 kHz were assumed to be measured perfectly, resulting in a 15 mode model for the beam. The transmission simulator was then removed using the approach in [6] using only the displacements at each node in the FEA models for each beam (not the rotations) for a total of 42 measurement points. In this process, seven negative TS modes are added to the system and seven constraints applied, so the total number of DOF is still 15. Of these 15 modes, 12 remain below 20 kHz and 10 of those\correspond closely with the free modes of the beam. The other two natural frequencies, at 695 and 1,037 Hz, are spurious modes that involve very little motion of the beam of interest. (The transmission simulator and its negative model dominate the motion of these modes; they would not make an important contribution to any FRF on the structure of interest.) Finally, the ML mode model has three additional modes above 20 kHz that involve other motions of the beam; these are the modes that allow the ML model to capture motions where the shear and moment at the connection point are nonzero.

Table 5.1 Natural frequencies (Hz) of FF and ML subcomponent models for the beam

Mode	FF	ML
1	0	0
2	0	0
3	0	0
–	–	695
–	–	1,037
4	1,082	1,083
5	2,982	2,993
6	5,845	5,892
7	8,422	8,424
8	9,663	9,809
9	14,435	14,831
10	16,869	16,892
11		25,954
12		31,480
13		2.9E + 09
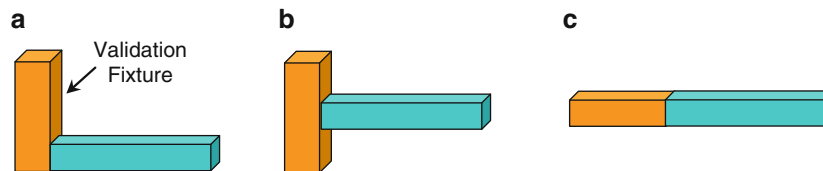
Fig. 5.2 Three potential validation experiments for the beam substructure shown in Fig. 5.1. A fixture with known properties is attached (*orange colored beam in the figure*) and the natural frequencies of the assembly are measured and compared to predictions

Table 5.2 Natural frequencies of FF and ML subcomponent models for the beam for validation case (a) in Fig. 5.2

Mode	True (Hz)	FF (Hz)	FF % error	ML (Hz)	ML % error
4	768.5	777.9	**1.2**	771.8	**0.4**
5	1699.1	1875.0	**10.4**	1721.1	**1.3**
6	3155.8	3452.8	**9.4**	3196.3	**1.3**
7	5710.8	5919.5	**3.7**	5767.1	**1.0**
8	7752.6	7785.4	**0.4**	7758.2	**0.1**
9	9167.7	9227.7	**0.7**	9240.6	**0.8**
10	12813.4	13310.6	**3.9**	12877.4	**0.5**
11	14534.8	15459.1	**6.4**	14757.8	**1.5**
12	17500.3	20110.2	14.9	17783.5	1.6
13	19691.8	30085.6	52.8	123620.1	527.8

5.3.1 *Validation Experiment: Simulating Perfect Measurements*

Now a validation experiment is simulated as follows. A finite element model is created for a validation fixture that is a beam of the same cross section at the transmission simulator, 3.0-in. long, modeled in FEA with 11 nodes. This validation fixture is attached to the full FEA of the beam at its end as shown in Fig. 5.2a and all of the modes below 20 kHz are extracted to use as validation data. (This assumes that one could extract all of the modes perfectly in a test, hence they are labeled "true" below.) Then the FF and ML substructure models are used with the FEM of the validation fixture to predict the modes the assembly. The natural frequencies obtained are shown below in Table 5.2. The results show that the ML model much more accurately predicts the first several modes of the system, having a maximum natural frequency error of 1.5% as compared to 10.4% for the FF model. The average error in each case is 0.9% for the ML model and 4.5% for the FF model. Hence, the validation experiment has revealed that the ML model is quite an accurate model for the subcomponent, while the FF model is less accurate although perhaps adequate for some purposes.

Table 5.3 Natural frequencies of FF and ML subcomponent models for the beam for validation case (b) in Fig. 5.2

Mode	True (Hz)	FF (Hz)	FF % error	ML (Hz)	ML % error
4	839.9	842.1	**0.3**	840.4	**0.1**
5	2261.5	2334.6	**3.2**	2271.1	**0.4**
6	3982.0	4476.0	**12.4**	4045.3	**1.6**
7	6157.0	6619.5	**7.5**	6246.8	**1.5**
8	7038.7	7689.8	**9.2**	7096.1	**0.8**
9	9805.2	10815.8	**10.3**	9996.7	**2.0**
10	12600.8	13277.4	**5.4**	12702.6	**0.8**
11	14605.8	15998.5	**9.5**	14921.6	**2.2**
12	17293.0	21921.1	26.8	17460.1	1.0
13	20203.7	33475.3	65.7	49402.7	144.5

This same procedure was repeated using the configuration shown in Fig. 5.2b, where the validation fixture is attached at its center in much the same way that the transmission simulator was attached, although recall that the TS was 6.0 in. long while the validation fixture is only 3.0 in. long, so its properties are quite different. The results in this case are shown in Table 5.3. The maximum and mean errors for the FF substructure model are 12.4% and 7.2% for this validation experiment, while the maximum and mean errors for the ML model are 2.2% and 1.2% respectively, significantly lower than those for the FF model.

A third validation experiment similar to the case in Fig. 5.2a was performed, only with a 6.0 in. long validation fixture (twice as long as the fixture used in the results presented in Table 5.2). Hence, the validation fixture is the same as the transmission simulator except that it is connected at its end rather than at its mid-point. In this case it was observed that the errors in the predictions of the FF substructure model were about 20% smaller than those reported in Table 5.2, while those of the ML model remained about the same. There were also quite a few additional modes in the testable bandwidth (0–20 kHz). This suggests, and it seems reasonable that, as the validation fixture becomes larger, that the modes obtained may become more dependent on the (known) properties of the validation fixture and less dependent on the substructure model.

A few other cases were also explored, but they will not be presented in detail since the results presented above are representative of all of the cases studied.

5.4 Conclusions

This work has proposed a methodology for validating experimentally derived models for substructures by performing an additional experiment with a known fixture attached. The experimentally measured natural frequencies in this configuration are then compared with the predicted natural frequencies to assess the quality of the substructure model. Some simple cases were studied where validation experiments were simulated for two substructure models, one based on free-free modes (and which was known to be fairly inaccurate) and another based on mass-loaded interface modes (which was thought to be superior). In all of the cases shown the validation experiment did suggest that the ML model was superior. The differences between the predicted natural frequencies (using the substructure model) and those obtained in the validation test are thought to be indicative of the quality of the substructure model. This will be explored in more detail in future works.

This work has sought to detect inadequacies in a substructure model caused by modal truncation (i.e. inadequate span of the modal basis of the subcomponent modes). Modal truncation is thought to be a significant contributor to the uncertainty in a modal substructure model, but there are other important sources of uncertainty as well. The same procedure might also be useful for quantifying the error in a substructure model due measurement uncertainty. Another potential source of error is the way in which the connection between two substructures (e.g. the bolted joint) is approximated. This interface is captured experimentally using the transmission simulator method, so this type of uncertainty might also be addressed using this approach. Future works will explore these issues.

References

1. Imregun M, Robb DA, Ewins DJ (1987) Structural modification and coupling dynamic analysis using measured FRF data. In: 5th international modal analysis conference (IMAC V), London
2. Ind P (2004) The non-intrusive modal testing of delicate and critical structures. Ph.D. thesis, Imperial College of Science, Technology & Medicine, University of London, London
3. Allen MS, Kammer DC, Mayes RL (2010) Uncertainty in experimental/analytical substructuring predictions: a review with illustrative examples. In: International Conference on Noise and Vibration Engineering 2010 (ISMA2010), Leuven
4. de Klerk D, Rixen DJ, Voormeeren SN (2008) General framework for dynamic substructuring: history, review, and classification of techniques. AIAA J 46:1169–1181
5. Allen MS, Gindlin HM, Mayes RL (2011) Experimental modal substructuring to estimate fixed-base modes from tests on a flexible fixture. J Sound Vib 330:4413–4428
6. Allen MS, Mayes RL, Bergman EJ (2010) Experimental modal substructuring to couple and uncouple substructures with flexible fixtures and multi-point connections. J Sound Vib 329:4891–4906
7. Sjovall P, Abrahamsson T (2008) Substructure system identification from coupled system test data. Mech Syst Signal Process 22:15–33
8. Nicgorski D, Avitabile P (2010) Conditioning of FRF measurements for use with frequency based substructuring. Mech Syst Signal Process 24:340–51
9. De Klerk D (2009) Dynamic response characterization of complex systems through operational identification and dynamic substructuring. Ph.D. thesis, Delft University of Technology
10. Kanda H, Wei ML, Allemang RJ, Brown DL (1986) Structural dynamic modification using mass additive technique. In 4th international modal analysis conference (IMAC IV), Los Angeles
11. Butland A, Avitabile P (2010) A reduced order, test verified component mode synthesis approach for system modeling applications. Mech Syst Signal Process 24:904–21
12. Voormeeren SN, de Klerk D, Rixen DJ (2010) Uncertainty quantification in experimental frequency based substructuring. Mech Syst Signal Process 24:106–18
13. Carne TG, Todd Griffith D, Casias ME (2007) Support conditions for experimental modal analysis. J Sound Vib 41:10–16
14. Rubin S (1975) Improved component-mode representation for structural dynamic analysis. AIAA J 13:995–1006
15. Martinez DR, Carne TG, Gregory DL, Miller AK (1984) Combined experimental/analytical modeling using component mode synthesis. In: AIAA/ASME/ASCE/AHS structures, structural dynamics & materials conference, Palm Springs, pp 140–152
16. Doebling SW, Peterson LD (1997) Computing statically complete flexibility from dynamically measured flexibility. J Sound Vib 205:631–645
17. Karpel M, Raveh D, Ricci S (1996) Ground modal tests of space-structure components using boundary masses. J Spacecraft Rockets 33:272–277
18. Mayes RL Arviso M (2010) Design studies for the transmission simulator method of experimental dynamic substructuring. In: International seminar on modal analysis 2010 (ISMA2010), Lueven
19. Allen MS, Kammer DC, Mayes RL (2011) Metrics for diagnosing negative mass and stiffness when uncoupling experimental and analytical substructures. In: 29th international modal analysis conference (IMAC XXIX), Jacksonville
20. Mayes RL, Allen MS, Kammer DC (2012) Correcting indefinite mass matrices with the transmission simulator method of substructuring. In: 30th international modal analysis conference, Jacksonville
21. Ginsberg JH (2001) Mechanical and structural vibrations, 1st edn. Wiley, New York

Chapter 6
Experimental Realization of System-Level Vibration by Use of Single Component Based on Virtual Boundary Condition Concept

Kohei Furuya, Tetsuki Hiyama, Nobuyuki Okubo, and Takeshi Toi

Abstract In order to meet the requirement of less vibration and less noise of complex machine, such as automobile, the system-level vibration test is carried out in spite of huge cost and time, which is conducted only when all components are able to be assembled. Although the vibration of individual component alone is different from the system-level, but a sophisticated component test is aimed to realize the system-level vibration at early development stage.

In this paper, a virtual boundary concept where the single component involved vibration source is excited by common uni-axial electro-magnetic exciters at proper point and direction with proper feed signal is proposed for experimental realization of the system-level vibration.

First the FRFs of the component are measured solely and the operating force can be identified based on operating vibration of the component. Then the FRFs of the rest component of the system and the system external force are given and consequently the transmitted forces through the connection points between the component and the rest can be determined. Therefore the target system-level vibration of the component can be predicted and the proper point and direction with proper feed signal of the exciters can be determined.

After verification by simple numerical model, the proposed method is applied to a Heating, Ventilating and Air Conditioning, HVAC component of automobile involved a blower motor. The difference of vibration and noise as well between the HVAC component and system level is revealed and finally two exciters are used to realize the system-level vibration and noise.

6.1 Introduction

In automobile companies, less vibration and less noise that affect directly on added value are strongly required and at the same time shortening development time and cost cut should be satisfied [1, 2]. However the conventional procedure which repeats try and error tests from component level till fully equipped level is time consuming with huge cost. Therefore in this paper a Virtual Boundary Condition (hereafter denoted as VBC) concept based on the following four steps is proposed to realize the system-level vibration and consequently noise by use of a single component that is interested in investigation, usually involves vibration source. As a result this enables us the evaluation of vibration and noise at early development stage.

First the Frequency Response Functions, FRFs of the individual component are independently measured. And the component under consideration is sorely operated to identify the generated force based on FRF matrix inversion with operating vibration responses [3, 4].

At the second step, the transmitted forces between the component and the rest can be determined by using the FRFs of the rest and given system external force and thus the system-level vibration as target can be predicted without assembling all components [5].

K. Furuya (✉) • T. Hiyama • N. Okubo • T. Toi
Department of Precision Mechanics, Chuo University, 1-13-27 Kasuga, Bunkyo-ku, Tokyo 113-8551, Japan
e-mail: furuya@mech.chuo-u.ac.jp

Then at the third step, in order to generate the target vibration at specified multiple frequencies (for example, harmonic order of rotating motor), the point and direction of the exciters are determined as the directional force vector and weighting factors as mentioned later.

Finally the VBC is realized to feed proper excitation signal to the exciters and the system-level vibration and noise of the component can be obtained for further investigation of vibration and noise improvement.

6.2 Influence of Component on System-Level Vibration

In this chapter, the difference of vibration between the component-level and system-level when all components are assembled is discussed and thus the problem of component test is revealed and the need of proposed method is mentioned.

The each case of component level is shown in Fig. 6.1; (a) a Heating, Ventilating and Air Conditioning, HVAC unit under consideration is shown, which involves a blower motor rotating around Z axis at constant speed, 2,580 rpm under free-free condition, which corresponds to the pure component test. (b) a beam which is assumed as the rest of car for simplification. (c) the HVAC and the beam is connected through three bolts under free-free condition. (d) In addition to (c), a pseudo force is exerted to the end of the beam in z direction which assumes the external road or engine excitation forces. In this case, composed two sinusoidal signals at 43 and 258 Hz which correspond to the first order and sixth order of rotating speed of the blower motor are fed to the other exciter.

The comparison of SPL among these levels at specified two frequencies, which is measured in semi unechoic room by a microphone at 10 cm apart from HVAC back in + x direction is shown in Fig. 6.2. The rhombus mark expresses the case (a), namely the component level test, the circle mark for case (c) where the SPL increase at the first order and the SPL decrease at the sixth order are observed, that proves the component-level vibration is influenced by the beam. Also the square mark expresses the case (d), namely the system-level which differs from component-level by 10 dB at both frequencies.

This concludes that the vibration and noise measured in component test is quite different from those in system test.

Fig. 6.1 Schematic representation for different conditions. (**a**) HVAC: motor in operation, (**b**) BEAM, (**c**) coupled system 1: motor on HVAC in operation, (**d**) coupled system 2: motor on HVAC and a pseudo engine/road force on BEAM in operation (Operating condition)
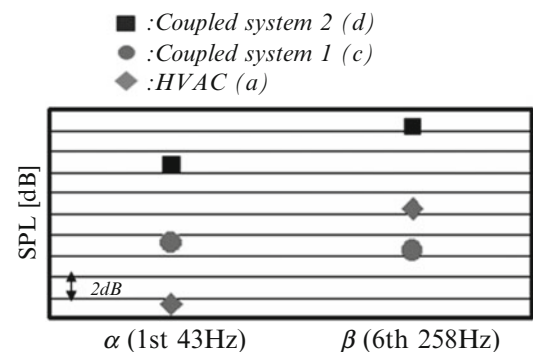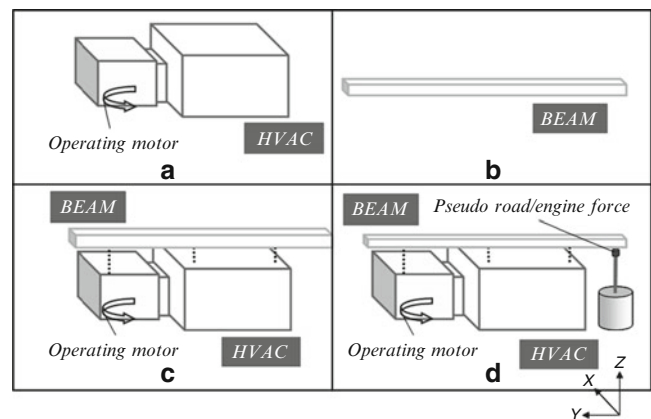
Fig. 6.2 Comparison of SPLs

6.3   Virtual Boundary Condition in Case of Simple FE Model

6.3.1   Identification of Transmitted Forces

The transmitted forces between the component and the rest which realize the system-level vibration without assembling all components can be predicted by use of FRF synthesize method.

Figure 6.3 shows two components system connected through two points rigidly under free-free condition as simple FE model. The component 1 under consideration is excited by constant force f_1 of 2[N] assumed an internal vibration source as a motor and the rest component 2 is acted by constant force f_2 of 1[N] as external force. Also in the lower part, the VBC concept is illustrated using only the component under free-free condition with two exciters.

The system-level vibration can be expressed by

$$x_i = H_{ij}^{comp.} f_j + H_{ik}^{comp.} r_k \tag{6.1}$$

Where x, f and r are the acceleration vector, the external force vector and the transmitted forces at boundary connection points respectively. The lower subscript i, j and k stand for the evaluation point, the system input point and the connection point respectively. H is the FRF matrix of individual component between the reference and the evaluation point and the upper subscript stands the component number.

Then this equation is rearranged into unknown and know part and the following equation can be derived where the system-level vibration and unknown transmitted force at boundary is left hand side.

$$\begin{Bmatrix} x_i \\ r_k \end{Bmatrix} = \begin{bmatrix} A & -H_{ik}^1 \\ B & H_{ik}^2 \end{bmatrix}^{-1} \begin{bmatrix} H_{ij}^1 & 0 \\ 0 & H_{ij}^2 \end{bmatrix} \begin{Bmatrix} f_{e1} \\ f_{e2} \end{Bmatrix} \tag{6.2}$$

Where

$$A = \begin{bmatrix} I & 0 \end{bmatrix}, \quad B = \begin{bmatrix} 0 & I \end{bmatrix}$$

By use of (6.2), the transmitted force can be determined by FRF of the component sorely and the external force. In this paper, two specific frequencies, 42 and 84 Hz which not coincides any resonances are chosen because in general the operating frequency is designed no to coincide the resonance and the directions of transmitted force are inherently different at these two frequencies while the uni-axial exciter only provides one directional force and therefore the direction of the exciter has to be optimized to minimize this inconsistency.
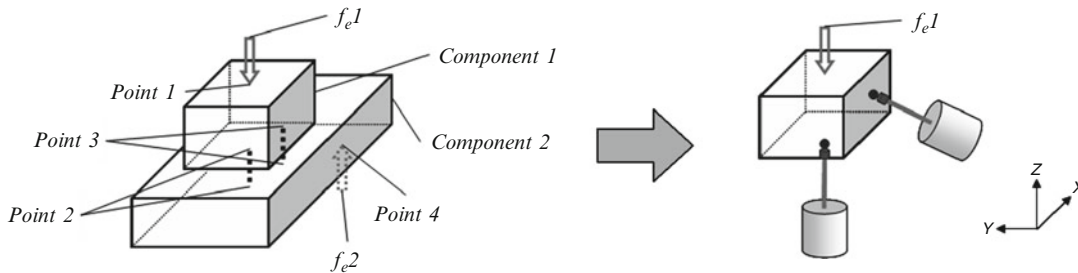
Fig. 6.3 Operating condition of a couple system and the conceptual scheme of a virtual boundary condition

Fig. 6.4 Candidate locations
for two exciters as VBC
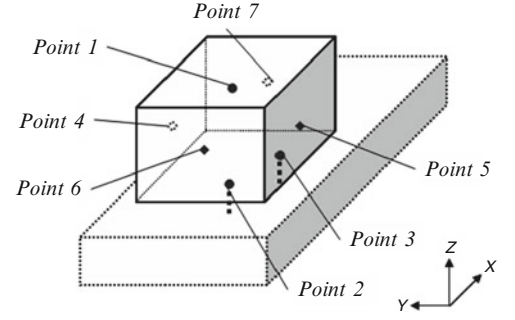
6.3.2 Setting VBC

In this section, the vibration at arbitrary points of the component is calculated as the target by transmitted forces and the setting of exciters, in this case two exciters is discussed. First the candidate excitation points are so chosen as to distribute at point 2 and 3 on the bottom surface of the component 1, that are connection point and at point 4 to 7 on 4 side surfaces except top one where the input force f_1 is located as shown in Fig. 6.4. The target acceleration vector x in system-level due to the transmitted forces is expressed as,

$$\overline{x_i} = H_{ik}^1 r_k \tag{6.3}$$

Then the directional force vector which defines uni-axial direction of each exciter and the weighting factor at two specified frequencies which defines the amplitude of feed signal are determined in the least square manner as follows. The directional force vector in x, y and z direction is denoted f_a, the weighting factor at two ω_1 and ω_2 are α and β and then the response difference ε square between the target vibration and VBC vibration can be written as,

$$\varepsilon^2 = \|\overline{x}(\omega_1) - \alpha \cdot x(\omega_1)\|^2 + \|\overline{x}(\omega_2) - \beta \cdot x(\omega_2)\|^2 \tag{6.4}$$

Where

$$x(\omega_1) = H(\omega_1)f_a, \quad x(\omega_2) = H(\omega_2)f_a$$

Therefore f_a, α and β can be determined as,

$$f_a = \left(H^H(\omega_1) \cdot H(\omega_1) + H^H(\omega_2) \cdot H(\omega_2)\right)^{-1} \cdot \left(H^H(\omega_1) \cdot \frac{\overline{x}(\omega_1)}{|\overline{x}(\omega_1)|} + H^H(\omega_2) \cdot \frac{\overline{x}(\omega_2)}{|\overline{x}(\omega_2)|}\right) \tag{6.5}$$

$$\alpha = \frac{\overline{x}(\omega_1) \cdot x(\omega_1)}{|x(\omega_1)|^2}, \quad \beta = \frac{\overline{x}(\omega_2) \cdot x(\omega_2)}{|x(\omega_2)|^2} \tag{6.6}$$

Where the upper subscript ^{H} means complex conjugate.

Because of two exciters used, the combination of exciters at point 2–7 are 15 and the least square norm of ε are shown in Fig. 6.5, which suggests the optimum combination is point 2 and 7 for two exciters. Also Fig. 6.6 shows the directional force vector and weighing factor at point 2 and 7 based on (6.5) and (6.6). At point 2 the force in z direction and at point 7 x direction is dominant. As a result the VBC is illustrated in Fig. 6.7. Also Fig. 6.8 shows the flow chart of proposed VBC concept.

Fig. 6.5 Error calculated values of VBC by two exciters
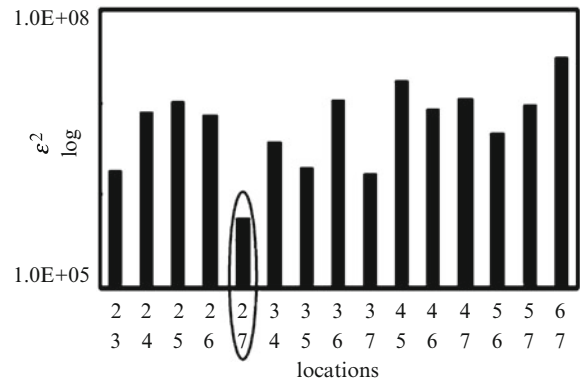
Fig. 6.6 Exciter setting as VBC: Directional force vector (*left*), Weighting factors (*right*)
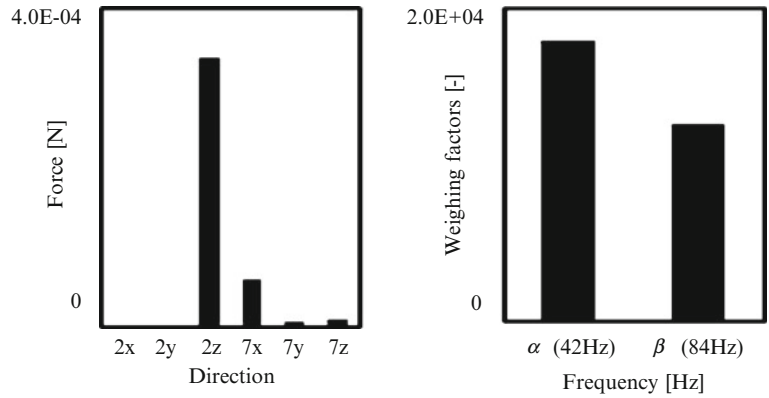
Fig. 6.7 Schematic of VBC by two exciters
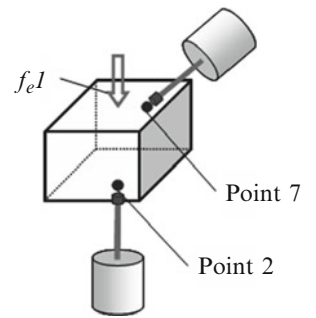
6.4 Application of VBC to HVAC

6.4.1 Force Identification of Blower Motor

In this section, the force generated by the blower motor in HVAC unit is identified by conventional FRF inverse method. From the practical point of view, the FRF at spindle of the motor is difficult to measure and thus the substitute point is chosen close to the spindle as shown in Fig. 6.9. The force identification is carried out to use the following equation as,

$$f_b = H^+ x_b \tag{6.7}$$

Fig. 6.8 Flow chart of VBC
concept
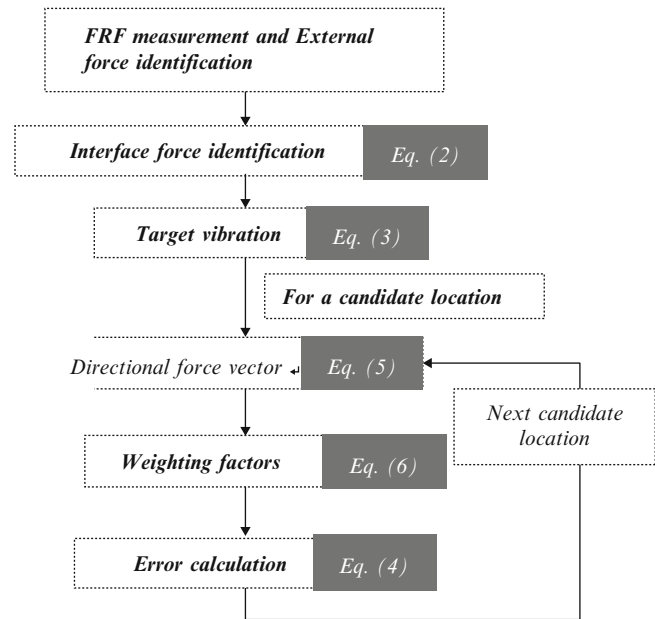
Fig. 6.9 Placement for
blower motor force
identification
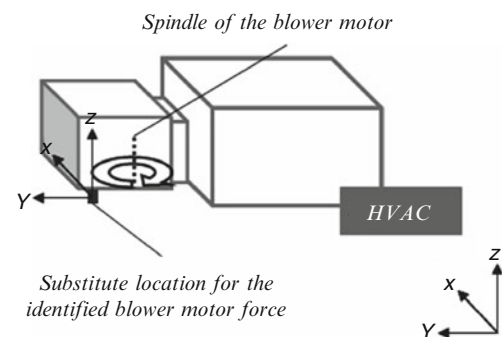
Where f_b is the identified force of the blower motor and the upper subscript $+$ means the pseudo inverse. The acceleration vector includes three connection points in three directions and six points in x direction located in the surface which contributes largely to radiate the noise.

Figure 6.10 shows the identified force where the first order of rotating speed is dominant and the harmonic order look small. But due to HVAC dynamic characteristic the six orders should be taken into account.

6.4.2 Identification of Transmitted Forces

In this section, the transmitted forces to HVAC are identified. Figure 6.11 shows a typical direct FRF of HVAC component at point 2 (indicated in Fig. 6.13) in x direction together with FRF of beam. Up to 300 Hz there are many resonances are existed in both components and consequently the system should be influenced mutually. The external system force exerted to the beam is assumed similar to the previous simple FE model. The identified transmitted force at point 2 is

Fig. 6.10 Identified blower motor force: frequency domain (*left*), time series (*right*). (2,580 rpm 43 Hz, 1 period 0.0227 s). (**a**) X direction, (**b**) Y direction, (**c**) Z direction

X direction

Y direction
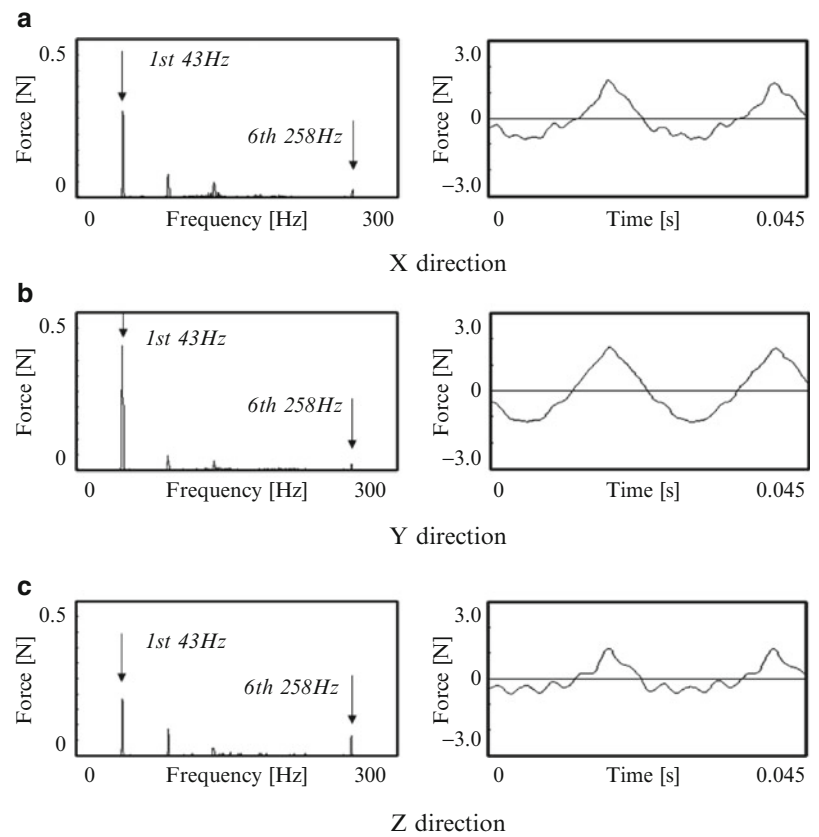
Z direction

Fig. 6.11 Driving point FRFs of components at point 2 (X direction)
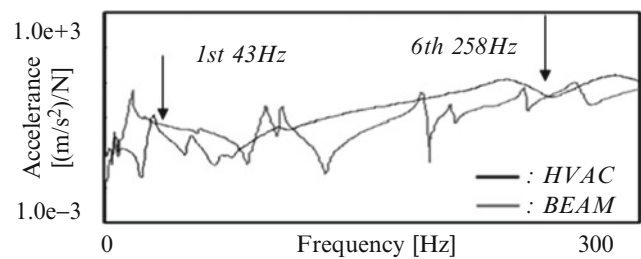
shown in Fig. 6.12 where not only the force in x and y direction but also that in z direction are found due to the rotation of the blower motor.

6.4.3 Setting VBC

In this section, the setting of VBC is discussed. Fig. 6.13 shows the candidate excitation points on HVAC unit from point 2 to 8 in which point 2, 3 and 4 are the connection points with the beam. Then the error against the target system-level vibration is shown in Fig. 6.14 for possible 21 combinations and point 2 and 4 for two exciters are found to minimize the error. Also the directional force vector and weighting factor are shown in Fig. 6.15 for two exciters. As you can see, three dimensional consideration is essential.

Fig. 6.12 Identified Interface force at Point 2 (2,580 rpm 43 Hz, 1 period 0.0227 s). (**a**) X direction, (**b**) Y direction, (**c**) Z direction
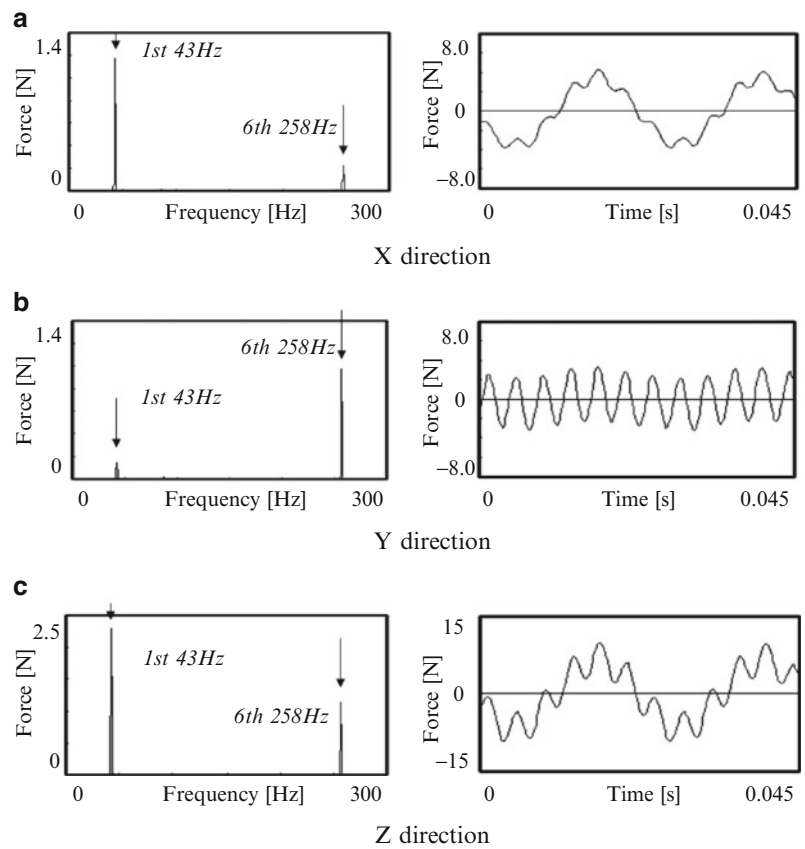
Fig. 6.13 Feasibility locations for exciters as VBC
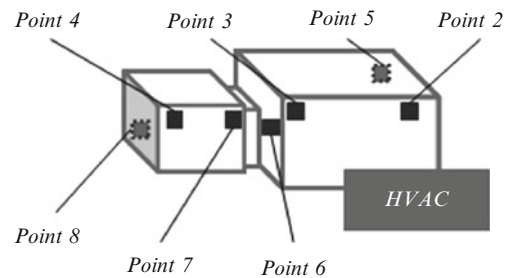
6.4.4 Application of VBC

The VBC is applied to the HVAC unit and SPL measured similar to the previous is compared with component-level and system-level. The HVAC unit under free-free condition is sorely excited by two exciters based on suggested VBC as shown in Fig. 6.16 while the blower motor rotates in 2,580 rpm. Figure 6.17 shows the comparison of SPL at evaluation point, where the difference between the system-level square marked and component-level by good use of VBC triangular marked is found about 2 dB at 43 Hz and 4 dB at 258 Hz, that improves significantly compared with rhombus mark, namely pure component test without VBC.

Fig. 6.14 Error calculated values of VBC by two exciters
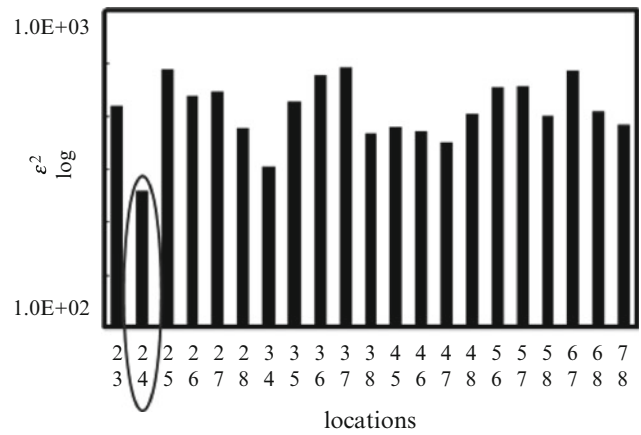
Fig. 6.15 Exciter setting as VBC: directional force vector (*left*), weighting factors (*right*)
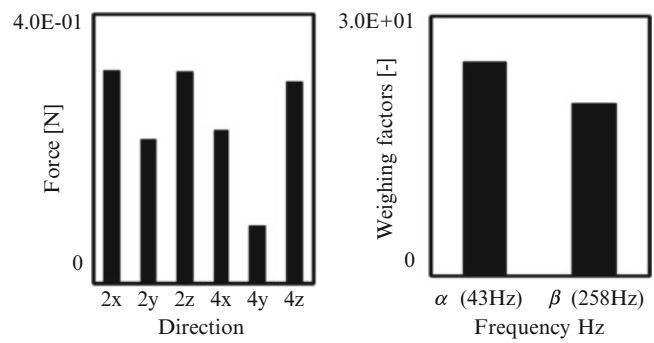
Fig. 6.16 Experimental setup for VBC by two exciters
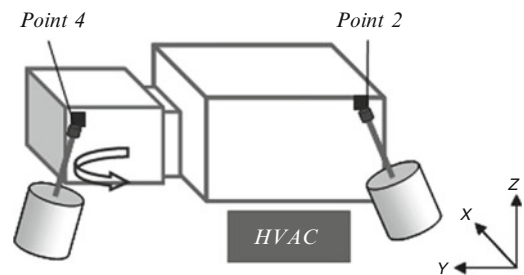
Fig. 6.17 Comparison of SPLs
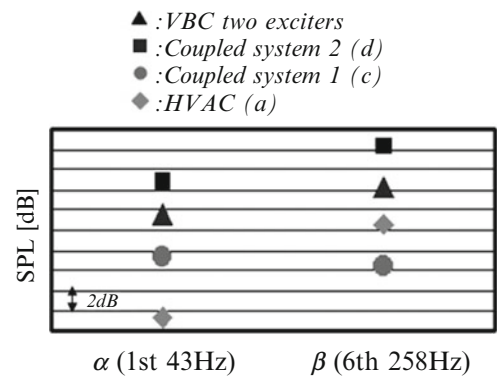
6.5 Conclusions

1. The transmitted forces between components in system level can be determined by FRFs of individual component and system external force. Therefore the target vibration of the component under consideration can be predicted.
2. This target vibration can be realized by uni-axial exciters at proper point and direction with proper feed signal, so called the Virtual Boundary Condition, VBC.
3. The VBC is successfully applied to actual HVAC unit and the system-level vibration and noise can be approximated at specified frequencies without assembling all components.

References

1. Okubo N (1982) Modal Analaysis of Machine. Chuo University Press, Tokyo
2. Heylen W, Lammens S, Sas P (2007) Modal analysis theory and testing. KUL Press, Leuven
3. Mas P, Sas P, Wyckaert K (1994) Indirect force identification based upon impedance matrix inversion: a study on statistical and deterministic accuracy. In: 19th international seminar on modal analysis conference proceedings, Leuven, pp 1049–1065
4. Parloo E, Verboven P, Guillaume P, Van Overmeire M (2003) Force identification by means of in-operation modal models. J Sound Vib 262:161–173
5. Aoyama K et al (1995) Prediction of transmitted forces between components under operating condition and its application to vibration and noise reduction. J JSPE 61(2):213–217

Chapter 7
An Introduction to the SEM Substructures Focus Group Test Bed – The Ampair 600 Wind Turbine*

Randy L. Mayes

Abstract Recent advances have provided renewed interest in the topic of experimental dynamic substructures. A focus group has been formed in the Society for Experimental Mechanics to advance the experimental dynamic substructures technology and theory. Sandia National Laboratories has developed two identical test beds to enable the focus group to advance the work. The system chosen was an Ampair 600 wind turbine with a fabricated tower and base. Some modifications were made to the system to make it more linear for initial studies. The test bed will be available for viewing in the technology booth of the IMAC exposition. A description of the turbine and modifications will be presented. Initial measurements on the full system will be described. Initial modal tests have been performed on six blades at the University of Massachusetts at Lowell [1]. Geometry and mass measurements for finite element modeling have been performed by the Atomic Weapons Establishment in the UK [2]. Initial efforts to quantify each blade as an experimental substructure are ongoing. One goal is to develop an experimental dynamic substructure of the blades and hub to couple with a finite element model of the nacelle and tower to predict parked system response.

7.1 Introduction

There has been a resurgence of interest in experimental dynamic substructures in the past few years that has been demonstrated by the number of papers and sessions at IMAC. In 2007 there were no substructures sessions, and of the 27 papers that mentioned the word "substructure", less than half a dozen addressed experimental substructures. Since then there have been three or four sessions on substructures each year. For a few years there was talk of developing a focus group on the topic and last year the group formed officially. One of the first actions was to develop a test bed structure that could be used for international collaboration. Sandia National Laboratories has developed two test beds that can be used for research, one of which is available for loan. In the experimental substructures focus group meeting at IMAC in 2011, initial plans were developed which led to the papers focused on the test bed this year.

7.2 Overview Description of the Experimental Dynamic Substructures Test Bed

In Fig. 7.1 one can see one of the two test beds. The test bed is founded upon an AMPAIR 600 wind turbine. The turbine was set upon a tapered aluminum pole representing the tower with an aluminum base plate softly supported on the trampoline. The base plate set on the trampoline should have a more consistent and more easily modeled boundary condition than the base plate set on some unknown foundation. The height is 1.85 m from the bottom of the base plate to the top of the generator housing. The rotor diameter is 1.7 m. The total mass of the test bed without the trampoline is 114 kg. For initial studies the rotor was parked by modifying the generator.

R.L. Mayes (✉)
Experimental Mechanics, NDE and Model Validation Department, Sandia National Laboratories,
5800 – MS0557, Albuquerque, NM 87185, USA
e-mail: rlmayes@sandia.gov

Fig. 7.1 Substructures focus
group test bed – Ampair 600
wind turbine

7.3   Description of the Blades

The blades are a glass reinforced polyester construction with local axes chosen as shown in Fig. 7.2. They are coated with a white epoxy. In addition to the six blades on the two test beds, six other blades were acquired for individual blade testing. The blades were given serial numbers. The blades are clamped to the hub by three bolts and two plates that sandwich the blade in place.

7.4   Description of the Hub

The hub to which the blades attach is shown in the center and bottom of Fig. 7.3. The hub has a mechanism which pitches the blades so they will not transmit power in high winds. Initial substructure studies will be focused on developing linear experimental substructures, so nonlinear elements of the system are minimized. For the test bed, the mechanism is defeated by potting the mechanism in the normal operating position to attempt to eliminate any nonlinear action such as gapping or rattling in the dynamics. The mechanism was activated by masses that were attached through bolts in the holes at the greatest radial distance from the center of the hub (seen on the black brackets in the figure). These masses were removed and only hardened steel bolts were inserted in those three locations. In addition the shaft was replaced with a modified shaft that bolts to the hub to ensure that there is no slip between the shaft and hub.

Fig. 7.2 One of the Ampair 600 blades
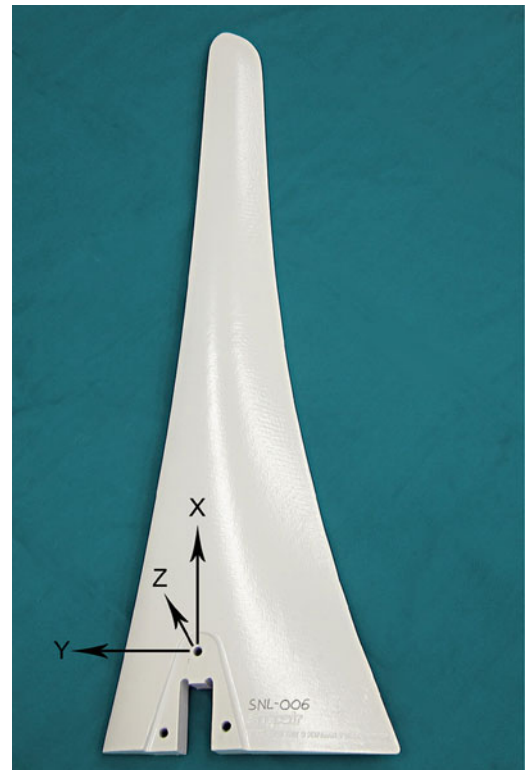
Fig. 7.3 Test bed parts – (*Left* to *Right*) – Generator housing, mass to replace the armature and field coils, coffee cup (for size comparison), hub, front bearing retainer, blade
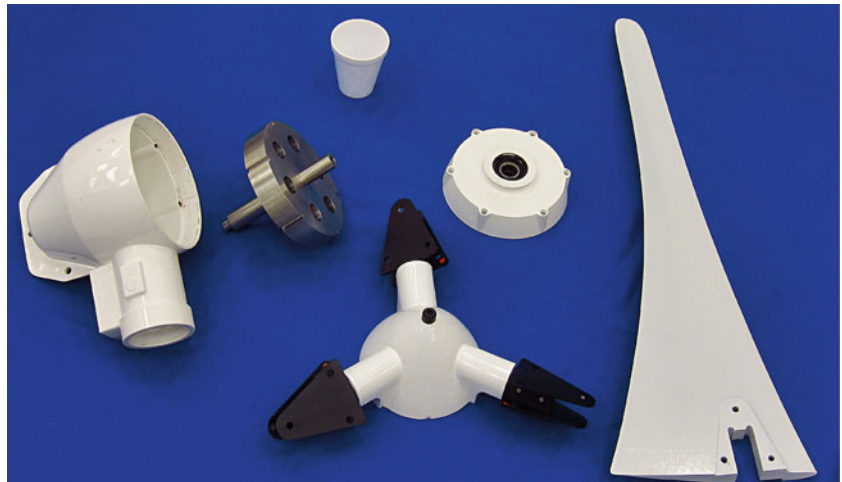
7.5 Description of the Generator

The generator is modified to make the system parked for initial studies. In Fig. 7.3 the generator parts can be seen. The white generator housing and front bearing retainer have the original bearings in them, but the armature and field coils are replaced by a single machined steel part that simulates their mass. The modified mass mounts in the bearings in the front bearing retainer and aft housing and is shown in the figure. When the front bearing retainer is bolted to the aft housing, it fixes the modified mass in the housing so that it cannot rotate in the bearings. This is another effort to minimize nonlinearity. Figure 7.4 shows the actual parts that are replaced by the modified mass. A smaller aluminum tail fin replaces the manufacturer's large tail fin to reduce the number of tail fin modes in the testable bandwidth (shown in Fig. 7.1).

Fig. 7.4 Removed generator
parts

7.6 Description of the Tower and Base

The base is made of a 7.62 cm thick by 76.2 cm diameter aluminum plate. It bolts to a 3.81 cm thick plug that is screwed and glued into the base of the pole representing the tower. The tower is made from a hollow tapered aluminum flag pole cut to 152.4 cm in length with 0.318 cm wall thickness. The tower base outside diameter is 7.62 cm and the top outside diameter is 6.39 cm. A hollow adapter sleeve that is 7.19 cm outside diameter is welded to the top of the tower to adapt to the generator housing. Three radial screws attach the base of the generator housing to the top of the tower. All this is set on a trampoline to provide a well-characterized boundary condition for the base. Setting the base on a floor was considered to be too variable a boundary condition, depending on floor roughness and material.

7.7 Linearization Attempts

The desire of the substructures focus group was to start with a linear experimental dynamic substructure, so efforts to remove possibly nonlinear parts were undertaken. In general, joints can be nonlinear. First the rotating shaft of the armature was replaced with the armature/field coil mass that would be locked to the housing when the front bearing retainer was bolted to the housing. Second, the overspeed mechanism which pitches the blades to reduce lift in high winds was potted to reduce the rattling and free play in that mechanism. The masses that activate this mechanism through centrifugal force were also removed. Third, the hub shaft was replaced with a shaft that would directly bolt to the hub to eliminate play between the hub/rotor and shaft.

7.8 A First Look at the Dynamics

A rudimentary impact modal test was performed to get a first look at the dynamics of some of the lower modes. There were not enough accelerometers to distinguish between first and second bending mode shapes of a blade or the tower. The elastic modes were extracted with the SMAC algorithm [3]. Low frequency rigid body frequencies were extracted from the peak in an autospectrum generated from a person exciting a specific rigid body motion of the test bed on the trampoline. Table 7.1 shows the modal parameters and a description of the modes extracted up to 50 Hz. Figures 7.5, 7.6, 7.7, 7.8, 7.9, 7.10, 7.11, and 7.12 show the mode shapes. Figure 7.13 shows the analytical synthesis of a complex mode indicator function from extracted modal parameters compared to the actual experimental data. The frequencies and damping change slightly with impact level, but the modal extraction was readily achievable.

Table 7.1 Modal parameters of the Ampair 600 test bed

Description	Frequency	Modal damping %
Pitch about X axis	0.875 Hz (.125 Hz resolution)	**
Pitch about Z axis	0.875 Hz (.125 Hz resolution)	**
Vertical Y bounce	2.75 Hz (.125 Hz resolution)	**
Lateral X	3.125 Hz (.125 Hz resolution)	**
Lateral Z	3.125 Hz (.125 Hz resolution)	**
Torsion about Y	3.375 Hz (.125 Hz resolution)	**
Blades bending about Y	16.97	1.5
Blades bending about X	17.68	1.8
Blades bending in phase in Z	18.76	1.87
First bend tower in X	20.4	1.74
First bend tower in Z	21.38	1.50
Second bend tower in X	29.57	2.37
Tail X motion out of phase with rotor Z motion	37.12	1.09
Rotor out of phase with nacelle rotation about X	50.80	1.36

**A few rigid body modes that were extracted from impact FRFs had damping on the order of 10%

Fig. 7.5 Top view 16.97 Hz

7.9 First Research Efforts

The substructures focus group consensus was to begin by characterizing just one blade. Initial plans of university and industry partners were to test blades in free and possibly mass loaded or fixed configurations. Also efforts were initiated to develop the solid geometry and a finite element model of the blade to aid studies. One proposal was to experimentally extract the parked rotor substructure and couple it to an analytical model of the tower and base. The hardware lends itself to these and many other possible approaches.

Fig. 7.6 YZ plane 17.68 Hz

Fig. 7.7 YZ plane 18.76 Hz

Mode 4
Frequency: 20.397 Hz
Damping: 1.743 %Cr
IDLine 1: Generated from reference 3X+

Fig. 7.8 XY plane 20.4 Hz

Mode 5
Frequency: 21.382 Hz
Damping: 1.496 %Cr
IDLine 1: Generated from reference 3Z+

Fig. 7.9 YZ plane 21.38 Hz

Fig. 7.10 XY plane 29.57 Hz

Fig. 7.11 Top view 37.12 Hz

Mode 10
 Frequency: 50.801 Hz
 Damping: 1.353 %Cr
 IDLine 1: Generated from reference 1001Z+

Fig. 7.12 YZ plane 50.80 Hz

Fig. 7.13 CMIF for 120 degree blade – analytical (*dashed*) versus experimental (solid)

References

1. Harvey J, Avitabile P (2012) Comparison of some wind turbine blade tests in various configurations. In: Proceedings of the 30th international modal analysis conference, paper no. 101, Jacksonville
2. Nurbhai M, et al (2012) Comparison modal assessment of wind turbine-blade in preparation of experimental substructuring. In: Proceedings of the 30th international modal analysis conference, paper no. 115, Jacksonville
3. Hensley DP, Mayes RL (2006) Extending SMAC to multiple references. In: Proceedings of the 24th international modal analysis conference, St. Louis, pp.220–230

Chapter 8
Modal Assessment of Wind Turbine Blade in Preparation of Experimental Substructuring

Mohsin Nurbhai and David Macknelly

Abstract As an active member of the International Modal Analysis Conference (IMAC) Substructuring Focus Group, AWE has agreed to participate in an international effort in the development of analytical and experimental substructuring techniques. The field of analytical and experimental substructuring in highly complex, especially the coupling of the two methods, and deservedly attracts an international audience. A large and diverse working group directly benefits this development activity, in order to make significant progress over the next few years. The overall aim of the programme is to engage parties interested in dynamic substructuring to attack and conquer the practical problems limiting the use of substructures. In response to the IMAC XXIX, Jacksonville, Florida, experimental substructuring focus group meeting, the Structural Dynamics team at AWE have conducted modal analysis work on a test bed, in preparation for future experimental substructuring efforts to be conducted by the focus group.

Following the first meeting of the technical focus group at IMAC XXIX, it was unanimously agreed by all stakeholders that the mechanism to carry out this development would be via the substructuring of a wind turbine, specifically the Ampair 600 Wind Turbine, manufactured by a UK based company. The longer term deliverable of this work stream would be to successfully model this wind turbine system where the turbine blades were modelled from experimentally derived substructures and other components were modelled as analytical substructures. This offers a unique capability to better model complex structures with complex material properties in an assembly configuration.

Three Ampair 600 Wind Turbine blades were procured with the aim to understand the characteristics of their structure. The blade is divided into sections, a Blade and an Anchor to the rotor. The Blade is believed to be made from a composite of glass fabric and polypropylene matrix, and the Anchor, from a foam of thermoplastic based syntactic polymer.

To derive high precision blade geometry, a non-contact scanning and reverse engineering approach was used. For complex freeform geometry, conventional contact measurement methods are unsuitable due to their low point density and rate of capture. For this reason a Romer Absolute articulated arm with Perceptron V5 laser scanner was used. This system was specifically used due to its tolerance of reflective surfaces and those with differing contrast, as present in the turbine blades. All three blades were measured and the resulting stitched surface meshes were put out in standardised CAD format. A master (average) mesh was constructed from the combinations of the individuals by averaging the errors between the three datasets over their complete geometry. A two-stage best fit alignment was used comprising of a coarse alignment by minimising deviations between a small number of sample points followed by a fine alignment using a more dense point sample. Mesh averaging the surfacing was done using Rapidform XOR3 and the final model generation was completed in Unigraphics NX5.

A full modal assessment was carried out by the authors, consisting of Modal free-free testing and Modal free and fixed analysis, together with an analytical model update and full correlation between the experimental and analytical results. Finite element models (FEM) for each of the blades, tuned to their relative mass, were generated in the ANSYS analysis code. Material models in these analytical models were further optimised following correlation with test data.

The three turbine blades were each scanned in a Free-Free condition using a Polytec 3D Scanning Laser Doppler Vibrometer. Using this technique it was possible to get a relatively high spatial density of measurement points compared to traditional techniques such as accelerometers. In addition to the high spatial density, translational DoFs were measured in all three axes. The measurements were post-processed and its modal parameters were fitted using the ICATS software package.

M. Nurbhai • D. Macknelly (✉)
Structural Dynamics Group, AWE Aldermaston, Reading RG7 4PR, UK
e-mail: david.macknelly@awe.co.uk

The results from the physical tests were mapped to a reduced FEM. This allowed like-for-like, test-to-test and test-to-FEM correlation using a number of standard correlation metrics.

As an immediate follow-on to this piece of work, the authors suggest that fixed-based modal tests of the three blades are carried out including to-test and to-FEM correlation for completeness at the least. It is also proposed that further material testing is carried out on blade material samples, including visual inspection of the fibre layup and Dynamic Material Analysis to help better characterise its mechanical response.

AWE (c) Crown Owned Copyright 2012

Chapter 9
Comparison of Some Wind Turbine Blade Tests in Various Configurations

Julie Harvie and Peter Avitabile

Abstract As part of the SEM Dynamic Substructuring Subgroup, several different dynamic modeling scenarios are to be studied in an attempt to identify an overall substructuring modeling strategy that can be used. A wind turbine system was chosen as a test bed to deploy some of those techniques. Two separate wind turbines with a total of six blades are available for this study.

Modal tests were performed with the six turbine blades in a free–free, built-in and mass loaded configuration to develop modal data bases for comparison of the blades. Each of the six blades were tested and compared to each other to identify the similarity and differences in the blades. The results of that study are presented in this paper.

9.1 Introduction

Dynamic substructuring techniques have been used for the development of analytical models for many years. Experimental techniques utilizing modal data have also been used for several decades and more recently use of frequency based substructuring techniques have gained popularity. However, many times the experimental data sets lack some of the necessary degrees of freedom for the development of the model or have been plagued by measurement issues pertaining to measurement noise that have often caused the approaches to not produce the high fidelity models that are expected for this type of modeling.

The Dynamic Substructuring Subgroup, newly formed as part of the SEM International modal Analysis Conference community, has placed emphasis on developing these approaches and to provide basic guidance in the utilization of these techniques. The group is focused on a "best practices" type of approach to help all of the experimental structural dynamic engineers in deploying these valuable modeling techniques in the best manner possible given the current understanding of the methodology and common pitfalls using actual experimental data to develop these models. The group is also focused on moving this technology forward in a meaningful and practical way to optimize the benefits of these modeling strategies.

As such, the SEM Dynamic Substructuring Subgroup has started to plan out a candidate structure that can be used to deploy these modeling strategies and provide guidance on the use of the approaches through the use of a small Ampair wind turbine blade. Sandia Labs has initiated the process and has companion papers at IMAC 30 (2012) [1] to describe the structure and the sets of data and databases that will be developed for general use in the structural dynamics community; a website has been set up for the group's activities [2].

The work presented in this paper focuses on the experimental modal tests that were performed on six turbine blades that were obtained from two separate Ampair wind turbines. The blades were tested in three separate configurations and all the blades were compared to each other as part of this exercise. Note that the majority of test and analysis results presented here were conducted as part of the University of Massachusetts Lowell's Vibrations course during the Spring 2011 semester; these results were part of educational studies for that class and as such, the results should be used with that in mind. The sets of cases studied along with the comparison of the results are presented next.

J. Harvie (✉) • P. Avitabile
Structural Dynamics and Acoustic Systems Laboratory, University of Massachusetts Lowell,
One University Avenue, Lowell, MA 01854, USA
e-mail: Harvie.Julie@gmail.com

9.2 Cases Studied

For this study, six Ampair wind turbine blades were used as the test subjects to explore the similarities and differences between blades. Impact tests were performed on the turbine blades in several configurations which can be summarized as:

Case 1 – Blade hanging free–free
Case 2 – Blade with mass loaded connection at root end
Case 3 – Blade clamped to sizeable anchor

9.2.1 Structure Description & General Modeling/Testing Performed

The six Ampair blades each weighed approximately 1.8 lb and were approximately 30" in length along the centerline. The blades had 20 impact points specified to be at roughly the same position on each blade. Note that the impact locations were defined using three consistent hole mounting locations for reference; slight errors in the locations of these reference holes did cause a small amount of variation that could visibly be seen in the actual geometric location for the 20 points identified for impact testing on each of the blades. All blades were serialized by Sandia Labs with the notation of #001, #002, #003, #004, #005, and #006 for reference. A photo of one of the turbine blades with impact locations identified is shown in Fig. 9.1.

Impact excitation was used to study the first few modes of the blades in the flapwise direction. For cases 1 and 2, the tests were performed as part of a class project where six teams of two students tested each blade. Various testing parameters were used by each group, but generally a bandwidth of either 300 Hz or 500 Hz was employed with 800 lines of spectral resolution. For case 3, testing was performed on all blades by a single individual with a bandwidth of 300 Hz and 1,600 lines of spectral resolution. Consistently five averages were taken for all tests. A reference accelerometer with a nominal sensitivity of 10 mV/g was attached to the back side of each of the blades at a point near the tip using wax; generally point 18 was chosen for the location of the accelerometer. Some modes were not able to be measured in a few cases where different points were chosen for the location of the reference accelerometer.

9.2.2 Case 1 – Blade Hanging Free–Free

The blades were each tested in a free–free condition by hanging them with bungee cords that were hooked to threaded rods fixed through the holes toward the root of the blades using nuts and washers. Illustration of test setup, similar for all blades, is shown in Fig. 9.2. Frequency results are displayed in Table 9.1 along with drive point FRFs up to 300 Hz for consistency. Consideration of the natural frequencies reveals that blade S/N #003 consistently had the highest frequency for each mode, suggesting that there might be something unique about its material properties; however the densities of all blades are likely equal because the weights of each blade were approximately the same. After extracting the normalized mode shapes from the test data, a MAC was performed between blades with the tip point excluded because it was observed to have inconsistent behavior for many of the mode shapes due to impact difficulties. The MAC is displayed in Table 9.2, where the strong mini-diagonals indicate good correlation of subsequent modes; the average MAC for the first three modes of all the blades was 98.3, with a minimum of 90.5. Note the gray boxes indicate immeasurable modes due to reference location.
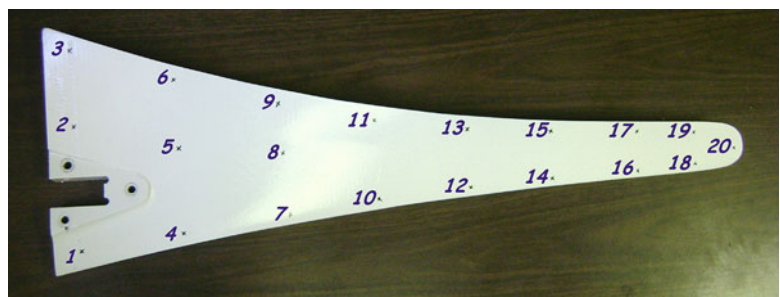
Fig. 9.1 Ampair blade with impact points labeled, consistent for all six blades

Fig. 9.2 General test setup
of blade in free–free
configuration
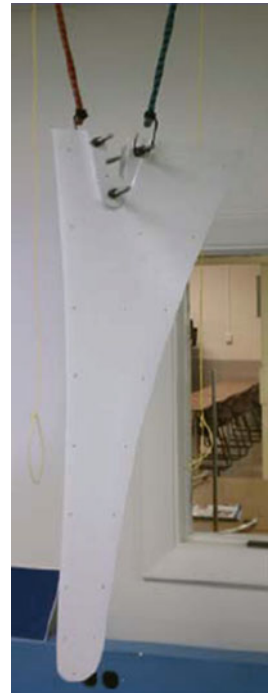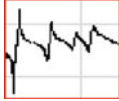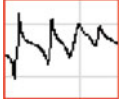
Table 9.1 First five natural frequencies of six Ampair blades in flapwise direction tested in free–free configuration

Blade	#001	#002	#003	#004	#005	#006
Mode	Hz	Hz	Hz	Hz	Hz	Hz
1	40.2	42.6	45.1	41.0	40.7	40.3
2	119.9	127.4	132.5	120.5	122.0	122.1
3	183.2	191.3	194.3	187.2	181.1	193.9
4	225.7	245.0	251.5	240.1	N/A	235.6
5	303.3	319.6	323.8	N/A	306.5	319.4
Ref dof	Pt 18	Pt 18	Pt 18	Pt 20	Pt 19	Pt 18
Drive pt FRF 300 Hz BW						

9.2.3 Case 2 – Blade with Mass Loaded Connection at Root End

The blades were each tested in a mass loaded condition by attaching a 2.45 lb aluminum block, slightly greater mass than that of the blades, to three threaded rods fixed through the holes toward the root of the blades using nuts and washers. The apparatus was then hung by two bungee cords that were hooked to the same threaded rods where the added mass was located. Illustration of test setup, similar for all blades, is shown in Fig. 9.3. Table 9.3 shows frequency results along with drive point FRFs up to 300 Hz for consistency. Consideration of the natural frequencies reveals that once again blade S/N #003 consistently had the highest frequency for each mode, supporting the notion that there is something unique about its material properties. After extracting the normalized mode shapes from the test data, a MAC was performed between blades with the tip point excluded because it was observed to have inconsistent behavior for many of the mode shapes due to impact difficulties. The MAC is displayed in Table 9.4, where the strong mini-diagonals indicate good correlation of subsequent modes; the average MAC for the first three modes of all the blades was 97.8, with a minimum of 88.4. Note that once again the gray boxes indicate immeasurable modes due to location of reference accelerometer.

Table 9.2 MAC correlation values for six Ampair blades in flapwise direction tested in free–free configuration

		Blade 1					Blade 2					Blade 3					Blade 4					Blade 5					Blade 6				
		1	2	3	4	5	1	2	3	4	5	1	2	3	4	5	1	2	3	4	5	1	2	3	4	5	1	2	3	4	5
Blade 1	1	100	0.9	2.7	10.3	7.1	99.5	2.5	0.9	6.9	2.3	99.8	0.6	6.5	15.0	12.7	99.7	1.7	2.1	13.1		99.3	3.9	0.1		1.4	99.1	2.6	0.5	5.4	0.5
	2	0.9	100	2.6	3.4	3.0	0.5	99.1	2.6	3.8	0.8	1.3	99.5	3.0	1.5	0.7	0.9	98.9	3.3	0.8		0.3	97.2	4.9		0.4	0.7	99.2	1.3	1.1	0.4
	3	2.7	2.6	100	7.5	13.3	1.9	2.1	97.5	2.5	5.0	2.1	1.8	98.5	4.4	10.1	1.9	2.9	99.2	2.1		1.5	0.6	96.3		4.2	3.4	1.9	95.3	0.0	5.3
	4	10.3	3.4	7.5	100	8.7	9.6	2.7	8.6	97.5	3.1	8.5	4.7	10.2	95.8	10.1	9.0	4.6	8.9	95.7		10.3	2.1	7.6		3.3	8.1	3.9	7.9	91.7	2.2
	5	7.1	3.0	13.3	8.7	100	5.5	2.8	12.7	4.5	95.1	5.7	3.1	16.6	4.8	96.1	5.5	4.1	13.2	3.9		6.6	2.7	12.2		93.4	6.7	2.7	13.7	1.3	92.1
Blade 2	1	99.5	0.5	1.9	9.6	5.5	100	1.7	0.6	6.7	1.4	99.6	0.2	5.2	14.5	10.1	99.6	1.2	1.5	12.6		99.6	2.9	0.0		0.7	98.6	1.8	0.2	5.3	0.1
	2	2.5	99.1	2.1	2.7	2.8	1.7	100	2.3	3.1	1.0	3.1	98.7	2.3	0.8	0.6	2.5	99.3	2.8	0.4		1.3	99.1	4.7		0.6	2.1	99.6	1.2	0.8	0.7
	3	0.9	2.6	97.5	8.6	12.7	0.6	2.3	100	3.5	4.9	0.6	1.7	94.0	5.0	8.3	0.5	3.0	98.3	2.6		0.3	0.7	98.8		4.2	1.2	2.1	99.0	0.2	5.7
	4	6.9	3.8	2.5	97.5	4.5	6.7	3.1	3.5	100	1.1	5.6	5.3	4.1	95.8	5.4	6.1	5.0	3.5	96.8		7.3	2.6	2.9		1.2	5.1	4.6	2.9	97.1	0.6
	5	2.3	0.8	5.0	3.1	95.1	1.4	1.0	4.9	1.1	100	1.6	0.8	6.6	0.8	92.6	1.5	1.5	4.9	0.7		2.1	1.2	4.9		99.3	2.0	0.8	6.2	0.1	99.0
Blade 3	1	99.8	1.3	2.1	8.5	5.7	99.6	3.1	0.6	5.6	1.6	100	0.9	5.4	13.1	10.8	99.8	2.3	1.6	11.4		99.3	4.5	0.0		0.9	99.1	3.2	0.3	4.4	0.2
	2	0.6	99.5	1.8	4.7	3.1	0.2	98.7	1.7	5.3	0.8	0.9	100	2.3	2.4	0.9	0.5	99.1	2.4	1.7		0.1	97.3	3.7		0.5	0.4	99.0	0.7	2.1	0.5
	3	6.5	3.0	98.5	10.2	16.6	5.2	2.3	94.0	4.1	6.6	5.4	2.3	100	7.0	13.8	5.1	3.3	97.3	4.0		4.6	0.7	91.7		5.4	7.6	2.2	90.5	0.4	6.4
	4	15.0	1.5	4.4	95.8	4.8	14.5	0.8	5.0	95.8	0.8	13.1	2.4	7.0	100	6.4	13.7	2.0	5.1	99.2		15.0	0.4	3.6		0.8	12.4	1.5	4.1	92.9	0.3
	5	12.7	0.7	10.1	10.1	96.1	10.1	0.6	8.3	5.4	92.6	10.8	0.9	13.8	6.4	100	10.6	1.4	9.5	5.6		11.8	0.6	7.6		90.9	12.2	0.5	9.2	2.2	88.0
Blade 4	1	99.7	0.9	1.9	9.0	5.5	99.6	2.5	0.5	6.1	1.5	99.8	0.5	5.1	13.7	10.6	100	1.8	1.4	11.9		99.6	3.8	0.0		0.8	99.2	2.6	0.2	4.9	0.2
	2	1.7	98.9	2.9	4.6	4.1	1.2	99.3	3.0	5.0	1.5	2.3	99.1	3.3	2.0	1.4	1.8	100	3.6	1.3		0.8	98.4	5.6		1.1	1.4	99.4	1.6	1.8	1.1
	3	2.1	3.3	99.2	8.9	13.2	1.5	2.8	98.3	3.5	4.9	1.6	2.4	97.3	5.1	9.5	1.4	3.6	100	2.7		1.2	1.0	97.7		4.2	2.7	2.6	96.3	0.2	5.3
	4	13.1	0.8	2.1	95.7	3.9	12.6	0.4	2.6	96.8	0.7	11.4	1.7	4.0	99.2	5.6	11.9	1.3	2.7	100		13.1	0.2	1.7		0.7	10.5	1.0	2.1	96.1	0.2
	5																														
Blade 5	1	99.3	0.3	1.5	10.3	6.6	99.6	1.3	0.3	7.3	2.1	99.3	0.1	4.6	15.0	11.8	99.6	0.8	1.2	13.1		100	2.3	0.0		1.3	98.5	1.4	0.1	5.8	0.4
	2	3.9	97.2	0.6	2.1	2.7	2.9	99.1	0.7	2.6	1.2	4.5	97.3	0.7	0.4	0.6	3.8	98.4	1.0	0.2		2.3	100	2.4		0.9	3.4	98.8	0.2	0.7	0.9
	3	0.1	4.9	96.3	7.6	12.2	0.0	4.7	98.8	2.9	4.9	0.0	3.7	91.7	3.6	7.6	0.0	5.6	97.7	1.7		0.0	2.4	100		4.3	0.2	4.4	98.2	0.1	5.8
	4																														
	5	1.4	0.4	4.2	3.3	93.4	0.7	0.6	4.2	1.2	99.3	0.9	0.5	5.4	0.8	90.9	0.8	1.1	4.2	0.7		1.3	0.9	4.3		100	1.2	0.5	5.6	0.1	99.0
Blade 6	1	99.1	0.7	3.4	8.1	6.7	98.6	2.1	1.2	5.1	2.0	99.1	0.4	7.6	12.4	12.2	99.2	1.4	2.7	10.5		98.5	3.4	0.2		1.2	100	2.1	0.6	3.7	0.3
	2	2.6	99.2	1.9	3.9	2.7	1.8	99.6	2.1	4.6	0.8	3.2	99.0	2.2	1.5	0.5	2.6	99.4	2.6	1.0		1.4	98.8	4.4		0.5	2.1	100	1.0	1.6	0.6
	3	0.5	1.3	95.3	7.9	13.7	0.2	1.2	99.0	2.9	6.2	0.3	0.7	90.5	4.1	9.2	0.2	1.6	96.3	2.1		0.1	0.2	98.2		5.6	0.6	1.0	100	0.1	7.3
	4	5.4	1.1	0.0	91.7	1.3	5.3	0.8	0.2	97.1	0.1	4.4	2.1	0.4	92.9	2.2	4.9	1.8	0.2	96.1		5.8	0.7	0.1		0.1	3.7	1.6	0.1	100	0.0
	5	0.5	0.4	5.3	2.2	92.1	0.1	0.7	5.7	0.6	99.0	0.2	0.5	6.4	0.3	88.0	0.2	1.1	5.3	0.2		0.4	0.9	5.8		99.0	0.3	0.6	7.3	0.0	100

Fig. 9.3 General test setup of blade in mass loaded configuration

Table 9.3 First five natural frequencies of six Ampair blades in flapwise direction tested in mass loaded configuration
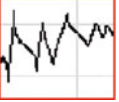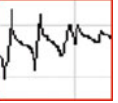
Blade	#001	#002	#003	#004	#005	#006
Mode	Hz	Hz	Hz	Hz	Hz	Hz
1	37.5	39.8	41.8	37.5	37.0	37.3
2	107.4	113.5	119.7	110.5	111.8	111.6
3	172.9	181.7	187.9	178.4	171.9	184.1
4	199.1	212.7	223.0	212.0	N/A	206.4
5	260.9	254.6	288.2	N/A	245.4	267.2
Ref dof	Pt 18	Pt 18	Pt 18	Pt 20	Pt 19	Pt 18
Drive pt FRF 300 Hz BW						

Table 9.4 MAC correlation values for six Ampair blades in flapwise direction tested in mass loaded configuration

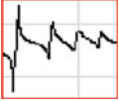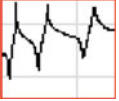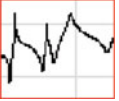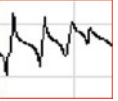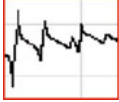			Blade 1					Blade 2					Blade 3					Blade 4					Blade 5					Blade 6				
		1	2	3	4	5	1	2	3	4	5	1	2	3	4	5	1	2	3	4	5	1	2	3	4	5	1	2	3	4	5
Blade 1	1	100	5.7	8.6	13.0	4.6	99.3	9.5	0.7	8.1	2.2	99.8	3.7	5.5	17.9	6.2	98.9	4.3	1.0	16.3		99.3	13.5	0.7		0.7	99.7	9.8	1.3	7.3	0.4
	2	5.7	100	0.2	15.5	0.8	4.4	99.1	2.2	17.4	0.2	6.2	99.4	1.5	8.6	0.2	3.8	99.5	3.6	7.0		4.2	97.2	3.9		1.3	5.0	99.0	1.9	11.4	0.4
	3	8.6	0.2	100	21.5	29.7	6.3	0.0	88.4	1.3	41.0	7.9	0.2	98.3	10.3	25.9	6.3	0.3	91.4	5.8		6.7	0.2	90.2		53.4	9.0	0.0	91.2	4.3	30.8
	4	13.0	15.5	21.5	100	12.2	13.5	11.4	22.0	83.1	15.7	12.0	16.4	23.3	94.5	14.5	12.0	17.1	23.8	89.5		13.0	10.5	26.9		34.4	14.4	13.1	23.5	90.1	9.8
	5	4.6	0.8	29.7	12.2	100	2.9	1.0	18.9	1.0	93.4	3.9	1.0	27.3	4.7	97.1	3.3	1.8	21.7	4.7		3.4	0.3	23.7		38.3	4.1	0.5	23.9	4.3	93.9
Blade 2	1	99.3	4.4	6.3	13.5	2.9	100	7.9	0.4	9.4	1.0	99.6	2.8	3.9	18.9	4.1	99.6	3.3	0.5	17.3		99.8	11.5	0.3		0.1	99.4	8.0	0.7	8.3	0.0
	2	9.5	99.1	0.0	11.4	1.0	7.9	100	1.4	13.7	0.2	10.1	98.2	0.8	5.4	0.3	7.0	98.7	2.6	4.5		7.6	99.0	2.9		1.0	8.8	99.5	1.2	8.6	0.8
	3	0.7	2.2	88.4	22.0	18.9	0.4	1.4	100	1.9	30.4	0.7	1.6	93.8	9.5	13.8	0.4	2.1	98.7	5.0		0.4	0.6	98.5		40.2	1.0	1.4	99.4	5.9	24.6
	4	8.1	17.4	1.3	83.1	1.0	9.4	13.7	1.9	100	1.5	7.5	19.1	1.7	92.1	2.3	8.2	19.1	2.4	94.5		8.6	14.8	3.6		11.4	9.0	16.4	2.1	95.5	0.3
	5	2.2	0.2	41.0	15.7	93.4	1.0	0.2	30.4	1.5	100	1.7	0.2	38.5	6.9	93.1	1.1	0.6	33.4	6.7		1.2	0.0	35.9		52.3	1.9	0.1	36.0	6.3	95.3
Blade 3	1	99.8	6.2	7.9	12.0	3.9	99.6	10.1	0.7	7.5	1.7	100	4.2	4.9	16.9	5.3	99.4	4.8	0.8	15.3		99.5	14.2	0.5		0.3	99.6	10.3	1.2	6.8	0.2
	2	3.7	99.4	0.2	16.4	1.0	2.8	98.2	1.6	19.1	0.2	4.2	100	1.3	9.7	0.4	2.3	99.7	3.0	8.1		2.6	96.3	3.3		1.4	3.2	97.9	1.4	12.2	0.4
	3	5.5	1.5	98.3	23.3	27.3	3.9	0.8	93.8	1.7	38.5	4.9	1.3	100	10.7	22.7	3.9	1.7	96.2	5.8		4.2	0.1	94.9		49.3	6.0	0.6	95.5	5.1	29.8
	4	17.9	8.6	10.3	94.5	4.7	18.9	5.4	9.5	92.1	6.9	16.9	9.7	10.7	100	7.2	16.7	9.9	10.5	97.8		17.9	5.3	12.7		23.7	19.3	7.0	10.4	94.7	2.7
	5	6.2	0.2	25.9	14.5	97.1	4.1	0.3	13.8	2.3	93.1	5.3	0.4	22.7	7.2	100	4.4	0.8	16.6	7.8		4.7	0.0	18.7		43.2	5.5	0.1	18.5	6.7	91.8
Blade 4	1	98.9	3.8	6.3	12.0	3.3	99.6	7.0	0.4	8.2	1.1	99.4	2.3	3.9	16.7	4.4	100	2.8	0.5	15.1		99.4	10.6	0.3		0.0	98.9	7.2	0.7	6.9	0.1
	2	4.3	99.5	0.3	17.1	1.8	3.3	98.7	2.1	19.1	0.6	4.8	99.7	1.7	9.9	0.8	2.8	100	3.6	8.3		3.1	96.7	3.9		1.9	3.8	98.3	1.9	12.8	1.0
	3	1.0	3.6	91.4	23.8	21.7	0.5	2.6	98.7	2.4	33.4	0.8	3.0	96.2	10.5	16.6	0.5	3.6	100	5.9		0.6	1.4	98.8		43.2	1.3	2.5	99.1	6.6	26.7
	4	16.3	7.0	5.8	89.5	4.7	17.3	4.5	5.0	94.5	6.7	15.3	8.1	5.8	97.8	7.8	15.1	8.3	5.9	100		16.3	4.6	7.5		19.4	17.5	5.9	5.8	97.0	2.9
	5																														
Blade 5	1	99.3	4.2	6.7	13.0	3.4	99.8	7.6	0.4	8.6	1.2	99.5	2.6	4.2	17.9	4.7	99.4	3.1	0.6	16.3		100	11.3	0.3		0.1	99.6	7.7	0.8	7.6	0.1
	2	13.5	97.2	0.2	10.5	0.3	11.5	99.0	0.6	14.8	0.0	14.2	96.3	0.1	5.3	0.0	10.6	96.7	1.4	4.6		11.3	100	1.7		0.6	12.7	99.1	0.4	9.2	0.2
	3	0.7	3.9	90.2	26.9	23.7	0.3	2.9	98.5	3.6	35.9	0.5	3.3	94.9	12.7	18.7	0.3	3.9	98.8	7.5		0.3	1.7	100		50.3	0.9	2.8	99.0	8.5	29.3
	4																														
	5	0.7	1.3	53.4	34.4	38.3	0.1	1.0	40.2	11.4	52.3	0.3	1.4	49.3	23.7	43.2	0.0	1.9	43.2	19.4		0.1	0.6	50.3		100	0.6	0.6	44.7	17.8	40.1
Blade 6	1	99.7	5.0	9.0	14.4	4.1	99.4	8.8	1.0	9.0	1.9	99.6	3.2	6.0	19.3	5.5	98.9	3.8	1.3	17.5		99.6	12.7	0.9		0.6	100	8.9	1.6	8.3	0.3
	2	9.8	99.0	0.0	13.1	0.5	8.0	99.5	1.4	16.4	0.1	10.3	97.9	0.6	7.0	0.1	7.2	98.3	2.5	5.9		7.7	99.1	2.8		0.6	8.9	100	1.2	10.7	0.4
	3	1.3	1.9	91.2	23.5	23.9	0.7	1.2	99.4	2.1	36.0	1.2	1.4	95.5	10.4	18.5	0.7	1.9	99.1	5.8		0.8	0.4	99.0		44.7	1.6	1.2	100	6.5	29.6
	4	7.3	11.4	4.3	90.1	4.3	8.3	8.6	5.9	95.5	6.3	6.8	12.2	5.1	94.7	6.7	6.9	12.8	6.6	97.0		7.6	9.2	8.5		17.8	8.3	10.7	6.5	100	3.5
	5	0.4	0.4	30.8	9.8	93.9	0.0	0.8	24.6	0.3	95.3	0.2	0.4	29.8	2.7	91.8	0.1	1.0	26.7	2.9		0.1	0.2	29.3		40.1	0.3	0.4	29.6	3.5	100

9.2.4 Case 3 – Blade Clamped to Sizeable Anchor

The blades were each tested in a clamped condition by bolting them to an 800-lb optical table. This was achieved by attaching an aluminum adapter plate to three threaded rods fixed through the holes toward the root of the blades using nuts and washers. The adapter plate was then bolted to the optical table at nine locations. A few photos regarding test setup are shown in Fig. 9.4. Table 9.5 shows frequency results for the first three modes of the blades along with the corresponding drive point frequency response functions; higher order modes were not studied in this configuration because the boundary condition seemed to have a noticeable contribution to the test subject's modal characteristics at higher frequencies. After extracting the normalized mode shapes from the test data, a MAC was performed between blades with the tip point excluded because it was observed to have inconsistent behavior for many of the mode shapes due to impact difficulties. The MAC is displayed in Table 9.6, where the strong mini-diagonals indicate good correlation of subsequent modes; the average MAC
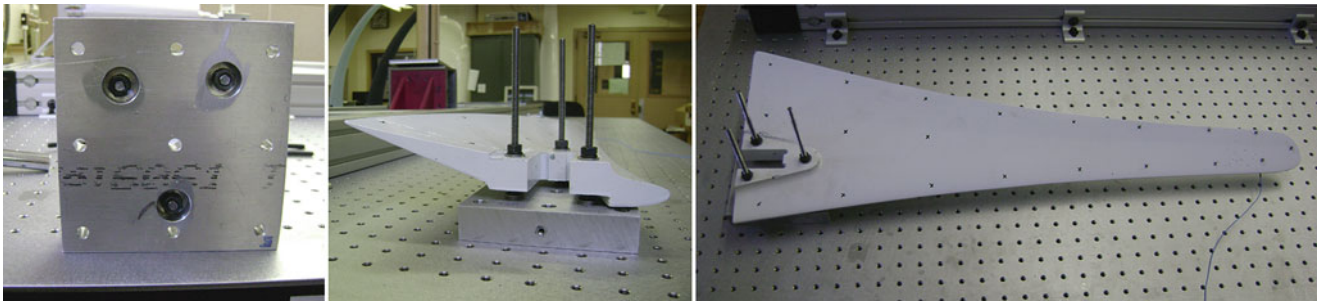
Fig. 9.4 General test setup of blade in clamped configuration

Table 9.5 First three natural frequencies of six Ampair blades in flapwise direction tested in clamped configuration

Blade	#001	#002	#003	#004	#005	#006
Mode	Hz	Hz	Hz	Hz	Hz	Hz
1	19.3	20.7	21.5	19.8	19.7	19.5
2	64.5	70.0	72.8	71.7	72.0	70.0
3	137.4	133.3	134.8	127.0	126.8	128.5
Ref dof	Pt 18	Pt 18	Pt 18	Pt 18	Pt 18	Pt 18
Drive pt FRF 300 Hz BW						

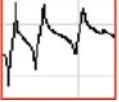**Table 9.6** MAC correlation values for six Ampair blades in flapwise direction tested in clamped configuration

		Blade 1			Blade 2			Blade 3			Blade 4			Blade 5			Blade 6		
		1	2	3	1	2	3	1	2	3	1	2	3	1	2	3	1	2	3
Blade 1	1	100	5.8	1.6	99.9	5.8	0.9	100	5.6	3.5	99.9	3.1	0.2	99.9	3.2	3.6	99.9	2.4	1.1
	2	5.8	100	18.5	5.0	99.8	47.5	5.4	99.8	25.9	5.9	99.5	35.1	6.3	99.5	33.5	6.1	99.1	32.1
	3	1.6	18.5	100	2.3	18.3	76.9	1.8	20.7	92.3	2.1	21.4	93.4	1.8	20.9	86.9	1.9	20.7	89.7
Blade 2	1	99.9	5.0	2.3	100	5.1	1.4	99.9	4.9	4.3	100.0	2.6	0.0	99.9	2.7	2.7	99.9	1.9	0.6
	2	5.8	99.8	18.3	5.1	100	47.9	5.4	99.7	26.2	6.0	99.4	34.8	6.4	99.4	33.7	6.2	99.1	32.3
	3	0.9	47.5	76.9	1.4	47.9	100	1.1	49.8	84.1	1.1	51.5	79.3	0.9	51.0	74.7	0.9	51.2	77.6
Blade 3	1	100	5.4	1.8	99.9	5.4	1.1	100	5.2	3.7	99.9	2.8	0.1	99.9	2.9	3.4	99.9	2.1	1.0
	2	5.6	99.8	20.7	4.9	99.7	49.8	5.2	100	28.2	5.7	99.4	37.6	6.1	99.4	36.0	5.9	99.1	34.6
	3	3.5	25.9	92.3	4.3	26.2	84.1	3.7	28.2	100	4.0	29.8	90.9	3.6	29.3	84.8	3.7	29.6	89.3
Blade 4	1	99.9	5.9	2.1	100.0	6.0	1.1	99.9	5.7	4.0	100	3.2	0.1	99.9	3.3	2.9	100.0	2.5	0.8
	2	3.1	99.5	21.4	2.6	99.4	51.5	2.8	99.4	29.8	3.2	100	37.9	3.5	99.9	35.1	3.4	99.8	34.3
	3	0.2	35.1	93.4	0.0	34.8	79.3	0.1	37.6	90.9	0.1	37.9	100	0.1	37.2	96.3	0.1	36.6	97.1
Blade 5	1	99.9	6.3	1.8	99.9	6.4	0.9	99.9	6.1	3.6	99.9	3.5	0.1	100	3.6	3.4	99.9	2.7	1.0
	2	3.2	99.5	20.9	2.7	99.4	51.0	2.9	99.4	29.3	3.3	99.9	37.2	3.6	100	34.5	3.5	99.8	33.6
	3	3.6	33.5	86.9	2.7	33.7	74.7	3.4	36.0	84.8	2.9	35.1	96.3	3.4	34.5	100	3.2	33.8	98.5
Blade 6	1	99.9	6.1	1.9	99.9	6.2	0.9	99.9	5.9	3.7	100.0	3.4	0.1	99.9	3.5	3.2	100	2.6	0.9
	2	2.4	99.1	20.7	1.9	99.1	51.2	2.1	99.1	29.6	2.5	99.8	36.6	2.7	99.8	33.8	2.6	100	33.3
	3	1.1	32.1	89.7	0.6	32.3	77.6	1.0	34.6	89.3	0.8	34.3	97.1	1.0	33.6	98.5	0.9	33.3	100

for the first three modes of all the blades was 95.6, with a minimum of 74.7. This somewhat low MAC can likely be attributed to blade S/N #002 since all MAC values under 80 involve blade S/N #002; when excluding this blade the average MAC for the first three mode increases to 97.1, with a minimum of 84.1.

9.3   Conclusions

The results of modal tests performed on six different Ampair turbine blades, tested in three different sets of boundary conditions, were presented. Frequency and shape correlation was presented for all of the studies performed.

These studies were performed as part of the SEM Dynamic Substructuring Subgroup work to identify "best practices" in the utilization of dynamic substructuring modeling methodologies. These results are archived as part of that project and are available for use in different dynamic modeling activities.

References

1. Mayes R (2012) An introduction to the SEM substructures focus group test bed – the ampair 600 wind turbine. In: Proceedings of the 30th International Modal Analysis Conference, Orlando
2. Dynamic Substructuring Group https://mywebspace.wisc.edu/xythoswfs/webui/_xy-40302674_1-t_RIQHeIA2

Chapter 10
Consideration of Interface Damping in Dynamic Substructuring

Pascal Reuss, Bernhard Zeumer, Jan Herrmann, and Lothar Gaul

Abstract Dynamic substructuring offers the possibility to simulate assembled systems efficiently. The coupling of the substructures can be established either by Component Mode Synthesis (CMS), or Frequency Response Functions (FRF) can be used to couple the substructures by Frequency Based Substructuring (FBS). In real systems, coupling is done by joints which can influence the dynamics of the assembled system significantly due to local damping and nonlinearities caused by friction. In this contribution the coupling of two beam-like substructures, which are assembled by a bolted joint, is considered using both coupling methods. While the substructures are linear, the implementation of the nonlinear friction forces requires special attendance in the equations of motion. The Harmonic Balance Method is therefore used to efficiently compute FRFs. Using FBS, the coupling is established directly in the frequency domain. The method provides the possibility to replace the dynamics of individual substructures by measured FRFs of the uncoupled system and combining numerical and experimental models. Alternatively, Component-Mode-Synthesis is used.

10.1 Introduction

Substructuring methods are of great interest for the computation of large finite element models of assembled structures. A separate consideration of each substructure offers several advantages in comparison with an investigation of the whole system. A validation of each substructure can be realized much easier compared to the consideration of the entire system. A substructure can be replaced without changing the whole model and even experimental data can be used to describe the dynamics of a substructure.

In real structures coupling is done by bolted joints where friction effects play an important role [3, 7, 8]. The damping contribution of the joints can significantly change the system behavior due to the fact that the damping is much higher than the overall material damping. Additionally, friction in joints is a local damping effect that requires a special attendance when modeling the substructure interface. In this paper, special focus lies on the dynamics within the interface and it is shown how this interface dynamic can be implemented in the system equations to compute FRFs.

In order to give an impression of the task which is treated in this work, Fig. 10.1 shows two substructures *a* and *b* which are coupled by two nonlinear elements. The elements are connected to the substructure at the interface node pairs (2, 4) and (3, 5). Now, the transfer path from the excitation point 1 to the considered output at point 6 is of interest. By reference to this example, two different coupling methods are presented in this paper, which is organized as follows. In the next section, Component Mode Synthesis is introduced and the Craig-Bampton reduction basis is reviewed for clarity. Then, it is demonstrated how to integrate a nonlinear local joint model in the component synthesis. Subsequently, the Frequency-based Substructuring is presented and both methods are tested using an example system. The suggested simulation approach is finally applied to a finite element model of two coupled beams. The paper closes with an short conclusion.

P. Reuss (✉) • B. Zeumer • J. Herrmann • L. Gaul
Institute of Applied and Experimental Mechanics, University of Stuttgart, Pfaffenwaldring 9, 70550 Stuttgart, Germany
e-mail: reuss@iam.uni-stuttgart.de; herrmann@iam.uni-stuttgart.de; gaul@iam.uni-stuttgart.de

Fig. 10.1 Coupling of two substructures with two nonlinear elements
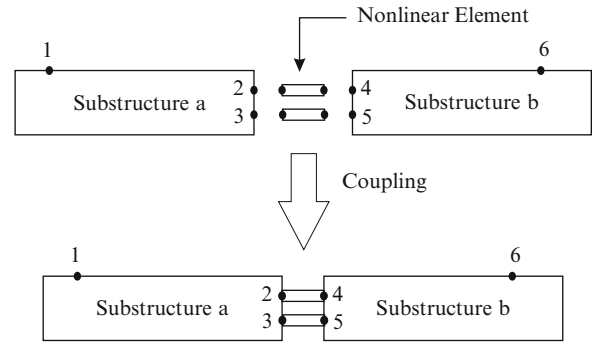
10.2 Component Mode Synthesis (CMS)

The concept of Component Mode Synthesis (CMS) combines model order reduction of component models with substructuring methods to obtain a model with a minimal set of degrees of freedom (DOF) and a sufficient approximation of the dynamic behavior of the assembled system [2, 9]. For large finite element models, the Craig-Bampton method is one of the standard methods to establish component model order reduction and subsequent coupling of substructures.

10.2.1 Craig-Bampton Recduction Basis

Using the Craig-Bampton method the reduced system represents a mixed formulation of the system dynamics in modal and physical coordinates. The idea is to let the interface DOFs, where forces can act on the substructure, in the physical domain and replace the free DOFs by a combination of so called *fixed interface modes* describing the dynamic part and static terms, the *constraint modes*. Therefore the matrices are partitioned to free (index *f*) and interface (index *i*) DOFs, i.e.

$$\begin{bmatrix} M_{ff} & M_{fi} \\ M_{if} & M_{ii} \end{bmatrix} \begin{bmatrix} \ddot{x}_f \\ \ddot{x}_i \end{bmatrix} + \begin{bmatrix} K_{ff} & K_{fi} \\ K_{if} & K_{ii} \end{bmatrix} \begin{bmatrix} x_f \\ x_i \end{bmatrix} = \begin{bmatrix} 0 \\ f_i \end{bmatrix}. \tag{10.1}$$

For the free degrees of freedom the *fixed interface modes* are computed by solving the EVP of the form

$$\left(K_{ff} - \omega_j^2 M_{ff} \right) \phi_j = 0. \tag{10.2}$$

The dynamic part of the reduction base is defined by the first *m* eigenvectors $\Phi = \phi_1, \ldots, \phi_m$ containing the desired frequency range. Additionally the reduction base is enriched by the *constraint modes* defining a unit displacement on the interface DOFs so that the reduction base Θ can be written as

$$\begin{bmatrix} x_f \\ x_i \end{bmatrix} = \begin{bmatrix} \Phi & -K_{ff}^{-1} K_{fi} \\ 0 & I \end{bmatrix} \begin{bmatrix} q \\ x_i \end{bmatrix} = \Theta \begin{bmatrix} q \\ x_i \end{bmatrix}. \tag{10.3}$$

The reduced matrices of each substructure can now be computed with the individual reduction base Θ

$$\tilde{M}^i = \Theta^T M^i \Theta, \quad \tilde{K}^i = \Theta^T K^i \Theta.$$

10.2.2 Coupling of Reduced Substructures by Nonlinear Elements

Following the approach of [5], the governing equation of an assembled system can be written as

$$M\ddot{x} + D\dot{x} + Kx = f + g, \tag{10.4}$$

where the matrices contain the reduced matrices of the substructures

$$M = diag\left(\tilde{M}^1, \ldots, \tilde{M}^p\right), \quad D = diag\left(\tilde{D}^1, \ldots, \tilde{D}^p\right), \quad K = diag\left(\tilde{K}^1, \ldots, \tilde{K}^p\right),$$

$$x = \left[q^1, x_i^1, \ldots, q^p, x_i^p\right]^T, \quad f = \left[\Theta^1 f^1, \ldots, \Theta^p f^p\right]^T, \quad g = \left[\Theta^1 g^1, \ldots, \Theta^p g^p\right]^T.$$

Here, f is the vector of the external forces and g the vector of the connecting forces. The force equilibrium at the interface is given by

$$L^T g = 0, \tag{10.5}$$

where L is a Boolean matrix localizing the interface DOFs of the substructure in the global set of DOFs. The forces g can be expressed by the Boolean matrix B with the relation $L = \text{null}(B)$. The Lagrange multipliers λ represent the interface forces, such that

$$g = -B^T \lambda. \tag{10.6}$$

The equilibrium condition can be written as

$$L^T g = -L^T B^T \lambda = 0. \tag{10.7}$$

Following [15], the Lagrange multipliers can be expressed by the stiffness and the damping quantities, K_b and D_b, of the coupling elements

$$\lambda = K_b u + D_b \dot{u}, \tag{10.8}$$

where u is the relative displacement between the coupling points. For the introductory example, u is

$$u = \begin{bmatrix} x_2 - x_4 \\ x_3 - x_5 \end{bmatrix} = Bx. \tag{10.9}$$

In the later application, the nonlinear coupling element is a friction model. The friction only acts in one direction and the other DOFs of the coupling points are fixed. Therefore the B matrix is partitioned into perfect and flexible interface DOFs, as presented in [15]:

$$B = \begin{bmatrix} B_f \\ B_p \end{bmatrix}. \tag{10.10}$$

The perfect interface is coupled by the null space of the constraint operator related to the perfect part of the interface

$$L_p = \text{null}(B_p), \tag{10.11}$$

whereas the interface forces of the friction are implemented using the flexible part of B

$$g = -B_f^T K_b B_f x - B_f^T D_b B_f \dot{x}. \tag{10.12}$$

The flexible part contains the Lagrange multiplier describing the friction forces F_T at the node pairs. The nonlinear friction forces can be approximated by an equivalent stiffness and damping term using the Harmonic Balance Method (HBM):

$$\lambda = F_T \approx K_{hbm} u + D_{hbm} \dot{u}. \tag{10.13}$$

Now, the interface forces can be expressed by

$$g = -B_f^T K_{hbm} B_f x - B_f^T D_{hbm} B_f \dot{x}. \tag{10.14}$$
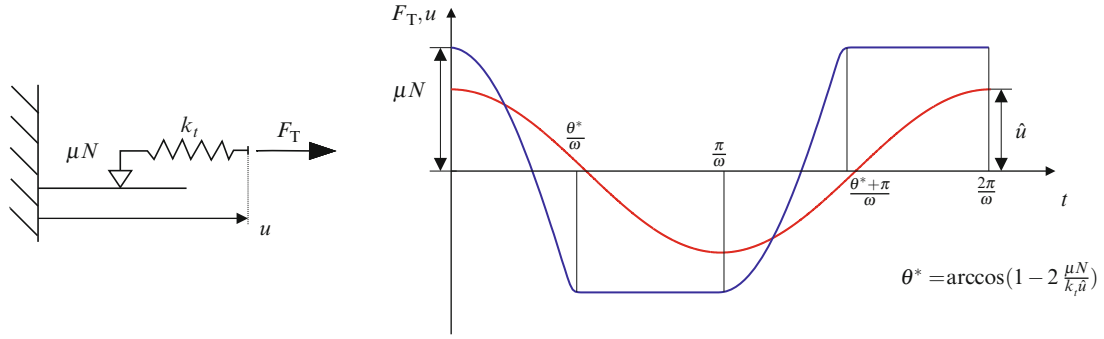
Fig. 10.2 Jenkins friction model (*left*) and friction behavior for a time harmonic relative displacement (*right*)

Table 10.1 Equivalent stiffness and damping of the Jenkins friction model for sticking and stick-slip

Coefficient	Sticking ($u^* < 1$)	Stick - Slip ($u^* \geq 1$)
k_{hbm}	k_T	$\frac{k_T}{\pi}\left(\arccos\left(1 - \frac{2}{u^*}\right) - \frac{2}{u^*}\left(1 - \frac{2}{u^*}\right)\sqrt{u^* - 1}\right)$
d_{hbm}	0	$\frac{4k_T}{\pi\omega u^*}\left(1 - \frac{1}{u^*}\right)$

The final equation which is solved iteratively in the frequency domain for time-harmonic behavior now reads

$$\left(L_p^T(K + B_f^T K_{hbm} B_f)L_p + i\omega L_p^T(D + B_f^T D_{hbm} B_f)L_p - \omega^2 L_p^T M L_p\right)\hat{x} = L_p^T \hat{f}. \tag{10.15}$$

10.3 Interface Flexibility and Damping

In order to linearize the nonlinear friction force F_T by the use of the Harmonic Balance Method [13], it is decomposed into an in phase part, i.e. stiffness and an out of phase part which corresponds to damping. Accordingly, the friction force can be substituted by a harmonic equivalent stiffness coefficient k_{hbm} and a harmonic equivalent damping coefficient d_{hbm} depending on the relative displacement u

$$F_T(u) \approx k_{hbm}u + d_{hbm}\dot{u}. \tag{10.16}$$

In this work, the so called Jenkins friction model is chosen which consists of a Coulomb friction model with an additional spring in series, as depicted in Fig. 10.2. The contact stiffness is denoted as k_t. For small displacement amplitudes $\hat{u}$, the model behaves like a pure elastic spring. No damping occurs until a critical amplitude is excessed. The critical amplitude when sliding begins is $\hat{u} = \mu N/k_t$, which can also be written in a normalized form, where sticking and sliding are separated for $u^* \geq 1$ and $u^* < 1$, respectively, to $u^* = \mu N/k_t\hat{u}$.

The Fourier coefficients of the equivalent stiffness and damping for the Jenkins model can be computed by a section-wise integration of the friction force for one period. The coefficients are given in Table 10.1 and can be found in the literature, see e.g. [1, 12]. In addition, other methods to obtain equivalent stiffness and damping coefficients are provided in [11].

10.4 Frequency-Based Substructuring (FBS)

Instead of using a modal representation, the system dynamics can also be represented by frequency response functions (FRF) and coupling is realized in the frequency domain directly [10]. With the difficulties of experimental data in mind [4, 14], numerical and experimental models can hereby be combined. A compact formulation of FBS can be found in [5]. In this

work, a formulation following the approach from [6] is used (with scalar quantities for clarity). Consequently, every point of the substructure possesses one DOF. Substructure a can be written in the frequency domain as

$$
\begin{bmatrix} \hat{x}_1 \\ \hat{x}_2 \\ \hat{x}_3 \end{bmatrix} = \begin{bmatrix} H_{11} & H_{12} & H_{13} \\ H_{21} & H_{22} & H_{23} \\ H_{31} & H_{32} & H_{33} \end{bmatrix} \begin{bmatrix} \hat{F}_1 \\ \hat{F}_2 \\ \hat{F}_3 \end{bmatrix},
\tag{10.17}
$$

and for substructure b

$$
\begin{bmatrix} \hat{x}_4 \\ \hat{x}_5 \\ \hat{x}_6 \end{bmatrix} = \begin{bmatrix} H_{44} & H_{45} & H_{46} \\ H_{54} & H_{55} & H_{56} \\ H_{64} & H_{65} & H_{66} \end{bmatrix} \begin{bmatrix} \hat{F}_4 \\ \hat{F}_5 \\ \hat{F}_6 \end{bmatrix}.
\tag{10.18}
$$

Here, H corresponds to the receptance $H = (K + i\omega D - \omega^2 M)^{-1}$. The equilibrium of the interface forces can be expressed by

$$
\hat{F}_2 + \hat{F}_4 = 0 \Rightarrow \hat{F}_2 = -\hat{F}_4 = \hat{\mathcal{F}}_1,
\tag{10.19}
$$

$$
\hat{F}_3 + \hat{F}_5 = 0 \Rightarrow \hat{F}_3 = -\hat{F}_5 = \hat{\mathcal{F}}_2,
\tag{10.20}
$$

where $\hat{\mathcal{F}}_1$ and $\hat{\mathcal{F}}_2$ are the nonlinear forces of the coupling elements. The interface forces can be computed by the relative displacements of the interface DOFs

$$
\hat{x}_2 - \hat{x}_4 = \hat{u}_1 = \frac{-\hat{\mathcal{F}}_1}{\mathcal{G}_{24}}, \quad \hat{x}_3 - \hat{x}_5 = \hat{u}_2 = \frac{-\hat{\mathcal{F}}_2}{\mathcal{G}_{35}}.
\tag{10.21}
$$

Here, $\mathcal{G}_{\bar{c}\bar{c}}$ is the complex describing function [6] representing the equivalent linearized stiffness and damping of the coupling element

$$
\mathcal{G}_{\bar{c}\bar{c}} = \frac{-\hat{\mathcal{F}}_j}{\hat{u}_j} = k_{hbm} + i\omega\, d_{hbm}.
\tag{10.22}
$$

With (10.19), (10.20) and the relation of (10.21), the coupled system is derived as

$$
\begin{bmatrix} \hat{x}_1 \\ \hat{x}_2 \\ \hat{x}_3 \\ \hat{x}_4 \\ \hat{x}_5 \\ \hat{x}_6 \\ 0 \\ 0 \end{bmatrix} = \begin{bmatrix} H_{11} & 0 & H_{12} & H_{13} \\ H_{21} & 0 & H_{22} & H_{23} \\ H_{31} & 0 & H_{32} & H_{33} \\ 0 & H_{46} & -H_{44} & -H_{45} \\ 0 & H_{56} & -H_{54} & -H_{55} \\ 0 & H_{66} & -H_{64} & -H_{65} \\ H_{21} & -H_{46} & H_{22} + H_{44} + 1/\mathcal{G}_{24} & H_{23} + H_{45} \\ H_{31} & -H_{56} & H_{32} + H_{54} & H_{33} + H_{55} + 1/\mathcal{G}_{35} \end{bmatrix} \begin{bmatrix} \hat{F}_1 \\ \hat{F}_6 \\ \hat{\mathcal{F}}_1 \\ \hat{\mathcal{F}}_2 \end{bmatrix}.
\tag{10.23}
$$

Introducing block matrices, the equation can be expressed in a more compact form

$$
\begin{bmatrix} \hat{x}_r \\ 0 \end{bmatrix} = \begin{bmatrix} H_{ri} & H_{rc} \\ H_{ci} & H_{cc} + \mathcal{G}_{\bar{c}\bar{c}}^{-1} \end{bmatrix} \begin{bmatrix} \hat{F}_i \\ \hat{\mathcal{F}}_j \end{bmatrix}.
\tag{10.24}
$$

Eliminating the coupling forces $\hat{\mathcal{F}}_j$, (10.24) yields

$$
\hat{x}_r = \left[H_{ri} - H_{rc} \left[H_{cc} + \mathcal{G}_{\bar{c}\bar{c}}^{-1} \right]^{-1} H_{ci} \right] \hat{F}_i.
\tag{10.25}
$$

This equation can be solved iteratively with the requirement that the Fourier coefficients of the coupling elements, $\mathcal{G}_{\bar{c}\bar{c}}$, depend on the amplitude $\hat{x}_r$.

10.5   Numerical Example

The two methods are applied to a system where the substructures consist of two equal two-mass-oscillators, see Fig. 10.3. Coupling is done by a linear spring-damper in parallel with a Jenkins friction model. Parameters of the system are given in Table 10.2. The excitation force F_{exc} is applied at substructure a and the displacement output x_4 is considered.

The FRFs in Fig. 10.4 (left) show that coupling by CMS (red) and FBS (dashed green) give equal results. Due to a local damping effect not all modes are damped depending on the mode shape. As a result of the additional stiffness in the friction model a shift in some eigenfrequencies can be seen compared to the linearly coupled system (blue). The right plot in Fig. 10.4 displays the development of the FRF for different values of the normal force N.
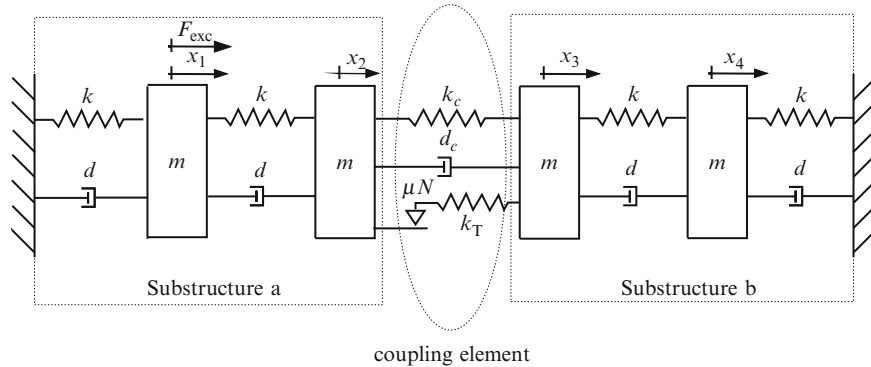
Fig. 10.3 Example system consisting of two substructures a and b coupled by a nonlinear element

Table 10.2 Parameter of the example system

Parameter	Value	Unit	Parameter	Value	Unit
m	1	kg	k_c	$4 \cdot 10^4$	N/m
d	4	Ns/m	k_t	$4 \cdot 10^4$	N/m
k	$4 \cdot 10^4$	N/m	μ	1	-
d_c	4	Ns/m	F_{exc}	15	N
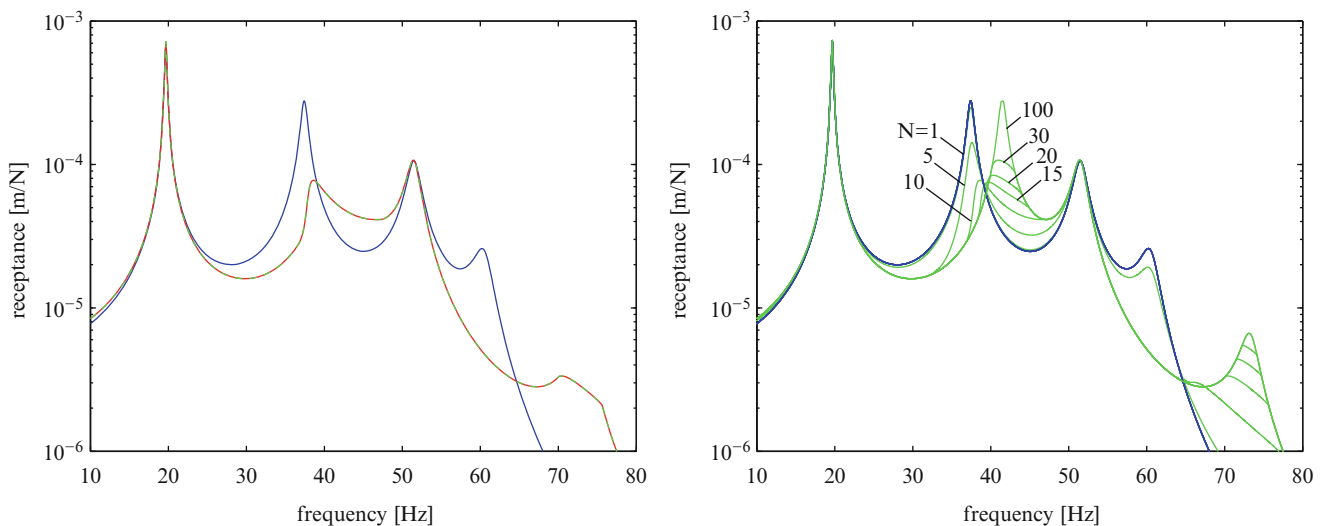
Fig. 10.4 *Left*: Comparison between CMS (*red*) and FBS coupling (*dashed green*) for $N = 10$ N for the example. Additionally the result of a linearly coupled (k_c,d_c) system is shown (*blue*). *Right*: FBS coupling (*green*) for different normal forces (color figure online)

10.6 Finite Element Model

Based on the results of the four-mass oscillator, the method is now applied to a finite element model shown in Fig. 10.5. The substructures are discretized by standard 8-node hexahedral solid elements having linear shape functions with three DOFs at each node. The two beams are coupled at four node pairs (1, 2, 3, 4) using CMS, whereby the two beams have coincident meshes at the interface. The excitation force $F_{exc} = 15$ N is applied at Substructure 1 and the displacement output at Substructure 2 is considered in the y-direction. In this situation only bending modes are excited.

The applied normal force N is equally distributed to the node pairs and results are presented in Fig. 10.6 for different values of N. Friction is implemented at the node pairs only in the z-direction, whereas the other directions are perfectly coupled. Contact stiffness is estimated by $k_t = 1 \cdot 10^8$ and the friction coefficient is $\mu = 1$. Geometrical and material parameter of a substructure can be found in Table 10.3. Damping in terms of Rayleigh is neglected to highlight the damping
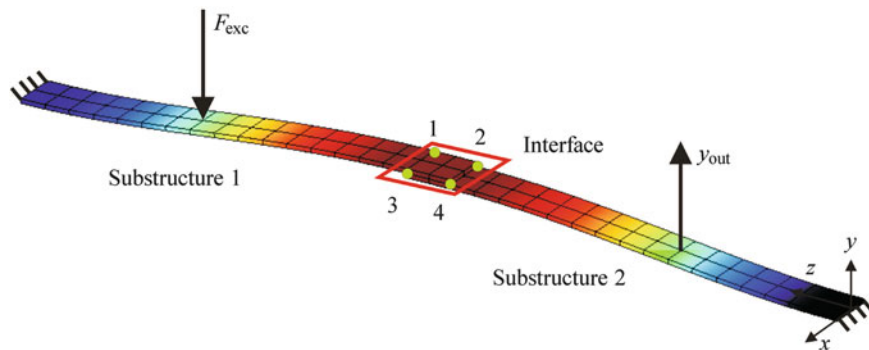
Fig. 10.5 Finite element model of two coupled beams
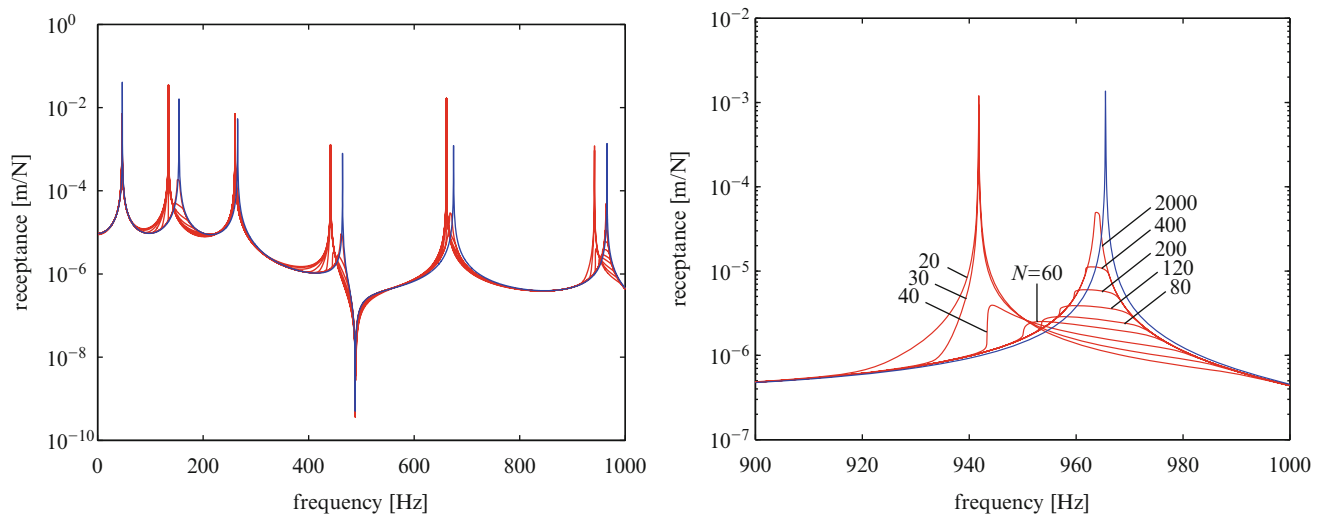
Fig. 10.6 *Left*: Frequency response function of the coupled beams with CMS (*red*) for different normal forces. Additionally the result of a perfect coupling is shown (*blue*). *Right*: Zoom on the sixth bending mode (color figure online)

Table 10.3 Geometrical and material parameter of a substructure

Parameter	Value	Unit	Parameter	Value	Unit
Length l	0.3	m	Density ρ	7850	kg/m^3
Width b	0.03	m	Young's modulus E	$210 \cdot 10^3$	N/mm^2
Height h	0.003	m	Poisson ratio v	0.3	–

effect caused by friction. Similar to the results of the four-mass oscillator, only selected modes are damped depending on the relative interface displacement of the corresponding mode shape. As with the oscillator, damping due to friction depends on the applied normal force N, as a closer consideration of the sixth bending mode shows.

10.7 Conclusion

In this work, the implementation of nonlinear coupling elements in a substructuring formulation using CMS and FBS is reviewed. The methods are used to compute frequency response functions of subsystems coupled by friction elements. For the four-mass oscillator, both methods give identical results. For the finite element model, CMS is used due to the fact that with increasing number of coupling nodes the handling of the system representation is much clearer. Furthermore, a higher-harmonic consideration of the system can be established much easier.

References

1. Balmer B (1993) Erhöhung der Dämpfung von Turbinenschaufeln durch Reibelemente, Serie 11, vol 197. VDI Fortschrittberichte, Düsseldorf
2. Becker J, Gaul L (2008) CMS-methods for efficient damping prediction for structures with friction. In: Proceedings of the IMAC-XXVI, Orlando, 2008
3. Bograd S, Reuss P, Schmidt A, Gaul L, Mayer M (2011) Modeling the dynamics of mechanical joints. Mech Syst Signal Process 25 (8):2801–2826
4. Brechlin E (2001) Methoden und Grenzen der Substrukturkopplung auf der Basis experimenteller Daten. PhD thesis, University of Stuttgart
5. De Klerk D, Rixen D, Voormeeren S (2008) General framework for dynamic substructuring: history, review and classification of techniques. AIAA J 46(5):1169–1181. doi:10.2514/1.33274
6. Ferreira JV (1998) Dynamic response analysis of structures with nonlinear components. PhD thesis, Imperial College London
7. Gaul L, Lenz J (1997) Nonlinear dynamics of structures assembled by bolted joints. Acta Mech 125:169–181
8. Gaul L, Nitsche R (2001) The role of friction in mechanical joints. Appl Mech Rev 54(2):93–106
9. Herrmann J, Maess M., Gaul L. (2010) Substructuring including interface reduction for the efficient vibro-acoustic simulation of fluid-filled piping systems. Mech Syst Signal Process 24(1):153–163
10. Jetmundsen B, Bielawa R, Flannelly W (1988) Generalized frequency domain substructure synthesis. J Am Helicopter Soc 33:55–64
11. Lazan B (1968) Damping of materials and members in structural mechanics. Pergamon Press, Oxford
12. Magnus K (1955) Über ein Verfahren zur Untersuchung nichtlinearer Schwingungs- und Regelungs-Systeme, vol 451. VDI-Forschungsheft, Düsseldorf
13. Popp K, Magnus K (2002) Schwingungen. Teubner, Wiesbaden
14. Voormeeren S, de Klerk D, Rixen D (2010) Uncertainty quantification in experimental frequency based substructuring. Mech Syst Signal Process 24(1):106–118
15. Voormeeren S, van der Valk P, Rixen D (2010) Practical aspects of dynamic substructuring in wind turbine engineering. In: Proceedings of the IMAC-XXVII, Jacksonville, 2010

Chapter 11
Direct Hybrid Formulation for Substructure Decoupling

Walter D'Ambrogio and Annalisa Fregolent

Abstract The paper considers the decoupling problem or subsystem subtraction, i.e. the identification of the dynamic behaviour of a structural subsystem, starting from the known dynamic behaviour of both the coupled system and the remaining part of the structural system (residual subsystem). Often it is necessary to combine numerical models (e.g. FEM) and test models (e.g. FRFs). In such cases, one speaks of experimental dynamic substructuring. Substructure decoupling techniques can be classified as inverse coupling or direct decoupling techniques. In inverse coupling, the equations describing the coupling problem are rearranged to isolate the unknown substructure instead of the coupled structure. Direct decoupling consists in adding to the coupled system a fictitious subsystem that is the negative of the residual subsystem. In this paper, starting from the 3-field formulation (dynamic balance, interface compatibility and equilibrium), a direct hybrid approach is developed by requiring that both compatibility and equilibrium conditions are satisfied exactly, either at coupling DoFs only, or at additional internal DoFs of the residual subsystem. Equilibrium and compatibility DoFs might not be the same: this generates the so-called non-collocated approach. The technique is applied using simulated data from a discrete system.

11.1 Introduction

The paper is focused on the decoupling problem or subsystem subtraction, namely how to extract a substructure model from the assembled system. A trivial application of decoupling is mass cancellation, to get rid of the effect of the accelerometer mass on FRF measurements. Another application is joint identification. More generally, decoupling is a relevant issue for subsystems that cannot be measured separately, but only when coupled to their neighboring substructure(s) (e.g. a fixture needed for testing or subsystems that are very delicate or in operational conditions). To be more precise, the decoupling problem is defined as the identification of the dynamic behaviour of a structural subsystem, starting from the known dynamic behaviour of the assembled system, and from information about the remaining part of the structural system (residual subsystem).

The decoupling problem can be seen as a special case of dynamic substructuring. However, while for subsystem addition many well established techniques exist when all substructures are modeled theoretically, in subsystem subtraction this would give rise to a trivial problem. Therefore, in subsystem subtraction the model of at least one subsystem must derive from experimental tests. Due to modal truncation problems, the use of FRFs (Frequency Based Substructuring) is preferred with respect to the use of modal parameters. The main algorithm for frequency based substructuring is the improved impedance coupling [1] that involves just one matrix inversion with respect to the classical impedance coupling technique that requires three inversions. A general framework for dynamic substructuring is provided in [2, 3], where primal and dual formulation are introduced.

W. D'Ambrogio (✉)
Dipartimento di Ingegneria Meccanica, Energetica e Gestionale, Università dell'Aquila, Via G. Gronchi, 18 – I-67100 L'Aquila, Italy
e-mail: walter.dambrogio@univaq.it

A. Fregolent
Dipartimento di Ingegneria Meccanica e Aerospaziale, Università di Roma La Sapienza, Via Eudossiana 18, I-00184 Rome, Italy
e-mail: annalisa.fregolent@uniroma1.it

Substructure decoupling techniques can be classified as inverse coupling techniques or direct decoupling techniques. In inverse coupling, the equations written for the coupling problem are rearranged to isolate (as unknown) one of the substructures instead of the assembled structure. Examples of inverse coupling are impedance and mobility approaches [4, 5].

Direct decoupling consists in adding to the assembled system a fictitious subsystem, which is the negative of the residual subsystem. The technique starts from the 3-field formulation: one set of equations expressing the dynamic balance of the assembled system and, separately, of the fictitious subsystem; one set of equations enforcing compatibility at interface DoFs, one set of equations enforcing equilibrium of constraint forces at interface DoFs. To solve the problem, a dual approach [6] or a primal approach [7] can be used. Compatibility and equilibrium can be required either at coupling DoFs only (standard interface), or at additional internal DoFs of the residual subsystem (extended interface). Furthermore, in [8, 9] it is pointed out that DoFs used to enforce equilibrium need not to be the same as DoFs used to enforce compatibility: this gives rise to the so called non collocated approach, as opposite to the traditional approach in which such DoFs are the same, which is called collocated. The choice of interface DoFs determines a set of frequencies at which the decoupling problem is ill conditioned, as shown in [6] for the dual approach. Apparently, when using an extended interface, the problem is singular at all frequencies, although this singularity is easily removed by using standard smart inversion techniques.

In this paper, an admittance and reduced version of the 3-field formulation (dynamic balance, interface compatibility and equilibrium) is developed: this formulation is particularly suited for experimental dynamic substructuring since it uses only measurements on the minimum set of DoFs that are necessary to enforce compatibility and equilibrium conditions. Starting from the 3-field formulation, the dual assembly is revisited and a hybrid assembly is developed by requiring that both compatibility and equilibrium conditions are satisfied exactly, either at coupling DoFs only, or at additional internal DoFs of the residual subsystem. Dual and hybrid assembly are compared both from the theoretical and the practical point of view, using simulated data from a discrete system.

11.2 Direct Decoupling Techniques

The coupled structural system RU (N_{RU} DoFs) is assumed to be made by an unknown subsystem U (N_U DoFs) and a residual subsystem R (N_R DoFs) joined through a number of couplings (see Fig. 11.1). The residual subsystem (R) can be made by one or more substructures. The degrees of freedom (DoFs) of the coupled system can be partitioned into internal DoFs (not belonging to the couplings) of subsystem U (u), internal DoFs of subsystem R (r), and coupling DoFs (c).

It is required to find the FRF of the unknown substructure U starting from the FRF of the coupled system RU. The subsystem U can be extracted from the coupled system RU by cancelling the dynamic effect of the residual subsystem R. This can be accomplished by adding to the coupled system RU a fictitious subsystem with a dynamic stiffness opposite to that of the residual subsystem R and satisfying compatibility and equilibrium conditions. The dynamic equilibrium of the coupled system RU and of the fictitious subsystem can be expressed in block diagonal format as:

$$\begin{bmatrix} \bar{\mathbf{Z}}^{RU} & \mathbf{0} \\ \mathbf{0} & -\bar{\mathbf{Z}}^{R} \end{bmatrix} \begin{Bmatrix} \mathbf{u}^{RU} \\ \mathbf{u}^{R} \end{Bmatrix} = \begin{Bmatrix} \bar{\mathbf{f}}^{RU} \\ \bar{\mathbf{f}}^{R} \end{Bmatrix} + \begin{Bmatrix} \bar{\mathbf{g}}^{RU} \\ \bar{\mathbf{g}}^{R} \end{Bmatrix} \tag{11.1}$$

where:

- $\bar{\mathbf{Z}}^{RU}$, $\bar{\mathbf{Z}}^{R}$ are the dynamic stiffness matrices of the coupled system RU and of the residual subsystem R, respectively;
- $\bar{\mathbf{u}}^{RU}$, $\bar{\mathbf{u}}^{R}$ are the vectors of degrees of freedom of the coupled system RU and of the residual subsystem R, respectively;
- $\bar{\mathbf{f}}^{RU}$, $\bar{\mathbf{f}}^{R}$ are the external force vectors on the coupled system RU and on the fictitious subsystem, respectively;
- $\bar{\mathbf{g}}^{RU}$, $\bar{\mathbf{g}}^{R}$ are the vectors of connecting forces between the coupled system and the fictitious subsystem, and viceversa (constraint forces associated with compatibility conditions).

According to this point of view, the interface between the coupled system RU and the fictitious subsystem should not only include all the coupling DoFs between subsystems U and R, but should as well include all the internal DoFs of subsystem R. However, since the problem can be solved by considering just coupling DoFs, the number of interface DoFs should be greater than or equal to the number of coupling DoFs n_c. Therefore, three options for interface DoFs can be considered:

- Standard interface, including only the coupling DoFs (c) between subsystems U and R;
- Extended interface, including also a subset of internal DoFs ($i \subseteq r$) of the residual subsystem R;
- Mixed interface, including subsets of coupling DoFs ($d \subseteq c$) and internal DoFs ($i \subseteq r$) of subsystem R.
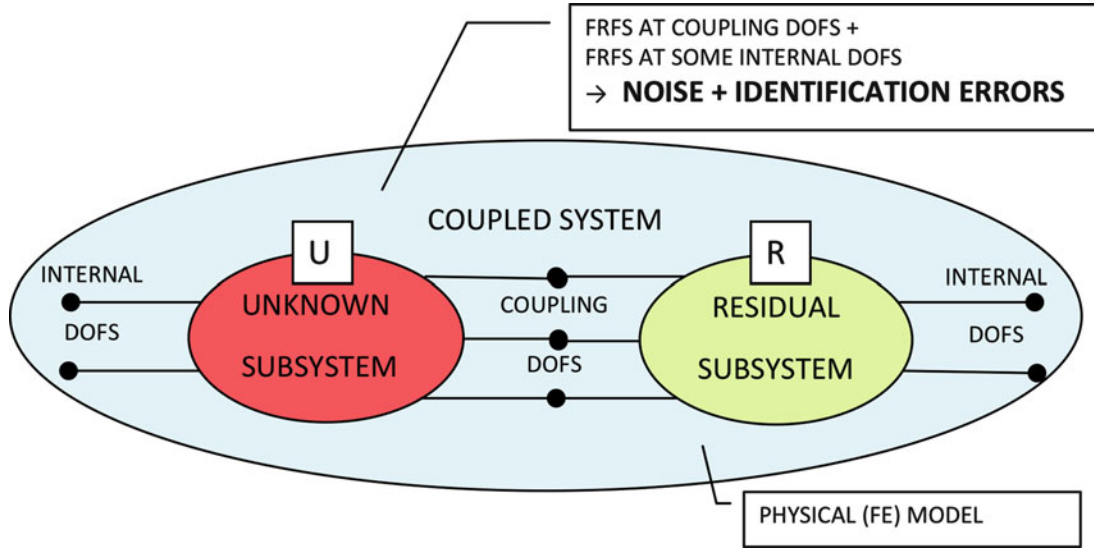
Fig. 11.1 Scheme of the decoupling problem

The compatibility condition at the (standard, extended, mixed) interface DoFs implies that any pair of matching DoFs $\bar{u}_l^{RU}$ and $\bar{u}_m^R$, i.e. DoF l on the coupled system RU and DoF m on subsystem R must have the same displacement, that is $\bar{u}_l^{RU} - \bar{u}_m^R = 0$. Let the number of interface DoFs on which compatibility is enforced be denoted as N_C.

The compatibility condition can be generally expressed as:

$$\begin{bmatrix} \bar{\mathbf{B}}_C^{RU} & \bar{\mathbf{B}}_C^R \end{bmatrix} \begin{Bmatrix} \bar{\mathbf{u}}^{RU} \\ \bar{\mathbf{u}}^R \end{Bmatrix} = \mathbf{0} \tag{11.2}$$

where each row of $\bar{\mathbf{B}}_C = \begin{bmatrix} \bar{\mathbf{B}}_C^{RU} & \bar{\mathbf{B}}_C^R \end{bmatrix}$ corresponds to a pair of matching DoFs. Note that $\bar{\mathbf{B}}_C$ has size $N_C \times (N_{RU} + N_R)$ and is, in most cases, a signed Boolean matrix.

Alternatively, the compatibility DoFs can be extracted from the full set of DoFs by an output selection matrix $\mathbf{P}$ as

$$\begin{Bmatrix} \mathbf{u}^{RU} \\ \mathbf{u}^R \end{Bmatrix} = \begin{bmatrix} \mathbf{P}^{RU} & \mathbf{0} \\ \mathbf{0} & \mathbf{P}^R \end{bmatrix} \begin{Bmatrix} \bar{\mathbf{u}}^{RU} \\ \bar{\mathbf{u}}^R \end{Bmatrix} \tag{11.3}$$

where $\mathbf{u}^{RU}$ and $\mathbf{u}^R$ are vectors of size N_C and $\mathbf{P}$ has size $2N_C \times (N_{RU} + N_R)$. In this case, the compatibility condition can be expressed as:

$$\begin{bmatrix} \mathbf{B}_C^{RU} & \mathbf{B}_C^R \end{bmatrix} \begin{Bmatrix} \mathbf{u}^{RU} \\ \mathbf{u}^R \end{Bmatrix} = \mathbf{0} \tag{11.4}$$

where $\mathbf{B}_C$ has size $N_C \times 2N_C$. Note that, in most cases, $\mathbf{B}_C^{RU}$ is a permutation matrix and $\mathbf{B}_C^R$ is the negative of a permutation matrix, or viceversa. (Recall that a permutation matrix is a square binary matrix that has exactly one entry 1 in each row and each column and zeroes elsewhere.)

Substituting (11.3) in (11.4), one obtains:

$$\begin{bmatrix} \mathbf{B}_C^{RU} & \mathbf{B}_C^R \end{bmatrix} \begin{bmatrix} \mathbf{P}^{RU} & \mathbf{0} \\ \mathbf{0} & \mathbf{P}^R \end{bmatrix} \begin{Bmatrix} \bar{\mathbf{u}}^{RU} \\ \bar{\mathbf{u}}^R \end{Bmatrix} = \mathbf{0} \tag{11.5}$$

from which

$$\begin{bmatrix} \bar{\mathbf{B}}_C^{RU} & \bar{\mathbf{B}}_C^R \end{bmatrix} = \begin{bmatrix} \mathbf{B}_C^{RU} & \mathbf{B}_C^R \end{bmatrix} \begin{bmatrix} \mathbf{P}^{RU} & \mathbf{0} \\ \mathbf{0} & \mathbf{P}^R \end{bmatrix} \tag{11.6}$$

Equation 11.5 shows how, starting from the full set of DoFs, the compatibility condition can be enforced in two steps: in one step, the matching DoFs are extracted from the full set of DoFs using the selection matrix **P**; in the second step, each pair of matching DoFs is constrained to have the same displacement by the **B**$_C$ matrix.

However, in case of experimental substructuring, it is reasonable to assume that only necessary measurements are performed, i.e. those on matching DoFs, and the first step becomes unnecessary. Therefore, (11.4) is the most suited for experimental dynamic substructuring.

Before deriving the equilibrium condition, it should be noted that the interface DoFs involved in the equilibrium condition are not necessarily the same used to enforce the compatibility condition, as long as controllability between equilibrium and compatibility DoFs is ensured. If the compatibility and the equilibrium DoFs are not the same, the approach is called non-collocated [8]. Note that a non-collocated approach requires an extended or mixed interface and therefore it is only possible in the decoupling problems (in coupling problems only standard interface can be defined). Obviously, the traditional approach, in which compatibility and equilibrium DoFs are the same, is called collocated.

Let N_E denote the number of interface DoFs on which equilibrium is enforced. The equilibrium condition for constraint forces implies that their sum must be zero for any pair of matching DoFs, i.e. $\bar{g}_r^{RU} + \bar{g}_s^R = 0$. Furthermore, if DoF k on the coupled system RU (or on the residual subsystem R) does not belong to the equilibrium interface, it must be $\bar{g}_k^{RU} = 0$ ($\bar{g}_k^R = 0$): this holds for any DoF not involved in the equilibrium condition.

Overall, the above conditions can be expressed as:

$$\begin{bmatrix} \bar{\mathbf{L}}_\mathbf{E}^{\mathbf{RU}} \\ \bar{\mathbf{L}}_\mathbf{E}^{\mathbf{R}} \end{bmatrix}^T \begin{Bmatrix} \bar{\mathbf{g}}^{\mathbf{RU}} \\ \bar{\mathbf{g}}^{\mathbf{R}} \end{Bmatrix} = \mathbf{0} \tag{11.7}$$

where the matrix $\bar{\mathbf{L}}_\mathbf{E} = \begin{bmatrix} \bar{\mathbf{L}}_\mathbf{E}^{\mathbf{RU}} & \bar{\mathbf{L}}_\mathbf{E}^{\mathbf{R}} \end{bmatrix}$ is a Boolean localisation matrix. Note that the number of columns of $\bar{\mathbf{L}}_\mathbf{E}$ is equal to the number N_E of equilibrium interface DoFs plus the number N_{NE} of DoFs not belonging to the equilibrium interface. Note that $N_{NE} = N_{RU} + N_R - 2N_E$: in fact, the number of DoFs belonging to the equilibrium interface must be subtracted once from N_{RU} and once from N_R. Therefore, the size of $\bar{\mathbf{L}}_E$ is $(N_{RU} + N_R) \times (N_{RU} + N_R - N_E)$.

Alternatively, the elements of $\bar{\mathbf{g}}^{RU}$ and $\bar{\mathbf{g}}^R$ not involved in the equilibrium condition can be set to zero by writing

$$\begin{Bmatrix} \bar{\mathbf{g}}^{\mathbf{RU}} \\ \bar{\mathbf{g}}^{\mathbf{R}} \end{Bmatrix} = \begin{bmatrix} \mathbf{Q}^{\mathbf{RU}} & \mathbf{0} \\ \mathbf{0} & \mathbf{Q}^{\mathbf{R}} \end{bmatrix} \begin{Bmatrix} \mathbf{g}^{\mathbf{RU}} \\ \mathbf{g}^{\mathbf{R}} \end{Bmatrix} \tag{11.8}$$

where the rows of **Q** corresponding to DoFs not involved in equilibrium conditions are zero, $\mathbf{g}^{RU}$ and $\mathbf{g}^R$ are vectors of size N_E, and **Q** has size $(N_{RU} + N_R) \times 2N_E$.

Limited to the equilibrium DoFs, the condition for matching constraint forces can be expressed as:

$$\begin{bmatrix} \mathbf{L}_\mathbf{E}^{\mathbf{RU}} \\ \mathbf{L}_\mathbf{E}^{\mathbf{R}} \end{bmatrix}^T \begin{Bmatrix} \mathbf{g}^{\mathbf{RU}} \\ \mathbf{g}^{\mathbf{R}} \end{Bmatrix} = \mathbf{0} \tag{11.9}$$

where the matrix $\mathbf{L}_\mathbf{E} = \begin{bmatrix} \mathbf{L}_\mathbf{E}^{\mathbf{RU}} & \mathbf{L}_\mathbf{E}^{\mathbf{R}} \end{bmatrix}$ has size $2N_E \times N_E$. Note that, in most cases, both $\mathbf{L}_\mathbf{E}^{\mathbf{RU}}$ and $\mathbf{L}_\mathbf{E}^{\mathbf{R}}$ are permutation matrices.

Again, (11.9) is the most suited for experimental dynamic substructuring, since in this case only necessary measurements are performed.

If it is further assumed that external forces act at most on interface DoFs involved in equilibrium conditions, it is possible to write

$$\begin{Bmatrix} \bar{\mathbf{f}}^{\mathbf{RU}} \\ \bar{\mathbf{f}}^{\mathbf{R}} \end{Bmatrix} = \begin{bmatrix} \mathbf{Q}^{\mathbf{RU}} & \mathbf{0} \\ \mathbf{0} & \mathbf{Q}^{\mathbf{R}} \end{bmatrix} \begin{Bmatrix} \mathbf{f}^{\mathbf{RU}} \\ \mathbf{f}^{\mathbf{R}} \end{Bmatrix} \tag{11.10}$$

where **Q** is the same as for the constraint forces.

The dynamic equilibrium equation (11.1) can be rewritten, by using (11.8) and (11.10) and by premultiplying by the inverse of the dynamic stiffness, as

$$\begin{Bmatrix} \bar{\mathbf{u}}^{\mathbf{RU}} \\ \bar{\mathbf{u}}^{\mathbf{R}} \end{Bmatrix} = \begin{bmatrix} \bar{\mathbf{Z}}^{\mathbf{RU}} & \mathbf{0} \\ \mathbf{0} & -\bar{\mathbf{Z}}^{\mathbf{R}} \end{bmatrix}^{-1} \begin{bmatrix} \mathbf{Q}^{\mathbf{RU}} & \mathbf{0} \\ \mathbf{0} & \mathbf{Q}^{\mathbf{R}} \end{bmatrix} \left(\begin{Bmatrix} \mathbf{f}^{\mathbf{RU}} \\ \mathbf{f}^{\mathbf{R}} \end{Bmatrix} + \begin{Bmatrix} \mathbf{g}^{\mathbf{RU}} \\ \mathbf{g}^{\mathbf{R}} \end{Bmatrix} \right) \tag{11.1*}$$

Using (11.3) to select only the N_C compatibility DoFs, (11.1 *) becomes:

$$\left\{ \begin{array}{c} \mathbf{u}^{RU} \\ \mathbf{u}^{R} \end{array} \right\} = \left[\begin{array}{cc} \mathbf{H}^{RU} & 0 \\ 0 & -\mathbf{H}^{R} \end{array} \right] \left(\left\{ \begin{array}{c} \mathbf{f}^{RU} \\ \mathbf{f}^{R} \end{array} \right\} + \left\{ \begin{array}{c} \mathbf{g}^{RU} \\ \mathbf{g}^{R} \end{array} \right\} \right) \tag{11.1**}$$

where the frequency response function matrix $\mathbf{H}$ ($2N_C \times 2N_E$) is defined as:

$$\left[\begin{array}{cc} \mathbf{H}^{RU} & 0 \\ 0 & -\mathbf{H}^{R} \end{array} \right] = \left[\begin{array}{cc} \mathbf{P}^{RU} & 0 \\ 0 & \mathbf{P}^{R} \end{array} \right] \left[\begin{array}{cc} \bar{\mathbf{Z}}^{RU} & 0 \\ 0 & -\bar{\mathbf{Z}}^{R} \end{array} \right]^{-1} \left[\begin{array}{cc} \mathbf{Q}^{RU} & 0 \\ 0 & \mathbf{Q}^{R} \end{array} \right] \tag{11.11}$$

Equation 11.1 ** is much more suited for experimental dynamic substructuring than (11.1) since the FRF matrices of the coupled system and of the residual subsystem can be directly measured among the minimum set of DoFs necessary to enforce the required compatibility and equilibrium conditions.

Equations 11.1 ** , 11.4 and 11.9 can be put together to obtain the admittance version of the 3-field formulation, suited for experimental dynamic substructuring:

$$\left\{ \begin{array}{l} \left\{ \begin{array}{c} \mathbf{u}^{RU} \\ \mathbf{u}^{R} \end{array} \right\} = \left[\begin{array}{cc} \mathbf{H}^{RU} & 0 \\ 0 & -\mathbf{H}^{R} \end{array} \right] \left\{ \begin{array}{c} \mathbf{f}^{RU} \\ \mathbf{f}^{R} \end{array} \right\} + \left[\begin{array}{cc} \mathbf{H}^{RU} & 0 \\ 0 & -\mathbf{H}^{R} \end{array} \right] \left\{ \begin{array}{c} \mathbf{g}^{RU} \\ \mathbf{g}^{R} \end{array} \right\} \\[16pt] \left[\begin{array}{cc} \mathbf{B}_{C}^{RU} & \mathbf{B}_{C}^{R} \end{array} \right] \left\{ \begin{array}{c} \mathbf{u}^{RU} \\ \mathbf{u}^{R} \end{array} \right\} = 0 \\[16pt] \left[\begin{array}{c} \mathbf{L}_{E}^{RU} \\ \mathbf{L}_{E}^{R} \end{array} \right]^{T} \left\{ \begin{array}{c} \mathbf{g}^{RU} \\ \mathbf{g}^{R} \end{array} \right\} = 0 \end{array} \right. \tag{11.1** , 11.4, 11.9}$$

Starting from the 3-field formulation, several assembly techniques can be devised. The classical ones are

- Primal assembly [2, 7] where the compatibility condition is satisfied exactly by defining a unique set of interface DoFs;
- Dual assembly [6, 8] where the equilibrium condition is satisfied exactly by defining a unique set of connecting force intensities.

In the sequel, after reviewing the dual assembly, the hybrid assembly is introduced aimed to satisfy both compatibility and equilibrium conditions.

11.2.1   Dual Assembly

In the dual assembly, the equilibrium condition $g_{r}^{RU} + g_{s}^{R} = 0$ at a pair of equilibrium interface DoFs is ensured by choosing, for instance, $g_{r}^{RU} = -\lambda$ and $g_{s}^{R} = \lambda$. If a Boolean matrix $\mathbf{B_E}$ is defined similarly to $\mathbf{B_C}$, but related to interface equilibrium DoFs, the overall interface equilibrium can be ensured by writing the connecting forces in the form:

$$\left\{ \begin{array}{c} \mathbf{g}^{RU} \\ \mathbf{g}^{R} \end{array} \right\} = - \left[\begin{array}{c} \mathbf{B}_{E}^{RU^{T}} \\ \mathbf{B}_{E}^{R^{T}} \end{array} \right] \lambda \tag{11.12}$$

where λ are Lagrange multipliers corresponding to connecting force intensities and $\mathbf{B_E}$ is a $N_E \times 2N_E$ matrix. Since there is a unique set of connecting force intensities λ, the interface equilibrium condition is satisfied automatically for any λ, i.e.

$$\left[\begin{array}{c} \mathbf{L}_{E}^{RU} \\ \mathbf{L}_{E}^{R} \end{array} \right]^{T} \left\{ \begin{array}{c} \mathbf{g}^{RU} \\ \mathbf{g}^{R} \end{array} \right\} = - \left[\begin{array}{c} \mathbf{L}_{E}^{RU} \\ \mathbf{L}_{E}^{R} \end{array} \right]^{T} \left[\begin{array}{c} \mathbf{B}_{E}^{RU^{T}} \\ \mathbf{B}_{E}^{R^{T}} \end{array} \right] \lambda = 0 \tag{11.13}$$

Then $\mathbf{B_E}^T$ is the nullspace of $\mathbf{L_E}^T$, and viceversa $\mathbf{L_E}$ is the nullspace of $\mathbf{B_E}$:

$$\begin{cases} \begin{bmatrix} \mathbf{B_E^{RU}} & \mathbf{B_E^R} \end{bmatrix} \begin{bmatrix} \mathbf{L_E^{RU}} \\ \mathbf{L_E^R} \end{bmatrix} = \mathbf{0} \\ \begin{bmatrix} \mathbf{L_E^{RU}} \\ \mathbf{L_E^R} \end{bmatrix}^T \begin{bmatrix} \mathbf{B_E^{RU}} & \mathbf{B_E^R} \end{bmatrix}^T = \mathbf{0} \end{cases} \tag{11.14}$$

In the dual assembly, the total set of DoFs is retained, i.e. each interface DoF is present as many times as there are substructures connected through that DoF. Since (11.13) is always satisfied, the 3-field formulation reduces to:

$$\begin{cases} \left\{ \begin{matrix} \mathbf{u^{RU}} \\ \mathbf{u^R} \end{matrix} \right\} = \begin{bmatrix} \mathbf{H^{RU}} & \mathbf{0} \\ \mathbf{0} & -\mathbf{H^R} \end{bmatrix} \begin{bmatrix} \mathbf{B_E^{RU}}^T \\ \mathbf{B_E^R}^T \end{bmatrix} \lambda + \begin{bmatrix} \mathbf{H^{RU}} & \mathbf{0} \\ \mathbf{0} & -\mathbf{H^R} \end{bmatrix} \left\{ \begin{matrix} \mathbf{f^{RU}} \\ \mathbf{f^R} \end{matrix} \right\} & (1^{**}) \\ \begin{bmatrix} \mathbf{B_C^{RU}} & \mathbf{B_C^R} \end{bmatrix} \left\{ \begin{matrix} \mathbf{u^{RU}} \\ \mathbf{u^R} \end{matrix} \right\} = \mathbf{0} & (4) \end{cases}$$

To eliminate λ, it is possible to proceed by writing (11.1**) in compact form, with obvious meaning of symbols:

$$\mathbf{u} = -\mathbf{H B_E}^T \lambda + \mathbf{H f} \tag{11.1**}$$

By substituting in (11.4) also written in compact form, it is:

$$\mathbf{B_C H B_E}^T \lambda = \mathbf{B_C H f} \tag{11.15}$$

from which λ, to be back-substituted in (11.1***), is found as:

$$\lambda = \left(\mathbf{B_C H B_E}^T \right)^+ \mathbf{B_C H f} \tag{11.16}$$

To obtain a determined or overdetermined matrix for the generalized inversion operation, the following condition must be satisfied:

$$\text{number of rows of } \mathbf{B_C} \geq \text{ number of rows of } \mathbf{B_E}$$

i.e.

$$N_C \geq N_E \geq n_c \tag{11.17}$$

Note that, if $N_C > N_E$, (11.15) is not satisfied exactly by vector λ given by (11.16), but only in the minimum square sense. This implies that also (11.4) is not satisfied exactly, i.e. compatibility conditions at interface are approximately satisfied. On the contrary, equilibrium is satisfied exactly due to the introduction of the connecting force intensities λ as in (11.12).

By substituting λ in (11.1***), it is obtained:

$$\mathbf{u} = \mathbf{H f} - \mathbf{H B_E}^T \left(\mathbf{B_C H B_E}^T \right)^+ \mathbf{B_C H f} = \mathbf{H^U f} \tag{11.18}$$

where $\mathbf{H^U}$ is the FRF matrix of the unknown subsystem U that can be rewritten in expanded form as:

$$\begin{aligned} \mathbf{H^U} = & \begin{bmatrix} \mathbf{H^{RU}} & \mathbf{0} \\ \mathbf{0} & -\mathbf{H^R} \end{bmatrix} - \begin{bmatrix} \mathbf{H^{RU}} & \mathbf{0} \\ \mathbf{0} & -\mathbf{H^R} \end{bmatrix} \begin{bmatrix} \mathbf{B_E^{RU}}^T \\ \mathbf{B_E^R}^T \end{bmatrix} \\ & \times \left(\begin{bmatrix} \mathbf{B_C^{RU}} & \mathbf{B_C^R} \end{bmatrix} \begin{bmatrix} \mathbf{H^{RU}} & \mathbf{0} \\ \mathbf{0} & -\mathbf{H^R} \end{bmatrix} \begin{bmatrix} \mathbf{B_E^{RU}}^T \\ \mathbf{B_E^R}^T \end{bmatrix} \right)^+ \\ & \times \begin{bmatrix} \mathbf{B_C^{RU}} & \mathbf{B_C^R} \end{bmatrix} \begin{bmatrix} \mathbf{H^{RU}} & \mathbf{0} \\ \mathbf{0} & -\mathbf{H^R} \end{bmatrix} \end{aligned} \tag{11.19}$$

With the dual assembly, the rows and the columns of $\mathbf{H}^U$ corresponding to compatibility and equilibrium DoFs appear twice. Furthermore, when using an extended or mixed interface, $\mathbf{H}^U$ contains some meaningless rows and columns: those corresponding to the internal DoFs of the residual substructure R. Obviously, only meaningful and independent entries are retained.

In (11.19), the product of the three matrices to be inverted can be defined as *interface flexibility matrix*. The interface flexibility matrix can be rewritten as:

$$\begin{bmatrix} \mathbf{B}_C^{RU} & \mathbf{B}_C^{R} \end{bmatrix} \begin{bmatrix} \mathbf{H}^{RU} & \mathbf{0} \\ \mathbf{0} & -\mathbf{H}^{R} \end{bmatrix} \begin{bmatrix} \mathbf{B}_E^{RU^T} \\ \mathbf{B}_E^{R^T} \end{bmatrix} = \mathbf{B}_C^{RU}\mathbf{H}^{RU}\mathbf{B}_E^{RU^T} - \mathbf{B}_C^{R}\mathbf{H}^{R}\mathbf{B}_E^{R^T} \tag{11.20}$$

It is possible to define:

$$\hat{\mathbf{H}}^{RU} = \mathbf{B}_C^{RU}\mathbf{H}^{RU}\mathbf{B}_E^{RU^T} \qquad \text{and} \qquad \hat{\mathbf{H}}^{R} = \mathbf{B}_C^{R}\mathbf{H}^{R}\mathbf{B}_E^{R^T}$$

where $\hat{\mathbf{H}}^{RU}$ and $\hat{\mathbf{H}}^{R}$ are permutations of the FRF matrices of the coupled structure and of the residual substructure.

Therefore, the interface flexibility matrix becomes:

$$\mathbf{B}_C^{RU}\mathbf{H}^{RU}\mathbf{B}_E^{RU^T} - \mathbf{B}_C^{R}\mathbf{H}^{R}\mathbf{B}_E^{R^T} = \hat{\mathbf{H}}^{RU} - \hat{\mathbf{H}}^{R} \tag{11.21}$$

11.2.2   Hybrid Assembly

In the hybrid assembly, it is sought to satisfy exactly both compatibility and equilibrium conditions. To satisfy the compatibility conditions, a unique set of DoFs is defined as in the primal assembly,

$$\left\{ \begin{array}{c} \mathbf{u}^{RU} \\ \mathbf{u}^{R} \end{array} \right\} = \begin{bmatrix} \mathbf{L}_C^{RU} \\ \mathbf{L}_C^{R} \end{bmatrix} \mathbf{q} \tag{11.22}$$

where $\mathbf{q}$ is the unique set of DoFs, and $\mathbf{L}_C$ is a localisation matrix similar to $\mathbf{L}_E$ introduced previously. Note that $\mathbf{L}_C$ is a $2N_C \times N_C$ matrix. Since there is a unique set of DoFs, $\mathbf{q}$, the compatibility condition is satisfied automatically for any set $\mathbf{q}$, i.e.

$$\begin{bmatrix} \mathbf{B}_C^{RU} & \mathbf{B}_C^{R} \end{bmatrix} \left\{ \begin{array}{c} \mathbf{u}^{RU} \\ \mathbf{u}^{R} \end{array} \right\} = \begin{bmatrix} \mathbf{B}_C^{RU} & \mathbf{B}_C^{R} \end{bmatrix} \begin{bmatrix} \mathbf{L}_C^{RU} \\ \mathbf{L}_C^{R} \end{bmatrix} \mathbf{q} = \mathbf{0} \qquad \forall \mathbf{q} \tag{11.23}$$

To satisfy exactly the equilibrium condition, it is possible to proceed as in the dual assembly i.e. by writing the connecting forces in the form given by (11.12).

By substituting (11.22) and (11.12) into (11.1 **), the 3-field formulation reduces to:

$$\begin{bmatrix} \mathbf{L}_C^{RU} \\ \mathbf{L}_C^{R} \end{bmatrix} \mathbf{q} + \begin{bmatrix} \mathbf{H}^{RU} & \mathbf{0} \\ \mathbf{0} & -\mathbf{H}^{R} \end{bmatrix} \begin{bmatrix} \mathbf{B}_E^{RU^T} \\ \mathbf{B}_E^{R^T} \end{bmatrix} \lambda = \begin{bmatrix} \mathbf{H}^{RU} & \mathbf{0} \\ \mathbf{0} & -\mathbf{H}^{R} \end{bmatrix} \left\{ \begin{array}{c} \mathbf{f}^{RU} \\ \mathbf{f}^{R} \end{array} \right\} \tag{11.1***}$$

or in more compact form:

$$\mathbf{L}_C\,\mathbf{q} + \mathbf{H}\,\mathbf{B}_E^{T}\lambda = \mathbf{H}\,\mathbf{f} \tag{11.1***}$$

By gathering $\mathbf{q}$ and λ in a single vector, one can rewrite:

$$\begin{bmatrix} \mathbf{L}_C & \mathbf{H}\,\mathbf{B}_E^{T} \end{bmatrix} \left\{ \begin{array}{c} \mathbf{q} \\ \lambda \end{array} \right\} = \mathbf{H}\,\mathbf{f} \tag{11.24}$$

where the block left matrix has size $2N_C \times (N_C + N_E)$.

Finally, from (11.24):

$$\left\{ \begin{array}{c} \mathbf{q} \\ \lambda \end{array} \right\} = \begin{bmatrix} \mathbf{L}_C & \mathbf{H}\,\mathbf{B}_E^{T} \end{bmatrix}^{+}\mathbf{H}\,\mathbf{f} \tag{11.25}$$

where the superscript + denotes the generalised inverse.

To obtain a determined or overdetermined matrix for the generalised inversion operation, the following condition must be satisfied:

$$2N_C \geq N_C + N_E \quad \Rightarrow \quad N_C \geq N_E \geq n_c \tag{11.26}$$

where it is worth to recall that n_c is the number of coupling DoFs.

Note that, if $N_C > N_E$, (11.24) is not satisfied exactly by the solution given by (11.25), but only in the minimum square sense, whilst equilibrium and compatibility conditions are satisfied exactly.

Equation 11.25 can be rewritten as:

$$\left\{ \begin{array}{c} \mathbf{q} \\ \lambda \end{array} \right\} = \left[\begin{array}{c} \mathbf{H^U}_{N_C \times 2N_E} \\ \mathbf{T}_{N_E \times 2N_E} \end{array} \right] \mathbf{f} \tag{11.27}$$

where $\mathbf{H^U}$ (i.e. the first N_C rows of the block matrix) is the FRF of the unknown subsystem U and $\mathbf{T}$ is the transmissibility between the external forces and the connecting force intensities.

With the hybrid assembly, the columns of $\mathbf{H^U}$ corresponding to the equilibrium interface DoFs appear twice. Furthermore, when using an extended interface, $\mathbf{H^U}$ contains some meaningless rows and columns: those corresponding to the internal DoFs of the residual substructure R. Obviously, only meaningful and independent entries are retained.

In (11.25), the matrix to be inverted $\left[\mathbf{L_C} \quad \mathbf{H\,B_E}^T \right]$, can be written in expanded form as:

$$\left[\begin{array}{cc} \mathbf{L_C^{RU}} & \left[\begin{array}{cc} \mathbf{H^{RU}} & \mathbf{0} \\ \mathbf{0} & -\mathbf{H^R} \end{array} \right] \left[\begin{array}{c} \mathbf{B_E^{RU}}^T \\ \mathbf{B_E^R}^T \end{array} \right] \end{array} \right] = \left[\begin{array}{cc} \mathbf{L_C^{RU}} & \mathbf{H^{RU} B_E^{RU}}^T \\ \mathbf{L_C^R} & -\mathbf{H^R B_E^R}^T \end{array} \right] \tag{11.28}$$

Similarly to $\mathbf{L_E^{RU}}$ and $\mathbf{L_E^R}$, $\mathbf{L_C^{RU}}$ and $\mathbf{L_C^R}$ are permutation matrices. Furthermore, similarly to $\mathbf{B_C^{RU}}$ and $\mathbf{B_C^R}$, $\mathbf{B_E^{RU}}$ is a permutation matrix and $\mathbf{B_E^R}$ is the negative of a permutation matrix.

If $N_C = N_E$, the matrix in (11.28) is square and it is possible to compute its determinant, taking into account that permutation matrices behave as identity matrices when computing the determinant:

$$\left| \begin{array}{cc} \mathbf{L_C^{RU}} & \mathbf{H^{RU} B_E^{RU}}^T \\ \mathbf{L_C^R} & -\mathbf{H^R B_E^R}^T \end{array} \right| = \left| \begin{array}{cc} \mathbf{I} & \mathbf{H^{RU}} \\ \mathbf{I} & \mathbf{H^R} \end{array} \right| = - \left| \mathbf{H^{RU}} - \mathbf{H^R} \right| \tag{11.29}$$

which is the negative of the determinant of the interface flexibility matrix, (11.21).

11.2.3 Singularity

Both for dual and hybrid assembly, the interface flexibility matrix is strictly related to singularity: for dual assembly the interface flexibility matrix must be inverted directly, for hybrid assembly the determinant of the matrix to be inverted is the negative of the determinant of the interface flexibility matrix.

In relation with dual assembly, it is shown in [6, 7] that the interface flexibility matrix is singular:

- At the resonant frequencies of the residual substructure with coupling DoFs grounded, both for standard interface and for non collocated extended interface;
- At all frequencies for collocated extended interface, although this kind of singularity can be easily removed by smart inversion techniques.

The above conclusions hold for the hybrid formulation too.

11.2.4 Hybrid vs Dual Formulation

In this section, the hybrid formulation and the dual formulation are compared to establish whether they provide the same result or not, and under which conditions. With regard to the hybrid formulation, By comparing (11.25) with (11.27), one obtains:

$$\begin{bmatrix} \mathbf{H^U} \\ \mathbf{T} \end{bmatrix} = \begin{bmatrix} \mathbf{L_C} & \mathbf{H\,B_E}^T \end{bmatrix}^+ \mathbf{H} \tag{11.30}$$

If $N_C = N_E$, (11.30) becomes:

$$\begin{bmatrix} \mathbf{H^U} \\ \mathbf{T} \end{bmatrix} = \begin{bmatrix} \mathbf{L_C} & \mathbf{H\,B_E}^T \end{bmatrix}^{-1} \mathbf{H} \tag{11.31}$$

Premultiplying by $[\mathbf{L_C}\ \mathbf{HB_E}^T]$, one obtains:

$$\begin{bmatrix} \mathbf{L_C} & \mathbf{H\,B_E}^T \end{bmatrix} \begin{bmatrix} \mathbf{H^U} \\ \mathbf{T} \end{bmatrix} = \mathbf{H} \tag{11.32}$$

i.e.:

$$\mathbf{L_C\,H^U} + \mathbf{H\,B_E}^T\mathbf{T} = \mathbf{H} \tag{11.33}$$

Premultiplying by $\mathbf{H}^{-1}$:

$$\mathbf{H}^{-1}\mathbf{L_C\,H^U} + \mathbf{B_E}^T\mathbf{T} = \mathbf{I} \tag{11.34}$$

Finally, premultiplying by $\mathbf{L_E}^T$, one obtains:

$$\mathbf{L_E}^T\mathbf{H}^{-1}\mathbf{L_C\,H^U} = \mathbf{L_E}^T \tag{11.35}$$

being $\mathbf{L_E}^T\mathbf{B_E}^T = 0$ since $\mathbf{B_E^T}$ is the nullspace of $\mathbf{L_E^T}$.

The FRF of the unknown subsystem U provided by dual formulation (see [6], Eq. 18) can be rewritten in compact form for $N_C = N_E$:

$$\mathbf{H^U}_D = \mathbf{H} - \mathbf{HB_E}^T\left(\mathbf{B_C HB_E}^T\right)^{-1}\mathbf{B_C H} \tag{11.36}$$

where the subscript D stands for dual. Premultiplying by $\mathbf{H}^{-1}$, one obtains:

$$\mathbf{H}^{-1}\mathbf{H^U}_D = \mathbf{I} - \mathbf{B_E}^T\left(\mathbf{B_C HB_E}^T\right)^{-1}\mathbf{B_C H} \tag{11.37}$$

Premultiplying by $\mathbf{L_E^T}$, one obtains:

$$\mathbf{L_E}^T\mathbf{H}^{-1}\mathbf{H^U}_D = \mathbf{L_E}^T \tag{11.38}$$

where again $\mathbf{L_E}^T\mathbf{B_E}^T = 0$.

By comparing (11.38) and (11.35), it is found that:

$$\mathbf{H^U}_D = \mathbf{L_C H^U} \tag{11.39}$$

The former equation shows that, if $N_C = N_E$, hybrid and dual formulations provide the same result. In fact, by considering the hybrid formulation, the relation between the unique set of DoFs $\mathbf{q}$ and the redundant set of DoFs $\mathbf{u}$ is given by $\mathbf{u} = \mathbf{L_C q}$.

On the contrary, if $N_C > N_E$, (11.32) cannot be obtained from (11.30) since:

$$\begin{bmatrix} \mathbf{L_C} & \mathbf{H\,B_E}^T \end{bmatrix}\begin{bmatrix} \mathbf{L_C} & \mathbf{H\,B_E}^T \end{bmatrix}^+ \neq \mathbf{I}$$

due to the definition of pseudoinverse for an overdetermined system.

Therefore, if $N_C > N_E$, the hybrid and the dual formulation provide different results.
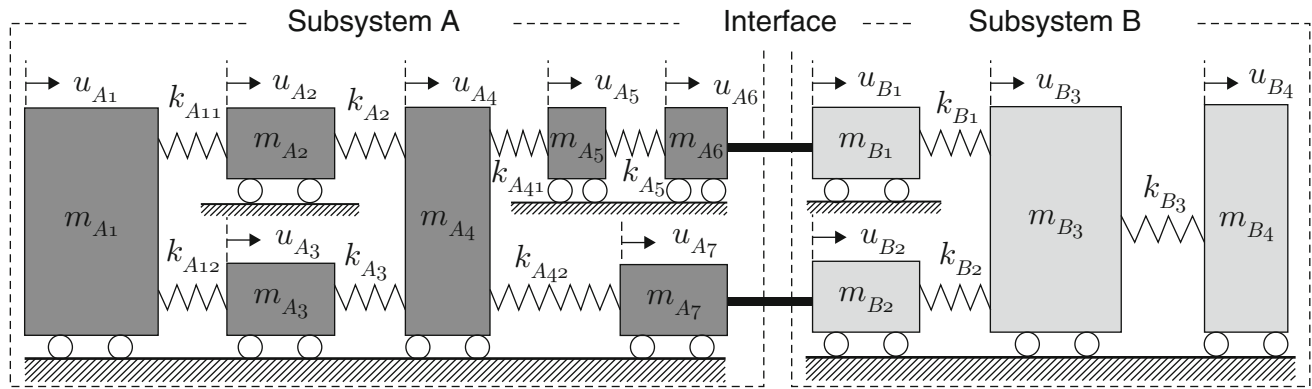
Fig. 11.2 Sketch of the test system

Table 11.1 Physical parameter values

Mass	(kg)	Stiffness	(N ·m)
m_{A1}	10	k_{A11}	2,000
m_{A2}	3	k_{A12}	2,000
m_{A3}	3	k_{A2}	1,000
m_{A4}	6	k_{A3}	1,000
m_{A5}	2	k_{A41}	500
m_{A6}	2	k_{A42}	1,000
m_{A7}	4	k_{A5}	200
m_{B1}	2	k_{B1}	1,000
m_{B2}	4	k_{B2}	1,000
m_{B3}	8	k_{B3}	2,000
m_{B4}	5	–	–

Table 11.2 Natural frequencies of the systems (Hz)

	System		
Mode	U (B)	R (A)	RU (AB)
1	0	0	0
2	2.6801	1.3168	1.1464
3	3.4287	2.1436	2.3974
4	4.7808	3.0046	2.5671
5	–	4.1146	3.0846
6	–	5.0329	4.0175
7	–	5.9736	4.5716
8	–	–	5.0329
9	–	–	5.9688

11.3 Application

A relatively simple application is considered on a discrete system already used as a case study in [8]. The complete system is a 9 DoFs system (see Fig. 11.2). The residual subsystem R is a 7 DoFs system, represented by subsystem A in figure, and the unknown subsystem U is a 4 DoFs system, represented by subsystem B. The two subsystems are coupled at a 2 DoFs interface.

Mass and stiffness values are shown in Table 11.1. Proportional damping is used: $\mathbf{C} = \alpha \mathbf{M} + \beta \mathbf{K}$, with $\alpha = 0.1$, $\beta = 0$.

To have an idea of the dynamic behaviour of the system, the natural frequencies of the subsystems U and R, and of the coupled system RU are shown in Table 11.2.

It is assumed that the FRFs (mobilities) describing the velocity/force relationship of the coupled system RU, and the mechanical impedance of the residual subsystem R are known. The mobility of subsystem U has to be determined. The exact

Fig. 11.3 H_{66}^{RU}: true (—), with noise (···), fitted (—)
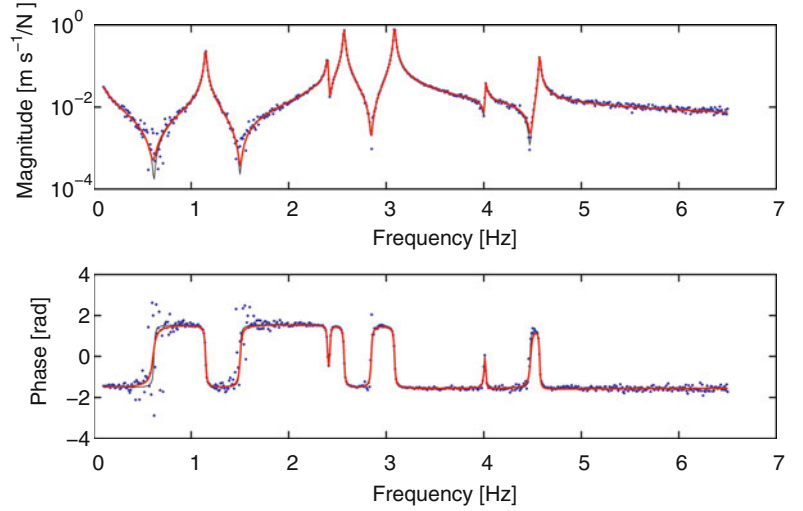
Fig. 11.4 H_{77}^{RU}: true (—), with noise (···), fitted (—)
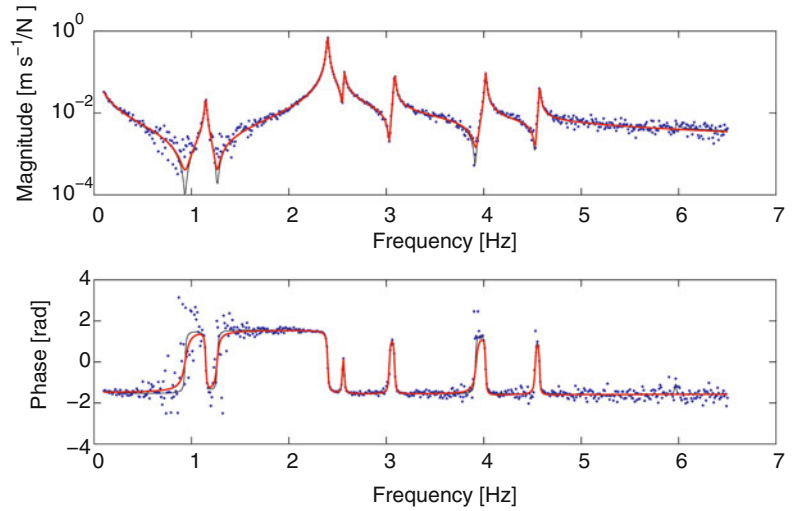
FRFs $\hat{H}_{ij}$ of the coupled system RU and the impedances of subsystem R are computed starting from the physical parameters of Table 11.1. To simulate the effect of noise on the FRFs of the coupled system, a complex random perturbation is added to true FRFs:

$$H_{ij}(\omega_k) = \hat{H}_{ij}(\omega_k) + m_{ij,k} + i\, n_{ij,k} \tag{11.40}$$

where $i = \sqrt{-1}$, $m_{ij,k}$ and $n_{ij,k}$ are independent random variables with gaussian distribution, zero mean and a standard deviation of $1 \cdot 10^{-3}$ m/(sN), chosen as about 5% of FRF mean value and about 0.1% of FRF peak value. The effect of such perturbation on the drive point mobilities at the coupling DoFs is shown in Figs. 11.3 and 11.4 together with the FRF obtained after curve-fitting.

In the sequel, only FRFs perturbed by simulated noise will be considered. In fact, if noise-free FRFs of the coupled system are used, the FRF of the unknown subsystem is predicted without errors (although the problem may be singular for several reasons, as stated in [6], the use of smart inversion techniques completely removes the singularity). Furthermore, perturbed FRFs are not used in raw form but are smoothed through a curve fitting procedure.

The mobility of subsystem U can be determined by using the procedure described previously where the compatibility and equilibrium DoFs are defined on a case by case basis. Results are compared with those obtained using the dual formulation [6].

Fig. 11.5 H_{11}^U: true (—),
computed without additional
internal dofs (···)
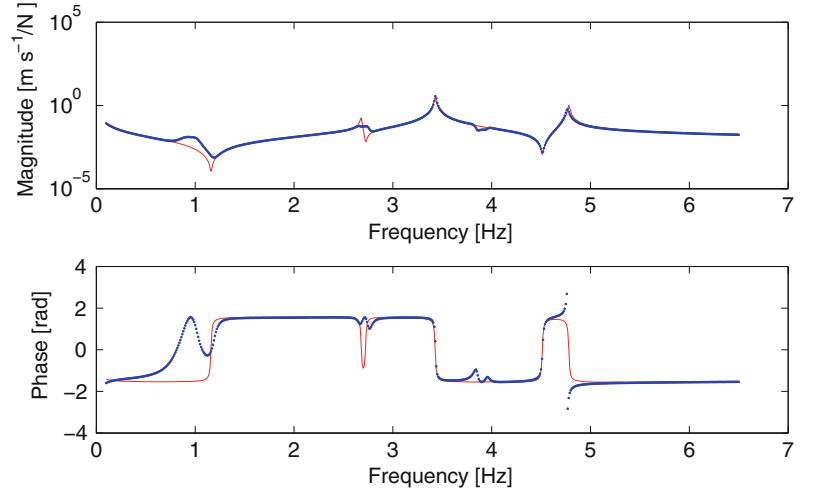
Fig. 11.6 H_{22}^U: true (—),
computed without additional
internal dofs (···)
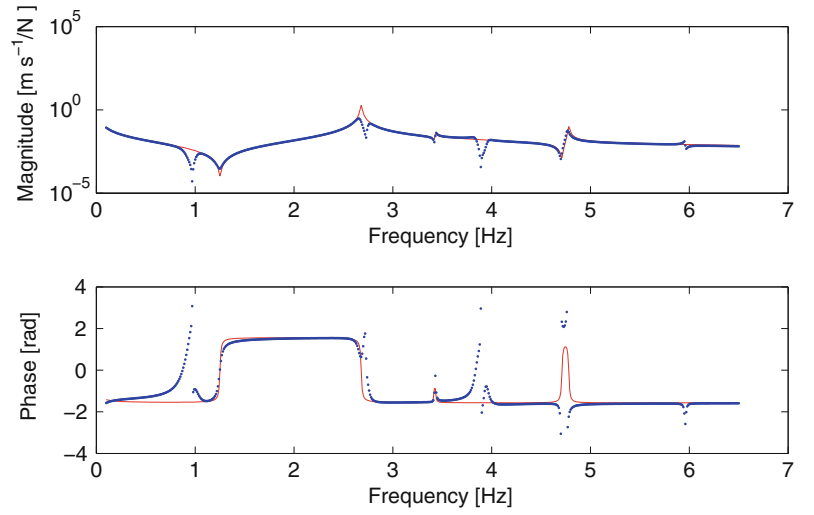
11.3.1 Decoupling

First of all, the case of standard interface (mobility known only at the coupling DoFs 6 and 7) is considered. In this case, $N_C = 2$, $N_E = 2$ and

$$
\mathbf{B_E} = \begin{matrix} u_6^{RU} & u_7^{RU} & u_6^{R} & u_7^{R} \end{matrix} \\
\begin{bmatrix} 1 & 0 & -1 & 0 \\ 0 & 1 & 0 & -1 \end{bmatrix} \\
\quad \mathbf{B_E^{RU}} \qquad \mathbf{B_E^{R}}
\tag{11.41}
$$

$$
\mathbf{L_C} = \begin{bmatrix} \mathbf{L_C^{RU}} \\ \mathbf{L_C^{R}} \end{bmatrix} = \begin{bmatrix} 1 & 0 \\ 0 & 1 \\ \hline 1 & 0 \\ 0 & 1 \end{bmatrix} \begin{matrix} \leftarrow u_6^{RU} \\ \leftarrow u_7^{RU} \\ \leftarrow u_6^{R} \\ \leftarrow u_7^{R} \end{matrix}
\tag{11.42}
$$

In Figs. 11.5 and 11.6, the true drive point mobilities at the coupling DoFs 1 and 2 of subsystem U are compared with the corresponding FRFs computed using the hybrid formulation, (11.25), starting from the fitted perturbed FRFs of the coupled system. As known, the same results are obtained using the dual formulation.

As discussed in previous papers [6, 10], the predicted mobility of subsystem U is badly identified at some frequencies. This depends on ill conditioning due to unmeasured internal DoFs. In fact, the coupled system RU and the residual subsystem R, with the "measured" coupling DoFs 6 and 7 grounded, share five resonance frequencies, namely $f_{n1} = 0.96$ Hz, $f_{n2} = 2.72$ Hz, $f_{n3} = 3.90$ Hz, $f_{n4} = 5.03$ Hz and $f_{n5} = 5.96$ Hz. Around these frequencies, the problem is ill-conditioned and noise can be greatly amplified.

A way to circumvent this problem is to use an extended interface, i.e. to assume that the FRF matrix of the coupled system is known not only at the coupling DoF but also at a subset of the five internal DoFs (1, 2, 3, 4, 5) of the residual subsystem R.

A possibility is to use a collocated approach with all the internal DoFs. In this case, $N_C = 7$, $N_E = 7$ and

$$
\mathbf{B_E} =
\begin{bmatrix}
\begin{array}{ccccccc|ccccccc}
u_1^{RU} & u_2^{RU} & u_3^{RU} & u_4^{RU} & u_5^{RU} & u_6^{RU} & u_7^{RU} & u_1^{R} & u_2^{R} & u_3^{R} & u_4^{R} & u_5^{R} & u_6^{R} & u_7^{R} \\
1 & 0 & 0 & 0 & 0 & 0 & 0 & -1 & 0 & 0 & 0 & 0 & 0 & 0 \\
0 & 1 & 0 & 0 & 0 & 0 & 0 & 0 & -1 & 0 & 0 & 0 & 0 & 0 \\
0 & 0 & 1 & 0 & 0 & 0 & 0 & 0 & 0 & -1 & 0 & 0 & 0 & 0 \\
0 & 0 & 0 & 1 & 0 & 0 & 0 & 0 & 0 & 0 & -1 & 0 & 0 & 0 \\
0 & 0 & 0 & 0 & 1 & 0 & 0 & 0 & 0 & 0 & 0 & -1 & 0 & 0 \\
0 & 0 & 0 & 0 & 0 & 1 & 0 & 0 & 0 & 0 & 0 & 0 & -1 & 0 \\
0 & 0 & 0 & 0 & 0 & 0 & 1 & 0 & 0 & 0 & 0 & 0 & 0 & -1
\end{array}
\end{bmatrix}
$$

with blocks $\mathbf{B_E^{RU}}$ and $\mathbf{B_E^{R}}$.

$$
\mathbf{L_C} =
\begin{bmatrix} \mathbf{L_C^{RU}} \\ \mathbf{L_C^{R}} \end{bmatrix} =
\begin{bmatrix}
1 & 0 & 0 & 0 & 0 & 0 & 0 \\
0 & 1 & 0 & 0 & 0 & 0 & 0 \\
0 & 0 & 1 & 0 & 0 & 0 & 0 \\
0 & 0 & 0 & 1 & 0 & 0 & 0 \\
0 & 0 & 0 & 0 & 1 & 0 & 0 \\
0 & 0 & 0 & 0 & 0 & 1 & 0 \\
0 & 0 & 0 & 0 & 0 & 0 & 1 \\
\hline
1 & 0 & 0 & 0 & 0 & 0 & 0 \\
0 & 1 & 0 & 0 & 0 & 0 & 0 \\
0 & 0 & 1 & 0 & 0 & 0 & 0 \\
0 & 0 & 0 & 1 & 0 & 0 & 0 \\
0 & 0 & 0 & 0 & 1 & 0 & 0 \\
0 & 0 & 0 & 0 & 0 & 1 & 0 \\
0 & 0 & 0 & 0 & 0 & 0 & 1
\end{bmatrix}
\begin{matrix}
\leftarrow u_1^{RU} \\ \leftarrow u_2^{RU} \\ \leftarrow u_3^{RU} \\ \leftarrow u_4^{RU} \\ \leftarrow u_5^{RU} \\ \leftarrow u_6^{RU} \\ \leftarrow u_7^{RU} \\ \leftarrow u_1^{R} \\ \leftarrow u_2^{R} \\ \leftarrow u_3^{R} \\ \leftarrow u_4^{R} \\ \leftarrow u_5^{R} \\ \leftarrow u_6^{R} \\ \leftarrow u_7^{R}
\end{matrix}
\tag{11.43}
$$

In Figs. 11.7 and 11.8, the true drive point mobilities at the coupling DoFs 1 and 2 of subsystem U are compared with the corresponding FRFs computed using the hybrid formulation, starting from the fitted perturbed FRFs of the coupled system. As known, the same results are obtained using the dual formulation. In this case, the residual subsystem is fully grounded and no ill-conditioned frequencies appear.

Using a non collocated approach enforcing compatibility at all DoFs and equilibrium only at the coupling DoFs 6 and 7, it is $N_C = 7$, $N_E = 2$, $\mathbf{B_E}$ is the same as in (11.41) and $\mathbf{L_C}$ is the same as in (11.43).

In Figs. 11.9 and 11.10, the true drive point mobilities at the coupling DoFs 1 and 2 of subsystem U are compared with the corresponding FRFs computed using once the hybrid formulation, (11.25), and once the dual formulation. The two approach provide very similar results, and ill conditioned frequencies are the same as for standard interface but they affect the predicted FRFs to a lower extent if compared with the standard interface.

Fig. 11.7 H_{11}^U: true (—),
computed with all the internal
dofs (...)
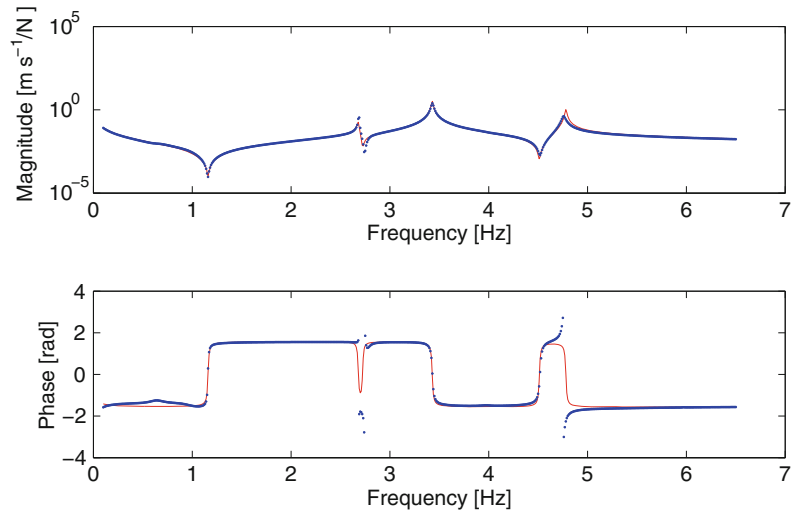
Fig. 11.8 H_{22}^U: true (—),
computed with all the internal
dofs (...)
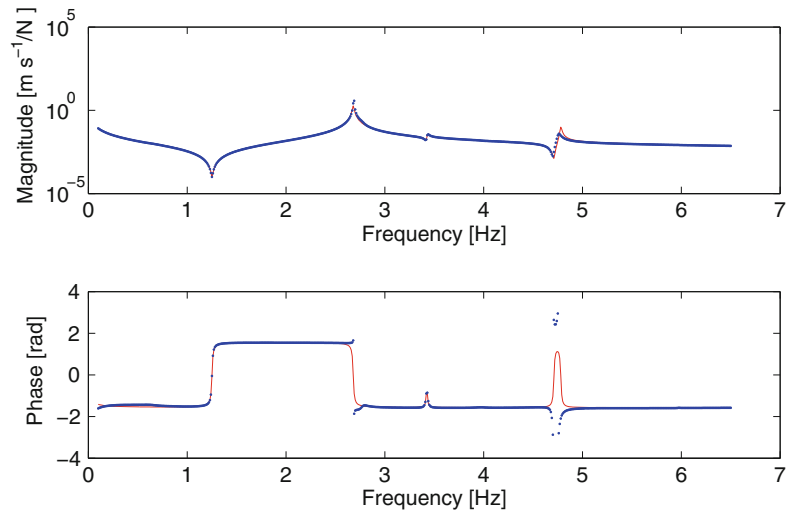
Since the full set of internal DoFs can be difficult to measure in practice, results obtained by adding only one internal DoF are considered. By enforcing compatibility at DoFs 2, 6, 7, and equilibrium only at coupling DoFs, it is $N_C = 3, N_E = 2, \mathbf{B_E}$ is the same as in (11.41) and

$$
\mathbf{L_C} = \begin{bmatrix} \mathbf{L_C^{RU}} \\ \mathbf{L_C^{R}} \end{bmatrix} = \begin{bmatrix} 1 & 0 & 0 \\ 0 & 1 & 0 \\ 0 & 0 & 1 \\ 1 & 0 & 0 \\ 0 & 1 & 0 \\ 0 & 0 & 1 \end{bmatrix} \begin{matrix} \leftarrow u_2^{RU} \\ \leftarrow u_6^{RU} \\ \leftarrow u_7^{RU} \\ \leftarrow u_2^{R} \\ \leftarrow u_6^{R} \\ \leftarrow u_7^{R} \end{matrix}
$$

In Figs. 11.11 and 11.12, the true drive point mobilities at the coupling DoFs 1 and 2 of subsystem U are compared with the corresponding FRFs computed using once the hybrid formulation, (11.25), and once the dual formulation. Again, results from the two formulations are very similar and show that noise is amplified around ill-conditioning frequencies which are the same as for standard interface.

Fig. 11.9 H_{11}^{U}: true (—),
computed with compatibility
at dofs 1–7 and equilibrium
at dofs 6 & 7 (⋯)

hybrid assembly

dual assembly
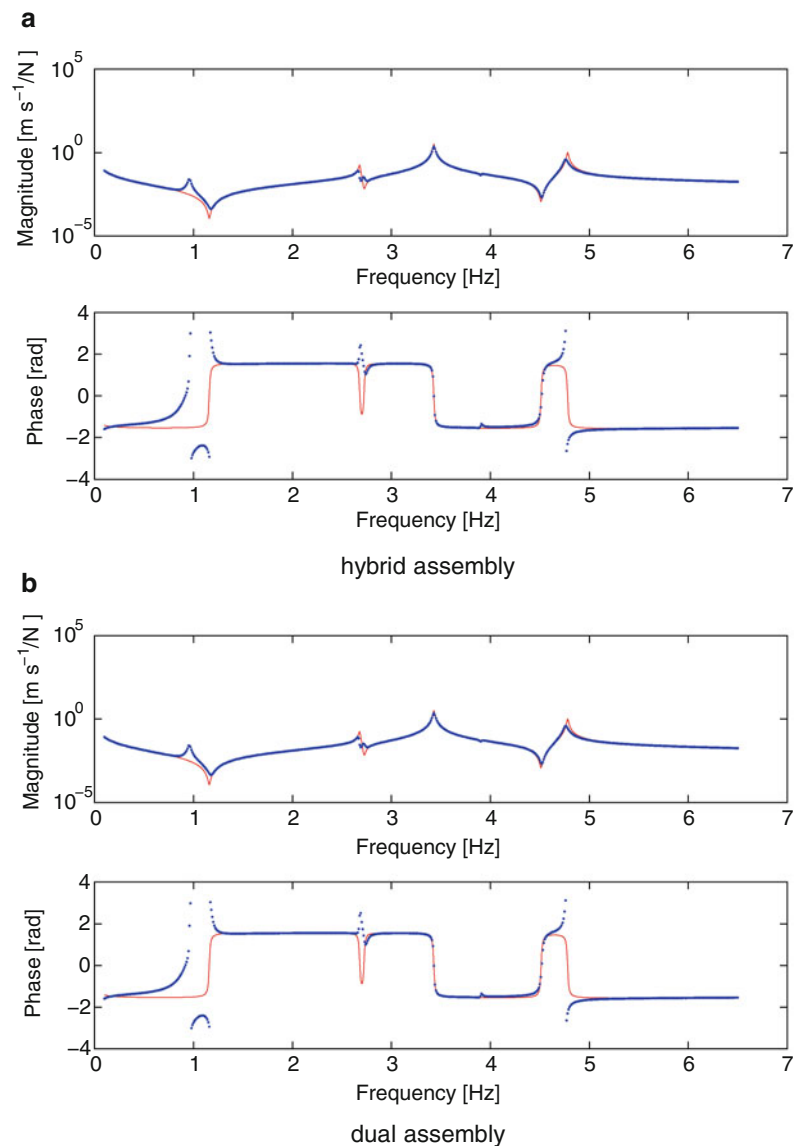
11.4 Summary and Discussion

The identification of the dynamic behaviour of a structural subsystem, starting from the known dynamic behaviour of the assembled system, and from information about the residual subsystem, (the remaining part of the structural system), i.e. decoupling problem, is considered in this paper. Direct decoupling techniques are considered, that consist in adding to the assembled system a fictitious subsystem, which is the negative of the residual subsystem. Starting from the 3-field formulation (dynamic balance, compatibility and equilibrium), a hybrid approach for decoupling is developed and compared with a dual approach.

Compatibility and equilibrium can be required either at coupling DoFs only (standard interface), or at additional internal DoFs of the residual subsystem (extended interface): the choice of interface DoFs determines a set of frequencies at which the decoupling problem is ill conditioned. An additional variant is the possibility to use the non collocated approach, in which DoFs used to enforce equilibrium are not the same as DoFs used to enforce compatibility: in this case the number of DoFs used to enforce compatibility must be not less than the number of DoFs used to enforce equilibrium.

As in dual assembly, also in hybrid assembly ill conditioning is strictly related to the interface flexibility matrix. Furthermore, hybrid assembly and dual assembly provide the same result when the number of DoFs used to enforce

Fig. 11.10 H_{22}^U: true (—),
computed with compatibility
at dofs 1–7 and equilibrium
at dofs 6 & 7 (···)

a

hybrid assembly

b

dual assembly
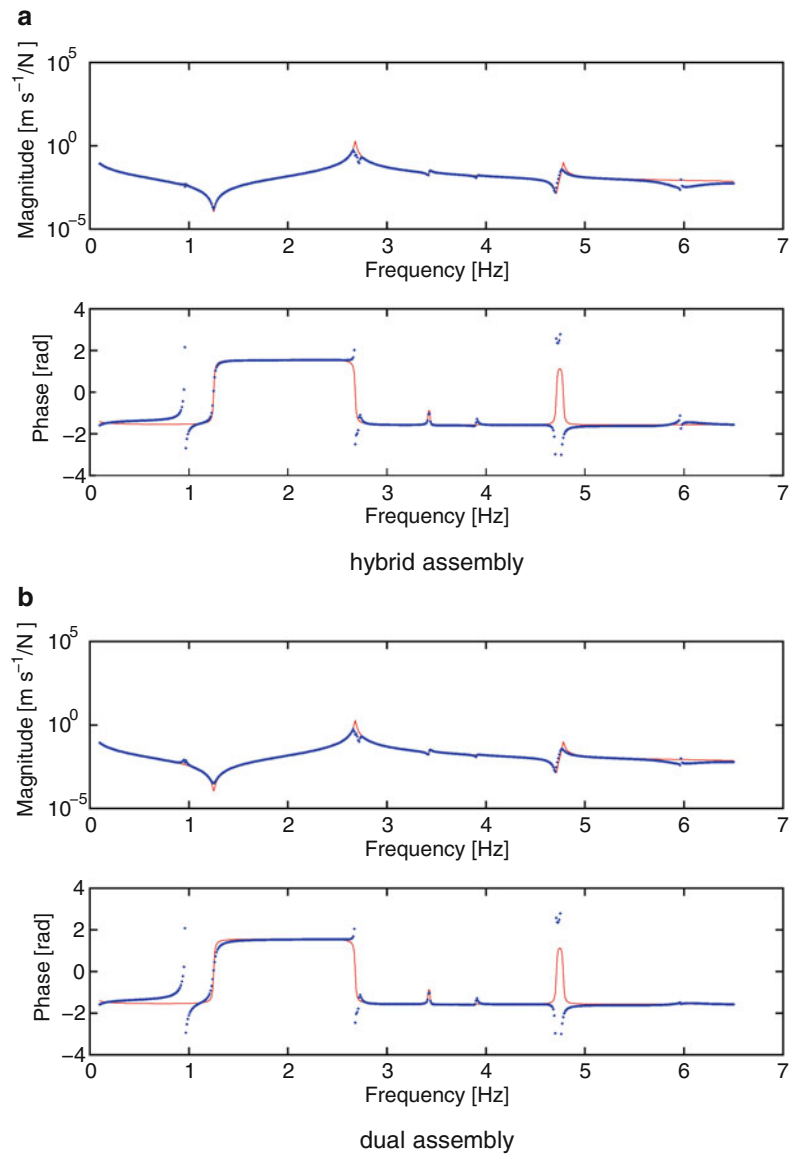
compatibility is equal to the number of DoFs used to enforce equilibrium, i.e. in the collocated approach and in some special case of non collocated approach. On the contrary, when the number of DoFs used to enforce compatibility is greater than the number of DoFs used to enforce equilibrium, the two approaches provide different results: in fact, using the hybrid approach, compatibility and equilibrium are enforced exactly; using the dual approach, compatibility is only approximate whilst equilibrium of constraint forces is enforced exactly.

Fig. 11.11 H_{11}^U: true (—), computed with compatibility at dofs 2, 6, 7 and equilibrium at dofs 6 & 7 ($\cdots$)

a

hybrid assembly

b

dual assembly
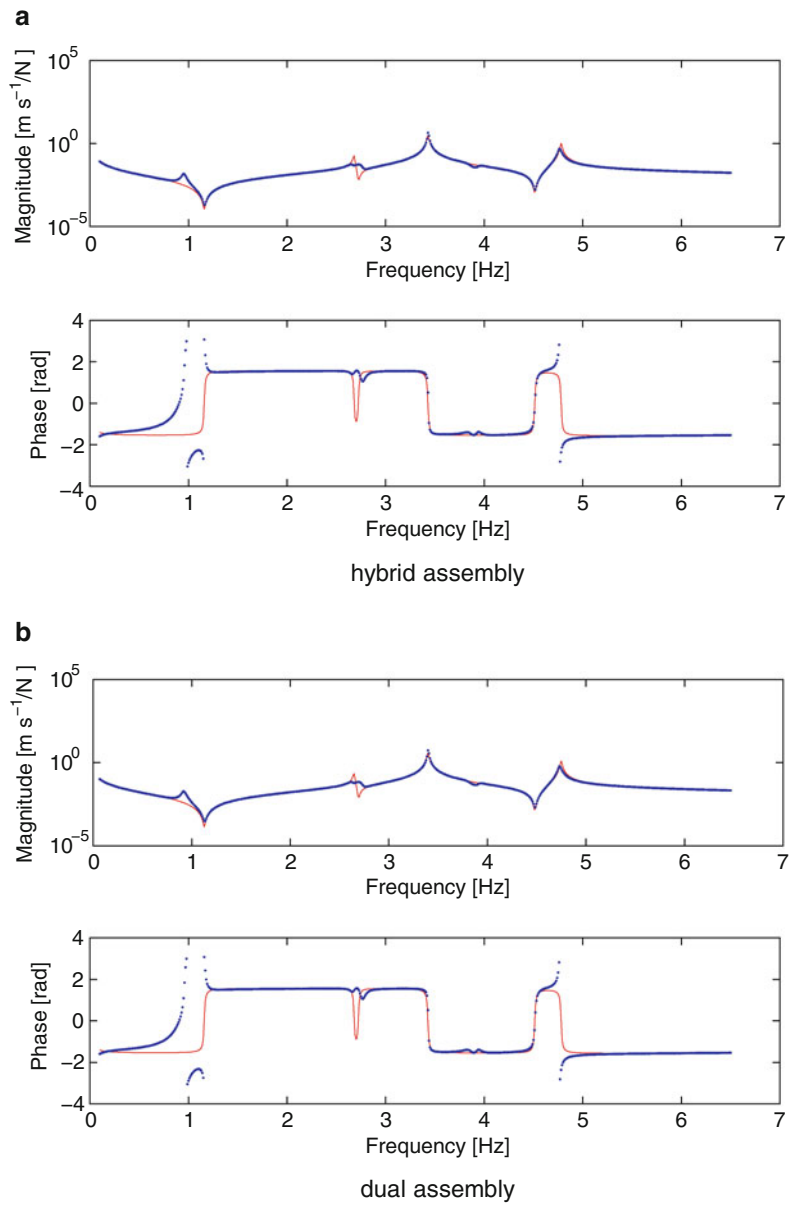
Fig. 11.12 H_{22}^U: true (—),
computed with compatibility
at dofs 2, 6, 7 and equilibrium
at dofs 6 & 7 (⋯)
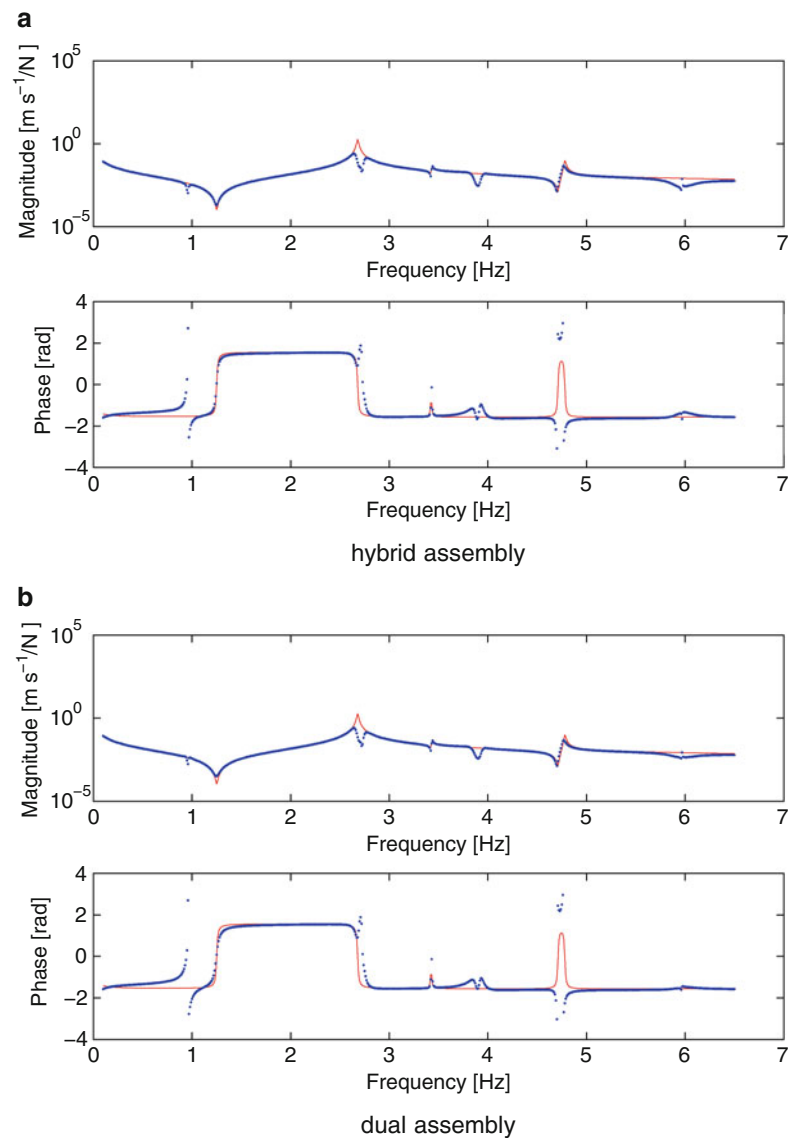
hybrid assembly

dual assembly

References

1. Jetmundsen B, Bielawa R, Flannelly W (1988) Generalised frequency domain substructure synthesis. J Am Helicopter Soc 33(1):55–64
2. de Klerk D, Rixen DJ, Voormeeren S (2008) General framework for dynamic substructuring: history, review, and classification of techniques. AIAA J 46(5):1169–1181
3. de Klerk D (2009) Dynamic response characterization of complex systems through operational identification and dynamic substructuring. Ph. D. thesis, TU Delft
4. D'Ambrogio W, Fregolent A (2008) Promises and pitfalls of decoupling procedures. Proceedings of 26th IMAC, Orlando, Feb 2008
5. Sjvall P, Abrahamsson T (2008) Substructure system identification from coupled system test data. Mech Syst Signal Process 22(1):15–33
6. D'Ambrogio W, Fregolent A (2010) The role of interface DoFs in decoupling of substructures based on the dual domain decomposition. Mech Syst Signal Process 24(7):2035–2048. doi:10.1016/j.ymssp.2010.05.007, also in Proceedings of ISMA 2010, 1863–1880, Leuven
7. D'Ambrogio W, Fregolent A (2011) Direct decoupling of substructures using primal and dual formulation. Proceedings of 29th IMAC, Jacksonville, Feb 2011
8. Vormeeren SN, Rixen DJ (2010) A dual approach to substructure decoupling techniques. Proceedings of 28th IMAC, Jacksonville, Feb 2010

9. Vormeeren SN, Rixen DJ (2010) A family of substructure decoupling techniques based on a dual assembly approach. In: Sas P, Bergen B (eds) Proceedings of ISMA 2010 – international conference on noise and vibration engineering. Leuven, pp 1955–1968, Sept 2010

10. D'Ambrogio W, Fregolent A (2009) Decoupling procedures in the general framework of frequency based substructuring. Proceedings of 27th IMAC, Orlando, Feb 2009

Chapter 12
Substructuring with Nonlinear Subcomponents: A Nonlinear Normal Mode Perspective

Matthew S. Allen and Robert J. Kuether

Abstract Substructure coupling techniques allow one to predict the response of an assembly from dynamic models for each subcomponent. Linear substructures are routinely used in analysis (e.g. the Craig-Bampton method) to reduce the computational cost of vibration, noise and load predictions for structures. They also provide a designer with insight into the influence that each subcomponent has on the assembled system's natural frequencies, mode shapes and damping. These concepts are currently limited to assemblies of linear substructures. This work explores substructuring with nonlinear subcomponents (substructures), using the nonlinear normal modes of each substructure to seek to understand how those contribute to the nonlinear modes of the assembly. The goal is to extend the insights that have been developed over the past several years for linear substructures, to nonlinear ones. A specific type of describing function model, which captures the variation of the structure's natural frequencies and mode shapes with energy is introduced, which is here dubbed a Representative Linear Modal Model (RLMM). The results show that this type of model can be used with linear substructuring techniques to effectively predict the dynamics of a nonlinear assembly, suggesting that linear substructuring concepts may be applied advantageously to nonlinear assemblies.

12.1 Introduction

Dynamic substructuring techniques allow one to predict the dynamics of an assembly from knowledge of the dynamics of each subcomponent and the way in which the subcomponents are assembled. For example, this is the basis of the finite element method, where individual elements with known stiffness and mass are assembled to approximate the behavior of a complicated structure. However, substructuring methods are more often employed in situations in which the subcomponents are more meaningful, for example, models of an engine and transmission may be assembled to predict the performance of a vehicle's powertrain. In applications such as this each subcomponent is likely to be described by a reduced order model. For example, when the subcomponents are linear, their low frequency modes (e.g. a Craig-Bampton model [1]) can be used to construct a reduced order model for each subcomponent and then dynamic substructuring procedures can be used to assemble the system; more simply, this approach allows one to predict the modes of an assembly from the known modes of the subcomponents. These techniques are also valid when the model for one of the subcomponents is derived experimentally (i.e. instead of using the finite element method to create the reduced-order modal model). Substructuring techniques are quite mature for linear assemblies comprised of analytical (e.g. Finite element) subcomponents, while, on the other hand, they are still not used very frequently with experimentally derived models. Work is ongoing in this area [2–4]. The reader is referred to a recent review [5] for additional details.

Substructuring methods can be classified as to whether they use modal models for the subcomponents, termed Modal Substructuring, or, for linear systems, the frequency response functions, called Frequency Based Substructuring in [5]. Modal substructuring will be the focus of this work. The concept of modes is very powerful. For example, one can show

M.S. Allen (✉) • R.J. Kuether
Department of Engineering Physics, University of Wisconsin, Madison, WI 53706, USA
e-mail: msallen@engr.wisc.edu; rkuether@wisc.edu

that each mode of an assembly is most strongly affected by those subcomponent modes that have similar frequencies [6] (or see the case study in [7]), so if an assembly has a mode at an undesirable frequency a designer can target specific subcomponent motions to alleviate the problem. Modes can also be used to construct very efficient subcomponent models. For example, while it may be prohibitively expensive to compute the modes of a structure that is modeled by millions of finite elements, the computational cost can be reduced dramatically by first breaking the substructure into subcomponents, using the Craig-Bampton method to construct modal models of each and then assembling the reduced-order models. Modal models are also convenient when a substructure is modeled experimentally, since the modes of the structure are readily manifest in the response and can be extracted to create a compact model for the subcomponent.

This work seeks to extend the concept of modal substructuring to nonlinear dynamic systems. A nonlinear system does not have modes if one remains bound to the classical definition, but many of the key concepts can be readily extended to nonlinear systems using the concept of a nonlinear normal mode (NNM). Specifically, a nonlinear normal mode describes the frequency of oscillation and the deformation shape of a nonlinear structure, and how those evolve with increasing energy (or amplitude). Here the definition pioneered by Rosenberg [8] will be used, which was developed further in recent years by Vakakis, Kerschen and others [9–11]. This work explores the relationship between the nonlinear normal modes of an assembly and those of its subcomponents, revealing that many concepts from linear substructuring can be readily extended to nonlinear systems. For example, this work shows that two nonlinear subcomponents with similar NNM frequencies interact to form new modes at distinct frequencies in the assembly, in much the same way that two linear modes combine in the classical vibration absorber.

The concept of modes with amplitude or energy dependent frequencies, which is central to this work, is well established although perhaps only more recently placed on a firmer theoretical basis using the nonlinear normal mode concept. (The concept of frequency energy dependence will be rigorously defined in Sect. 12.2.3.) For example, many structures are only weakly nonlinear so that the nonlinearity is thought to have little effect besides causing the effective natural frequencies and/or mode shapes to change somewhat as the forcing amplitude is increased. Hence, it has often been suggested that one can simply ignore the nonlinearity and obtain adequate accuracy with a linear model so long as the appropriate natural frequency (for the forcing level of interest) is used when simulating the response or performing substructuring. (See, for example [12]. This idea is also closely related to the describing function approach used in nonlinear controls [13], also called quasi-linearization). This work explores the validity of this approach and seeks to understand its merits and limitations with regard to substructuring. The results presented here suggest that this approach is remarkably useful. The examples presented show that the amplitude dependent modal parameters of two subcomponents can be combined with linear modal substructuring to accurately predict the frequency-energy evolution of the nonlinear normal modes of the assembly. This approximate substructuring approach could be very valuable when designing systems with nonlinear subcomponents, since it allows the analyst to predict how the NNMs of an assembly will react to a structural modification.

The paper is organized as follows. The following section briefly reviews substructuring theory for both linear and nonlinear systems. Then the nonlinear normal mode concept is introduced and explained in this context. An approximate substructuring method is then proposed in Sect. 12.2.4, which reveals how changes in the effective frequency and mode shape of a nonlinear subcomponent affect those of the assembly. The proposed methods are demonstrated on some relatively simple, nonlinear, spring-mass models in Sect. 12.3 and the conclusions are presented in Sect. 12.4.

12.2 Theory

12.2.1 Review of Substructuring Theory for Linear and Nonlinear Systems

Figure 12.1 shows a schematic of a general substructuring problem, adapted from [5], where two substructures, denoted A and B, are assembled at three connection points in order to form the built-up system.

A general, nonlinear dynamic system can be described with the following equation of motion in terms of the state vector, $\mathbf{x}$, and the input forces, $\mathbf{u}$, which are comprised of both the forces applied at the interface (i) and elsewhere (app) $\mathbf{u}(t) = \mathbf{F}^A_i + \mathbf{F}_{app}^A$. The superscript $()^A$ identifies the quantities that pertain to substructure A and similarly for B.

$$\dot{\mathbf{x}}^A(t) = \mathbf{f}^A\big(\mathbf{x}^A(t), \mathbf{u}(t)\big)$$
$$\dot{\mathbf{x}}^B(t) = \mathbf{f}^B\big(\mathbf{x}^B(t), \mathbf{u}(t)\big) \tag{12.1}$$
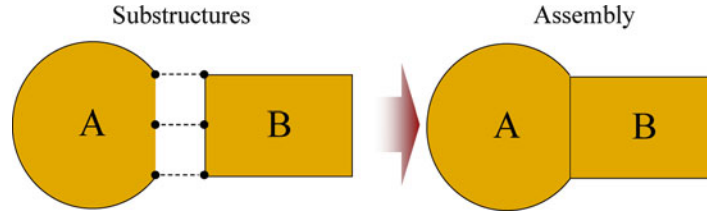
Fig. 12.1 Schematic of general substructuring problem. Subcomponents A and B are assembled at a series of connection points to form the assembly of interest
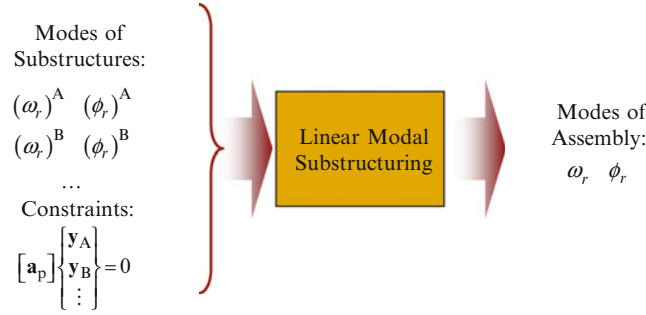
Fig. 12.2 Overview of linear modal substructuring process. Modal models for the substructures are combined, constraints are enforced between the components, and the result is an estimate of the mode shapes and natural frequencies of the assembly

The derivative of the state vector is, in general, a nonlinear function, $\mathbf{f}^A()$, of the states and the input forces. A similar set of equations is written for B and the process could be repeated for any number of subcomponents. The goal is to assemble the subcomponent models in order to obtain a dynamic model for the built-up system.

Assembly is accomplished by enforcing equal displacement at certain points, e.g. $\mathbf{x}_1{}^A = \mathbf{x}_3{}^B$ if the first node of A is joined to the third node of B. Common constraints are linear and can be written as follows

$$\mathbf{a}\left\{\begin{array}{c}\mathbf{x}^A\\\mathbf{x}^B\end{array}\right\} = \mathbf{0} \tag{12.2}$$

Where $\mathbf{a}$ is a matrix of constants, e.g. for the case where the constraint is $\mathbf{x}_1{}^A = \mathbf{x}_3{}^B$, $\mathbf{a}$ is a row vector with a value of 1 in the first column and with -1 in the column corresponding to $\mathbf{x}_3{}^B$. The state vector contains both displacements and velocities, but typically only the displacements need to be constrained. One must also enforce equilibrium, or in other words that the net force at each point on the interface should be zero after assembly (assuming that no external forces are applied at the interface).

Equations 12.1 and 12.2 constitute a set of differential-algebraic equations (see Ginsberg [14]) or constrained ordinary differential equations, since the state vector is not free to assume any value for each state but must satisfy (12.2). Equations such as these can be solved by various methods. When the substructures are linear one typically uses (12.2) to eliminate some of the states in order to form an unconstrained set of generalized coordinates (see [15] or [5]). The basic linear substructuring process is summarized in Fig. 12.2 below. Further mathematical details are provided in the Appendix.

12.2.2   Linearization

It is important to contrast the approach that shall be presented in this work with linearization. One can use the Taylor series expansion of the equations of motion in (12.1) to obtain the following linearized system,

$$\dot{\mathbf{x}}^A(t) = \mathbf{A}\mathbf{x}^A(t) + \mathbf{B}\mathbf{u}(t)$$
$$\mathbf{A} = \left[\frac{\partial \mathbf{f}_i}{\partial \mathbf{x}_j}\right]_{\bar{\mathbf{x}},\bar{\mathbf{u}}}, \quad \mathbf{B} = \left[\frac{\partial \mathbf{f}_i}{\partial \mathbf{u}_j}\right]_{\bar{\mathbf{x}},\bar{\mathbf{u}}} \tag{12.3}$$
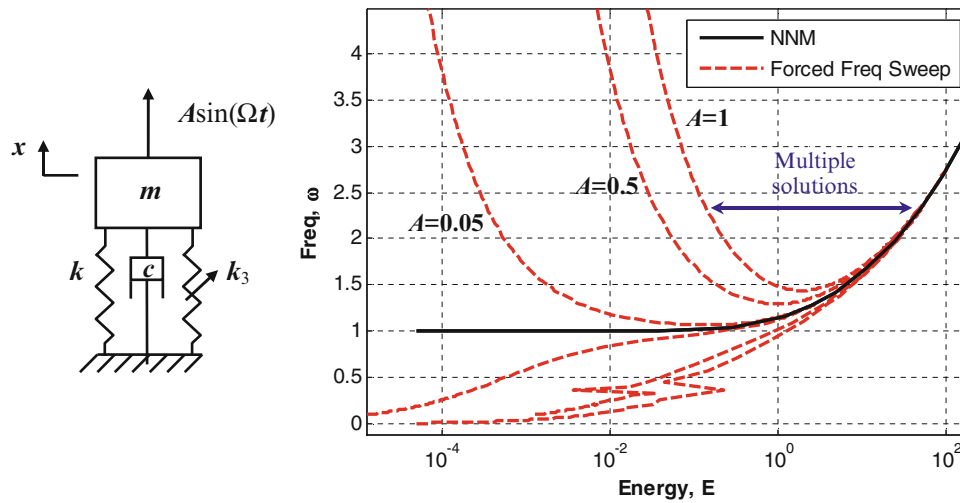
Fig. 12.3 (*solid black*) Frequency-energy plot for the nonlinear normal mode of a single-degree-of-freedom Duffing oscillator. (*dashed red*) Frequency response curves of Duffing oscillator at various forcing amplitudes. The NNM provides tremendous insight into the free and forced response of the system (color figure online)

where the notation signifies that the (i, j)th element of the A matrix is the derivative of the ith function in **f** with respect to the jth element of **x** (see [16] for further details). Note that the Jacobians must be evaluated at a fixed value of the state and input, $\bar{\mathbf{x}}, \bar{\mathbf{u}}$, to obtain a linear time invariant model. One could evaluate the Jacobians at every point along a trajectory but then a time-varying model would be obtained. (See, e.g. [17].)

This derivation reveals that one cannot obtain a linear time invariant model for a system by linearizing about a certain amplitude or input level. Only the mean value of the displacement or forcing may be varied if one wishes to obtain a rigorous linear time invariant model. However, in many applications of interest the resonance frequencies of a structure seem to change in response to the amplitude of the forcing or response, but an alternate methodology is needed to describe this phenomenon.

12.2.3   Undamped Nonlinear Normal Modes (NNMs)

While a few definitions exist for nonlinear modes, the definition that will be used here is that a nonlinear normal mode (NNM) is simply a vibration in unison of a system or a "not necessarily synchronous periodic solution" to the equations of motion [9]. This definition is essentially the same as the definition of a linear mode, since linear modes are also found by solving for the periodic solutions of the linear equations of motion. However, there are several important differences the most significant being that the response of a nonlinear system is not a linear superposition of its nonlinear normal modes. Vakakis provided an excellent review of the literature in this area, explaining how NNMs relate to the response of the system and highlighting methods for finding them analytically [10]. Kerschen also recently provided an excellent overview [9].

It is helpful to illustrate the nonlinear normal mode concept with a single-degree-of-freedom (SDOF) system before proceeding. Figure 12.3 shows the fundamental frequency of the NNM of a Duffing oscillator whose equation of motion is given below in nondimensional form. The parameters used in this example are: $\zeta = 0.01$, $\omega_1 = 1$ and $\omega_3 = 0.5$.

$$\ddot{x} + 2\zeta\omega_1\dot{x} + \omega_1 x + \omega_3 x^3 = f(t) \tag{12.4}$$

The NNM is merely a periodic solution to the undamped ($\zeta = 0$) equation of motion for the system; so if the system were linear then a possible periodic solution would be a pure sinusoid at a specific natural frequency, with a certain magnitude and phase. The analogous solution to the nonlinear equation of motion is a fundamental frequency plus a series of harmonics.

Figure 12.3 shows how the fundamental frequency of this solution evolves as the total energy in the system increases. The black line gives the fundamental frequency of the response, or frequency of the NNM, at each energy level. As expected for this system (whose nonlinearity is of the hardening type) the fundamental frequency increases as the energy increases. For example, if the undamped system were given an initial energy of E = 10^2 (dimensionless) and released, the system would oscillate at a fundamental frequency of 2.7 rad/s. It is clear that the NNM concept captures how the oscillation frequency of structure may change with amplitude. For convenience, the nonlinear normal mode frequency of the rth mode will be denoted $\omega^{\mathrm{NNM}}(E)_r$, where the dependence on energy is explicit noted, or more simply, $\omega^{\mathrm{NNM}}{}_r$. Note that the NNM frequency may be multi-valued, that is, the NNM curve may fold back so that there are several possible frequencies for rth NNM at certain energy levels; this is termed an internal resonance of the nonlinear system and will be observed in the example in Sect. 12.3.

The NNMs of a system are closely related to its forced response, analogous to the way in which the linear modes can be used to explain the forced response of a linear system (see, e.g. [10]). The red curves in Fig. 12.3 show the forced response of the Duffing oscillator at different excitation levels. Contrary to the usual convention, frequency is on the vertical axis in this figure. The curves for nondimensional forcing amplitudes $A = 0.05$, 0.5 and 1.0 are shown, all computed with $\zeta = 0.01$. The NNM forms the backbone of the frequency response curves, which reach further up the NNM as the amplitude increases. At high enough amplitude, the frequency response curves bend upward and a region emerges where three possible solutions exist (i.e. three possible response amplitudes for a fixed forcing frequency and amplitude). One of the solutions is unstable, but either the other might be observed at that forcing level, depending on the structure's initial conditions. One can also see that peaks begin to emerge at lower frequencies as the amplitude increases. These peak occur at integer fractions of the NNM frequency and correspond to superharmonic resonances of the system [18]. Nonlinear normal modes and nonlinear forced response curves such as these are relatively straightforward to compute using recently developed continuation techniques, and they provide tremendous insight into the dynamics of the system. The nonlinear mode of the Duffing oscillator shown above was found using the methods in [9, 11] implemented in their "NNMcont" Matlab package. The nonlinear frequency response curves were computed using the closely related method that is described in [19].

The nonlinear normal modes of a system depend on its nonlinear stiffness and mass, in much the same way that the linear modes of a structure depend on its linear stiffness and mass. For example, Fig. 12.4 shows how the NNM of the Duffing system changes as (a) its nonlinear stiffness increases from 0.5 (black line) to 0.75 1.0 1.25 and 1.5, (b) its linear stiffness increases from 1.0 (black line) to 1.25 1.5 1.75 and 2.0 or (c) its mass increases from 1.0 (black line) to 1.25 1.5 1.75 and 2.0. The behavior of the NNM is quite intuitive in this simple example. The changes in the frequency at low energy due to increasing the mass and stiffness are exactly what one would predict with linear theory.

When a system possesses multiple degrees of freedom, there are several nonlinear normal modes. Each mode can be characterized by a frequency-energy backbone curve such as that shown above for the Duffing oscillator. As with a linear mode, the structure also exhibits a particular deformation shape during each NNM. When a linear structure vibrates in a linear modal motion, the deformation of the structure can be written as

$$\mathbf{x} = [\phi_{1r} \quad \phi_{2r} \quad \cdots \quad \phi_{Nr}]^{\mathrm{T}} q_r = \boldsymbol{\varphi}_r(q_r) \tag{12.5}$$

where q_r is the amplitude of the rth mode of vibration and ϕ_{jr} is the shape of the rth mode at the jth node. One could also think of the mode shape as expressing a functional relationship between all of the nodes of the structure and the modal amplitude, q_r, so one could write the structural deformation as a vector function $\boldsymbol{\varphi}_r(q_r)$. In the case of a linear system as shown above, each element of the function $\boldsymbol{\varphi}_r(q_r)$ is simply proportional to, or a linear function of q_r. As one might expect, when the system is nonlinear the NNMs become nonlinear functions of the modal displacement. For example, Fig. 12.5 shows the shape, in the (x_1, x_2) space, of the first nonlinear normal mode of a two-DOF system that is described later (shown in Fig. 12.7). It is clear that x_2 and x_1 are nonlinear functions of the amplitude. If the system were linear, the relative amplitudes would obey a linear trend as is shown with the dashed red line.

A NNM shape such as that shown with a blue line in Fig. 12.5 is only valid for a single energy level. Hence, the rth NNM of a nonlinear system will here be denoted $\boldsymbol{\varphi}^{\mathrm{NNM}}(E, q_r)_r$ to make the dependence on energy explicit, or more simply, $\boldsymbol{\varphi}^{\mathrm{NNM}}{}_r$. It is important to note that the NNM curve at a low energy is not necessarily a subset of the NNM at a higher energy. For example, if a second curve was added to Fig. 12.5 showing the NNM at a higher energy level, the two curves would not generally overlay. Also, in some situations the modal amplitude is a complicated function of the physical displacements, so it is often more convenient to write the NNM shape as a function of time $\boldsymbol{\varphi}^{\mathrm{NNM}}(E, t)_r$, where time is only defined within the fundamental period $0 \leq t < 2\pi/\omega^{\mathrm{NNM}}(E)_r$.
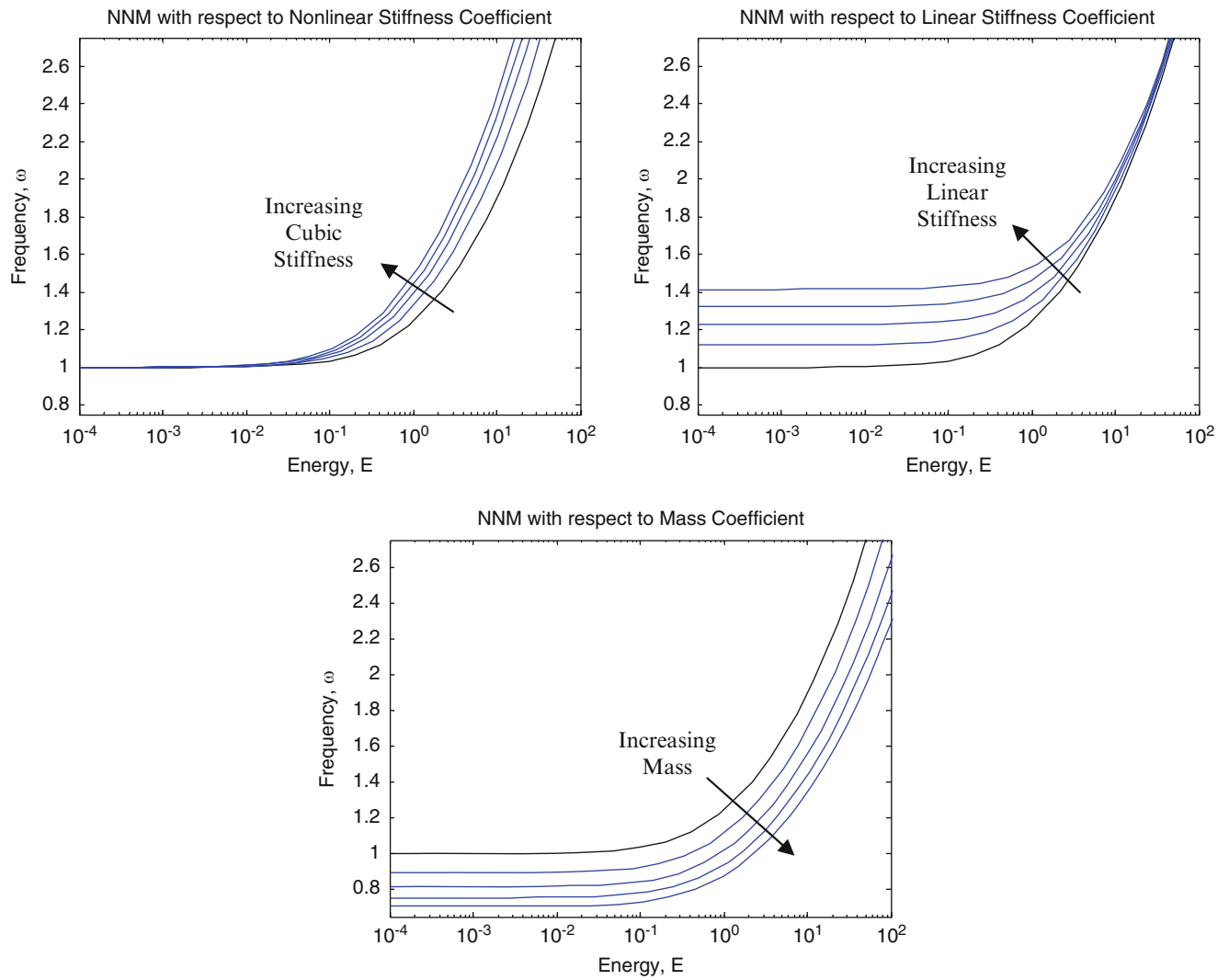
Fig. 12.4 Frequency-energy plots for the nonlinear normal mode of the single-degree-of-freedom Duffing oscillator. (*Black*) Reference NNM curve (same as in Fig. 12.3). (*Blue*) Changes in NNM frequency with mass, linear stiffness and nonlinear stiffness (color figure online)
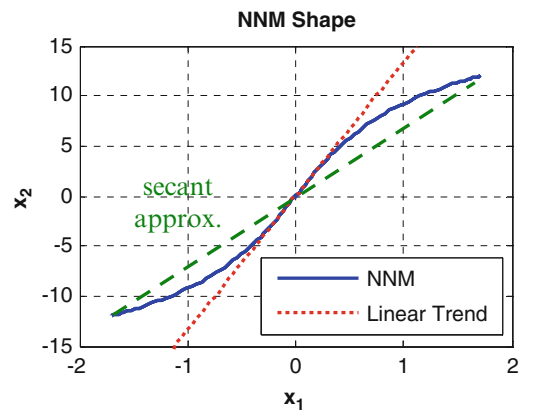
Fig. 12.5 Shape of the first NNM of the system shown in *red* in Fig. 12.7 at E = 13.2 (color figure online)

12.2.4   Proposed Approximate Nonlinear Substructuring Methodology Based on Representative Linear Modal Models (RLMMs)

At the most basic level, one can think of a nonlinear normal mode as providing the frequency and mode shape of a system as a function of energy. As explained in the previous section the NNM shapes are not simple linear functions of modal amplitude and the frequency of the NNM is only the fundamental frequency of a multi-frequency oscillation. In any event, this leads one to question: To what degree is the behavior of the nonlinear system well described simply by the change in the fundamental frequency of oscillation of the nonlinear system with energy? If the system can be described by a linear model with the appropriate frequency and mode shape then modeling, simulation and test could all be simplified dramatically. Section 12.2.2 established the fact that linearization will not generally capture a nonlinear system's frequency-energy dependence. Here an alternative description is proposed based on the nonlinear normal mode concept and which is dubbed a Representative Linear Modal Model (RLMM). This concept is closely related to the describing function concept, which has various definitions and uses [13, 20].

A representative linear modal model is a linear system defined by a set of natural frequencies and mode shapes, both of which are functions of energy. The RLMM natural frequency, $\omega^R(E)_r$, is taken to be the fundamental frequency of the NNM curve of the system.

$$\omega^R(E)_r = \omega^{NNM}(E)_r \tag{12.6}$$

In cases where the NNM frequency is multi-valued one could retain the various values, or simply select a single branch of interest and discard the others. The mode shape might be obtained in a number of ways. In this work we propose to use a secant approximation to the NNM. Specifically, the mode shape is taken to be the maximal deformation of the structure, defined as the deformation at the instant when the velocity is zero (assuming a predominantly synchronous motion),

$$\phi^R(E)_r = \boldsymbol{\varphi}^{NNM}(E, t_{dpk})_r \tag{12.7}$$

where t_{dpk} is the time instant at which $\dot{\mathbf{x}} = 0$. At a particular energy level the mode shape is a vector of constants akin to a linear mode shape. For example, consider the NNM shape shown in Fig. 12.5. The maximal deformation occurs at the extremes of the blue curve, so the proposed RLMM mode shape approximates the NNM with a line connecting the maximum positive and negative deformations of the structure, or a secant line connecting the two extremes of the NNM shape.

The goal in defining representative linear modal models is to characterize the response of the nonlinear system and to facilitate substructuring predictions when various subcomponents are assembled. Towards the latter goal, this work proposes to treat the RLMMs of two subcomponents as linear models. Hence, given the RLMMs of two subcomponents at various energy levels, one would simply use linear modal substructuring techniques to predict the modes of the assembly. The resulting modes of the assembly would then be an RLMM model describing the frequency-energy and mode shape-energy dependence of the assembled system. The procedure is outlined in Fig. 12.6 and specific examples will be presented in the following section.
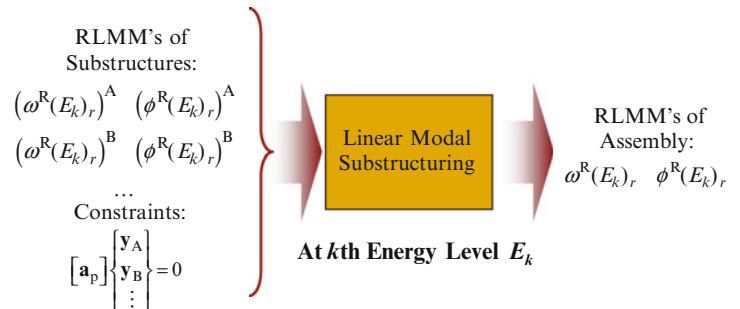
Fig. 12.6 Overview of the proposed approximate substructuring procedure based on representative linear modal models for each subcomponent

It is interesting to contrast this approach with a complete nonlinear model for the assembly. For example, Apiwattanalunggarn Shaw, and Pierre [21] adapted the Craig-Bampton approach to accommodate nonlinear normal mode models, but found that it was quite impractical to compute nonlinear normal modes that contained the required nonlinear couplings and also to simulate the response of the assembly using the NNM subcomponent models. In contrast, the operations outlined in Fig. 12.6 could be performed at negligible computational cost even if each subcomponent has dozens of RLMMs.

12.3   Case Study

The fundamentals of nonlinear substructuring will be explored with the simple substructuring problem that is depicted in Fig. 12.7, where two nonlinear spring-mass systems are joined forming a 2DOF built-up system. The parameters used are: $m_1 = 1$, $m_2 = 0.5$, $m_3 = 0.5$, $k_1 = 1$, $k_2 = 0.2$, and the nonlinear springs are cubic with coefficients $k_{nl,1} = 0.5$ and $k_{nl,2} = $ 1e-5. The figure shows the frequency-energy dependence of the nonlinear normal modes of each of the subcomponents, as well as those of the assembled system. The NNMs of the assembled system were computed directly from the model for system C shown below; there was no approximation of the system so these NNMs can be taken to be the truth model for the nonlinear system.

This system is linearizable, so it is helpful to first consider what insights the linearized system provides. Each NNM of the system reduces to the linearized natural frequency of the structure at sufficiently low energy (at the far left edge of the plot). The system parameters are such that the linearized natural frequency of the base system, A, (blue line) is $\omega_1^A = 1$ rad/s, which is close to the second linearized natural frequency, $\omega_2^B = (2k_2/m_2)^{(1/2)} \approx 0.89$, of the attached system, B, (green line). (Note that $\omega_1^B = 0$.) The dashed red lines in Fig. 12.7 give the natural frequencies obtained by combining the linearized models ($k_{nl,1} = k_{nl,2} = 0$), revealing that the two modes of the subcomponents that have similar natural frequencies combine to form two new modes of system C that have distinct natural frequencies. This is similar to the standard vibration absorber or mass-tuned damper problem (see, e.g. [22]), where the two modes of the subcomponents combine to form two new modes, one above and the other below the original resonance frequency.
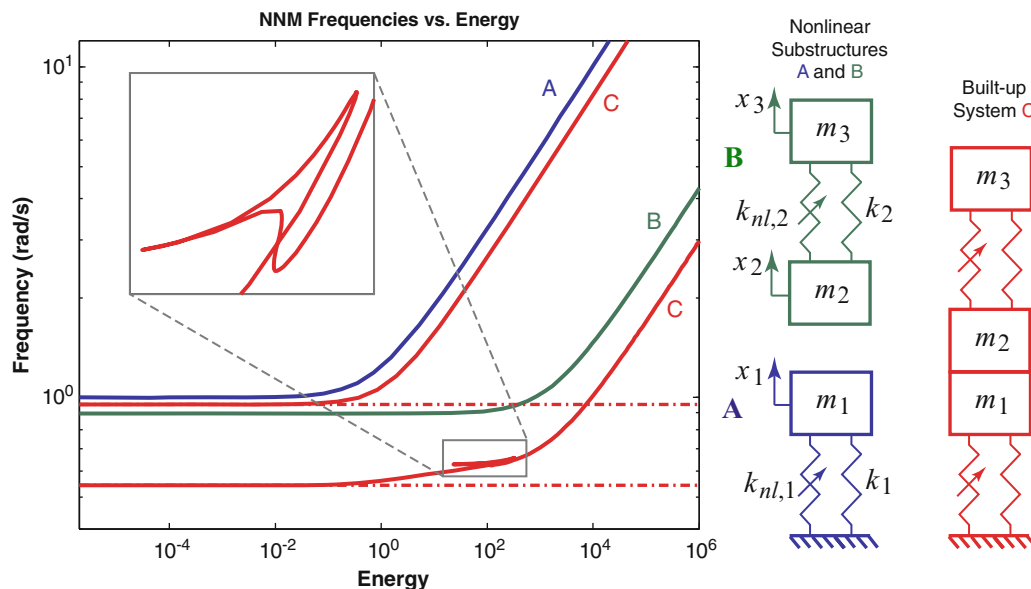
Fig. 12.7 (*right*) Simple substructuring problem where a nonlinear SDOF system is coupled to a nonlinear 2DOF system. The system is assembled, as shown on the far *right*, by enforcing the constraint $x_1 = x_2$. (*left*) Plot showing frequency versus energy dependence of the nonlinear normal modes of the subcomponents (*blue and green lines*) and of the assembled system (*red*). At low energy the NNMs of the assembled system converge to the frequencies predicted by a linear analysis (*dashed red lines*) (color figure online)

12.3.1   Rigorous Analysis of the Nonlinear Assembly

Now consider the nonlinear system. At low energy the subcomponents are well approximated as linear and the linearized analysis predicts their natural frequencies precisely. As energy increases, the NNM of subsystem A increases in frequency, beginning at an energy of E = 0.1. Subsystem B has a weaker nonlinearity ($k_{nl,2}$ is four orders of magnitude smaller than $k_{nl,1}$), so its NNM frequency does not begin to increase until E = 100. Interestingly, the two NNMs of the assembly, C, seem to track the frequencies of subsystems A and B, with the higher NNM of C following the curve for system A's nonlinear mode and the lower one following the curve for B's nonlinear mode.

Viewing the substructuring problem in terms of nonlinear normal modes in this manner leads to a number of important insights. First, it seems that the first NNM of the built-up structure is primarily influenced by the nonlinear mode of subsystem B. The NNM of subsystem A seems to dominate the second NNM of the assembly. This information can be very valuable during the design process. For example, if the response analysis were to reveal that the 1st NNM of the assembled system was responsible for excessive vibration, then one might target the NNM of subsystem B in order to cause the greatest change.

The inset in Fig. 12.7 shows a magnified view of the 1st NNM frequency over a small range of energy, revealing a feature which is unique to nonlinear systems. The natural frequency of the first NNM is seen to change in a very erratic way at this energy level. The mode shape also changes dramatically in this region (not shown) as the system exhibits a 1:3 internal resonance (the first mass moves at three times the frequency of the second). This type of response could be detrimental, since it could lead to high vibration levels at unexpected frequencies. On the other hand, this phenomenon has also been proposed as a mechanism for very effective nonlinear vibration absorbers [23]. It is also important to note that one could have predicted that subharmonic resonance was possible at this energy level because the 2nd NNM frequency is three times the 1st NNM frequency at that energy and the nonlinearities are cubic. The NNM frequency-energy dependence of the coupled system seems to follow the trend of the individual subcomponent NNMs except in this relatively small region where this internal resonance occurs.

12.3.2   Substructuring Analysis with Representative Linear Modal Models

The frequency-energy plot in Sect. 12.3.1 presented the true dynamics of the assembly of nonlinear subcomponents. This section considers the result that one obtains using RLMMs for the substructures A and B.

Substructure A is a single degree-of-freedom system, so it has a single nonlinear mode whose frequency-energy dependence, $\left(\omega^R(E)_1\right)^A$, is shown with a blue line in Fig. 12.7, ranging from 1 rad/s at low energy to 17.8 rad/s at E = 10^5. The corresponding nonlinear mode shape is a scalar value which, after mass-normalizing, remains unchanged, $\left(\phi^R(E)_1\right)^A = 1$. Substructure B is a two degree-of freedom system, but its first NNM is equivalent to its linear rigid body mode so $\left(\omega^R(E)_1\right)^B = 0$ and $\left(\phi^R(E)_1\right)^B = [\,1 \quad 1\,]^T$. The frequency dependence of its second RLMM, $\left(\omega^R(E)_2\right)^B$, is shown with a green line in Fig. 12.7, ranging from 0.89 to 2.45 rad/s at E = 10^5. The corresponding shape also happens to be constant with energy, $\left(\phi^R(E)_2\right)^B = [\,1 \quad -1\,]^T$. Now the procedure outlined in Fig. 12.6 can be applied to predict the RLMMs of the assembled system. This was implemented using the freely available "ritzscomb" Matlab routine which implements the method described in [3, 15]. The frequency-energy curves for each of the RLMMs computed using this approach are shown in Fig. 12.8.

Figure 12.8 shows that the RLMM method reproduces the nonlinear modes of the assembly with surprising accuracy. The RLMMs are linear models and they were assembled using linear substructuring techniques, so this results suggests that the frequency-energy dependence of the assembly is governed primarily by the effective natural frequencies (or RLMM frequencies) of the underlying substructures. Other nonlinear effects, such as nonlinear coupling between the underlying linear modes, seem to be much less significant. On the other hand, the inset shows that the linear RLMM model is incapable of describing the internal resonance that occurs when the energy is near E = 100, so that feature of the response is completely missed.

In order to better understand how well the RLMM approximation captures the response of the nonlinear system, the first nonlinear normal mode of the assembly is shown in Fig. 12.9 for an energy level of E = 250. (Recall that the NNM is simply a periodic response of the nonlinear structure). The corresponding response of the RLMM model is also shown, which is a pure cosine since the RLMM is a linear model. Comparing the curves, the RLMM can be seen to approximate the motion of $x_2(t)$ quite well; $x_2(t)$ dominates the response of this NNM at this energy level. On the other hand, the NNM shape of $x_1(t)$ is dominated by higher frequency motion that cannot be captured by the RLMM model.

Fig. 12.8 Frequency energy curves of the subcomponents and assembly shown in Fig. 12.7. *Blue*: RLMM frequency of substructure A, *Green*: second RLMM frequency of substructure B, *Black Dashed*: RLMM frequencies of the substructuring prediction using the method in Sect. 12.2.4, *Red*: True frequency-energy curves of the assembly, repeated from Fig. 12.7 (color figure online)
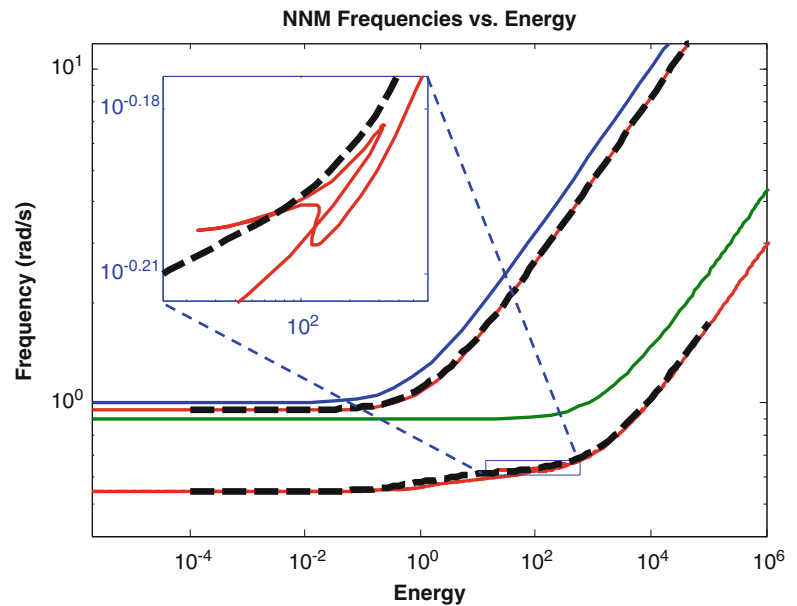
Fig. 12.9 Periodic responses (e.g. NNM responses) of each degree of freedom for the true nonlinear assembly (*solid lines*) and the linear RLMM approximation (*dashed lines*)
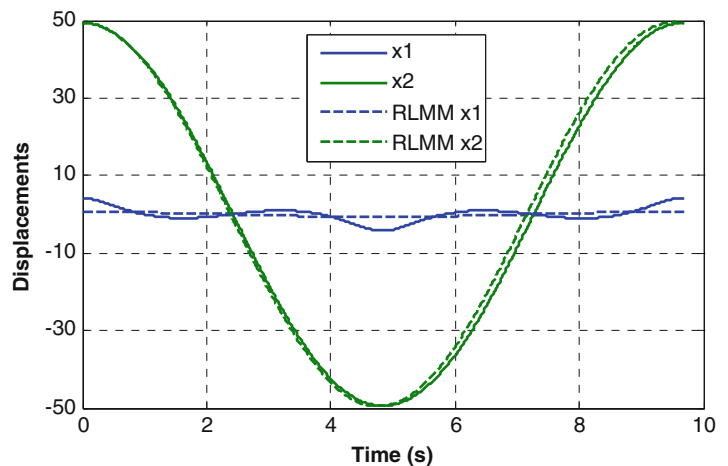
12.3.3 Three Degree of Freedom Example of RLMM Substructuring

It was noted previously that both of the subcomponents used in the example in the previous subsection had constant RLMM mode shapes, and this might cause one to question whether those results were simply an anomaly arising because the mode shapes were constant. This was evaluated by using the RLMM substructuring procedure to add yet another copy of subsystem B to assembly described in Figs. 12.7 and 12.8. The result, summarized in Fig. 12.10 below, shows that once again very accurate results were obtained using the RLMM procedure, even though the shapes of the RLMM modes of one of the substructures changed very significantly in this second example.

It is important to note that the actual nonlinear normal modes of this system show several internal resonances which are not visible due to the coarse scale of the frequency-energy plot in Fig. 12.10. Indeed, some effort was required to compute
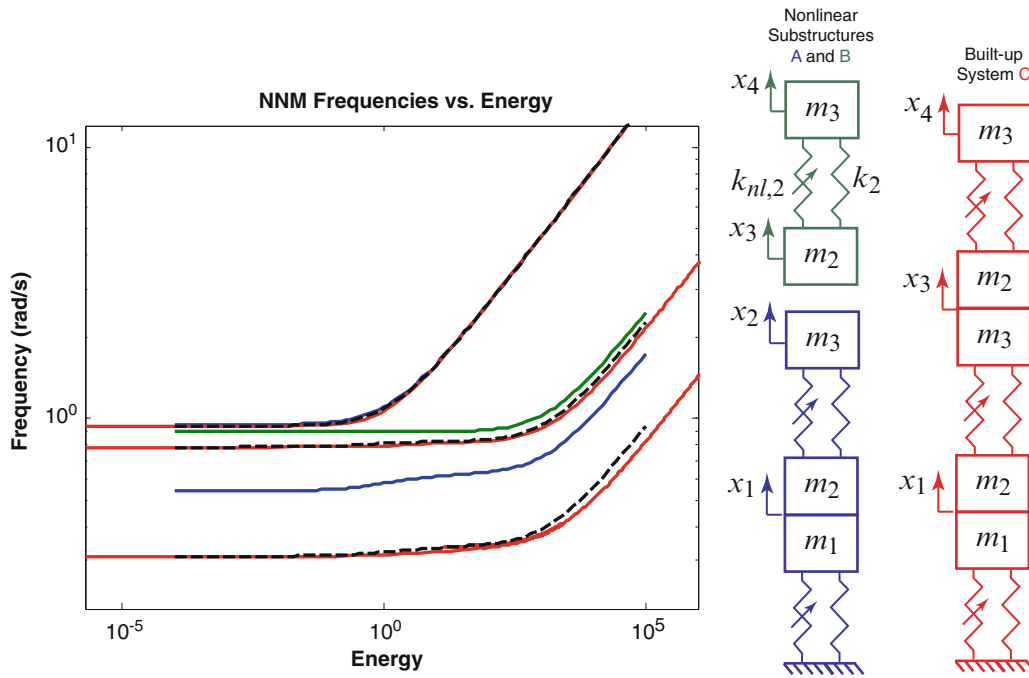
Fig. 12.10 Nonlinear normal modes and RLMM approximations for a 3DOF substructuring problem. Substructure B in this example is the built-up system C in Fig. 12.7

the true NNMs of this system since the 1st NNM curve suddenly doubles back upon itself several times. The RLMM method does not capture any of this complexity, but it does capture the overall trend in the NNM curves, and it does so at a miniscule computational cost compared to the rigorous nonlinear model.

12.4   Conclusions

This work has extended concepts from linear modal substructuring to assemblies of nonlinear subcomponents using the nonlinear normal mode concept. Nonlinear normal modes provide important insights into both the forced and free response of a system, and this work has shown that the basic evolution of the nonlinear normal modes of an assembly can be predicted very accurately if the NNMs of the subcomponents are known. Their evolution seems to be dominated by the frequency-energy dependence of the individual subcomponents, so concepts from linear substructuring can be readily applied to understand how each subcomponent contributes to the dynamic behavior of the assembly. Furthermore, these observations were exploited by presenting a new substructuring technique that uses linear modal substructuring techniques to assemble linear models for the subcomponents, here called Representative Linear Modal Models (RLMMs), in order to predict the frequency-energy dependence of the assembly. This method was found to predict the frequency-energy evolution very accurately and with minimal computational cost.

Of course, it is important to remember that linear models are not able to capture exclusively nonlinear phenomena such as internal resonance, instabilities or chaos, so any linear analysis should be followed by a more detailed nonlinear analysis at key energy levels in order to assure that important dynamics have not been missed. Fortunately, in many cases one can predict the energy levels at which internal resonances might occur based on the NNM curves. For example when a system has cubic springs, internal resonance typically occurs when one mode has a frequency that is three times that of another mode [18]. The first NNM in Fig. 12.7 is three times the second at only one energy level, precisely that at which the internal resonance was observed. Hence, for a system such as this one could predict the general evolution of the NNMs using the substructure RLMMs and linear substructuring and then identify the energy at which internal resonances are possible.

Appendix

This section explains how two linear substructures, each described by a set of linear modes can be joined so that the modes of the assembly can be computed. The natural frequencies, ω_r, and the matrix of mass-normalized mode shapes, Φ, are known for each substructure. The concatenated equations of motion (in second order form) are then the following.

$$\begin{bmatrix} \mathbf{I}_A & 0 \\ 0 & \mathbf{I}_B \end{bmatrix} \begin{Bmatrix} \ddot{\mathbf{q}}_A \\ \ddot{\mathbf{q}}_B \end{Bmatrix} + \begin{bmatrix} [\backslash \omega_r^2 \backslash]_A & \mathbf{0} \\ \mathbf{0} & [\backslash \omega_r^2 \backslash]_B \end{bmatrix} \begin{Bmatrix} \mathbf{q}_A \\ \mathbf{q}_B \end{Bmatrix} = \begin{Bmatrix} \Phi_A{}^T \mathbf{F}_A \\ \Phi_B{}^T \mathbf{F}_B \end{Bmatrix}$$
$$\begin{Bmatrix} \mathbf{y}_A \\ \mathbf{y}_B \end{Bmatrix} = \begin{bmatrix} \Phi_A & \mathbf{0} \\ \mathbf{0} & \Phi_B \end{bmatrix} \begin{Bmatrix} \mathbf{q}_A \\ \mathbf{q}_B \end{Bmatrix} \tag{12.8}$$

The constraints can then be expressed in terms of the physical or modal coordinates as follows:

$$[\mathbf{a}_p] \begin{Bmatrix} \mathbf{y}_A \\ \mathbf{y}_B \end{Bmatrix} = 0 \quad \rightarrow \quad [\mathbf{a}_p] \begin{bmatrix} \Phi_A & 0 \\ 0 & \Phi_B \end{bmatrix} \begin{Bmatrix} \mathbf{q}_A \\ \mathbf{q}_B \end{Bmatrix} = 0 \tag{12.9}$$

Then the constrained generalized coordinates can be eliminated by defining a nonsquare matrix $\mathbf{B}$ that transforms the concatenated coordinates into a set of unconstrained coordinates using either the method described in [15] or the method in [5] where

$$\begin{Bmatrix} \mathbf{q}_C \\ \mathbf{q}_A \end{Bmatrix} = \mathbf{B}\mathbf{q}_u \tag{12.10}$$

and $\mathbf{B}$ is in the null space of the matrix of constraints in (12.9). The equations of motion of the system in unconstrained coordinates then become the following

$$\mathbf{M}_u \ddot{\mathbf{q}}_u + \mathbf{K}_u \mathbf{q}_u = \mathbf{B}^T \begin{Bmatrix} \Phi_A{}^T \mathbf{F}_A \\ \Phi_B{}^T \mathbf{F}_B \end{Bmatrix}$$
$$\begin{Bmatrix} \mathbf{y}_A \\ \mathbf{y}_B \end{Bmatrix} = \begin{bmatrix} \Phi_A & \mathbf{0} \\ \mathbf{0} & \Phi_B \end{bmatrix} \mathbf{B}\mathbf{q}_u \tag{12.11}$$

where the mass and stiffness matrices of the coupled system are.

$$\mathbf{M}_u = \mathbf{B}^T \begin{bmatrix} \mathbf{I}_A & 0 \\ 0 & \mathbf{I}_B \end{bmatrix} \mathbf{B}, \quad \mathbf{K}_u = \mathbf{B}^T \begin{bmatrix} [\backslash \omega_r^2 \backslash]_A & \mathbf{0} \\ \mathbf{0} & [\backslash \omega_r^2 \backslash]_B \end{bmatrix} \mathbf{B} \tag{12.12}$$

One can show that multiplying the forces by $\mathbf{B}^T$ eliminates the constraint forces, ensuring that compatibility is satisfied (see Chap. 9 in [15]). The modes of the assembly can then be computed by solving an eigenvalue problem with $\mathbf{M}_u$, $\mathbf{K}_u$ and then relating the mode shapes in $\mathbf{q}_u$ coordinates back to the physical coordinates with (12.11).

References

1. Craig RRJ, Bampton MCC (1968) Coupling of substructures using component mode synthesis. AIAA J 6:1313–1319
2. Allen MS, Gindlin HM, Mayes RL (2011) Experimental modal substructuring to estimate fixed-base modes from tests on a flexible fixture. J Sound Vib 330:4413–4428
3. Allen MS, Mayes RL, Bergman EJ (2010) Experimental modal substructuring to couple and uncouple substructures with flexible fixtures and multi-point connections. J Sound Vib 329:4891–4906
4. Allen MS, Kammer DC, Mayes RL (2011) Metrics for diagnosing negative mass and stiffness when uncoupling experimental and analytical substructures. In: 29th international modal analysis conference (IMAC XXIX), Jacksonville

5. de Klerk D, Rixen DJ, Voormeeren SN (2008) General framework for dynamic substructuring: history, review, and classification of techniques. AIAA J 46:1169–1181
6. Bourquin F (1990) Analysis and comparison of several component mode synthesis methods on one-dimensional domains. Numer Math 58:11–34
7. Allen MS, Kammer DC, Mayes RL (2010) Uncertainty in experimental/analytical substructuring predictions: a review with illustrative examples. In: ISMA2010 – international conference on noise and vibration engineering, Leuven
8. Rosenberg RM (1960) Normal modes of nonlinear dual-mode systems. J Appl Mech 27:263–268
9. Kerschen G, Peeters M, Golinval JC, Vakakis AF (2009) Nonlinear normal modes, part I. A useful framework for the structural dynamicist. Mech Syst Signal Process 23:170–94
10. Vakakis AF (1997) Non-linear normal modes (NNMs) and their applications in vibration theory: an overview. Mech Syst Signal Process 11:3–22
11. Peeters M, Viguie R, Serandour G, Kerschen G, Golinval JC (2009) Nonlinear normal modes, part II: toward a practical computation using numerical continuation techniques. Mech Syst Signal Process 23:195–216
12. Pickrel CR (2002) Airplane ground vibration testing: correlation with nominal modal model. In: 20th international modal analysis conference (IMAC-XX), Los Angeles
13. Slotine J-JE, Li W (1991) Applied nonlinear control. Prentice Hall, Upper Saddle River
14. Ginsberg JH (2005) Engineering dynamics, 3rd edn. Cambridge University Press, Cambridge, MA
15. Ginsberg JH (2001) Mechanical and structural vibrations, 1st edn. Wiley, New York
16. Bay JS (1999) Fundamentals of linear state space systems. McGraw-Hill, Boston
17. Sracic MW, Allen MS (2011) Method for identifying models of nonlinear systems using linear time periodic approximations. Mech Syst Signal Process 25:2705–2721
18. Nayfeh AH (1981) Introduction to perturbation techniques. Wiley, New York
19. Sracic MW, Allen MS (2011) Numerical continuation of periodic orbits for harmonically forced nonlinear systems. In: 29th international modal analysis conference (IMAC XXIX), Jacksonville
20. Ozer MB, Ozguven HN, Royston TJ (2009) Identification of structural non-linearities using describing functions and the Sherman-Morrison method. Mech Syst Signal Process 23:30–44
21. Apiwattanalunggarn P, Shaw SW, Pierre C (2005) Component mode synthesis using nonlinear normal modes. Nonlinear Dyn 41:17–46
22. Meirovich L (2001) Fundamentals of vibrations. McGraw-Hill, New York
23. Vakakis AF, McFarland DM, Bergman L, Manevitch LI, Gendelman O (2004) Isolated resonance captures and resonance capture cascades leading to single- or multi-mode passive energy pumping in damped coupled oscillators. J Vib Acoust 126:235–244

Chapter 13
An Effective Method for Assembling Impulse Response Functions to Linear and Non-linear Finite Element Models

P.L.C. van der Valk and D.J. Rixen

Abstract The Impulse Based Substructuring (IBS) method has been proposed lately as an effective approach to evaluate the dynamic response of a system, using either the numerically or experimentally obtained Impulse Response Functions (IRFs) of its components. In this paper, the method will be combined with the (non-linear) Newmark time integration scheme in order to couple IRFs with linear and non-linear finite element models. In the linear case this is done by performing, for each time step, the Newmark step for the FE substructures and solving the convolution integrals for the IRFs simultaneously. After this, the interface forces are computed that are required to enforce compatibility between all the substructures. For the non-linear case, all the neighboring linear subsystems are condensed in the non-linear subsystems, which is then solved using Newton-Raphson iterations on this condensed (non-linear) problem. A general multi-degree-of-freedom case will be shown to illustrate the accuracy and versatility of the method. From the numerical results it is shown that the method yields the same results as a Newmark time integration, thereby showing that the IBS method can be an efficient method to quickly compute the response of a system obtained by assembling precomputed numerical components or measured substructures.

Nomenclature

$\mathbf{M}$	Mass matrix
$\mathbf{C}$	Damping matrix
$\mathbf{K}$	Stiffness matrix
$\mathbf{u}$	Array of degrees of freedom
$\mathbf{f}$	External force vector
$\mathbf{g}$	Connection force vector
$\mathbf{p}$	Internal elastic and damping force vector
$\mathbf{B}$	Compatibility matrix (Boolean)
$\mathbf{L}$	Localization matrix (Boolean)
$\boldsymbol{\lambda}$	Vector of Lagrange multipliers
$\mathbf{S}$	Time stepping matrix
$\mathbf{S}_t$	Jacobian (iteration) matrix
IRF	Impulse Response Function
IBS	Impulse Based Substructuring

P.L.C. van der Valk (✉)
Delft University of Technology, Mekelweg 2, 2628CD Delft, The Netherlands
e-mail: p.l.c.vandervalk@tudelft.nl

D.J. Rixen
Section Engineering Dynamics, Delft University of Technology, Mekelweg 2, 2628CD Delft, The Netherlands

13.1   Introduction

Dynamic substructuring is a family of methods based on the ancient idea of "divide and conquer"; by dividing a large and complex system into smaller and simpler subsystems, one is able to compute the dynamic behavior, which might otherwise not be possible, or greatly improve the efficiency of doing so. The first successful implementation of this idea in mathematics was done by Schwarz in 1890 [15], but the idea of substructuring didn't find its way to mechanics for another 70 years. In 1960 Hurty [6] was the first to propose the so called Component Mode Synthesis technique, which triggered an entire new field and was soon followed by the methods from Hurty [7], Gladwell [4], Guyan [5], Craig [1], MacNeal [10] and Rubin [14] in the 1960s and 1970s.

In the 1980s a second class of substructuring methods originated from the desire to assemble measured substructures. In 1984 Crowley et al. [2] presented a method for the direct assembly of frequency response functions (FRFs), SMURF (structural modification using experimental frequency response functions), which did not get much attention from the engineering community. Jetmundsen et al. [8] proposed an alternative method, which is often referred to as the classical Frequency Based Substructuring method (FBS).

Nowadays, a third class of substructuring techniques can be identified, which is referred to by Rixen as Impulse Based Substructuring (IBS) using either numerical models [13], or experimentally obtained models [12]. Similar ideas where already used by Lehmann [9] for coupling finite element models and infinite domains in the field of soil-structure interaction.

Section 13.2 handles some of the basic topics, such as time integration using IRFs, discretization of the duhamel integral and how to numerically obtain the impulse response functions. In Sect. 13.3 the Impulse Based Substructuring (IBS) methods for both linear and non-linear finite element models (FEM) are presented. Both methods are demonstrated using an academic example and the results are shown in Sect. 13.4. Finally, conclusions and discussion can be found in Sect. 13.5.

13.2   Time Integration Using Impulse Response Functions

As the name implies, Impulse Response Functions (IRFs) show the response of the system at hand to a unit impulse force over time. Hence, they give the input–output relationship of a system or structure. As any force, that is a function of time, can be expressed as subsequent force impulses over time, IRFs can be used to determine the time response of a system. In this section it will be shown how to obtain and use these IRFs for time integration.

13.2.1   Time Integration Using the Impulse Response Functions

Firstly, starting from the equation of motion of a general linear dynamic system:

$$M\ddot{u}(t) + C\dot{u}(t) + Ku(t) = f(t) \tag{13.1}$$

Here, M denotes the mass matrix, C the viscous damping matrix, K the stiffness matrix, $f(t)$ the external force, which is a function of time and $u(t), \dot{u}(t), \ddot{u}(t)$ respectively the displacements, velocities and accelerations, which are also a function of time. Assuming that $\ddot{u}(\omega) = i\omega\dot{u}(\omega) = -\omega^2 u(\omega)$, it can be rewritten into:

$$\left(-\omega^2 M + i\omega C + K\right)u(\omega) = Z(\omega)u(\omega) = f(\omega), \tag{13.2}$$

where $Z(\omega)$ is the dynamic stiffness matrix. The reader can easily verify that the equations of motion (13.1) have been transformed from the time to the frequency domain (13.2).

$$Z(\omega)^{-1}f(\omega) = Y(\omega)f(\omega) = u(\omega), \tag{13.3}$$

where $Y(\omega)$ is the dynamic flexibility matrix. So, if one would be interested in the time response of a certain system caused by a certain input force, (13.3) can be transformed back to the time domain by means of an inverse fourier transform, which would result in:

$$u(t) = \int\limits_{\tau=0}^{t} Y(t-\tau)f(\tau)d\tau, \tag{13.4}$$

Fig. 13.1 Force impulse in the constant average acceleration Newmark scheme
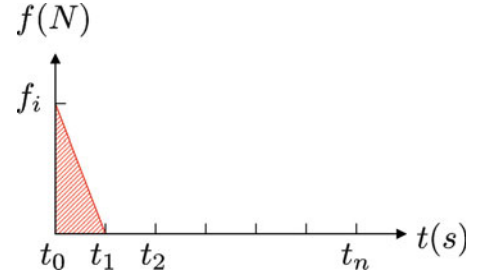
where, $Y(t)$ is the impulse response function of the dynamic system at hand. This integral equation is known as a convolution product or Duhamel integral, and needs to be discretized to allow for numerical computations.

13.2.2 Discretization of a Convolution Product

The obtained convolution integral (13.4) is a continues equation and needs to be discretized in order to use it for numerical computations. By looking at the applied force $f(t)$ as a sum of discrete impulses, one could interpret this integral as being a sum of the responses to impulse excitations between $t = 0$ and $t = \tau$.

In general however, the analytical impulse response function is not available, therefore one can compute a discrete numerical approximation $Y(t_i)$, for $t_i = 0 \ldots t_n$. Due to this, the integral of (13.4) is replaced by a finite sum, which converges to the exact solution if dt goes to zero.

$$u(t_n) = u_n = dt \sum_{i=0}^{n-1} Y_{n-i} f_i \tag{13.5}$$

Note that the sum in (13.4) is from 0 to $n - 1$, since $Y(0) = 0$. This is due to the fact that the response of a system in terms of displacements at $t = 0$ to an impulse at $t = 0$ is zero, as only the accelerations and velocities respond directly to the impact. In this sum, it is assumed that both the impulse response function and the forcing function are piecewise *constant*. A more accurate approximation would be to assume a piecewise *linear variation* of the forcing function a the different time stations, which would result in the following sum and is also known as the *trapezoidal rule*.

$$u_n = \frac{dt}{2} \sum_{i=0}^{n-1} Y_{n-i}(f_i + f_{i+1}) \tag{13.6}$$

A brief introduction to discrete time integration using the impulse response matrices and the convolution product has been given. In the next sections this will be used to apply these methods directly in different substructuring analysis.

13.2.3 Computing the Unit Impulse Response Functions

For computing the unit impulse force response functions, the Newmark time integration scheme is used. There are several initial conditions one can use to compute the impulse force response functions [13]. In this paper it is assumed that an initial force is given in the first time step ($t_0 = 0$), this is chosen as it is consistent with the constant average Newmark method. From this assumption, the following initial conditions can be derived.

$$\begin{aligned} u_0 &= 0 \\ \dot{u}_0 &= 0 \\ \ddot{u}_0 &= M^{-1} \frac{\mathbf{1}_{[j]}}{dt}, \end{aligned} \tag{13.7}$$

where $\mathbf{1}_{[j]}$ is a vector with a unit coefficient for DoF j. Note that, throughout this paper the constant average acceleration variant of the Newmark ($\gamma = 0.5, \beta = 0.25$) is used. This thus implies that the values of the forcing function vary linearly between the different time stations, as can be seen in Fig. 13.1. Due to this, the system is in fact excited not by a *unit* pulse,

but by a *half unit* pulse and the final result has to be corrected for this. Using (13.7) as the initial conditions and performing a time simulation, one is able to obtain the accelerations, velocities and displacements at all DoF as a result of the impulse force at DoF j. Thereby determining the jth column of the Unit Impulse Force Response Matrices. Hence obtaining the entire set of IRFs needed in (13.6).

$$\mathbf{Y}(t_i) = \begin{bmatrix} Y_{[11]}(t_i) & \dots & Y_{[1j]}(t_i) & \dots & Y_{[1N]}(t_i) \\ \vdots & \ddots & \vdots & \ddots & \vdots \\ Y_{[j1]}(t_i) & \dots & Y_{[jj]}(t_i) & \dots & Y_{[jN]}(t_i) \\ \vdots & \ddots & \vdots & \ddots & \vdots \\ Y_{[N1]}(t_i) & \dots & Y_{[Nj]}(t_i) & \dots & Y_{[NN]}(t_i) \end{bmatrix} \tag{13.8}$$

13.3 The Impulse Based Substructuring Method

As the basics of Sect. 13.2 have been discussed now, the different Impulse Based Substructuring (IBS) methods can be presented in this section. In this section it will be shown how to assemble an IRF to a linear or non-linear FE model, as is visualized in Fig. 13.2. Firstly, from the conditions necessary for coupling, the set of coupled equations of motion will be derived. Using this set of coupled equations and the Newmark time integration scheme, a method is developed to obtain coupled dynamic load simulations for combining both linear (Sect. 13.3.2) and non-linear (Sect. 13.3.3) finite element models with impulse response functions.

13.3.1 Conditions for Assembly: Compatibility and Equilibrium

The goal of this section is to come from the set of uncoupled equations (13.9), where the variables with superscript (s) denote the linear substructures described in their IRFs, the variables with superscript (r) denote the models given as (non) linear FE models and $\mathbf{p}^{(r)}(\dot{\mathbf{u}}_n^{(r)}, \mathbf{u}_n^{(r)})$ is a vector of linear and non-linear internal forces, to the set of coupled equations of motion.

$$\begin{cases} \mathbf{u}_n^{(s)} = \frac{dt}{2} \sum_{i=0}^{n-1} \mathbf{Y}_{n-i}^{(s)} \left(\mathbf{f}_i^{(s)} + \mathbf{f}_{i+1}^{(s)} + \mathbf{g}_i^{(s)} + \mathbf{g}_{i+1}^{(s)} \right) \\ \mathbf{M}^{(r)} \ddot{\mathbf{u}}_n^{(r)} + \mathbf{p}^{(r)} \left(\dot{\mathbf{u}}_n^{(r)}, \mathbf{u}_n^{(r)} \right) = \mathbf{f}_n^{(r)} + \mathbf{g}_n^{(r)} \end{cases} \tag{13.9}$$

Here, $\mathbf{g}$ denotes the interface forces coming from the neighboring substructures, which are needed to enforce coupling between these substructures. It is known that in order to obtain a fully coupled set of equations, two conditions have to be satisfied. The first one being *compatibility*, which means that the the displacements of the nodes on both sides of the interface have to be equal, and thus no gap is allowed between the different substructures.

$$\mathbf{u}_{[b]}^{(s)} = \mathbf{u}_{[b]}^{(r)}, \tag{13.10}$$

where the subscript $[b]$ denotes the interface (or boundary) nodes. The compatibility condition can also be written using Boolean operators that work on the boundary DoF within the full set of DoF, such that
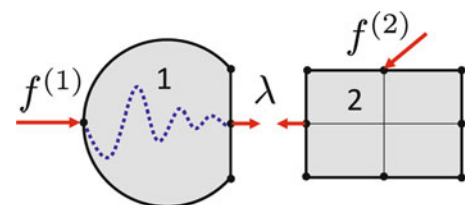
Fig. 13.2 Conceptual view of coupling FEM to IRFs

$$\begin{bmatrix} \boldsymbol{B}^{(s)} & \cdots & \boldsymbol{B}^{(r)} \end{bmatrix} \begin{bmatrix} \boldsymbol{u}^{(s)} \\ \vdots \\ \boldsymbol{u}^{(r)} \end{bmatrix} = \boldsymbol{B}\boldsymbol{u} = 0 \tag{13.11}$$

The second condition is *Equilibrium*, which states that the sum of the forces at the connecting nodes have to be equal to zero, such that no resulting force between the substructures exists. This means that the interface forces have to be opposite in sign and equal in magnitude.

$$\boldsymbol{g}_b^{(s)} + \boldsymbol{g}_b^{(r)} = 0 \tag{13.12}$$

Using the Boolean operator $\boldsymbol{B}$ from (13.11), this can be written as:

$$\begin{bmatrix} \boldsymbol{g}^{(s)} \\ \boldsymbol{g}^{(r)} \end{bmatrix} = -\boldsymbol{B}^T\boldsymbol{\lambda}, \tag{13.13}$$

where $\boldsymbol{\lambda}$ are known as *Lagrange Multipliers* that denote the magnitudes of the interface forces. Hence, by using (13.13), the number of unknowns is reduced. Substitution of both the compatibility condition (13.11) and the equilibrium condition (13.13), results in the set of coupled equations.

$$\begin{cases} \boldsymbol{u}_n^{(s)} = \frac{dt}{2}\sum_{i=0}^{n-1}\boldsymbol{Y}_{n-i}^{(s)}(\boldsymbol{f}_i + \boldsymbol{f}_{i+1} - \boldsymbol{B}^{(s)^T}(\boldsymbol{\lambda}_i + \boldsymbol{\lambda}_{i+1})) \\ \boldsymbol{M}^{(r)}\ddot{\boldsymbol{u}}_n^{(r)} + \boldsymbol{p}^{(r)}(\dot{\boldsymbol{u}}_n^{(r)}, \boldsymbol{u}_n^{(r)}) = \boldsymbol{f}_n^{(r)} - \boldsymbol{B}^{(r)^T}\boldsymbol{\lambda}_n \\ \boldsymbol{B}\boldsymbol{u}_n = 0, \end{cases} \tag{13.14}$$

Note that solving these equations is not straight forward and in addition one needs to consider the time discretization relations for the velocities and accelerations in the Finite Element submodels. In the next sections, it will be discussed how to rewrite these equations in order to solve them in a time stepping scheme. Firstly, in Sect. 13.3.2, it is assumed that the FE model at hand is a linear model, hence $\boldsymbol{p}^{(r)}\left(\dot{\boldsymbol{u}}_n^{(r)}, \boldsymbol{u}_n^{(r)}\right)$ is replaced by the sum of internal (linear) damping and elastic forces. Finally, Sect. 13.3.3 covers the assembly of non-linear finite element models and (linear) impulse response functions. For more details on Boolean operators and assembly of substructures, the interested reader is referred to [3, 16].

13.3.2 Assembly of Linear FE Models and Impulse Response Functions

First, the linear case will be handled, therefore the non linear forces are discarded and $\boldsymbol{p}^{(r)}\left(\dot{\boldsymbol{u}}_n^{(r)}, \boldsymbol{u}_n^{(r)}\right)$ is replaced by $\boldsymbol{C}^{(r)}\dot{\boldsymbol{u}}_n^{(r)} + \boldsymbol{K}^{(r)}\boldsymbol{u}_n^{(r)}$. The sets of equations of motion for the different subsystems are now:

$$\begin{cases} \boldsymbol{u}_n^{(s)} = \frac{dt}{2}\sum_{i=0}^{n-1}\boldsymbol{Y}_{n-i}^{(s)}(\boldsymbol{f}_i + \boldsymbol{f}_{i+1} - \boldsymbol{B}^{(s)^T}(\boldsymbol{\lambda}_i + \boldsymbol{\lambda}_{i+1})) \\ \boldsymbol{M}^{(r)}\ddot{\boldsymbol{u}}_n^{(r)} + \boldsymbol{C}^{(r)}\dot{\boldsymbol{u}}_n^{(r)} + \boldsymbol{K}^{(r)}\boldsymbol{u}_n^{(r)} = \boldsymbol{f}_n^{(r)} - \boldsymbol{B}^{(r)^T}\boldsymbol{\lambda}_n \\ \boldsymbol{B}\boldsymbol{u}_n = 0, \end{cases} \tag{13.15}$$

Again, the compatibility and equilibrium conditions stated in Sect. 13.3.1 have to be satisfied for a successful coupling of the subsystems. Since the outcome of this substructuring analysis would be to obtain the response of the total system to a certain set of input forces, the equations are solved in a time stepping scheme. Since the Newmark method is one of the most popular and most common time stepping schemes, it will also be used in this research. In the Newmark scheme, a Taylor expansion is used to deduce the velocities and displacements of the next time station, according to:

$$\dot{\boldsymbol{u}}_n = \dot{\boldsymbol{u}}_{n-1} + (1-\gamma)dt\ddot{\boldsymbol{u}}_{n-1} + \gamma dt\ddot{\boldsymbol{u}}_n$$

$$\boldsymbol{u}_n = \boldsymbol{u}_{n-1} + dt\dot{\boldsymbol{u}}_{n-1} + dt^2\left(\frac{1}{2} - \beta\right)\ddot{\boldsymbol{u}}_{n-1} + dt^2\beta\ddot{\boldsymbol{u}}_n \tag{13.16}$$

Substituting the velocities and displacements according to (13.16) into (13.15), results in the numerical scheme to compute the accelerations of the next time step.

$$S^{(r)}\ddot{u}_n^{(r)} = f_n^{(r)} - B^{(r)^T}\lambda_n - C^{(r)}\dot{\hat{u}}_n^{(r)} - K^{(r)}\hat{u}_n^{(r)} \tag{13.17}$$

where,

$$
\begin{aligned}
S^{(r)} &= M^{(r)} + \gamma dt C^{(r)} + \beta dt^2 K^{(r)} \\
\dot{\hat{u}}_n^{(r)} &= \dot{u}_{n-1}^{(r)} + (1-\gamma)dt\ddot{u}_{n-1}^{(r)} \\
\hat{u}_n^{(r)} &= u_{n-1}^{(r)} + dt\dot{u}_{n-1}^{(r)} + dt^2\left(\frac{1}{2}-\beta\right)\ddot{u}_{n-1}^{(r)}
\end{aligned}
\tag{13.18}
$$

As compatibility is enforced on the interface displacements (13.15), an expression for $u_n^{(r)}$ is required. Firstly, note that (13.17) can be rewritten into:

$$\ddot{u}_n^{(r)} = S^{(r)^{-1}}\left(f_n^{(r)} - B^{(r)^T}\lambda_n - C^{(r)}\dot{\hat{u}}_n^{(r)} - K^{(r)}\hat{u}_n^{(r)}\right) \tag{13.19}$$

Substituting (13.19) into (13.16) and separating the known part ($\tilde{u}_n^{(r)}$) from the unknown part, this leads to an expression for the displacements at t_n.

$$u_n^{(r)} = \tilde{u}_n^{(r)} - dt^2\beta S^{(r)^{-1}}B^{(r)^T}\lambda_n \tag{13.20}$$

where,

$$\tilde{u}_n^{(r)} = \hat{u}_n^{(r)} + dt^2\beta S^{(r)^{-1}}\left(f_n^{(r)} - C^{(r)}\dot{\hat{u}}_n^{(r)} - K^{(r)}\hat{u}_n^{(r)}\right) \tag{13.21}$$

Now, the same approach is taken to obtain an expression for the unknown displacements for the subsystems denoted by the superscripts (s) at t_n, the duhamel integral from (13.15) is also separated into a known and unknown part.

$$u_n^{(s)} = \tilde{u}_n^{(s)} - \frac{dt}{2}Y_1^{(s)}B^{(s)^T}\lambda_n, \tag{13.22}$$

where:

$$\tilde{u}_n^{(s)} = \frac{dt}{2}\sum_{i=0}^{n-2}Y_{n-i}^{(s)}(f_i + f_{i+1} - B^{(s)^T}(\lambda_i + \lambda_{i+1})) + \frac{dt}{2}Y_1^{(s)}(f_{n-1}^{(s)} + f_n^{(s)} - B^{(s)^T}\lambda_{n-1}) \tag{13.23}$$

Note that in both (13.20) and (13.22), the "known" part of the displacements is in fact the uncoupled response of the different subsystems. Due to all the steps taken so far, (13.15) is rewritten into (13.24).

$$
\begin{cases}
u_n^{(s)} = \tilde{u}_n^{(s)} - \frac{dt}{2}Y_1^{(s)}B^{(s)^T}\lambda_n \\
u_n^{(r)} = \tilde{u}_n^{(r)} - dt^2\beta S^{(r)^{-1}}B^{(r)^T}\lambda_n \\
Bu_n = 0
\end{cases}
\tag{13.24}
$$

It can be seen that the unknowns at this point are still $u_n^{(s)}$, $u_n^{(r)}$ and λ_n. By now substituting the first two lines of (13.24) into the last line, the compatibility condition, and rewriting the result, the direct relation between the known part of the displacements $\tilde{u}_n$ and interface forces λ_n is obtained.

$$\lambda_n = \left(BW\,B^T\right)^{-1}B\tilde{u}_n \tag{13.25}$$

where,

$$W = \begin{bmatrix} \frac{dt}{2}Y_1^{(s)} & 0 \\ 0 & dt^2\beta S^{(r)^{-1}} \end{bmatrix}$$

Substituting the result from (13.25) back into (13.24) and (13.16) leads to the actual coupled displacements, velocities and accelerations at time t_n, which is then the starting point to compute the coupled response at time t_{n+1}. The integration scheme discussed here is also summarized in Fig. 13.3.

13.3.3 Assembly of Non-linear FE Models and Impulse Response Functions

In addition to linear finite element models, one should also be possible to handle non-linear finite element models. Recalling (13.14), it is clear that the internal force vector $\boldsymbol{p}^{(r)}\left(\dot{\boldsymbol{u}}_n^{(r)}, \boldsymbol{u}_n^{(r)}\right)$ contains all the internal linear and non-linear elastic and damping forces. As for the non-linear case, the accelerations, velocities and displacements cannot be found in one step. The non-linear (finite element) subsystems of (13.14) are solved using the non-linear Newmark scheme [11], which uses Newton-Raphson iterations in order to solve the set of non-linear equations of motion. For solving the displacements of the linear part, expressed in IRFs, only the Lagrange multipliers ($\boldsymbol{\lambda}_n$) are needed.

In this section it will be shown how to re-arrange the equations, in order to solve the set of coupled equations. First of all, it will be shown how to condense all the linear subsystems in the non-linear subsystems, as this will ensure that the contribution of the linear subsystems is included in the Newton-Raphson iterations on the non-linear subsystems. Finally, it is shown how to update the accelerations, velocities and displacements of the non-linear subsystems using a non-linear Newmark scheme and how to use these to explicitly obtain the Lagrange multipliers, which are required to update the displacements of the linear subsystems (as can be seen in (13.6)).

Repeating the second line from (13.14) here:

$$\boldsymbol{M}^{(r)}\ddot{\boldsymbol{u}}_n^{(r)} + \boldsymbol{p}^{(r)}\left(\dot{\boldsymbol{u}}_n^{(r)}, \boldsymbol{u}_n^{(r)}\right) + \boldsymbol{B}^{(r)^T}\boldsymbol{\lambda}_n = \boldsymbol{f}_n^{(r)} \tag{13.26}$$

Note that $\boldsymbol{B}^{(r)^T}\boldsymbol{\lambda}_n$ is the interface force, which is there due to the coupling to other substructures. Now, if one wants to solve for the accelerations, velocities and displacements, the most common method is to use a Newton-Raphson scheme, which requires an iteration matrix. This iteration matrix $\boldsymbol{S}_t\left(\boldsymbol{u}_n^{(r)}\right)$, is a local linearization of the non-linear problem and can be interpreted as a tangent dynamic stiffness matrix.

$$\boldsymbol{S}_t\left(\boldsymbol{u}^{(r)}\right) = \frac{\partial \boldsymbol{p}^{(r)}}{\partial \boldsymbol{u}^{(r)}} + \frac{\partial \boldsymbol{p}^{(r)}}{\partial \dot{\boldsymbol{u}}^{(r)}}\frac{\partial \dot{\boldsymbol{u}}^{(r)}}{\partial \boldsymbol{u}^{(r)}} + \boldsymbol{M}^{(r)}\frac{\partial \ddot{\boldsymbol{u}}^{(r)}}{\partial \boldsymbol{u}^{(r)}} - \frac{\partial \boldsymbol{f}^{(r)}}{\partial \boldsymbol{u}^{(r)}} + \frac{\partial \boldsymbol{B}^{(r)^T}\boldsymbol{\lambda}}{\partial \boldsymbol{u}^{(r)}} \tag{13.27}$$

Note that, in order to compute this matrix, a direct relationship between $\boldsymbol{\lambda}$ and $\boldsymbol{u}^{(r)}$ is required and needs to be computed. Recalling the compatibility equation (13.11), the IRFs describing the linear subsystems (13.14) can be substituted in this compatibility condition and is rewritten into:

$$\begin{bmatrix} \boldsymbol{B}^{(r)} & \boldsymbol{B}^{(s)} \end{bmatrix}\begin{bmatrix} \boldsymbol{u}_n^{(r)} \\ \tilde{\boldsymbol{u}}_n^{(s)} \end{bmatrix} + \begin{bmatrix} \boldsymbol{B}^{(r)} & \boldsymbol{B}^{(s)} \end{bmatrix}\begin{bmatrix} 0 & 0 \\ 0 & \frac{dt}{2}\boldsymbol{Y}_1^{(s)} \end{bmatrix}\begin{bmatrix} \boldsymbol{B}^{(r)^T} \\ \boldsymbol{B}^{(s)^T} \end{bmatrix}\boldsymbol{\lambda}_n = 0, \tag{13.28}$$

where $\tilde{\boldsymbol{u}}_n^{(s)}$ is given in (13.30).

$$\tilde{\boldsymbol{u}}_n^{(s)} = \frac{dt}{2}\sum_{i=0}^{n-2}\boldsymbol{Y}_{n-i}^{(s)}(\boldsymbol{f}_i + \boldsymbol{f}_{i+1} - \boldsymbol{B}^{(s)^T}(\boldsymbol{\lambda}_i + \boldsymbol{\lambda}_{i+1})) + \frac{dt}{2}\boldsymbol{Y}_1^{(s)}\left(\boldsymbol{f}_{n-1}^{(s)} + \boldsymbol{f}_n^{(s)} - \boldsymbol{B}^{(s)^T}\boldsymbol{\lambda}_{n-1}\right) \tag{13.29}$$

It can be seen, that from (13.29), the relation between $\boldsymbol{\lambda}$ and $\boldsymbol{u}^{(r)}$ is easily obtained.

$$\boldsymbol{\lambda}_n = \left(\boldsymbol{B}^{(s)}\frac{dt}{2}\boldsymbol{Y}_1^{(s)}\boldsymbol{B}^{(s)^T}\right)^{-1}\boldsymbol{B}\bar{\boldsymbol{u}}_n, \tag{13.30}$$

where, $\bar{\boldsymbol{u}}_n = \begin{bmatrix} \boldsymbol{u}_n^{(r)^T} & \tilde{\boldsymbol{u}}_n^{(s)^T} \end{bmatrix}^T$. As can be seen, $\boldsymbol{B}\bar{\boldsymbol{u}}_n$ denotes the compatibility error (due to the fact that the displacements of the linear part are not updated yet), which is multiplied by the equivalent interface *stiffness* of the linear subsystem and thus results in the interface force that is required to close the "gap". Note that this is an *implicit* equation, as $\boldsymbol{u}_n^{(s)}$ is also a function

$$\boldsymbol{Y}^{(s)}, \ \boldsymbol{f}^{(s)}$$

$$\boldsymbol{M}^{(r)}, \ \boldsymbol{C}^{(r)}, \ \boldsymbol{K}^{(r)},$$
$$\boldsymbol{u}_0^{(r)}, \ \dot{\boldsymbol{u}}_0^{(r)}, \ \boldsymbol{f}^{(r)}$$

Initial accelerations

$$\ddot{\boldsymbol{u}}_0^{(r)} = \boldsymbol{M}^{(r)^{-1}} \left(\boldsymbol{f}_0^{(r)} - \boldsymbol{K}^{(r)} \boldsymbol{u}_0^{(r)} - \boldsymbol{C}^{(r)} \dot{\boldsymbol{u}}_0^{(r)} \right)$$

$$t = t + dt$$

$$t = t + dt$$

Prediction

$$\boldsymbol{u}_n^{(s)} = \frac{dt}{2} \sum_{i=0}^{n-2} \boldsymbol{Y}_{n-i}^{(s)} \left(\boldsymbol{f}_i^{(s)} + \boldsymbol{f}_{i+1}^{(s)} - \boldsymbol{B}^{(s)^T} \boldsymbol{\lambda}_i \right.$$
$$\left. - \boldsymbol{B}^{(s)^T} \boldsymbol{\lambda}_{i+1} \right) + \frac{dt}{2} \boldsymbol{Y}_1^{(s)} \left(\boldsymbol{f}_{n-1}^{(s)} - \boldsymbol{B}^{(s)^T} \boldsymbol{\lambda}_{n-1} \right)$$

Prediction

$$\dot{\boldsymbol{u}}_n^{(r)} = \dot{\boldsymbol{u}}_{n-1}^{(r)} + (1-\gamma) dt \ddot{\boldsymbol{u}}_{n-1}^{(r)}$$
$$\boldsymbol{u}_n^{(r)} = \boldsymbol{u}_{n-1}^{(r)} + dt^2 \left(\frac{1}{2} - \beta \right) \ddot{\boldsymbol{u}}_{n-1}^{(r)}$$

"Uncoupled" response to an external force

$$\boldsymbol{u}_n^{(s)} = \boldsymbol{u}_n^{(s)} + \frac{dt}{2} \boldsymbol{Y}_1^{(s)} \boldsymbol{f}_n^{(s)}$$

"Uncoupled" response to an external force

$$\ddot{\boldsymbol{u}}_n^{(r)} = \boldsymbol{S}^{(r)^{-1}} \left(\boldsymbol{f}_n^{(r)} - \boldsymbol{K}^{(r)} \boldsymbol{u}_n^{(r)} - \boldsymbol{C}^{(r)} \dot{\boldsymbol{u}}_n^{(r)} \right)$$
$$\dot{\boldsymbol{u}}_n^{(r)} = \dot{\boldsymbol{u}}_n^{(r)} + \gamma dt \ddot{\boldsymbol{u}}_n^{(r)}$$
$$\boldsymbol{u}_n^{(r)} = \boldsymbol{u}_n^{(r)} + dt^2 \beta \ddot{\boldsymbol{u}}_n^{(r)}$$

Interface force

$$\boldsymbol{\lambda}_n = \left(\boldsymbol{B} \boldsymbol{W} \boldsymbol{B}^T \right)^{-1} \boldsymbol{B} \boldsymbol{u}_n$$

Correction

$$\boldsymbol{u}_n^{(s)} = \boldsymbol{u}_n^{(s)} - \frac{dt}{2} \boldsymbol{Y}_1^{(s)} \boldsymbol{B}^{(s)^T} \boldsymbol{\lambda}_n$$

Correction

$$\ddot{\boldsymbol{u}}_n^{(r)} = \ddot{\boldsymbol{u}}_n^{(r)} - \boldsymbol{S}^{(r)^{-1}} \boldsymbol{B}^{(r)^T} \boldsymbol{\lambda}_n$$
$$\dot{\boldsymbol{u}}_n^{(r)} = \dot{\boldsymbol{u}}_n^{(r)} + \gamma dt \ddot{\boldsymbol{u}}_n^{(r)}$$
$$\boldsymbol{u}_n^{(r)} = \boldsymbol{u}_n^{(r)} + dt^2 \beta \ddot{\boldsymbol{u}}_n^{(r)}$$
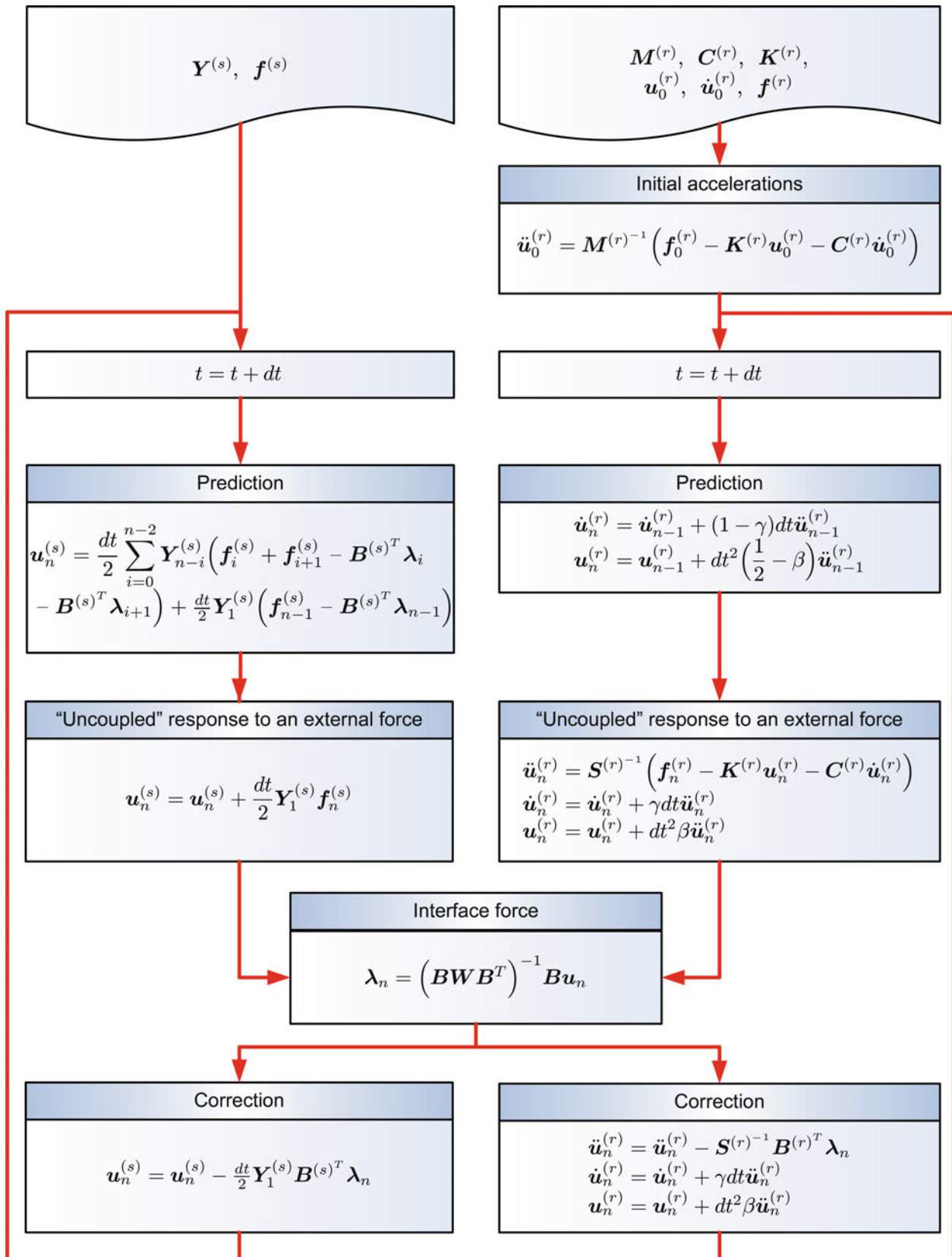
Fig. 13.3 Integration scheme for the linear IBS case

of the interface force $\boldsymbol{\lambda}_n$ (13.14). Nevertheless, (13.31) can be substituted in the equations of motion of the non-linear part of the total problem (13.14). This results in the following set of equations.

$$\boldsymbol{M}^{(r)}\ddot{\boldsymbol{u}}_n^{(r)} + \left(\boldsymbol{p}^{(r)}(\dot{\boldsymbol{u}}_n^{(r)}, \boldsymbol{u}_n^{(r)})\right) + \boldsymbol{B}^{(r)^T}\left(\boldsymbol{B}^{(s)}\tfrac{dt}{2}\boldsymbol{Y}_1^{(s)}\boldsymbol{B}^{(s)^T}\right)^{-1}\boldsymbol{B}\bar{\boldsymbol{u}}_n = \boldsymbol{f}_n^{(r)} \tag{13.31}$$

This is in fact a condensation of the linear subsystems, described in their IRFs, into the non-linear subsystems. Using (13.32), the tangent iteration matrix $\boldsymbol{S}_t(\boldsymbol{u}^{(r)})$ can be computed.

$$\boldsymbol{S}_t\left(\boldsymbol{u}_n^{(r)}\right) = \boldsymbol{K}_t^{(r)} + \frac{\gamma}{\beta dt}\boldsymbol{C}_t^{(r)} + \frac{1}{\beta dt^2}\boldsymbol{M}^{(r)} + \boldsymbol{B}^{(r)^T}\left(\boldsymbol{B}^{(s)}\frac{dt}{2}\boldsymbol{Y}_1^{(s)}\boldsymbol{B}^{(s)^T}\right)^{-1}\boldsymbol{B}^{(r)} \tag{13.32}$$

Using the relations obtained so far, the time stepping scheme (Fig. 13.4) can now be discussed. The scheme consists of two simultaneous loops over time; the first being the discretized convolution product and the second being the modified non-linear Newmark time integration scheme. As with any time integration scheme, one starts with the initial conditions and computes the initial accelerations. In the next step, the so called predictors are computed. In the case of the convolution product, this is in fact the "uncoupled" response of the subsystem, as is given in (13.30). For the non-linear Newmark scheme one computes, at each new time step, predictions for the displacements, velocities and accelerations.

$$\begin{aligned}
\boldsymbol{u}_n^{(r)} &= \boldsymbol{u}_{n-1}^{(r)} + dt^2\left(\frac{1}{2} - \beta\right)\ddot{\boldsymbol{u}}_{n-1}^{(r)} \\
\dot{\boldsymbol{u}}_n^{(r)} &= \dot{\boldsymbol{u}}_{n-1}^{(r)} + (1 - \gamma)dt\ddot{\boldsymbol{u}}_{n-1}^{(r)} \\
\ddot{\boldsymbol{u}}_n^{(r)} &= 0
\end{aligned} \tag{13.33}$$

Using these predictions, the error on the equilibrium is computed, which can be interpreted as a residual force vector.

$$\boldsymbol{r}_n^{(r)} = \boldsymbol{M}^{(r)}\ddot{\boldsymbol{u}}_n^{(r)} + \boldsymbol{p}^{(r)}(\dot{\boldsymbol{u}}_n^{(r)}, \boldsymbol{u}_n^{(r)}) - \boldsymbol{f}_n^{(r)} + \boldsymbol{B}^{(r)^T}\boldsymbol{\lambda}_n \tag{13.34}$$

Note that $\boldsymbol{\lambda}$ is computed using (13.31). The goal is to minimize this residual to a given convergence criterium $|\boldsymbol{r}_n^{(r)}| < \varepsilon|\boldsymbol{f}_{int}^{(r)}|$, where $\boldsymbol{f}_{int}^{(r)}$ is the sum of all the internal forces and ε is a constant dictating the strictness of convergence. This minimization of the residual is achieved by successive Newton-Raphson iterations

$$\boldsymbol{S}_t(\boldsymbol{u}_n^{(r)})\Delta\boldsymbol{u}^{(r)} = -\boldsymbol{r}_n^{(r)}, \tag{13.35}$$

here, $\Delta\boldsymbol{u}^{(r)}$ is the correction on the displacements and the iteration matrix $\boldsymbol{S}_t(\boldsymbol{u}_n^{(r)})$ is the Jacobian of the equations of motion as computed in (13.33). Using $\Delta\boldsymbol{u}^{(r)}$, the displacements, velocities and accelerations are updated.

$$\begin{aligned}
\ddot{\boldsymbol{u}}_n^{(r)} &= \ddot{\boldsymbol{u}}_n^{(r)} + \frac{1}{\beta dt^2}\Delta\boldsymbol{u}^{(r)} \\
\dot{\boldsymbol{u}}_n^{(r)} &= \dot{\boldsymbol{u}}_n^{(r)} + \frac{\gamma}{\beta dt}\Delta\boldsymbol{u}^{(r)} \\
\boldsymbol{u}_n^{(r)} &= \boldsymbol{u}_n^{(r)} + \Delta\boldsymbol{u}^{(r)}
\end{aligned} \tag{13.36}$$

Using the updated displacements, a new interface force $\boldsymbol{\lambda}_n$ is computed for each iteration using (13.31). Substituting the new interface force and the updated displacements, velocities and accelerations into (13.35), results in the "updated" residual force, which is used for the next iteration. After the non-linear part has converged, the linear substructures can be updated

$$\boldsymbol{u}_n^{(s)} = \tilde{\boldsymbol{u}}_n^{(s)} - \frac{dt}{2}\boldsymbol{Y}_1^{(s)}\boldsymbol{B}^{(s)^T}\boldsymbol{\lambda}_n, \tag{13.37}$$

and a new time step is started. The method for coupling IRFs and non-linear FE models is shown in Fig. 13.4, where the iteration-loop is indicated by the green dotted line. It is clear that the Impulse Based Substructuring method can also be used to couple IRFs with non-linear finite element models and that the implementation only requires some small modifications to the original Newmark time integration scheme for non-linear problems.
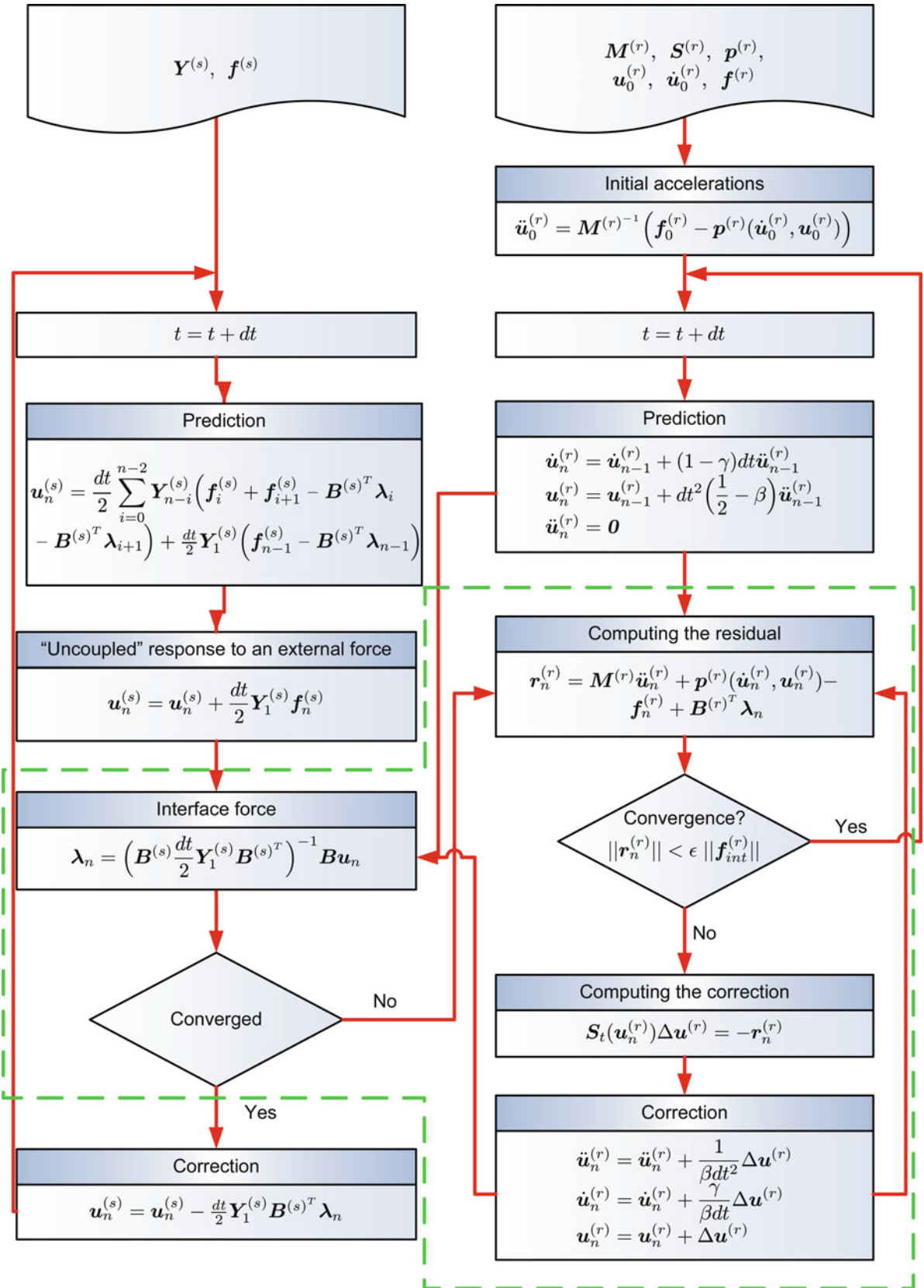
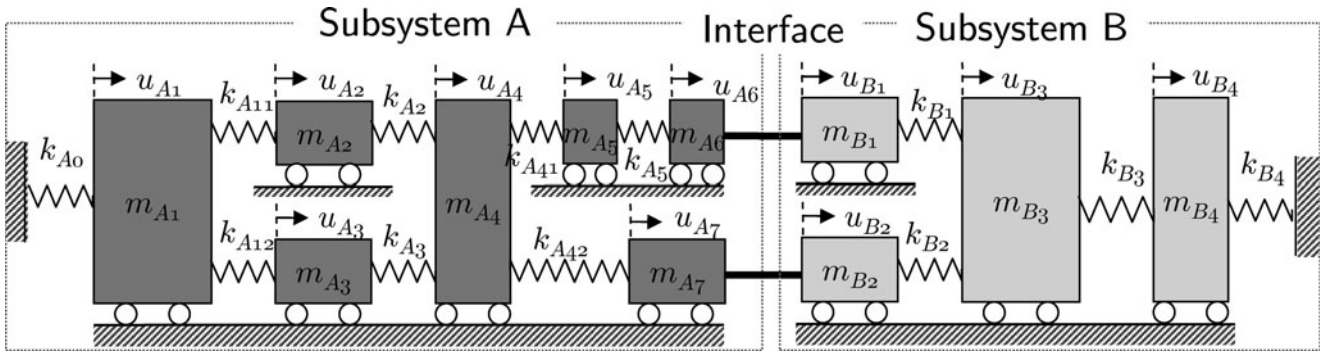**Fig. 13.4** Integration scheme for the non-linear IBS case

Fig. 13.5 Simple system used for case study

Table 13.1 Parameters of mass-spring systems

| | System parameters | | | |
| | Subsystem A | | Subsystem B | |
	Mass (kg)	Stiffness (N/m)	Mass (kg)	Stiffness (N/m)
General	$m_{A1} = 10$	$k_{A11} = 2 \cdot 10^3$	$m_{B1} = 2$	$k_{B1} = 1 \cdot 10^3$
	$m_{A2} = 3$	$k_{A12} = 2 \cdot 10^3$	$m_{B2} = 4$	$k_{B2} = 1 \cdot 10^3$
	$m_{A3} = 3$	$k_{A2} = 1 \cdot 10^3$	$m_{A3} = 8$	$k_{B3} = 2 \cdot 10^3$
	$m_{A4} = 6$	$k_{A3} = 1 \cdot 10^3$	$m_{B4} = 5$	$k_{B4} = 2 \cdot 10^2$
	$m_{A5} = 2$	$k_{A41} = 0. 5 \cdot 10^3$		
	$m_{A6} = 2$	$k_{A42} = 1 \cdot 10^3$		
	$m_{A7} = 4$	$k_{A5} = 0. 2 \cdot 10^3$		
Linear case		$k_{A0} = 1 \cdot 10^3$		
Non-linear case		$k_{A0} = 5 \cdot 10^7$		

13.4 Case Study

The methods presented above, will be demonstrated using both a linear and a non-linear academic test case. Both test cases are based on the same model (Fig. 13.5 and Table 13.1), where in the non-linear case one of the linear springs is replaced by a cubic spring. Subsystem A is a 7 DoF system and is modeled using the finite element method, subsystem B is a 4 DoF system and is modeled using impulse response functions. The total system consists of 9 DoF, as u_{A6} is rigidly connected to u_{B1} and u_{A7} is rigidly connected to u_{B2}. In order to demonstrate the method, the system is excited by an impulse on m_{A1} at $t = 0. 1s$ and the computed displacements are compared to a reference solution, which is obtained by performing a Newmark time integration on the total system. The results of the linear test case are shown in Fig. 13.6. In the upper graph, the displacements u_{A1} is shown for both the reference solutions as well as the solution computed using the IBS method; it is clear that the responses are the same. The interface forces are shown in the lower graph, where λ_1 is the interface force between m_{A6} and m_{B1} and λ_2 is the interface force between m_{A7} and m_{B2}. In the non-linear case, the linear spring denoted k_{A0} in Fig. 13.5 is replaced by a cubic spring, with the following behavior

$$f = k_{A0}u_{A1}^3$$

and m_{A1} is excited by the same impulse. The results of the non-linear test case are shown in Fig. 13.7. The effect of the non-linear spring is apparent in the results and it can easily be verified by the reader that, again, the method gives perfect results.

13.5 Conclusions and Discussion

In this paper it was shown how to assemble both linear and non-linear finite element models to impulse response functions. From Figs. 13.3 and 13.4 it is easy to see that the IBS method can actually be seen as and "add-on" to the standard Newmark time integration schemes and require only a limited number of modifications. From the results it can be concluded that the method works excellent for both the linear and non-linear cases.
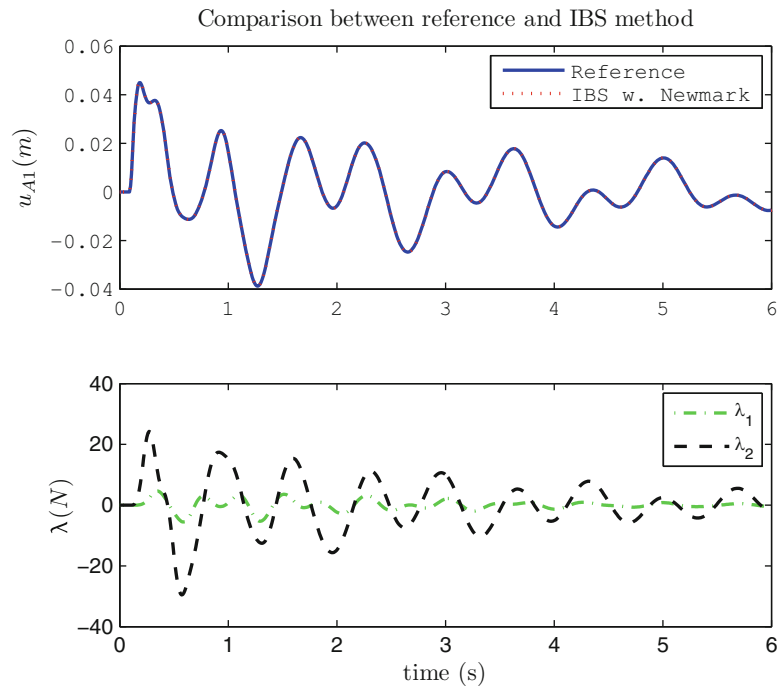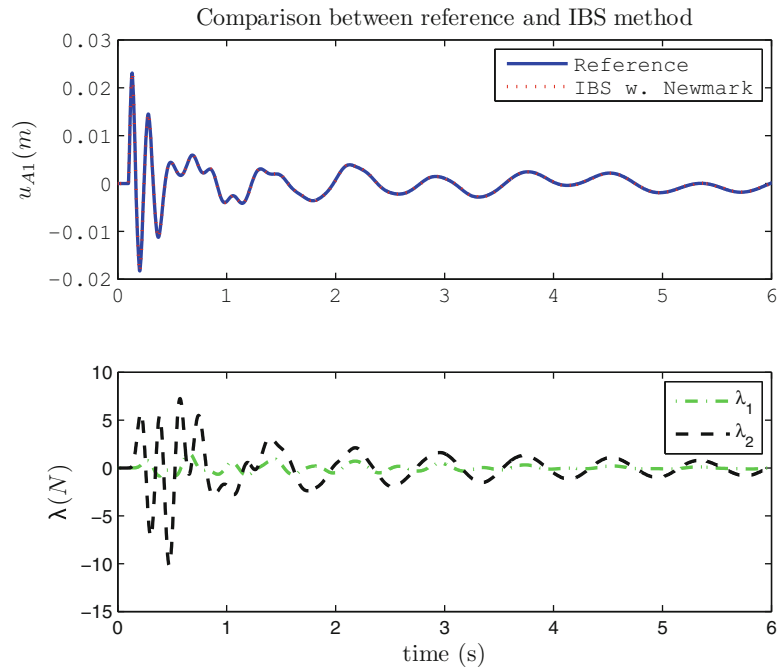
Fig. 13.6 Results of the linear test case

Fig. 13.7 Results of the non-linear test case

In addition to this, in theory, the method can also be used for combining numerical models with experimentally obtained impulse response functions. Although working with measurements is altogether challenging, the technique should allow for time integrations which include measured components.

References

1. Craig R, Bampton M (1968) Coupling of substructures for dynamic analysis. AIAA J 6(7):1313–1319
2. Crowley J, Klosterman A, Rocklin G, Vold H (1984) Direct structural modification using frequency response functions. In: Proceedings of the second international modal analysis conference, Orlando, FL, Society for experimental mechanics, Bethel, pp 58–65
3. de Klerk D, Rixen D, Voormeeren S (2008) General framework for dynamic substructuring: history, review and classification of techniques. AIAA J 46(5):1169–1181
4. Gladwell G (1964) Branch mode analysis of vibrating systems. J Sound Vib 1:41–59
5. Guyan R (1965) Reduction of stiffness and mass matrices. AIAA J 3:380
6. Hurty WC (1960) Vibrations of structural systems by component mode synthesis. J Eng Mech, Division American Society of Civil Engineers 86(4):51–69
7. Hurty W (1965) Dynamic analysis of structural systems using component modes. AIAA J 3(4):678–685
8. Jetmundsen B, Bielawa R, Flannelly W (1988) Generalized frequency domain substructure synthesis. J Am Helicopter Soc 33:55–65
9. Lehmann L (2005) An effective finite element approach for soil-structure analysis in the time-domain. Struct Eng Mech 21:437–450
10. MacNeal R (1971) A hybrid method of component mode synthesis. Comput Struct 1(4):581–601
11. Newmark N (1959) A method of computation for structural dynamics. In: Proceedings of the American society of civil engineers, J Eng Mech Div 85:67–94
12. Rixen D (2010a) A substructuring technique based on measured and computed impulse response functions of components. In: Proceedings of the international conference on noise and vibration engineering (ISMA 2010), Leuven, 20–22 Sept 2010
13. Rixen D (2010b) Substructuring using impulse response functions for impact analysis. In: Proceedings of the IMAC - XXVIII, Jacksonville
14. Rubin S (1975) Improved component-mode representation for structural dynamic analysis. AIAA J 13:995–1006
15. Schwarz HA (1890) Gesammelte Mathematische Abhandlungen, vol 2, pp 133–143. First published in Vierteljahrsschrift der Naturforschenden Gesellschaft in Zürich, 1870, vol 15, pp 272–286
16. Voormeeren S, van der Valk P, Rixen D (2011) Generalized methodology for assembly and reduction of component models for dynamic substructuring. AIAA J 49(5):1010–1020. doi:10.2514/1.54302

Chapter 14
Truncating the Impulse Responses of Substructures to Speed Up the Impulse-Based Substructuring

Daniel Rixen and Nazgol Haghighat

Abstract Recently a time-domain substructuring method was proposed based on the assembly of series of impulse responses of components: the Impulse Base Substructuring (IBS). Although theoretically the IBS is the time-domain equivalent to the Frequency Based Substrcutring method (FBS), it has several advantages when computing shock responses for instance. However a major drawback of the IBS is the rapid increase of computational costs when the simulated time increases. In this contribution we propose a truncation and windowing procedure in order to limit the cost involved by the discretized convolution product inherent to the IBS method. We describe how to truncate the Impulse Response Functions of floating and non-floating substructures, and describe a cosine windowing function to improve the accuracy and stability of the dynamic response obtained from the superposition of truncated impulse responses. A simple bar example is used to illustrate the numerical performance of the truncated IBS.

14.1   Nomenclature

FRF	Frequency response functions
FBS	Frequency based substructuring
IBS	Impulse based substructuring
IRF	Impulse response functions
$\boldsymbol{u}$	Array of degrees of freedom
$\boldsymbol{f}$	Array of external forces
$\boldsymbol{H}(t)$	Matrix of impulse response function
$\star^{(s)}$	Pertaining to substructure s
N^s	Number of substructures in the system
$\boldsymbol{B}$	Signed Boolean matrix defining compatibility constraints
λ	Lagrange multipliers on interface
$\boldsymbol{M}, \boldsymbol{K}, \boldsymbol{C}$	Mass, stiffness and damping matrix of a linear(ized) system
$\boldsymbol{R}$	Matrix of rigid body modes of a floating substructure
dt	Time-step size
$\star_n$	Pertaining to time-step n
$[\star_i$	Component i of an array
β, γ	Parameters of the Newmark time-integration scheme
ε	Relative amplitude threshold for the truncation of the IRF
t_c	Cutoff time for the truncation of the IRF

D. Rixen (✉) • N. Haghighat
Faculty of Mechanics, Maritime and Material Engineering, Department of Precision and Microsystems Engineering, Engineering Dynamics, Delft University of Technology, Mekelweg 2, 2628CD Delft, The Netherlands
e-mail: d.j.rixen@tudelft.nl

14.2   Introduction

The Impulse Based Substructuring (IBS) method was proposed in [3] as a time-domain counter-part of the Frequency Based Substructuring (FBS) (see for instance [1] for an overview of the FBS approach). The FBS represents the dynamics of the substructures through the Frequency Response Functions (FRFs) in the frequency domain at the interface, input and output degrees of freedom. The IBS describes the substructure dynamics using impulse response functions (IRF) which, in theory, are the inverse Fourier transforms of the FRFs.

Although the IBS approach is the direct counterpart of the FBS in the time domain, it has some advantages when one wants to compute the response of a system to shock loads using the measured or simulated response of its components.

In the present contribution we deal with one of the shortcomings of the IBS method, namely the fact that computing the response through a discretized convolution product can become computationally expensive when the time interval one is interested in for the simulation is not small. To alleviate the cost involved in the IBS computation, we investigate the possibility to apply truncation and windowing to the impulse responses of the components. Although such an approach seems straightforward, special caution must be taken when a component is floating, namely when it has not enough constraints to fix it in space once it is disconnected from its neighboring components.

In Sect. 14.2 we will shortly recall the basic principles of the IBS method and in Sect. 14.3 we discuss the truncation procedures for the IRFs of the components. We first describe the truncation and windowing for a non-floating component, then we develop a truncation procedure for floating ones. In Sect. 14.4 a simple numerical example is presented in order to illustrate the accuracy and stability of the solution computed by the truncated IBS approach.

14.3   The Impulse Based Substructuring in a Nutshell

14.3.1   Convolution of Impulse Response Functions and Inputs

The impulse based computation of the response of a dynamical system is described by the Duhamel's integral stating that a dynamic response is obtained from the convolution of the impulse response $h(t)$ (i.e. the response to a unit impulse at time $t = 0$) and the applied force $f(t)$. For a system with several inputs and outputs, we call $H(t)$ the matrix of the impulse response functions between inputs and outputs. The system responses at the outputs are denoted by the array $u(t)$ and the applied forces (the inputs) are denoted by an array $f(t)$. The Duhamel's integral can then be written as

$$u(t) = \int_0^t H(t - \tau) f(\tau) d\tau \tag{14.1}$$

In practice, for engineering systems, the IRFs, namely $H(t)$ are not known analytically but can be measured (see [2]) or simulated (see [3]). So the IRF is available in a time-discretized form. Calling H_n, f_n and u_n, the IRF matrix, input and output arrays at time t_n, the Duhamel's integral (14.1) can be approximated by the finite difference form

$$u_n = \sum_{i=0}^{n-1} \left(H_{n-i} f_i + H_{n-i-1} f_{i+1} \right) dt/2 \tag{14.2}$$

This approximation is obtained by applying the trapezoidal rule to the Duhamel's integral. It was observed in [3] that, if the IRF matrix is computed using a Newmark scheme, the discretization (14.2) yields the some dynamic response as when a Newmark scheme is applied to compute the response to the excitation f.

14.3.2   Assembling the Dynamic Response of Substructures

Let us now assume that a system is described by the impulse response of its N_s substructures and let as call $H^{(s)}$ the IRFs of substructure $\Omega^{(s)}$. The assembly of the substructure is perform in a dual manner by imposing the compatibility between matching degrees of freedom on the interface between substructures. This can be written as

$$\sum_{s=1}^{N^s} B^{(s)} u^{(s)} = 0 \tag{14.3}$$

where $B^{(s)}$ are signed Boolean matrices identifying the matching degrees of freedom on the interfaces (see [1] for instance). This relation merely states that for any matching pair $(u_i^{(s)}, u_j^{(r)})$ one must impose $u_i^{(s)} - u_j^{(r)} = 0$. This compatibility condition is enforced using Lagrange multipliers λ, representing the internal forces on the interfaces. Hence for a partitioned problem the Duhamel's integral (14.1) can be written as[1]

$$\begin{cases} u^{(s)}(t) = \int_0^t H^{(s)}(t-\tau)\Big(f^{(s)}(\tau) + B^{(s)^T}\lambda(\tau)\Big)d\tau \\[2mm] \sum_{s=1}^{N_s} B^{(s)} u^{(s)}(t) = 0 \end{cases} \tag{14.4}$$

Considering the same time-discretization as in (14.2), taking into account that $H_0 = 0$, the dual assembly (14.4) can be discretized as

$$\begin{cases} u^{(s)}{}_n = H_n^{(s)}\left(f_0^{(s)}\frac{dt}{2} + B^{(s)^T}\lambda_0\right) + \sum_{i=1}^{n-1} H_{n-i}^{(s)}\Big(f_i^{(s)}dt + B^{(s)^T}\lambda_i\Big) \\[2mm] \sum_{s=1}^{N^s} B^{(s)} u_n^{(s)} = 0 \end{cases} \tag{14.5}$$

In practice this system is solved for every time instance t_n by first predicting the substructure response as if the interface impulses λ_{n-1} are null, then computing the λ_{n-1} necessary to satisfy compatibility at time t_n, and finally correcting the substructure responses for the interface force. In summary,

$$\tilde{u}_n^{(s)} = H_n^{(s)}\left(f_0^{(s)}\frac{dt}{2} + B^{(s)^T}\lambda_0\right) + \sum_{i=1}^{n-2} H_{n-i}^{(s)}\Big(f_i^{(s)}dt + B^{(s)^T}\lambda_i\Big) + H_1^{(s)}f_n - 1^{(s)}dt \tag{14.6}$$

$$\lambda_{n-1} = -\left(\sum_{s=1}^{N^s} B^{(s)} H_1^{(s)} B^{(s)^T}\right)^{-1} \sum_{s=1}^{N^s} B^{(s)} \tilde{u}_n^{(s)} \tag{14.7}$$

$$u_n^{(s)} = \tilde{u}_n^{(s)} + H_1^{(s)} B^{(s)^T}\lambda_{n-1} \tag{14.8}$$

14.4   Truncating the Impulse Responses

Clearly the cost of the discretized convolution (14.6) is increasing rapidly when the simulation time t_n is getting large. This is due to the fact that all the forces that have been acting on the system from time t_0 to time t_{n-1} determine the dynamic response at t_n through the history transmitted over the time domain according to the impulse response H. For instance the force f_0 applied at time t_0 will influence the response at time t_n through the value of the IRFs H_n. If however the IRFs at t_n have significantly decreased due to the damping in the system, it seems acceptable to neglect the contribution of f_0 to the response u_n. In essence one then truncates the IRFs of the system. This will be investigated in this section, first for a non-floating component, then for a floating component.

---

[1] In the time-discrete form λ are chosen to represent interface impulses.

14.4.1 Non-Floating Substructures

Let us split the Duhamel's integral (14.2) in the following two convolution products:

$$u_n = \int_0^{t_n} H(t_n - \tau)f(\tau)\ d\tau = \int_0^{t_n - t_c} H(t_n - \tau)f(\tau)\ d\tau + \int_{t_n - t_c}^{t_n} H(t_n - \tau)f(\tau)\ d\tau \qquad (14.9)$$

Let us further assume that after time t_c the IRFs have decayed so that they can be assumed to be zero:

$$H(t_n - \tau) \simeq 0 \qquad for\, t_n - \tau > t_c, namely\, for\, \tau < t_n - t_c$$

Note that this will occur only if damping is present and if the structure is not floating. Indeed if the structure (or substructure in the case of the IBS) are not restrained by enough imposed displacements, the IRFs will grow steadily due to the rigid body motion generated by the initial impulse. This case will be discussed in Sect. 14.3.2. Assuming thus that enough damping is present and that the (sub)structure is not floating, one can then write the approximation[2]

$$u_n \simeq \int_{\max\{0, t_n - t_c\}}^{t_n} H(t_n - \tau)f(\tau)d\tau \qquad (14.10)$$

$$\simeq \sum_{i=\max\{0, n-c\}}^{n-1} \left(H_{n-i}f_i + H_{n-i-1}f_{i+1}\right)dt/2 \qquad (14.11)$$

This approximation can significantly reduce the cost of the convolution computation. It corresponds to cutting the IRF after time t_c, and can thus be seen as windowing the IRF with a rectangular window of width equal to t_c. Obviously other windows can be defined in order to force the IRFs to zero in a smoother manner. This is discussed next.

Let us consider a user defined threshold ε. Then the cutoff time t_c can be chosen as the time for which all the impulse responses in H have a vibrational amplitude lower than ε (see Fig. 14.1). The approximation (14.11) can then be interpreted as applying a rectangular window on the IRFs in order to set them to zero after time t_c. Such a rectangular window can formally be written as

$$W_{rect}(t) = \begin{cases} 1 & if\, t < t_c \\ 0 & if\, t > t_c \end{cases} \qquad (14.12)$$

where t_c is such that the amplitude of all the IRFs in H have reached an oscillatory amplitude ε-times lower than their maximum value over time.[3] Obviously, forcing the impulse response to zero can seriously perturb the dynamic response computed by superposition of impulse responses since it corresponds to introducing parasitic impulses after time t_c in order to "kill" the impulse response of forces that have been acting on the system c time steps earlier. Thus applying smoother windows is desirable in order to improve the accuracy and the stability of the dynamic response constructed on truncated IRFs. Here we will investigate a simple *cosine* window defined as

$$W_{cos}(t) = \begin{cases} \cos\left(\dfrac{\pi t}{2t_c}\right) & if\, t < t_c \\ 0 & if\, t > t_c. \end{cases} \qquad (14.13)$$

An illustration of such a window is given in Fig. 14.2. This cosine window has the advantage to introduce only very small additional damping at the beginning of the IRF, therefore not perturbing to much the dynamical properties of the system.

---

[2] In case of substructures, one must also add the interface forces $B^{(s)^T}\lambda$ in these equations. Nevertheless, to simplify the text, we will omit the interface forces in this section.

[3] In our work the oscillatory amplitude is detected by evaluating the peak values of the IRFs.
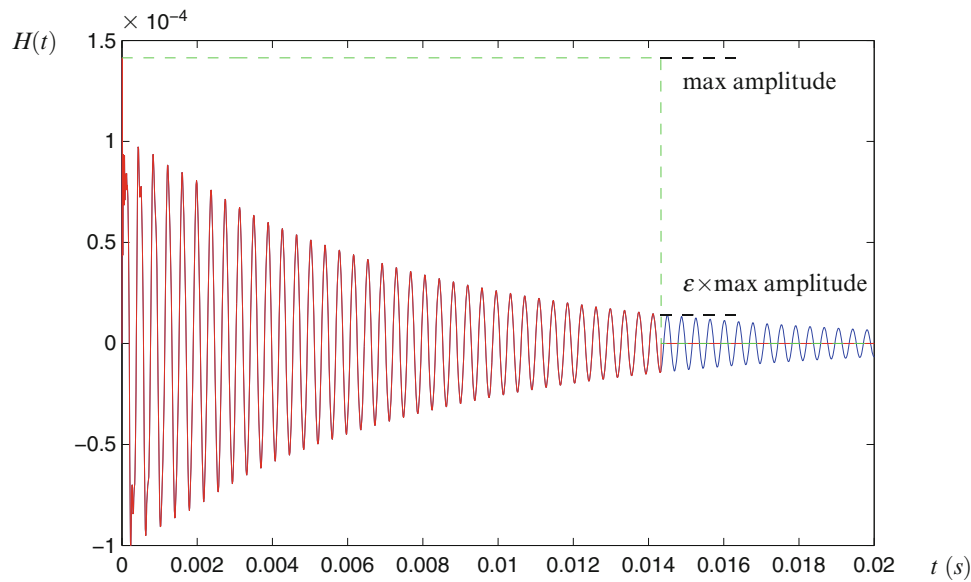
Fig. 14.1 IRF truncated by a rectangular window
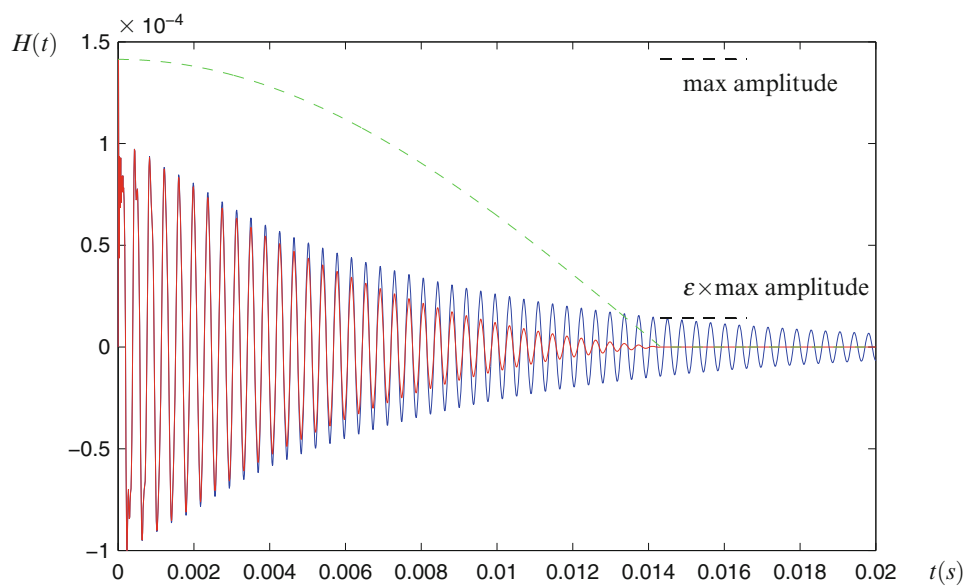
Fig. 14.2 IRF truncated by a cosinus window

Nevertheless one should be aware that such a window, unlike for instance a classical exponential window, transforms the IRF in a dynamic response that isnot mechanically interpretable. Furthermore, the high slope of the cosine window close to the cutoff time might induce significant velocity and acceleration perturbations.

When such a non-rectangular window is applied one first multiplies the IRFs up to t_c by W_{cos} to obtain the weighted IRFs $\bar{H}$ (red curve in Fig. 14.2) and uses the truncated convolution (14.11) where H is replaced by $\bar{H}$. Obviously such a procedure can be introduced in the IBS approach (14.5) by simply restricting the convolution computation and replacing the IRFs by the weighted ones.

14.4.2   *Floating Substructures*

Let us now consider the case of a floating (sub)structure and split again the convolution product as in (14.9)

$$u_n = \int_0^{t_n} H(t_n - \tau)f(\tau) \ d\tau = \int_0^{t_n - t_c} H(t_n - \tau)f(\tau) \ d\tau + \int_{t_n - t_c}^{t_n} H(t_n - \tau)f(\tau) \ d\tau$$

When the substructure is floating, namely when there are not enough boundary conditions to block its rigid body motion, one can no longer assume that the IRF is close to zero after a time t_c since the initial impulse has generated an initial velocity causing the (sub)structure to drift away. In fact the IRF can be seen as a vibration superimposed on a global rigid body motion.

The approach proposed here is then to truncate and apply a window on the part of the IRF remaining when one has removed the rigid body motion due to a unit impulse. The overall rigid body motion in the IRF will be accounted for during the full length of the convolution and thus is not truncated.

To build the rigid body response, one can either estimate the constant velocity part from the measured or simulated IRF, or if the global inertia of the (sub)structure is known, it can be computed. Calling $\boldsymbol{R}$ the matrix containing in its columns the rigid body modes of the (sub)structure (i.e. the nullspace of the stiffness matrix $\boldsymbol{K}$), the overall motion is found by setting

$$u = R\alpha \tag{14.14}$$

where α are the unknown rigid body mode amplitudes. Let as write the linear(ized) equilibrium equation of the system as

$$M\ddot{u} + C\dot{u} + Ku = f \tag{14.15}$$

where $\boldsymbol{M}$, $\boldsymbol{C}$ and $\boldsymbol{K}$ are respectively the mass, damping and stiffness matrices. Introducing the assumption (14.14) in the equilibrium equation and noting that $\boldsymbol{KR} = \boldsymbol{0}$ by definition, and assuming further that $\boldsymbol{CR} = \boldsymbol{0}$,[4] one finds

$$R^T M R\ddot{\alpha} = R^T f \tag{14.16}$$

Thus, when $\boldsymbol{f}$ is an initial unit impulse, one can write

$$\int_0^t \int_0^t R^T M R\ddot{\alpha} dt = \int_0^t \int_0^t R^T f = R^T 11 \ t$$

where 11 is an array containing zeros for all entries except at the degree of freedom excited by the impulse, where the value of 11 is 1. Defining then

$$M_{tot} = R^T M R \tag{14.17}$$

the total inertia related to the rigid body modes $\boldsymbol{R}$ and recalling that for the IRF, initial conditions are null, one finds

$$\alpha = M_{tot}^{-1} R^T 11 \ t \tag{14.18}$$

Substituting now in (14.14) one finds the rigid body motion related to a unit impulse:

$$u_{rigid} = R_{tot}^{-1} R^T 11 \ t \tag{14.19}$$

So computing the rigid body motion associated to every input of the IRF matrix $\boldsymbol{H}$, one builds the rigid body response matrix

---

[4] This assumption means that the damping in the (sub)structure is internal and does not produce any damping force when no deformations are present.

$$H^{rig} = R M_{tot}^{-1} R^T \ t \tag{14.20}$$

and the vibrational part of the IRF is obtained from[5]

$$H^{vib} = H - H^{rig} \tag{14.21}$$

The truncation of the IRF for a floating (sub)structure then consists in truncating only its vibrational part since that portion of the IRF can be assumed to decay to a negligible contribution after the cutoff time t_c. Mathematically speaking we write

$$
\begin{aligned}
_n &= \int_0^{t_n} H(t_n - \tau) f(\tau) \ d\tau \\
&= \int_0^{t_n} \left(H^{rig}(t_n - \tau) + H^{vib}(t_n - \tau) \right) f(\tau) \ d\tau \\
&\simeq \int_0^{t_n} {}^{rig}(t_n - \tau) f(\tau) d\tau + \int_{t_n - t_c}^{t_n} {}^{vib}(t_n - \tau) f(\tau) \ d\tau \\
&\text{where} \quad {}^{rig}(t_n - \tau) = R_{tot}^{-1} R^T \ [t_n - \tau] \ d\tau
\end{aligned}
\tag{14.22}
$$

The first part represents the rigid body response to the force f and, introducing the simplified notation

$$\mathcal{M}^{-1} = R M_{tot}^{-1} R^T \quad, \tag{14.23}$$

it can be written as

$$u_n^{rig} = \int_0^{t_n} \mathcal{M}^{-1} \ [t_n - \tau] f(\tau) \ d\tau \tag{14.24}$$

$$
\begin{aligned}
&= \int_0^{t_{n-1}} \mathcal{M}^{-1} \ [t_{n-1} + dt - \tau] f(\tau) \ d\tau + \int_{t_{n-1}}^{t_n} \mathcal{M}^{-1} \ [t_n - \tau] f(\tau) d\tau \\
&= \int_0^{t_{n-1}} \mathcal{M}^{-1} \ [t_{n-1} - \tau] f(\tau) \tau + \mathcal{M}^{-1} \ dt \int_0^{t_{n-1}} f(\tau) \ d\tau + \mathcal{M}^{-1} \int_{t_{n-1}}^{t_n} [t_n - \tau] f(\tau) d\tau \\
&= u_{n-1}^{rig} + \mathcal{M}^{-1} \left\{ dt \int_0^{t_{n-1}} f(\tau) \ d\tau + \int_{t_{n-1}}^{t_n} [t_n - \tau] f(\tau) d\tau \right\}
\end{aligned}
\tag{14.25}
$$

This last relation is interesting since it indicates that the rigid body part of the response can be computed by time stepping and does not need a lengthy convolution. Let us observe that the second term in (14.25) can be given a clear physical interpretation by noting that $\mathcal{M}^{-1} \int_0^{t_{n-1}} f(\tau) \ d\tau$, basically the accumulated impulses divided by the inertia, corresponds to the overall velocity at time t_{n-1}. So the second term expresses the increase of displacement during the time increment dt due to that velocity. The third term is related to the additional acceleration produced by the force applied between t_{n-1} and t_n.

The discretization of (14.25) can be performed using the same finite difference approach as done earlier for the convolution product. For that let us restart from the definition (14.24) of the rigid response and discretize it in time following the trapezoidal rule also used in (14.2):

---

[5] Let us note that since the impulse response for a linear dynamic system can be seen as the superposition of its impulse modal responses, an equivalent way to compute the vibrational part of the IRF is to project the IRF M-orthogonal to the rigid body modes, namely

$$H^{vib} = (I - R M_{tot}^{-1} R^T) H$$

and the rigid part is

$$H^{rig} = R \ M_{tot}^{-1} \ R^T \ H$$

$$u_n^{rig} = \int_0^{t_n} \mathcal{M}^{-1} [t_n - \tau] f(\tau) \tau$$

$$\simeq \mathcal{M}^{-1} \sum_{i=0}^{n-1} \left\{ [(n\, dt - \tau) f(\tau)]_{\tau=i\, dt} + [(n\, dt - \tau) f(\tau)]_{\tau=(i+1)dt} \right\} \frac{dt}{2} \tag{14.26}$$

$$\simeq \mathcal{M}^{-1} \sum_{i=0}^{n-1} \left\{ (n-i) f_i + (n-i-1) f_{i+1} \right\} \frac{dt^2}{2}$$

Following now the same steps as from (14.24) to (14.25), but now in the time-discrete case,

$$u_n^{rig} \simeq \mathcal{M}^{-1} \sum_{i=0}^{n-1} \left\{ (n-i) f_i + (n-i-1) f_{i+1} \right\} \frac{dt^2}{2}$$

$$\simeq \mathcal{M}^{-1} \sum_{i=0}^{n-2} \left\{ (n-i) f_i + (n-i-1) f_{i+1} \right\} \frac{dt^2}{2} + \mathcal{M}^{-1} f_{n-1} \frac{dt^2}{2}$$

$$\simeq \mathcal{M}^{-1} \sum_{i=0}^{n-2} \left\{ ((n-1)-i) f_i + ((n-1)-i-1) f_{i+1} \right\} \frac{dt^2}{2} + \mathcal{M}^{-1} \sum_{i=0}^{n-2} \left\{ f_i + f_{i+1} \right\} \frac{dt^2}{2} + \mathcal{M}^{-1} f_{n-1} \frac{dt^2}{2} \tag{14.27}$$

$$\simeq u_{n-1}^{rig} + \mathcal{M}^{-1} \sum_{i=0}^{n-2} \left\{ f_i + f_{i+1} \right\} \frac{dt^2}{2} + \mathcal{M}^{-1} f_{n-1} \frac{dt^2}{2}$$

which reveals the time-discrete form of (14.25). Finally we can summarize the discretized and truncated IRFs for floating domains by substituting in (14.22) the discretization (14.27) for the rigid part and considering the truncation (14.11) for the vibrational term:

$$\mathcal{I}_0 = f_0 \frac{dt}{2} \tag{14.28}$$

$$\mathcal{I}_n = \mathcal{I}_{n-1} + f_{n-1}\, dt \tag{14.29}$$

$$u_n^{rig} = u_{n-1}^{rig} + \mathcal{M}^{-1} \mathcal{I}_n\, dt \tag{14.30}$$

$$u_n \simeq u_n^{rig} + \sum_{i=max\{0,n-c\}}^{n-1} \left(\bar{H}_{n-i}^{vib} f_i + \bar{H}_{n-i-1}^{vib} f_{i+1} \right) dt/2 \tag{14.31}$$

where the effect of the applied forces is accumulated in the total impulse $\mathcal{I}_n$ and where $\bar{H}^{vib}$ denotes the vibrational part of the IRFs possibly weighted by, for instance, the cosine window described in the previous section. In the context of the IBS, the truncation of the convolution product for floating subdomains can be introduced in the dually assembled form (14.5).

14.5   A Simple Example

In this contribution we consider the same example as the one treated in [3]. We consider the bar structure described in Fig. 14.3 excited by a load at its end. The structure is divided in two substructures of equal length, each substructure being modeled by 25 bar finite elements (the consistent mass matrices are used here). The bar is made of steel ($E = 2.\,1\,10^{11}$ Pa, $\rho = 7500$ kg/m^3), has a uniform cross-section of $A = 3.14\,10^{-4}\,m^2$ and each substructure has a length of $L = 0.\,5\,m$. In the model damping has been introduced by constructing $C = 1\,10^{-6} K$.
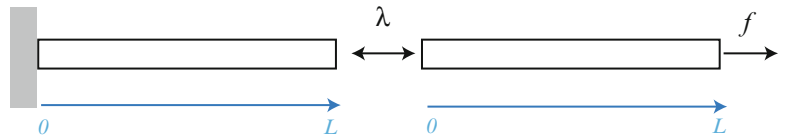
Fig. 14.3 Example of a beam with two substructures
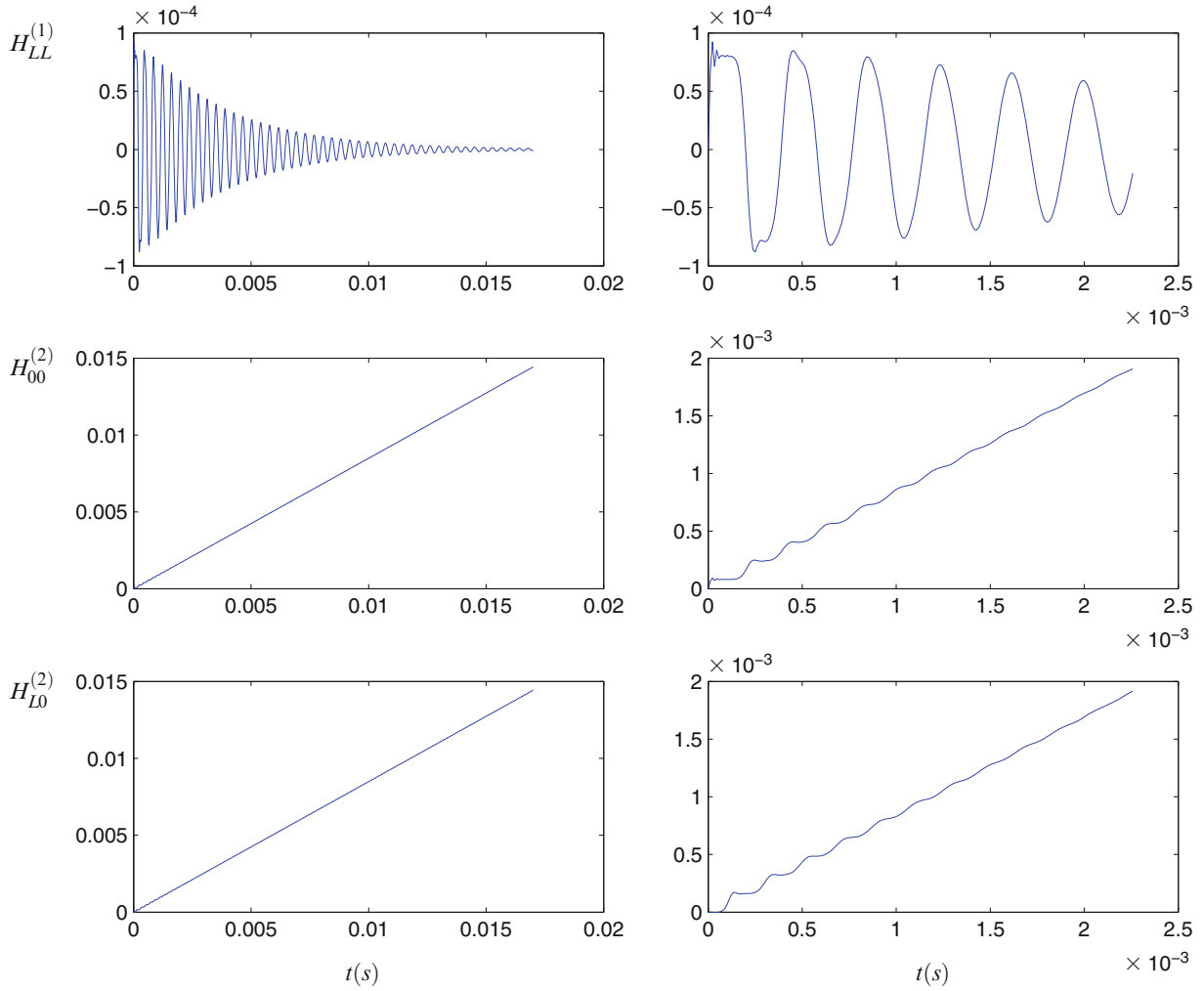
Fig. 14.4 IRFs for the bar substructures (zoomed on the *right*)

Assuming the dofs of the substructures are numbered from left to right, the Boolean constraining matrices are

$$B^{(1)} = \begin{bmatrix} 0 \cdots 0 - 1 \end{bmatrix}$$
$$B^{(2)} = \begin{bmatrix} 1 \cdots 0\ 0 \end{bmatrix}$$

The impulse responses are computed using a Newmark scheme $\gamma = 1/2, \beta = 1/4$ for a unit force applied at time $t = 0$ at the interface degrees of freedom and at the end of the second substructure (this will be the input of the force in our example). The time-step is chosen equal to $3dt_{crit}$ where dt_{crit} is the critical time step, namely the stability limit if the integration scheme would be explicit. The obtained IRFs are plotted in Fig. 14.4 for inputs on the interface and on the end of the bar. On the right of that figure the IRFs are zoomed. The IRFs for this problem are shown in Fig. 14.4. It can be clearly seen that the IRFs for the right substructure converge to a monotonically increasing line, illustrating the drift of the displacement for a floating substructure. In this case the rigid body mode of the second substructures is simply an array with all ones as entries and the total mass matrix $\boldsymbol{M}_total$ is equal to the total translation mass of the second substructure.

Now, using the IBS approach described by (14.7), we compute the response of the assembled bar to a step load of unit amplitude applied at the right end (see [3] for a detailed outline of the algorithm for this example). The threshold ε for the truncation (see Sect. 14.3.1, Figs. 14.1 and 14.2) was chosen successively to be 10^{-1}, 10^{-2} and 10^{-3}.

In Fig. 14.5 we report the dynamic response obtained at the interface of the bar, under a unit step load applied at the end of the bar, when applying the IBS approach with and without truncation. Here a simple rectangular window is applied (as illustrated in Fig. 14.1). When the threshold ε is chosen to high (in this case $\varepsilon = 10^{-1}$) the truncation introduces too many

$\varepsilon = 10^{-1}$

Rectangular window

$\varepsilon = 10^{-2}$

$\varepsilon = 10^{-3}$
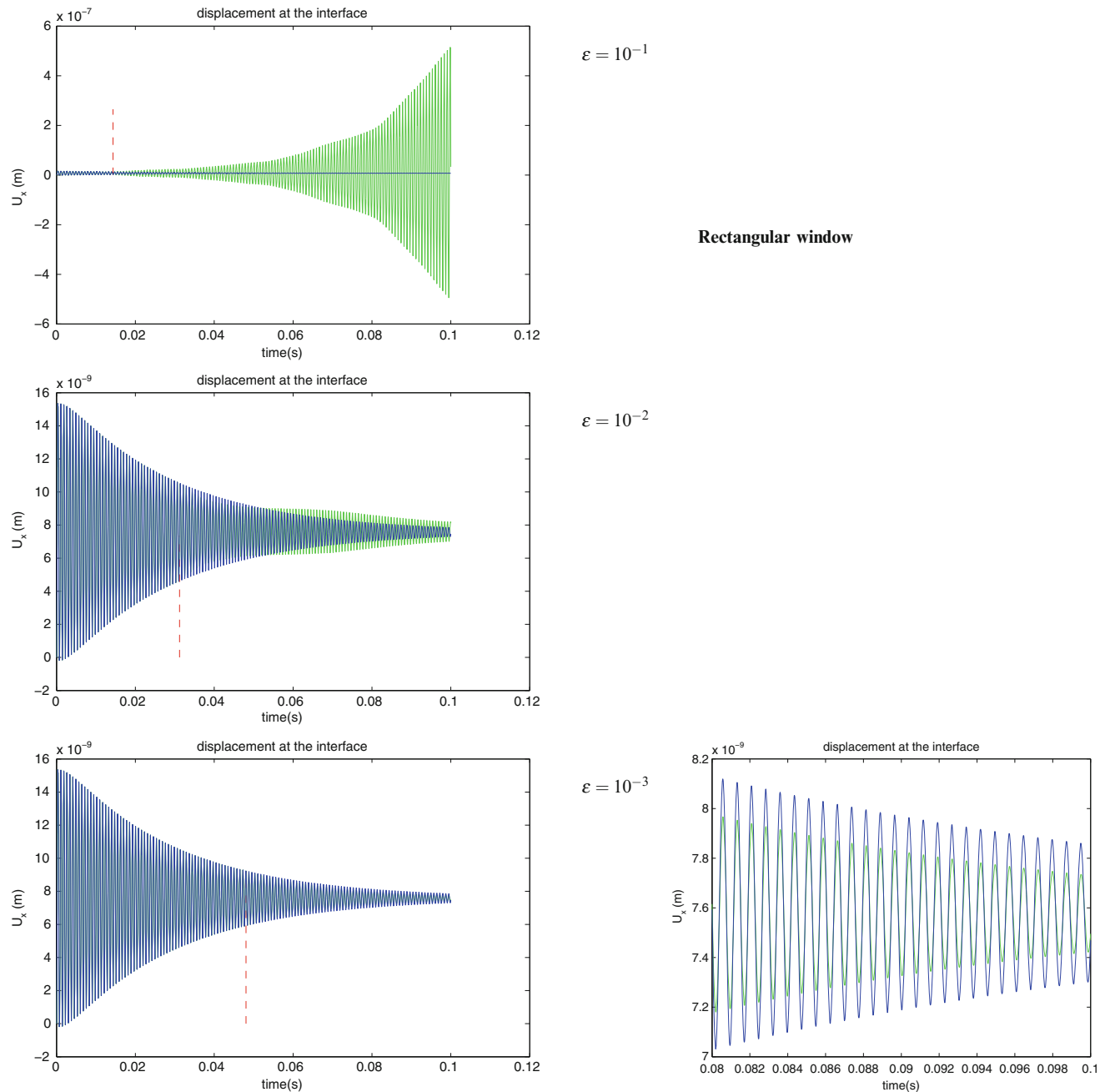
Fig. 14.5 Interface displacement of the full bar to a unit step, computed by IBS, with (*green*) and without (*blue*) truncation: rectangular window. The *red line* indicates the cutoff time for the truncation

residual impulses leading to an unstable response in the IBS. For $\varepsilon = 10^{-2}$ the solution is stable, but clearly the truncation significantly affects the accuracy of the solution. For $\varepsilon = 10^{-3}$, the solution computed by the truncated IBS is rather accurate, although zooming in the curves (right side of Fig. 14.5) it is clear that a noticeable error has been introduced by the truncation. Note that for this last case, namely $\varepsilon = 10^{-3}$, the cutoff time is $t_c = 0.048$, resulting in only a small computational saving in our computation where the simulation is run until $t_{final} = 0.1$.

Applying now a cosine window, we obtain the results reported in Fig. 14.6. It is very interesting to observe that with the cosine window the IBS method results in a stable and rather accurate dynamic response, even for $\varepsilon = 10^{-1}$. This threshold corresponds to a cutoff time $t_c = 0.014$ and the truncation yields a significant reduction of computational effort in computing the convolution product. Finally we observe that when the threshold is further reduced (to 10^{-2} and 10^{-3}) the results of the truncated IBS is nearly identical to the results without truncation. Nevertheless the cutoff time is higher and thus more computational effort is required.
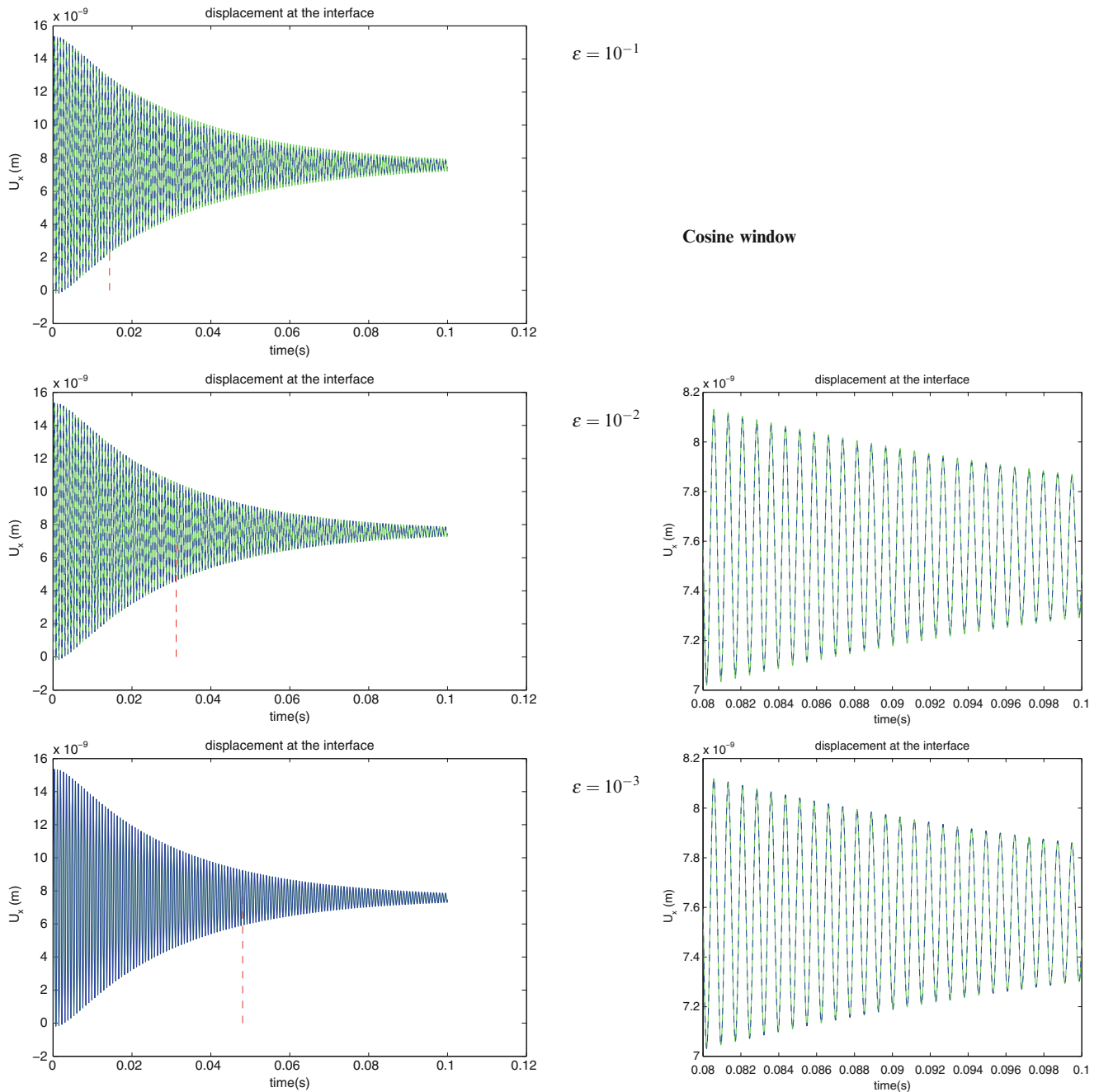
Fig. 14.6 Interface displacement of the full bar to a unit step, computed by IBS, with (*green*) and without (*blue*) truncation: cosine window. The *red* line indicates the cutoff time for the truncation (color figure online)

14.6 Conclusion

In this contribution we have shown how to apply truncation and windowing on the Impulse Response Functions (IRF) of substructures, so that one can significantly reduce the computational burden related to the convolution product in the Impulse Based Substructuring (IBS) method.

Special care must be taken when truncating the IRFs of floating substructure: the overall rigid body motion can not be truncated since it does not decay to zero. We have indicated how the truncation can be applied only to the vibrational part of the IRF in that case.

We have described a cosine window in order to force the IRF smoothly to zero at the cutoff time, without introducing significant damping in the system. The results on a simple bar example decomposed in two substructures have indicated that the truncated IBS with the cosine window can produce accurate results while significantly reducing the necessary number of operations in the computation of the convolution product.

Future work will concentrate on investigating other time windows and on applying windowing directly on the IRF expressed for the velocities or the accelerations. Also more detailed analysis must be performed to investigate the stability conditions for the truncated IBS. Currently, the truncated IBS is being applied to a three-dimensional engineering structure in order to estimate the gain in computational time when applying an appropriate truncation.

References

1. Klerk DD, Rixen DJ, Voormeeren SN (2008) General framework for dynamic substructuring: history, review and classification of techniques. AIAA J 46(5):1169–1181
2. Rixen DJ (2010) Substructuring technique based on measured and computed impulse response functions of components. In: Sas P, Bergen B (eds) ISMA, KU Leuven
3. Rixen DJ (2010) Substructuring using impulse response functions for impact analysis. In: IMAC-XXVIII: international modal analysis conference, Jacksonville, Society for experimental mechanics, Bethel

Chapter 15
Application of Residual Vectors to Superelement Modeling of an Offshore Wind Turbine Foundation

B.P. Nortier, S.N. Voormeeren, and D.J. Rixen

Abstract Traditionally, wind turbine dynamics are analyzed using aero-elastic codes based on geometrically simplified models. As hundreds of simulations are required per wind farm for verification purposes, such coarse models allow reasonable computation while still capturing the overall dynamic behavior. With offshore turbines being installed in deeper waters, the industry nowadays moves gradually towards more complex foundation structures such as jackets and tripods. Even the simplest models of such structures have many more DoF than the complete wind turbine model, leading to excessive computation times. To cope with this, reduced "superelement" modeling of the foundation structure can be employed. However, since these structures are subjected to wave loading at a large portion of their DoF, traditional reduction methods such as Craig-Bampton fail to properly describe the component's response due to this excitation. Hence in this work we propose to use the concept of modal truncation augmentation, which consists in extending the reduction basis by adding "residual vectors". Furthermore we use principal component analysis to find the predominant wave loading on the foundation structure. Through application on a realistic model of a wind turbine and complex offshore foundation, it will be shown that this approach gives a very compact yet accurate model of the combined structure.

15.1 Introduction

15.1.1 Offshore Wind Energy

At present there are few topics as heavily debated as "sustainability". On a daily basis the media are full of items on climate change, oil prices, CO_2 reductions, rising energy consumptions and so on. Regardless of one's opinion on the subject, a fact is that more sustainable ways of power generation need to be found simply because the currently used resources will some day be exhausted.

One of the more promising ways of generating "green" electricity on a large scale is provided by wind energy. As a result, the wind turbine industry has undergone a huge transition: from a small group of mainly Danish enthusiasts in the early 1980s, the modern wind power industry now has grown to a global multi billion dollar industry.

However, wind energy has not been without debate. Opponents point at the intermittency and variability of wind generated electricity, furthermore noise and "landscape pollution" are often heard complaints. In an attempt to mitigate these negative effects, developers have turned to a new place to install wind turbines: the sea. Offshore, average wind speeds are higher and acoustic and visual nuisance is hardly relevant. In Northern Europe, many offshore wind farms have been installed over the last years and many more are currently planned or under construction. In fact, few high wind/shallow water sites are still available. As a result, there is a trend towards deeper water with even higher average wind speeds.

B.P. Nortier • S.N. Voormeeren (✉) • D.J. Rixen
Section Engineering Dynamics, Delft University of Technology, Mekelweg 2, 2628CD Delft, The Netherlands
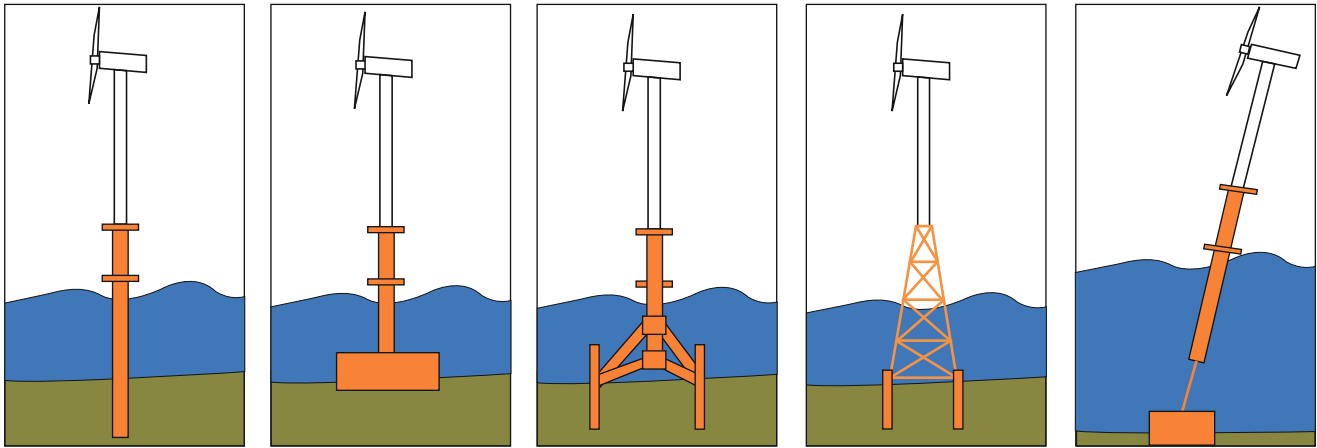e-mail: s.n.voormeeren@tudelft.nl

Fig. 15.1 Different foundation types for increasing water depths

All in all, it is clear that wind turbine manufacturers are faced with many challenges in order to make their wind turbines operate efficiently and reliably in these harsh conditions. One of these challenges concerns the correct modeling and analysis of the structural dynamic behavior of the wind turbine.

15.1.2 Offshore Wind Turbine Dynamic Analysis

Since the environmental conditions (water depth, soil properties) and ambient excitations (wind, wave and current loading) can vary greatly across different offshore sites, every offshore wind farm is custom engineered. This means that a standard rotor-nacelle assembly (RNA) is combined with a specifically designed tower and offshore foundation. An important part of the engineering process is to perform dynamic simulations to assess whether the design can withstand the loads during its specified lifetime. For certification purposes, several hundreds or even thousands of load cases need to be evaluated.

To efficiently perform these dynamic simulations, wind turbine manufacturers, research institutes and universities have developed many different aero-elastic codes [13]. These advanced codes are designed to analyze the global dynamics of a wind turbine, taking into account aerodynamic loads and coupling, and wave loads. Given the number of load cases that need to be run, these models must be as coarse as possible to keep the computation times at an acceptable level. Such aero-elastic models typically consist of 300–400 degrees of freedom (DoF).

For offshore wind turbines, by far the most popular type of foundation is the monopile due to its simplicity and robustness. When installing wind turbines in deeper water, however, such monopiles become less attractive as a disproportional amount of material is needed for it to withstand the more severe loading. More complex types of foundations then become economical, with the jacket structures as the most interesting option. See Fig. 15.1.

However, a jacket type of foundation is considerably more complex then a monopile and so is its dynamic behavior. Consequently, a more detailed dynamic model is needed to predict these dynamics. Where a monopile can typically be represented with a few beam elements leading to a model of approximately 50 DoF, a jacket structural model easily consists of more than 1,000 DoF. Needless to say, this negatively impacts the computation times of the dynamic simulations. Simplifying the jacket dynamics cannot be done in general since coupling can occur between vibrations in the jacket and RNA.

In this work we therefore propose to use a reduced component model (or *superelement*) to represent the jacket structure. However, since these structures are subjected to wave loading at a large portion of their DoF, traditional reduction methods such as Craig-Bampton fail to properly describe the components response due to this excitation. Hence in this work we propose to use the concept of modal truncation augmentation, which consists in extending the reduction basis by adding "residual vectors" which are dependent on the external loading.

15.1.3 Paper Outline

This paper is organized as follows. In the next Section, the classic component model reduction technique of Craig-Bampton is explained. Thereafter, Sect. 15.3 addresses the theory of modal truncation augmentation, which can be used to augment the Craig-Bampton reduction basis in order to improve the accuracy of the forced response predictions of the reduced model.

Sect. 15.4 then outlines the proper orthogonal decomposition (POD) method, which can be used to extract the dominant wave loading on the foundation structure. The use of the methods is illustrated through application to a reference structure in Sect. 15.5. Finally, some conclusions and recommendations are given in Sect. 15.6.

15.2 Component Model Reduction: Craig-Bampton Method

In structural dynamic analysis a technique that is often applied to analyze large or complex systems is dynamic substructuring (DS). This methodology combines the ideas of a componentwise "divide and conquer" approach and model reduction techniques as follows:

1. The complete system is decomposed into components or substructure.
2. Each component is modeled and reduced separately, using a suitable reduction basis. This basis usually consists of a set of static modes describing the interaction with neighboring components, and some vibration modes to account for the dynamics.
3. The reduced component models are assembled to form the model of the complete system.

This approach is often also called *component mode synthesis* (CMS) and was first introduced in the 1960s [8, 7]. One very popular CMS method often used today is the Craig-Bampton method [3]. This is the method considered in this work and will be explained hereafter.

As a starting point we take the equations of motion of a discretized dynamic component model *s*:

$$\boldsymbol{M}^{(s)}\ddot{\boldsymbol{u}}^{(s)}(t) + \boldsymbol{C}^{(s)}\dot{\boldsymbol{u}}^{(s)}(t) + \boldsymbol{K}^{(s)}\boldsymbol{u}^{(s)}(t) = \boldsymbol{f}^{(s)}(t) + \boldsymbol{g}^{(s)}(t) \tag{15.1}$$

Here $\boldsymbol{M}^{(s)}$, $\boldsymbol{C}^{(s)}$ and $\boldsymbol{K}^{(s)}$ are the components mass, damping and stiffness matrix, respectively. Vector $\boldsymbol{u}^{(s)}(t)$ denotes the degrees of freedom, and $\dot{\boldsymbol{u}}^{(s)}(t)$ and $\ddot{\boldsymbol{u}}^{(s)}(t)$ its respective time derivatives, $\boldsymbol{f}^{(s)}(t)$ the external force vector and $\boldsymbol{g}^{(s)}(t)$ the vector of the connection forces with other component models. To simplify the expressions we will drop the explicit time dependency and the component model notation in subsequent equations. Furthermore, damping will not be considered here, but it can be included in the developments.

To allow assembly with other component models we partition the DoF vector $\boldsymbol{u}$ into a part belonging the interface (boundary) DoF, denoted by $\boldsymbol{u}_b$, and the internal DoF, denoted by $\boldsymbol{u}_i$. This gives the partitioned equations of motion of a component model as:

$$\begin{bmatrix} \boldsymbol{M}_{bb} & \boldsymbol{M}_{bi} \\ \boldsymbol{M}_{ib} & \boldsymbol{M}_{ii} \end{bmatrix} \begin{bmatrix} \ddot{\boldsymbol{u}}_b \\ \ddot{\boldsymbol{u}}_i \end{bmatrix} + \begin{bmatrix} \boldsymbol{K}_{bb} & \boldsymbol{K}_{bi} \\ \boldsymbol{K}_{ib} & \boldsymbol{K}_{ii} \end{bmatrix} \begin{bmatrix} \boldsymbol{u}_b \\ \boldsymbol{u}_i \end{bmatrix} = \begin{bmatrix} \boldsymbol{f}_b \\ \boldsymbol{f}_i \end{bmatrix} + \begin{bmatrix} \boldsymbol{g}_b \\ 0 \end{bmatrix} \tag{15.2}$$

The Craig-Bampton method now consists in retaining the boundary and finding a good approximation for the internal DoF. This is done by splitting the response of the internal DoF into a static and a dynamic part:

$$\boldsymbol{u}_i = \boldsymbol{u}_{i,stat} + \boldsymbol{u}_{i,dyn} \tag{15.3}$$

The static response $\boldsymbol{u}_{i,\,stat}$ is obtained from the second line of (15.2) by setting the force on internal DoF to zero (i.e. $\boldsymbol{f}_i = \boldsymbol{0}$) and neglecting the inertia forces by taking $\ddot{\boldsymbol{u}}_i$ and $\ddot{\boldsymbol{u}}_b$ to zero, by doing so we obtain:

$$\boldsymbol{u}_{i,stat} = -\boldsymbol{K}_{ii}^{-1}\boldsymbol{K}_{ib}\boldsymbol{u}_b = \boldsymbol{\Psi}_{C,i}\boldsymbol{u}_b \tag{15.4}$$

Here $\boldsymbol{\Psi}_{C,i}$ are the so-called static constraint modes. Each column of $\boldsymbol{\Psi}_{C,i}$ represents the static response of $\boldsymbol{u}_i$ to a unit displacement of an interface DoF, while the other interface DoF are constrained. The number of static modes thus equals the number of boundary DoF. For components with large or refined interfaces this could be a limiting factor for the reduction process. To overcome this issue interface reduction techniques can be used which approximate the interface dynamic behavior, thereby reducing the number of interface DoF. See for instance [4, 2, 21, 17, 18].

The dynamic response $\boldsymbol{u}_{i,dyn}$ is also obtained from the second line of (15.2), where again we set the force acting on the internal DoF to zero and restrain the interface DoF. The dynamic response can then be approximated using a superposition of a truncated number of vibration modes:

$$\boldsymbol{u}_{i,dyn} \approx \boldsymbol{\Phi}_i\boldsymbol{\eta}_i \tag{15.5}$$

Where matrix $\boldsymbol{\Phi}_i$ contains a truncated collection of so-called fixed interface vibration modes, obtained from the eigenproblem (15.6), and η_i is a vector which contains the corresponding modal amplitudes.

$$\left(\boldsymbol{K}_{ii} - \omega_{i,n}^2 \boldsymbol{M}_{ii}\right)\boldsymbol{\Phi}_{i,n} = 0 \tag{15.6}$$

Here $\boldsymbol{\Phi}_{i,\,n}$ represents a single fixed interface vibration mode with unit modal mass and $\omega_{i,n}^2$ its corresponding eigenfrequency. Combining (15.4) and (15.5) an approximation for the response of the internal DoF is obtained:

$$\boldsymbol{u}_i \approx \boldsymbol{\Psi}_{C,i}\boldsymbol{u}_b + \boldsymbol{\Phi}_i\boldsymbol{\eta}_i \tag{15.7}$$

Since for obtaining $\boldsymbol{u}_{i,stat}$ and $\boldsymbol{u}_{i,dyn}$ the force external on the internal DoF was set to zero the approximation in (15.7) does not take this force into account. The accuracy of the response is dependent on how well the static constraint and fixed interface vibration modes represent the response to this force. The reduction matrix of the Craig-Bampton method is now found as:

$$\begin{bmatrix} \boldsymbol{u}_b \\ \boldsymbol{u}_i \end{bmatrix} \approx \begin{bmatrix} \boldsymbol{I} & \boldsymbol{0} \\ \boldsymbol{\Psi}_{C,i} & \Phi_i \end{bmatrix} \begin{bmatrix} \boldsymbol{u}_b \\ \boldsymbol{\eta}_i \end{bmatrix} = \boldsymbol{R}_{CB} \begin{bmatrix} \boldsymbol{u}_b \\ \boldsymbol{\eta}_i \end{bmatrix} \tag{15.8}$$

Using the reduction matrix $\boldsymbol{R}_{CB}$ the equations of motion in (15.2) can be reduced to obtain:

$$\tilde{\boldsymbol{M}} = \boldsymbol{R}_{CB}^T\boldsymbol{M}\boldsymbol{R}_{CB} \tag{15.9}$$

$$\tilde{\boldsymbol{K}} = \boldsymbol{R}_{CB}^T\boldsymbol{K}\boldsymbol{R}_{CB}$$

Where $\tilde{\boldsymbol{M}}$ and $\tilde{\boldsymbol{K}}$ have the following form

$$\begin{aligned} \tilde{\boldsymbol{K}} &= \begin{bmatrix} \tilde{\boldsymbol{K}}_{bb} & \boldsymbol{0} \\ \boldsymbol{0} & \boldsymbol{\Omega}_i^2 \end{bmatrix} \\ \tilde{\boldsymbol{K}}_{bb} &= \boldsymbol{K}_{bb} - \boldsymbol{K}_{bi}\boldsymbol{K}_{ii}^{-1}\boldsymbol{K}_{ib} \\ \tilde{\boldsymbol{M}} &= \begin{bmatrix} \tilde{\boldsymbol{M}}_{bb} & \tilde{\boldsymbol{M}}_{b\phi} \\ \tilde{\boldsymbol{M}}_{\phi b} & \boldsymbol{I} \end{bmatrix} \\ \tilde{\boldsymbol{M}}_{bb} &= \boldsymbol{M}_{bb} - \boldsymbol{M}_{bi}\boldsymbol{K}_{ii}^{-1}\boldsymbol{K}_{ib} - \boldsymbol{K}_{bi}\boldsymbol{K}_{ii}^{-1}\boldsymbol{M}_{ib} + \boldsymbol{K}_{bi}\boldsymbol{K}_{ii}^{-1}\boldsymbol{M}_{ii}\boldsymbol{K}_{ii}^{-1}\boldsymbol{K}_{ib} \\ \tilde{\boldsymbol{M}}_{\phi b} &= \boldsymbol{\Phi}_i^T\left(\boldsymbol{M}_{ib} - \boldsymbol{M}_{ii}\boldsymbol{K}_{ii}^{-1}\boldsymbol{K}_{ib}\right) = \tilde{\boldsymbol{M}}_{b\Phi}^T \end{aligned} \tag{15.10}$$

In (15.10) $\boldsymbol{\Omega}_i^2$ is a diagonal matrix containing the fixed interface eigenfrequencies. One of the advantages of the CB reduction is that all the interface DoF are retained, thereby allowing for easy assembly with other component models.

15.3 Modal Truncation Augmentation

As discussed in the previous section, the external force acting on the internal DoF is not considered in the Craig-Bampton method. The fixed interface vibration modes used for the reduction are usually selected based on their eigenfrequency in order to cover the frequency content of the external excitation, which leads to spectral convergence. However, spatial convergence is rarely considered which can lead to an inadequate representation of the response.

To improve this spatial convergence the CB reduction basis can be augmented by a set of correction vectors (also called residual or load dependent vectors). For this the *modal truncation augmentation* (MTA) method is used which can be seen as a generalization of the *mode acceleration* (MA) method [14]. The MTA method was introduced in [5, 15] where it was shown that it can greatly improve the dynamic response by including correction vectors in the reduction basis.

In this section we will derive the MTA method for a Craig-Bampton reduced component. As a starting point we take the second line of (15.2):

$$\boldsymbol{M}_{ii}\ddot{\boldsymbol{u}}_i + \boldsymbol{K}_{ii}\boldsymbol{u}_i = -\boldsymbol{M}_{ib}\ddot{\boldsymbol{u}}_b - \boldsymbol{K}_{ib}\boldsymbol{u}_b + \boldsymbol{f}_i \tag{15.11}$$

Where we note that the external force on the internal DoF is kept in the expression. As is done for the Craig-Bampton method a solution is sought for the internal DoF $u\}_i$ by splitting the response into a static and dynamic part, see (15.3). The static response of the internal DoF is again obtained by substituting (15.3) into (15.11) and neglecting the inertia forces:

$$u_{i,stat} = \Psi_{C,i}u_b + K_{ii}^{-1}f_i \tag{15.12}$$

It is observed that $u_{i,stat}$ now is not only described by the static constraint modes but also includes the response to external loading. By substituting (15.3) and (15.12) into (15.11) and rewriting for the dynamic solution $u_{i,dyn}$ the following can be obtained:

$$\begin{aligned} M_{ii}\ddot{u}_{i,dyn} + K_{ii}u_{i,dyn} &= \left(-M_{ii}\Psi_{C,i} - M_{ib}\right)\ddot{u}_b - M_{ii}K_{ii}^{-1}\ddot{f}_i \\ &= Y\ddot{u}_b - M_{ii}K_{ii}^{-1}\ddot{f}_i \end{aligned} \tag{15.13}$$

Here we have defined the matrix $Y = \left(-M_{ii}\Psi_{C,i} - M_{ib}\right)$, where its columns can be seen as load vectors associated to the interface. We now split $u_{i,dyn}$ into a quasi-static solution $y_{i,stat}$ and a relative dynamic solution $y_{i,dyn}$. The quasi-static part $y_{i,stat}$ is obtained by setting $\ddot{u}_{i,dyn} = 0$ in (15.13).

$$y_{i,stat} = K_{ii}^{-1}Y\ddot{u}_b - K_{ii}^{-1}M_{ii}K_{ii}^{-1}\ddot{f}_i \tag{15.14}$$

In (15.14) the $K_{ii}^{-1}Y$ term can be interpreted as the static response of the internal DoF associated to internal inertia loads due to unit accelerations of the interface DoF. The separation of $u_{i,dyn}$ together with the definition of $y_{i,stat}$, given in (15.14), can be substituted into (15.13). If this is rewritten for the dynamic solution, now $y_{i,dyn}$, the following is obtained:

$$M_{ii}\ddot{y}_{i,dyn} + K_{ii}y_{i,dyn} = K_{ii}^{-1}M_{ii}K_{ii}^{-1}Y\frac{d^4u_b}{dt^4} + \left(M_{ii}K_{ii}^{-1}\right)^2\frac{d^4f_i}{dt^4} \tag{15.15}$$

By repeating this process the response of u_i is represented as a sequence of (high order) correction modes:

$$u_i = u_{i,stat} + y_{i,stat} + z_{i,stat} + \ldots + w_{i,dyn} \tag{15.16}$$

By substituting the obtained results for the (quasi-)static and dynamic response the following is obtained:

$$\begin{aligned} u_i = &\Psi_{C,i}u_b + K_{ii}^{-1}Y\ddot{u}_b - K_{ii}^{-1}M_{ii}K_{ii}^{-1}Y\frac{d^4u_b}{dt^4} + \ldots \\ &+ K_{ii}^{-1}f_i - K_{ii}^{-1}M_{ii}K_{ii}^{-1}\ddot{f}_i + \left(K_{ii}^{-1}M_{ii}\right)^2K_{ii}^{-1}\frac{d^4f_i}{dt^4} + \ldots \end{aligned} \tag{15.17}$$

The first term on the right hand in (15.17) are the static constraint modes which are already present in the Craig-Bampton reduction basis. The last term is the dynamic solution $w_{i,dyn}$ which is approximated by a superposition of the fixed-interface vibration modes, i.e. $w_{i,dyn} \approx \Phi_i\eta_i$. The remaining terms of the expression can be separated into a group involving the external force acting on the internal DoF (the terms containing f_i) and a second involving the interface excitation (the term containing u_b). These terms are the so-called MTA vectors which will be discussed in further detail below.

First we define a representation of the external force acting on the internal DoF. In general this can be represented by a superposition of g spatial (time-independent) force vectors which are modulated by their time dependent amplitudes:

$$f_i = \sum_{p=1}^{g} f_{i,p}\alpha_p(t) \tag{15.18}$$

Where $f_{i,p}$ is the pth spatial force vector and $\alpha_p(t)$ its corresponding (time dependent) amplitude. The spatial force vectors can represent different types of forces such as point forces, gravity and wind or wave loads. Here we assume that the external force can be represented by a number of these spatial force vectors, contained in the matrix F_i. In the next section it will be

shown that these spatial force vectors can be obtained from time varying load data using the *proper orthogonal decomposition* (POD) method.

The correction terms in (15.17) can be written as the MTA vectors, where we assume unitary interface displacements (and its time derivatives), from this we obtain:

$$\bar{\Phi}_{MTA} = \begin{bmatrix} \bar{\Phi}_{MTA,0} \dots \bar{\Phi}_{MTA,j} \dots \bar{\Phi}_{MTA,m-1} \end{bmatrix} \tag{15.19}$$

Where $\bar{\Phi}_{MTA}$ is a collection of the MTA vectors of different orders, given by j. Each order of MTA vector(s) is computed by:

$$\bar{\Phi}_{MTA,j} = \boldsymbol{P} \big(\boldsymbol{K}_{ii}^{-1} \boldsymbol{M}_{ii} \big)^j \boldsymbol{K}_{ii}^{-1} \begin{bmatrix} \boldsymbol{YF}_i \end{bmatrix} \qquad j = 0, \dots, m \tag{15.20}$$

Here we have applied a projection matrix, defined as $\boldsymbol{P} = \boldsymbol{I} - \boldsymbol{\Phi}_i \boldsymbol{\Phi}_i^T \boldsymbol{M}_{ii}$, which orthogonalizes the MTA vectors to the fixed interface vibration modes since they both capture a part of the dynamic response. This could lead to linear dependency in the columns of the reduction matrix which can cause numerical problems. In [16] it was shown that the MTA vectors can be efficiently computed by post-processing the Lanczos iterations created by the computation of the fixed interface vibrations modes. For this the starting vectors for the algorithm have to be chosen as the columns of $K_{ii}^{-1} \begin{bmatrix} Y \ F_i \end{bmatrix}$. To further improve the numerical robustness the columns of $\bar{\Phi}_{MTA}$ are mutually orthogonalized by solving an eigenvalue problem defined as:

$$\big(\bar{\Phi}_{MTA}^T \boldsymbol{K}_{ii} \bar{\Phi}_{MTA} \big) \boldsymbol{y} = \boldsymbol{\mu}^2 \big(\bar{\Phi}_{MTA}^T \boldsymbol{M}_{ii} \bar{\Phi}_{MTA} \big) \boldsymbol{y} \tag{15.21}$$

Where μ^2 is a diagonal matrix containing the "pseudo-frequencies" corresponding to the MTAs. These frequencies are always higher than those of the fixed interface vibration modes and provide an indication for what frequency range a dynamic correction is supplied. The orthonormalized MTAs are computed by

$$\Phi_{MTA} = \bar{\Phi}_{MTA} y \tag{15.22}$$

Where the properties of the MTA vectors are:

$$\begin{aligned} \boldsymbol{\Phi}_{MTA}^T \boldsymbol{M}_{ii} \boldsymbol{\Phi}_{MTA} &= \boldsymbol{I} \\ \boldsymbol{\Phi}_{MTA}^T \boldsymbol{K}_{ii} \boldsymbol{\Phi}_{MTA} &= \boldsymbol{\mu}^2 \end{aligned} \tag{15.23}$$

Including the MTA vectors, the solution of the internal DoF using the Craig-Bampton method can now be represented by

$$\boldsymbol{u}_i \approx \boldsymbol{\Psi}_{C,i} \boldsymbol{u}_b + \boldsymbol{\Phi}_i \boldsymbol{\eta}_i + \boldsymbol{\Phi}_{MTA} \boldsymbol{\zeta} \tag{15.24}$$

Where ζ are the modal amplitudes of the MTAs. The augmented Craig-Bampton reduction basis can thus be written as:

$$\begin{bmatrix} \boldsymbol{u}_b \\ \boldsymbol{u}_i \end{bmatrix} \approx \begin{bmatrix} \boldsymbol{I} & \boldsymbol{0} & \boldsymbol{0} \\ \boldsymbol{\Psi}_{C,i} & \boldsymbol{\Phi}_i & \boldsymbol{\Phi}_{MTA} \end{bmatrix} \begin{bmatrix} \boldsymbol{u}_b \\ \boldsymbol{\eta}_i \\ \boldsymbol{\zeta} \end{bmatrix} = \boldsymbol{R}_{ACB} \begin{bmatrix} \boldsymbol{u}_b \\ \boldsymbol{\eta}_i \\ \boldsymbol{\zeta} \end{bmatrix} \tag{15.25}$$

Similar to the standard reduced Craig-Bampton model, all interface DoF are retained which allows assembly of the reduced component model as a superelement.

15.4 Proper Orthogonal Decomposition

The proper orthogonal decomposition (POD), also known as principle component analysis (PCA) or the Karhunen–Loève transform (KLT), is a mathematical data analysis method which is used to efficiently analyze complex data. The POD method is an orthogonal linear transformation that transforms the data dependent on n possibly correlated variables into a reduced or equal set of uncorrelated variables, called principal components. First a brief explanation of the theory will be given together with a physical interpretation of the components.

From a time varying data series a number of snapshots m can be obtained, these snapshots can for instance represent the response of a structure or the magnitude of the wave loads on the structure at a specific time. Each snapshot consists of a vector z_i containing n variables. All these snapshots can be collected into a matrix Z, which has dimensions $n \times m$.

$$Z = \begin{bmatrix} z_1 & \cdots & z_m \end{bmatrix} = \begin{bmatrix} z_{11} & \cdots & z_{m1} \\ \vdots & \ddots & \vdots \\ z_{1n} & \cdots & z_{mn} \end{bmatrix} \tag{15.26}$$

The snapshots can be chosen such that they have a zero mean $x_i = z_i - \mu_a$, where μ_a is the average of all the snapshots. The matrix containing the new snapshots x_i is called the *response matrix*, denoted as X. A singular value decomposition (SVD) can be performed on this matrix, such that:

$$X = U \Sigma V^T \tag{15.27}$$

The matrix U is a square $(n \times n)$ matrix of left singular vectors, Σ is a $(n \times m)$ matrix containing the singular values and V is a $(m \times m)$ matrix of right singular vectors. By dividing the left singular vectors by the number of snapshots the *proper orthogonal modes* (POMs) are obtained. By doing the same for the singular value contained in Σ the *proper orthogonal values* (POVs) are obtained.

The POVs represent the relative amount of the total energy is captured by their corresponding POMs. It can be shown that, due to its formulation, the POD is optimal in a least squares sense when considering the energy in the snapshots. This means that the POMs form a vector basis that captures more energy per mode than any other set of basis vectors [10, 11, 12]. Hence, often surprisingly few modes are needed to capture a large amount of the system's energy.

15.4.1 Obtaining Force Vectors Using POD

The POD method can be used to obtain spatial force vectors from time varying load data. This is done by taking as the response matrix the time varying load data, where the dimension m is thus given by time.

The obtained POMs now represent time-independent spatial force vectors which capture a part of the total energy present in the force data, this is given by the corresponding POV. As described in Sect. 15.3, MTA vectors can be computed based on these spatial force vectors. In Sect. 15.5 these force vectors will be used to compute MTA vectors and added to the reduction basis of an offshore wind turbine support structure.

15.4.2 Comparison Methods Based on POD

The dynamic response of a reduced system obtained from time integration can show phase shifts with respect to a reference solution. These phase shifts occur because the eigenfrequencies of the reduced model are an approximation of those of the unreduced system and can be different for various reduced models. As a result direct comparison of calculated time responses becomes troublesome.

In this work it is proposed to analyze the dynamic response using the POD method and to compare the POMs and POVs of the reduced system response to those of the unreduced system. The POMs can be treated similarly to eigenmodes and compared using the modal assurance criterion (MAC) [1]. The POVs can be treated as eigenfrequencies and compared by computing the relative error. However, to take into account that the relative energy captured by the POMs diminishes quickly, the relative error is scaled using the relative energy captured by the corresponding POM, so:

$$e_{\sigma,i} = \frac{\tilde{\sigma}_i - \sigma_i}{\sigma_i} \cdot \frac{\sigma_i}{\sum_{i=1}^{n} \sigma_i} \tag{15.28}$$

Here $e_{\sigma,i}$ is the error of the ith POV, which is computed using σ_i and $\tilde{\sigma}_i$ which are the corresponding POVs from the unreduced and reduced system, respectively.

15.5 Case Study

In this section the presented approach will be applied to a representative offshore wind turbine model to test its effectiveness. To this end, a numerical model of a 5 MW offshore wind turbine with a jacket support structure has been created, which will be described next. Thereafter, Sect. 15.5.2 describes the numerical experiments performed on this model, while results will be presented in Sect. 15.5.3.

15.5.1 System Description

The reference model consists of a 5 MW wind turbine on a jacket offshore support structure. For the turbine model the one created by the U.S. Department of Energy's National Renewable Energy Laboratory (NREL) was chosen. This baseline turbine, known as the "NREL 5 MW baseline wind turbine" is, as the name suggests, a 5 MW wind turbine. The turbine is a conventional horizontal axis, three bladed, upwind type and its specifications can be found in detail in [9].

For the support structure the jacket model is used that was initially created for the Offshore Code Comparison Collaboration Continuation (OC4) project. The details of this jacket structure can be found in [20]. Therein also some modifications are given for the NREL turbine model which are also taken into account in the subsequent model description.

Both the 5 MW baseline turbine and the OC4 jacket have been modeled, using Matlab and ANSYS/ASAS. Both models will be briefly described next.

15.5.1.1 NREL 5 MW Baseline Turbine

The NREL turbine consists of a standard tubular tower, a nacelle, hub and three blades, see Fig. 15.2 for the dimensions. These components are modeled as follows:

- **Tower**: a conical tower is created according to the specifications given in [20]. The tower is 68 m in height, with a base diameter of 5.6 m and top diameter of 4.0 m, and is modeled using 8 three-dimensional linear beam elements. The tower has two 6 DoF interfaces, one at the bottom (tower bottom), which will be connected to the jacket structure and one at the top (tower top) which will be connected to the rotor-nacelle assembly.
- **Nacelle**: modeled as one single rigid and massless linear beam element with on one end a point mass representing the nacelle's mass (240,000 kg) and inertia, and on the other a 6 DoF interface which connects to the tower top. The large stiffness and low mass of the element are created using a high Young's modulus and a low density value. The parallel axis theorem was used to calculate the moments of inertia around its local axes.
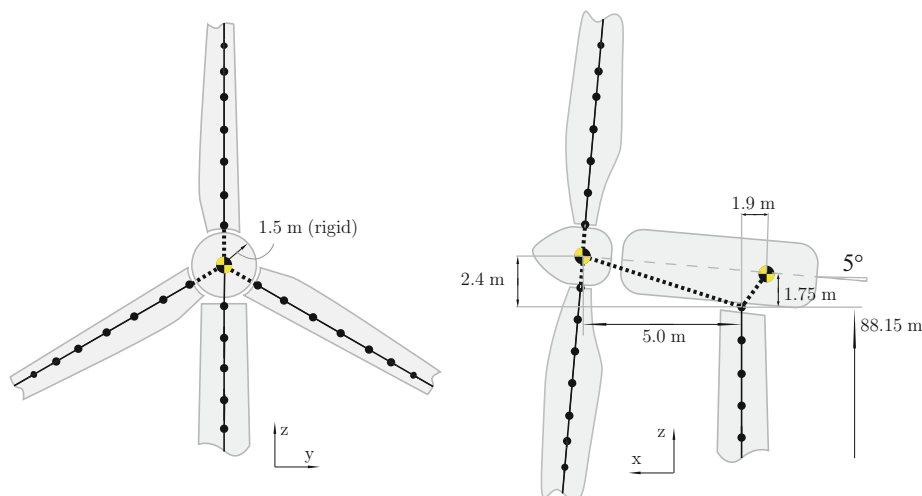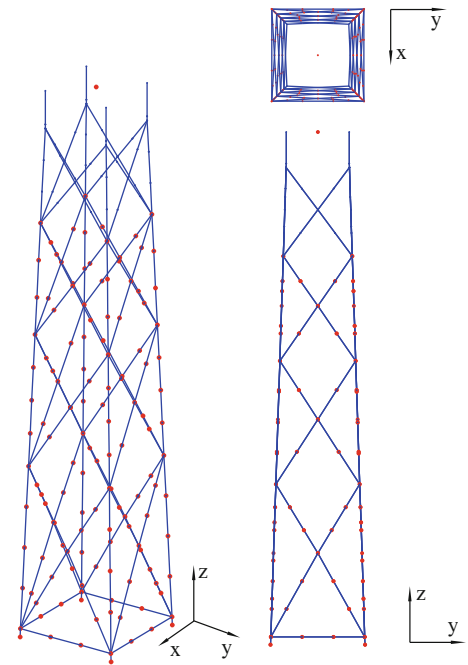

Fig. 15.2 RNA of the NREL 5 MW baseline turbine

Fig. 15.3 Matlab model of
the OC4 jacket

- **Hub**: modeled similar to the nacelle as a single rigid and massless linear beam element. The hub has a virtual distance of 1.5 m between its center and the connection to the blades. The hub's mass (56,780 kg) is added as a point mass at one end of the element together with its moments of inertia. The element has two 6 DoF interfaces, one end connects to the tower top, the other to the three blades.
- **Blades**: the blades are 61.5 m in length and each weighs 17,740 kg. They are modeled using 49 three-dimensional linear beam elements. A root-element, located at the base of each blade, is modeled as a 1.5 m long rigid and massless element to account for the virtual distance discussed earlier. The root-element has a 6 DoF interface which connects to the hub element.

The assembled turbine model consists of 157 elements and possesses 948 DoF.

15.5.1.2 OC4 Jacket Structure

The jacket designed for the OC4 project, which hereafter will be called the OC4 jacket, consists of four main legs which are interconnected via four levels of X-braces, see Fig. 15.3. The height of the jacket is 68 m and is designed for water depths of 50 m. As was described in [20], the stiffness of the connection to the seabed is assumed to be high and is therefore modeled as rigid. The connection between the turbine and jacket is realized using a concrete transition piece weighing 666 ton. This transition piece rigidly connects the top elements of the jacket. The interface to the tower is realized using a 6 DoF interface.

The jacket is modeled in ANSYS according to the specification given in [20] and hereafter converted into a Matlab model. To account for the added mass created by the surrounding water when the jacket structure moves, additional point masses (with directional properties) are added to the structure's nodes, shown as red dots in Fig. 15.3. The total jacket model consists of 229 linear beam elements and 1,014 DoF.

15.5.1.3 Properties of the Model

The correctness of the numerical models of the NREL turbine and OC4 jacket has been checked by comparing the manually calculated mass to that resulting from the application of (translational) unit accelerations. The total mass of the turbine model was found to be 567 ton, which is 1.3% higher than the manually calculated 560 ton. Although there is a difference between the two values the accuracy was found to be adequate. The total mass of the jacket structure model was found to be 1,205 ton, including the 666 ton concrete transition piece and without the added masses, which is in agreement with the manually calculated value. Preferably an eigenfrequency comparison should be performed on both models, when clamped at their interfaces. Unfortunately, no such data was found in literature, so this comparison could not be made.

Table 15.1 First ten eigenfrequencies and mode shape description of turbine model

Mode number [-]	Frequency [Hz]	Modeshape description
1	0.32	1st global side-side
2	0.33	1st global fore-aft
3	0.73	1st asymmetric flapwise yaw
4	0.77	1st asymmetric flapwise pitch
5	0.80	1st flapwise collective
6	1.04	1st edgewise collective
7	1.16	1st asymmetric edgewise pitch
8	1.24	1st asymmetric edgewise yaw
9	1.26	2nd global fore-aft
10	1.33	2nd global side-side

The first ten eigenfrequencies and eigenmodes of the assembled turbine-jacket model are given in Table 15.1. The obtained eigenfrequencies are comparable to those found in literature, see [19].

15.5.2 Numerical Experiments

The model described in the previous section is used for a number of numerical experiments. The goal is to compare the accuracy of different reduced models by comparing their modal results and dynamic response to those of the unreduced model. Here the interest lies in the creation of an accurate superelement of the jacket model, the wind turbine is not reduced.

As outlined in the introduction the number of DoF of the jacket model has to be minimized in order to limit the simulation time of aero-elastic codes. As mentioned in the introduction currently monopile support structures are modeled using around 50 DoF. For the jacket model we further reduce this number by allowing only 26 DoF as a maximum.

To create the reduced jacket model the (augmented) Craig-Bampton method is used. So for the reduction basis a combination of static constraint modes $\boldsymbol{\Psi}_{C,\,i}$, fixed interface vibration modes $\boldsymbol{\Phi}_i$ and MTA vectors $\boldsymbol{\Phi}_{MTA}$ can be used. In total seven reduced jacket models are created and assembled to the unreduced turbine model. In order for the reduced models to be at least statically correct all static constraint modes $\boldsymbol{\Psi}_{C,i}$ are included in the reduced models. Then 20 additional DoF are used for both fixed interface vibration modes and MTA vectors. To investigate the improvement of adding vibration modes the jacket model it is also reduced by the static constraint modes only, resulting in a 6 DoF model. This type of reduction is known as the Guyan method [6].

In Sect. 15.3 it was shown that MTA vectors can be based on force vectors arising from the interface or from external loading. Here the focus lies on the latter, by creating MTAs based on the spatial force vectors obtained from time data using the POD method.

This time varying data for the jacket structure is obtained from ASAS, which is an extension of ANSYS specialized for offshore and maritime applications, for four sea conditions namely: low, medium, high and "freak" waves. The importance of dynamic analysis of this wave loading is underlined by the fact that the frequency content of the wave loads is in the range of the eigenfrequencies of the turbine model, so modal excitation is likely to occur. For each sea condition a (quasi-) stochastic time series of 100 s is obtained with time steps of 0.04 s, so 2,500 samples in total. The time step is such that the highest frequency that can be represented in the data is higher than the highest frequency present in the signal. From the POMs obtained using the method described in Sect. 15.4 the first five are selected, capturing more than 93% of the total energy. This shows the effectiveness of the POD method.

A limitation of the POMs, and thus the resulting MTAs, obtained using this method is that they are based on a single wave type. Therefore, it is likely that they are able to only accurately capture the response to that specific wave type. This would limit the use of the reduced jacket model to a single wave type. To overcome this issue a generalized method of obtaining force vectors is also investigated. An extended time series is obtained by simply combining all wave condition specific time series, forming one long time series.[1] Generalized force vectors can be obtained from this data and used to compute

---

[1] To prevent the introduction of high frequencies in the combined data a signal window was used to scale the magnitude of the wave loads to zero at the transitions between time series. Furthermore, because the magnitude of the force data varies for different wave types, one can imagine that high waves produce larger forces than low waves, a normalization step is taken, explicitly scaling the maximum occurring value of the individual time series to unity.
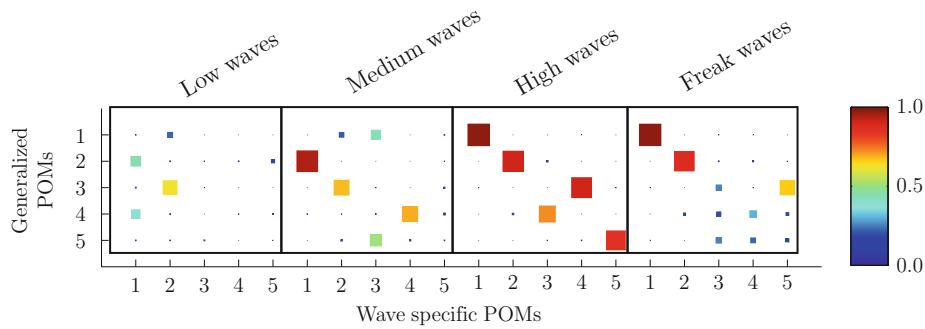
Fig. 15.4 Modal results of the reduced wind turbine models

Table 15.2 Overview of numerical models of baseline offshore turbine

Wave conditions	# of $\Psi_{C,i}$	# of Φ_i	# of Φ_{MTA}	MTA order	Total # of DoF	Name
–	–	–	–	–	1,956	REF
–	6	–	–	–	948	CB00
–	6	20	0	–	968	CB20
Low	6	10	10	2	968	MTA10l
Medium	6	10	10	2	968	MTA10m
High	6	10	10	2	968	MTA10h
Freak	6	10	10	2	968	MTA10f
Combined	6	10	10	2	968	MTA10c

generalized MTA vectors. The first five generalized POMs showed to capture 93% of the total energy. From a cross correlation between the wave specific and generalized POMs using the MAC, it can be seen that the generalized POMs show reasonable correlation with the POMs of the medium, high and freak wave, but a low correlation to those of the low waves. See Fig. 15.4.

Based on these POMs the first and second order MTAs are created and added to the reduction basis, so 10 MTAs in total. Since we decided to allocate 20 DoF in total, the reduced jacket models including MTAs have ten fixed interface vibration modes in their basis. An overview of the reduced assemblies and the ingredients for the jacket's reduction bases are given in Table 15.2. The last letter in the name of the reduced models with MTAs indicates the wave conditions on which the MTA vectors are based (l = low, m = medium, h = high, f = freak and c = combined).

15.5.3   Results

15.5.3.1   Modal Comparison

In Fig. 15.5 the modal results for the first 60 eigensolutions of the different reduced assemblies are plotted. All results are relative to the reference (unreduced) model. From the figure it can be observed that the addition of fixed interface vibration modes and MTA vectors improves the modal results compared to the system where the jacket is reduced using only the static constraint modes, the CB00 model. Furthermore, it can be noticed that the modal results of systems including MTA vectors are very similar. For the first 20 modes the results on both the eigenmodes and eigenfrequencies are of similar quality as the CB20 model, hereafter however the CB20 system produces better results.

From the modal results a high correlation is observed between the unreduced and reduced assemblies (with the exception of the CB00 model) for the eigenmodes 20, 26 and 31. On further inspection of these modes it was found that they show very localized deformation of the jacket structure which is exactly represented by the fixed interface vibration modes. These modes are present in all reduction bases (with the exception of the CB00 model) and thus explain the high correlation.
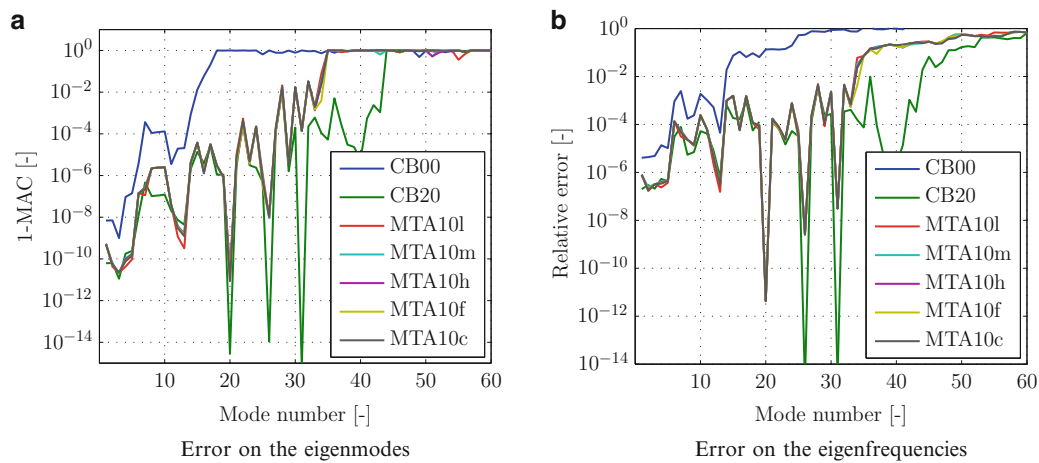
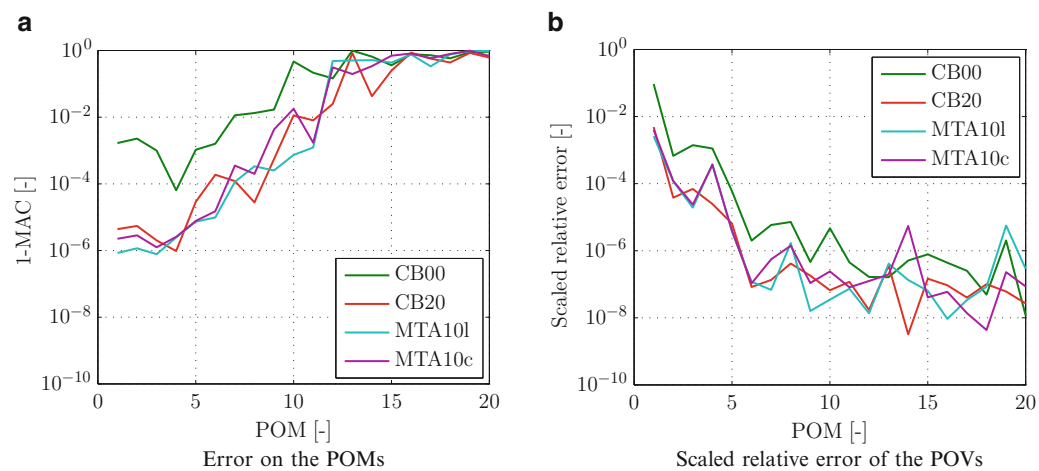**Fig. 15.5** Modal results of the reduced wind turbine models

Fig. 15.6 Comparing POD results to reference solution, low waves

15.5.3.2 Time Integration Results

In Figs. 15.6–15.9 the results of the POMs and POVs for various wave conditions are shown. From all figures it can be observed that the CB00 model gives the least accurate results, which was to be expected since the jacket model is statically reduced to a 6 DoF model. The addition of both fixed interface vibration modes and MTA vectors improve these results, resulting in higher correlation with the POMs and POVs of the unreduced assembly. Note that although the results of the first 20 POMs and POVs are compared, a large part of the energy is captured by just the first few modes.

An interesting comparison is that between the results of the CB20 system and the corresponding system including the wave condition specific MTA vectors (i.e. MTA10l, MTA10m, MTA10h or MTA10f):

- For the results for the low waves (Fig. 15.6), the CB20 and MTA10l systems do not show a clear difference in the results. Hence for this case the MTA vectors do not give better description than the fixed interface vibration modes they replace. Investigation of the shape of the POMs for this wave type showed that they create very localized excitation around the mean sea level (around the height of the second level of X-braces). From analysis of the fixed interface modes of the jacket structure it was found that these also include very localized deformations at this height. These modes could already be sufficient to capture the response to this loading and hence explain why the accuracy is not improved by adding the MTAs.
- For the medium waves (Fig. 15.7), it can be observed that for the first 11 POMs the MTA10m model shows improved results compared to the CB20 model. For the POV values we can see that the first five are better approximated, hereafter no clear trend is observed.
- The results for the high and freak waves, Figs. 15.8 and 15.9, also show similar results, where the system including MTA vectors shows improved results on the first POMs and POV values.
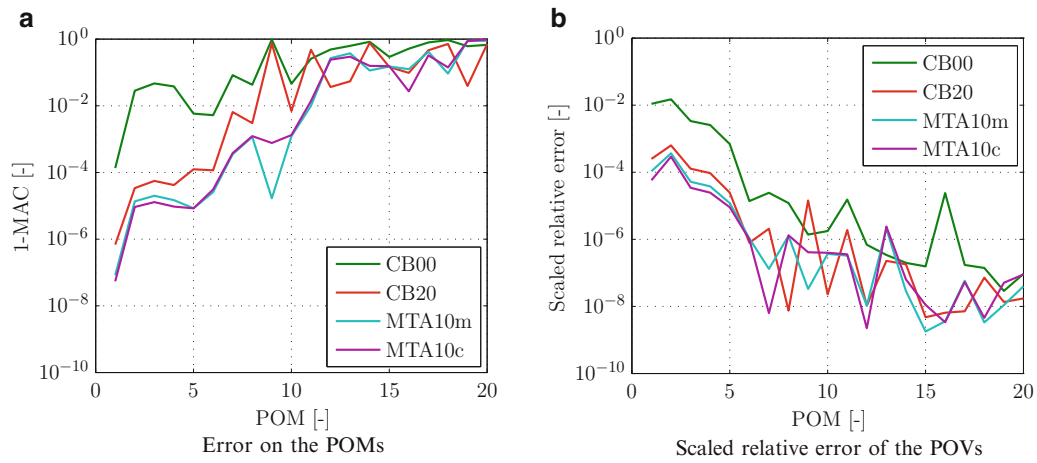
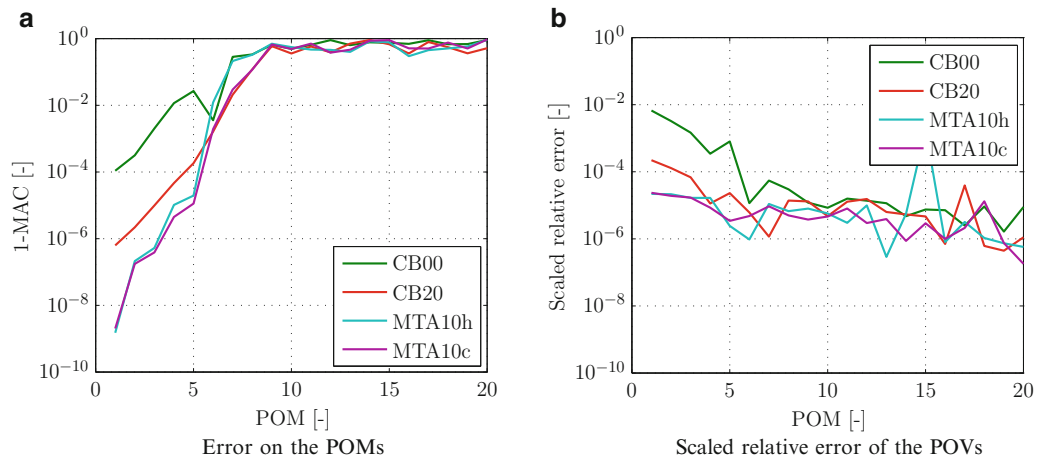**Fig. 15.7** Comparing POD results to reference solution, medium waves

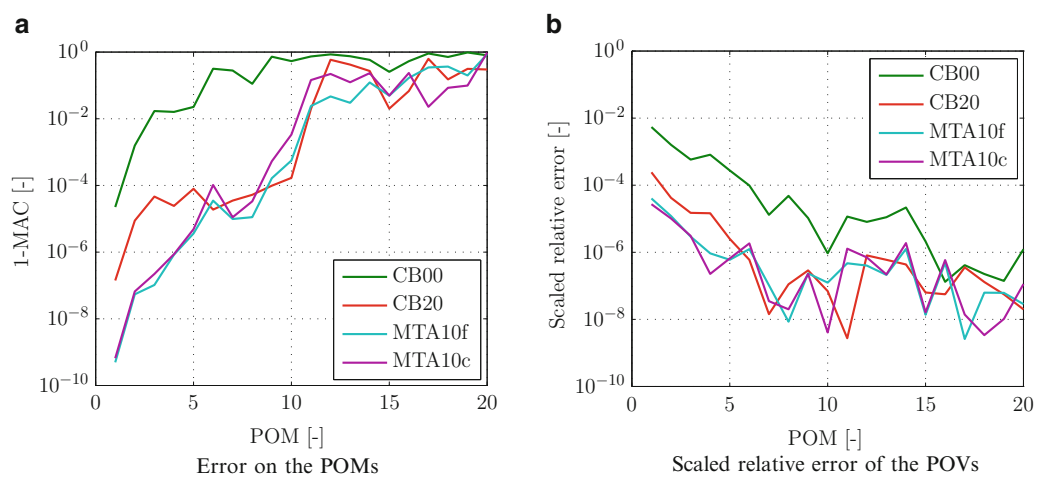**Fig. 15.8** Comparing POD results to reference solution, high waves

Fig. 15.9 Comparing POD results to reference solution, freak waves

Another interesting observation is that the system where the MTA vectors are based on the combined POMs (MTA10c), results are found that are comparable to those of when wave type specific MTA vectors are used. This thus shows that the obtained POMs for the combined wave load data produce MTAs which are suitable for different wave conditions, so that a generalized reduced model can be created.

15.6   Conclusions and Recommendations

The current trend in wind turbine engineering is to install wind turbines further offshore on more complex foundation structures such as jackets. In order to efficiently perform integrated dynamic analysis, this work proposed the use of reduced component models for the foundation. However, one of the shortcomings of the common component reduction methods is their inability to accurately represent the response to external excitation. It was explained how this shortcoming can be overcome by augmenting the reduction basis using the MTA method. Furthermore, it was shown how spatial force vectors can be extracted from time varying load data using the proper orthogonal decomposition (POD) method.

To test the methodology, a case study was performed on the NREL 5 MW reference wind turbine attached to the OC4 benchmark jacket support structure. The dynamic response of various reduced models was compared, showing that the addition of the MTA vectors gave a more accurate response for almost all wave conditions compared to an equal sized normal reduced model. It can therefore be concluded that combining the component model reduction and the MTA method, adequate models can be obtained for complex offshore wind turbine foundations.

A number of open issues require additional research. One topic worth investigating is including damping in the reduced model. Simple mass/stiffness proportional damping can be readily applied, but more complex damping types (e.g. hydrodynamic and soil damping) are less straightforward. Furthermore, research is required on calculating even more general MTAs that can be used for example for wave loads coming from different directions.

References

1. Allemang R, Brown D (1982) A correlation coefficient for modal vector analysis. In: Proceedings of the International Modal Analysis Conference, Society for Experimental Mechanics, Bethel, pp 110–116
2. Balmès E (1996) Use of generalized interface degrees of freedom in component mode synthesis. In: Proceedings of the Fourteenth International Modal Analysis Conference, Dearborn. Society for Experimental Mechanics, Bethel
3. Craig R, Bampton M (1968) Coupling of substructures for dynamic analysis. AIAA J 6(7):1313–1319
4. Craig R, Chang C (1976) A review of substructure coupling methods for dynamic analysis. NASA. Langley Res Center Adv Eng Sci 2(CR-2781):393–408
5. Dickens J (1997) A critique of mode acceleration and modal truncation augmentation methods for modal response analysis. Comput Struct 62 (6):985–998
6. Guyan R (1965) Reduction of stiffness and mass matrices. AIAA J 3:380
7. Hurty W (1965) Dynamic analysis of structural systems using component modes. AIAA J 3(4):678–685
8. Hurty WC (1960) Vibrations of structural systems by component mode synthesis. J Eng Mech Div Am Soc Civil Eng 86(4):51–69
9. Jonkman J, Butterfield S, Musial W, Scott G (2009) Definition of a 5-MW reference wind turbine for offshore system development. Technical report, National Renewable Energy Laboratory
10. Kerschen G, Golinval J (2002) Physical interpretation of the proper orthogonal modes using the singular value decomposition. J Sound Vib 249 (5):849–865
11. Kerschen G, Golinval JC, Vakakis A, Bergman L (2005) The method of proper orthogonal decomposition for dynamical characterization and order reduction of mechanical systems: an overview. Nonlinear Dyn 41:147–169
12. Liang Y, Lee H, Lim S, Lin W, Lee K, Wu C (2002) Proper orthogonal decomposition and its applications—part I: theory. J Sound Vib 252:527–544
13. Passon P, Kühn M, Butterfield S, Jonkman J, Camp T, Larsen T (2007) OC3-Benchmark exercise of aero-elastic offshore wind turbine codes. J Phys: Conf Ser 75:1–12
14. Rayleigh J (1896) The theory of sound. Dover Publications, New York
15. Rixen D (2001) Generalized mode acceleration methods and modal truncation augmentation. In: Structures, structural dynamics and material conference and exhibit. 42st AIAA/ASME/ASCE/AHS/ASC, Seattle. AIAA 2001-1300
16. Rixen D (2002) A lanczos procedure for efficient mode superposition in dynamic analysis. In: Structures, structural dynamics and material conference and exhibit. 43st AIAA/ASME/ASCE/AHS/ASC, Denver. AIAA 2002-1393
17. Tran DM (2001) Component mode synthesis methods using interface modes: application to structures with cyclic symmetry. Comput Struct 79:209–222
18. van der Valk P (2010) Model reduction and interface modeling in dynamic substructuring. Master's thesis, Delft University of Technology, Delft

19. Vorpahl F, Popko W (2011) IEA wind annex 30—OC4 project. The offshore code comparison collaboration continuation. IEA wind side event at EWEA, EWEA 2011 annual event, Brussels
20. Vorpahl F, Popko W, Kaufer D (2011) Description of a basic model of the "Upwind refrence jacket" for code comparison in the OC4 project under IEA wind annex XXX. Technical report, Frauenhofer university
21. Witteveen W, Irschik H (2007) Efficient modal formulation for vibration analysis of solid structures with bolted joints. In: Proceedings of the twenty fifth international modal analysis conference, Orlando. Society for Experimental Mechanics, Bethel

Chapter 16
Demonstrating Predictive Capability of Validated Wind Turbine Blade Models

Kendra L. Van Buren, François M. Hemez, and Sezer Atamturktur

Abstract Verification and Validation (V&V) activities provide a means by which credibility can be established for simulation models developed to predict the behavior of wind turbines. This paper discusses the use of validation activities in the development of finite element (FE) models for wind turbine blades. The nine-meter CX-100 wind turbine blade, developed at Sandia National Laboratories (SNL), is utilized in this study. The FE model is developed using design specifications for the geometry of the blade, and the rule of mixtures is applied to smear the cross section so that it can be represented using isotropic material properties. Experimental modal data from laboratory tests of the CX-100 blade at the National Renewable Energy Laboratory (NREL), is collected for a fixed-free boundary condition, in which the blade is bolted to a 20 t steel frame. The experimental modal data is collected in two configurations: (1) in the original fixed-free condition and, (2) with two masses attached to the blade at the 1.6 and 6.75 m stations. To mimic the second experimental configuration, the FE model is modified by incorporating point masses attached to the blade with springs. Calibration of the fixed-free and mass-added FE models is limited to use of the natural frequencies only. By exploring these different configurations of the wind turbine blade, credibility can be established regarding the ability of the FE model to predict the response to different loading conditions. Through the use of test-analysis correlation, the experimental data can be compared to model output and an assessment is given of the predictive capability of the model. *(Publication approved for unlimited, public release on September 26, 2011, LA-UR-11-5490, Unclassified.)*

16.1 Introduction

16.1.1 Motivation

Wind energy is being pursued in the United States to supply 20% of power by the year 2030 [1]. Wind plants, and consequently wind turbines, are being produced at a larger scale to capture and produce more energy to meet the growing demands of the wind energy industry [2]. However, it is absolutely crucial to understand the dynamics and vibrations of wind turbine blades to efficiently increase the performance of wind turbines. The blades are responsible for only 10–15% of the cost of the wind turbine system [2], however, they capture all of the energy produced from wind turbines, and damage to the blades can result in rotor instability that can lead to damage of the entire wind turbine system [3, 4]. Because blade damage to turbines is perhaps the most prohibitive cost of wind energy [5], condition-based blade maintenance schemes are critical to lowering operational and maintenance costs [6]. Such schemes are only possible through a better understanding of wind turbine blade vibrations.

The development of modeling and simulation (M&S) techniques for studying the vibrations of wind turbine blades offers an economical alternative to constructing new generation blades and maintaining current blades in optimal condition. It is forecasted that the wind energy industry will benefit from the financial benefits provided by M&S due to the increasing

K.L. Van Buren (✉) • S. Atamturktur
Department of Civil Engineering, Clemson University, 110 Lowry Hall, Clemson, SC 29634-0911
e-mail: klvan@clemson.edu

F.M. Hemez
Los Alamos National Laboratory, XTD-3, Mail Stop T087, Los Alamos, NM 87545

costs of full-scale testing as wind turbine blades are produced at larger scales [2]. M&S also provides a means to efficiently evaluate the structural design [7]. Recently, finite element (FE) models calibrated against experimental data have gained acceptance for routine use in studying wind turbine blades, owing to their versatility in predicting many complex load cases [8], whereas only idealized loads can be implemented in full scale experiments [9].

The ultimate goal of this study is to demonstrate the predictive capability of a validated FE model of the CX-100 wind turbine blade developed at Sandia National Laboratories (SNL). Here, "predictive capability" is defined as the ability to accurately predict different configurations of experimentally obtained data that has not been previously considered with the FE model. The FE model used in this study has previously gone through rigorous **V**erification and **V**alidation (V&V) exercises as reported in Reference [10, 11]. The FE model employed in this study is developed using the rule of mixtures to smear the cross-sectional areas of the blade and characterize the materials with isotropic properties, instead of modeling the multiple composite layers embedded in an epoxy matrix. This study demonstrates the potentials and limitations of FE models to predict the behavior of wind turbine blades by comparing the FE model predictions to new data that have not yet been used during the calibration of the FE model.

16.1.2 Related Literature

FE models suffer from many, unavoidable sources of uncertainty, such as variability of the manufactured product from design specifications, deviation of material properties from coupon properties used to represent the material behavior, and unique stress loading behaviors in critical sections of the model [9]. Furthermore, to reduce the complexity of FE models assumptions and simplifications of known, or unknown, physics are inevitably applied. Assumptions and simplifications, such as neglecting damping or assuming a two-dimensional flow over the blades, [12, 13] limit the ability of the model to replicate reality. It has been shown that FE models of composite structures that assume smeared cross sections, such as the FE model implemented in this paper, can accurately model the global response but are limited in predicting the behavior of thick laminates, stress and strain near geometric and material discontinuities, and the kinematics of delamination [14]. In using predictive simulation models, it is imperative to understand the limitations imposed by such assumptions and simplifications to the model.

In the development of simulation models, reliable experimental data for use in calibration and validation exercises is also necessary. Experimental testing has been pursued in several studies to provide a description of the structural response of wind turbine components. For example, a 25-m wind turbine blade was exercised in a full-scale static flapwise test to provide measurements of local deflection and strain for comparison to FE models [15]. Modal testing is also a common experiment to perform, due to the ease in which it can be assessed in simulation models [16]. Although experimental data are useful for comparison to model output, research can be limited due to its lack of availability. Efforts have been put forth to collect experimental data for different types of wind turbines [17], however, public access to such data is typically limited.

An example of an analytical study utilizing experimental data is provided in Reference [18], in which a full static test to failure of a wind turbine blade was performed to confirm the FE predictions of the buckling behavior of the blade. Similarly, a FE model was successfully developed to study the buckling collapse observed during experimental flap-wise loading of a wind turbine blade [8]. In subsequent experimentation, modeling is utilized to investigate fatigue damage to study why 300 kW wind turbine blades were failing prior to the design life of 20 years. Failure scenarios were categorized from coupons of a failed wind turbine blade, and FE modeling was used to investigate areas of high stress and to determine the critical mode of failure [19]. FE modeling has also been demonstrated as a tool that can be used during the design phase of wind turbine blades. This was demonstrated in Reference [20], when the optimal design of a wind turbine blade was developed through parametric studies, and various load cases specified by the International Electrotechnical Commission 61400-1 for wind turbine blade design requirements were applied to the wind turbine FE model. Consequently, the wind turbine blade was manufactured for experimental studies, and comparison to the FE model output found that the final product was within 4% error of the mass, span-wise center of gravity, blade tip deflection, and first-flap natural frequency.

In addition to studying and replicating laboratory tests, simulation models can be used to study complex load cases or events that cannot be measured experimentally. One application is to study the onset of damage. In an effort to study the increasingly complex load cases that wind turbines will experience in off-shore conditions, a FE model of a wind turbine blade was coupled to a Computational Fluid Dynamics (CFD) model to study the interaction of the flexible wind turbine blade with wind loading [21]. Another study employed FE modeling to investigate the fatigue failure of wind turbine blades [22]. The study concluded that at best, the wind turbine blade used in their study could survive a 24-year life span, just barely meeting the 20–30 year design lifetime. A recent study used a calibrated model of a wind turbine to explore the onset of damage, concluding that modal properties produced changes that were too insensitive to damage [6]. The study

was able to demonstrate that the use of statistical modeling has the potential to detect damage; however, more simulation modeling and testing would be necessary to confirm this hypothesis. These studies demonstrate the potential of FE modeling to be used in a predictive capacity to model the behavior of wind turbine blades. The current study aims to contribute to these efforts by investigating the level of accuracy that can be provided by FE models through the use of validation exercises and test-analysis correlation to quantify the model agreement to experimental data.

16.2 Model Development and Experimental Campaign

16.2.1 Development of the CX-100 FE Model

This section provides a review of the development process of the FE model of the CX-100 blade, as discussed in-depth in Refs. [10, 11]. The model is developed from design specifications of the geometry using the NuMAD preprocessor developed at SNL, and imported into ANSYS v 12.1 with Shell-281 elements. The mesh discretization is based on an element size of $\Delta x = 8$ cm, producing an overall solution uncertainty of 1.78%, comparable to a 3-σ experimental variability of 1.62% estimated from free-free modal testing performed at Los Alamos National Laboratory (LANL) [23].

Six independent sections are defined in the development of the FE model: shear web, root, spar cap, trailing edge, leading edge with balsa, and leading edge without balsa. The sections are illustrated in Fig. 16.1; however, the shear web is not shown because it is an internal component of the wind turbine blade. Isotropic materials with smeared cross-sectional properties are used to define the material sections. Free-free and clamped-free modal testing performed at LANL is used in the calibration and validation of the FE model. Reference [11] describes the calibration of model parameters to the free-free experimental natural frequencies. The FE model is also compared to the results of the clamped-free modal testing, in which a 250-kg steel bookend was used to create the boundary condition. Springs are introduced to the base of the blade to create a condition that is neither "fixed" nor "free," and to mitigate the uncertainty associated with the experimentally implemented clamped-free testing.

16.2.2 NREL Modal Testing of the CX-100 Wind Turbine Blade

Experimental modal testing performed at the National Renewable Energy Laboratory allows the possibility of examining the predictive capability of such a simplified model. The CX-100 blade is attached to a 20-t (18,000 kg) steel frame, effectively allowing for a fixed-free setup of the blade. Modal testing is performed using a roving impact hammer test of the CX-100 blade under two different set-ups: first, in a fixed-free condition, and second with large masses clamped to the blade. The addition of a 582-kg mass and 145-kg mass at the 1.6 and 6.75-m locations, respectively, is inspired by their utility in performing fatigue testing on the blade. Four uni-axial accelerometers and one tri-axial accelerometer are used to collect data for hammer impacts at 65 locations: 47 in the flapwise directions, and 18 in the edgewise directions. Three test repeats are performed with a linear average and 150 Hz sampling frequency. The acceleration response is collected with 4,096 sampling points without a window function due to the relatively long sampling period of 11 s.
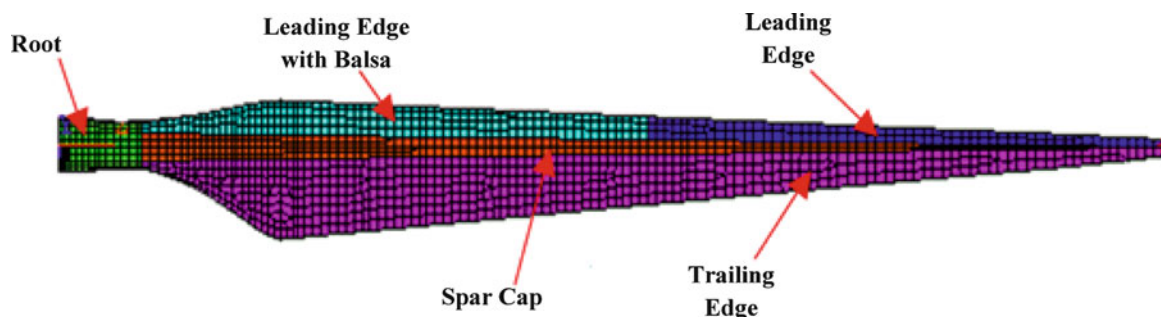

Fig. 16.1 Illustration of the ANSYS model showing different sections of the blade
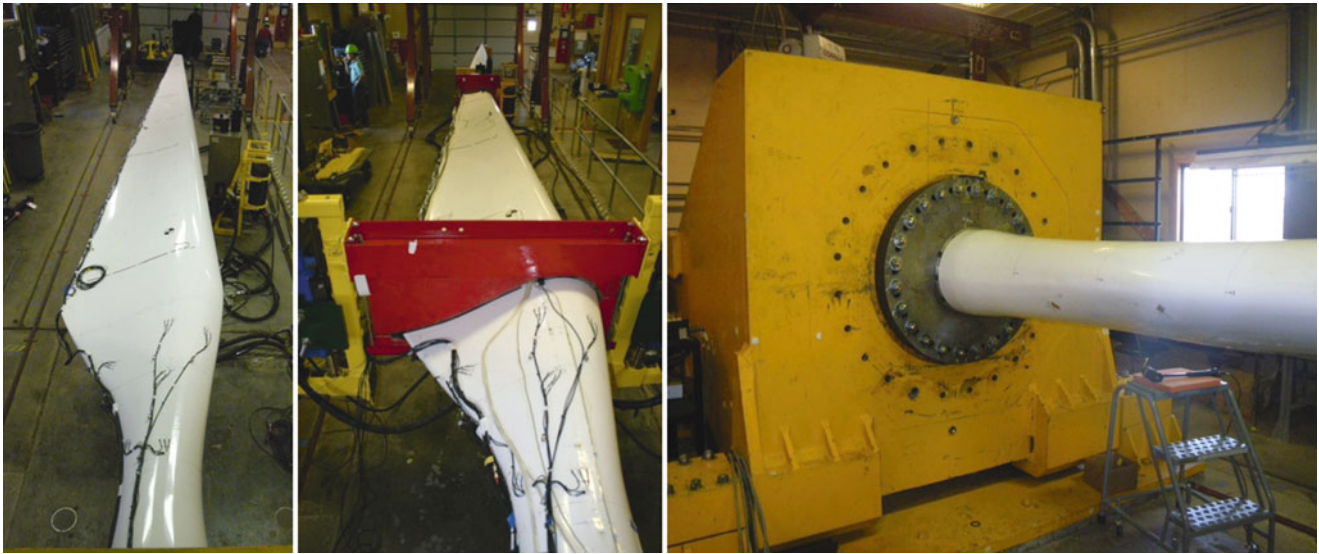
Fig. 16.2 Experimental fixed-free (*left*) configuration, mass-added (*middle*) configuration, and base fixity (*right*)

Table 16.1 Comparison of prior and posterior uncertainty of the FE model parameters

FE model parameter	Prior uncertainty			Posterior uncertainty		
	Lower	Upper	Range	Mean	Std. dev.	$\pm 2\sigma$ range
Trailing edge, ρ (kg·m^{-3})	484.37	729.81	245.44	607.34	68.25	272.95
Spar cap, E (MPa)	29.92	53.56	23.64	47.81	4.51	18.04
Z spring, k_2 ($\times 10^{+6}$ N·m^{-1})	1.00	100.0	99.00	48.13	30.25	131.00

The experimental set-ups and base fixity are shown in Fig. 16.2. Note that the boundary condition provided in the NREL testing is different from the boundary condition found in previous modal testing performed at LANL [11, 23].

16.2.3 Fixed-Free CX-100 Model

As mentioned in Sect. 16.2.1, the data from previous clamped-free testing employed a 250-kg steel bookend fixture; however, the experimental boundary condition is created using an 18,000-kg steel frame in the current study. Due to this change in boundary condition, calibration of the fixed-free model is re-considered.

Three statistically significant model parameters of the fixed-free FE model of the wind turbine blade are identified using a forward propagation of uncertainty and sensitivity analysis in Reference [11]. The influential parameters are: translational springs used to model the boundary condition perpendicular to the base fixity, the modulus of elasticity of the spar cap, and the density of the trailing edge. Measurements of the natural frequencies obtained during the NREL testing are utilized to calibrate the FE model. Instead of performing calibration as an optimization of model parameters to best-fit the experimental data, inference uncertainty quantification is performed to explore the posterior probability distribution of these three parameters. To efficiently perform the inference uncertainty quantification, the FE model is executed using full-factorial design-of-computer-experiments to provide simulation data to train a fast-running Gaussian Process Model (GPM). A Markov Chain Monte Carlo (MCMC) algorithm is used to explore the posterior distribution of the GPM utilizing the computational methodology proposed in Refs. [24, 25].

The results of the inference are summarized in Table 16.1. Columns 2–4 summarize the prior uncertainty, which represents the range of values used in the full-factorial design to train the GPMs. Columns 5–7 provide the posterior uncertainty, which are the statistics inferred from the MCMC search algorithm. The inference is most successful at "learning" the value of the spar cap modulus of elasticity, as indicated by the reduction of its uncertainty relative to the initial range used in the design.

Fig. 16.3 Marginal distribution and correlation functions corresponding to Table 16.1
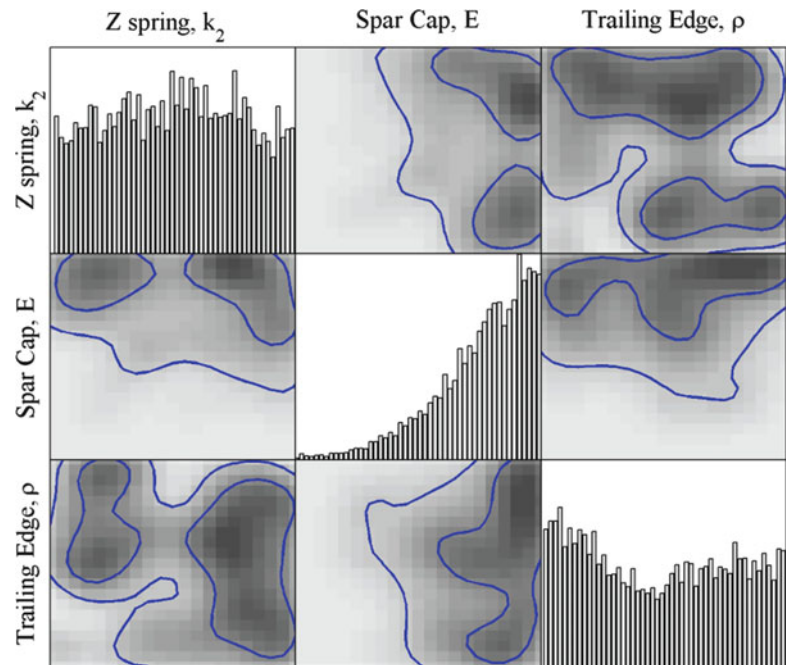

Table 16.2 Comparison of experimental and simulated results for the fixed-free model

Mode	Description	Experimental (Hz)	Simulated (Hz)	Difference (%)
1	First flap	4.35	3.61	−17.0
2	First lag	6.43	4.72	−26.6
3	Second flap	11.51	9.80	−14.8
4	Third flap	20.54	16.79	−18.2
5	Second lag	23.11	19.51	−15.6
6	Fourth flap	35.33	29.86	−15.5
7	First torsion	46.27	35.39	−23.5
8	Third lag	48.64	40.02	−17.7

A graphical representation of the posterior distribution is provided in Fig. 16.3, which plots the marginal distribution of each parameter on the diagonal and a probability contour of the pairs of parameters in the off-diagonal boxes. The inference is not capable of reducing the uncertainty of the spring constants or trailing edge density. It is possible that there is an interaction between the density and the spring during calibration that produces compensating effects, thus making it difficult to calibrate using the present methodology. On the other hand, the inference is successful in reducing the uncertainty of the spar cap modulus, as observed in Table 16.1, when comparing the prior range to the posterior range. However, the visual representation of the posterior, shown in Fig. 16.3, and the clustering of samples drawn towards the upper bound, suggest that the algorithm may be attracted to values outside of the initial range provided to the GPM.

Table 16.2 compares the experimentally obtained natural frequencies to those predicted by the FE model with the parameters set to the mean values of the posterior distribution. The simulation consistently under-predicts the experimental results by approximately 15–26%. While this seems to be a large deviation, the absolute differences for the first three frequencies are only 0.74, 1.71, and 1.71 Hz, respectively. This under-prediction also provides a possible explanation for why the inference uncertainty quantification appears to be searching for larger values in the posterior distribution for the spar cap modulus, shown in Fig. 16.3, because a stiffer blade would potentially provide higher values for the natural frequencies.

16.2.4 Mass-Added CX-100 Model

To implement the masses into the simulation, a central point mass is added at each cross section and then connected by springs to the nodes of the blade to adjust for the interaction between the blade and the added masses. The configuration of the springs, with the point mass in the middle, is shown in Fig. 16.4. This modeling is adopted because exploratory FE

Fig. 16.4 Illustration of the
blade cross-section with added
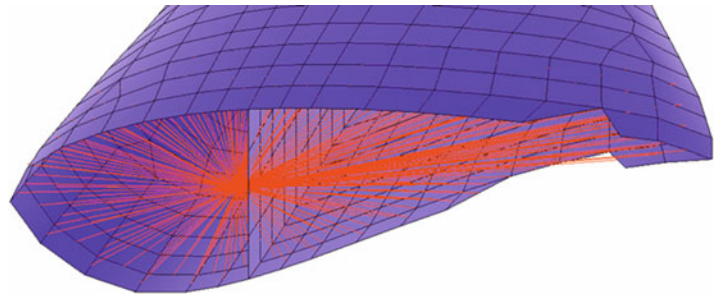point mass and springs

Fig. 16.5 Effect of spring
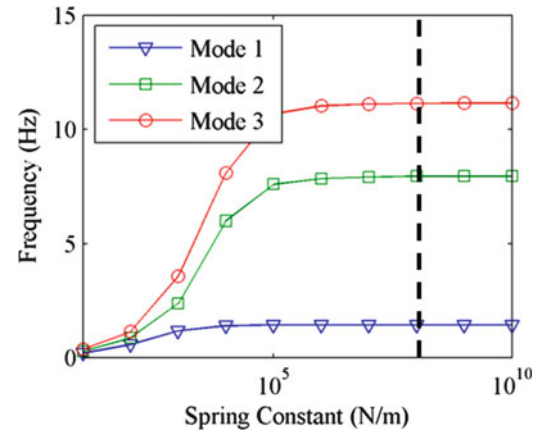stiffness constants on the first
three frequencies

Table 16.3 Comparison of
experimental and simulated
results for the mass-added
model

Mode	Description	Experimental (Hz)	Simulated (Hz)	Difference (%)
1	First flap	1.82	1.44	−21.1
2	First lag	2.68	1.94	−27.8
3	Second flap	9.23	7.93	−14.0
4	Third flap	12.72	10.27	−19.3
5	Second lag	14.68	11.14	−24.1
6	Fourth flap	18.86	18.52	−1.8
7	Third lag	24.43	24.51	0.4

simulations indicate that representing the masses simply as concentrated values does not adequately account for the rigidity
introduced. A way to model this rigidity is through the introduction of fictitious springs.

To preserve the fixed-free model, the spring stiffness constants are the only parameters considered for calibration in the
mass-added model. A parametric study is performed first to evaluate how the model output changes as the spring stiffness
coefficients are varied.

Figure 16.5 shows the frequency predictions as the spring stiffness values are varied from 10 to 10^8 N/m. As the spring
stiffness is increased, the natural frequencies also increase, due to the change in interaction between the blade and the
springs. Around a value of 10^6 N/m, the natural frequencies plateau to values that consistently under-predict the experimen-
tal natural frequencies. This under-prediction is likely an extension of the observed results from the fixed-free model.
Because of the inability of the parametric spring study to form an envelope around the experimentally obtained natural
frequencies, a calibration of the model parameters would likely converge to the upper bound of the spring stiffness values.
Therefore, a value of 10^8 N/m is chosen for the spring stiffness value, indicated by the vertical black line in Fig. 16.5.

Table 16.3 compares natural frequencies from the experiments to the model output. Again, the natural frequencies are
consistently under-predicted by the model; however, the absolute differences for the first three modes, 0.38, 0.74, and
1.30 Hz, demonstrate an acceptable fidelity to experimental data despite the minimal calibration activities performed after
the model was modified to include the added masses.

16.3 Test-Analysis Correlation for Validation

16.3.1 Mode Shapes

Our contention is that a model can be considered *validated* only when it is able to accurately predict data that have not previously been considered during calibration exercises, and is an important component to establish the credibility of FE models. Ideally, experimental data used for validation is independent of the data used for calibration [16]. This constraint can often times be difficult to achieve for engineering applications involving complex structures. One reason, as discussed in Reference [26], is because calibration exercises sometimes have the tendency to over-fit simulation models, in which case the model may have good fidelity to the data to which it was calibrated but low predictive capability. It is also possible that the model is being used to provide predictions for cases outside of what it was intended to predict during the initial model development process. These concerns make validation an important step in the development of FE models to ensure the credibility of predictions.

The mode shape deflections are used to illustrate the predictive capability of the FE model through Test-Analysis Correlation (TAC). The parameters are set to the mean values of the posterior distributions for comparison to the experimental mode shapes. Figures 16.6 and 16.7 provide a comparison of the experimental and simulation mode shapes, with the simulated shape plotted in red, experimental shape in black, and un-deformed shape in blue. The flapwise and edgewise bending behaviors are decoupled for the graphical and quantitative comparisons (see Sect. 16.3.2) due to noise present in components of the experimentally-obtained mode shapes.

The agreement of mode shapes for the fixed-free FE model is shown in Fig. 16.6. However, the correlation breaks down for the first and third edgewise, bending modes. As shown in the simulation figures and Table 16.2, these modes are dominated by flapwise bending, providing a possible explanation for why noise is introduced into the experimentally obtained edgewise bending of the mode shapes.

The agreement of the mode shapes for the mass-added FE model is shown in Fig. 16.7. An excellent degree of correlation is obtained for the flapwise bending component of the mode shapes, however, the same agreement is not observed for the edgewise bending component. While it is possible that the FE model may not be producing accurate predictions, it is also likely due to the noise in the experimentally obtained mode shapes.

16.3.2 Modal Assurance Criterion

The Modal Assurance Criterion (MAC) is a well-known metric used to quantify the degree to which mode shapes obtained experimentally and computationally are correlated:

$$\text{MAC} = \frac{\left(\Phi_{\text{Test}}^{\text{T}} \cdot \Phi_{\text{Model}}\right)^2}{\left(\Phi_{\text{Test}}^{\text{T}} \cdot \Phi_{\text{Test}}\right)\left(\Phi_{\text{Model}}^{\text{T}} \cdot \Phi_{\text{Model}}\right)}, \tag{16.1}$$

where Φ_{Test} and Φ_{Model} are the measured and simulated mode shapes, respectively, expressed at the same degrees-of-freedom. The MAC is used to identify the corroboration between the experimental mode shapes and deflection shapes predicted by the fixed-free or mass-added FE models. This procedure allows both the equivalence of the modal results in the two experimental set-ups and the quantification of the agreement. Due to limited access to the experimental data, only the first five modes are considered. It is emphasized that the mode shape vectors are not considered during calibration, thus allowing them to be used as a validation data set.

The comparison of the simulated shapes obtained from the fixed-free model and the experimental mode shapes is shown in Fig. 16.8. The lowest diagonal flapwise MAC is 78.3%, corresponding to the second mode shape, which potentially contains noisy measurements of the mode shape vector, as shown in Fig. 16.6. The edgewise modes, however, have significantly low MAC values for the first and third mode, also consistent with the observed noise in Fig. 16.6. The introduction of noise into the edgewise bending of these mode shapes is likely due to the fact that the first and third modes are flapwise modes. When not considering these two modes, the lowest diagonal term in the edgewise MAC is 94.2%, demonstrating an excellent degree of
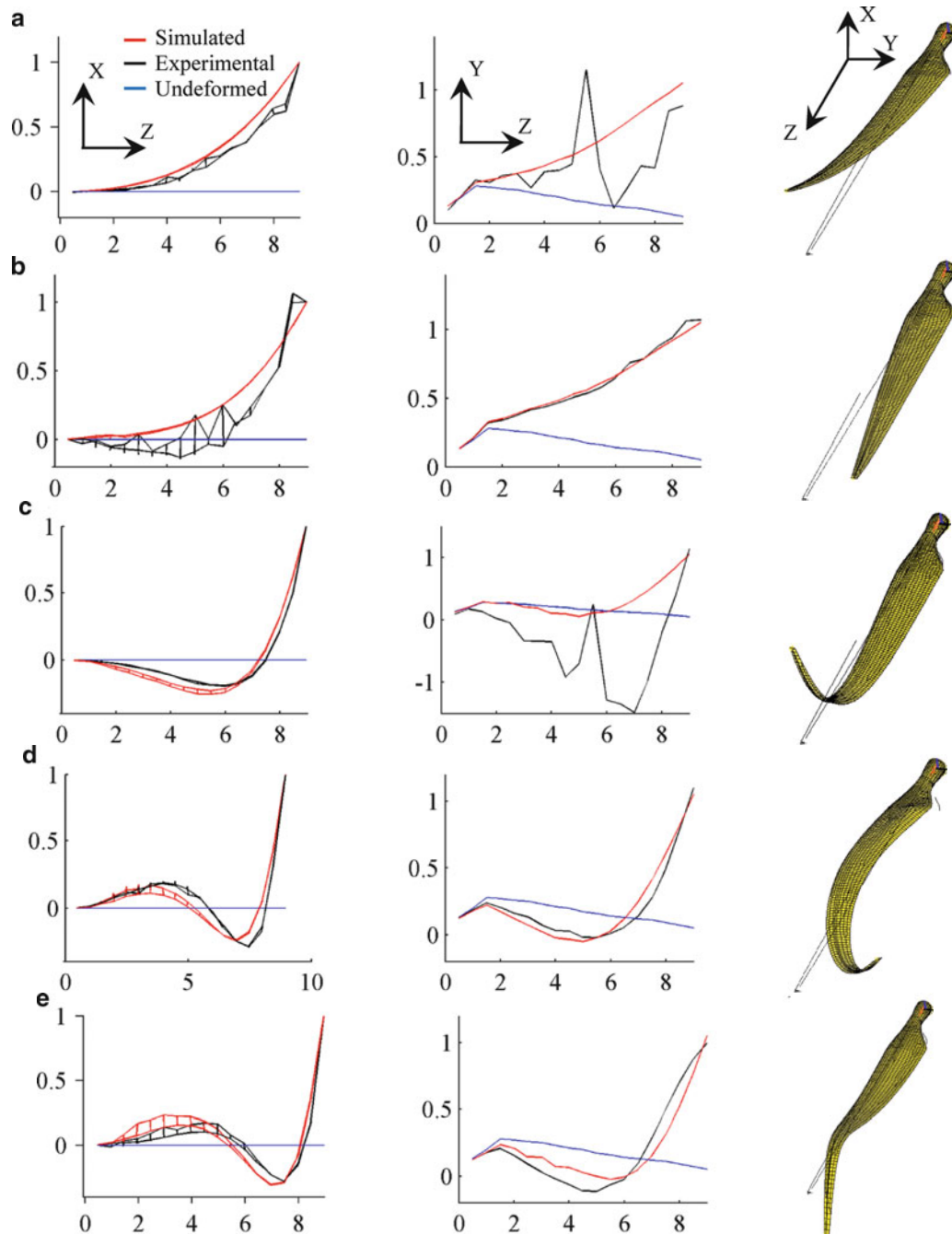
Fig. 16.6 Measured (*black line*) and simulated (*red line*) mode shapes for the fixed-free configuration. (**a**) Flapwise bending (*left*), edgewise bending (*middle*), and simulated deflection (*right*) for the first mode. (**b**) Flapwise bending (*left*), edgewise bending (*middle*), and simulated deflection (*right*) for the second mode. (**c**) Flapwise bending (*left*), edgewise bending (*middle*), and simulated Mode (*right*) for the third mode. (**d**) Flapwise bending (*left*), edgewise bending (*middle*), and simulated mode (*right*) for the fourth mode. (**e**) Flapwise bending (*left*), edgewise bending (*middle*), and simulated deflection (*right*) for the fifth mode (color figure online)

correlation between the experiments and simulation. In addition, the repeated mode shapes that occur when transitioning between flap and lag bending modes can explain the significantly high off-diagonal terms shown in Fig. 16.8.

The MACs obtained from the mass-added model are shown in Fig. 16.9. Despite the minimal calibration performed, the modes obtained demonstrate an acceptable correlation to data. The lowest diagonal MAC for the flapwise bending is
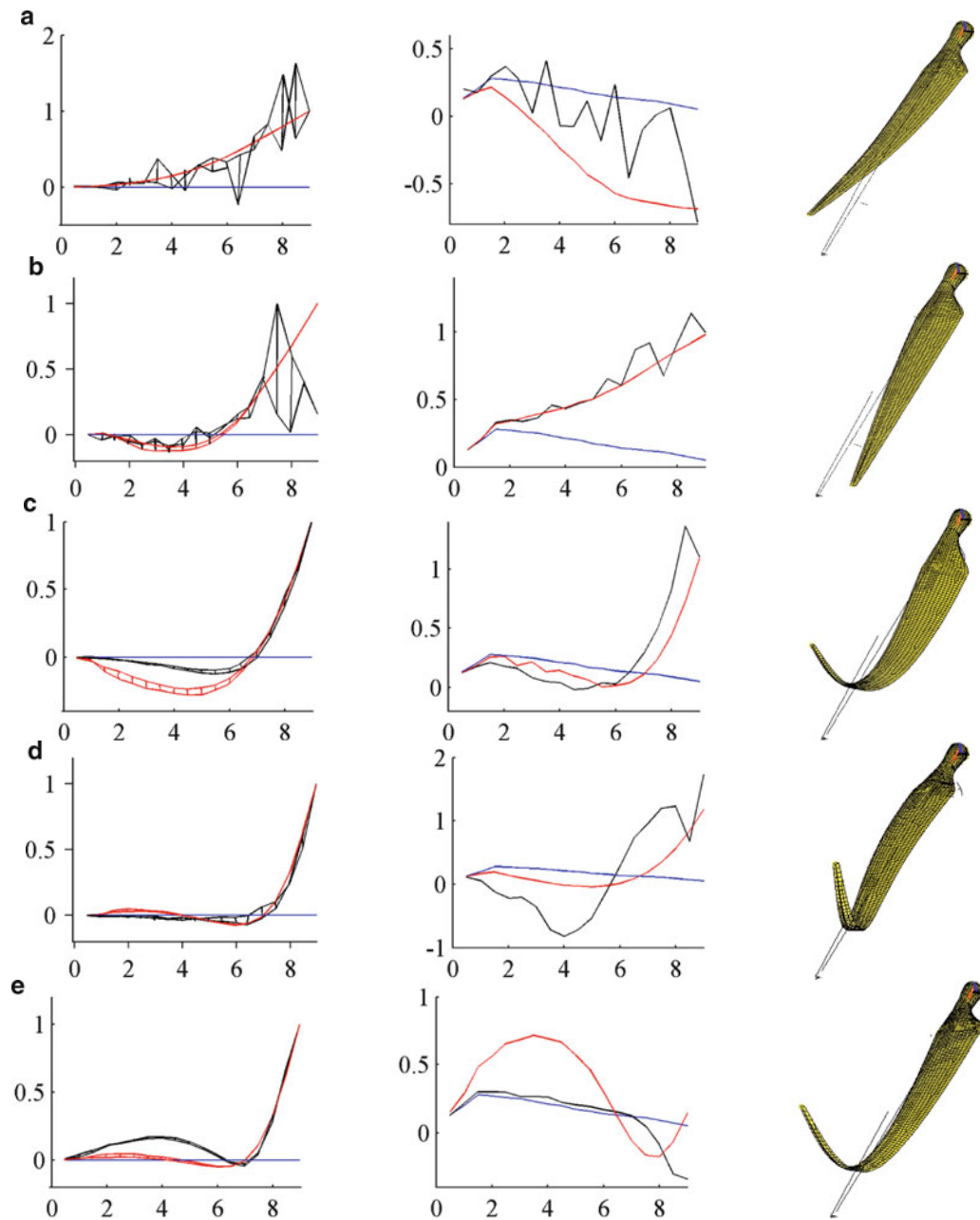
Fig. 16.7 Measured and simulated mode shapes for the mass-added configuration. (**a**) Flapwise bending (*left*), edgewise bending (*middle*), and simulated deflection (*right*) for the first mode. (**b**) Flapwise bending (*left*), edgewise bending (*middle*), and simulated deflection (*right*) for the second mode. (**c**) Flapwise bending (*left*), edgewise bending (*middle*), and simulated deflection (*right*) for the third mode. (**d**) Flapwise bending (*left*), edgewise bending (*middle*), and simulated deflection (*right*) for the fourth mode. (**e**) Flapwise bending (*left*), edgewise bending (*middle*), and simulated deflection (*right*) for the fifth mode

obtained for mode 2, as shown in Fig. 16.9. However, in reference to Fig. 16.7, this mode contains a significant amount of noise and is characterized as a lag-bending mode. Consistent with the graphical representation of the mode shapes in Fig. 16.7, the correlation of the mode shape vectors breaks down for the edgewise, bending component of the mode shapes. This slight disagreement can again be explained by the noise present in the experimentally obtained mode shapes.
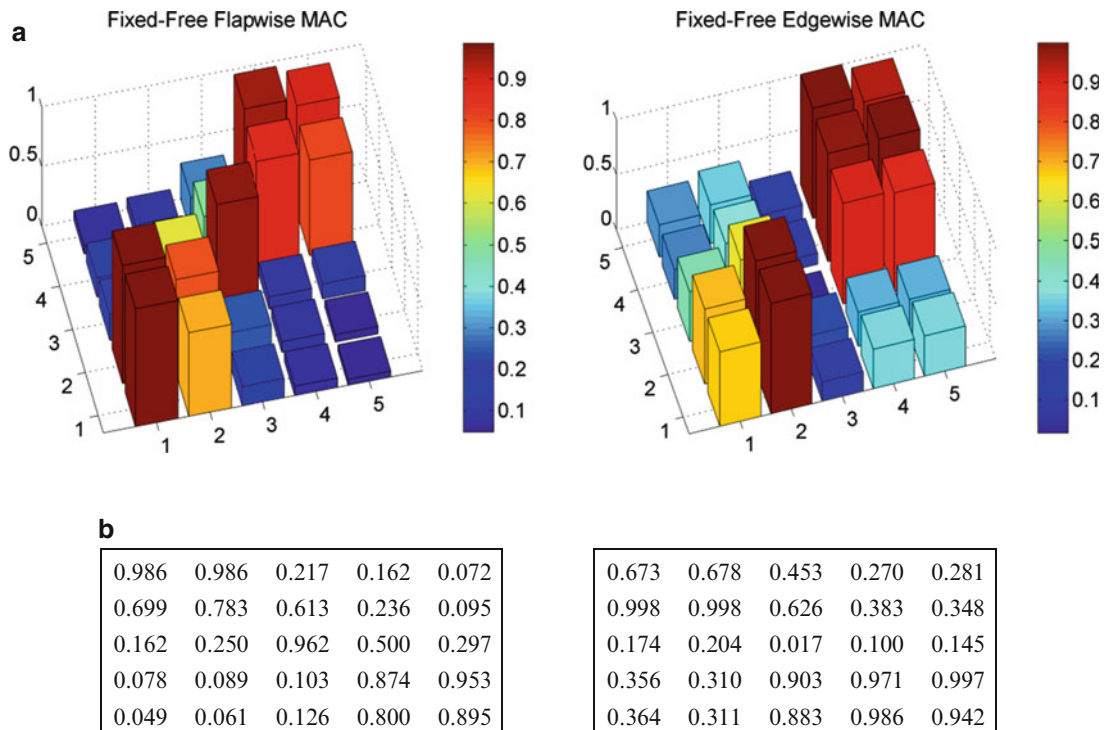
Fig. 16.8 Mode shape MACs for the fixed-free model. (**a**) Graphical comparison of the flapwise MAC (*left*) to the edgewise MAC (*right*).
(**b**) Numerical comparison of the flapwise MAC (*left*) and edgewise MAC (*right*)

0.986	0.986	0.217	0.162	0.072
0.699	0.783	0.613	0.236	0.095
0.162	0.250	0.962	0.500	0.297
0.078	0.089	0.103	0.874	0.953
0.049	0.061	0.126	0.800	0.895

0.673	0.678	0.453	0.270	0.281
0.998	0.998	0.626	0.383	0.348
0.174	0.204	0.017	0.100	0.145
0.356	0.310	0.903	0.971	0.997
0.364	0.311	0.883	0.986	0.942
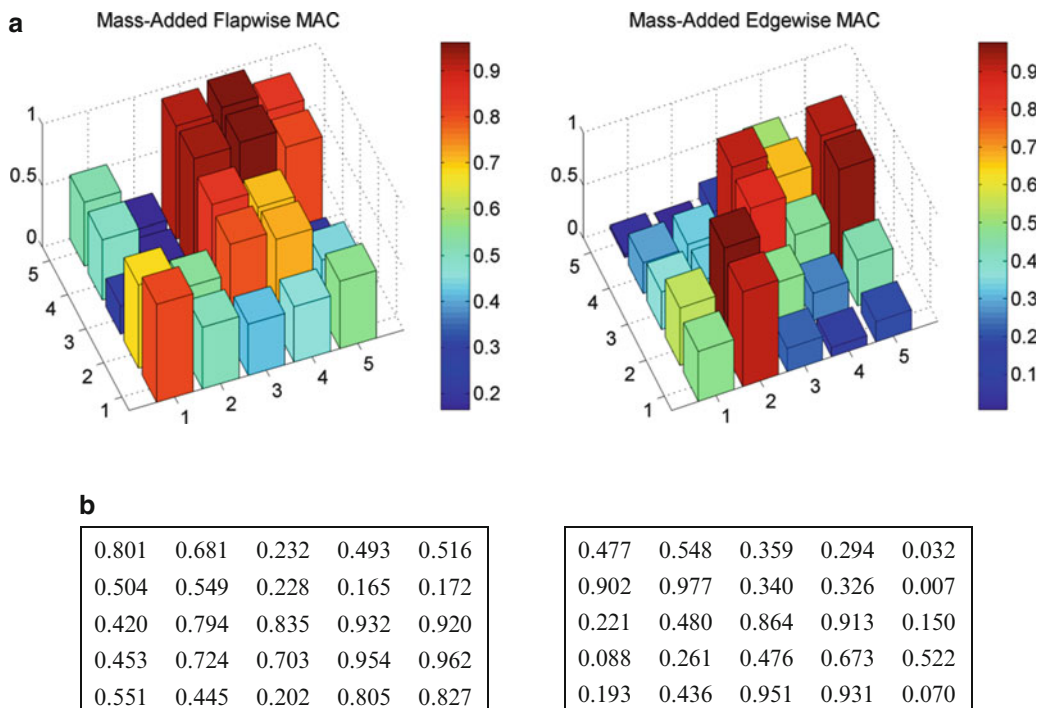
Fig. 16.9 Mode shape MACs for the mass-added model. (**a**) Graphical comparison of the flapwise MAC (*left*) to the edgewise MAC (*right*).
(**b**) Numerical comparison of the flapwise MAC (*left*) and edgewise MAC (*right*)

0.801	0.681	0.232	0.493	0.516
0.504	0.549	0.228	0.165	0.172
0.420	0.794	0.835	0.932	0.920
0.453	0.724	0.703	0.954	0.962
0.551	0.445	0.202	0.805	0.827

0.477	0.548	0.359	0.294	0.032
0.902	0.977	0.340	0.326	0.007
0.221	0.480	0.864	0.913	0.150
0.088	0.261	0.476	0.673	0.522
0.193	0.436	0.951	0.931	0.070

16.4 Conclusion

This manuscript discusses the use of validation datasets to assess the predictive capability of the FE model of the CX-100 wind turbine blade. In an effort to assure the credibility of the FE model despite the use of simplifications during the model development process, **V&V** exercises are applied in the model development process. Natural frequencies identified from experimental modal laboratory tests performed at the NREL are utilized for calibration of the model, and the corresponding mode shape vectors are utilized for validation.

Emphasized in this study is that calibration studies should be limited to reduce the occurrence of over-fitting, in which the simulation is able to accurately replicate data to which it was calibrated but has low predictive power. Furthermore, performing validation exercises provides a means by which the predictive capability of the model is objectively assessed. In this study, validation is carried out by calculating the degree of correlation between mode shape deflections predicted by the model and those measured experimentally. Even though this exercise can be viewed as "weak" validation because the resonant frequencies and mode shape vectors originate from the same identification procedure and, therefore, are not completely independent, the MACs obtained demonstrate that the simplified FE model accurately predicts the mode shape vectors. The study also concludes that it is important to consider the coupling between mode shapes due to the decision to analyze the flapwise and edgewise mode shapes independently.

The quality of the experimental data is called into question in the analysis of mode shape deflections. Figures 16.6 and 16.7 demonstrate undeniable noise in the experimentally obtained mode shapes, likely due to the combination of low-order frequencies at which the blade vibrates and specific choices of experimental procedures. Future studies could improve on the validation presented herein by applying data cleansing filters to minimize the noisy data. Experiments could also be repeated when the quality of the data acquired is questionable. Furthermore, test-to-test and specimen-to-specimen replicates would provide an envelope of expected responses that quantify the overall level of experimental variability and could allow for a more comprehensive TAC.

This study demonstrates the steps necessary to validate FE models, in an effort to assess their predictive capability. This is an important step to establish the credibility of simulation models that incorporate important simplifications for wind energy.

References

1. U.S Department of Energy (2008) 20% wind energy by 2030. U.S. Dept. of Energy, Energy Efficiency and Renewable Energy, Washington, DC
2. Veers PS, Ashwill TD, Sutherland HJ, Laird DL, Lobitz DW, Griffin DA, Mandell JF, Musial WD, Jackson K, Zuteck M, Miravete A, Tsai SW, Richmond JL (2003) Trends in the design, manufacture, and evaluation of wind turbine blades. Wind Energy 6(3):245–259
3. Ciang CC, Lee JR, Bang HJ (2008) Structural health monitoring for a wind turbine system: a review of damage detection methods. Meas Sci Technol 19(12):122001
4. Liu W, Tang B, Jiang Y (2010) Status and problems of wind turbine structural health monitoring techniques in China. Renew Energy 35(7):1414–1418
5. Larsen FM, Sørensen T (2003) New lightning qualification test procedure for large wind turbine blades. In: proceedings of international conference on lightning and static electricity, Blackpool
6. Adams D, White J, Rumsey M, Farrar C (2011) Structural health monitoring of wind turbines: method and application to a HAWT. Wind Energy 14(4):603–623
7. Overgaard LCT, Lund E, Thomsen OT (2010) Structural collapse of a wind turbine blade. Part a: static test and equivalent single layered models. Compos Pt A App Sci Manuf 41(2):257–270
8. Jensen FM, Falzon BG, Ankersen J, Stang H (2006) Structural testing and numerical simulation of a 34m composite wind turbine blade. Compos Struct 76(1–2):52–61
9. Freebury G, Musial W (2000) Determining equivalent damage loading for full-scale wind turbine blade fatigue tests. In: 19th ASME wind energy symposium, Reno
10. Mollineaux MG, Van Buren KL, Hemez FM (2011) Simulating the dynamics of wind turbine blades: part I, model development and verification. In: 13th AIAA non-deterministic approaches conference, Denver (Also, Los Alamos report LA-UR-10-5604)
11. Van Buren KL, Mollineuax MG, Hemez FM (2011) Simulating the dynamics of wind turbine blades, part II, model validation and uncertainty quantification. In: 13th AIAA non-deterministic approaches conference, Denver (Also, Los Alamos report LA-UR-10-5605)

12. Martins M, Perdana A, Ledesma P, Agneholm E, Carlson O (2007) Validation of fixed speed wind turbine dynamic models with measured data. Renew Energy 32(8):1301–1316
13. Snel H (2003) Review of aerodynamics for wind turbines. Wind Energy 6(3):203–211
14. Van Paepegem W, Degrieck J (2001) Modelling strategies for fatigue damage behaviour of fibre-reinforced polymer composites. Eur J Mech Environ Eng 46(4):217–227
15. Jørgensen ER, Borum KK, McGugan M, Thomsen CL, Jensen FM, Debel CP, Søresnen BF (2004) Full scale testing of wind turbine blade to failure – flapwise loading. Risø-R-1392(EN) report, Risø National Laboratory, Denmark
16. Griffith DT, Carne TG, Paquette JA (2008) Modal testing for validation of blade models. Wind Eng 32(2):91–102
17. Tande JOG, Muljadi E, Carlson O, Pierik J, Estanqueiro A, Sørensen P, O'Malley M, Mullane A, Anaya-Lara O, Lemstrom B (2004) Dynamic models of wind farms for power system studies – status by IEA Wind R&D Annex 21. In: European wind energy conference, London
18. Sørensen BF, Jørgensen E, Debel CP, Jensen FM, Jensen HM, Jacobsen TK, Halling KM (2004) Improved design of large wind turbine blades of fibre composites based on studies of scale effects (phase 1) – summary report. Risø-R-1390(EN) report, Risø National Laboratory, Denmark
19. Marín JC, Barroso A, París F, Cañas J (2009) Study of fatigue damage in wind turbine blades. Eng Fail Anal 16(2):656–668
20. Kong C, Bang J, Sugiyama Y (2005) Structural investigation of composite wind turbine blade considering various load cases and fatigue life. Energy 30(11–12):2101–2114
21. Zhang JP, Pan LL (2009) Three-dimensional modeling and aeroelastic coupling analysis for the wind turbine blade. In: World non-grid-connected wind power and energy conference, Nanjing
22. Shokrieh MM, Rafiee R (2006) Simulation of fatigue failure in a full composite wind turbine blade. Compos Struct 74(3):332–342
23. Deines K, Marinone T, Schultz R, Farinholt K, Park G (2011) Modal analysis and structural health monitoring investigation of CX-100 wind turbine blade. In: 29th international modal analysis conference, Jacksonville
24. Kennedy M, O'Hagan A (2000) Predicting the output from a complex computer code when fast approximations are available. Biometrika 87:1–13
25. Higdon D, Gattiker J, Williams B, Rightley M (2008) Computer model calibration using high-dimensional output. J Am Stat Assoc 103:570–583
26. Hemez FM, Ben-Haim Y (2004) The good, the bad, and the ugly of predictive science. In: 4th international conference on sensitivity analysis of model output, Santa

Chapter 17
Towards the Experimental Assessment of *NLBeam* for Modeling Large Deformation Structural Dynamics

Sarah Dalton, Lisa Monahan, Ian Stevenson, D.J. Luscher, Gyuhae Park, and Kevin Farinholt

Abstract With the growth of the wind energy industry, it has become apparent that gear boxes in wind turbines, which link the blades to the generator, tend to wear down faster than anticipated. This phenomenon is not clearly understood; one theory is that existing wind turbine modeling approaches used to design the turbines do not properly account for nonlinearities caused by large amplitude blade deformations. To help understand the effects of geometric nonlinearities, a finite element based code, *NLBeam*, has been developed to simulate structural dynamic responses of wind turbine blades by employing the geometrically exact beam theory. This research focuses on assessing the adequacy of *NLBeam* by comparing simulation to experimental results. Three aluminum blade surrogates with different geometries were tested by applying large amplitude base excitations while assuring the surrogates stayed within the elastic range. A variety of orientations were utilized changing the dynamic characteristics of the surrogates and reflecting actual turbine blade behavior. The results are used to guide future development of *NLBeam* which will be coupled with large scale simulations of wind plants in a Computational Fluid Dynamics based program developed at Los Alamos National Laboratory called *WindBlade*.

17.1   Introduction

In a 2008 report published by the Department of Energy, the possibility of providing 20% of the United States' power supply through wind energy by 2030 was assessed [1]. To accomplish such a feat, it is projected that wind energy production must increase beyond 300 gigawatts (GW) by 2030, an increase of 25 orders of magnitude in 23 years. In order to meet this increase in energy demand, wind plants are expanding in size and requiring the optimization of turbine placement to most efficiently produce power for a given wind input. Concurrently, individual wind turbines are manufactured larger and with higher capacities. Turbine blade lengths are continually increasing in order to more efficiently extract power from wind, however, a corresponding increase in displacement and, even more importantly, large magnitudes of rotation associated with deformation also occur. Such deformations, for example, blade torsion, influence angle-of-attack and ultimately affect wind flow at the plant scale in a coupled manner. To model the wind and turbine-turbine interactions at a plant scale, Los Alamos National Laboratory has developed a computational fluid dynamics (CFD)-based wind plant simulation code called *WindBlade* [2].

To realize such production, it is imperative that wind power production not only increase in capacity, but also become more economically viable. A clear area to reduce wind energy costs is to increase wind turbine reliability. Wind turbines include multiple assemblages which interact and transfer loads to the foundation. Evidence has been found indicating certain

S. Dalton
Clemson University, Clemson, SC 29634, USA

L. Monahan
University of Pittsburgh, Pittsburgh, PA 15260, USA

I. Stevenson
Rose-Hulman Institute of Technology, Terre Haute, IN 47803, USA

D.J. Luscher (✉) • G. Park • K. Farinholt
Los Alamos National Laboratory, Los Alamos, NM 87545, USA
e-mail: djl@lanl.gov

assemblies, such as the gearbox, are plagued by premature failures [3]. The cause is not clearly understood; one theory is that existing wind turbine modeling approaches do not properly account for nonlinearities caused by large amplitude blade deformations. Consequently, the actual loads transmitted through the wind turbine blades are higher than anticipated.

With the growing desire to harvest wind power at increased demand levels, the length of turbine blades and the number of turbines erected in wind plants is ever increasing. Modeling these plants to determine the most efficient layout is difficult due to the complex nature of aerodynamic loading on turbines, mainly due to variable inflow conditions as shown by Robinson et al. [4]. The deeper the wind penetrates into the plant, the more turbines it interacts with, creating noise effects on the wind flow. The noisy wind conditions imposed upon downwind turbines complicate both the modeling of structural loading on the turbines and the modeling of their ability to capture energy [5]. LANL's *WindBlade* aims to model the interactions of wind and turbines [2]; however, it currently assumes rigid body dynamical motion of the turbine rotors. This simplification does not account for the change in angle of attack with respect to the wind when blades deform and rotate. Furthermore, the actual loads being transmitted throughout the wind turbine system are not computed, thus losing available insight on the influence of the dynamic wind field on the structural loading. Essentially, key aspects of the aeroelastic interaction between the wind and wind turbines are not captured. To improve this plant scale simulation capability, a more complete representation of wind turbine structural dynamics must be implemented into *WindBlade*.

One such approach has been developed by the National Renewable Energy Laboratory (NREL) leading to the implementation of a code coined FAST (Fatigue, Aerodynamics, Structures, and Turbulence) [6, 7]. FAST utilizes equations of motion for the modeling of complex dynamic systems derived from Kane's method. This theory differs from other methods for obtaining equations of motion such as Lagrange's method, D'Alembert's method, and Newton-Euler's method, in that Kane's method parameterizes the motion of deformation into decoupled orthogonal modes [8, 9]. In order to model flexible elements, FAST utilizes linear modal characterization assuming small deformations [7]. This approach can be inauspicious in that (1) the small deformation assumption is often not held; inducing geometric nonlinearities and (2) the reliability of the model depends on the validity of mode shapes over a range of operating conditions which are input into FAST from a separate code [6].

Another approach is to develop detailed, high fidelity three-dimensional finite element (FE) models to couple with the fluid–structure interactions of wind turbine blades [10–12]. These high fidelity models are advantageous in modeling both the spatial and temporal multi-scale physics throughout the entire system over a given time period. However, the computational costs associated with running simulations of this level of sophistication preclude application at the plant scale as accomplished by *WindBlade*.

An alternative approach, as employed in this paper, strikes a balance between accurately representing generally nonlinear behavior with the computational costs when considered as an integral part of a plant-scale simulation code. In particular, this research uses the geometrically exact beam theory such as developed by Reissner [13, 14], Simo [15], Simo and Vu-Quoc [16], Jelenic and Crisfield [17], for example. The use of this method is advantageous in comparison to those modeling techniques of rigid body systems, linear modal representations, or high fidelity modeling due to its ability to handle the nonlinear problem in a computationally efficient manner [17, 18]. In the context of this paper, it is important to note that *geometrically exact* implies the treatment of finite rotation of each cross section as exact, obviating any small-angle approximations [19]. The geometrically exact beam theory exploits the slenderness of beams, allowing for dimensional reduction, i.e., the simplification of a geometrically nonlinear 3D problem by decoupling the problem into a linear 2D cross-sectional analysis and a nonlinear beam problem along a reference axis [19]. This approach preserves geometric nonlinearities in a computationally tractable manner when representing beam deformations [17–19].

A finite element code, *NLBeam*, was developed to implement this theory for application to modeling coupled fluid–structure dynamics within *WindBlade*. The research presented in this paper aims to initiate validation of that code by (1) developing an experimental methodology to isolate geometric nonlinearity in structural dynamics of flexible beams, and (2) assess the predictive modeling capabilities of *NLBeam* in capturing large amplitude blade dynamics by comparing experimental results with *NLBeam* simulations for dynamically driven surrogate blades. Moreover, a secondary objective aims to contribute to a body of evidence which can be used to aid in the future development and validation of *NLBeam*.

17.2 Geometrically Exact Beam Theory

NLBeam employs the geometrically exact beam theory to represent the geometric nonlinearity associated with generally large rotations. Geometrically exact beam theory dates back to the pioneering work of Reissner and Simo and Vu-Quoc and has been extensively developed over the last three decades [14–19] and applied, for example, to helicopter rotor dynamics [18]. The theory is only briefly summarized here.
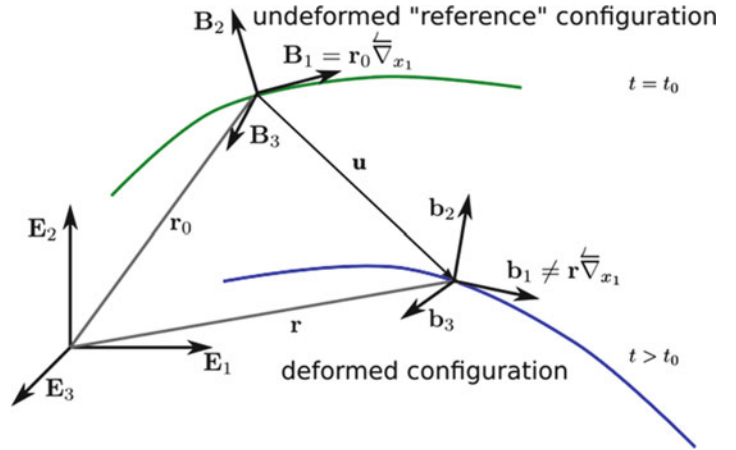
The kinematic description underlying the geometrically exact beam theory is essentially that shown in Fig. 17.1. The green curve in this figure depicts a beam reference axis in its undeformed configuration whilst the blue curve represents the same reference axis in a deformed configuration. Each point along the reference axis is located within the fixed inertial frame, $\mathbf{E}_i$, by the vector, $\mathbf{r}_0$. Associated with each point along the reference axis is a cross section whose orientation is defined by the orthogonal triad of unit vectors $\mathbf{B}_i$. Note that the orientation of $\mathbf{B}_i$ within the fixed inertial frame is defined by the initial sectional rotation tensor, $\mathbf{\Lambda}_0$, i.e., $\mathbf{B}_i = \mathbf{\Lambda}_0 \cdot \mathbf{E}_i$. At some later time, $t > t_0$, the beam reference axis has deformed into a different configuration where each point previously located at $\mathbf{r}_0$ in the undeformed configuration is now located by the vector $\mathbf{r}$ in the inertial frame $\mathbf{E}_i$. In addition, the cross section associated with a particular point along the reference axis has an orientation defined by the orthonormal basis, $\mathbf{b}_i$, which differs from $\mathbf{B}_i$ according to $\mathbf{b}_i = \tilde{\mathbf{\Lambda}} \cdot \mathbf{B}_i$. Here, $\mathbf{\Lambda}_0$ describes initial orientation, $\tilde{\mathbf{\Lambda}}$ is the rotation of a cross-section due to deformation, and $\mathbf{\Lambda}$ is the total rotation aligning the fixed inertial basis, $\mathbf{E}_i$, with the deformed beam cross section axes $\mathbf{b}_i$, i.e., $\mathbf{b}_i = \mathbf{\Lambda} \cdot \mathbf{E}_i$ where $\mathbf{\Lambda} = \tilde{\mathbf{\Lambda}} \cdot \mathbf{\Lambda}_0$.

A key ingredient of the geometrically exact beam theory is that the position of any point in the three-dimensional continuum body (beam in this case) can be expressed as

$$\mathbf{R}_0 = \mathbf{r}_0 + \mathbf{\Lambda}_0 \cdot \boldsymbol{\xi}_0 \tag{17.1}$$

or

$$\mathbf{R} = \mathbf{r}_0 + \mathbf{u} + \mathbf{\Lambda} \cdot \boldsymbol{\xi}_0 \tag{17.2}$$

in the undeformed and deformed configurations, respectively, where contributions due to cross-sectional warping are omitted (Cf. Hodges, et al. [19] for a more general representation accounting for warping) and the vector, $\boldsymbol{\xi}_0$, expresses the cross-sectional position $\{0, x_2, x_3\}$ within the reference frame $\mathbf{B}_i$. This enables a continuum displacement field, i.e., $\mathbf{U} = \mathbf{R} - \mathbf{R}_0$ from which classical continuum strain measures can be computed. An important point is that the continuum motion of every point in the three dimensional beam is tracked by a total of six kinematical parameters, namely, three vector components of the reference axis displacement, $\mathbf{u}$, and three rotation vector parameters, $\boldsymbol{\theta}$, comprising the sectional rotation, $\tilde{\mathbf{\Lambda}}(\boldsymbol{\theta})$.

In this paper, isotropic Hooke's law describes the elastic constitutive response such that the continuum stresses, $\boldsymbol{\sigma}$, are related to strains, $\boldsymbol{\varepsilon}$, by $\boldsymbol{\sigma} = \lambda \operatorname{Tr}[\boldsymbol{\varepsilon}] \mathbf{I} + 2\mu \boldsymbol{\varepsilon}$ where μ is the elastic shear modulus and the Lamé constant related to Young's modulus, E, and Poisson ratio, v, as indicated in (17.3), I is the second order identity tensor, and $\operatorname{Tr}[*]$ denotes the trace of *.

$$\mu = \frac{E}{2(1+v)} \quad \text{and} \quad \lambda = \frac{vE}{(1+v)(1-2v)} \tag{17.3}$$

Note, however, that *NLBeam* employs a generally anisotropic Hooke's law suitable for representation of composite cross-sections. The stresses thus obtained allow the strong form of conservation of momentum within the 3D continuum to be

expressed as $\nabla \cdot \boldsymbol{\sigma} + \rho \mathbf{f}_b = \rho \ddot{\mathbf{U}}$ where ∇ is the divergence operator, ρ the material mass density per unit volume, $\mathbf{f}_b$ is a body force per unit mass, for example due to gravity, and $\ddot{\mathbf{U}}$ is the acceleration of a given material point. The strong form of the conservation of momentum is integrated across the beam cross-section to get a suitable weak form in terms of generalized sectional forces and strains. Likewise, the local strain energy can be integrated across a cross-section yielding an expression for the strain energy, W, at each point along the beam reference axis in terms of cross-sectional strains, $\boldsymbol{\gamma}$, and curvatures, $\boldsymbol{\kappa}$, i.e.,

$$W = \frac{1}{2}\left\{\begin{matrix}\boldsymbol{\gamma}\\\boldsymbol{\kappa}\end{matrix}\right\}^{T}[\mathbf{C}]\left\{\begin{matrix}\boldsymbol{\gamma}\\\boldsymbol{\kappa}\end{matrix}\right\} \tag{17.4}$$

where the sectional strains and curvatures are computed by

$$\boldsymbol{\gamma} = \boldsymbol{\Lambda}^T \mathbf{r}' - \mathbf{b}_1 \quad \text{and} \quad \boldsymbol{\kappa} = \boldsymbol{\Lambda}^T \boldsymbol{\Lambda}' \tag{17.5}$$

and' denotes differentiation with respect to the coordinate along the undeformed beam reference axis, x_1. The components of the sectional strain vector comprise axial strain and transverse shear strains in two directions. The curvature vector comprises the torsional rate of twist about the beam reference axis as well as bending curvature about the other two axes. Differentiating the cross-sectional elastic strain energy of (17.4) with respect to the sectional strains and curvatures yields the sectional forces and moments, respectively, i.e.,

$$\mathbf{F}_N = \frac{\partial W}{\partial \boldsymbol{\gamma}} \quad \text{and} \quad \mathbf{F}_M = \frac{\partial W}{\partial \boldsymbol{\kappa}} \tag{17.6}$$

For the case of a homogeneous cross-section, as studied in this paper, the cross-sectional elastic matrix is simply, $[\mathbf{C}] = \text{Diag}[EA, GA_2, GA_3, GJ, EI_2, EI_3]$, where Diag indicates a diagonal matrix, A is the area of the cross section, I_2 and I_3 are geometric moments of inertia about the corresponding section axes, J is the polar geometric moment of inertia, and A_2 and A_3 are effective shear areas along the corresponding section axes. Accordingly the sectional forces and moments are simply

$$\begin{matrix} F_{Na} = EA\,\gamma_1, & F_{Nv2} = GA_2\,\gamma_2, & F_{Nv3} = GA_3\,\gamma_3 \\ F_{Mt} = GJ\,\kappa_1, & F_{Mb2} = EI_2\,\kappa_2, & F_{Mb3} = EI_3\,\kappa_3 \end{matrix} \tag{17.7}$$

where F_{Na}, F_{vi} are the axial and shear forces, respective, and F_{Mt}, F_{Mbi} are the axial torque and bending moments, respective. Equation (17.7) reflects a linear force-to-strain relationship in the local section coordinate system along the beam; however, the rotation used in transforming into fixed inertial frame is inherently nonlinear (as all rotations are strictly speaking).

The strong form of conservation of momentum is weakened and then implemented into a numerical form (*NLBeam*) using a Petrov-Galerkin finite element discretization in space. The weak form of the equations of motion are expressed as

$$R_I = R_I^m + R_I^d - R_I^e = 0 \tag{17.8}$$

where the total residual, R_I, at node I, is expressed in terms of contributions from material stress, R_I^m, inertia, R_I^d, and external forces, R_I^e, as computed by

$$\begin{aligned} R_I{}^m &= \int_0^L \begin{bmatrix} N_I'I & 0 \\ N_I'\tilde{r}' & N_I'I \end{bmatrix} \left\{ \begin{matrix} \boldsymbol{\Lambda} \cdot \mathbf{F}_N \\ \boldsymbol{\Lambda} \cdot \mathbf{F}_M \end{matrix} \right\} dx_1 \\ R_I{}^d &= \int_0^L N_I(x_1) \left\{ \begin{matrix} \rho A \ddot{u} \\ \tilde{\mathbf{W}} \mathbf{J}_\rho \mathbf{W} + \mathbf{J}_\rho \mathbf{A} \end{matrix} \right\} dx_1 \\ R_I{}^e &= \int_0^L \left\{ \begin{matrix} N_I \rho A\, \mathbf{f}_b \\ 0 \end{matrix} \right\} dx + \sum_k N_I(x_1{}^k) \sum \begin{bmatrix} \boldsymbol{\Lambda} \cdot \bar{\mathbf{f}}_k \\ \boldsymbol{\Lambda} \cdot \bar{\mathbf{m}}_k \end{bmatrix} \end{aligned} \tag{17.9}$$

In (17.9), $\mathbf{W}$ and $\mathbf{A}$ are the angular velocity and acceleration, respectively, of a point on the beam reference axis, $\mathbf{J}_\rho$ is the cross-sectional inertia tensor (a cross-sectional property), and $\bar{\mathbf{f}}$ and $\bar{\mathbf{m}}$ are concentrated forces and moments, respectively. Additionally, the elemental shape functions, N_I, have been introduced and are quadratic Lagrange interpolating polynomials

in *NLBeam*, thus each element comprises three nodes. Integration of these terms is carried out using (reduced) two point Gauss quadrature over the length of each element. Equation 17.8 reflects a nonlinear system of equations whose independent variables are the incremental nodal degrees of freedom, $\Delta\mathbf{u}$ and $\Delta\boldsymbol{\theta}$, and is solved using a Newton–Raphson iterative scheme.

17.3 Experimental Approach

Toward the overarching research goal, experimental procedures were performed with the role of providing data for comparison to numerical results from *NLBeam* simulations. It was intended that surrogate beams be driven into large, i.e., nonlinear, deformation. The experimental effort consisted of imposing base excitations on three blades of differing geometry in three different orientations under varying excitation amplitudes in order to create and observe the desired nonlinearities.

To accomplish the experimental goal of driving and identifying geometrically nonlinear deformation, specific test specimens were designed with differing geometries. Each geometry consists of a different tapered width profile and a constant thickness of 0.32 cm selected for practical reasons during fabrication, as seen in Fig. 17.2. These width profiles were selected in order to evaluate *NLBeam's* modeling capabilities for nonprismatic beams, a purely geometric consideration. To minimize experimental variability and model uncertainty the specimens were fabricated of Aluminum 6061. Although typical wind turbine blades are made of optimized fiber reinforced composite lay-ups, aluminum was chosen due to its well-documented homogenous, isotropic material properties.

The physical experimental setup consists of a surrogate blade specimen fixed to a base, replicating a fixed-free cantilever beam which is fairly representative of operating turbine-blade boundary conditions. The base is then bolted to a VTS Model VG 100-6 shaker, suitable for driving the desired base excitations. Each specimen was excited in the flap-wise bending direction in three different orientations, viz. horizontal-flat, horizontal-edge, vertical, as seen in Fig. 17.3, to explore geometric nonlinearities due to differing gravitational loads. This is a relevant response condition because wind turbine blades experience changing stress fields which are attributed to varying gravitational loading throughout their rotations. A small mass of approximately 50 g was attached to the end of each surrogate blade as seen in Fig. 17.4. The mass served to exaggerate geometric nonlinearities observed in the experimental procedures; however, the additional inertial forces induced rocking motion of the base. This rocking complicated the boundary conditions input to the model.

Excitation signals used to dynamically drive the system originate from a *Dactron* data acquisition system which sends the desired excitation voltage through a power amplifier and, ultimately, to the shaker which drives the surrogate blade. Excitation signals used comprise of (1) random and (2) sine dwell. *Dactron* configurations for each excitation are shown below in Table 17.1. Random base excitations were used to generate a comprehensive baseline frequency response function (FRF) to identify natural frequencies and screen for nonlinear responses. Sine dwells were then utilized to focus on specific frequencies for generating data that could easily be compared to simulation results. Sine dwell excitation was advantageous to this research in that the degree of nonlinearity of response data can be easily measured using a harmonic distortion metric, represented in (17.10), where a_n represents the magnitude of the response at the nth harmonic. A large value for this metric implies a highly nonlinear system.

$$H_D = \frac{1}{a_1} \sqrt{\sum_n a_n^2} \tag{17.10}$$
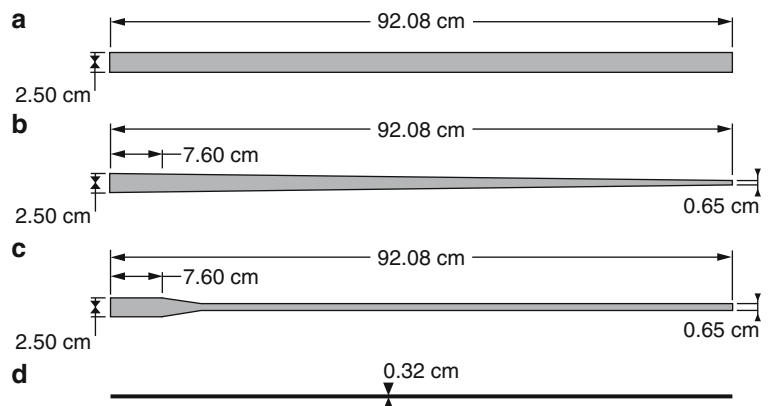
Fig. 17.2 Geometry of the surrogate blade test specimen used in experiments; (**a**) non-tapered, (**b**) linear taper, (**c**) radiused taper, (**d**) uniform thickness profile for all geometries
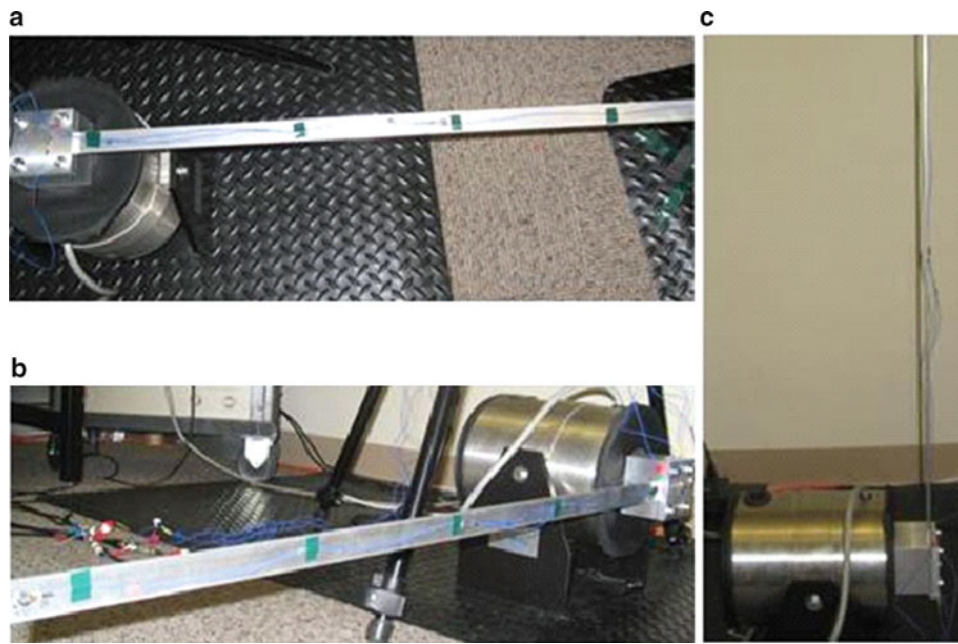
Fig. 17.3 Three blade orientations investigated; (**a**) horizontal flat (**b**) horizontal edge (**c**) vertical

Fig. 17.4 Mass attached at tip to help drive geometrically nonlinear deformation

Table 17.1 Dactron settings for each excitation type		Cutoff frequency	Data points	Spectral lines	Other
	Random	250	4,096	1,600	0.5 Vrms
	On-resonance sine	500	4,096	1,600	57 Hz
	Off-resonance sine	250	4,096	1,600	35 Hz
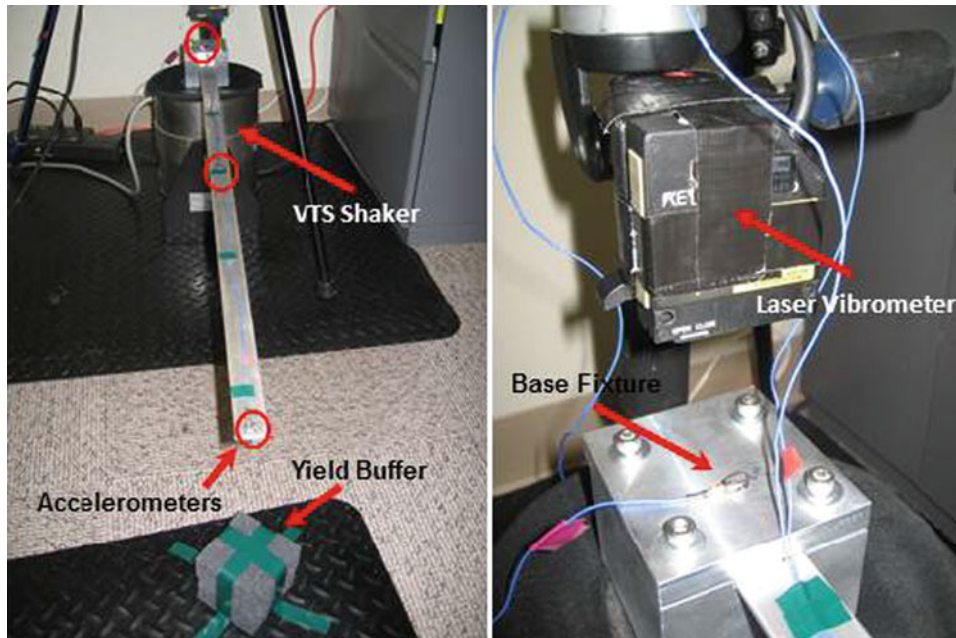
Fig. 17.5 Experimental setup

Because the Dactron system restricts the total number of data input channels to four, careful channel allocation and sensor placement was important. To aid in this task, a solid/continuum finite element model of one blade geometry was developed to estimate representative modal characteristics using the commercial finite element software, *Abaqus*. The preliminary mode shapes were used to aid sensor placement on the test specimens and also provide some frame of reference for specifying excitation signal parameters. Two accelerometers were placed on the base fixture, one on the back end and one on the front end in order to capture any base rocking, one accelerometer is placed approximately at the midspan of the beam, and one accelerometer is placed near the beam's tip, as seen in Fig. 17.5. Early experiments collected base displacement data from a laser vibrometer (as shown in Fig. 17.5), but this approach was aborted because (1) it could not capture the rotation of the base and (2) the data contained prohibitive levels of noise for use as boundary conditions for input to a numerical model.

17.4 Numerical Modeling

Toward the goal of establishing the predictive capability of *NLBeam* and highlighting nonlinear structural dynamic response when present, two different FE modeling approaches were utilized to simulate the experiments. The two modeling approaches used were (1) a geometrically nonlinear model using *NLBeam* and (2) a linear modal superposition model using the commercial FE modeling package *Abaqus*. The role of the nonlinear model is to demonstrate acceptable agreement between *NLBeam* and experimental results, while the use of a linear model aims to highlight geometric nonlinearities in observed response. In both cases, simulation output results are directly compared with experimental data to substantiate quantitative and qualitative assessments.

To model surrogate blades, *NLBeam* uses quadratic beam elements based on the geometrically exact beam theory as described above. Each node includes six degrees of freedom (DOF); three translations and three rotations in (and about, respectively) the global x, y, and z directions. At each elemental integration point along the length of the beam, two-dimensional cross-sectional properties, shown in Table 17.2, are defined via a sectional properties pre-processor developed as part of this work.

The linear superposition model employs the *Abaqus* beam element, *B32*, which is a quadratic beam element in space, also accounting for six degrees of freedom at each node. Rectangular beam cross-section properties are calculated directly within *Abaqus* from sectional widths and thicknesses corresponding to the center node of each element given as input. The response data from the modal superposition model reflects a superposition of the first four modal responses accounting for each mode's participation factor.

Table 17.2 Material and sectional property relations used in pre-processor

Parameter	Symbol	Value
Young's modulus	E	69 GPa
Shear modulus	G	26 GPa
Density	ρ	2.70 g/cm^3
Area	A	wh
Torsion constant	J	$hw^3\left(\frac{1}{3} - 0.21\frac{w}{h}\left(1 - \frac{w^4}{12h^4}\right)\right)$
Moments of inertia (y-dir)	I_y	$\dfrac{wh^3}{12}$
Moments of inertia (z-dir)	I_z	$\dfrac{hw^3}{12}$

Boundary condition input data (displacement/acceleration time histories) for both models were generated from base accelerometer data measured in experiments. *NLBeam* is limited to accept only displacement (rather than acceleration) time histories as boundary conditions; therefore the measured experimental acceleration data was converted into suitable displacement data. Rocking (rotation about global z-axis) of the base, attributed to the addition of a tip mass, was observed in experimental data. This feature of the boundary conditions was significant enough that it was necessarily accounted for in a manner ensuring both the translational and rotational base accelerations were preserved.

To achieve this, assumed rigid body translational and angular acceleration are computed from both accelerometers on the base according to (17.11), where a_b is translational acceleration, α_b is rotational acceleration, and a_1, a_2 are the measured accelerations from two sensors on the assumedly rigid base.

$$a_b = \frac{a_1 + a_2}{2} \quad \alpha_b = \frac{a_1 + a_2}{r_{12}} \tag{17.11}$$

These rigid body accelerations were high-pass filtered, H_h, and doubly integrated to obtain displacement and rotation data, i.e.,

$$u_b = \iint H_h(a_b)dt \quad \theta_b = \iint H_h(\alpha_b)dt \tag{17.12}$$

Finally, pure translational displacements applicable to nodes on the base are calculated according to (17.13) and low pass filtered, H_l, to reduce high frequency noise. The key reason for calculating displacement in this manner is to preserve relative phase information between translational displacement and angular rotation that is essential for parity of simulations and experiment.

$$u_1 = H_l\left(u_b + \frac{r_{12}}{2} * \theta_b\right) u_2 = H_l\left(u_b - \frac{r_{12}}{2} * \theta_b\right) \tag{17.13}$$

The result of this scheme is highlighted in Fig. 17.6 where a representative measured experimental acceleration time history is compared with the acceleration time history as computed by *NLBeam* given the displacement input boundary conditions. It is clear from this figure that the angular and translational motion including the relative phase is preserved.

The nominal *NLBeam* model consisted of 24 elements, of which, one element corresponded to the relatively rigid base holding the surrogate blade. This element was effectively stiffened to reflect the rigid body motion of the base fixture. The base displacement input time history computed according to (17.13) was specified as nodal boundary conditions for the first and last node of this "fixture-base-beam" element. A point mass was included at the tip node corresponding to the experimental tip mass. Simulation results from the *NLBeam* model used for comparison to experiment in this paper come from a node located 86 cm from the base of the blade corresponding to the location of tip accelerometer. As suggested by (17.9), *NLBeam* directly includes contributions from gravitational forces as well as the nonlinear geometric stiffening due to stresses in the beam. Accordingly, simulations were conducted using the *NLBeam* model for all three surrogate blade geometries across all three orientations to compare to assess the influence of the orientation with respect to gravity.
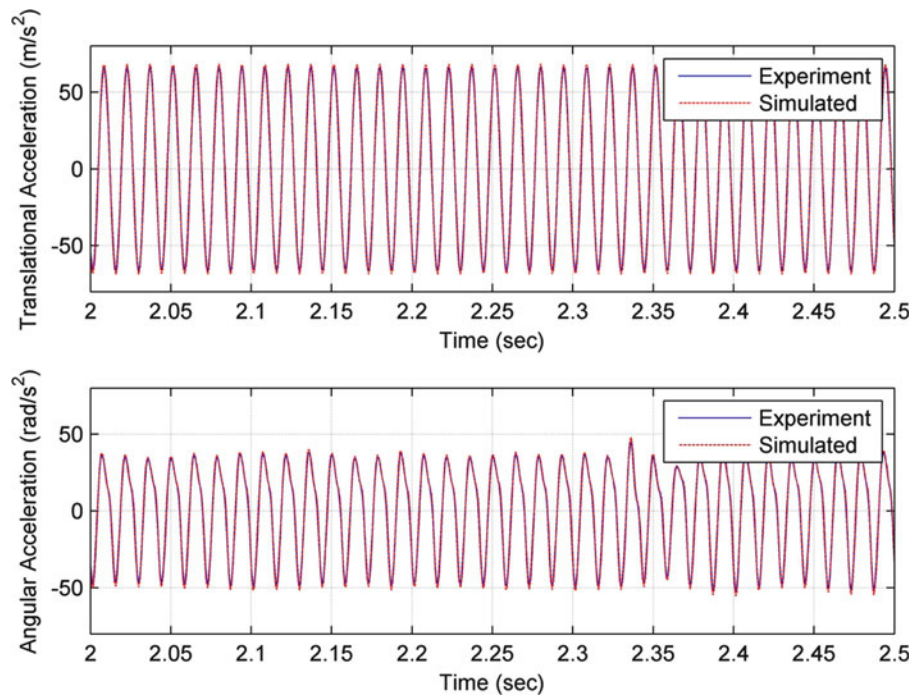
Fig. 17.6 Comparison of translational *(top)* and rotational *(bottom)* acceleration at the base between *NLBeam* and experiment

Much consideration was given to ensuring that parameters and boundary conditions for the modal superposition model, utilizing *Abaqus,* were as close to those employed in *NLBeam* as the software would allow, in order for meaningful comparisons. Thus, the nominal modal superposition model consisted of 23 elements with one element allocated to the base fixture of the experimental setup. Similar to the *NLBeam* case, this element was stiffened in order to ensure the assumed rigid body motion boundary condition; however, since acceleration time histories can be specified directly as boundary conditions within this FE code, base accelerometer data measured in experiments were used as excitation sources for the linear superposition model. Likewise, a point mass corresponding to the mass used in experimentation was applied to the final node in the model. All data extracted from the modal superposition model and presented herein are from a node located 86 cm from the base of the blade which corresponds to the location of the tip accelerometer. The surrogate's response across all three orientations was simulated using a gravitational preload in an effort to explore the effects of gravity on a linear (perturbation) model.

17.5   Results and Discussion

Ultimately, it is desired to experimentally validate *NLBeam* over a range of response regimes including behavior that exhibits varying levels of geometric nonlinearity. Achieving such conditions in this study proved to be difficult with the available experimental hardware and code capabilities. Physical restraint of the shaker system was difficult under cases of large deformations because of the large accelerations and resulting base moments associated with such motion. The base moments also induced the aforementioned rotations (rocking) of the base of the blade where it affixes to the shaker. Furthermore, the shaker itself has internal physical stops which limited the amplitude of base displacement. In light of these experimental limitations, the most efficient manner to drive large deformations was to operate the shaker near a resonant frequency of the beam. However, simulating this behavior near resonance was complicated because the model did not directly include physical damping. Accordingly, this section compares simulation and experiment results for near resonance and off resonance cases and, perhaps more importantly, discusses improvements in both experiment and model that can be used in the future.

17.5.1 Fixture Base Rotation Complexities

As was discussed previously, a mass of approximately 50 g was added to the tip of the surrogate blades to enhance any nonlinearity in the response of the test specimen. The addition of this mass increases the inertial loading, in turn, causing the "rocking" motion of the base. This rocking is not driven by the shaker, per se, but is permitted due to the compliance of that system. The kinematic motion of this rocking behavior is captured and input as boundary conditions to the model as discussed in Sects. 17.3 and 17.4. Figure 17.7 shows a representative normalized power spectral density (PSD) of an experimental case prior to and following the addition of the 50 g mass. The tip acceleration of the surrogate blade with tip mass contains several harmonics of the fundamental excitation frequency (57 Hz in this case), whereas the signal from the case without a tip mass does not. Presumably this difference is a manifestation of nonlinearity in the system response which is enhanced by adding the mass.

However, the source of nonlinearity in this experimental configuration cannot be isolated to the surrogate blade response and it is believed to be attributable, as least in part, to a nonlinear interaction between the shaker and the test specimen. This coupling cannot be directly accounted for in the simulations because they model the surrogate blade only, i.e., there is not a direct model of the shaker system or its interface with the surrogate beam. With the objective of model validation this is viewed as a limitation of the experiment (in permitting such induced rotations) rather than the model, as there is no desire to develop a physical model of the shaker system.

It is interesting that the induced rocking behavior is characteristic of a bi-stable phase orientation between the rigid base translation and base rotation. Figure 17.8 illustrates this behavior as follows. A representative experimental case (non-tapered beam, horizontal-flat orientation, with a normalized input amplitude of 2.0 at 57 Hz), was repeated ten times. The acceleration time histories measured by two accelerometers located on the shaker base fixture are plotted in Fig. 17.8. The rear-most accelerometer data appears relatively repeatable and is plotted in blue with sinusoidal amplitude of approximately 4 m/s^2. Data from the forward-most accelerometer separates into two distinct categories of response classified by their respective amplitudes, i.e., approximately 2 and 6 m/s^2. This indicates a base rotation that falls into one of two bistable operational modes; one is in phase with the base translation and contributes additively to the forward-most accelerometer and the other mode is 180° out of phase with the base translation, thus contributing subtractively to the forward-most accelerometer.

As suggested in Sect. 17.3, one measure of system nonlinearity is the harmonic distortion of an output signal observed when the system's input is a pure sinusoid at a single frequency. The relevance of this metric is revealed by considering that a nonlinear model, M, relating inputs, x, to outputs, y, can be expressed in a power series. If x is a pure sinusoid then harmonics of the frequency of x appear in the output

$$Y = M(X) = \sum_{n=0}^{\infty} M_n (X - C)^n \tag{17.14}$$

If, for the sake of discussion, $X = a \sin(\omega t) + b \cos(\omega t)$, then (17.14) yields a Fourier series, i.e.,

$$Y = A_0 + \sum_{n=0}^{\infty} A_n \sin(n \omega t) + B_n \cos(n \omega t) \tag{17.15}$$

where a, b, A_i, B_j, are constants pertaining to the model and input data, n is an integer specifying each harmonic of the original signal input frequency, ω. Clearly, if the system is nonlinear, then the output will contain harmonics of the original input frequency. Figure 17.9 presents the harmonic distortion computed from measured tip acceleration collected from experiments conducted at each orientation for the prismatic beam versus a normalized magnitude of the input excitation amplitude. The harmonic distortion increases with the input amplitude up to a maximum value that is unique for each case. Further increases in input amplitude result in a decrease in the observed nonlinearity. The source of this behavior is unclear, but we speculate that such experimental nonlinearity is caused by the mechanical connection between the surrogate blade and the shaker fixture. This type of behavior is consistent with a stick–slip transition in this mechanical connection where nonlinearity is most profound near the incipient transition from stick to slip response. At low amplitudes the connection behaves essentially linearly, at increasing amplitudes up to some point the connection spends more time near the stick–slip transition. However, as amplitudes continue to increase the response is dominated by the slip condition manifest as frictional dissipation (itself a nonlinearity, though perhaps not as profound as the transition.) The experiments generating this data
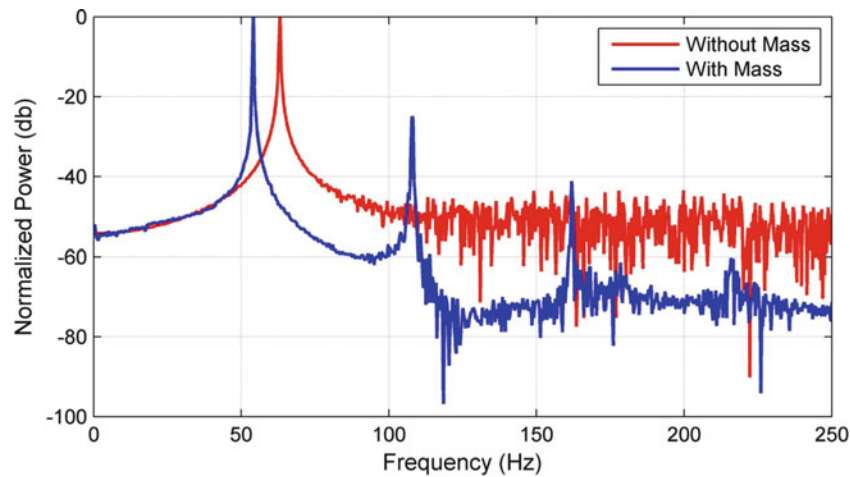
Fig. 17.7 PSD of tip acceleration without mass (*red*) and with mass (*blue*) (color figure online)
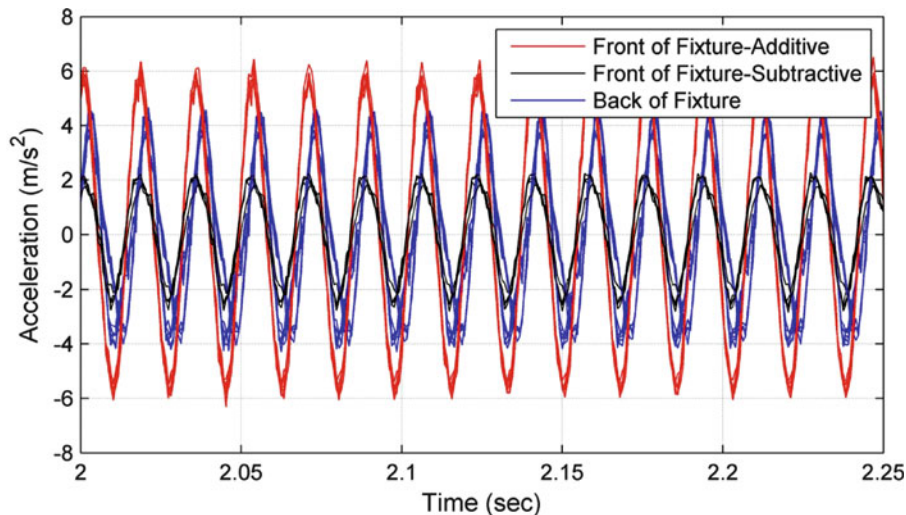
Fig. 17.8 Representative measured acceleration time histories from multiple experimental repeats. Data from accelerometer on rear of fixture is plotted in *blue*. Data from accelerometer near the front of base fixture separates into two distinct phases of base rotation: additive (*plotted in red*) and subtractive (*plotted in black*) (color figure online)

were conducted in turn at each orientation in the order: (1) flat-horizontal, (2) edge-horizontal, (3) vertical. Immediately after completing the experiment in the vertical orientation, the experiment was repeated under the flat-horizontal orientation. Results from this final case are plotted in green in Fig. 17.9 and clearly differ from the original experiment conducted in this orientation (shown in blue). The lack of agreement between this data and that from the initial flat-horizontal case indicates a change in the system throughout the progression of these experiments. This change is consistent with the theory of the stick–slip transition nonlinearity. Such behavior would probably be influenced by the specific details of the interface between the surrogate blade and base fixture. The apparatus was disassembled and reassembled between each experimental case, accordingly, such connection details, for example bolt preload, are most likely different between each case. No attempt was made to characterize or control these connection details.

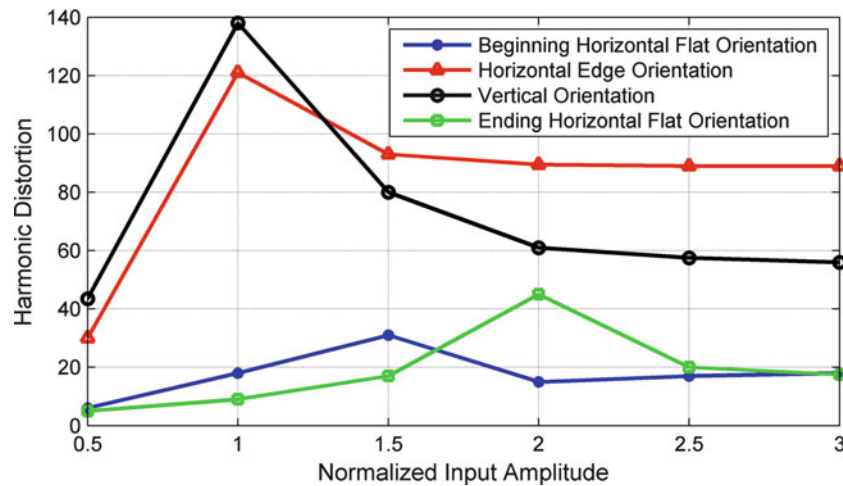**Fig. 17.9** Harmonic distortion of measured tip acceleration response versus input amplitude (*normalized*) for various orientations of surrogate blade
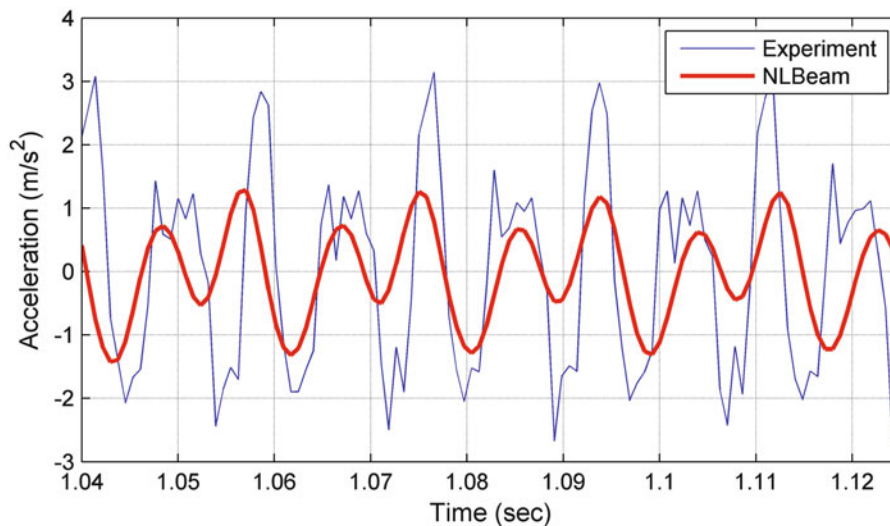
Fig. 17.10 Comparison of tip acceleration time history for horizontal-flat orientation excited with sine dwell near resonance (57 Hz)

17.5.2   On-Resonance Results

Predicting response under sine-dwell excitation at a frequency near resonance is complicated because of the base rocking complexities previously discussed as well as the lack of physical damping in *NLBeam*. The first issue is addressed to a limited extent by specifying a rotational motion of the base in the finite element models that coincides with the observed rocking accelerations. The latter issue is handled to some extent by numerical damping associated with the Newmark time integration scheme employed by *NLBeam*. Physical damping mechanisms in this system comprise friction at the fixture base and material damping in the beam. *NLBeam* was developed to represent the structural dynamic response within an aeroelastically coupled wind turbine modeling code. In this context the actual damping mechanisms are expected to be dominated by interaction of relative velocity and aerodynamic drag. Accordingly, little attention thus far has been devoted to modeling material or frictional damping within *NLBeam*. One consequence is poor agreement (over predicting amplitudes) in predicting structural response near resonance where the numerical model is unstable for truly zero damping.

Aside from damping, another issue is the complexity associated with the shaker-fixture-beam interface, which is not being modeled. It is unclear precisely the influence of this coupling, but it is possible to represent the nonlinearly coupled

Table 17.3 Experimental harmonic distortion for tip acceleration response for no taper, horizontal flat orientation

Orientation	Sine at 35 Hz	Sine at 57 Hz (third mode)
Horizontal flat	1.00	26.48
Horizontal edge	1.00	8.42
Vertical	1.00	6.72

Table 17.4 Computed frequency domain response correlation metric values

	No taper			Linear taper			Radiused taper		
	Flat	Edge	Vert	Flat	Edge	Vert	Flat	Edge	Vert
Exp. – NLB	0.985	0.985	0.977	0.977	0.981	0.952	0.979	0.982	0.975
Exp. – ABQ	0.984	0.982	0.974	0.978	0.982	0.956	0.982	0.984	0.976
ABQ – NLB	0.995	0.992	0.996	0.998	0.998	0.993	0.995	0.994	0.992

behavior by simply specifying base rotations, while conceptually sound, overly constrains the response of the model. Also, it is important to note that the addition of mass to the tip of the blade necessitated relocating the tip accelerometer toward the base of the blade, essentially placing it near a node of the operational deflected shape point. Thus, the acceleration reported at this point is presumably sensitive to details such as the precise location of the sensor and/or FE-node. Attributing the discrepancy between model and experiment to these issues is somewhat speculative; however, it is recommended that the experimental program be adjusted to eliminate these uncertainties.

Figure 17.10 presents a representative comparison between experimentally observed and *NLBeam* prediction of tip acceleration for the surrogate blade without taper in the horizontal-flat orientation. The general response is captured by *NLBeam*, albeit with a significantly subdued amplitude for this particular period of the total time history. Other orientations and surrogate geometries are not discussed here because of the issues described previously.

17.5.3   Off-Resonance Results

In order to eliminate many of the issues discussed in the previous sections, an off-resonance low-amplitude set of experiments was also conducted. Results from these tests enable a more meaningful (and consequently, better quantitative) comparison between experiment and models. On the other hand, the very nature of these experiments restricts comparisons to a fundamentally linear regime of response. For example, consider Table 17.3, which reports the harmonic distortion of the experimentally measured tip acceleration for the surrogate blade with no taper in a horizontal flat orientation for near- (57 Hz) and off- (35 Hz) resonance cases. Clearly, there is no significant nonlinearity present in the response for this case.

In order to make some comparison, a frequency domain correlation metric is defined as

$$C_{12} = \frac{A_1(\omega) \cdot A_2(\omega)}{\|A_1(\omega)\| \ \|A_2(\omega)\|} \tag{17.16}$$

where $A_i(\omega)$ is the acceleration response in the frequency domain for the ith signal and the inner product is taken over the frequency domain. This particular correlation metric is used because it measures how well the shape of the two signals match in the frequency domain, although it does not strongly penalize discrepancy in the magnitudes of those signals. Computed values of this correlation metric between experimental data and each of the two modeling approaches are shown in Table 17.4. Generally, both modeling approaches do well, although when comparing only simulated data to experimental data, the models are better able to predict responses in both the horizontal-edge (average correlation value of 0.983) and horizontal-flat (average correlation value of 0.980) orientations. As expected, the modal superposition and geometrically nonlinear model are highly correlated in the frequency domain. Thus, the geometrically nonlinear approach offers negligible advantage for modeling dynamic response dominated by linear behavior. Comparisons of acceleration time histories shown in Figs. 17.11, 17.12, and 17.13 affirm this conclusion; although, in some cases *NLBeam* compares more favorably than the model superposition results. Such "eyeball" comparisons can be misleading and development of a quantitative metric for comparing nuances of time history data is recommended for future work. Note in particular, acceleration time histories for

Fig. 17.11 Comparison of tip acceleration response for no taper and horizontal-flat orientation
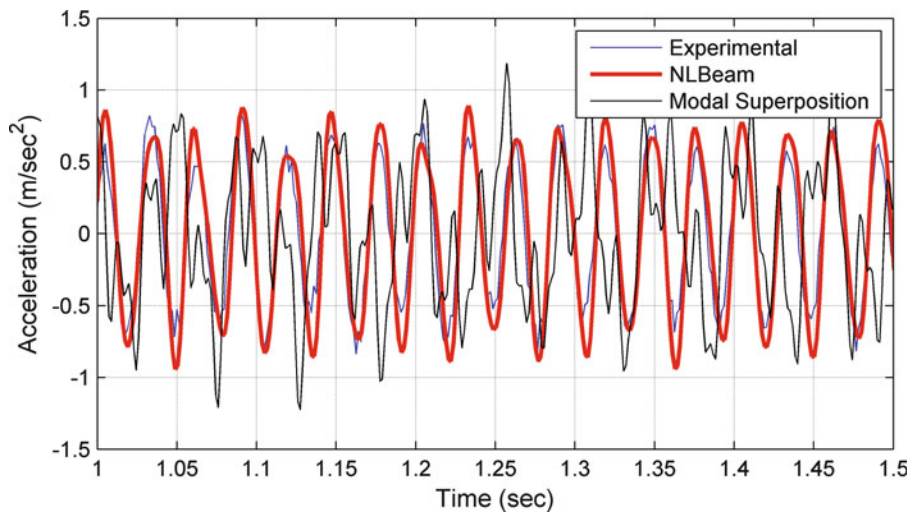
Fig. 17.12 Comparison of tip acceleration response for no taper and horizontal-edge orientation
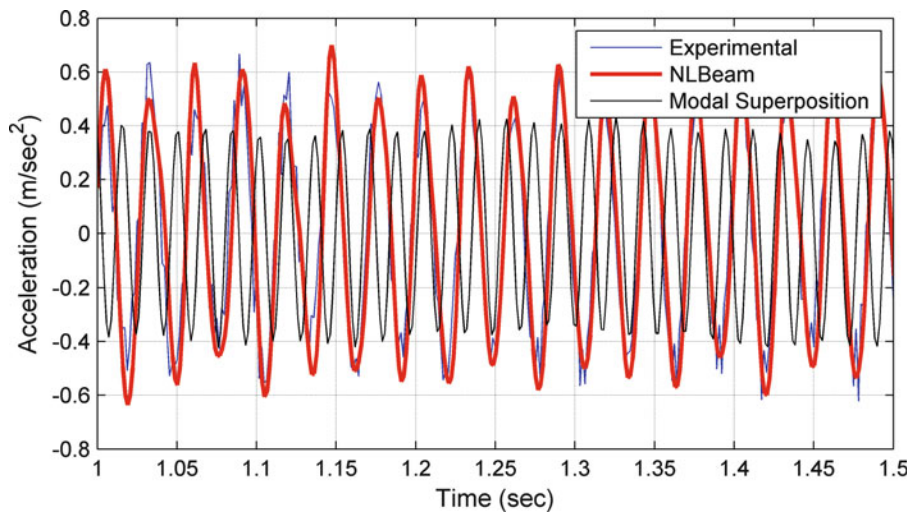
Fig. 17.13 Comparison of tip acceleration response for no taper and vertical orientation
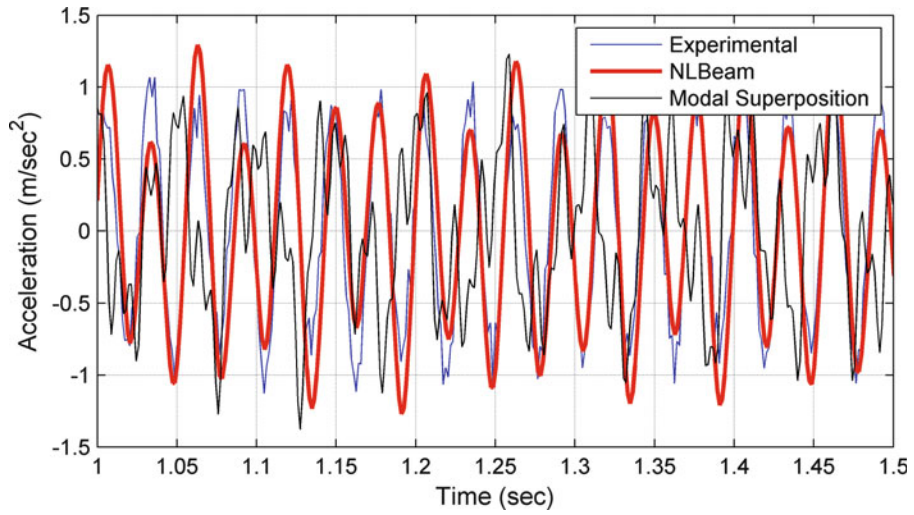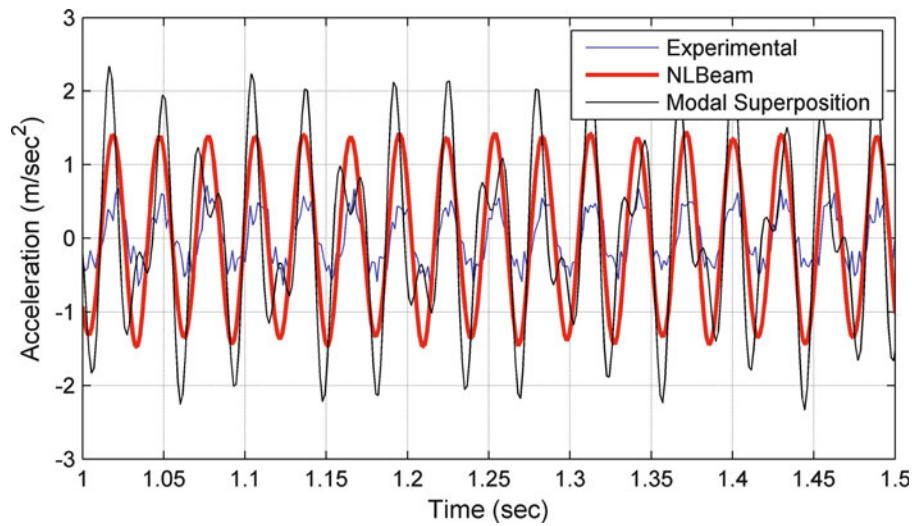
Fig. 17.14 Comparison of tip acceleration response for linear taper and horizontal-flat orientation
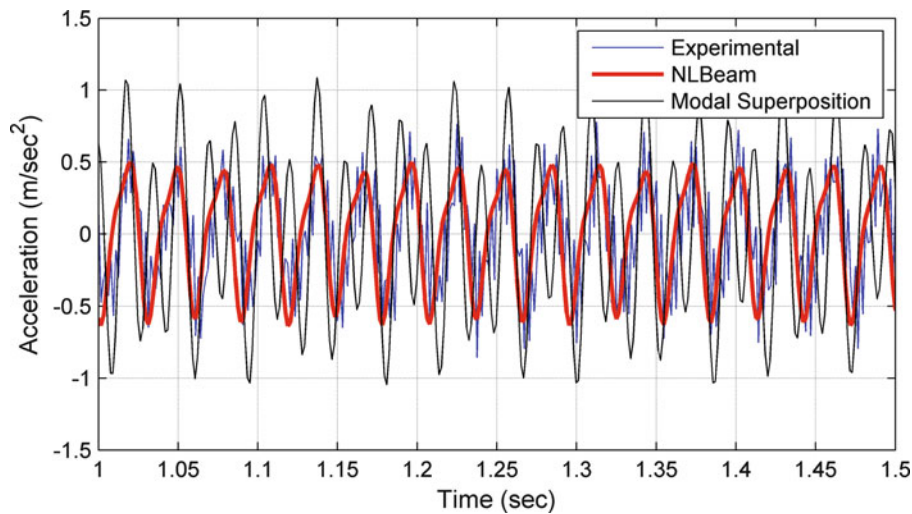
Fig. 17.15 Comparison of tip acceleration response for radius taper and horizontal-flat orientation

both models compare reasonably with experiment for the non-tapered beam (Cf. Fig. 17.11, 17.12 and 17.13). On the other hand, neither model does well matching experimental response for the linear tapered beam as shown in Fig. 17.14. A possible source of error is that the relatively coarse mesh cannot adequately capture the varying geometry. While a thorough grid convergence study has not been performed to assess the accuracy of the results for the linear taper case, it is expected that is not the sole source of discrepancy between the experiment and model and more work needs to be done to rectify this case. Finally, results for the radiused taper case are presented in Fig. 17.15. In this case, *NLBeam* appears to capture the experimental response with better agreement than modal superposition.

17.6 Conclusions

This paper presents work conducted within the scope of the 2011 Los Alamos Dynamics Summer School. The intention was to develop an experimental program supporting validation of a geometrically nonlinear structural dynamics code under development as part of Los Alamos National Laboratory's effort to expand modeling capabilities for wind turbines amenable

to simulation of entire operating plants. The experimental technique and modeling presented in this paper are directly capable of assessing the influence of orientation of laboratory-size surrogate blades under small base excitation. Experimental validation of simulation capabilities under conditions of truly large deformation response remains elusive, but will benefit from the findings reported in this paper. For conditions of small deformation and varying orientations with respect to gravity, simulation results from the code *NLBeam* compare favorably with experimental results in most cases. Future capability enhancements to this code consist of the addition of physical damping mechanisms to enable simulation of response near resonance, allowing specification of rotation time histories as nodal boundary conditions, and providing for the input of accelerations rather than displacement or rotation for boundary conditions. Future improvements to the experimental program that would enable validation over a broader range of nonlinear deformation response include the addition of sensors to measure the resultant base forces and moments, an actuation system that eliminates inadvertent base rotations and that permits large displacement and acceleration amplitudes.

References

1. U.S. Department of Energy (2008) 20% Wind Energy by 2030. U.S. Dept. of Energy, Energy Efficiency and Renewable Energy, Washington, DC
2. US Department of Energy (2010) HIGRAD/windblade wind generation modeling and simulation. http://techportal.eere.energy.gov/technology.do/techID=276
3. Walford CA (2006) Wind turbine reliability: understanding and minimizing wind turbine operation and maintenance costs Sandia report. SAND2006-1100
4. Robinson MC, Luttges MW, Miller MS, Shipley DE, Young TS (1994) Wind turbine blade aerodynamics: the analysis of field test data. National Renewable Energy Lab. NREL/TP-441- 7108 CONF-940113-11
5. National Wind Technology Center (2010) Wind energy aerodynamics/aeroacoustics. National Renewable Energy Laboratory. NREL/FS-5000-48830
6. Jonkman JM, Buhl Jr ML (2005) FAST user's guide NREL/EL-500-29798. Golden, Colorado: National Renewable Energy Laboratory
7. Jonkman JM (2010) NWTC design codes. http://wind.nrel.gov/designcodes/simulators/fast/. Last modified 05 Nov 2010. Accessed 20 June 2011
8. Kane TR, Wang CF (1965) On the derivation of equations of motion. J Soc Ind Appl Math 13(2):478–492
9. Kane TR, Levinson DA (1997) Dynamics: theory and applications, MacGraw-hill series in mechanical engineering. MacGraw-Hill Book Company, New York
10. Bazilevs Y, Hsu MC, Akkerman I, Wright S, Takizawa K, Henicke B, Spielman T, Tezduyar TE (2011) 3D simulation of wind turbine rotors at full scale. Part I: geometry modeling and aerodynamics. Int J Numer Meth Fl 65:207–235
11. Bazilevs Y, Hsu MC, Kiendl J, Wuchner R, Bletzinger KU (2011) 3D simulation of wind turbine rotors at full scale. Part II: fluid-structure interaction modeling with composite blades. Int J Numer Meth Fl 65:236–253
12. Zhang JP, Pan LL (2009) Three-dimensional modeling and aeroelastic coupling analysis for the wind turbine blade. In: WNWEC 2009 – 2009 world non-grid-connected wind power and energy conference, Nanjing
13. Reissner E (1972) On One-dimensional finite-strain beam theory: the plane problem. J Appl Math Phy 32:795–804
14. Reissner E (1981) On finite deformations of space-curved beams. J Appl Math Phys 32:734–744
15. Simo JC (1985) A finite strain beam formulation. The three-dimensional dynamic problem, part I. Comp Meth Appl Mech Eng 58:55–70
16. Simo JC, Vu-Quoc L (1986) Á three-dimensional finite-strain rod model. Part II: computational aspects. Comp Meth Appl Mech Eng 58:79–116
17. Jelenic G, Crisfield MA (1999) Geometrically exact 3D beam theory: implementation of a strain-invariant finite element for statics and dynamics. Comp Meth Appl Mech Eng 171:141–171
18. Bauchau OA (2011) Flexible multibody dynamics, vol 176, Solid mechanics and its applications. Springer, New York
19. Hodges DH, Yu W (2006) A rigorous engineer-friendly approach for modeling realistic composite rotor blades. Wind Energy 10:179–193

Chapter 18
Wind Turbine Experimental Dynamic Substructure Development*

Randy L. Mayes

Abstract Structural dynamic development of modern wind turbines is important for control and to maximize the fatigue life of the wind turbine components. Modeling can be used in development to aid designs. In some cases an experimental dynamic model, or substructure, may be cheaper to develop and more accurate than an analytical model. Some applications for which dynamic substructures could be useful for wind turbine development are presented. Recent advances have provided renewed interest in the topic of experimental dynamic substructures. A focus group has been formed in the Society for Experimental Mechanics to advance the experimental dynamic substructures technology and theory. Sandia National Laboratories has developed two identical test beds to enable the focus group to advance the work. The system chosen was an Ampair 600 wind turbine with a fabricated tower and base. Some modifications were made to the system to make it more linear for initial studies. The test bed will be available for viewing in the technology booth of the IMAC exposition. A description of the turbine and modifications will be presented. Initial measurements on the full system will be described. Organizations already performing experiments on the test bed are the UK Atomic Weapons Establishment, University of Massachusetts-Lowell, Technical University-Delft and University of Wisconsin.

18.1 Introduction

There has been interest in being able to couple experimental and analytical substructures for a long time [1], but difficulties in the experimental methods prevented the common use of experimental substructures. There has been a resurgence of interest in experimental dynamic substructures in the past few years that has been demonstrated by the number of papers and sessions at IMAC. In 2007 there were no substructures sessions, and of the 27 papers that mentioned the word "substructure", less than half a dozen addressed experimental substructures. Since then there have been three or four sessions on substructures each year. For a few years there was talk of developing a focus group on the topic and last year the group actually formed officially. One of the first actions was to develop a test bed structure that could be used for international collaboration. Sandia National Laboratories has developed two test beds that can be used for research, one of which is available for loan. In the experimental substructures focus group meeting at IMAC in 2011, initial plans were developed which led to the papers focused on the test bed this year. Interest in wind turbines has also soared over the last several years. Several possible applications of experimental dynamic substructures may be useful for wind turbine structural dynamic development. In Sect. 18.2 some possible applications for experimental dynamic substructures are proposed. In the other sections, some initial work of the SEM substructures focus group on the AMPAIR 600 wind turbine test bed will be described.

R.L. Mayes (✉)
Experimental Mechanics, NDE and Model Validation Department, Sandia National Laboratories,
5800 – MS0557, Albuquerque, NM 87185, USA
e-mail: rlmayes@sandia.gov

18.2 Possible Applications of Experimental Dynamic Substructures for Wind Turbine Dynamic Development

In Fig. 18.1 is shown a small wind turbine which will be used as an example for discussion of possible applications of experimental dynamic substructures for wind turbine development. One of the most logical uses of experimental dynamic substructuring based simply on maximum utilization of resources is to develop an experimental model of a portion (a substructure) of the wind turbine system because it is cheaper or more accurate than developing an analytical model. The experimental models can be coupled with validated analytical substructures of the other portions of the wind turbine to accurately predict full system response. It seems plausible that the tower and the hub of the rotor might be reasonably modeled with finite elements, since they have relatively well understood geometry and are often made of an isotropic material such as steel. However, certain portions of the wind turbine are not well understood which makes them difficult to model accurately. One other advantage of a finite element substructure over an experimental substructure is that it can be easily modified for updated designs. Experimental substructures are constructed from input/output relationships which may not easily be related back to design change parameters. In the following paragraphs, some suggested uses of experimental dynamic substructures for wind turbines are proposed. The author is most familiar with the transmission simulator method [2, 3] of experimental dynamic substructures, so applications for which that method is applicable are emphasized.

18.2.1 Experimental Dynamic Substructure of the Foundation

In the figure, the base of the wind turbine is set on a trampoline, simply because it provides a much more consistent and easily modeled boundary condition than setting the base on a floor with unknown mass, stiffness and contact mechanics. This emphasizes one of the difficult modeling problems for field wind turbines. The foundation of the wind turbine is often difficult

Fig. 18.1 Substructures focus group test bed – Ampair 600 wind turbine

to model, requiring an understanding of how a base fixture, bolts, concrete materials and soil interact together, which may not be well understood. But the boundary condition of the base has a huge effect on the frequency of the first bending mode of the tower. The damping that is caused by the foundation is an order of magnitude more difficult to model than the stiffness and mass (most damping values for FE models are derived from measured experimental data). Experimental dynamic substructuring might be the cheapest and fastest way to get a substructure model of the foundation that could be connected to a FE model of the tower. In fact, if an accurate model of the tower exists, the transmission simulator method of dynamic substructuring can be used to determine the experimental substructure model of the foundation. With this method, an instrumented fixture is attached to the connection points of the foundation. The tower could be used as the fixture since it generally already exists. The transmission simulator method provides a mass, stiffness and damping matrix directly from translation force and acceleration measurements made on the tower, which is connected to the foundation. No measurements directly on the foundation have to be made. In the end, the stiffness, mass and damping of the tower can be subtracted analytically, leaving simply a stiffness, mass and damping matrix for the foundation and the joint between the foundation and the tower.

18.2.2   Experimental Dynamic Substructure of the Blade

Some development wind turbine blades are difficult to model because of complex geometries and uncertain material properties making the analytical stiffness, mass and (especially) damping matrices difficult to generate. Experimental substructure models of the blades may be valuable for certain analyses. The transmission simulator method might be performed with the actual hub used as a fixture connected to a blade. Then the hub can be subtracted, and a model of the blade that includes the joint stiffness and damping between blade and hub results.

18.2.3   Experimental Dynamic Substructure of the Nacelle and Its Components

Because of the complex geometry, bearings, joints, gears, cables and mechanisms in the generator, the nacelle and its internal parts may be more easily and accurately modeled with an experimental substructure than an analytical model. However, the experimental setup may be logistically challenging. Since it has a connection to the hub and a connection to the tower, two fixtures would be necessary to capture the connection dynamics. The hub could perhaps be used for the connection to the rotor, but a special fixture would probably be needed to capture the connection to the tower.

18.2.4   Experimental Dynamic Substructure of the Nacelle/Tower/Foundation

Logistically it might be easier to model the shaft, nacelle and components, tower and foundation all as one experimental substructure, rather than modeling the foundation and tower experimentally and the tower analytically. If an analytical model of the rotor was available, it could be connected to this substructure to predict full system response.

18.3   Overview Description of the Experimental Dynamic Substructures Test Bed

In Fig. 18.1 one can see one of the two test beds. The test bed is founded upon an AMPAIR 600 wind turbine. The turbine was set upon a tapered aluminum pole representing the tower with an aluminum base plate softly supported on the trampoline. The base plate set on the trampoline should have a more consistent and more easily modeled boundary condition than the base plate set on some unknown foundation. The height is 1.85 m from the bottom of the base plate to the top of the generator housing. The rotor diameter is 1.7 m. The total mass of the test bed without the trampoline is 114 kg. For initial studies the rotor was parked by modifying the generator.

18.4   Description of the Blades

The blades are a glass reinforced polyester construction with local axes chosen as shown in Fig. 18.2. They are coated with a white epoxy. In addition to the six blades on the two test beds, six other blades were acquired for individual blade testing. The blades were given serial numbers. The blades are clamped to the hub by three bolts and two plates that sandwich the blade in place.

18.5   Description of the Hub

The hub to which the blades attach is shown in the center and bottom of Fig. 18.3. The hub has a mechanism which pitches the blades so they will not transmit power in high winds. Initial substructure studies will be focused on developing linear experimental substructures, so nonlinear elements of the system are minimized. For the test bed, the mechanism is defeated by potting the mechanism in the normal operating position to attempt to eliminate any nonlinear action such as gapping or rattling in the dynamics. The mechanism was activated by masses that were attached through bolts in the holes at the greatest radial distance from the center of the hub (seen on the black brackets in the figure). These masses were removed and only hardened steel bolts were inserted in those three locations. In addition the shaft was replaced with a modified shaft that bolts to the hub to ensure that there is no slip between the shaft and hub.

18.6   Description of the Generator

The generator is modified to make the system parked for initial studies. In Fig. 18.3 the generator parts can be seen. The white generator housing and front bearing retainer have the original bearings in them, but the armature and field coils are replaced by a single machined steel part that simulates their mass. The modified mass mounts in the bearings in the front bearing retainer and aft housing and is shown in the figure. When the front bearing retainer is bolted to the aft housing,
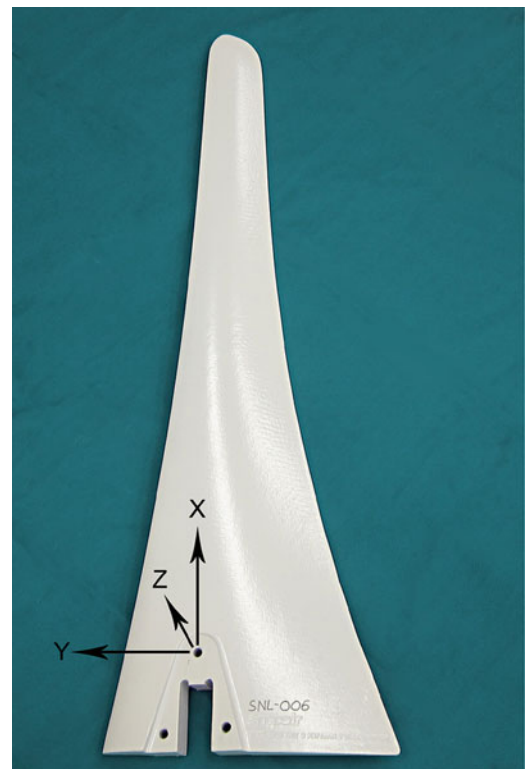
Fig. 18.2 One of the Ampair 600 blades

Fig. 18.3 Test bed parts –
(*Left to Right*) – generator
housing, mass to replace
the armature and field coils,
coffee cup (for size
comparison), hub, front
bearing retainer, blade
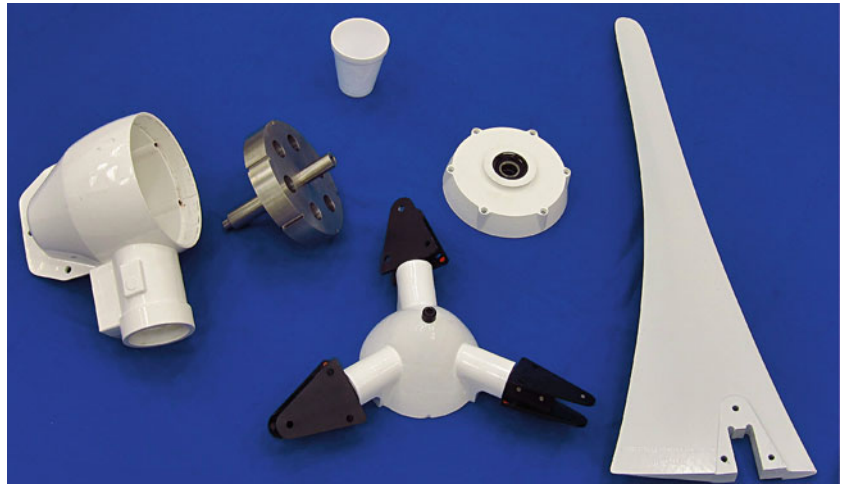
Fig. 18.4 Removed
generator parts

it fixes the modified mass in the housing so that it cannot rotate in the bearings. This is another effort to minimize nonlinearity. Figure 18.4 shows the actual parts that are replaced by the modified mass. A smaller aluminum tail fin replaces the manufacturer's large tail fin to reduce the number of tail fin modes in the testable bandwidth (shown in Fig. 18.1).

18.7   Description of the Tower and Base

The base is made of a 7.62 cm thick by 76.2 cm diameter aluminum plate. It bolts to a 3.81 cm thick plug that is screwed and glued into the base of the pole representing the tower. The tower is made from a hollow tapered aluminum flag pole cut to 152.4 cm in length with 0.318 cm wall thickness. The tower base outside diameter is 7.62 cm and the top outside diameter is 6.39 cm. A hollow adapter sleeve that is 7.19 cm outside diameter is welded to the top of the tower to adapt to the generator housing. Three radial screws attach the base of the generator housing to the top of the tower. All this is set on a trampoline to provide a well-characterized boundary condition for the base. Setting the base on a floor was considered to be too variable a boundary condition, depending on floor roughness and material.

18.8   Linearization Attempts

The desire of the substructures focus group was to start with a linear experimental dynamic substructure, so efforts to remove possibly nonlinear parts were undertaken. In general, joints can be nonlinear. First the rotating shaft of the armature was replaced with the armature/field coil mass that would be locked to the housing when the front bearing retainer was bolted to the housing. Second, the overspeed mechanism which pitches the blades to reduce lift in high winds was potted to reduce the rattling and free play in that mechanism. The masses that activate this mechanism through centrifugal force were also removed. Third, the hub shaft was replaced with a shaft that would directly bolt to the hub to eliminate play between the hub/rotor and shaft.

18.9   A First Look at the Dynamics

A rudimentary impact modal test was performed to get a first look at the dynamics of some of the lower modes. There were not enough accelerometers to distinguish between first and second bending mode shapes of a blade or the tower. The elastic modes were extracted with the SMAC algorithm [4]. Low frequency rigid body frequencies were extracted from the peak in an autospectrum generated from a person exciting a specific rigid body motion of the test bed on the trampoline. Table 18.1 shows the modal parameters and a description of the modes extracted up to 50 Hz. Figures 18.5, 18.6, 18.7, 18.8, 18.9, 18.10, 18.11 through 18.12 show the mode shapes. Figure 18.13 shows the analytical synthesis of a complex mode indicator function from extracted modal parameters compared to the actual experimental data. The frequencies and damping change slightly with impact level, but the modal extraction was readily achievable.

18.10   First Research Efforts

The substructures focus group consensus was to begin by characterizing just one blade. Initial plans of university and industry partners were to test blades in free and possibly mass loaded or fixed configurations. Also efforts were initiated to develop the solid geometry and a finite element model of the blade to aid studies. One proposal was to experimentally extract the parked rotor substructure and couple it to an analytical model of the tower and base. The hardware lends itself to these and many other possible approaches.

Table 18.1 Modal parameters of the Ampair 600 test bed

Description	Frequency	Modal damping%
Pitch about X axis	0.875 Hz (.125 Hz resolution)	**
Pitch about Z axis	0.875 Hz (.125 Hz resolution)	**
Vertical Y bounce	2.75 Hz (.125 Hz resolution)	**
Lateral X	3.125 Hz (.125 Hz resolution)	**
Lateral Z	3.125 Hz (.125 Hz resolution)	**
Torsion about Y	3.375 Hz (.125 Hz resolution)	**
Blades bending about Y	16.97	1.5
Blades bending about X	17.68	1.8
Blades bending in phase in Z	18.76	1.87
First bend tower in X	20.4	1.74
First bend tTower in Z	21.38	1.50
Second bend tower in X	29.57	2.37
Tail X motion out of phase with rotor Z motion	37.12	1.09
Rotor out of phase with nacelle rotation about X	50.80	1.36

**A few rigid body modes that were extracted from impact FRFs had damping on the order of 10%

Mode 3
Frequency: 16.966 Hz
Damping: 1.675 %Cr
IDLine 1: Generated from reference 1001Z+
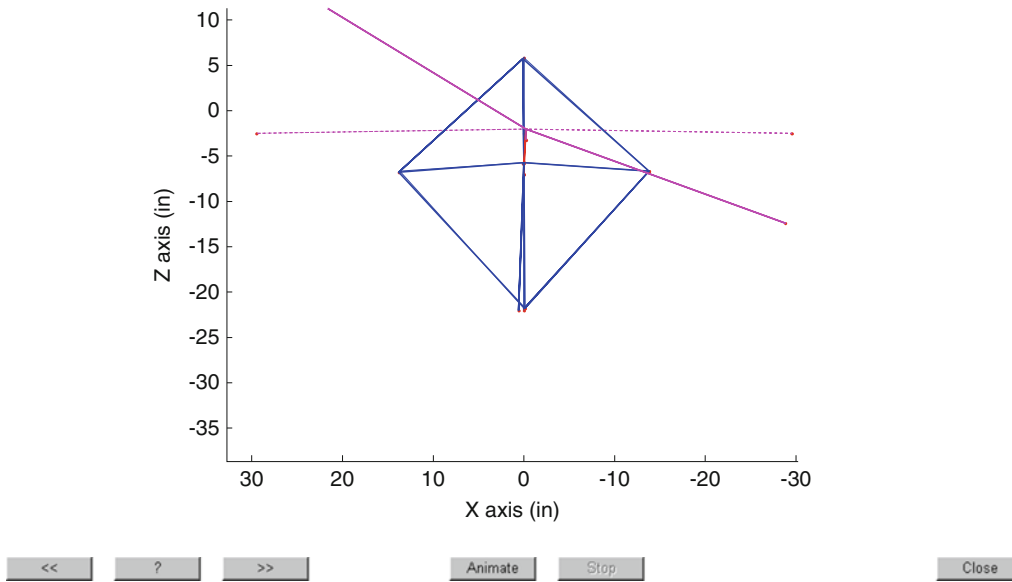
Fig. 18.5 Top view 16.97 Hz

Mode 3
Frequency: 17.679 Hz
Damping: 1.800 %Cr
IDLine 1: Generated from reference 1101Z+
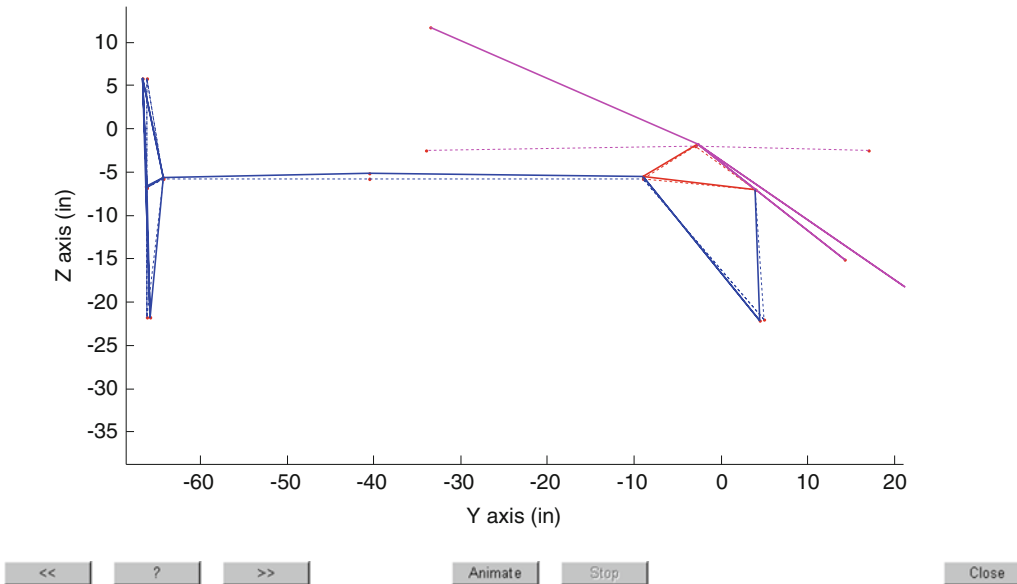
Fig. 18.6 YZ plane 17.68 Hz

Mode 4
Frequency: 18.759 Hz
Damping: 1.874 %Cr
IDLine 1: Generated from reference 1101Z+

Fig. 18.7 YZ plane 18.76 Hz

Mode 4
Frequency: 20.397 Hz
Damping: 1.743 %Cr
IDLine 1: Generated from reference 3X+

Fig. 18.8 XY plane 20.4 Hz

Mode 5
Frequency: 21.382 Hz
Damping: 1.496 %Cr
IDLine 1: Generated from reference 3Z+

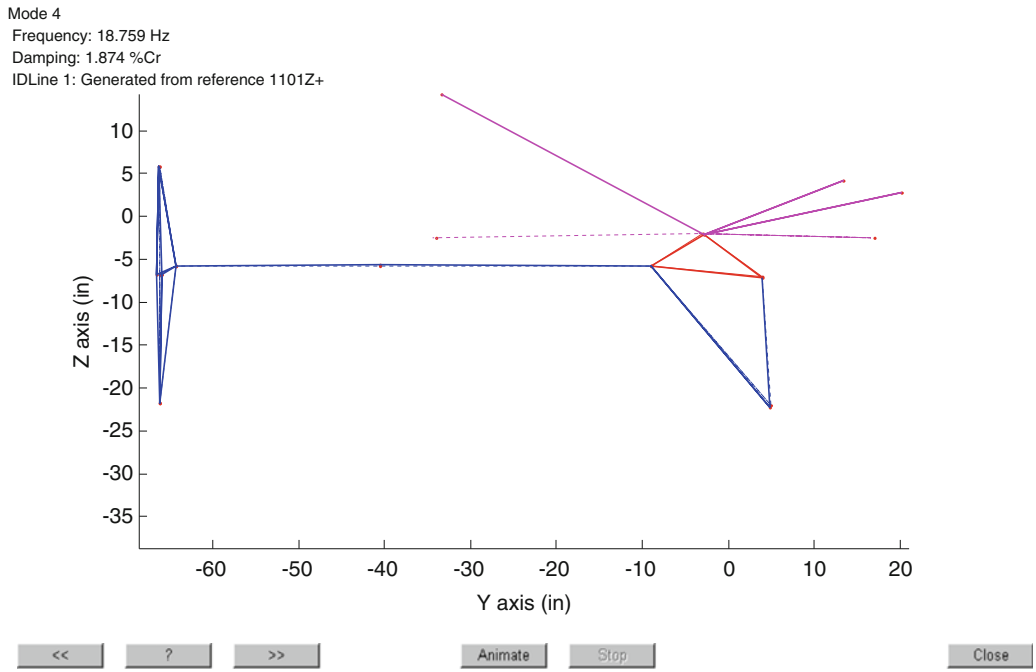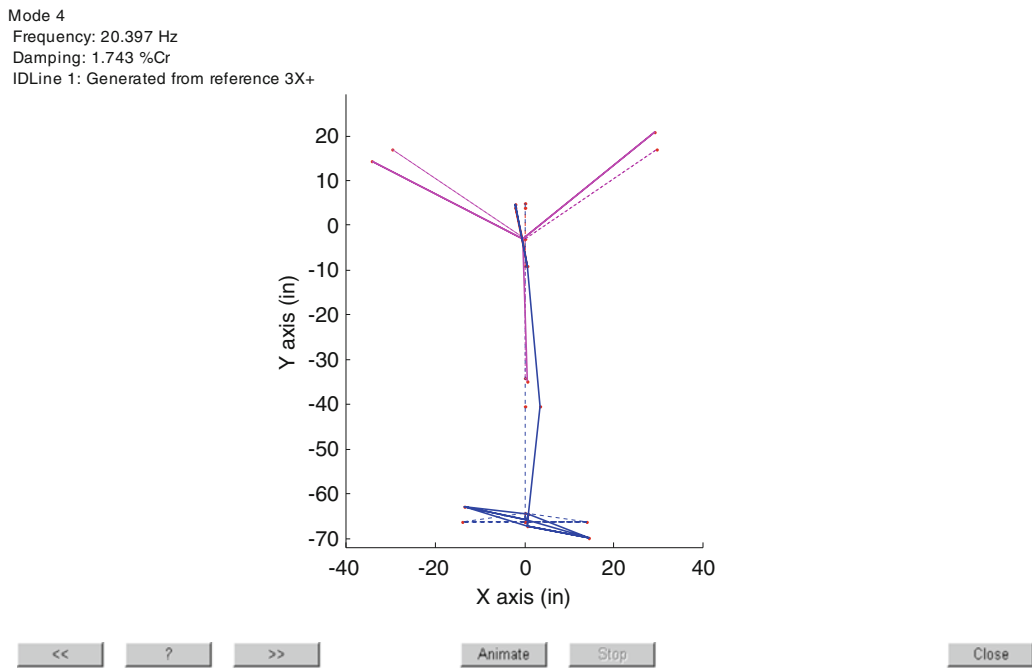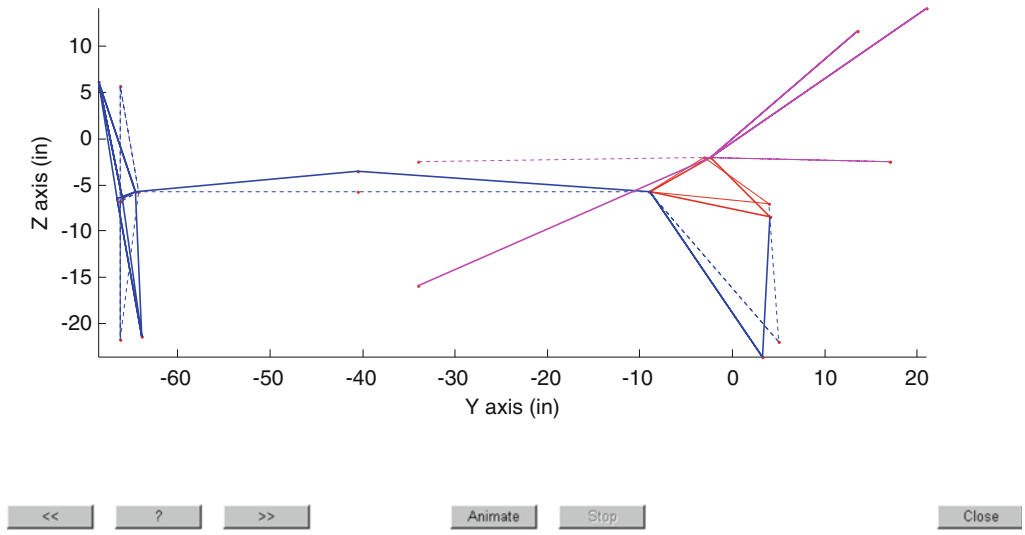

Fig. 18.9 YZ plane 21.38 Hz

Mode 5
Frequency: 29.572 Hz
Damping: 2.374 %Cr
IDLine 1: Generated from reference 9X+
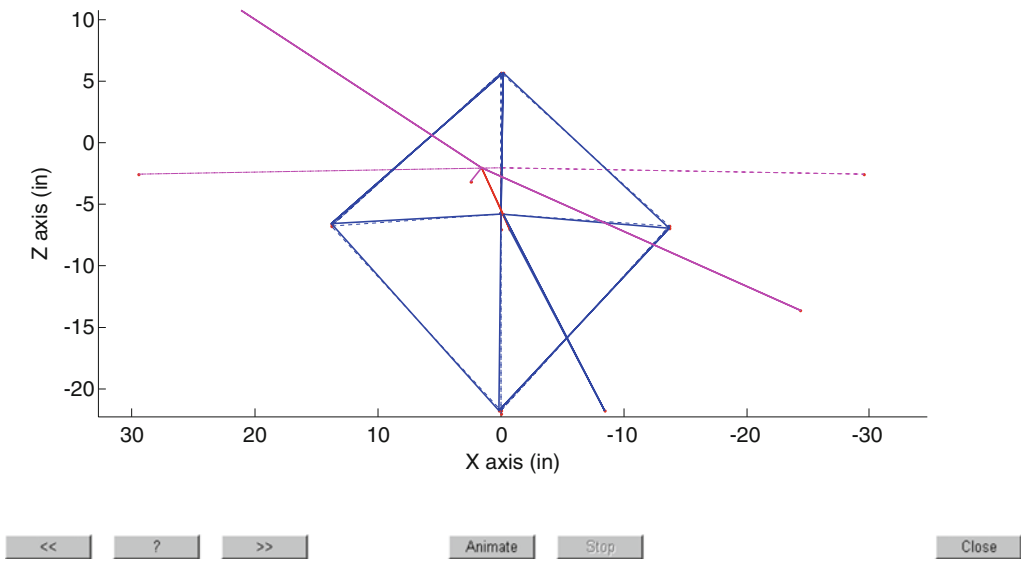
Fig. 18.10 XY plane 29.57 Hz

Fig. 18.11 Top view 37.12 Hz
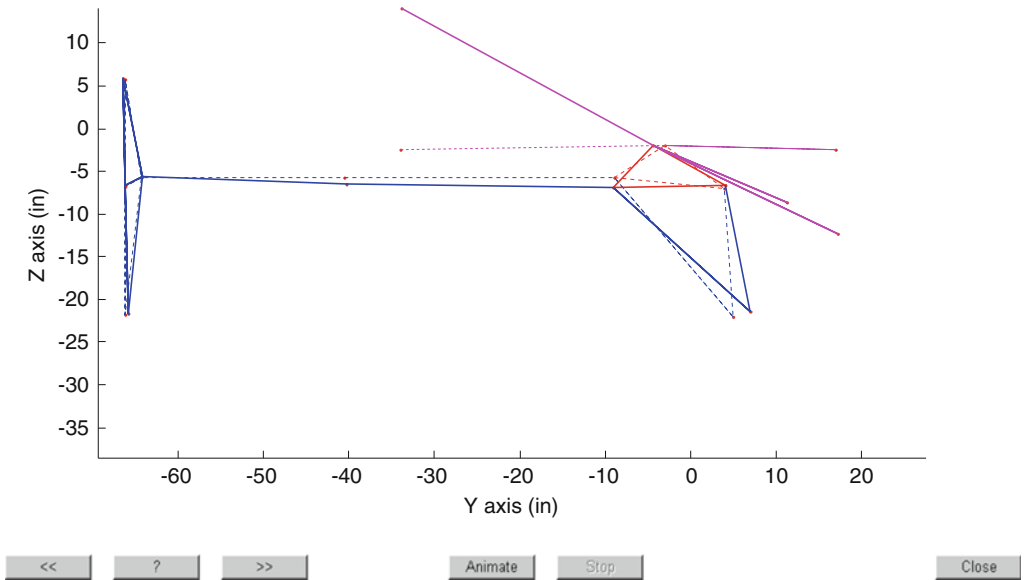
Fig. 18.12 YZ plane 50.80 Hz
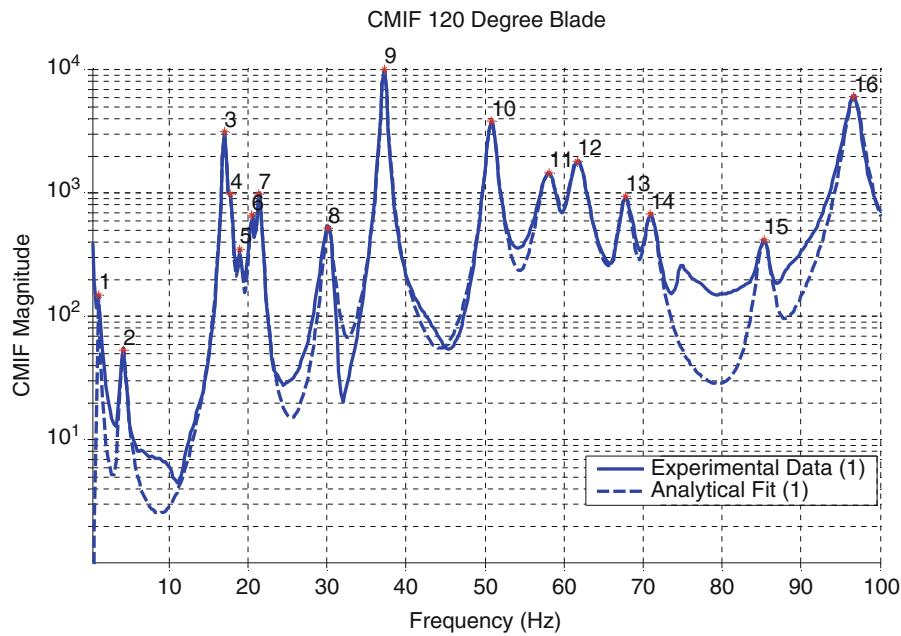
Fig. 18.13 CMIF for 120° blade – analytical (*dashed*) versus experimental (*Solid*)

18.11   Concluding Remarks

Experimental dynamic substructuring can be applied to a wind turbine: experimental substructure models for foundation (land-based and offshore), drive train and blades could be combined in a relevant way with analytical substructure modes for design analysis predictions of dynamics. There are several potential applications in which structural dynamic wind turbine development could possible benefit from the use of experimental dynamic substructuring technology. In the cases when a portion of a wind turbine needs to be modeled, it may be more cost effective and more accurate to obtain an experimental dynamic substructure of that portion instead of an analytical model. This is especially true when the substructure model may be extremely difficult to develop analytically from first principles. Possible experimental substructure applications discussed were: (1) Wind turbine foundation; (2) A blade with complex geometry and uncertain material properties; (3) The nacelle and its components with many joints, bearings and mechanisms; and (4) The nacelle/tower/foundation assembly. The substructures focus group of SEM has established two test beds for development of experimental substructuring methods. The test beds are two wind turbines based on Ampair 600 machines mounted to a tower and base. Testing and modeling of the blades and system has already commenced with participation internationally from both academia and industry. Over 20 participants were involved in the first focus group workshop and planning meeting at IMAC in 2011. Their work is demonstrated in four sessions on substructuring methods at IMAC in 2012.

References

1. Martinez DR, Carne TG, Gregory DL, Miller AK (1984) Combined experimental/analytical modeling using component mode synthesis. In: Proceedings of the AIAA/ASME/ASCE/AHS structures, structural dynamics and materials conference, Palm Springs, pp 140–152
2. Allen MS, Mayes RL, Bergman EJ (2010) Experimental modal substructuring to couple and uncouple substructures with flexible fixtures and multi-point connections. J Sound Vib 329(23):4891–4906
3. Mayes RL, Hunter PS, Simmermacher TW, Allen MS (2008) Combining experimental and analytical substructures with multiple connections. In: Proceedings of the 26th international modal analysis conference (IMAC XXVI), Orlando
4. Hensley DP, Mayes RL (2006) Extending SMAC to multiple references. In: Proceedings of the 24th international modal analysis conference, St. Louis, pp 220–230

Chapter 19
Validation of a Finite Element Model Used for Dynamic Stress–Strain Prediction

Jack LoPiccolo, Jennifer Carr, Christopher Niezrecki, Peter Avitabile, and Micheal Slattery

Abstract Modal testing is performed on wind turbine blades to provide information that is necessary for model updating and validation. In this work, a finite element model of a small wind turbine blade is developed and is used to perform dynamic stress–strain prediction using digital image correlation techniques. In order to assure that the model is appropriate for this work, a modal test is performed and correlated to the finite element model. Several blades are tested to identify the variability expected in the as-built configuration. This paper presents the test, analysis and correlation for this wind turbine blade.

19.1   Introduction

As part of the certification process for wind turbine blades, static and dynamic tests are conducted to validate the structural configuration. Load tests are performed along with fatigue testing on the blades. Generally, the blades are instrumented with various measurement transducers and, in particular, strain gages are generally included as part of the measurement system.

As part of the work performed on these blades, a new approach was used for the identification of the stress–strain experienced by the blade during static and dynamic testing. Typically, only a handful of strain gages are used for the identification of the blade stress–strain. However, in these tests, digital image correlation (DIC) was used allowing for the measurement of full-field surface strain. The primary benefit to using DIC is that the measurement approach is not limited to identifying the strain at only the point discrete strain gage locations.

As part of the certification process, many times the finite element model generated is validated through the use of experimental modal data to assure that the model is an accurate representation of the structure. For this work, the correlation of the model is also important for the correlation of the test results obtained from the DIC to be compared to the finite element model results.

At the time of the writing of this paper, the solid finite element model had not been finalized. Therefore a simpler beam like representation of the blade was used for the correlation studies presented in this paper. A future paper will present the solid model and correlation to the test data along with the comparison of the data to the stress–strain results. The presentation of the methodology for the static [1] and dynamic [2] results for this blade are presented in companion papers. This paper focuses on the correlation of the test data collected for several representative blades to the finite element model of the blade.

J. LoPiccolo (✉) • J. Carr • C. Niezrecki • P. Avitabile
Structural Dynamics and Acoustic Systems Laboratory, University of Massachusetts Lowell,
One University Avenue, Lowell, MA 01854, USA
e-mail: Jack_LoPiccolo@student.uml.edu

M. Slattery
Southwest Windpower, 1801 W.Route 66, Flagstaff, AZ 86001, USA

19.2   Finite Element Model Developed and Analysis Performed

A solid model of the blade was in the final stages of development at the time of the writing of this paper. The solid model is shown in Fig. 19.1 for reference. A preliminary finite element model of the blade was also developed from the solid model but was also not finalized at the time the paper was finalized. The rough model of the blade is shown in Fig. 19.2.
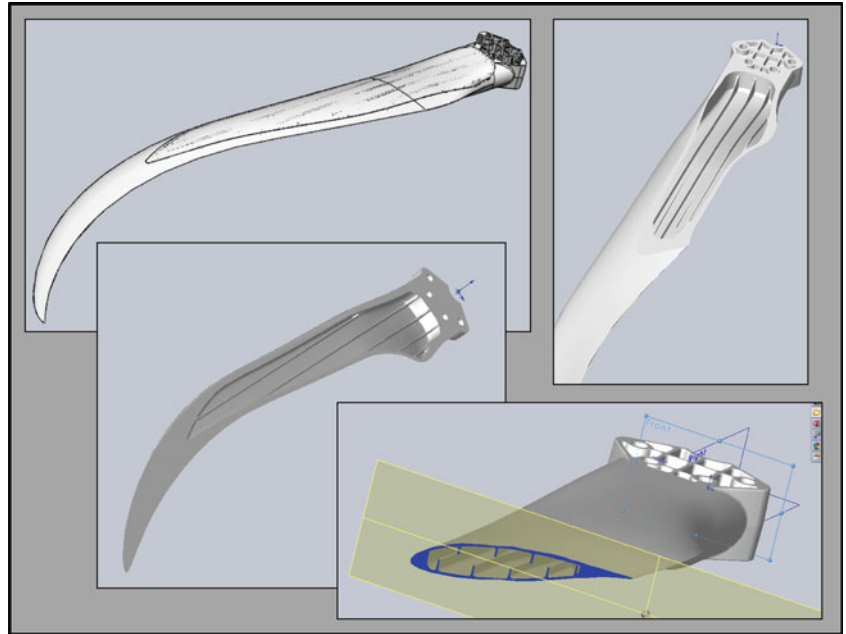
Fig. 19.1 Schematic of solid model and several related cross sections [3]
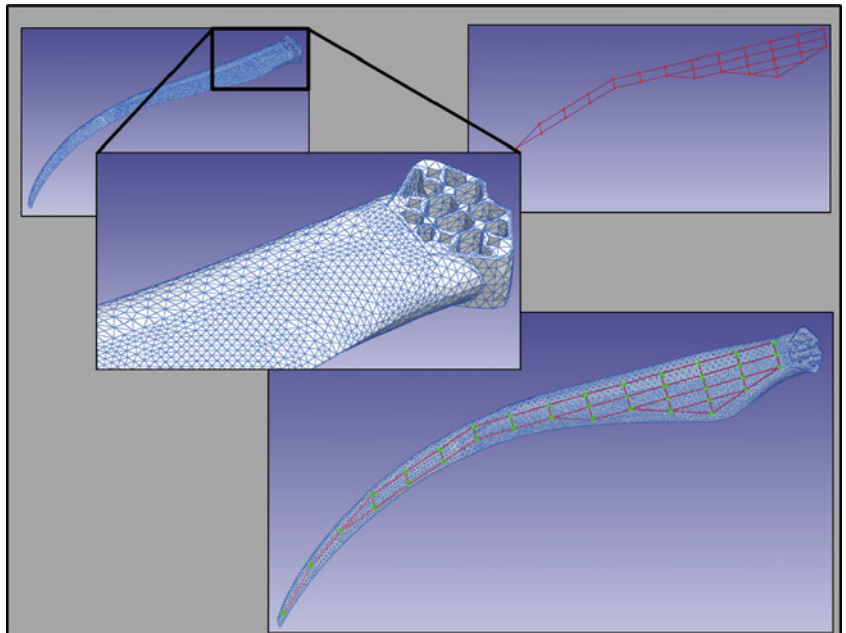
Fig. 19.2 Preliminary solid finite element model with test data (In progress)
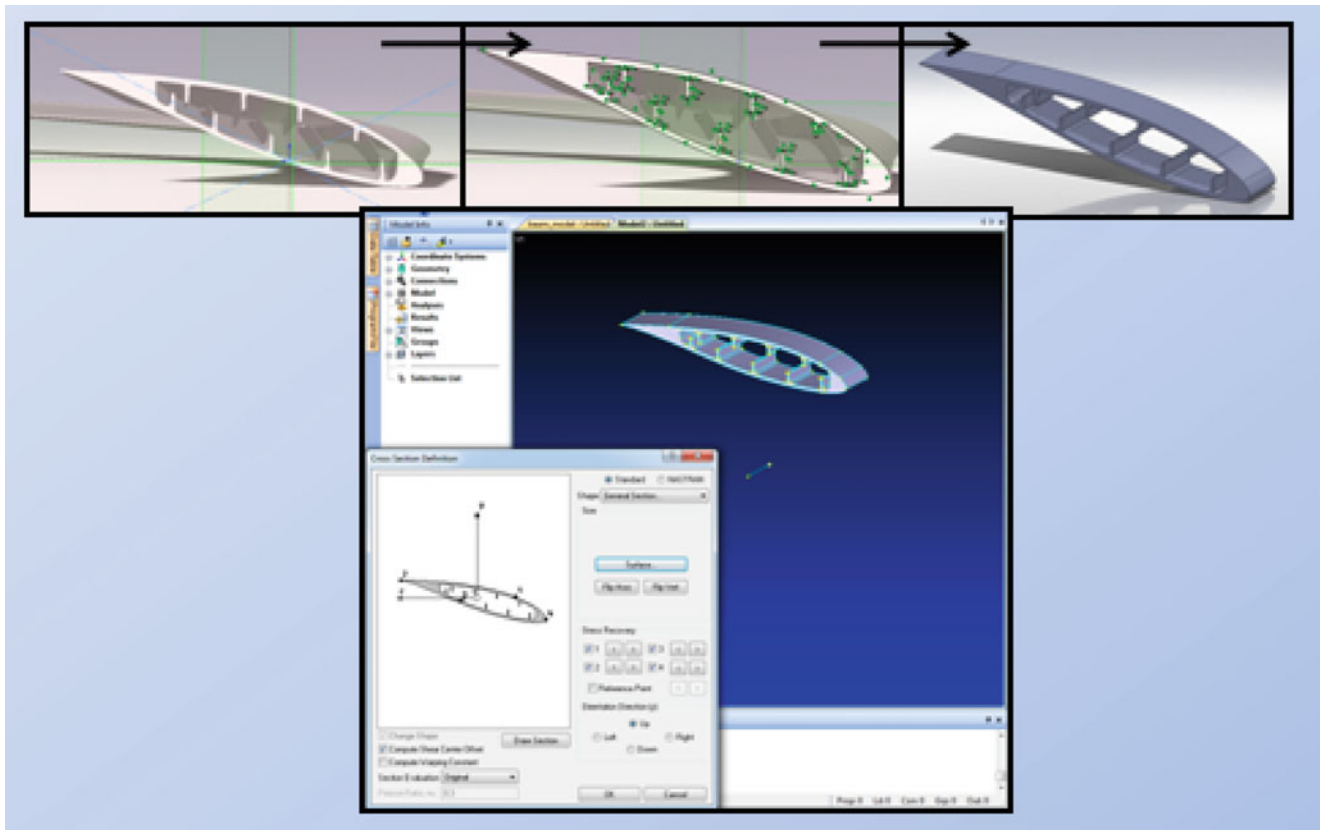
Fig. 19.3 Process of FE formulation

In order to provide preliminary information in regards to the dynamic characteristics of the blade, a simpler finite element (FE) model of the blade was created. This model was created using beam elements to represent the blade. The cross section of the blade was taken from a CAD model that had been provided by the manufacturer [3]. Cross sectional properties were recorded for every 0.5 in. along the length of the blade. A new CAD part was then created for each cross section sketch, where the cross-section was extruded to a 0.5-in. beam. The CAD parts for each cross-section were imported into FEMAP. This process is illustrated in Fig. 19.3.

Each beam element of the FE model was given a length of 0.5 in. and the cross-sectional properties to match the cross-sections imported from the CAD cross sections. The beam elements followed a line based on the centroids of the cross-sectional areas taken from the CAD model. This line formed the curve of the blade. The final FE model is shown in Fig. 19.4. The image on the top shows the beam elements of the FE model, while the image on the bottom illustrates the cross-section of each beam element. The solid elements on which the FE model is overlaid, are imported from the parts of each cross-section from the CAD model.

Based on the high refinement of the beam elements, the simplified FE model was an acceptable model of the blade and could be used further for analysis. As a check to the accuracy of the model, the mass of the blade in FEMAP was checked. The weight of the FE blade was found to be 15.9 lbf. The actual blade weighs approximately 18 lbf which is an 11.7% difference.

An analysis was performed that characterized the blade FE model for a free-free boundary condition. For the analysis, eight modes were calculated in order to obtain six modes in the flap-wise direction. Figure 19.5 shows the flexible mode shapes and frequencies for the free-free condition. The highlighted modes are edge-wise dominant and not important for this analysis here, that is mainly focused on flap-wise blade motion.
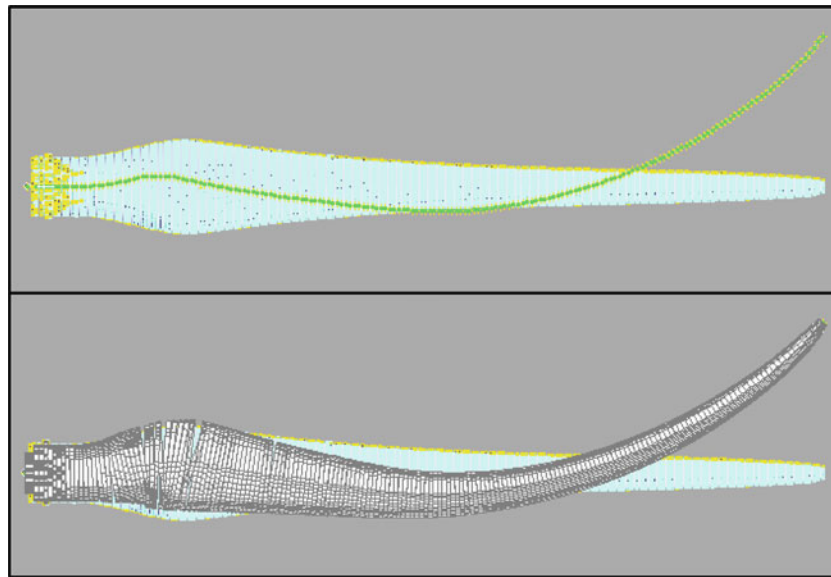
Fig. 19.4 Finite element model from beam elements with cross section

Mode	Frequency (Hz)
1	13.78
2	25.90
3	49.92
4	57.49
5	83.45
6	121.87
7	155.65
8	169.35

= Edgewise
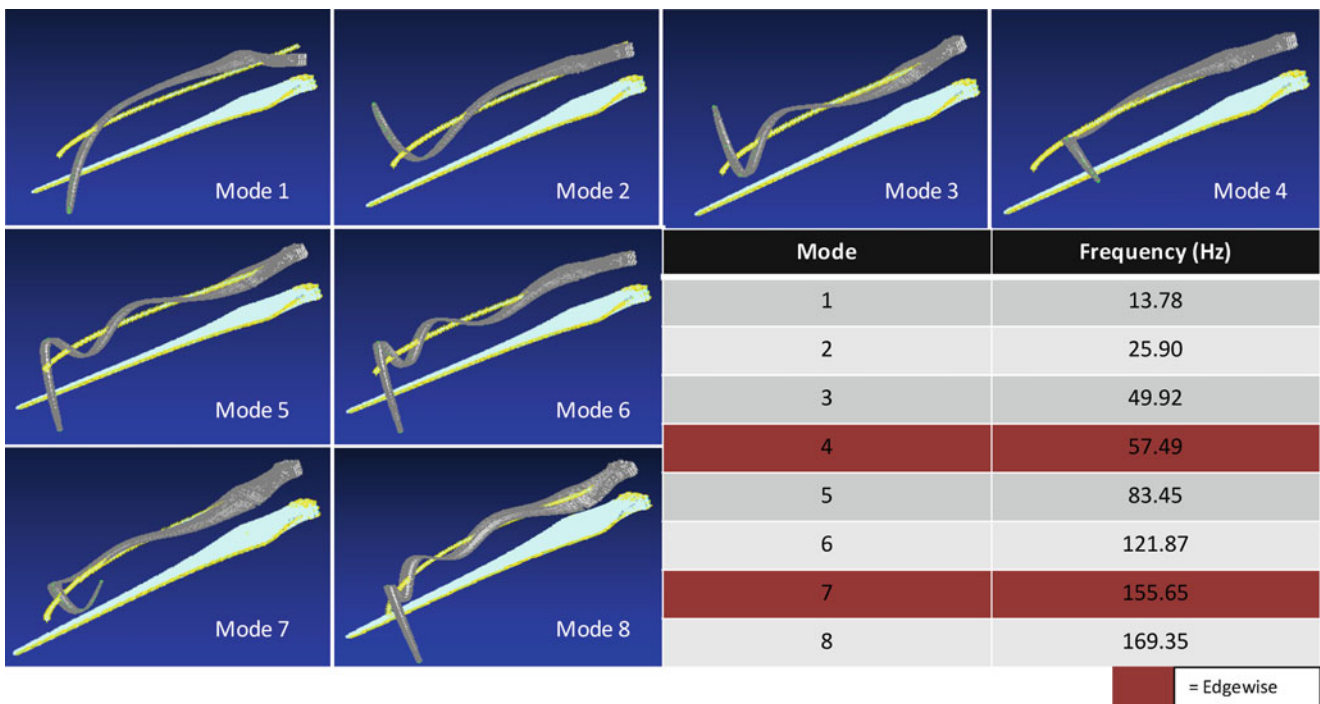
Fig. 19.5 Free-free shapes and frequencies

19.3 Dynamic Testing and Results

Testing was performed on four 7-ft wind turbine blades. The blades were serialized, and are referred to as "Blade 1," "Blade 2," "Blade 3," and "Blade 4." For experimental testing, each blade was hung vertically from the root using two bungee cords to simulate a free-free condition for flap-wise response. An impact test was performed on each blade using 37 impact
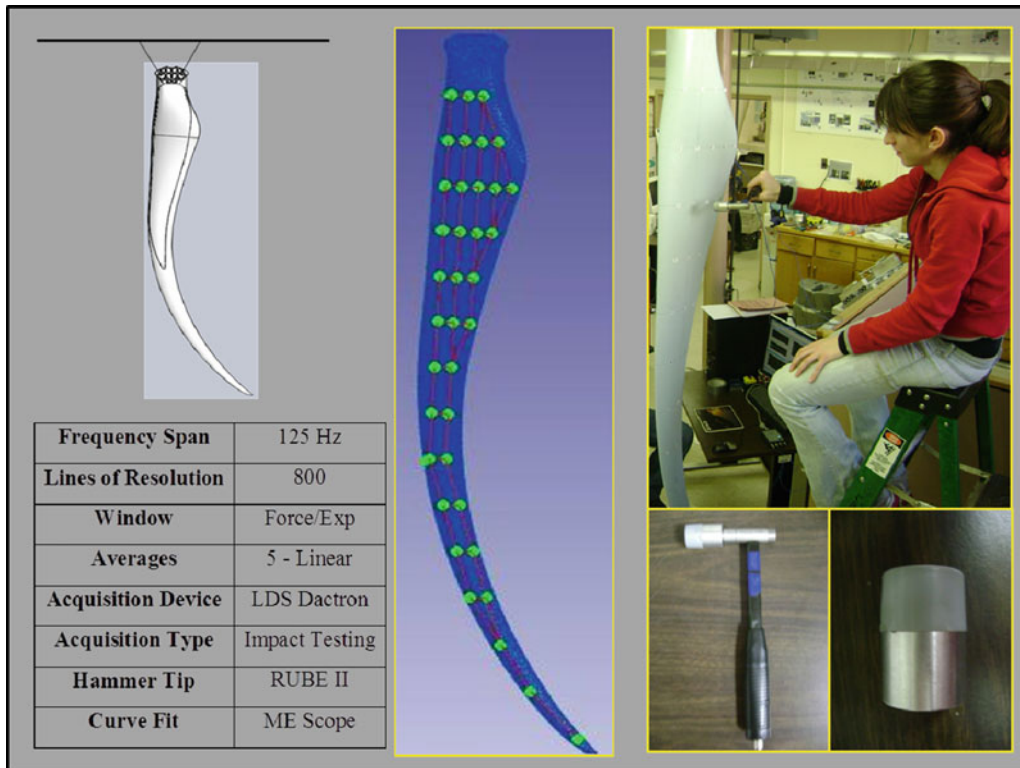
Fig. 19.6 Test setup and measurement parameters

Table 19.1 Weights of blades

Blade 1	Blade 2	Blade 3	Blade 4
17 lbs	17 lbs	18 lbs	20 lbs

Table 19.2 Natural frequencies of blades

Mode	Blade 1 (Hz)	Blade 2 (Hz)	Blade 3 (Hz)	Blade 4 (Hz)
1	14.5	13.6	13.1	13.3
2	28.8	26.4	25.6	25.9
3	54.2	50.1	49.0	49.6
4	65.6	56.6	56.4	56.2
5	90.1	83.3	81.5	82.5
6	130.1	120.1	117.7	119.7

locations with five averages at each point. Two reference accelerometers were placed on the turbine blade. One reference accelerometer was placed at the tip of the blade. The second reference accelerometer was placed closer to the root of the blade, off the center axis. A 4-channel LDS Dactron Photon II Analyzer was used for data acquisition during the modal tests. The test data was then processed with MEScope for the modal parameter estimation. The test setup, along with a map of the impact locations, is shown in Fig. 19.6.

To study the variability that can be expected in the blades, four blades were subjected to modal tests to obtain multiple data sets for future analyses. Additionally, each blade was weighed, as differences in mass would result in changes in dynamic characteristics. The weights of the blades are listed in Table 19.1.

The first six modes of each blade were captured during impact testing. A comparison of the natural frequency results is shown in Table 19.2.

19.4 Data Corelations

To further study the variability in the blades, a modal assurance criterion (MAC) was performed between the mode shapes of each blade. The MAC results are shown in Table 19.3.

The diagonals and sub-diagonals highlighted in gray show the high level of correlation of the mode shapes between the modal test results for each of the blades. However, the fourth mode of Blade 4 does not correlate well with the other blades. This is due to differences in the tip displacement, as shown in Fig. 19.7, which overlays the mode shapes for Blade 1 and Blade 3.

Measurements at the tip are difficult to obtain because the high response at this location results in double impacts for many measurement averages and distorts the measurement. To obtain better correlation between the blades, the two measurement points nearest the tip of the blades were deleted and another MAC was performed. These results are shown in Table 19.4.

The correlation of all blades improved, with Blade 3 improving the most. The average MAC for each of the blade correlations has been compiled in Table 19.5.

A comparison between blades was performed to determine expected variance between blades. The weight varied by as much as 17% and was determined to be 18.3 ± 1.2 lbs. The frequency of the first mode varied by as much as 9.7% and was

Table 19.3 MAC of all blades

MAC	Mode	Blade 1						Blade 2						Blade 3						Blade 4					
		1	2	3	4	5	6	1	2	3	4	5	6	1	2	3	4	5	6	1	2	3	4	5	6
Blade 1	1	100.0	16.8	11.6	41.5	12.6	12.8	96.4	14.7	16.1	46.6	12.5	13.2	96.7	12.0	14.2	17.5	9.3	11.9	96.0	13.5	13.4	48.1	8.8	13.0
	2	16.8	100.0	44.3	40.0	27.5	32.2	31.6	99.7	46.6	39.2	27.3	33.6	29.3	99.3	44.7	4.9	16.6	32.0	31.8	99.4	42.9	24.4	15.8	31.8
	3	11.6	44.3	100.0	78.0	40.3	33.0	17.6	46.8	98.9	74.4	34.7	35.1	21.0	46.6	99.0	58.1	23.1	30.5	24.2	49.5	99.0	66.4	23.4	31.2
	4	41.5	40.0	78.0	100.0	52.5	38.7	47.5	41.1	84.7	99.0	48.8	39.4	53.6	37.7	83.0	64.5	37.4	33.8	55.2	41.4	82.5	94.4	36.9	35.8
	5	12.6	27.5	40.3	52.5	100.0	47.4	15.7	27.5	47.3	49.4	98.9	43.4	17.0	26.3	45.2	40.1	95.6	39.4	19.3	30.2	49.0	39.6	96.3	40.7
	6	12.8	32.2	33.0	38.7	47.4	100.0	17.3	31.6	35.4	35.8	49.7	98.9	17.2	30.7	32.6	30.3	41.6	97.9	19.4	34.1	38.7	25.6	42.8	98.5
Blade 2	1	96.4	31.6	17.6	47.5	15.7	17.3	100.0	29.0	22.7	52.7	15.6	17.8	98.8	25.5	20.5	16.0	10.8	16.3	98.8	27.2	19.2	50.5	10.2	17.4
	2	14.7	99.7	46.8	41.1	27.5	31.6	29.0	100.0	49.0	39.9	27.1	33.1	27.1	99.6	47.3	5.1	16.3	31.4	29.4	99.6	45.2	25.0	15.6	31.2
	3	16.1	46.6	98.9	84.7	47.3	35.4	22.7	49.0	100.0	81.2	41.9	37.1	26.8	48.0	99.8	58.9	29.5	32.0	29.9	51.3	99.3	72.8	29.5	32.9
	4	46.6	39.2	74.4	99.0	49.4	35.8	52.7	39.9	81.2	100.0	46.0	36.0	58.8	36.5	79.5	64.5	35.1	30.6	60.4	40.0	78.7	96.0	34.5	32.8
	5	12.5	27.3	34.7	48.8	98.9	49.7	15.6	27.1	41.9	46.0	100.0	45.0	16.8	25.8	39.9	34.5	97.7	40.9	18.8	29.6	43.2	36.7	97.2	42.0
	6	13.2	33.6	35.1	39.4	43.4	98.9	17.8	33.1	37.1	36.0	45.0	100.0	17.7	32.3	34.1	30.3	36.5	99.4	20.1	35.7	40.3	25.9	37.8	99.2
Blade 3	1	96.7	29.3	21.0	53.6	17.0	17.2	98.8	27.1	26.8	58.8	16.8	17.7	100.0	23.5	24.6	19.9	11.8	15.7	99.1	25.4	22.9	58.1	11.0	17.0
	2	12.0	99.3	46.6	37.7	26.3	30.7	25.5	99.6	48.0	36.5	25.8	32.3	23.5	100.0	46.4	4.8	15.2	30.8	26.0	99.7	44.6	22.0	14.6	30.5
	3	14.2	44.7	99.0	83.0	45.2	32.6	20.5	47.3	99.8	79.5	39.9	34.1	24.6	46.4	100.0	57.6	27.8	29.1	27.4	49.5	99.0	71.7	27.7	29.9
	4	17.5	4.9	58.1	64.5	40.1	30.3	16.0	5.1	58.9	64.5	34.5	30.3	19.9	4.8	57.6	100.0	29.5	26.7	23.1	6.4	63.4	67.6	31.7	28.8
	5	9.3	16.6	23.1	37.4	95.6	41.6	10.8	16.3	29.5	35.1	97.7	36.5	11.8	15.2	27.8	29.5	100.0	32.9	13.2	18.4	31.0	28.2	99.4	34.0
	6	11.9	32.0	30.5	33.8	39.4	97.9	16.3	31.4	32.0	30.6	40.9	99.4	15.7	30.8	29.1	26.7	32.9	100.0	18.2	33.9	35.3	21.0	34.6	99.6
Blade 4	1	96.0	31.8	24.2	55.2	19.3	19.4	98.8	29.4	29.9	60.4	18.8	20.1	99.1	26.0	27.4	23.1	13.2	18.2	100.0	28.1	26.1	58.8	12.6	19.4
	2	13.5	99.4	49.5	41.4	30.2	34.1	27.2	99.6	51.3	40.0	29.6	35.7	25.4	99.7	49.5	6.4	18.4	33.9	28.1	100.0	47.9	25.0	17.7	33.7
	3	13.4	42.9	99.0	82.5	49.0	38.7	19.2	45.2	99.3	78.7	43.2	40.3	22.9	44.6	99.0	63.4	31.0	35.3	26.1	47.9	100.0	70.1	31.4	36.3
	4	48.1	24.4	66.4	94.4	39.6	25.6	50.5	25.0	72.8	96.0	36.7	25.9	58.1	22.0	71.7	67.6	28.2	21.0	58.8	25.0	70.1	100.0	27.1	22.7
	5	8.8	15.8	23.4	36.9	96.3	42.8	10.2	15.6	29.5	34.5	97.2	37.8	11.0	14.6	27.7	31.7	99.4	34.6	12.6	17.7	31.4	27.1	100.0	35.8
	6	13.0	31.8	31.2	35.8	40.7	98.5	17.4	31.2	32.9	32.8	42.0	99.2	17.0	30.5	29.9	28.8	34.0	99.6	19.4	33.7	36.3	22.7	35.8	100.0
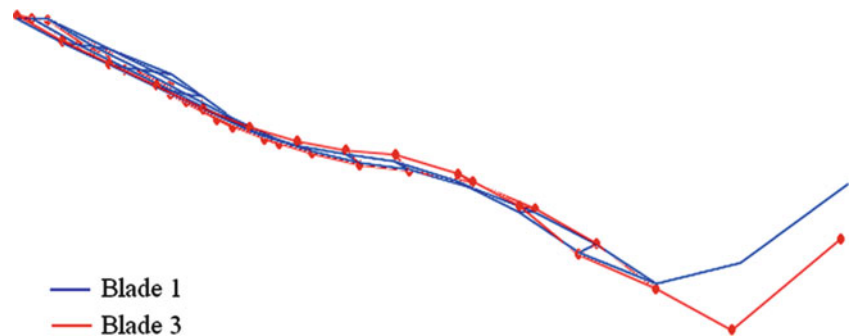
Fig. 19.7 Blade 1 and 3, mode 4 revealing a difference in tip displacement

— Blade 1
— Blade 3

Table 19.4 MAC of blades with tip points deleted

MAC	Mode	Blade 1 1	2	3	4	5	6	Blade 2 1	2	3	4	5	6	Blade 3 1	2	3	4	5	6	Blade 4 1	2	3	4	5	6
Blade 1	1	100.0	15.9	9.3	6.5	0.4	0.1	96.4	23.2	7.3	12.9	0.5	0.2	98.7	22.8	9.0	11.3	0.1	0.4	97.1	23.0	7.8	14.9	0.0	0.8
	2	15.9	100.0	0.3	49.5	10.6	0.6	5.7	98.8	2.5	43.1	8.6	0.2	12.7	98.6	2.3	40.1	10.9	0.0	8.9	98.4	3.0	50.4	12.1	0.1
	3	9.3	0.3	100.0	37.2	2.5	13.4	11.1	0.0	98.2	30.6	5.8	10.1	6.4	0.1	97.9	33.4	8.3	14.3	4.6	0.2	98.0	28.1	9.7	16.1
	4	6.5	49.5	37.2	100.0	2.0	6.0	2.1	47.4	45.3	95.4	0.4	5.8	7.3	43.5	43.5	95.3	0.4	10.2	6.9	43.7	47.1	96.3	0.4	8.7
	5	0.4	10.6	2.5	2.0	100.0	1.4	1.8	11.2	0.2	1.7	97.4	5.6	1.1	10.8	0.1	1.3	96.6	8.8	1.3	9.2	0.3	2.4	96.8	9.1
	6	0.1	0.6	13.4	6.0	1.4	100.0	0.1	1.0	14.9	5.5	0.1	95.8	0.1	1.3	14.5	3.0	0.2	92.8	0.0	1.0	12.5	2.8	0.0	94.6
Blade 2	1	96.4	5.7	11.1	2.1	1.8	0.1	100.0	10.7	10.1	7.2	1.8	0.2	97.3	10.5	12.0	6.1	0.9	0.6	97.6	10.7	10.8	8.0	0.6	1.0
	2	23.2	98.8	0.0	47.4	11.2	1.0	10.7	100.0	1.0	43.1	9.5	0.4	19.3	99.7	0.8	40.1	12.2	0.0	14.6	99.4	1.3	50.5	13.4	0.3
	3	7.3	2.5	98.2	45.3	0.2	14.9	10.1	1.0	100.0	37.5	1.9	12.3	5.1	0.4	99.7	40.3	3.3	17.6	3.7	0.3	99.7	35.4	4.1	19.4
	4	12.9	43.1	30.6	95.4	1.7	5.5	7.2	43.1	37.5	100.0	0.3	6.2	14.8	39.3	35.9	97.5	0.4	10.4	14.3	39.6	39.1	97.0	0.4	8.2
	5	0.5	8.6	5.8	0.4	97.4	0.1	1.8	9.5	1.9	0.3	100.0	0.9	1.3	9.3	1.5	0.3	99.4	2.3	1.6	7.7	1.9	0.8	98.4	2.4
	6	0.2	0.2	10.1	5.8	5.6	95.8	0.2	0.4	12.3	6.2	0.9	100.0	0.1	0.6	12.3	3.2	0.7	98.5	0.0	0.4	10.2	2.9	1.5	97.6
Blade 3	1	98.7	12.7	6.4	7.3	1.1	0.1	97.3	19.3	5.1	14.8	1.3	0.1	100.0	18.7	6.6	13.2	0.5	0.3	98.6	18.9	5.6	16.3	0.3	0.6
	2	22.8	98.6	0.1	43.5	10.8	1.3	10.5	99.7	0.4	39.3	9.3	0.6	18.7	100.0	0.3	36.1	12.1	0.1	13.9	99.7	0.6	46.4	13.4	0.5
	3	9.0	2.3	97.9	43.5	0.1	14.5	12.0	0.8	99.7	35.9	1.5	12.3	6.6	0.3	100.0	38.1	2.8	17.8	5.0	0.3	99.5	33.4	3.6	19.4
	4	11.3	40.1	33.4	95.3	1.3	3.0	6.1	40.1	40.3	97.5	0.3	3.2	13.2	36.1	38.1	100.0	0.3	6.5	13.0	36.2	42.1	98.0	0.2	5.2
	5	0.1	10.9	8.3	0.4	96.6	0.2	0.9	12.2	3.3	0.4	99.4	0.7	0.5	12.1	2.8	0.3	100.0	2.0	0.8	10.3	3.2	0.9	99.5	2.0
	6	0.4	0.0	14.3	10.2	8.8	92.8	0.6	0.0	17.6	10.4	2.3	98.5	0.3	0.1	17.8	6.5	2.0	100.0	0.1	0.0	15.4	6.0	3.1	98.6
Blade 4	1	97.1	8.9	4.6	6.9	1.3	0.0	97.6	14.6	3.7	14.3	1.6	0.0	98.6	13.9	5.0	13.0	0.8	0.1	100.0	14.0	4.2	15.7	0.6	0.2
	2	23.0	98.4	0.2	43.7	9.2	1.0	10.7	99.4	0.3	39.6	7.7	0.4	18.9	99.7	0.3	36.2	10.3	0.0	14.0	100.0	0.5	46.2	11.7	0.3
	3	7.8	3.0	98.0	47.1	0.3	12.5	10.8	1.3	99.7	39.1	1.9	10.2	5.6	0.6	99.5	42.1	3.2	15.4	4.2	0.5	100.0	37.0	4.1	16.8
	4	14.9	50.4	28.1	96.3	2.4	2.8	8.0	50.5	35.4	97.0	0.4	2.9	16.3	46.4	33.4	98.0	0.9	6.0	15.7	46.2	37.0	100.0	0.9	4.8
	5	0.0	12.1	9.7	0.4	96.8	0.0	0.6	13.4	4.1	0.4	98.4	1.5	0.3	13.4	3.6	0.2	99.5	3.1	0.6	11.7	4.1	0.9	100.0	3.0
	6	0.8	0.1	16.1	8.7	9.1	94.6	1.0	0.3	19.4	8.2	2.4	97.6	0.6	0.5	19.4	5.2	2.0	98.6	0.2	0.3	16.8	4.8	3.0	100.0

Table 19.5 Improvement of Average MAC values by removing tip points

Correlation	Average MAC Original	Tip points removed
Blade 1 and 2	82.0	97.0
Blade 1 and 3	82.2	96.7
Blade 1 and 4	82.1	96.9
Blade 2 and 3	98.2	98.7
Blade 2 and 4	97.5	98.3
Blade 3 and 4	99.0	99.0

Table 19.6 Comparison between FE and test natural frequencies

Mode	Frequency (Hz) FE model	Blade 1	Blade 2	Blade 3	Blade 4	Largest% Diff
1	13.8	14.5	13.6	13.1	13.3	4.9%
2	25.9	28.8	26.4	25.6	25.9	9.9%
3	50.1	54.2	50.1	49.0	49.6	7.5%
4	57.7	65.6	56.6	56.4	56.2	12%
5	84.2	90.1	83.3	81.5	82.5	6.5%
6	123.7	130.1	120.1	117.7	119.7	4.9%

determined to be 13.6 ± 0.5 Hz. The frequency of the second mode varied by as much as 11.1% and was determined to be 26.7 ± 1.3 Hz. All MAC comparisons were above 95% once the poor tip measurements were deleted.

The four sets of blade data were then compared to the FE model predictions. Table 19.6 compares the predicted natural frequencies of the blade from the FE model with the measured natural frequencies of the four tested blades.

Table 19.6 lists the largest percent differences found among all the blades for each natural frequency. Every largest percent difference was found to be associated with Blade 1, highlighted in gray. All measured values of natural frequency for Blade 1 resulted in a higher natural frequency for each mode when compared to the FE prediction. On the contrary, Blades 2, 3, and 4 test results in lower values for natural frequencies when compared to the FE predictions for each mode.

Table 19.7 MAC values for first six modes of turbine blade compared to FE model

| Mode | MAC | | | | Description |
	Blade 1	Blade 2	Blade 3	Blade 4	
1	91.4	90.7	90.6	88.5	Flap-wise
2	96.6	96.5	95.6	94.4	Flap-wise
3	92.3	93.8	94.3	90.0	Flap-wise
4	90.2	90.6	57.9	88.4	Torsional
5	90.0	91.8	85.9	83.2	Flap-wise
6	89.6	91.3	87.6	86.6	Flap-wise
Average	91.68	92.45	85.32	88.52	
Average, Omitting Mode 4	91.98	92.82	90.80	88.54	

Experience has shown that the finite element method generally produces frequency values that are greater than what is measured in the field. Table 19.6 shows that this is consistent for Blades 2, 3, and 4. To validate the finite element model predictions for mode shapes, a MAC calculation was performed. Table 19.7 shows the MAC calculation for each of the blades.

Table 19.7 shows that most of the MAC values are 90 or above. The lowest value is found at mode 4 of blade 3. Mode 4 is classified as a torsional mode. Testing was performed using a single axis accelerometer and excitation in the Flap-wise direction. Although the mode shape of mode 4 has components of both flap-wise and torsion, the torsional component is dominant, and only the small component of flap-wise motion could be measured during testing. Therefore, the average MAC was calculated again omitting mode 4. By omitting mode 4, the average MAC increased slightly for Blades 1, 2, 4, and significantly increased for Blade 3.

The results were examined to determine if there were any particular measured degrees of freedom that were mostly responsible for the poor MAC values. The mode shape pairs were examined, and several test points were causing errors in the correlation calculations. Table 19.8 shows graphics of the mode shape pairs for each mode.

Table 19.8 shows that mode shape correlation is poor at the tip of the blade for all modes. The blade is very compliant near the tip and the measurements at the tip were not consistent for all of the blades, thus contaminating the MAC values of all blades. The correlation improvements for test data seen in Table 19.4 were a result from deleting the node point pairs at the tip of the blade. Table 19.9 shows the updated MAC values resulting from deleting erroneous node point pairs near the tip and root of the blade.

Overall the updated MAC values are improved by deleting the inaccurate node point pairs from the correlation calculation. Table 19.10 compares the original Average MAC values which were contaminated with the inaccurate node point pairs, to the updated Average MAC values. The greatest improvement of Average MAC is observed in Blades 2, 3, and 4. The greatest improvement is observed for Blade 4, and yields a 2.959% difference due to the tip and root node point pair deletion.

The results of these preliminary correlations provide important information for the future correlation effort for the blade using the full solid finite element model currently in progress. These preliminary results are very useful to help understand the dynamic characteristics of the blade for future efforts to predict dynamic stress–strain.

19.5 Conclusion

As part of an overall assessment of a turbine blade for static and fatigue loading, modal testing was performed for several wind turbine blades to understand the overall dynamic characteristics and variability from a set of turbine blades. Modal characteristics of the test data was compared to each other to identify any obvious differences between the blades. MAC values for all the Flap-wise modes were very good overall.

In addition, a simple beam finite element model was developed (while the solid model of the blade was being prepared) for comparison to the measured data. The beam model was correlated to the test data collected for each of the blades tested. Overall the correlation to the model was very good. Improvements to the correlation were observed as certain measurements (suspected to be prone to measurement error) were removed from the data set. Further correlation studies are yet to be performed once the solid model is available.

Table 19.8 Correlated mode shape pairs
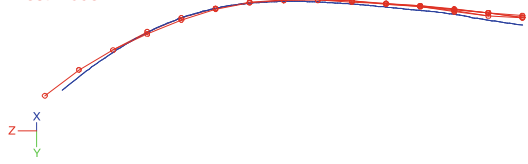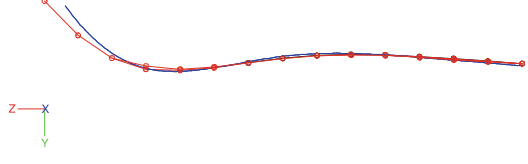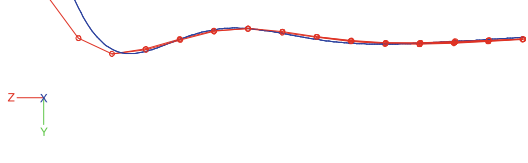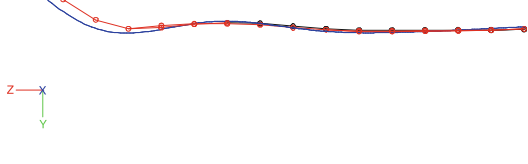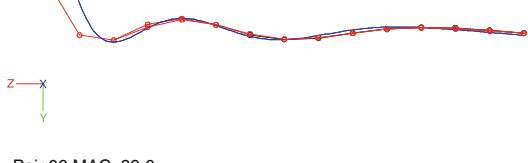
Mode	Mode shape pair	Cause of error
1	Pair 01 MAC 91.4 FE Model Test Model 	Tip root
2	Pair 02 MAC 96.6 FE Model Test Model 	Tip
3	Pair 03 MAC 92.3 FE Model Test Model 	Tip
4	Pair 04 MAC 90.2 FE Model Test Model 	Tip
5	Pair 05 MAC 90.0 FE Model Test Model 	Tip
6	Pair 06 MAC 89.6 FE Model Test Model 	Tip

Table 19.9 Updated MAC values for flap-wise modes of the turbine blade compared to FE model

| Mode | MAC | | | | Description |
	Blade 1	Blade 2	Blade 3	Blade 4	
1	90.4	86.1	84.5	82.9	Flap-wise
2	97.9	99.0	99.0	98.9	Flap-wise
3	95.1	97.4	96.7	95.5	Flap-wise
5	90.7	92.6	88.9	88.5	Flap-wise
6	85.8	91.9	88.7	90.4	Flap-wise
Average	92.0	93.40	91.60	91.24	Flap-wise

Table 19.10 Comparison of average MAC values for flap-wise modes of the turbine blade

Blade	Average MAC	Average MAC updated	% Diff
1	91.98	92.00	<0.01
2	92.82	93.40	0.615
3	90.80	91.60	0.873
4	88.54	91.24	2.959

References

1. Carr J, Avitabile P, Niezrecki C (2012) Dynamic stress–strain on turbine blade using digital image correlation techniques (Part 1 – Static load and calibration). In: Paper accepted for 30th international modal analysis conference, Jacksonville
2. Carr J, Avitabile P, Niezrecki C (2012) Dynamic stress–strain on turbine blade using digital image correlation techniques (Part 2 – Dynamic measurements). In: Paper accepted for 30th international modal analysis conference, Jacksonville
3. Southwest Windpower, Blade CAD models provided for analyses performed, AZ, USA

Chapter 20
Dynamic Stress–Strain on Turbine Blade Using Digital Image Correlation Techniques Part 1: Static Load and Calibration

Jennifer Carr, Javad Baqersad, Christopher Niezrecki, Peter Avitabile, and Micheal Slattery

Abstract Often times, wind turbine blades are subjected to static and dynamic testing to identify the performance levels that can be achieved for a particular configuration. These tests are a necessary part of the validation process. Typically, a variety of different static and dynamic measurements are made using a variety of different transducers. Typically, only a handful of strain gages are deployed to capture strain information.

Recent advances in digital image correlation (DIC) and dynamic photogrammetry (DP) have allowed new opportunities for blade inspection, structural health monitoring, and full-field vibration testing. The primary benefit to using DIC is that the measurement approach is not limited to identifying the displacement or strain at only a few discrete measurement locations, but instead makes full-field surface measurements possible. These techniques are currently being explored on several wind turbine blade applications and can provide a wealth of additional information that was previously unobtainable.

This paper, which is the first part of a two part paper, presents the static strain measurements and calibration of the system overall. The strain distribution along the length of the structure is compared to the finite element model. The data analysis is used to assure that the model is calibrated for the dynamic testing results; dynamic testing results are presented in the second part of this paper.

20.1 Introduction

As part of the certification process for wind turbine blades, static and dynamic tests are conducted to validate the structural configuration. Load tests are performed along with fatigue testing on the blades. Generally, the blades are instrumented with various measurement transducers and, in particular, many strain gages are generally included as part of the measurement system.

These strain gages are used to identify the stress and strain from the test. However, these gages are located at discrete points and information regarding the full-field distribution of the stress–strain is not available. Using digital image correlation (DIC) techniques, the full-field stress–strain can be obtained.

This work focuses on the use of DIC techniques to measure full-field stress and strain for both static and dynamic tests. Part 1 (this paper) focuses on the static testing and general calibration of the system. Part 2 focuses on the dynamic testing results. The test configuration is described and the results of conventional strain gages are compared to the DIC technique to show the advantages of the full-field approach.

J. Carr (✉) • J. Baqersad • C. Niezrecki • P. Avitabile
Structural Dynamics and Acoustic Systems Laboratory, University of Massachusetts Lowell,
One University Avenue, Lowell, MA 01854, USA
e-mail: Jennifer_Carr@student.uml.edu

M. Slattery
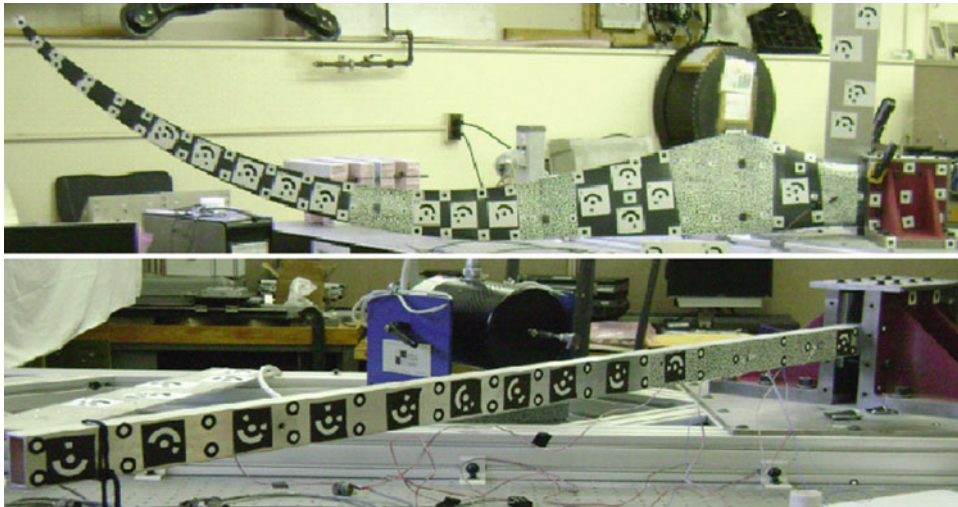Southwest Windpower, 1801 W.Route 66, Flagstaff, AZ 86001, USA

Fig. 20.1 Test setup for turbine blade (*top*) and aluminum beam (*bottom*)

In preparation for the testing of an actual wind turbine blade, a simple beam like structure was used for the validation of the test set up and methodology for the actual testing (see Fig. 20.1). The beam is very easy to characterize from both a test and model standpoint and the results provide more credibility for the proposed approach. (The actual testing of the Southwest Windpower turbine blade was underway at the time of this writing and the results will be presented in a future paper.) The test rig is described followed by the static testing performed prior to the dynamic tests; the dynamic testing results are presented in Part 2 of this paper.

20.2 Test Rig for Testing Blades

To perform testing on the turbine blades, a test rig was designed, manufactured, and assembled [1]. During the design process, information on loading procedure and experimental requirements was based upon a test report from the National Renewable Energy Laboratory (NREL) [2]. An overview of the test setup is shown in Fig. 20.2.

An optical table was chosen as the base of the test rig. To prevent transferring of forces generated by testing to the table, a frame was used to connect the fixture to the table. The frame was constructed with 3 in. by 3 in. aluminum extrusion beams. A 3/8 in. steel plate was bolted over a 2 ft by 2 ft area of the frame on which the fixture holding the blade was bolted. A CAD model of the frame is shown in Fig. 20.3.

The fixture is designed to secure the root of the blade during testing and consists of two cast iron angle blocks, two shear plates, two spacer plates, and assorted hardware. The cast iron angle blocks clamp against the blade and secure the blade to the frame. The shear plates are used to increase torsional rigidity of the fixture. The aluminum spacer plates were used to adapt the face of the root, which has compression limiters and a triangular extrusion that interfere with clamping, to the face of the angle blocks. The fixture is shown in Fig. 20.4.

The load applied to the blade was distributed using a whiffle tree. The design of the whiffle tree was based on the NREL test report [2], but pink insulation foam was used for the saddles instead of machined delrin pieces. The whiffle tree is shown in Fig. 20.5.

The designed loading mechanism consists of a 3 in. pneumatic (air) ram controlled by three precision air flow valves and fed by a small compressor. A controller was designed and manufactured to allow the load to be increased or decreased. This device permitted a user-controlled loading speed. The ram was mounted to the frame using a square post and a swiveling mounting bracket. The swiveling bracket allows the pneumatic ram to maintain a perpendicular pulling angle with respect to the whiffle tree. The air ram is connected to the whiffle tree with rope that has a force gage in the middle to measure the load. The pneumatic ram is shown in Fig. 20.6.
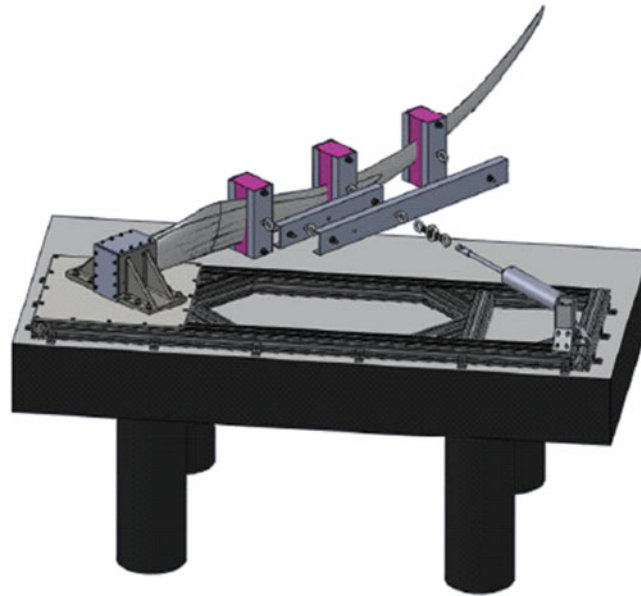
Fig. 20.2 Test rig including the mounting fixture, turbine blade, whiffle tree, and pneumatic actuator

Fig. 20.3 Frame design
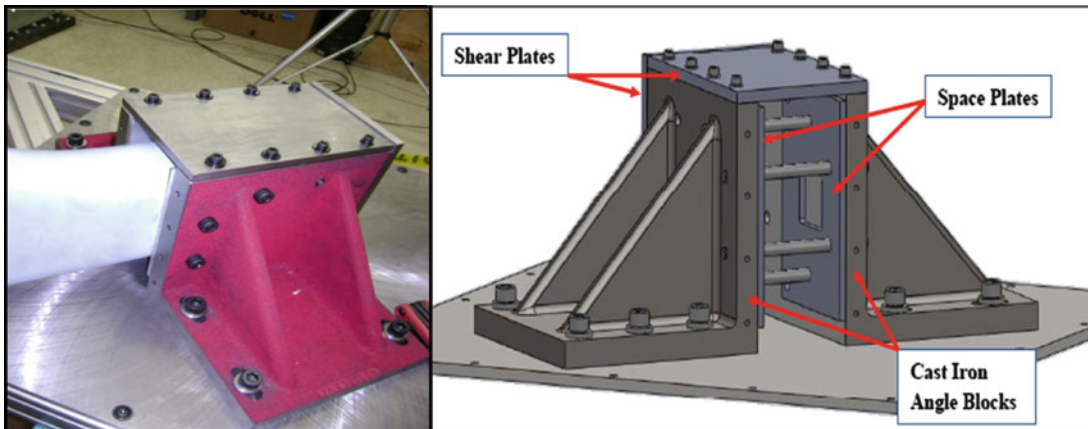
Fig. 20.4 Fixture realization and CAD model
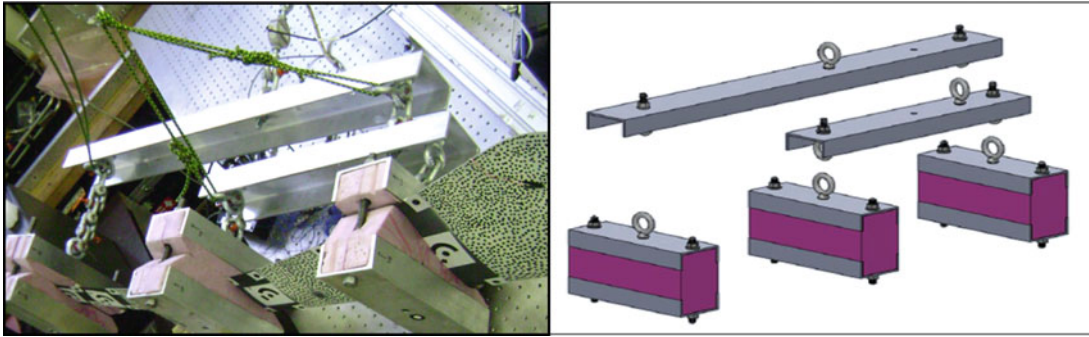
Fig. 20.5 Whiffle tree
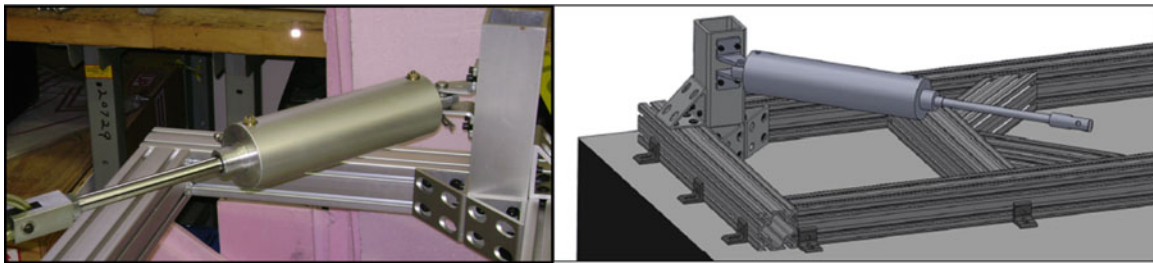
Fig. 20.6 Pneumatic ram actuator used to provide the turbine blade loading

20.3 Structure Description

Testing and analysis was performed on a 5-ft long aluminum beam. The cross-section of the beam was a rectangular tube with dimensions of 1-in. by 2-in. and a thickness of 1/8-in. The beam was clamped in a fixture specifically designed for testing a wind turbine blade. The beam was used as a simplified structure for preliminary testing to validate the test set up and methodology for the actual testing. The beam is very easy to characterize from both a test and model standpoint and the results provide more credibility for the proposed approach. The test methods were designed for wind turbine blade applications and will be implemented on a wind turbine blade when the testing procedures and equipment are better understood and successfully performed on the beam.

20.4 Testing Performed

For validation and calibration of the system and finite element model, a static test was performed on the structure. The load was applied using the pneumatic ram described earlier. Incremental loads of 25 lbs were applied up to a 125 lb load. At each loading stage, data was taken using strain gages and DIC cameras, and the results were compared. A visual comparison of the finite element model to the DIC results when the structure was subjected to a 125 lb load, along with graphical strain comparisons of the strain gage results and DIC results, are shown in Fig. 20.7.
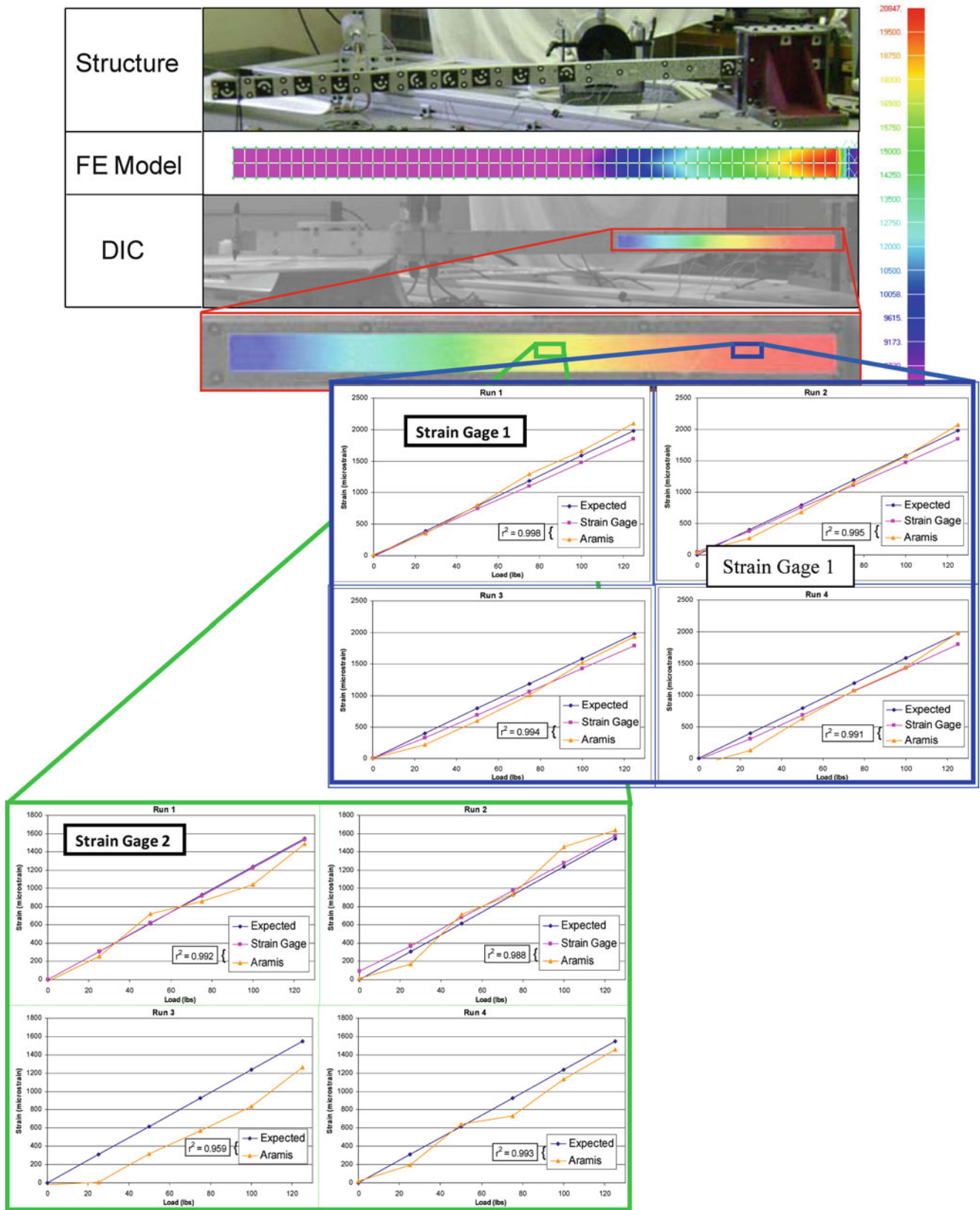
Fig. 20.7 Comparison of the full-field DIC results and the measurement from two strain sensors

Table 20.1 Coefficient of determination for strain gage and DIC data

Run #	Strain gage 1 (near base)	Strain gage 2 (near tip)
1	0.998	0.993
2	0.995	0.988
3	0.994	0.959
4	0.991	0.993

The DIC data provides a full-field strain plot over the measured length of the beam. This plot shows a similar trend compared to the finite element model over the same field of the beam. To compare the results of the strain gages and the DIC data, the results from one measurement point of the speckle pattern located in the center of the strain gages was compared to the strain gage data, as shown in the plots of Fig. 20.7. In addition to the strain gages and DIC results, an expected value of strain at those locations was calculated to ensure the results were reasonable. Although there was variance on the DIC data due to the proximity to the noise floor of the DIC measurement, the data is comparable to the strain gage results. Table 20.1 shows the coefficient of determination (R^2) values between the strain gage data and the DIC data (Note: Strain gage data for the location nearest the tip of the structure was not measured for runs 3 or 4, so an R^2 correlation was performed between the DIC data and the calculated strain). All the R^2 values are greater than 0.98, except in Run 3 in the data closer to the tip of the beam in which the DIC data were offset from the expected strain values. Overall, the results from the strain gage, model, and DIC compare very well. The acceptable correlation of data from a static test validates the testing approach and permits dynamic testing to be performed with confidence. The dynamic testing is presented in Part 2 of this paper.

Using DIC techniques to measure strain provides full-field strain results on a structure, that has a large advantage over conventional discrete strain measurement techniques. Because strain gages only measure discrete points, unexpected strain values due to defects in the structure would only be captured if a strain gage were placed at that precise location. However, current studies show that measuring strain along a structure using DIC techniques allows for the detection of defects due to changes in the full-field strain results. Additionally, using DIC permits measurements to be taken without the preparation time and wiring required when using strain gages.

20.5 Conclusion

Static and dynamic measurements for wind turbine blades are generally required for validation procedures. Digital image correlation has been used for making full-field surface measurements of displacement and strain in many applications and is currently being explored for measurement on turbine blades. For this work, in Part 1 of this paper, a static load test was performed on a cantilevered aluminum beam to validate the test setup and methodology for testing that will be performed for a turbine blade. Strain gages measured strain at discrete points on the structure while DIC measurement techniques were also employed to capture a full-field strain measurement. The DIC results and strain gage data compared very well; all strain measurements between the two techniques had R^2 correlation coefficients greater than 0.98, and the use of DIC for this application was validated. The full-field strain contour from the DIC measurement was also compared to a strain contour of the finite element model, and the contour plots exhibited the same trend along the length of the structure.

References

1. Carr J, Dyas S, Ertsos M, LoPiccolo J, Nonis C, Romano J (2011) Static and dynamic testing of a 7-ft wind turbine blade. University of Massachusetts Lowell, James B. Francis College of Engineering, Department of Mechanical Engineering, Capstone Design, 6 May 2011
2. National Renewable Energy Laboratory (2010) Blade static test report SWWP SS47 2.3-m wind turbine blade. Test report 100804, 4 Aug 2010

Chapter 21
Dynamic Stress–Strain on Turbine Blades Using Digital Image Correlation Techniques Part 2: Dynamic Measurements

Jennifer Carr, Javad Baqersad, Christopher Niezrecki, Peter Avitabile, and Micheal Slattery

Abstract Often times, wind turbine blades are subjected to static and dynamic testing to identify the performance levels that can be achieved for a particular configuration. Many times only a handful of strain gages are deployed to capture that information.

The first paper (part 1) presents the static strain measurements and calibration of the system overall. The strain distribution obtained by using digital image correlation (DIC) along the length of the beam is compared to discrete strain gage measurements and with a finite element model. In this second paper, DIC techniques are used to identify the full-field stress–strain on the turbine blade during dynamic testing. Comparison of the full-field stress–strain and the conventional strain gages are presented to show the usefulness of the image correlation approaches.

21.1 Introduction

As part of the certification process for wind turbine blades, static and dynamic tests are conducted to validate the structural configuration. Load tests are performed along with fatigue testing on the blades. Generally, the blades are instrumented with various measurement transducers and, in particular, many strain gages are generally included as part of the measurement system.

These strain gages are used to identify the stress and strain from the test. However, these gages are located at discrete points and information regarding the full-field distribution of the stress–strain is not available. Using digital image correlation (DIC) techniques, the full-field stress–strain can be obtained.

This work focuses on the use of DIC techniques to measure full-field stress and strain for both static and dynamic tests. Part 1 focuses on the static testing and general calibration of the system. Part 2 (this paper) focuses on the dynamic testing results. The test configuration is described and the results of conventional strain gages are compared to the DIC technique to show the advantages of the full-field approach.

In preparation for the testing of an actual wind turbine blade, a simple beam like structure was used for the validation of the test set up and methodology for the actual testing (see Fig. 21.1). The beam is very easy to characterize from both a test and model standpoint and the results provide more credibility for the proposed approach. (The actual testing of the Southwest Windpower turbine blade was underway at the time of this writing and the results will be presented in a future paper). The dynamic testing results measured using strain gages and DIC techniques are presented and analyzed.

J. Carr (✉) • J. Baqersad • C. Niezrecki • P. Avitabile
Structural Dynamics and Acoustic Systems Laboratory, University of Massachusetts Lowell,
One University Avenue, Lowell, MA 01854, USA
e-mail: Jennifer_Carr@student.uml.edu

M. Slattery
Southwest Windpower, 1801 W.Route 66, Flagstaff, AZ 86001, USA

Fig. 21.1 Test setup for turbine blade (*Top*) and aluminum beam (*Bottom*)

21.2 Structure Description

Testing and analysis was performed on a 5-ft long aluminum beam. The cross-section of the beam was a rectangular tube with dimensions of 1-in. by 2-in. and a thickness of 1/8-in. The beam was clamped in a fixture specifically designed for testing a wind turbine blade; for a description of the test rig, see Part 1 of this paper [1]. The beam was used as a simplified structure for preliminary testing to validate the test set up and methodology for the actual testing. The beam is very easy to characterize from both a test and model standpoint and the results provide more credibility for the proposed approach. The test methods were designed for wind turbine blade applications and will be implemented on a wind turbine blade when the testing procedures and equipment are better understood and successfully performed on the beam.

21.3 Testing Performed

Two different dynamic tests were performed to study the effectiveness of the image correlation techniques. The first dynamic test performed on the beam was a pluck test. For this test, the tip of the beam was displaced a certain distance. The beam was then released and allowed to oscillate. Three of these tests were performed, with tip displacements of approximately 1, 2, and 3 in., respectively. When the beam tip was displaced, the entire optical table, which sits upon pneumatic legs, also moved; when the beam was released, the table also oscillated, but at a much lower frequency. Tip displacements were measured with respect to the table. The results of the pluck tests are shown in Fig. 21.2.

As displayed in Fig. 21.2, the DIC data contains noise. A 100 Hz filter was applied to the strain gage measurements during testing, and the strain gage data is smoothed. The calculation of strain from the DIC measurement involves spatial filtering of the images. For this test, the default settings were used in the Aramis^TM software. Other filter settings may affect the processed data however, further studies on the effects of applying a filter to the DIC data are beyond the scope of this paper. Also, within the DIC data, there is a low frequency oscillation that is caused by the movement of the optical table. If this table oscillation were removed from the data, the peak strain results would match better. Although there is noise on the DIC data, the strain gage and DIC measurements match very well. In Fig. 21.2, the peak-to-peak values of strain are comparable between the strain gage and DIC measurements, which demonstrates that the DIC produces measurements of strain that are comparable to strain gage measurements.

When using DIC techniques, full-field strain of the structure can be produced at any slice in time, whereas strain gages can provide strain values for a discrete point on the structure over a period of time. This powerful aspect of the DIC approach is demonstrated in Fig. 21.3, that displays strain fields at two separate points in time. Having the full-field strain measurements provides data about structural defects or abnormalities that strain gages could only detect if placed at that discrete location.

Fig. 21.2 Dynamic strain measurements from the Pluck test for three different tip displacements comparing DIC to strain gages at two beam locations
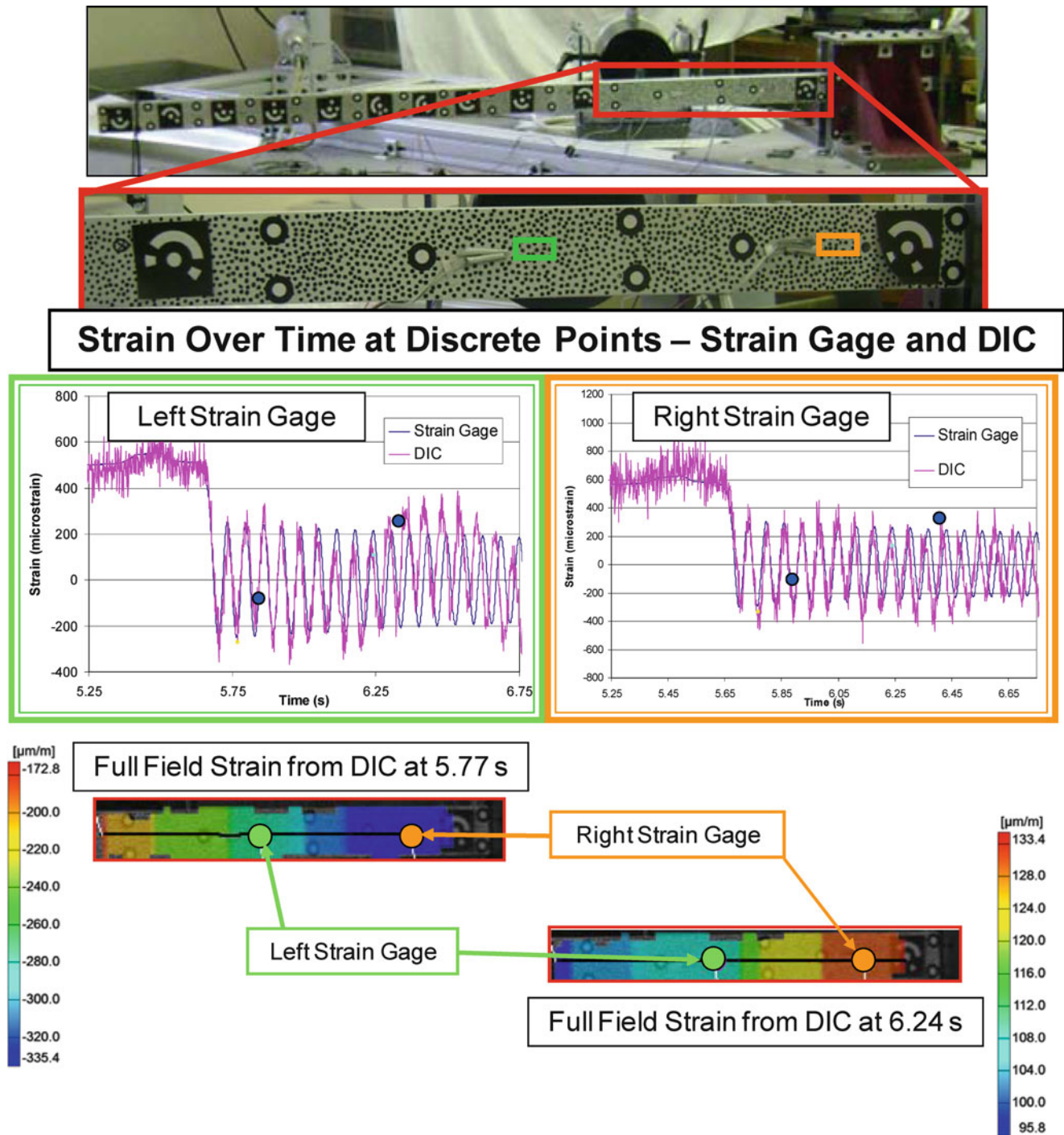
Fig. 21.3 Full-field strain measurements from DIC during Pluck test

For the second dynamic test a shaker was placed 8.25 in. from the base on the back side of the beam. A discrete sine input at the first natural frequency (determined to be 14.8 Hz through modal testing) of the system was applied. The strain on the beam was measured using both strain gages and DIC, and the results were compared. A comparison of the results is shown in Fig. 21.4. Again, there is noise in the DIC data that can be filtered but is beyond the scope of work for this paper. For the discrete sine test, the peak strain measurements are again comparable. DIC techniques that provide full-field strain values at any given instant in time can also be applied to this type of testing.
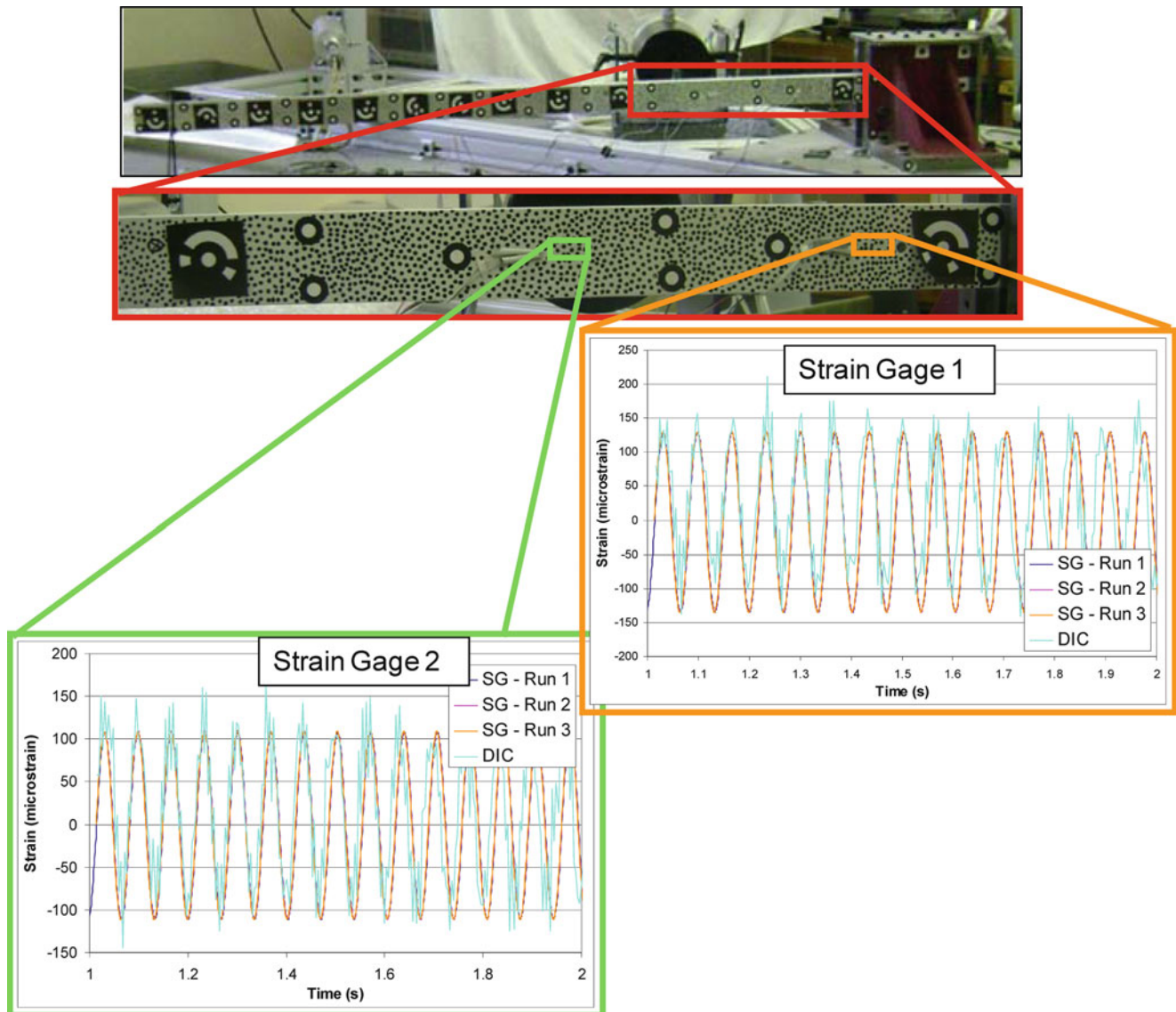
Fig. 21.4 Strain measurements from Shaker test at the first natural frequency

21.4 Conclusion

Static and dynamic measurements for wind turbine blades are generally required for validation of numerical models. Digital image correlation has been used for making full-field surface measurements of strain in many applications and is being explored for turbine blade applications. Within this paper, dynamic testing was performed on a cantilevered aluminum beam to compare the measurements between strain gages and DIC. The next phase of the testing will involve measurements that will be performed on a turbine blade. First, a pluck test, was performed where the tip of the beam was displaced a certain amount, released, and the beam oscillated. In another dynamic test a shaker was located near the base of the beam and oscillated at the first natural frequency of the system. Strain gages measured strain at discrete points on the structure while DIC measurement techniques were also employed to capture a full-field strain measurement. The DIC results and strain gage data compared very well, and the use of DIC for this application was validated.

Using DIC techniques as a measurement tool provides great potential in gathering data. The DIC measurements produce full-field strain measurements at any instant in time for dynamic testing. Full-field measurements can detect abnormalities in the strain field that a strain gage can only measure if placed at that precise location.

Reference

1. Carr J, Baqersad J, Avitabile P, Niezrecki C (2011) Dynamic stress- strain on turbine blade using digital image correlation techniques part 1- static load and calibration. In: Proceedings of the IMAC-XXX, Jacksonville, 30 Jan–2 Feb 2011

Chapter 22
Structural Health Monitoring of Wind Turbine Blades Under Fatigue Loads

Samuel J. Dyas, Justin Scheidler, Stuart G. Taylor, Kevin Farinholt, and Gyuhae Park

Abstract This paper presents the results of dynamic characterization and preparation of a full-scale fatigue test of a 9 m CX-100 blade. Sensors and actuators utilized include accelerometers and piezoelectric sensors. To dynamically characterize a 9 m CX-100 blade, full scale modal analyses were completed with varying boundary conditions and blade orientations. Also, multi-scale sensing damage detection techniques were explored; high frequency active-sensing was used in identifying fatigue damage initiation, while low frequency passive-sensing was used in assessing damage progression. Ultimately, high and low frequency response functions, wave propagations, and sensor diagnostic methods were utilized to monitor and analyze the condition of the wind turbine blade under fatigue loading.

22.1 Introduction

22.1.1 *Background*

Wind Energy is the fastest growing renewable domestic energy source in the United States. The DOE recently proposed that 20% of the nation's energy needs may be met through wind energy by 2030 [1]. In order to accomplish a larger wind power presence in the US, significant investments are being made in wind turbine technology, thus motivating manufactures to produce more efficient and more complex wind turbines. These trends are producing larger, longer, and lighter blades, ultimately generating greater power with increased efficiency. Given the demand for wind, and significant investments required, great effort is being expended to improve the design and manufacturability of wind turbine blades [2–4].

Maximizing wind turbine design reliability is a key to providing safe and cost effective operation. In order to increase wind turbine reliability, a non-destructive structural health monitoring (SHM) system specifically designed for the blades of the turbines would allow real-time monitoring of the blades while in a working state. Monitoring the health of the blades is practically important as they account for 15–20% of the total cost of the system. Also, if blade damage goes undetected, it may cause rotating unbalance, causing secondary damage to various other components of the turbine [5]. SHM could lead to condition based (as opposed to time based) maintenance, which saves operators unnecessary maintenance costs, while still alerting operators of real-time problems. SHM may ultimately lead to less downtime of wind turbines, and more efficient operation of the US wind energy national network.

This study will utilize a multi-scale sensing strategy which will lead to the characterization of both damage initiation and progression within the CX-100 blade. The multi-scale strategy will include the use of accelerometers, strain gages, piezoelectric transducers and acoustic emission sensors. High frequency sensing will be used in identifying fatigue damage

S.J. Dyas
Department of Mechanical Engineering, Colorado School of Mines, Golden, CO 80401, USA

J. Scheidler
Department of Mechanical Engineering, Ohio State University, Columbus, OH 43210, USA

S.G. Taylor • K. Farinholt • G. Park (✉)
The Engineering Institute, Los Alamos National Laboratory, Los Alamos, NM 87545, USA
e-mail: gpark@lanl.gov

initiation, while low frequency sensing will be used in assessing damage progression. Methods including high and low frequency response functions, wave propagations, and sensor diagnostics will be utilized to monitor and analyze the condition of the blade under the fatigue loads [6].

22.1.2   Previous Work

Many SHM techniques rely upon blade frequency response data. It has been shown during modal analyses of research-sized wind turbine blades that the boundary conditions prescribed during testing can have a significant effect on the frequencies and magnitudes of the blade's mode shapes [7–10]. For a research-sized blade supported by bungees, to simulate free conditions, percent differences of 2% and 52% in the first edgewise bending mode frequency and damping, respectively, were observed after support stiffness and locations were altered [10]. The same study also illustrated, theoretically, that measured damping could be far from the true value even for softly supported structures, and that the ideal location of support straps was at the nodes of the most relevant modes. By simply changing the location of straps used to support a CX-100 blade in a free-free condition, an average percent difference of 8.20% from the baseline was measured in the frequencies of the first three flap-wise modes [8]. From this research, it is apparent that the boundary conditions applied during validation of various SHM techniques must be closely monitored. The effect of random errors sources (such as force level, input force location, and algorithmic) and bias error sources (such as mass loading, data transmission cables, and ambient environment) on experimentally measured modal frequencies and damping has also been studied [11]. It was found that bias errors tend to be more significant than random errors. Further, mass loading from instrumentation cables and sensors (having 0.7% of the structure mass) can result in as much as 35% increases in damping and 4% decreases in frequency, with torsional modes affected the most [11].

The use of SHM strategies on research-sized wind turbine blades has also been investigated. The SHM strategies can generally be divided into low-frequency and high-frequency categories. In the low-frequency regime, frequency response functions (FRFs) were used in conjunction with data from an FE model to monitor changes in resonant frequencies and mode shapes [12], deviations in the root-mean-square of an FRF and a neural network were used to identify delamination in composites [13], and a modal-based approach used PZT patches to observe changes in resonant frequencies [14, 15]. The low-frequency techniques are typically used for damage detection on a global scale. These low-frequency methods usually lack sufficient sensitivity, and are affected by changes to boundary or operational conditions [16].

In the high-frequency regime, piezoelectric-based MFC (macro-fiber composite) self-sensing actuators were used to measure mechanical impedance from the sensor electrical impedance [17–19], acoustic emission sensors have been used to measure changes in acoustic velocity and attenuation [14, 17, 20, 21], MFC and piezoelectric actuators and sensors were used to track and obtain time domain responses [22], variations in blade loading were measured using accelerometers and piezoelectric [17], surface displacements were monitored by a coherent optical technique [20], changes in piezoelectric sensor response to lamb wave propagations were investigated [22], and changes to frequency response measurements were observed using piezoelectric actuating and sensing [16, 17, 22]. Results showed that acoustic emission strategies face challenges due to the vast range of materials in a wind turbine blade, and that while many techniques are promising, additional research is needed to determine the optimal SHM strategy for a particular wind turbine system. A challenge facing many high-frequency techniques is the relatively high memory usage and power consumption [22]. High-frequency techniques are used to detect damage on a local scale, and therefore require location of the sensors close to the failure region (which presents challenges to detecting small scale damage, while also monitoring the entire blade).

Since the damage detection range for many SHM techniques is limited, it is important to locate the sensors at critical locations on the blade. Static testing of a TX-100 blade resulted in failure between 1 and 3 m from the root, near maximum chord, on the compression side. Also, fatigue testing of similar 9 m blades yielded failure near the maximum chord. However, recent fatigue testing of a TX-100 blade resulted in failure on the tension side at the spar cap termination point [17]. A number of damage "hot spots" on wind turbine blades have also been identified as (1) 30–35% and 70% in blade length from the blade root, (2) the blade root, (3) the maximum chord, and (4) the upper spar cap/flange of the spar [5].

Equally important or possibly more important than sensor location is sensor diagnostics. Sensor diagnostics determine whether a sensor is in a healthy condition and therefore if its measurements can be trusted. In this field, monitoring of PZT sensor electrical admittance (and effectively the capacitance) has shown much promise [23–25]. The electrical admittance monitoring method has been shown to identify sensor debonding progression and degradation of the electromechanical properties of the PZT in situ [23].

22.1.3   Purpose and Goals

There are two primary objectives of this study. The first is to dynamically characterize the CX-100 in various boundary conditions. This is crucial to the development and validation of finite element (FE) models of the CX-100 blade. This study will not be involved with the development or validation of the FE models, but data from this study will be provided to other research projects involved with the effort. The second primary objective is to prepare working and validated tools and methods for the SHM of the CX-100 once the blade has begun a full-scale fatigue test at the National Energy Renewable Laboratory (NREL). When the full-scale fatigue tests commences, the CX-100 will be oscillated to failure, while various sensor provide real-time data that will serve as inputs to the SHM analysis techniques developed in this research.

22.2   Modal Analysis Discussion

22.2.1   LANL Free-Free Analysis

A free-free modal analysis on this blade was completed [8]. The support straps were placed at the node of the first mode in order to minimize the effects of the boundary condition. A photo of the set-up is shown in Fig. 22.1, while the modal test data acquisition parameters are shown in Table 22.1.

The modal results of the free-free modal analysis are shown in Table 22.2.

22.2.2   LANL Vertical Fixed-Free Analysis

In this test, a modal analysis was performed under a vertical fixed-free configuration. A photo of the experimental set-up is shown in Fig. 22.2. The data acquisition parameters used were the same as the free-free analysis (Table 22.1).

Fig. 22.1 Set-up of free-free modal test of CX-100, completed summer 2010 [8]

Table 22.1 Data acquisition parameter of free-free modal test of CX-100, completed summer 2010 [8]

Sampling frequency (Hz)	150
Number of data points	4,096
Number of averages	5
Sampling time (s)	11
Type of average	Linear
Window	None

Table 22.2 Modal results of CX-100 in free-free configuration [8]

Mode	Frequency (Hz)	Damping (% critical)	Description
1	7.61	0.195	First flap bending
2	18.1	2.960	First lag bending
3	20.2	0.752	Second flap bending
4	32.2	0.353	Third flap bending
5	45.1	0.733	Second lag bending
6	50.5	0.630	Fourth flap bending
7	63.9	0.740	First torsion
8	70.1	0.568	Third lag bending

Fig. 22.2 Set-up of vertical fixed-free modal test of CX-100
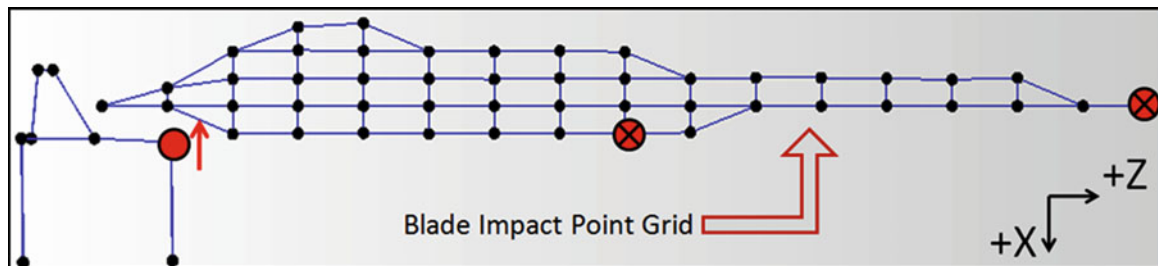
Fig. 22.3 Impact grid and accelerometer placement for vertical fixed-free modal analysis of CX-100

The experimental procedure for the fixed-free analysis included impacting 73 total points on the blade and frame. (49 on the blade and 24 on the support structure). Also there were three accelerometers utilized, two on the blade and one on the frame. The impact grid, placement and direction of the accelerometers are shown in Fig. 22.3.

The results of the vertical fixed-free modal analysis are shown in Table 22.3.

Table 22.3 Modal results of CX-100 in vertical free-free configuration

Mode	Frequency (Hz)	Damping (%)	Description
1	3.22	0.241	First flap bending
2	4.16	0.251	First lag bending
3	7.10	0.361	Second flap bending
4	8.80	0.275	Second flap bending
5	16.9	0.325	Third flap bending
6	19.2	0.330	Second lag bending
7	30.9	0.255	Fourth flap bending
8	39.3	0.565	First torsion
9	47.5	0.291	Fifth flap bending

Fig. 22.4 Tuned absorber effect of frame on CX-100 at 2nd bending mode
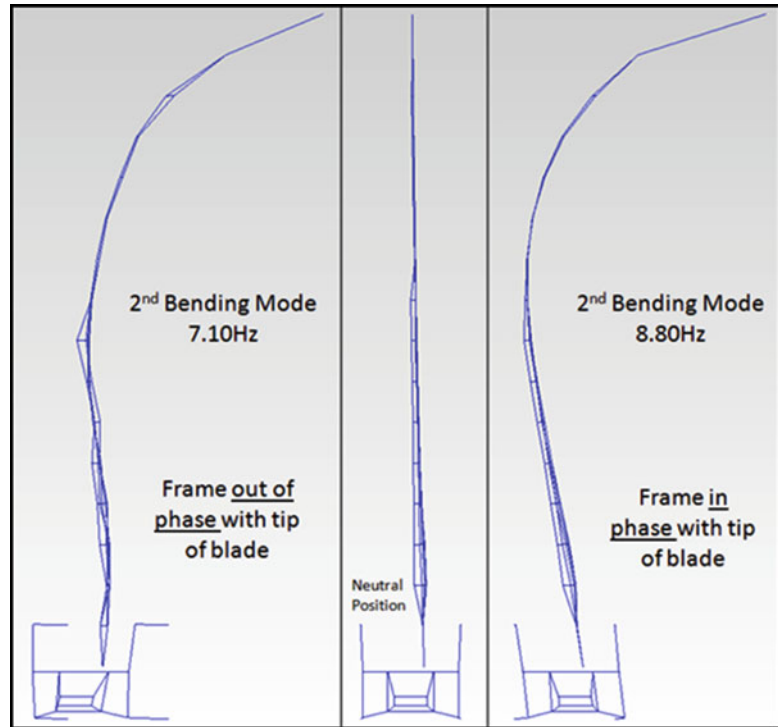
As shown in Table 22.3, there were two 2nd flap bending modes observed when testing in the vertical fixed-free orientation (modes 3 and 4). Upon further investigation of the two modes, it can seen in Fig. 22.4 that at 7.10 Hz the frame is out of phase with the tip of the blade, while at 8.80 Hz the frame is in phase with the tip of the blade.

The splitting of the 2nd bending mode due to fixture movement confirmed the suspicion of a relatively non-stiff and non-massive constraint. Due to the fixtures excessive movement and interaction with the blades mode shapes, a full modal analysis was performed on the blade support fixture.

22.2.3 LANL CX-100 Fixture Modal Analysis

A photo of the CX-100 support fixture is shown in Fig. 22.5.

The fixture shown in Fig. 22.5 weighs approximately 800 lbs and is primarily 80–20 aluminum and 1″ steel plate. The results of the fixture modal analysis are shown in Table 22.4.

In order for the 2nd bending mode of the blade to be split, due to interactions with the fixture, the frame must have a mode between 7.1 and 8.8 Hz. The modal test revealed there was a mode located at 8.37 Hz, in the same direction as the vertical orientation blade's bending modes. This confirmed that the frame was acting as a tuned absorber.

Fig. 22.5 LANL CX-100
fixture

Table 22.4 Results of fixture
modal analysis

Mode	Frequency (Hz)	Damping (%)	Description
1	8.37	0.409	Side-to-side oscillation
2	27.1	0.388	Side-to-side torsion
3	45.7	0.555	Vertical oscillation

Fig. 22.6 Set-up of horizontal fixed-free modal test of CX-100

22.2.4 LANL Horizontal Fixed-Free Analysis

In addition to the vertical fixed-free analysis, the blade was rotated 90° and tested in the horizontal fixed-free orientation. The horizontal fixed-free analysis was completed primarily to check for non-linearity due to mass loading of the blade in the flap-wise direction. A photo of the horizontal fixed-free analysis is shown in Fig. 22.6.

The testing parameters provided in Table 22.1 were used for data acquisition of the horizontal fixed-free modal analysis. Due to vibration forces in the vertical direction in combination with concerns of the strength of the fixture, a reduced number of points were impacted. There were 28 total impact points in the vertical direction, 20 on the blade and eight on the fixture.

Fig. 22.7 Impact grid for horizontal fixed-free modal analysis of CX-100
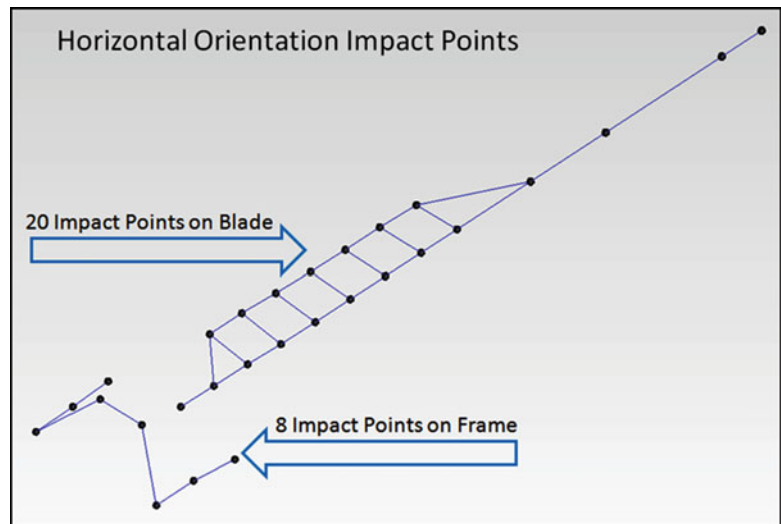
Table 22.5 Results of horizontal fixed-free modal analysis of CX-100

Mode	Frequency (Hz)	Damping (%)	Description
1	3.37	0.287	First flap bending
2	8.77	0.242	Second flap bending
3	16.8	0.311	Third flap bending
4	31.0	0.312	Fourth flap bending
5	38.8	0.419	First torsion
6	52.3	1.14	Fifth flap bending

Table 22.6 Comparison of fixed-free vertical versus horizontal

Mode	Description	Vertical orientation		Horizontal orientation		Percent difference	
		Frequency (Hz)	Damping (%)	Frequency (Hz)	Damping (%)	Frequency (Hz) (%)	Damping (%)
1	First flap bending	3.22	0.24	3.37	0.29	4.55	19.0
2	Second flap bending	8.80	0.28	8.77	0.24	0.34	15.5
3	Third flap bending	16.9	0.33	16.8	0.31	0.59	6.26
4	Fourth flap bending	30.9	0.26	31.0	0.31	0.32	17.7
5	First torsion	39.3	0.57	38.8	0.42	1.28	31.0
6	Fifth flap Bending	47.5	0.29	52.3	1.14	9.64%	184%

Again, three accelerometers were used, all in the same placements as in the vertical testing (Fig. 22.3). Although, unlike the vertical modal test where one accelerometer measured a different direction from the other two, all three accelerometers where placed to measure in the vertical direction, thus only flap-wise and torsional modes could be observed. See Fig. 22.7 for horizontal impact point layout.

The results of the horizontal fixed-free modal analysis are presented in Table 22.5.

22.2.5 Comparison of Fixed-Free Vertical Versus Horizontal Modal Analyses

Table 22.6 presents the percent differences between the vertical and horizontal modal analyses of the CX-100. Only the flap bending modes were compared, as only the flap bending modes were observed during the horizontal modal test.

A MAC comparing the mode shapes of vertical versus horizontal orientation CX-100 modal analyses is presented is Fig. 22.8.

The agreement observed in the natural frequencies and mode shapes of the two different orientations of the CX-100 may answer some important questions. Assuming the vertical orientation of the blade returned linear behavior of the blade, and
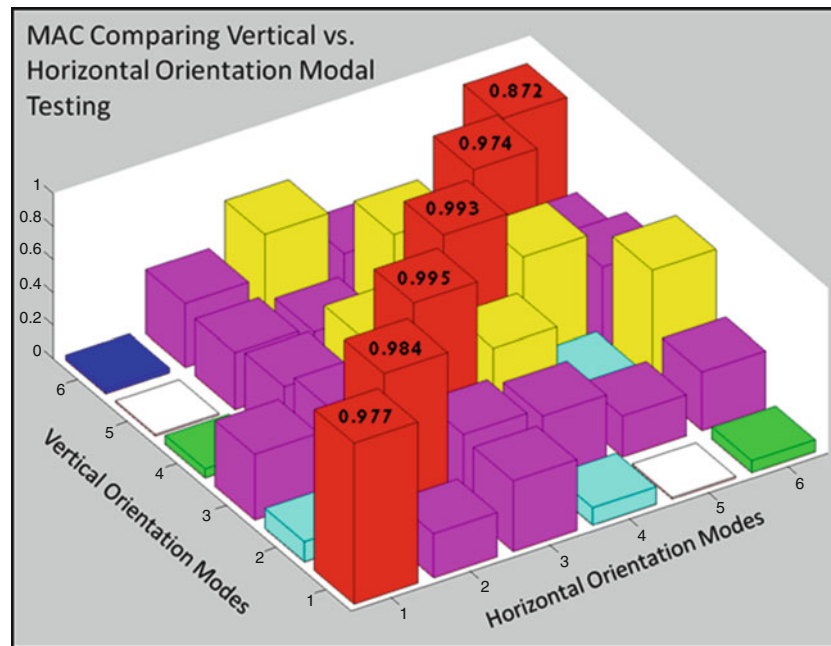
Fig. 22.8 MAC comparing fixed-free vertical versus horizontal orientation modal analyses of CX-100

Fig. 22.9 NREL fixed boundary condition

given the MAC agreement (Fig. 22.8), it may be concluded that there is minimal non-linearity due to mass loading in the horizontal orientation. The conclusion of minimal non-linearity due to mass loading of the blade in the horizontal direction also assumes there is no aerodynamic loading on the blade and an attack angle of zero. Finally, the disappearance of the split 2nd bending mode (compare Table 22.3, 22.5) further substantiates the LANL fixture is in fact acting as a tuned absorber when the blade is in the vertical orientation.

22.2.6 Fixed-Free Modal Analysis with a Seismic Fixed-Free Condition

There were two modal tests performed on the CX-100 under a different boundary condition. These tests were done at National Renewable Energy Laboratory (NREL). Both were performed with fixed-free boundary conditions. The fixed boundary condition at NREL is made of a relatively seismic concrete/steel block; a photo of the boundary condition is shown in Fig. 22.9.

Fig. 22.10 NREL horizontal
fixed-free modal analysis
set-up

Table 22.7 Modal results
of CX-100 in horizontal
free-free configuration
at NREL

Mode	Frequency (Hz)	Damping (%)	Description
1	4.35	0.200	First flap bending
2	6.42	0.253	First lag bending
3	11.5	0.243	Second flap bending
4	20.5	0.283	Third flap bending
5	23.1	0.310	Second lag bending
6	35.3	0.307	Fourth flap bending
7	46.4	0.428	First torsion
8	48.6	0.422	Third lag bending
9	54.6	0.455	Fifth flap bending

The first modal test of the CX-100 at NREL was a horizontal fixed-free condition modal test. A photo of the set-up is shown in Fig. 22.10.

The results of the NREL horizontal Fixed-Free modal analysis are presented in Table 22.7.

22.2.7   NREL Fixed-Free Modal Analysis with Fatigue Masses Attached

The final modal analysis performed was a Fixed-Free analysis of the CX-100 at NREL with two fatigue masses attached to the blade. The fatigue masses are attached to the blade at strategic locations (shown in Fig. 22.11), as to inflict maximum damage during fatigue testing.

A photo of the mass loaded CX-100 is shown in Fig. 22.12.
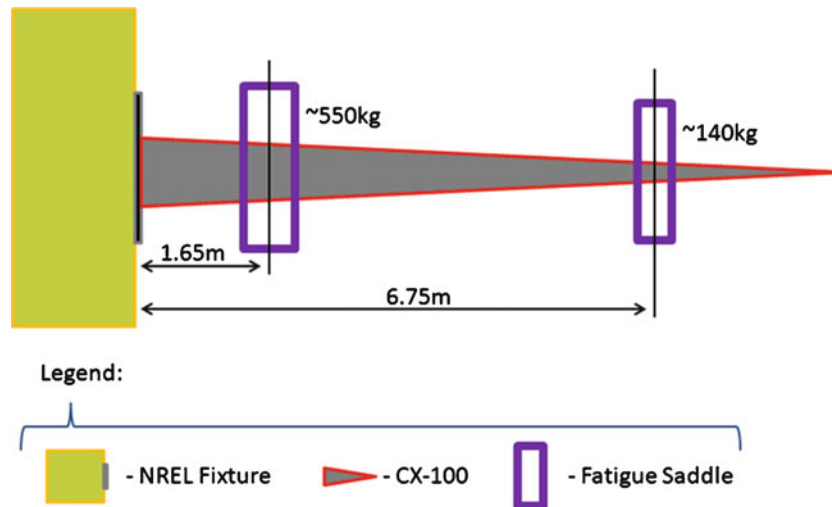
Fig. 22.11 Locations and weights of fatigue masses placed on CX-100

Fig. 22.12 Mass loaded CX-100, final set-up of full-scale fatigue test

Table 22.8 Natural frequencies of mass loaded CX-100

Mode	Frequency (Hz)	Damping (%)	Mode Description
1	1.82	0.132	First flap bending
2	2.68	0.312	First lag bending
3	9.23	0.546	Second flap bending
4	12.7	0.868	Third flap bending
5	14.7	1.50	Second lag bending
6	18.9	0.958	Fourth flap bending
7	24.4	1.33	Third lag bending

A modal test was performed on the mass loaded CX-100 for two primary reasons. The first was to determine the first natural frequency of the final mass loaded system. The first natural frequency would then be used to excite the blade for the duration of the fatigue test. The second was to obtain baseline natural frequencies of the system. Then throughout the duration of the fatigue test, modal tests will be performed, and changes in natural frequencies will be tracked. Changes in natural frequencies may be clues to damage initiation or damage propagation. The results of the mass loaded CX-100 modal analysis are presented in Table 22.8.
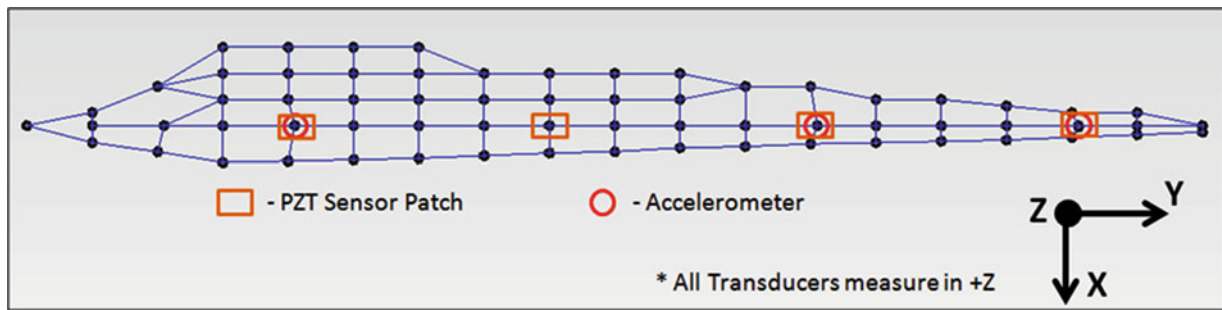
Fig. 22.13 Placements of accelerometers and PZT sensors on CX-100

Table 22.9 Accelerometer versus PZT sensor modal results of NREL fixed-free horizontal orientation

	Accelerometer data		PZT sensor data		% Difference	
Mode	Frequency (Hz)	Damping (%)	Frequency (Hz)	Damping (%)	Frequency (Hz)	Damping (%)
1	4.35	0.170	4.35	0.176	0.00	3.47
2	6.42	0.255	6.42	0.257	0.00	0.78
3	11.5	0.260	11.5	0.254	0.00	2.33
4	20.5	0.284	20.5	0.278	0.00	2.14
5	23.1	0.324	23.1	0.318	0.00	1.87
6	35.3	0.313	35.3	0.302	0.00	3.58

Modal analysis tracking is only one form of SHM to be performed on the CX-100 throughout the full scale fatigue test. There would also be several multi-scale sensing techniques employed on the CX-100 throughout the fatigue test.

22.3 Accelerometers Versus piezoelectric button sensors for modal analysis

Piezoelectric button sensors are routinely employed for use in SHM, but for modal analyses, accelerometers are the first choice for a transducer, while piezoelectrics are not regularly used. Compared to piezoelectric button sensors, accelerometers are significantly more expensive. Further, a multi-scale sensing approach to SHM was desired, employing both high and low frequency sensing techniques. Therefore, to reduce the complexity of a multi-scale sensing SHM system and reduce costs, it was desired to utilize piezoelectric button sensors as both actuators and sensors for both the high and low frequency sensing methods.

In order compare an accelerometer-based modal analysis to a piezoelectric button-based sensor modal analysis, the NREL CX-100 was outfitted with both accelerometers and piezoelectric sensor patches. Figure 22.13 shows the placements of the three accelerometers and four piezoelectric buttons. As shown, each of the accelerometers was co-located with piezoelectric button sensors (specifically PZT-based elements).

A modal test of the CX-100 was completed in the NREL Fixed-Free boundary condition. After, the accelerometer and PZT sensor modal data was processed separately. The results are shown in Table 22.9.

The high level of agreement between the accelerometers and PZT sensors suggest that piezoelectric button sensors offer the same fidelity as accelerometers for measuring the low-frequency modal frequencies and damping. Therefore, the piezoelectric sensors can be utilized for high and low frequency sensing techniques in a multi-scale sensing approach.

22.4 Structural Health Monitoring

One of the major challenges hindering the expansion of wind power is reliability. Since the trend in the wind energy field has led to increasing blade length and tower height, insufficient research has gone into blade reliability. Additionally, as stated earlier, blades account for 15–20% of the total wind turbine cost, and blade failure can lead to significant secondary damage [5]. Thus, real-time monitoring of blade health is of great importance.

Fig. 22.14 Electric impedance sensor diagnostic method [23]
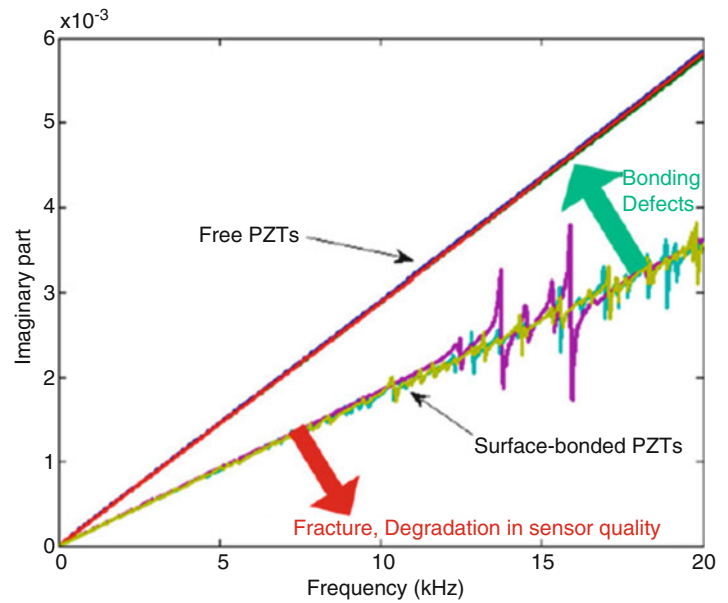
A full scale fatigue test of a 9 m CX-100 wind turbine blade will occur at NREL. The goal of this and subsequent research is to develop and refine techniques that will be utilized to detect and monitor the progression of damage in the CX-100 blade during the fatigue test.

A multi-scale sensing approach to SHM is presented in this research. For this application, multi-scale sensing refers to a use of both high and low frequency SHM methods. As is common, high-frequency techniques will be utilized to detect and locate damage on a region localized around the sensing array. To determine if the localized damage poses a significant threat to the health of the entire wind turbine system, low-frequency SHM methods will be employed to determine if global damage (i.e. changes to the global mass, damping, and/or stiffness) has occurred. The high-frequency methods of interest include frequency response function analysis and lamb wave propagation analysis, each utilizing piezoelectric elements as sensors, actuators, or both. The low-frequency damage-sensing technique of interest is a modal characterization utilizing piezoelectric elements in place of the typical accelerometers.

22.4.1 Sensor Diagnostics

Sensor diagnostics are crucial to successful SHM. In order to accurately monitor or detect damage, sensor health must first be determined to prevent false positives from occurring. Sensor diagnostics strive to detect a variety of false positives, from the fracture/breakage/degradation of sensors to debonding/delamination of sensors to poor cable connections from sensors to data acquisition systems.

The sensor diagnostic system used on the CX-100 SHM system is the Electrical Impedance (EI) method, developed at LANL [23]. The basic process of EI sensor diagnostics is as follows:

1. Bond PZT sensor to structure surface
2. Measure electrical admittance (inverse of electrical impedance) of PZT sensor

   (a) Use initial admittance of sensor as baseline

3. Measure admittance of sensors periodically to check for defects

   (a) Deviations from baseline infer a variety of sensor issues

The slope of the electrical admittance of the PZT sensors is a measure of the capacitance of said sensors. Thus, this method monitors the PZT sensors for changes in their capacitance. Figure 22.14 is a visual of the EI method.

A MATLAB code was developed to quickly identify sensor defects based on electrical admittance measurements of sensors. Figure 22.15 shows an example of the code's output for a single day when measuring a sensor array of eight sensors.
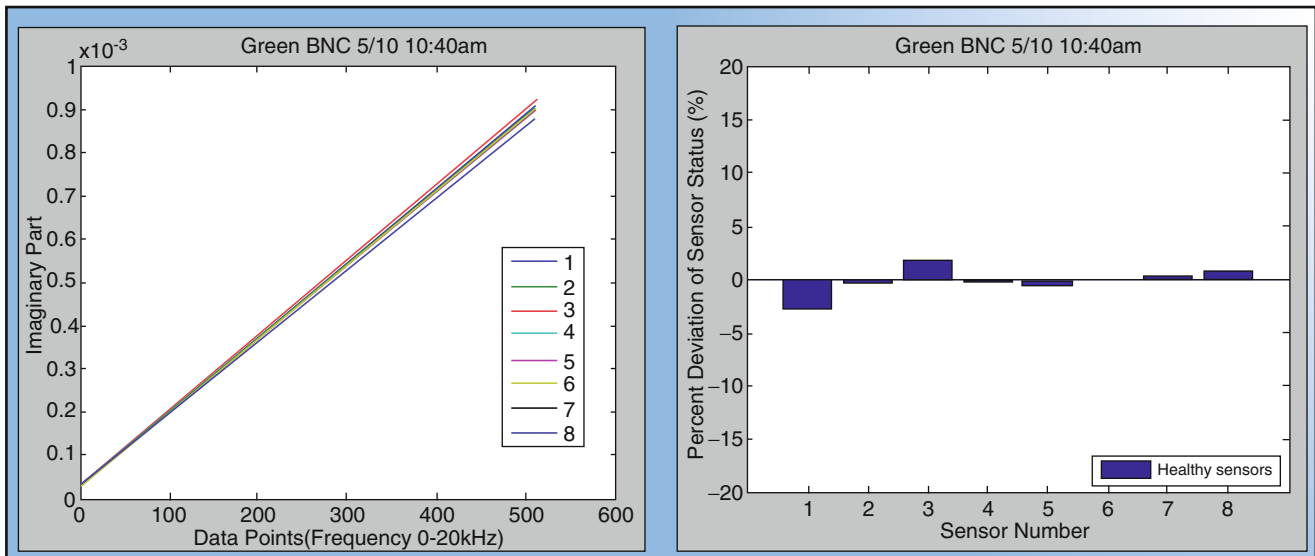
Fig. 22.15 Electric admittance measurements for a single date

The admittance measurements (left side of Fig. 22.15) are the baselines, from which an average sensor status is determined. Based on deviations of each sensor from the average, a Percent Deviation of Sensor Status is determined for each sensor (right side of Fig. 22.15).

Periodically a set of EI measurements are acquired for the same array of eight sensors.

Figure 22.16 shows the progression of EI measurements from 5/10/2011 to 6/10/2011. Sensor issues can be seen from significant (as governed by a predetermined threshold) changes in the "percent deviation of sensor status" from date-to-date. A significant change in sensor status is shown on the upper right of Fig. 22.18. The cause of this sensor problem was determined to be a loose wire connection. After fixing the connection, the sensor status's returned to normal, as seen on the subsequent date. This is an example of a successful sensor diagnosis, and illustrates how the technique may be utilized prior to SHM investigations.

22.4.2 SHM Experimental Setup

Structural health monitoring of the 9 m CX-100 wind turbine blade at NREL was performed. Health monitoring was conducted using high-frequency lamb-wave propagation and FRF techniques, employing inexpensive piezoelectric buttons as actuators and sensors. For each technique, one piezoelectric actuator was surrounded by an array of piezoelectric sensors. The high-frequency FRFs were measured using two mutually exclusive sensing arrays (an inner array and an outer array), while lamb-wave propagation responses were obtained using only the inner array. The location of the piezoelectric actuator and the locations of the piezoelectric sensors relative to the actuator for the inner and outer sensor arrays are shown in Figs. 22.17 and 22.18, respectively. The actuators and sensors were located on the low-pressure side of the blade.

To obtain lamb wave propagations, the piezoelectric actuator was excited with a tone-burst sine signal having a specifically controlled frequency. Eleven excitation frequencies ranging from 50 to 275 kHz were used. The reason for multiple excitation frequencies is the complex composite structure of the CX-100 wind turbine blade. A cross-section of the blade is shown in Fig. 22.19. In this method, the sensors measure propagating lamb waves in the composite blade. When damage occurs, propagating waves are reflected, attenuated, and/or dispersed. Due to the complex composite structure, lamb wave speeds, reflections, attenuations, and/or dispersion change depending upon the sensing path location on the blade. Time-domain responses to the tone-burst sine signal were measured at each sensor in the array using a Metis Intelli-Connector digital SHM system. As seen in Fig. 22.17, six sensing paths were monitored. A fast Fourier transform (FFT) of each sensor response was calculated, and the integral of each FFT was estimated using trapezoidal numerical integration in MATLAB. This resulted in a single metric (representing the energy content of the response) for the wave propagation between the actuator and each sensor, that could be tracked over time to assess changes in the wave propagation response.
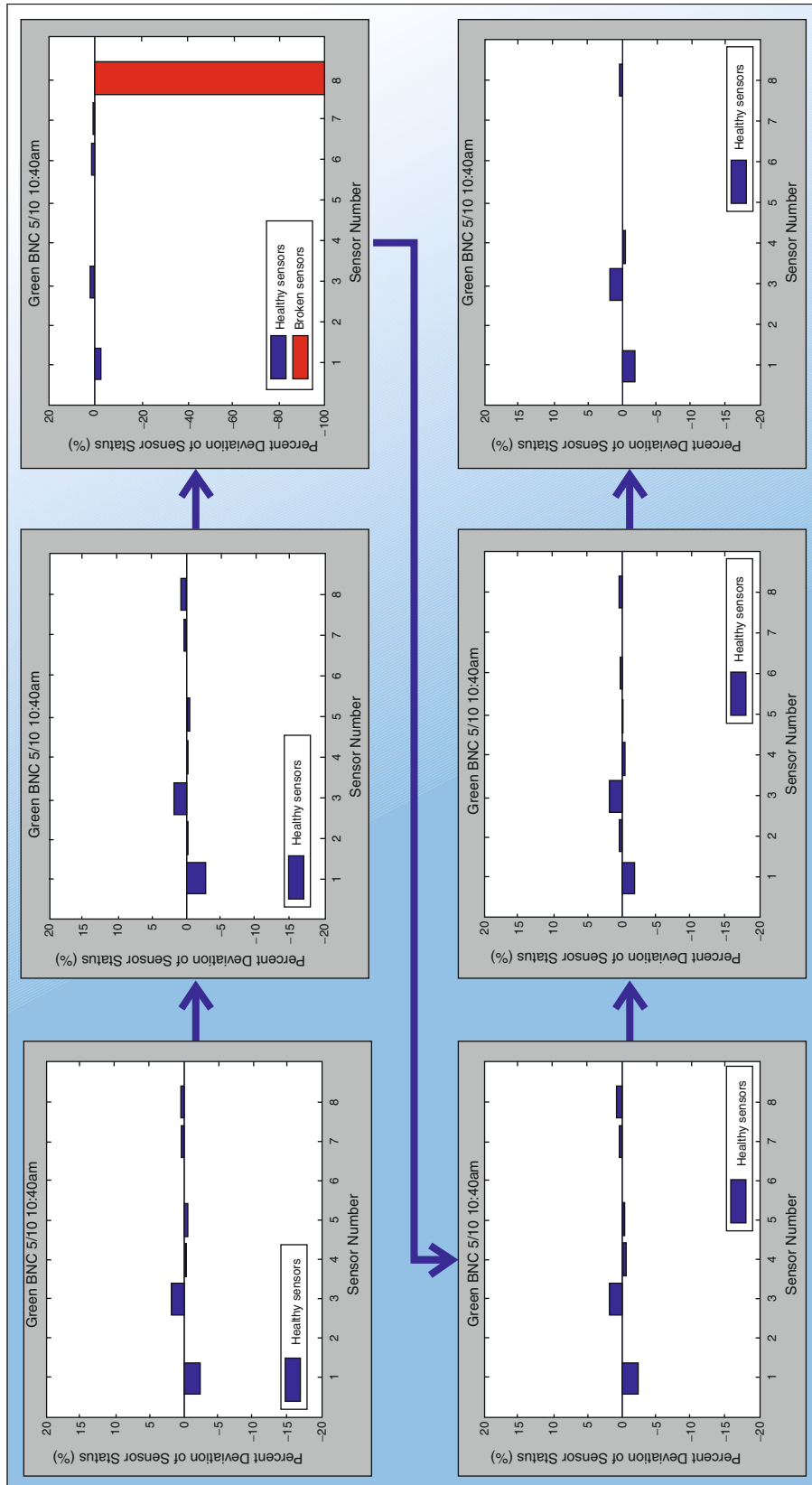
Fig. 22.16 Time lapse of EI sensor measurements from 5/10/2011 to 6/10/2011

Fig. 22.17 Sensor and actuator locations for inner sensor array
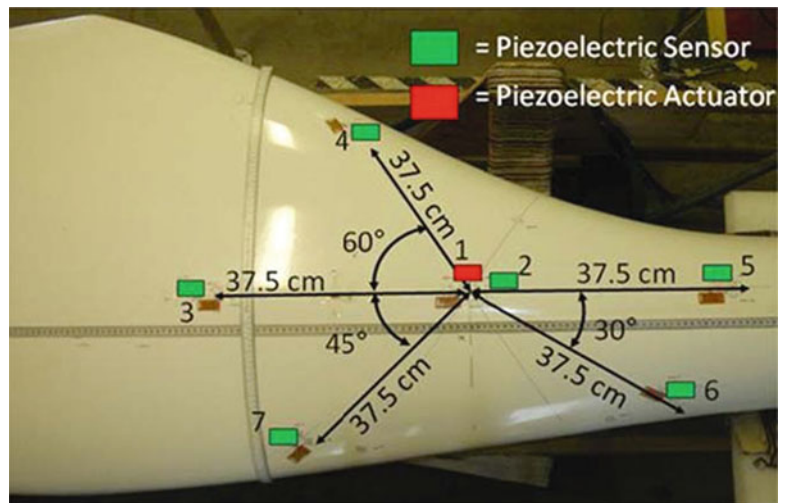
Fig. 22.18 Sensor and actuator locations for outer sensor array
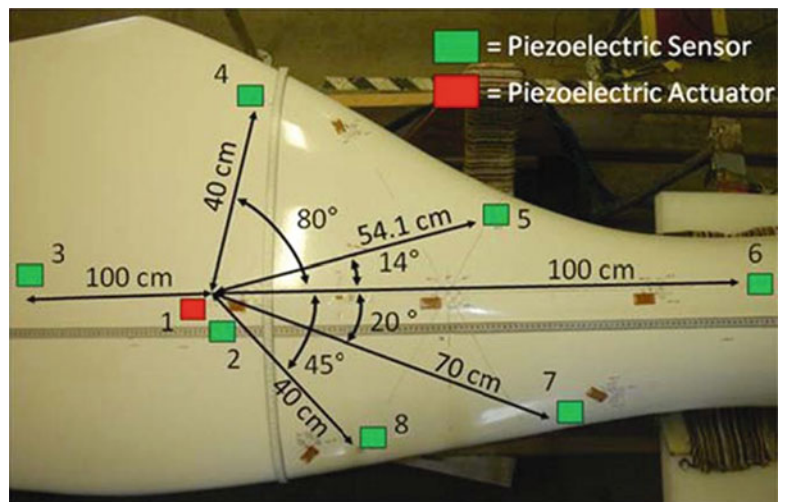
Fig. 22.19 CX-100 wind turbine blade cross section

For each sensor array, FRFs between each sensor and the actuator to a random excitation were measured using a Brüel and Kjaer Laser USB data acquisition system. As seen in Figs. 22.17 and 22.18, this resulted in six and seven sensing paths for the inner and outer arrays, respectively. The FRFs were measured at a sampling frequency of 96 kHz for a total of 16,384 points, and utilized a hanning window. The output of the data acquisition system was a single FRF calculated by linearly averaging 20 FRFs for each sensor-actuator pair. FRFs were measured in this manner over a period of weeks. In order to

Fig. 22.20 FRF damage
progression as measured
by the inner sensor array
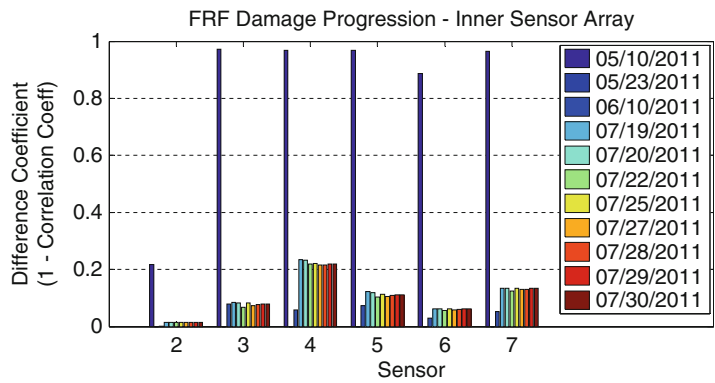
Fig. 22.21 FRF damage
progression as measured
by the outer sensor array
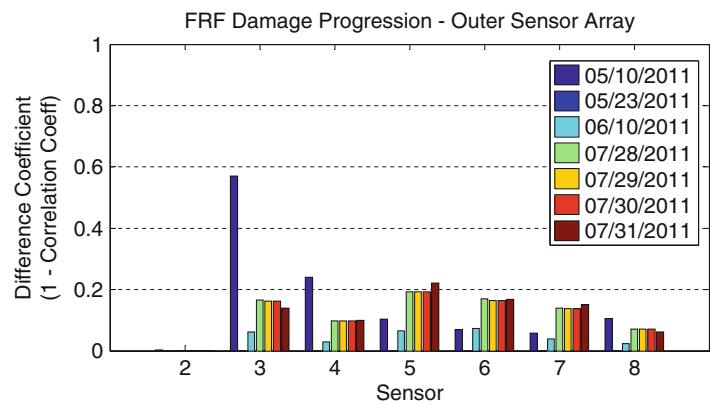
Table 22.10 Changes to the CX-100 blade during SHM testing

Date	Description of the change to or test on the blade
5/10/2011–5/23/2011	Fatigue masses at X ft (X m) and 22 ft (6.7 m) added on the blade, Ref. Fig. 22.13
5/25/2011–6/10/2011	Surface of the blade was painted across the sensing region
7/28/2011–7/29/2011	500 lb (2,220 N) dead weight added to the fatigue mass at 22 ft (6.7 m), Ref. Fig. 22.13
7/29/2011–7/30/2011	Edgewise pull test of 500 lb (2,220 N) in the +y direction at 22 ft (6.7 m) from the root, Ref. Figs. 22.11 and 22.13
7/30/2011–7/31/2011	Edgewise pull test of 500 lb (2,220 N) in the −y direction at 22 ft (6.7 m) from the root, Ref. Figs. 22.11 and 22.13

assess the progression of damage, a linear correlation coefficient between a current FRF and the baseline FRF was calculated for each sensor and measurement period. The linear correlation coefficient is simply a measure of how linearly related two data sets are, with one signifying a perfect linear relationship and zero signifying no linear relationship. The correlation coefficients were then subtracted from one to obtain a damage coefficient, such that as damage or differences from baseline increased, the damage coefficient increased. This provided a single metric to monitor for each sensing path.

22.4.3   SHM Results

The progression of damage coefficients, calculated from high-frequency FRF measurements, over an 11 week period for the inner and outer sensor arrays are shown in Figs. 22.20 and 22.21, respectively. In these plots, the FRF responses on 05/23/2011 are used as the baseline measurement, and therefore have zero damage coefficients. Throughout the 11 week measurement period, a number of tests on and modifications to the blade were enacted. These alterations are summarized in Table 22.10. A huge change in the FRF responses was seen from 05/10/2011 to 05/23/2011. Referring to Table 22.10, the likely cause can be identified as the addition of the 900 and 300 lb (4,000 N and 1,330 N) fatigue masses. With the addition of the fatigue masses to the stock blade, cracking and settling of the composite material from the as manufactured condition likely occurred. This is a typical occurrence for wind turbine blades. This would result in stiffness and damping changes in
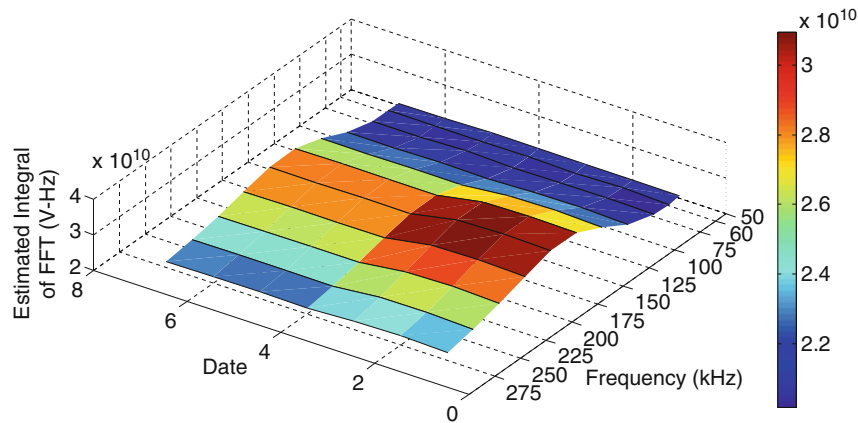
Fig. 22.22 Wave propagation damage progression for sensor 3
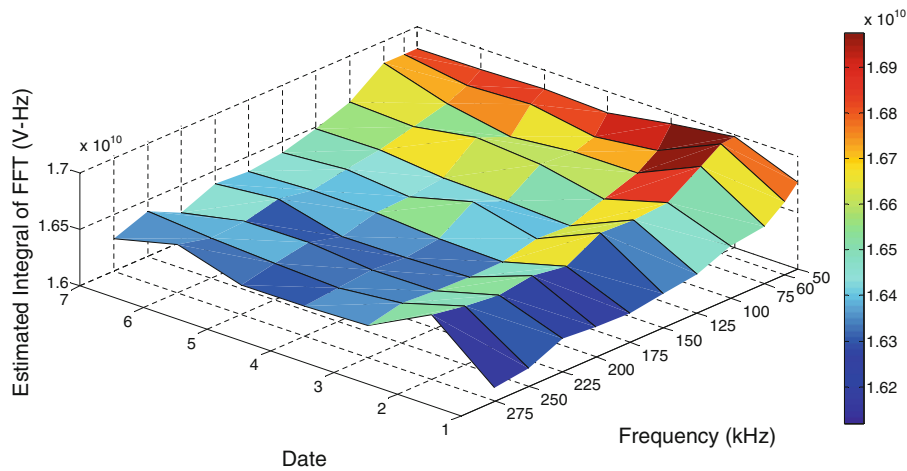
Fig. 22.23 Wave propagation damage progression for sensor 4

the blade, leading to changes in the FRF responses. The next shift in damage coefficient occurs between 05/23/2011 and 06/10/2011 for both sensing arrays. Referencing Table 22.10, this damage can be reasonably identified as due to the painting of the blade. It is interesting to note that the high-frequency FRFs were not sensitive to the static strains induced by the pull tests, as described in Table 22.10. This was an expected result due to the high frequency sensing used. Had low-frequency sensing been analyzed, frequency shifts and attenuation in the FRFs would have been expected. Thus, once the blade had moved through the settling in period, the high-frequency sensing FRF technique was insensitive to operational conditions.

Wave propagation results for all excitation frequencies of sensors three and four are shown in Figs. 22.22 and 22.23, respectively. In these plots, the progression of the estimated integral as a function of date for each excitation frequency is of interest. All of the frequencies are plotted together for comparison, in order to ascertain at which frequencies the lamb wave propagation technique was most sensitive to damage or modifications to the blade for the specific sensing path.

Comparing Tables 22.10 and 22.11 with Fig. 22.22, it can been seen that lamb wave propagation frequencies between 125 and 250 kHz were sensitive to the painting of the blade surface. As seen in Fig. 22.23, sensing path 4 was insensitive to the painting of the blade. At the time of writing, the fatigue test at NREL had not been started. Additionally, the sample set of lamb wave propagation data analyzed is very small. Thus, the applicability of this frequency range to sensing actual damage cannot be assessed. This illustrates the difficulty in selecting an excitation frequency. Depending upon location on the blade, some excitation frequencies may result in damage detection, while others may be insensitive.

Table 22.11 Wave propagation
date explanations

Date#	Corresponding date
1	5/24/2011 – Run 1
2	5/24/2011 – Run 2
3	5/25/2011 – Run 1
4	6/10/2011 – Run 1
5	6/10/2011 – Run 2
6	6/10/2011 – Run 3
7	6/10/2011 – Run 4

Due to the lack of damaged blade data and the small data set, an effective baseline, used to assess if damage has occurred, could not be established for each sensing path. However, the framework for quickly analyzing high-frequency lamb-wave propagation and high-frequency response function data, and for identifying ideal excitation frequencies was developed.

22.5 Conclusions

The 9 m CX-100 blade was tested in various boundary conditions, including fixed-free in two drastically different fixtures, and in both the vertical and horizontal orientation. From comparisons of vertical versus horizontal orientation fixed-free modal analyses, it was concluded that there is minimal non-linearity when the blade was mass loaded in the horizontal direction. This assumes that non-linearity is absent in the vertical orientation, the blade has no aerodynamic loading, and a blade attack angle of zero. Also, when performing fixed-free modal analysis in the vertical orientation, a tuned absorber was found in the LANL fixture. This was one indication the LANL fixture was a relatively flexible, fixed boundary condition. It was determined that mode shapes and natural frequencies from fixed-free modal testing on the LANL fixture were not accurate representations of the CX-100. The mode shapes and natural frequencies found from fixed-free testing at LANL were that of the coupled system of the CX-100 blade and fixture. This is a crucial distinction, as a finite element model should be validated from experimental tests whose boundary conditions can be accurately modeled in the software. Also, the natural frequencies of a mass-loaded CX-100 were determined prior to the full-scale fatigue test commencement. This was important for two reasons, (1) for determination of the first natural frequency, as it would be used as the excitation frequency for the duration of the fatigue test, and (2) for the determination of a baseline of natural frequencies, as any changes throughout the fatigue test, may point to damage initiation or propagation.

It was shown through a modal analysis of the CX-100 blade, that piezoelectric button sensors provide the same fidelity as accelerometers in measuring modal frequencies and damping. This result is significant in that it offers the ability to not only replace expensive accelerometers with inexpensive piezoelectrics, but also to serve as the backbone for multi-scale sensing structural health monitoring. Piezoelectric buttons can operate as sensors or accelerometers for both high-frequency sensing and low-frequency sensing. High-frequency sensing techniques analyzed in this research were frequency response functions and lamb wave propagations. High-frequency frequency response functions were shown to be insensitive to operational conditions following a settling in period of the CX-100 blade. The excitation frequency for high-frequency lamb wave propagations was shown to be very difficult to ascertain, and to depend upon sensor location on the blade. At the time of writing, fatigue data for the CX-100 blade was not available. However, a framework was developed for both high-frequency methods that will allow for quick determination of damage location and progression.

References

1. U.S. Department of Energy 20% wind energy by 2030. July 2030
2. TPI Composites, Inc. (2003) Innovative design approaches for large wind turbine blades. Project report for SNL, SAND2003-0723
3. TPI Composites (2004) Innovative design approaches for large wind turbine blades; final report, SAND2004-0074, Sandia National Laboratories, Albuquerque
4. Ashwill TD (2006) Some recent trends & activities in turbines and blades. Sandia National Labortories 2nd Wind Turbine Blade Workshop, Albuquerque
5. Ciang Chia Chen, Jung-Ryul Lee, Hyung-Joon Bang (2008) Structural health monitoring for a wind turbine system: a review of damage detection methods. Meas Sci Technol 19:1–20
6. TPI Composites, Inc (2007) Design of 9-meter carbon-fiberglass prototype blades: CX-100 and TX-100 final project report, SAND2007-0201

7. White JR, Adams DE, Rumsey MA (2010) Modal analysis of CX-100 rotor blade and micon 65/13 wind turbine. In: proceedings of the IMAC-XXVII, Jacksonville, 1–4 Feb 2010

8. Deines K, Marinone T, Schultz R, Farinholt K, Park G (2011) Modal analysis and SHM investigation of CX-100 wind turbine blade. Rotating Machinery Struct Health Monitor Shock Vib 5:413–438

9. Griffith DT, Hunter PS, Kelton DW, Carne TG, Paquette JA (2009) Boundary condition considerations for validation of wind turbine blade structural models. In: Proceedings of the SEM annual conference, Albuquerque, 1–4 Jun 2009

10. Carne TG, Griffith DT, Casias ME (2007) Support conditions for experimental modal analysis. Sound Vib Mag 41:10–15

11. Griffith DT, Carne TG (2007) Experimental uncertainty quantification of modal test data. In: 25th international modal analysis conference, Orlando

12. Kessler SS, Spearing SM, Atalla MJ, Cesnik CE, Soutis C (2002) Damage detection in composite materials using frequency response methods. Compos Pt B: Eng 33(1):87–95

13. Amraoui MY, Lieven NAJ (2004) Laser vibrometry based detection of delaminations in glass/epoxy composites. ASME J Vib Acoust 126 (3):430–437

14. Sundaresan MJ, Schulz MJ, Ghoshal A (2002) Structural health monitoring static test of a wind turbine blade. NREL/SR-500-28719, North Carolina A&T State University report for NREL, Golden

15. Ghoshal A, Sundaresan MJ, Schulz MJ, Pai PF (2000) Structural health monitoring techniques for wind turbine blades. J Wind Eng Ind Aerodyn 85:309–324

16. Park G, Rutherford AC, Wait JR, Nadler B, Farrar CR, Clayton TN (2005) High-frequency response functions for composite plate monitoring with ultrasonic validation. AIAA J 43(11):2431–2437

17. Rumsey MA, Paquette JA Structural health monitoring of wind turbine blades. Sandia National Laboratories, Albuquerque

18. Park G, Inman DJ (2005) Impedance-based structural health monitoring. In: Inman DJ et al (eds) Damage prognosis – for aerospace, civil and mechanical system. Wiley, Chichester, pp 275–292, Chap 18

19. Park G, Sohn H, Farrar CR, Inman DJ (2003) Overview of piezoelectric impedance-based health monitoring and path forward. Shock Vibr Dig 35(6):451–463

20. Sutherland HJ, Beattie A, Hansche B, Musial W, Alread J, Johnson J, Summers M (1994) The application of non-destructive techniques to the testing of a wind turbine blade. SAND93-1380, Sandia National Laboratories, Albuquerque

21. Sorensen BF, Lading L, Sendrup P, McGugan M, Debel P, Kristensen OJD, Larsen G, Hansen AM, Rheinlander J, Rusborg J, Vestergaard JD (2002) Fundamentals for remote structural health monitoring of wind turbine blades – a Preproject. Annex B – sensors and non-destructive testing methods for damage detection in wind turbine blades, Riso National laboratory, Roskilde

22. Light-Marquez A, Sobin A, Park G, Farinholt K (2010) Structural damage identification in wind turbine blades using piezoelectric active-sensing. In: proceedings of the IMAC XXVII, Jacksonville, 1–4 Feb 2010

23. Overly TG, Park G, Farinholt KM, Farrar CR (2009) Piezoelectric active-sensor diagnostics and validation using instantaneous baseline data. IEEE Sens J 9(11):1414–1421

24. Park G, Farrar CR, Rutherford CA, Robertson AN (2006) Piezoelectric active sensor self-diagnostics using electrical admittance measurements. ASME J Vib Acoust 128(4):469–476

25. Park G, Farrar CR, di Scalea FL, Coccia S (2006) Performance assessment and validation of piezoelectric active sensors in structural health monitoring. Smart Mater Struct 16(6):1673–1683

Chapter 23
Dynamic Characterization of Whisper 500 Turbine Blade

Christopher Nonis, Samuel Garrett, Stuart G. Taylor, Kevin M. Farinholt, and Gyuhae Park

Abstract The aim of this research is to analyze the dynamic behavior of a 2.2 m whisper 500 wind turbine blade. Several roving impact hammer modal tests were carried out in both free-free and fixed-free conditions. A reduced order model to capture the essential dynamics of the blade is also developed to represent the actual blade. This reduced order model can be used in embedded sensors for damage identification. The prediction capability of this reduced model is tested and validated, where "simulated" damage is introduced to the blade in the form of masses loading the blade. After characterizing the blade, a Kalman filter is implemented to estimate the blade t4ip deflection from accelerometer data. First, a simplified two degree of freedom model is developed in Matlab to verify the performance of the filter. The blade model is then combined with accelerometer data from impulse tests to infer tip deflection which is then compared to laser vibrometer data (measuring tip deflection) during the same impulse tests.

23.1 Introduction

23.1.1 Background

The DOE has projected that wind turbines could produce as much as 20% of the United States' electricity by 2030 [1]. Considering their potential economic importance, it is critical to develop cost-effective methods of maintaining these systems. Wind turbines are subject to constant loads which over time result in damage. Damage to the blades is of particular interest as they constitute approximately 20% of the cost of the system. Furthermore, they are one of the most expensive parts to repair and can cause secondary damage to other components of the system if they are functioning improperly [2].

Embedded sensing in turbine blades is an emerging field in the area of wind turbine Structural Health Monitoring (SHM). These sensors, however, have limited computational capacity and limited electrical supply. It is therefore necessary that a reduced order model be developed which is simplified enough to be run in conjunction with these embedded systems yet is still sufficiently accurate to properly detect changes in the blades.

Having a way to monitor tip deflection can be important for more cheaply maintaining wind turbines. Tip deflection influences load transmission which is a significant source of damage for blades. Also tip deflection is sometimes an indicator of already existing damage so it also has structural health monitoring applications. Finally, tip deflection measurements may be able to determine when tower strikes are imminent. This is especially relevant because a tower strike can destroy an entire wind turbine installation.

C. Nonis
Department of Mechanical Engineering, University of Massachusetts Lowell, Lowell, MA 01854, USA

S. Garrett
Department of Mechanical Engineering, Stanford University, Stanford, CA 94305, USA

S.G. Taylor • K.M. Farinholt • G. Park (✉)
The Engineering Institute, Los Alamos National Laboratory, Los Alamos, NM 87545, USA
e-mail: gpark@lanl.gov

23.1.2 Previous Work

Many researchers have applied Kalman filtering techniques to wind turbine measurement applications. Haynes et al. [3] used a Kalman filter to determine tip deflection in a 1 m turbine blade. They used this data to study load transmission from the tip of the blade to the hub. Donders [4] has used a Kalman filter to determine wind speed incident on a turbine from the actuator gain in a pitch-to-vane control wind turbine. Bottasso et al. [5] used strain gauges and accelerometers placed on structural members of a wind turbine and a Kalman filter to approximate vertical and horizontal wind shear and yawed flow on the turbine. A software package called SHMTools is under development by Flynn et al. [6] which includes C-code that can be embedded in sensors and includes routines for data acquisition, feature extraction, and feature classification. This will provide an integrated software platform for structural health monitoring systems.

23.1.3 Purpose

The purpose of this paper is to present the results of a full dynamic characterization of a Whisper 500 turbine blade including free-free and fixed-free boundary conditions. It will also be to determine whether or not a reduced-order model can accurately predict the effect of damaged conditions on the overall dynamics of the blade. Finally, it has the goal of using a Kalman filter to estimate tip deflection using data from just one accelerometer mounted at the tip of the blade.

23.2 Experimental Procedure

23.2.1 Impact Grid

A roving impact hammer modal test was used to dynamically characterize the blade. To start, the Whisper 500 was measured for length and then marked with a 36 point grid. The grid extends over 84 in. from the tip of the blade to just 2 in. from the root. Impact points are distributed in rows 6 in. apart. Depending on the width of the blade section there are either two or three impact points per row. Because the blade is relatively flat it can be reasonably approximated as a beam with impact points coplanar. Three reference accelerometer locations were used during the tests. Figure 23.1 shows the impact grid and reference accelerometer locations. See Appendix A for more details on the experimental setup.

For the first two modal tests reference accelerometers were placed at 9 and 36. Point 9 was chosen to detect torsional modes. Point 36 was chosen to measure flapwise bending modes because the tip experiences maximum displacement. In later tests reference accelerometers were placed at 35 and 36. Reference accelerometer 35 was used to measure edgewise bending modes. All data was recorded using an RT Pro Photon Dactron and all curve fitting was done in ME Scope.

23.2.2 Free-Free Modal Tests

Six Free-Free modal tests were conducted in total on two different blades. For these tests the blade was suspended in a vertical orientation. The set up consisted of a single steel portal frame. The blade was hung from a set of bungee cords and
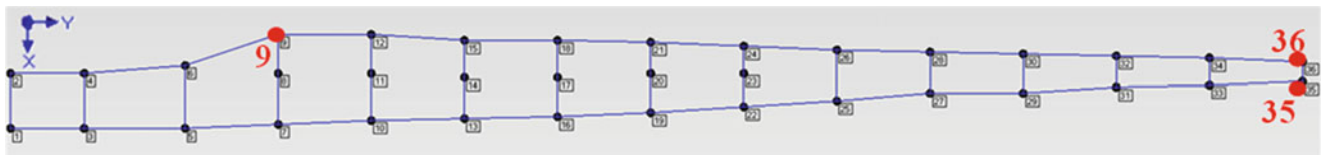
Fig. 23.1 Impact grid

Fig. 23.2 Free-free test
configuration

fishing line. The bungee cords were connected to the frame and the fishing line. The fishing line was looped through the first two bolt holes on the whisper 500. The free-free test configuration is shown in Fig. 23.2.

23.2.2.1   Flapwise Test

The first two modal test conducted measured the flapwise bending modes of Blades 1 and 2.

23.2.2.2   Flapwise/Edgewise Test

Inspecting the results of the flapwise modal tests showed 2 s order bending modes, which was very suspicious. It was estimated one of the modes was actually an edgewise bending. To confirm this and account for edgewise modes in future tests a reference accelerometer was moved from the flap to the tip to measure edgewise displacement.

One edgewise was conducted by impacting the leading edge of the blade. The next test was a full test, where both flapwise and edgewise modes were measured.

The next modal tests carried out were combined edgewise/flapwise tests. In these modal tests both blades were tested again. This test allowed the creation of cleaner and more accurate animations of mode shapes. It also eliminated uncertainty about which were flapwise and which were edgewise modes.

Fig. 23.3 Mass loaded tip
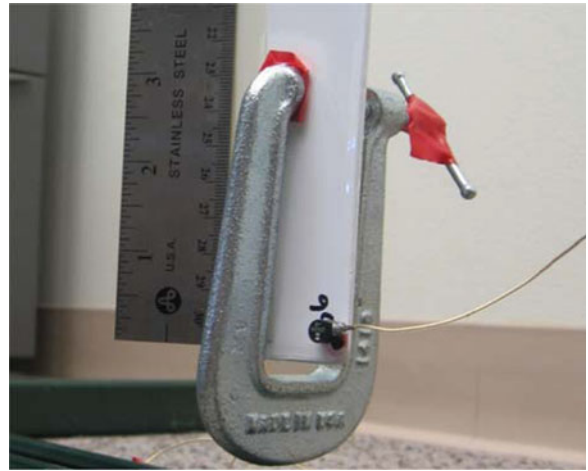
Fig. 23.4 Mass loaded root

23.2.3 "Damaged" Modal Tests

Two modal tests were conducted with simulated damage added to the blade in the form of C-clamps attached at various points. The first was a .444 lbm clamp attached at the tip. The second case was a 1.3 lbm clamp attached at the top of the blade. These tests were conducted to check the accuracy of the finite element model. Figure 23.3 shows the mass loaded tip with the 0.444 lbm clamp. Figure 23.4 shows the root mass loaded with the 1.3 lbm clamp.

23.2.4 Fixed-Free Modal Tests

Six fixed-free modal tests were carried out on Blade 1. Only one blade was used because it had been established that blades 1 and 2 behaved identically. It was attached to an 800 lbm Aluminum-Steel structure normally used to hold a CX-100 9 m turbine blade shown in Fig. 23.5.

Fig. 23.5 Fixed free set up
(mass loaded)

23.2.4.1 "Damaged" Fixed Free

After one fixed-free test, five mass loaded tests were run.

- 0.444 lbm C-clamp at tip
- 0.444 lbm C-clamp at middle, Point 20
- 0.3 lbm C-Clamp at root, Point 7
- 0.3 lbm C-Clamp at middle, Point 25
- 1.3 lbm C-Clamp at root, Point 7

23.2.4.2 Vibrometer

To verify the accuracy of the Kalman Filter's ability to predict tip displacement, actual tip displacement was measured with a laser vibrometer along with acceleration. The blade was excited with an impulse at Points 5, 14, 16, 23, and 33. These vibrometer tests were done during the sequence of fixed-free modal tests. The record of the laser vibrometer time series analyses is in Appendix B. The vibrometer set up is shown in Fig. 23.6.

Fig. 23.6 Laser vibrometer
set up
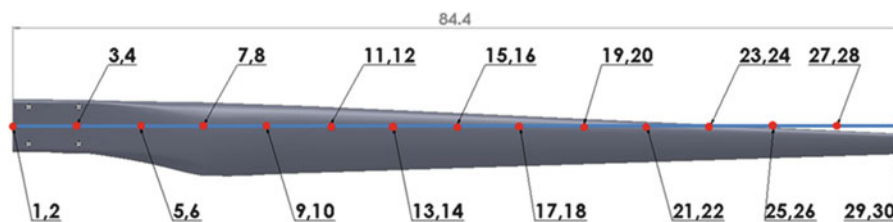
Fig. 23.7 Finite element model node and degree of freedom locations

Table 23.1 Finite element
model parameters

Parameter	Value
Number of elements	14
Number of nodes	15
Elastic modulus	2.5 Mpsi [8]
Density	.0492 lbm/in.^{3}
Element length	6″
Cross sectional area	Section dependent
Area moment of inertia (flapwise bending)	Section dependent

23.2.5 Model

A simple finite element model was created in Matlab based on a previous study reported by Avitabile [7]. A finite element model is used to develop the state space model required by the Kalman Filter. A simple Matlab 30 degree of freedom beam model was used because it could be run quickly and the Stiffness and Mass matrix were easily extracted and implemented into the Matlab Kalman Filter.

The model is comprised of 14 6 in. length beam elements and 15 nodes. Each node has a vertical and rotary degree of freedom. The location of the elements, nodes and degrees of freedom, DOF, are shown in Fig. 23.7. Odd number DOFs correspond to vertical translation and even to rotation.

The parameters used to define the beam model are shown in Table 23.1.

The cross sectional area and area moment of inertia were measured using Solidwork's section properties tools (Fig. 23.8). These parameters were measured at the location of each node and were assumed to be constant along the length of the beam element. The blade is constructed of a foam core and fiberglass and carbon fiber shell. It was assumed that the foam did not contribute significantly to the stiffness or weight of the blade, therefore only the composite shell was measured.

Some additional assumptions are made in the model. The composite material is assumed to be homogenous and isotropic, therefore density is constant and elastic modulus is not directional dependent. The flapwise bending modes were assumed to account for most of the tip deflection and therefore, the model only calculates flapwise bending modes.

Fig. 23.8 Measuring blade
with solidworks sections
properties tool
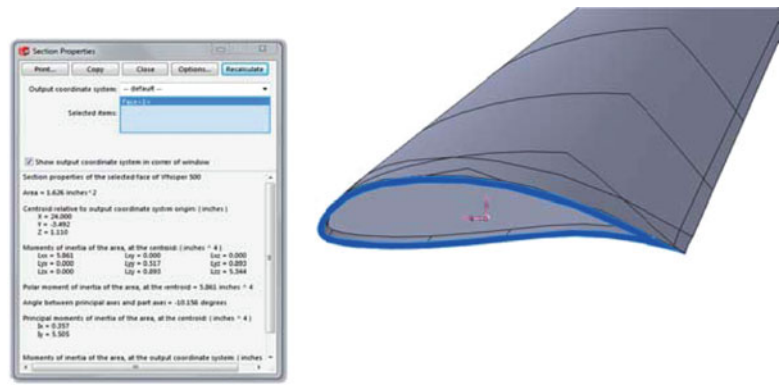
Fig. 23.9 Free-free boundary
condition
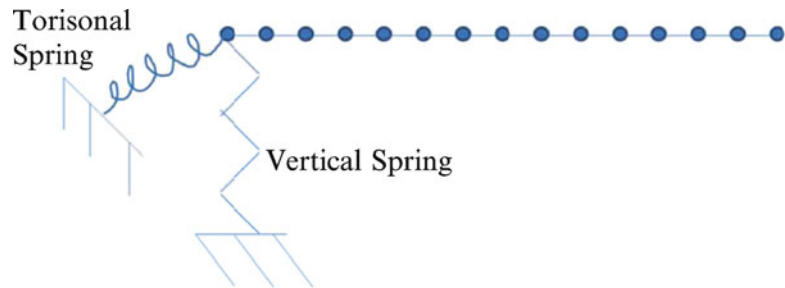
Table 23.2 Free-free
boundary condition
stiffness

Spring	Stiffness
Vertical spring	2 lbf/in.
Torsional spring	2 lb-in./rad

23.2.5.1   Modeling Boundary Conditions

There were two boundary conditions that needed to be modeled, free-free and fixed-free. To simulate free-free, a soft vertical
spring and soft torsional spring supported the root of the blade. Figure 23.9 shows the free-free model and Table 23.2 lists the
spring values.

   To simulate fixed-free stiff vertical and torsional springs as well as a large mass were attached to the root. Figure 23.10
shows the fixed-free model and Table 23.3 lists the mass and spring values.

23.2.5.2   Modeling Attached Mass

In seven modal tests the blade was mass loaded using C-clamps. To model these additional masses, point masses were added
to the closest vertical degree of freedom. Mass moment of inertia was modeled because it was difficult to measure and when
it was added it had minimal effect, especially on lower order modes.

   The validity of the model and all the assumptions made were confirmed by comparing FEM natural frequencies and mode
shapes to experimental results.

23.2.6   Kalman Filter

The Kalman filter is an algorithmic method for simultaneously reducing measurement noise and inferring one measurement
from another. It does this by comparing measurement readings against what a theoretical model predicts should be
the behavior of the object under question. Then, depending upon how much either the model or the readings are "trusted"
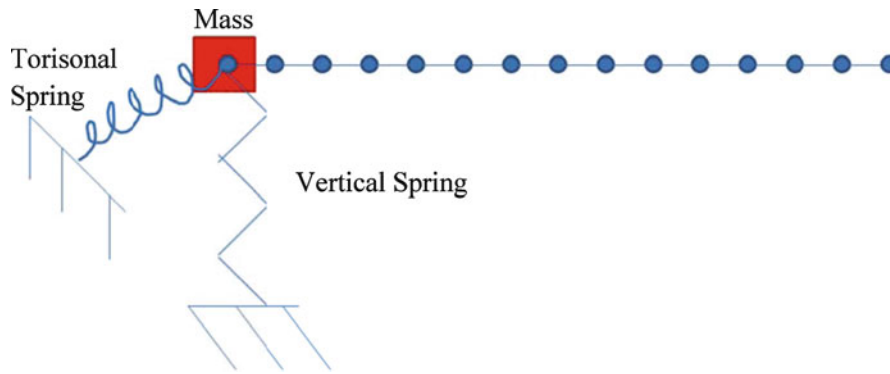
Fig. 23.10 Fixed-free boundary condition

Table 23.3 Fixed free boundary condition mass and stiffness

Parameter	Value
Vertical spring	2,000,000 lbf/in.
Torsional spring	2,000,000 lb-in./rad
Mass	1,000,000 lbm
Mass moment of inertia	1,000,000 lbm*in.^{2}

Fig. 23.11 Diagram of two degree of freedom system
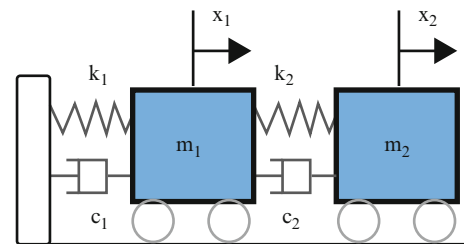
(this is supplied by the user), the filter weights the result toward one or the other and typically delivers quite accurate results. It infers one reading from another simply by using a state space model wherein the matrices can be arranged such that an input of one type of data produces a different type in the output, so long as the equations of motion for the system are known.

23.2.6.1 Two Degree of Freedom Model

This project attempts to use a 30 degree of freedom model of a Whisper 500 blade and tip-mounted accelerometer measurements to infer tip deflection with a Kalman filter. To validate this approach a two degree of freedom mass-spring-damper system model was first developed in Matlab. See Fig. 23.11 for a diagram of the system. The dynamics of this system are well known and can be modeled quite accurately, thus serving as a reliable benchmark to test the Kalman filter. An LSIM model fed "fake" accelerometer data from a 1 Hz sinusoidal excitation of the system to the Kalman filter. Before it entered the filter, however, randomized signal "noise" was added to the data. The Kalman filter then processed this data and output predicted displacement data.

23.3 Results

All free-free data was recorded using RT Pro Photon Dactron and mode shapes, natural frequencies and damping were calculated by curve fitting in ME Scope.

Table 23.4 Free-free frequency results

Mode	Frequencies (Hz)		Description
	Blade 1	Blade 2	
1	25.1	26.2	First flapwise bending
2	63.0	65.8	Second flapwise bending
3	104.0	101.5	First edgewise bending
4	118.7	122.3	Third flapwise bending
5	188.9	194.5	Fourth flapwise bending
6	260.8	256.2	Second edgewise bending
7	277.4	282.0	Fifth flapwise bending
8	368.0	379.4	Sixth flapwise bending
9	387.9	406.7	First torsional
10	469.8	488.2	Seventh flapwise bending

Fig. 23.12 Free-free MAC comparing Blade 1 to Blade 2
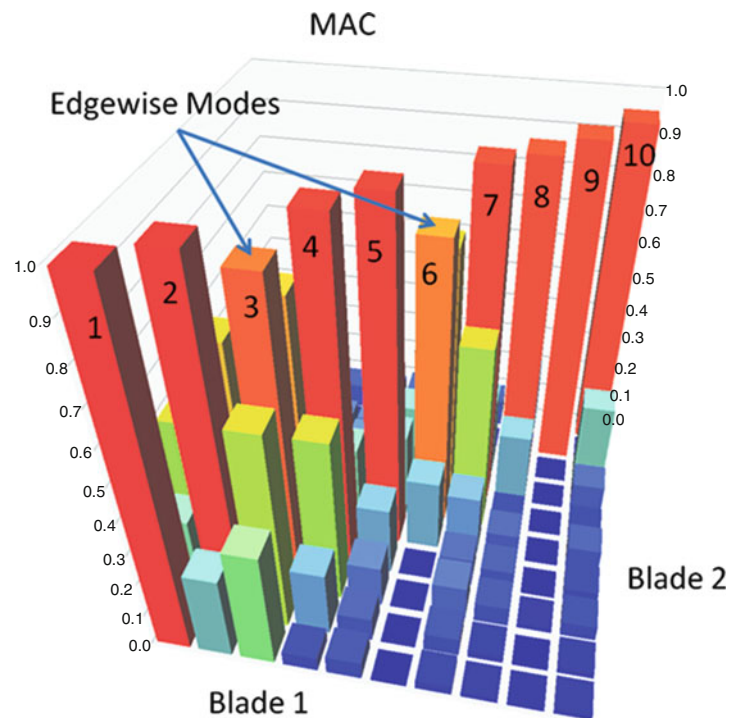
23.3.1 Free-Free Modal Tests Results

By comparing natural frequencies and mode shapes it was determined the dynamic characteristics of Blade 1 and Blade 2 are nearly identical. Because the blades have nearly identical dynamics further tests were not duplicated on each blade.

23.3.1.1 Free-Free Natural Frequencies

The natural frequencies of the free-free test are summarized in Table 23.4. Table 23.4 shows Blade 1 and Blade 2 have similar natural frequencies.

23.3.1.2 Free-Free Mode Shape Comparisons

A modal assurance criterion was used to compare the mode shapes of Blade 1 to Blade 2. Figure 23.12 shows very similar mode shapes.

Table 23.5 Fixed-free natural frequencies

Mode	Frequencies (Hz)	Description
1	11.1	First flapwise bending
2	32.9	Second fapwise bending
3	37.5	First lag bending
4	75.7	Third flapwise bending
5	124.2	First edgewise bending
6	135.1	Fourth flapwise bending
7	210.4	Fifth flapwise bending
8	280.0	Second edgewise bending
9	295.7	Sixth flapwise bending
10	314.2	First torsional
11	388.6	Seventh flapwise bending

Table 23.6 Free-free natural frequency comparison, FEM to experimental

Mode	Frequencies (Hz)				
	Blade 1	Blade 2	Test Avg.	FEM	% Diff.
1	25.1	26.2	25.7	25.1	2
2	63.0	65.8	64.4	65.5	2
3	118.7	122.3	120.5	126.7	5
4	188.9	194.5	191.7	204.2	6

23.3.2 Fixed-Free Modal Test Results

The frequency results of the fixed-free test are shown in Table 23.5.

23.3.3 Finite Element Model Validation

To validate the FEM, a variety of boundary conditions and mass loading situations were simulated and compared to experimental mode shapes and natural frequencies.

23.3.3.1 Free-Free Model Validation

Table 23.6 shows the comparison of natural frequencies. The percent difference is quite low, indicating the FEM can accurately predict frequencies.

To confirm the FEM can accurately predict flapwise bending modes, a MAC was created that compared FEM shapes to experimental mode shapes. Only the experimental measurement points on the leading edge of the blade were used in the MAC. This was necessary because the experimental geometry was two dimensional and the FEM was only one dimensional. A MAC of the free-free mode shapes is shown in Fig. 23.13. The MAC shows high correlation, confirming the FEM can accurately predict free-free mode shapes.

23.3.3.2 Fixed-Free Model Validation

Table 23.7 shows a comparison of the fixed-free natural frequencies. The low percent difference between experimental and FEM confirms the model accurately predicts fixed-free frequencies.

There is a relatively high percent difference between mode two natural frequencies. This is likely caused by the presence of a lag bending mode, the coupling of edgewise and flapwise ending modes. The FEM does not account for this, and is likely the cause for this error.

Figure 23.14 shows a MAC comparing experimental fixed-free mode shapes to FEM shapes.

The MAC shows high correlation for flapwise bending modes 1, 3 and 4 and slightly lower for Mode 2. Again this error is likely caused by the model not accounting for the lag bending mode.

Fig. 23.13 Free-free MAC, experimental Blade 2 to finite element model
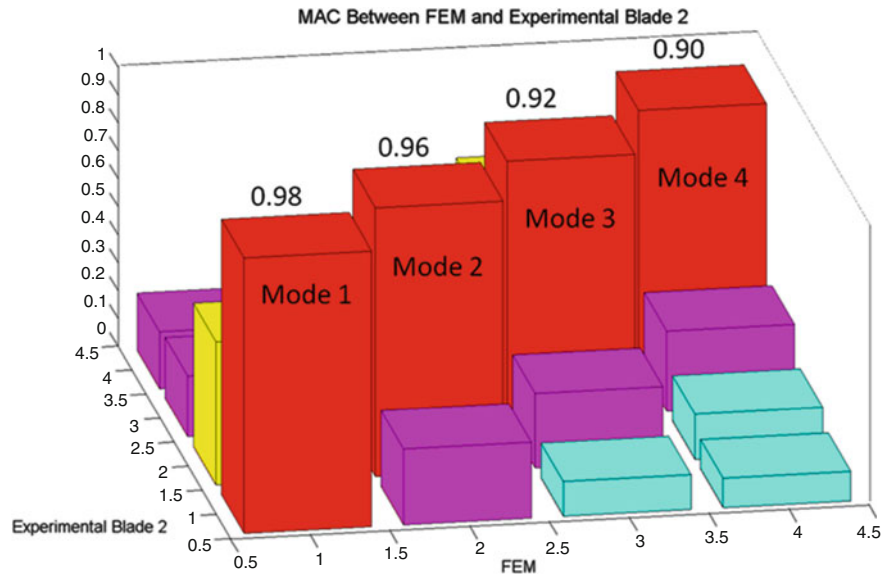
Table 23.7 Fixed-free natural frequency comparison, FEM to experimental

Mode	Frequencies (Hz)		% Difference
	Experimental	FEM	
1	11.1	11.0	0.6
2	32.9	38.0	−15.6
3	75.7	82.2	−8.6
4	135.1	145.0	−7.4

Fig. 23.14 Fixed-free MAC, experimental Blade 1 to finite element model
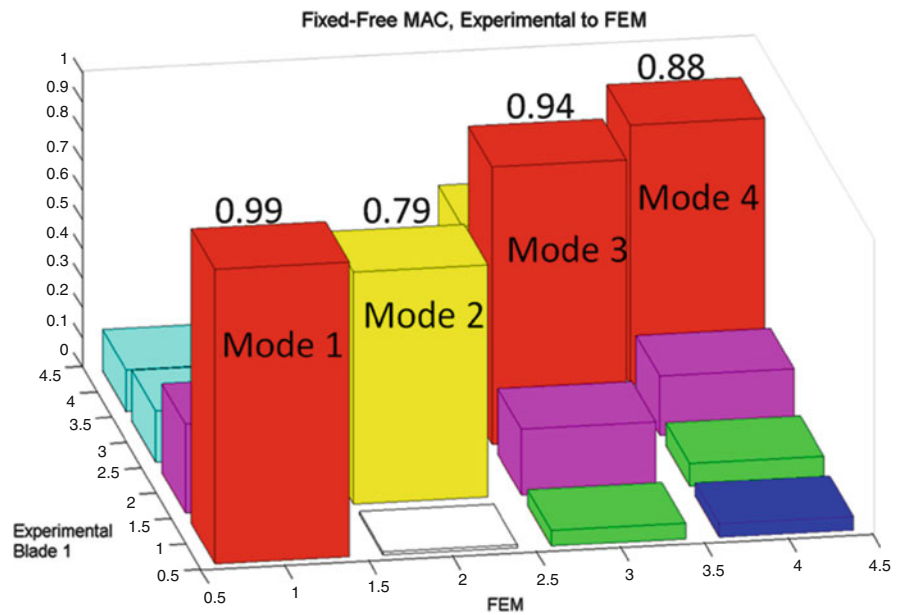
23.3.3.3   Mass Loaded Model Validation

Seven additional modal tests were completed where the blade was mass loaded with a variety of C-Clamps. In general, the FEM was able to accurately predict frequencies and mode shapes. The frequency comparisons, MACs and other details are in Appendix C.

Table 23.8 Frequency comparison of free-free tip loaded blade

| | Frequencies (Hz) | | |
Mode	Experimental	FEM	% Difference
1	17.3	16.4	5
2	70.4	49.4	29
3	121.9	105.6	13
4	194.7	180.6	7

Fig. 23.15 Tip loaded free-free MAC, experimental Blade 2 to finite element model
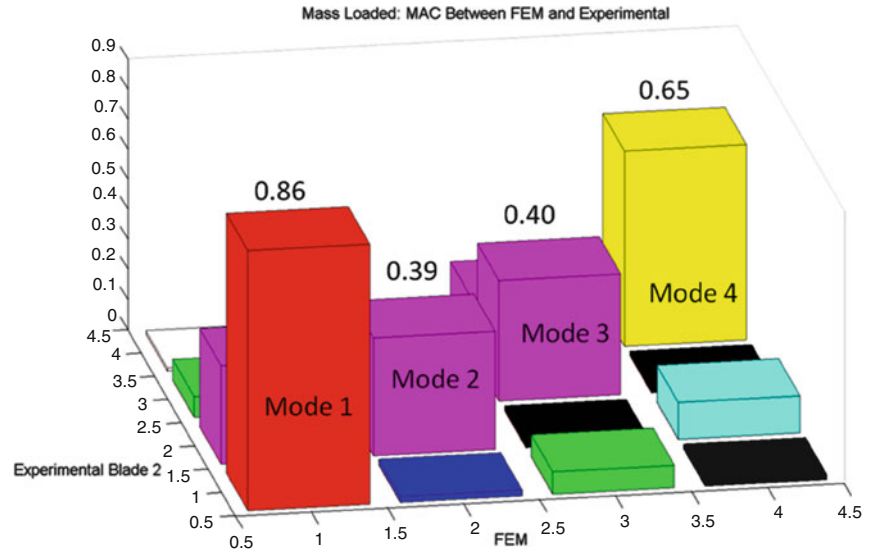
Table 23.9 Comparison of frequencies with mass attached at root

| | Frequencies (Hz) | | |
Mode	Experimental	FEM	% Difference
1	24.3	24.2	0.4
2	61.5	63.2	−2.8
3	129.7	122.1	5.9
4	196.6	196.6	0.0

While the FEM was able to accurately simulate most tests, some loading conditions can induce effects not accounted for in the model. One example is the free-free test with a tip mass. See Fig. 23.3. In the experimental setup, the blade is hanging vertically, reference Fig. 23.2, and the mass is at the tip (bottom). As a result, there is an axial load applied to the blade which affects mode shapes and frequencies. The model does not account for this load, therefore the results were poor. Table 23.8 shows a comparison of the natural frequencies.

The error caused by the axial load can also be seen in the MAC shown in Fig. 23.15.

To confirm that the poor model prediction was caused by the axial force, a clamp was attached to the root (top), effectively eliminating the axial load. See Fig. 23.4 for clamp location. The model's prediction of this mass loaded condition was much more accurate. The frequency comparison is shown in Table 23.9.

The MAC comparing experimental to FEM is shown in Fig. 23.16.

The model was also able to accurately simulate masses added in the fixed free condition. Five different tests were carried out to confirm this. Table 23.10 shows the comparison of a fixed free condition with a .444 lbm mass at point 20 near the middle of the blade. MAC values are shown to be very good for this condition shown in Fig. 23.17.

Fig. 23.16 Root loaded
free-free MAC, experimental
Blade 2 to finite element
model
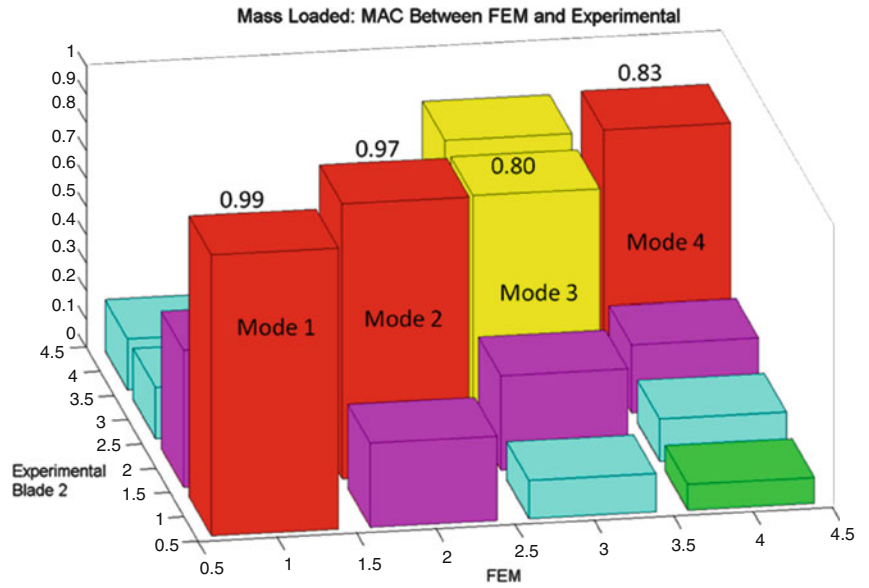
Table 23.10 Comparison of
fixed free blade with .444 lbm
mass load in middle

| Mode | Frequencies (Hz) | | % Difference |
	Experimental	FEM	
1	11	10.8302	1.54
2	31.3	34.8631	−11.38
3	72.7	79.7708	−9.73
4	134.6	141.5375	−5.15

Fig. 23.17 Fixed free mass
loaded near middle of blade
with .444 lbm
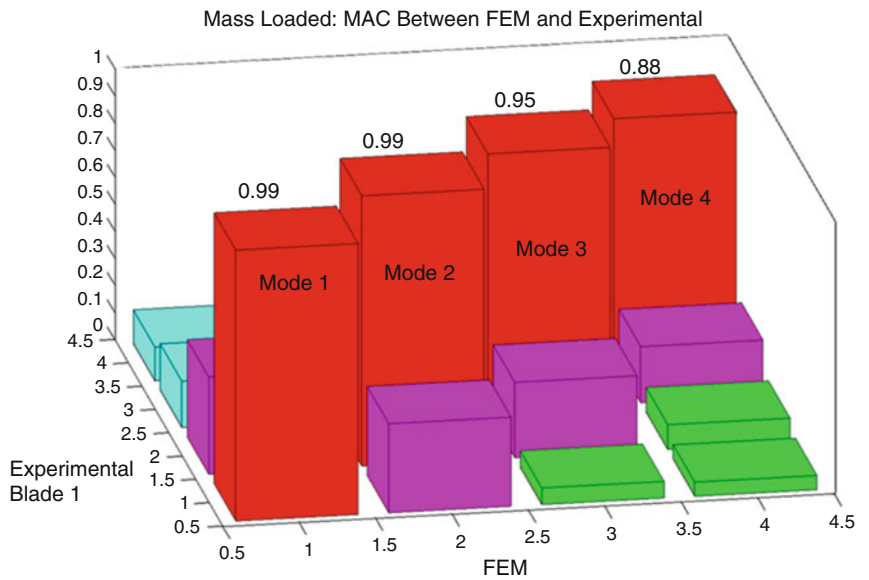
Fig. 23.18 Kalman versus actual at signal to noise ratio of 40
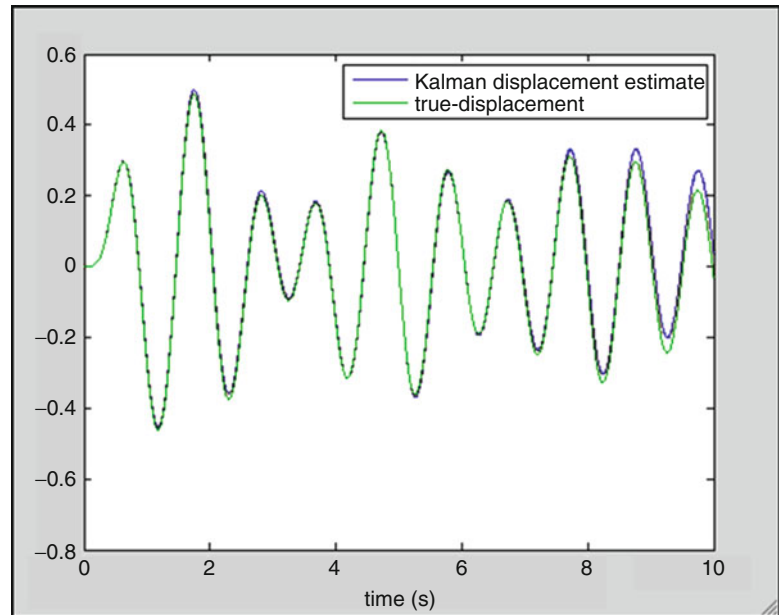
Fig. 23.19 Kalman versus actual at signal to noise ratio of 10
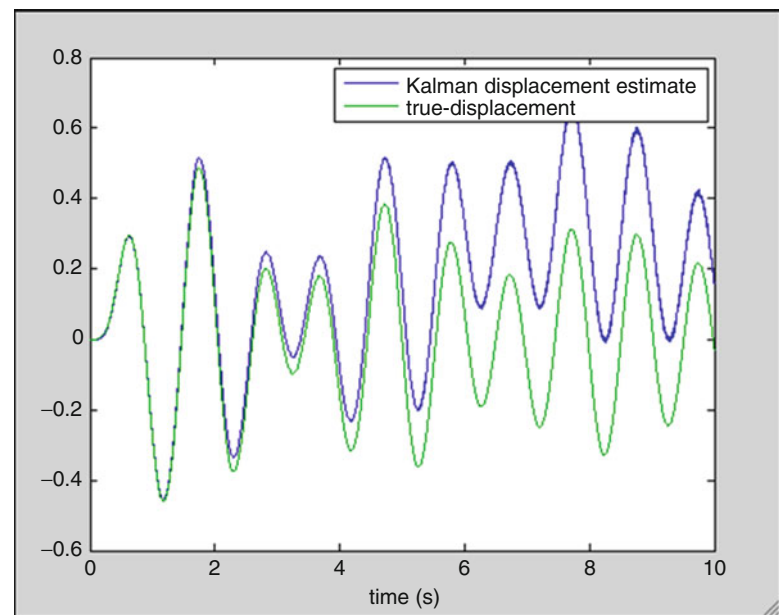
23.3.4 Kalman Filter Results

23.3.4.1 Two Degree of Freedom Model Results

This data was then compared to displacement data output by the same LSIM model and was found to match with a high degree of accuracy, shown in Fig. 23.18.

The complication with this model is that it could only sustain a small amount of measurement noise before the displacement estimate began to diverge. The plot in Fig. 23.18 has a signal to noise ratio of 40 to 1. At a signal to noise ratio of 10 to 1 the measurement begins to diverge and become unusable, shown in Fig. 23.19.

It is probable that a lack of necessary computational power is to blame for this relatively limited filtering capacity. The tests shown were restricted to a 1,000 Hz sample rate. The computers available were not able to handle sample rates much higher than this. If they were then it is conceivable that much lower signal to noise ratios could have been subject to the filter and returned accurate results. To further confirm the validity of the two degree of freedom model, several parameters were varied to determine their effect on the output of the Kalman filter.

23.3.4.2 Thirty Degree of Freedom Model

After validating the Kalman filter with a two degree of freedom system, the same strategy was used to filter the 30 degree of freedom model of the Whisper 500 blade. However, when attempting to supply the filter with data produced by simulation, the output of the Kalman filtering loop quickly diverged to infinity. It is suspected that lack of sufficient computational power is also to blame here. The state matrix is much larger and computational intensity much higher, therefore divergent behavior is to be expected with the very limited sampling rate available. Due to severe time constraints further investigation into this behavior was not possible.

23.4 Conclusions

Modal testing of the Whisper 500 was completed in free-free and fixed free configurations. The natural frequencies and mode shapes were identified for the first few modes. Results of the free-free modal tests confirmed the two blades had almost identical dynamic characteristics. A reduced-order model that was developed in this study was shown to be able to accurately predict frequencies and mode shapes for a variety of boundary and mass loaded conditions. This reduced order model can be used in embedded sensors for detecting changes in the properties of wind turbine blades. Determining changes in the characteristics of turbine blades can allow detection of damage before total failure of a blade occurs.

The Kalman filter accurately inferred the displacement of a two degree of freedom system from accelerometer measurements under relatively high signal to noise ratio conditions. As noise became a larger component of the measurement though, the predictive capacity of the Kalman filter became unstable. This is likely due to a low sampling rate which is the result of limited computational capacity. For unknown reasons when the 30 degree of freedom model is subjected to the same Kalman code, its results rapidly diverge to infinity. It is possible this is due to insufficient computational power as well.

Appendix A

Modal Test Record

Test #	Modal test	Blade	ME scope file	Description	Mass
1	Modal test 1 6_23_2011	1	Whisper 500 Blade 1	Free free flapwise	NONE
2	Modal test 2 7_6_2011	2	Whisper 500 Blade 2	Free free flapwise	NONE
3	Modal test 3 7_7_2011	1	Whisper 500 Blade 1	Free free edgewise	NONE
4	Modal test 4 7_18_2011	2	Whisper 500 Blade 2 test 4	Free free edgewise and flap	NONE
5	Modal test 5 7_18_2011_Mass	2	Whisper 500 Blade 2 test 5	Free free mass @ tip	.444 lbm clamp
6	Modal test 6 7_22_2011_Mass_II	2	Whisper 500 Blade 2 test 6	Free free mass @ top	1.3 lbm clamp
7	Modal test fixed bld 1 7_27_2011	1	Whisper 500 Blade 1 Fixed free	Fixed free	
8	Modal test fixed bld 1 Mass 7_27_2011	1	Whisper 500 Blade 1 Fixed free	Fixed free w/tip mass	.444 lbm clamp
9	Modal test fixed bld 1 Mass2 7_27_2011	1	Whisper 500 Blade 1 Fixed free	Fixed free mass @ 20	.444 lbm clamp
10	Modal test fixed bld 1 Mass3 7_28_2011	1	Whisper 500 Blade 1 Fixed free	Fixed free mass @ 7	.3 lbm clamp
11	Modal test fixed bld 1 Mass4 7_28_2011	1	Whisper 500 Blade 1 Fixed free	Fixed free mass @ 25	.3 lbm clamp
12	Modal test fixed bld 1 Mass5 7_28_2011	1	Whisper 500 Blade 1 Fixed free	Fixed free mass @ 7	1.3 lbm clamp

Data Acquisition

Software: ProPhoton Version 5.1
Hardware: Dactron
Lines: 800
Bandwidth: 500 Hz
Points: 2048
ΔT: 781.3
Linear Averages: 5
Window: None

Appendix B

Laser Vibrometer Time Series Record

1	Modal test fixed bld 1 7_27_2011	1	Whisper 500 Blade 1 Fixed free	Fixed free	None
2	Modal test fixed bld 1 Mass 7_27_2011	1	Whisper 500 Blade 1 Fixed free	Fixed free w/tip mass	.444 lbm clamp
3	Modal test fixed bld 1 Mass2 7_27_2011	1	Whisper 500 Blade 1 Fixed free	Fixed free mass @ 20	.444 lbm clamp
4	Modal test fixed bld 1 Mass3 7_28_2011	1	Whisper 500 Blade 1 Fixed free	Fixed free mass @ 7	.3 lbm clamp
5	Modal test fixed bld 1 Mass4 7_28_2011	1	Whisper 500 Blade 1 Fixed free	Fixed free mass @ 25	.3 lbm clamp
6	Modal test fixed bld 1 Mass5 7_28_2011	1	Whisper 500 Blade 1 Fixed free	Fixed free mass @ 7	1.3 lbm clamp

Impact Map
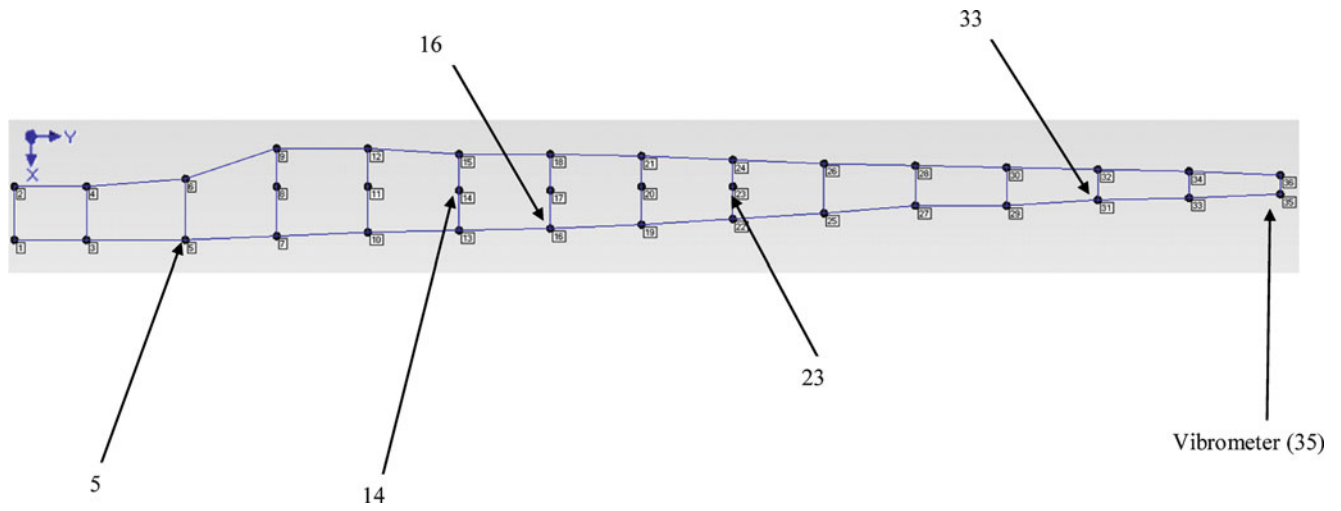
Appendix C

MAC Figures
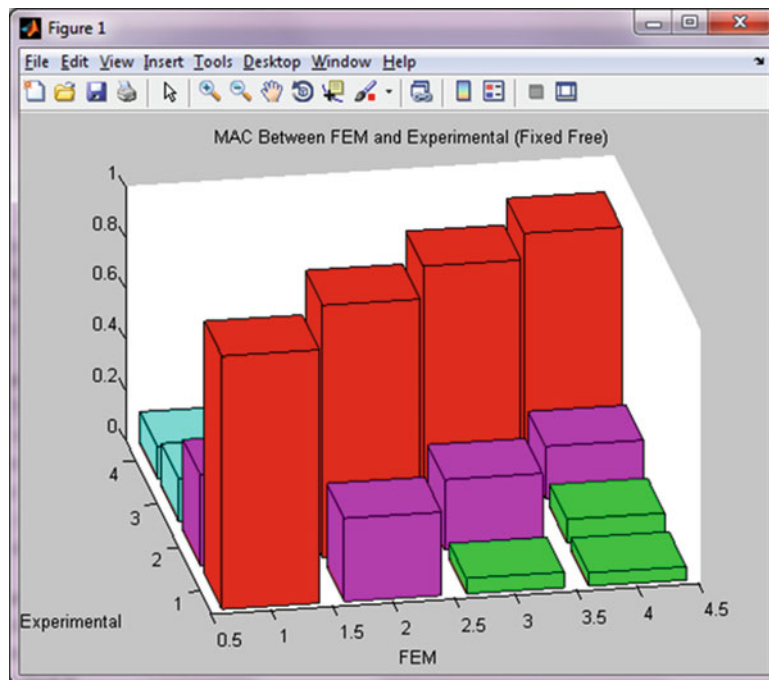
Fig. C.1 MAC of .444 lbm mass clamped at point 20
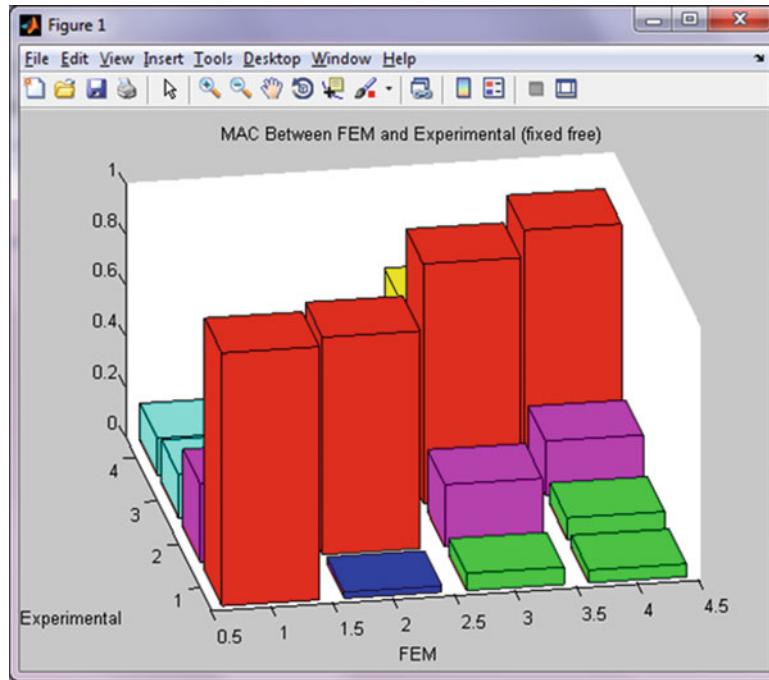
Fig. C.2 MAC of .3 lbm mass clapmed at point 7
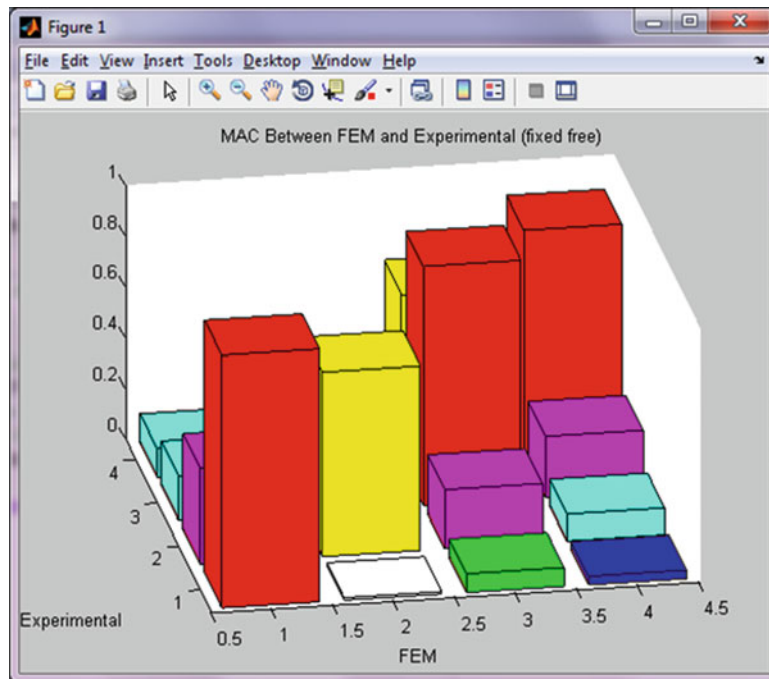
Fig. C.3 Mac of .3 lbm mass clamped at point 25
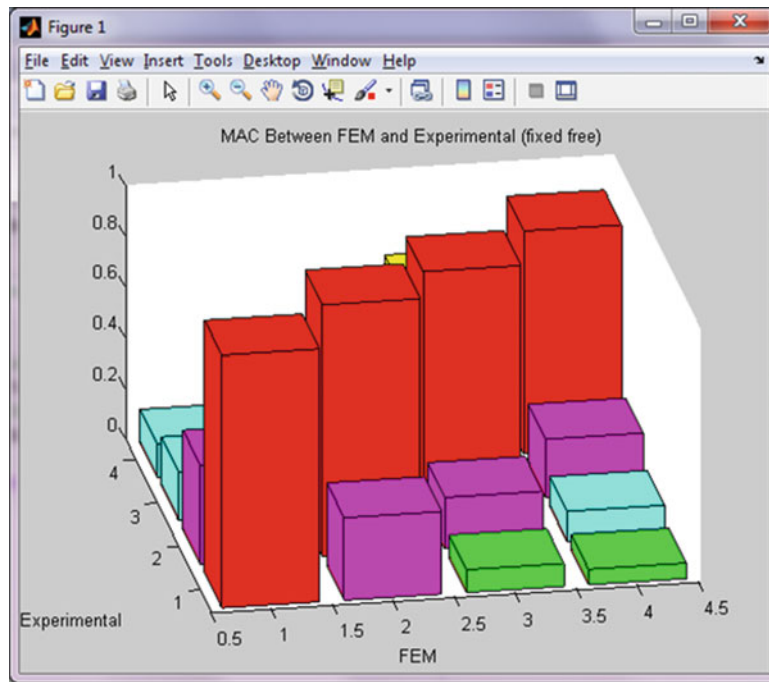
Fig. C.4 MAC of 1.3 lbm mass clamped at point 7
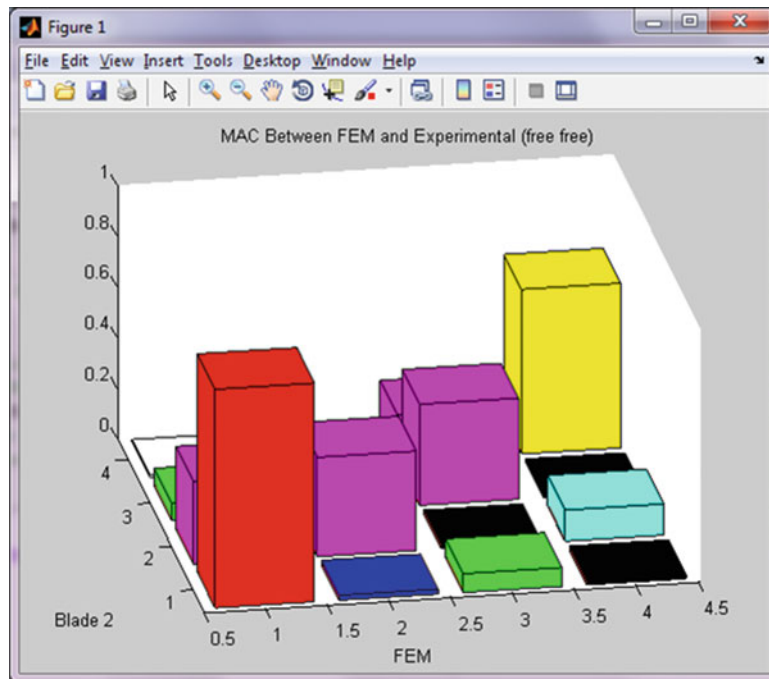
Fig. C.5 MAC of .444 lbm mass clamped at tip
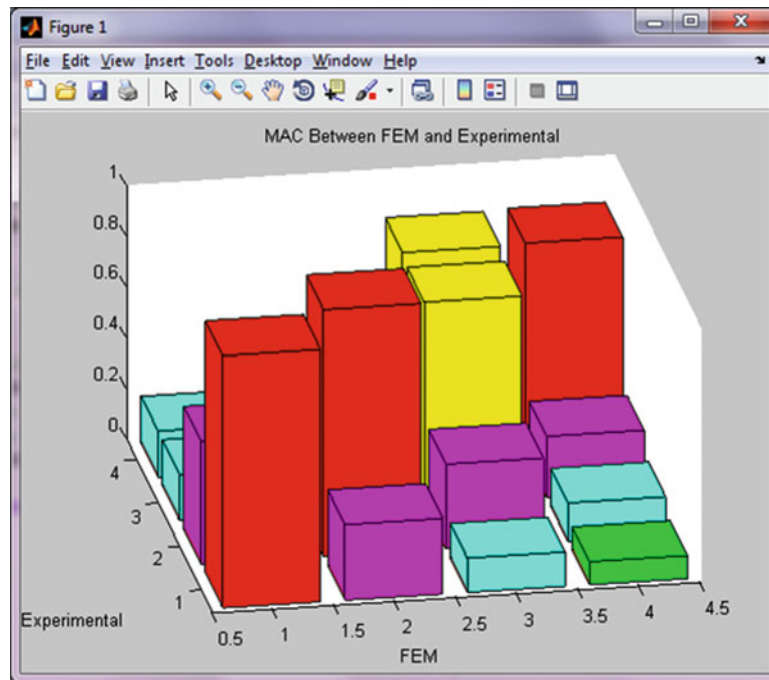
Fig. C.6 MAC of 1.3 lbm mass clamped at root

References

1. U.S. Department of Energy (2008) 20% wind energy by 2030: increasing wind energy's contribution to U.S. electricity supply. Wind and hydropower technologies program, Washington, DC, http://www.nrel.gov/docs/fy08osti/41869.pdf
2. Ciang CC, Jung-Ryul L, Hyung-Joon B (2008) Structural health monitoring for a wind turbine system: a review of damage detection methods. Meas Sci Technol 19(12):1–20
3. Haynes C, Konchuba N, Park G, Farinholt KM (2008) Modeling, estimation, and monitoring of force transmission in wind turbines. In: Proceedings of the IMAC- XXVIII, Jacksonville, http://institute.lanl.gov/ei/LADSS/2009/modeling_estiamtion_and.pdf
4. Donders S (2002) Fault detection and identification for wind turbine systems: a closed-loop analysis. Master's thesis, University of Twente. http://www.stijndonders.nl/wind/scriptie.pdf
5. Bottasso CL, Croce A (2009) Cascading Kalman observers of structural flexible and wind states for wind turbine control. Scientific report DIA-SR 09-02. Dipartimento di Ingegneria Aerospaziale, Politecnico di Milano.http://www.docstoc.com/docs/48223509/Cascading-Kalman-Observers-of-Structural-Flexible-and-Wind-States—rossir24-0017
6. Flynn E, Kpotufe S, Harvey D, Figueiredo E, Taylor S, Dondi D, Mollov T, Todd M, Rosing TS, Park G, Farrar C. SHMTools: a new embeddable software package from SHM applications
7. Avitabile P. Matlab beam finite element script. SDASL UML
8. Kopeliovich D (2011) Polyester matrix composite reinforced by glass fibers (Fiberglass) [SubsTech]. Main_page [SubsTech]. http://www.substech.com/dokuwiki/doku.php?id=polyester_matrix_composite_reinforced_by_glass_fibers_fiberglass. Accessed 1 Aug 2011

Chapter 24
Developing a Finite Element Model in Conjunction with Modal Test for Wind Turbine Blade Models

Eric Harvey, Peter Avitabile, and Christopher Niezrecki

Abstract There are numerous modeling approaches that can be employed in the generation of composite models for wind turbine applications. Several more traditional approaches have been used over the past few decades. However, one modeling approach used for the generation of manufacturing models uses what is referred to as the unit cell approach. This modeling approach has been used for large deformation applications where the orientation realignment of the composite plies needs to be considered in the forming process. This modeling approach has been used for static and large deformation applications but not for dynamic modeling scenarios. There would be a significant advantage to use this approach for the complete modeling of wind turbine blades. A comparison of the traditional composite ply modeling approach and the unit cell approach is studied to determine similarities and differences in the approaches. A panel section is modeled and tested in various conditions followed by correlation and updating studies. A comparison of the different modeling approaches is performed.

The use of this modeling technique is specifically intended to be used in conjunction with the determination of dynamic stress–strain prediction for turbine blade applications. A simple break-out section of a turbine blade comprised of balsa and resin/fiber is used to identify typical model properties needed to properly model the turbine blade. A panel section is modeled and tested and then the model is updated to reflect the properties to best represent the panel structure. The test is performed with several different perturbed boundary conditions to assure that the updated model has appropriate and realistic properties identified for the model.

24.1 Background

Finite element models of a system are composed of elemental and material properties with multiple degrees of freedom. There are many possible ways in which the model can be developed to capture the dynamics of interest. Models are used to represent existing structures where dynamic behaviors are of interest. Using numerical analyses, the system's response to a given input is predicted and often correlated to test data, validating the models accuracy. Improvement of the model's accuracy depends on the information provided to each property; consequently, updates to the properties are made to best represent the structure. Several different modeling techniques and properties can be used to validate the model, but the engineer must filter out unreasonable results, depending on the desired solution.

A composite panel provided by TPI Composites Inc. (TPI) is provided to do several different expansion and stress–strain tests. To do the analysis on the panel an accurate finite element model is required. FEMAP [1] and Nastran [2] are used to develop two finite element models, using different techniques in modeling. Modal tests are done on the plate and the models are updated to converge to mode shapes and frequencies.

Two methods of modeling were utilized in the development of the finite element model. The first method uses a unit cell [3] produced by 2-D plate and 1-D beam elements that mimic the resin and fibers of the composite, respectively. The unit cell was developed for the purpose of preserving material properties during the forming of the composite in a mold. The plate and beam

E. Harvey (✉) • P. Avitabile • C. Niezrecki
Structural Dynamics and Acoustic Systems Laboratory, University of Massachusetts Lowell,
One University Avenue, Lowell, MA 01854, USA
e-mail: Eric_Harvey@student.uml.edu

Fig. 24.1 Modeling of a composite plate using the unit cell and orthotropic shell methods
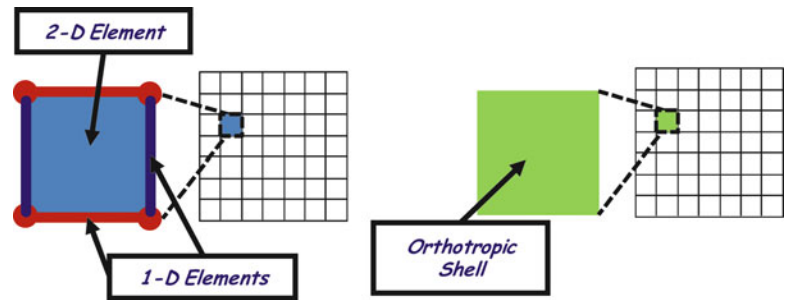
Fig. 24.2 Composite panel test structure for model updating
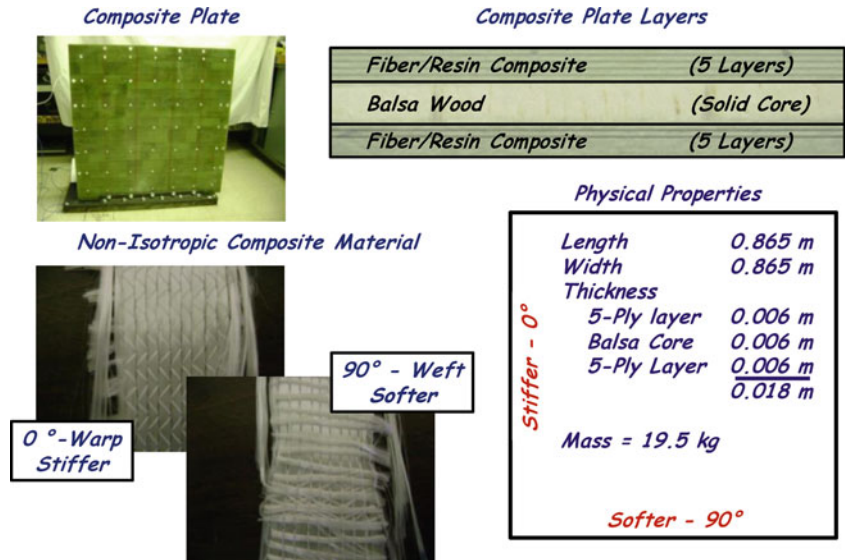
elements shift and translate just like the behavior of the fiber and resin. Traditionally, composites are developed using orthotropic plates. The second method uses an orthotropic plate to capture the effective directional properties. Figure 24.1 shows the layout of the elements in a composite layer for each modeling method.

24.2 Test Structure Description

The structure to be analyzed is a panel, manufactured by TPI Composites, consisting of a fiber/resin composite material and an end-grain balsa core. Five-plies of composite are laid on each side of the balsa core, in the same direction, with each layer consisting of a 0–90° warp-weft architecture. The combined plate is a 0.865 m square with an overall thickness of 0.018 m and a mass of 19.5 kg. Figure 24.2 shows the physical properties of the composite structure.

24.3 Modal Test Description

Traditional modal impact techniques were used to collect data from the test structure using three different boundary conditions: one free-free and two fixed boundary conditions. Configurations can be seen in Fig. 24.3, where the panel is designated into four upright positions. Configurations 1 and 3 fix the panel along the softer, 90°, axis primarily utilizing bending in the stiffer direction and configurations 2 and 4 are fixed along the stiffer. The plates were clamped to a 500 lb steel anchor for clamped testing configurations.

Fig. 24.3 Composite panel test configurations
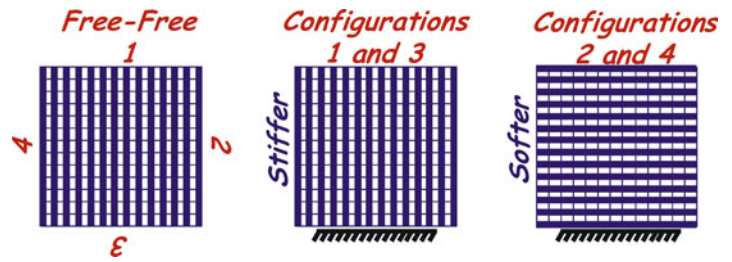
Table 24.1 List of natural frequencies of the composite plate in free-free, and configurations 1 through 4

Mode	Free-Free (Hz)	Configurations 1 and 3 (stiffer)				Configurations 2 and 4 (softer)			
		Conf. 1 (Hz)	Conf. 3 (Hz)	Diff. (%)	MAC	Conf. 2 (Hz)	Conf. 4 (Hz)	Diff. (%)	MAC
1	49.90	19.19	18.82	1.95	99.6	12.69	12.47	1.77	98.1
2	84.34	31.97	31.84	0.42	99.5	29.54	29.36	0.59	98.6
3	129.9	98.19	98.28	-0.09	99.6	84.56	83.96	0.71	97.3
4	138.5	127.2	126.7	0.40	97.6	109.3	108.5	0.68	99.6
5	166.5	135.6	135.2	0.31	97.0	147.4	148.0	-0.43	99.8
6	230.3	204.2	203.3	0.42	99.4	208.6	207.8	0.41	99.1
7	252.1	241.3	242.2	-0.36	99.6	230.0	228.7	0.53	99.4
8	267.5	298.1	293.7	1.50	93.3	240.4	239.7	0.29	98.6
9	359.3	317.4	315.0	0.76	88.4	338.7	338.8	-0.02	99.7
10	382.8	354.8	356.5	-0.47	97.6	363.5	365.5	-0.54	99.1
11	386.9	387.8	383.0	1.25	98.6	409.3	407.1	0.55	91.6
12	434.6	442.4	442.7	-0.08	98.5	418.0	413.8	1.02	89.7
13	452.7	459.5	449.89	2.14	95.2	430.8	429.0	0.43	95.5
14	471.6	499.8	494.6	1.05	92.8	508.9	506.2	0.53	93.0
15	574.7	541.2	539.6	0.29	95.6	533.2	532.1	0.20	96.4
16	582.9	567.7	569.4	-0.29	93.5	598.6	597.7	0.15	85.4
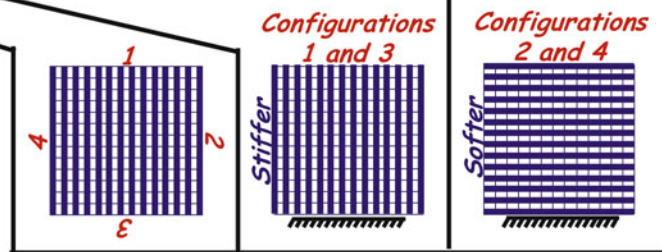
Using LMS Test.Lab [4], five impacts were made at 25 different locations with three reference accelerometers. Impacts were measured at 1,800 lines over a band of 650 Hz and curvefit using LMS's Polymax. Sixteen modes in each configuration were observed and are listed in Table 24.1. Configurations 1 and 3 as well as 2 and 4 were compared to each other to check for uniformity. The overall structure is highly directional. Bending modes in the stiffer and softer directions are clearly observed and can be seen in Fig. 24.4. The first ten flexible modes in each configuration are shown.
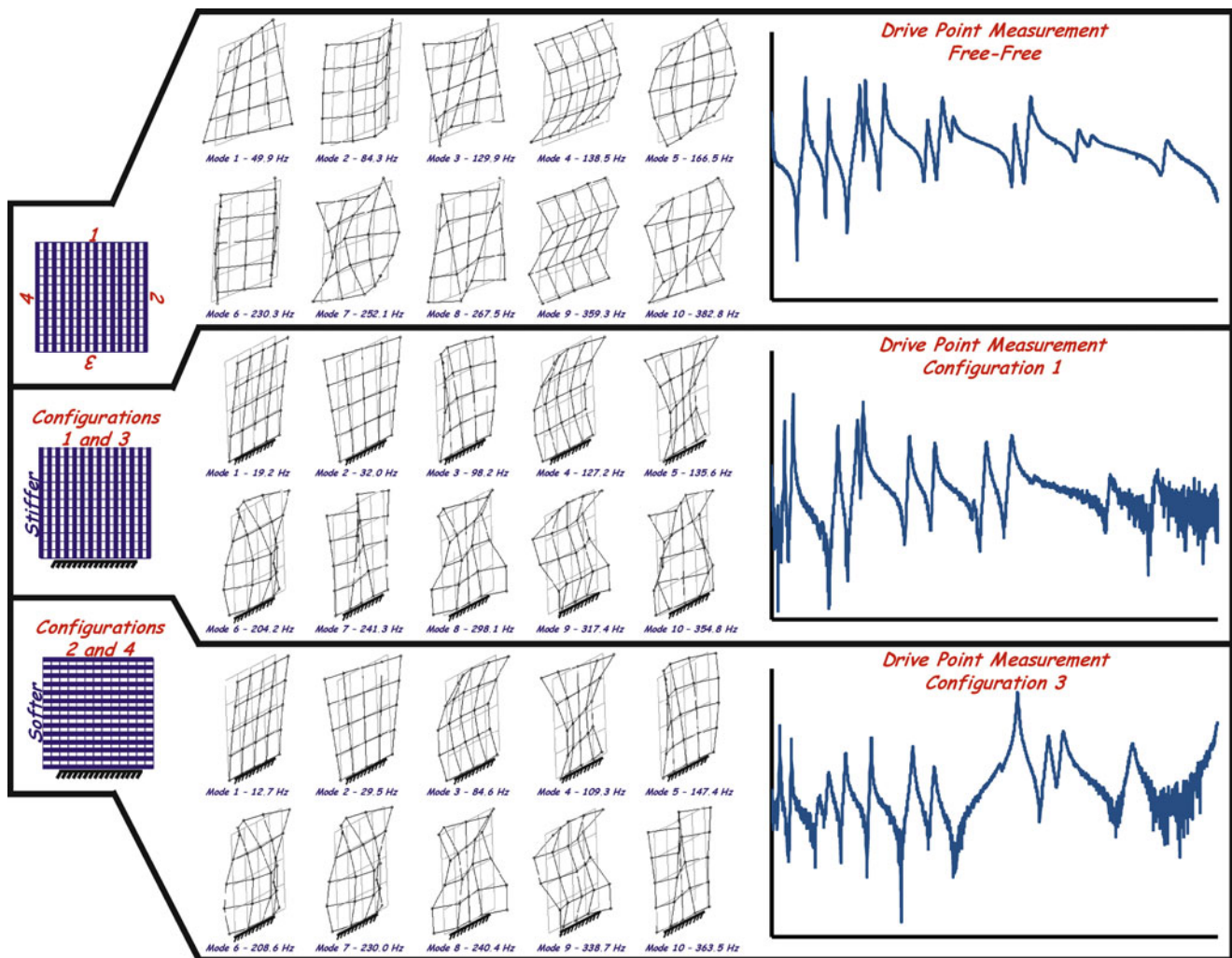
Fig. 24.4 Modes of the composite plate in all configurations and a typical drive point measurement

24.4 Model Description and Cases Studied

Using FEMAP, multiple model configurations were assembled and studied. For the analysis of the composite plate, two models are presented. Each model consists of an isotropic balsa core sandwiched between 5-plies of composite material on each side. Model A uses the unit cell method to model the composite layer and Model B employs the orthotropic shell technique. Each model is compared to the test data in all three configurations and updated using the free-free data. The two clamped configurations are used as perturbations to confirm the update parameters provide reasonable dynamic characteristics.

24.4.1 Model A: Unit Cell

The first model produced uses the unit cell to model the composite portion of the plate. Properties of the beams and elements, specific to the composite material used, were provided by the UMASS Lowell Advanced Composite Materials and Textile Research Laboratory. Material properties were obtained by using static material characterization tests. Figure 24.5 shows the geometry and the parameters for a unit cell. The 1-D elements represent the fibers of the composite and the 2-D elements are of resin. Table 24.2 is a list of the material properties provided by TPI Composites Inc.
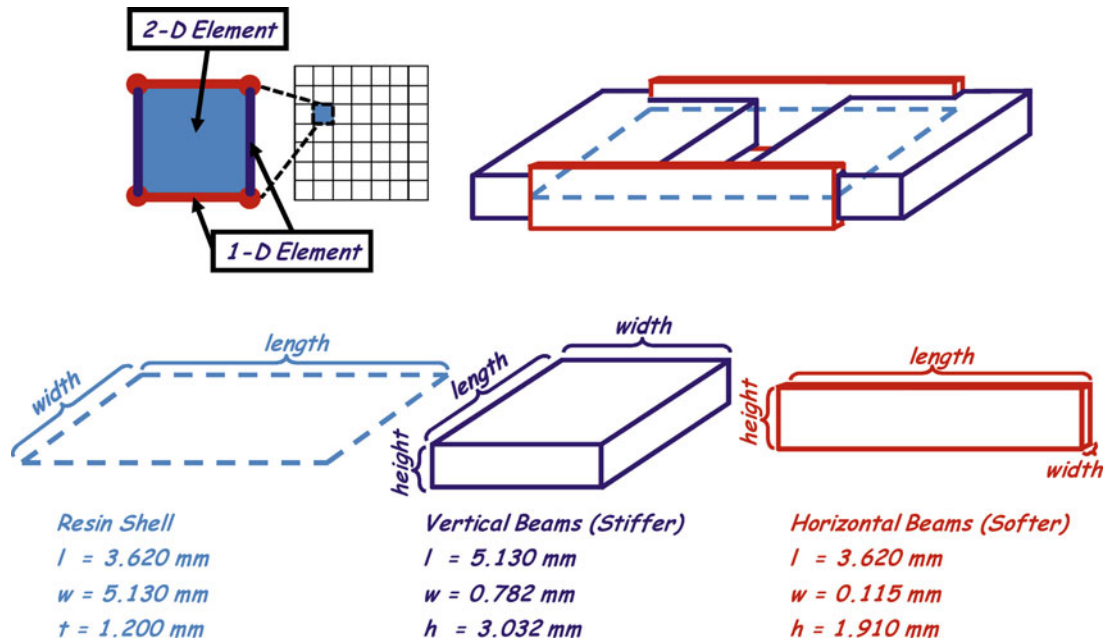
Fig. 24.5 Unit cell parameters

Table 24.2 Material properties used in Model A

Material	Young's Modulus [GPa]	Poisson's ratio	Mass density [kg/m3]
Balsa	1.51	0.3	155
Fiber	60.6	0.2	2,600
Resin	3.00	0.3	1,200

Fig. 24.6 Combination of unit cell with rigid connections to make a multiple layers
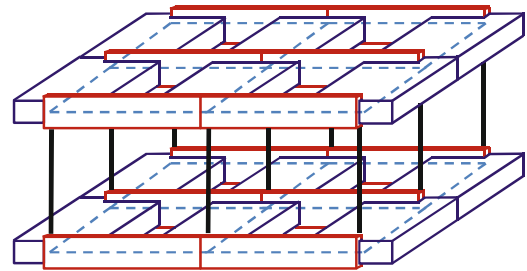
Assembly of the composite plate combines each unit cell in order to make one layer. The layers are then offset and connected rigidly to each other as seen in Fig. 24.6. Two composite sections of 5-plies are then connected to the balsa core, which is made out of isotropic shell elements. Nastran is used to compile the data and solve for 16 modes in each configuration. FEMtools is used to correlate Model A to test data in the free-free configuration. Figure 24.7 shows the correlation.

There is a strong diagonal showing the mode shapes correlated well for around the first ten modes with an average Modal Assurance Criterion (MAC) over all the collected modes of 96.5. The frequencies show a different trend with an average difference of 45.4%. The shift in frequencies is something global in the model, from material properties to modeling methods. Because the unit cell was provided, the properties of the composite are assumed to be correct, leaving balsa as the only possible characteristic to change in the updating. FEMtools [5] was used to update the model to match frequencies and mode shapes. From the optimization, the balsa was much more sensitive to the updating and changed significantly whereas the

#	FEA	Hz	EMA	Hz	% Diff.	MAC
1	1	22.13	1	49.90	-55.66	99.9
2	2	48.82	2	84.34	-42.12	99.3
3	3	65.20	3	129.94	-49.82	99.7
4	4	101.74	4	138.49	-26.53	98.7
5	5	109.56	5	166.55	-34.22	99.8
6	6	128.46	6	230.26	-44.21	99.6
7	7	135.95	7	252.14	-46.08	99.3
8	8	142.08	8	267.53	-46.89	99.3
9	9	194.58	11	386.93	-49.71	96.6
10	10	204.93	9	359.29	-42.96	97.6
11	11	212.52	10	382.79	-44.48	96.2
12	12	233.34	13	452.71	-48.46	84.7
13	13	235.87	12	434.61	-45.73	98.7
14	14	247.99	14	471.64	-47.42	84.8

Average Diff. = -45.4
Average MAC = 96.5
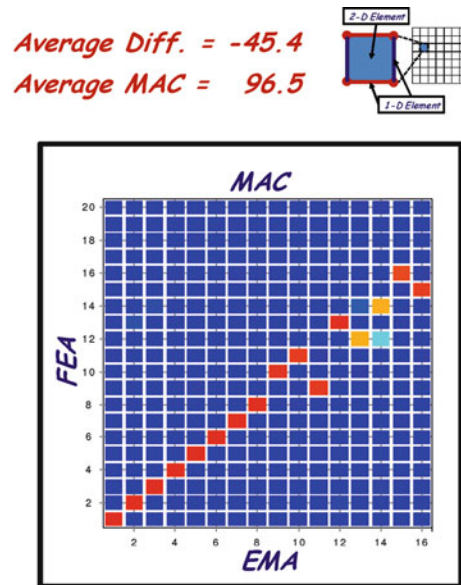
Fig. 24.7 Correlation of Model A to test data in free-free

composite material also changed but not as significantly as the balsa properties. After multiple runs, the only convergence of the model occurs when the Young's modulus is updated. Table 24.3 shows the updated properties of Model A.

In order for the model to converge, the Young's modulus of the balsa material needed to be increased by a factor of 100. While this value may seem unreasonable, these changes produce frequencies with an average difference of −0.53% in the free-free configuration. The model is then checked against the two different perturbed configurations to validate the parameter change. Correlations in the free-free and fixed configurations can be seen in Figs. 24.8, 24.9, and 24.10. Due to a strong correlation between the fixed configurations (1 and 3) and (2 and 4), the model was correlated to only configurations 1 and 2.

Without specifically reviewing the actual material properties obtained, the updated model does satisfy the measured modes from the free-free test. In addition, the two perturbed boundary condition models also confirm that the properties can replicate the different test conditions measured. If the specific material characteristics are not of interest and only the response is of concern, then these models are acceptable for use in further dynamic studies. Both mode shapes and frequencies are preserved; however, the questionable value of balsa draws a concern and the material properties of the unit cell are re-evaluated. Updates to the material properties of the composite layers show no significant improvement to the overall system. Using the unit cell model approach, there was a difference between the model and test data. Therefore a secondary model was constructed using more traditional methods of composite modeling.

24.4.2 Model B: Orthotropic Shell

The composite portion of the plate is modeled using an orthotropic shell. The orthotropic shell has an independent stiffness value in both the x and y directions as shown in Fig. 24.11. The same size shell is used as the unit cell. Analytical models and studies were performed to produce an orthotropic plate from the unit cell. Effective material properties can be seen in Table 24.4.

Assembly of the composite plate is similar to that of the unit cell by combining each orthotropic shell to make one layer. Using FEMAP's layup tool the composite layers are combined to make two 5-ply sections. The 5-ply sections are offset and connected to the balsa core through rigid connections. The balsa core is made of the same with isotropic shells and Nastran is used to compile the data and solve for 16 modes in each configuration. FEMtools is used to correlate Model B to test data in the free-free configuration. Figure 24.12 shows the correlation.

Again the MAC values show excellent correlation, but as seen before the average frequency difference is 22.0% lower than the test. Allowing the balsa to stay within reasonable range, the model was updated to the free-free test data. Properties of the updated material are shown in Table 24.5.

Table 24.3 Updated material properties used in Model A

Material	Young's modulus [GPa]	Poisson's ratio	Mass density [kg/m3]
Balsa	1.51 → 145	0.3	155
Fiber	60.6 → 61	0.2	2,600
Resin	3.00 → 11	0.3	1,200

#	FEA	Hz	EMA	Hz	% Diff.	MAC
1	1	49.64	1	49.90	-0.52	100
2	2	87.19	2	84.34	3.38	99.8
3	3	131.23	3	129.94	0.99	99.9
4	4	134.28	4	138.49	-3.04	99.6
5	5	163.65	5	166.55	-1.74	99.9
6	6	229.83	6	230.26	-0.19	99.8
7	7	249.63	7	252.11	-1.00	99.8
8	8	266.60	8	267.53	-0.35	99.8
9	9	355.74	9	359.29	-0.99	99.5
10	10	381.52	10	382.79	-0.33	97.1
11	11	383.29	11	386.93	-0.94	97.7
12	13	446.31	12	452.71	-1.41	87.1
13	14	466.30	13	471.64	-1.13	90.4
14	16	581.73	14	582.90	-0.20	96.4

Average Diff. = -0.53
Average MAC = 97.6
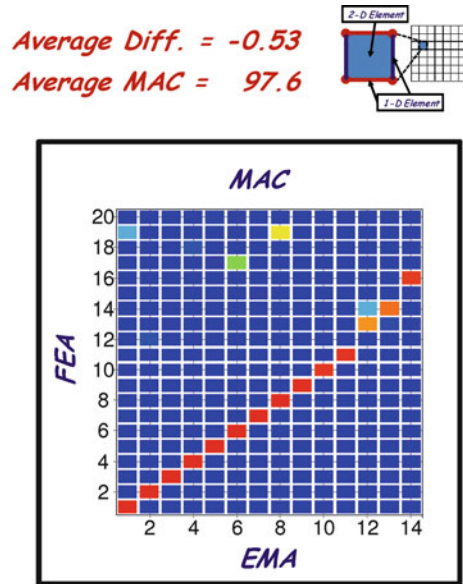
Fig. 24.8 Updated Model A free-free correlation

#	FEA	Hz	EMA	Hz	% Diff.	MAC
1	1	20.06	1	19.19	4.53	99.1
2	2	32.86	2	31.98	2.77	99.1
3	3	99.69	3	98.19	1.54	98.9
4	4	124.61	4	127.25	-2.07	97.8
5	5	133.35	5	135.64	-1.69	98.2
6	7	199.99	6	204.16	-2.04	99.4
7	8	241.21	7	241.29	-0.03	99.2
8	10	281.52	8	298.25	-5.61	97.5
9	12	307.01	9	317.41	-3.27	94.4
10	13	355.27	10	354.81	0.13	98.1
11	14	376.92	11	387.77	-2.80	95.8
12	16	430.13	12	442.38	-2.77	99.2
13	17	435.79	13	459.52	-5.16	96.6
14	18	484.13	14	499.68	-3.11	94.0
15	19	525.81	15	540.99	-2.81	96.6

Average Diff. = -1.49
Average MAC = 97.6
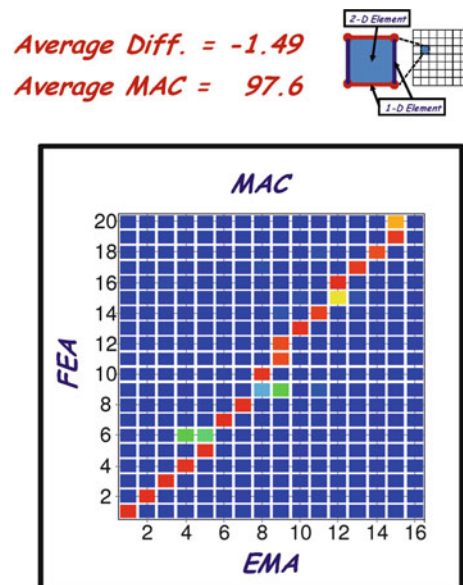
Fig. 24.9 Updated Model A correlated to configuration 1

#	FEA	Hz	EMA	Hz	% Diff.	MAC
1	1	13.93	1	12.68	9.89	99.2
2	2	30.2	2	29.54	2.24	99.6
3	3	82.12	4	84.58	-2.91	94.7
4	4	108.58	5	109.27	-0.64	99.6
5	6	143.58	6	147.37	-2.57	99.8
6	7	203.78	7	208.57	-2.29	99.0
7	8	224.81	8	229.96	-2.24	97.6
8	10	236.02	9	240.43	-1.83	99.1
9	12	329.4	10	338.66	-2.73	99.0
10	13	360.7	11	363.54	-0.78	98.0
11	14	395.24	12	409.29	-3.43	89.2
12	15	400.76	13	417.93	-4.11	96.0
13	17	424.44	14	430.85	-1.49	91.9
14	18	487.18	15	508.84	-4.26	92.4
15	19	522.78	16	533.12	-1.94	92.6

Average Diff. = -1.27
Average MAC = 96.5

Fig. 24.10 Updated Model A correlated to configuration 2

Orthotropic Shell
l = 3.620 mm
w = 5.130 mm
t = 1.200 mm
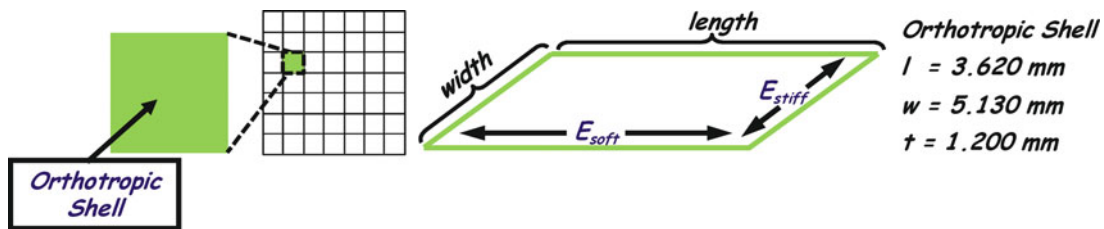
Fig. 24.11 Orthotropic shell parameters

Table 24.4 Derived material properties of orthotropic shell

Material		Young's modulus [GPa]	Poisson's ratio	Mass density [kg/m3]
Balsa		1.51	0.3	155
Fiber/Resin	Ex	8.65		
	Ey	17.2	0.3	1823
	Gxy	5.00		

In order for the model to converge, the fiber and resin are updated in the x and y directions. The updated parameters for the fiber and resin (which were originally assumed to be valid from the unit cell model approach) did change fairly significantly. From the manufacturer's specification sheet, the updated parameters seemed to be in agreement with the expected material properties. The values were in the same ballpark with Ex = 18.2 GPa and Ey = 47.8 GPa, a max difference of 1% from the updated values. Correlation in the free-free and the two different fixed configurations can be seen in Figs. 24.13, 24.14 and 24.15. Due to a strong correlation between the fixed configurations (1 and 3) and (2 and 4), the model was correlated to only configurations 1 and 2.

The two different updated models developed were compared to each other and the correlation between them is very good overall. However, the material properties for each of these updated models are significantly different than the material properties obtained from the unit cell modeling approach. The correlation of these two models in a free-free condition is shown in Fig. 24.16; note that the correlation of the two models to each other for the two different perturbed boundary conditions also correlates very well with similar levels of correlation as seen in Fig. 24.16 and are not shown for brevity.

#	FEA	Hz	EMA	Hz	% Diff.	MAC
1	1	44.95	1	49.90	-9.91	100
2	2	57.86	2	84.34	-31.40	93.5
3	3	92.09	4	138.49	-33.51	92.9
4	4	108.51	3	129.94	-16.49	99.5
5	5	121.58	5	166.55	-27.00	98.3
6	6	174.61	6	230.26	-24.17	97.0
7	7	209.32	8	267.53	-21.76	95.8
8	8	210.63	7	252.14	-16.46	99.7
9	9	240.51	9	359.29	-33.06	98.5
10	10	276.73	10	382.79	-27.71	90.9
11	11	329.38	11	386.93	-14.87	96.3
12	12	330.69	12	434.61	-23.91	98.3
13	13	350.42	13	452.71	-22.59	95.5
14	14	383.66	14	471.64	-18.65	95.7
15	17	490.72	15	574.71	-14.61	71.8
16	18	491.39	16	582.90	-15.70	96.2

Average Diff. = -22.0
Average MAC = 95.0
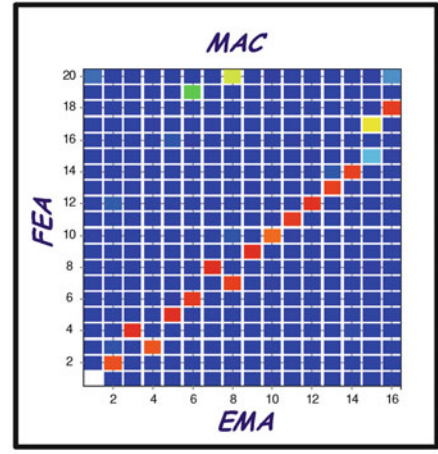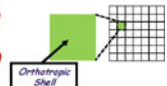
Fig. 24.12 Correlation of Model B to free-free test data

Table 24.5 Updated material properties used in Model B

Material	Young's modulus [GPa]		Poisson's ratio	Mass density [kg/m3]
Balsa		1.51	0.3	155
Fiber/Resin	Ex	8.65 → 18.0		
	Ey	17.15 → 45.0	0.3	1,823
	Gxy	5.00 → 6.10		

#	FEA	Hz	EMA	Hz	% Diff.	MAC
1	1	49.46	1	49.9	-0.87	100
2	2	83.73	2	84.34	-0.73	98.2
3	3	129.77	3	129.94	-0.13	99.6
4	4	140.2	4	138.49	1.24	97.7
5	5	163.16	5	166.55	-2.03	99.0
6	6	235.48	6	230.26	2.27	98.3
7	7	252.56	7	252.14	0.17	99.8
8	8	265.41	8	267.53	-0.79	98.9
9	9	358.35	9	359.29	-0.26	98.3
10	10	384.32	10	382.79	0.40	95.2
11	11	388.76	11	386.93	0.47	96.4
12	12	432.53	12	434.61	-0.48	99.1
13	13	445.35	13	452.71	-1.63	93.0
14	14	479.43	14	471.64	1.65	95.2
15	15	570.43	15	574.71	-0.74	94.8
16	16	583.86	16	582.9	0.17	96.3

Average Diff. = -0.01
Average MAC = 97.5
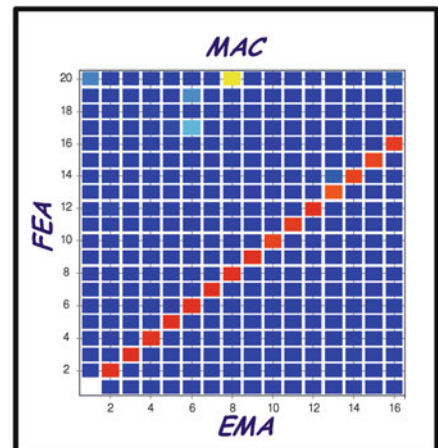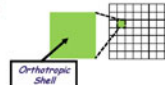
Fig. 24.13 Updated Model B free-free correlation

#	FEA	Hz	EMA	Hz	% Diff.	MAC
1	1	19.80	1	18.82	5.20	99.8
2	2	33.35	2	31.84	4.75	99.7
3	3	96.85	3	98.28	-1.45	97.9
4	4	132.80	4	126.74	4.78	97.7
5	5	134.20	5	135.22	-0.76	99.6
6	6	205.86	6	203.32	1.25	98.3
7	7	246.15	7	242.17	1.64	97.9
8	8	282.22	8	293.71	-3.91	92.7
9	9	304.44	9	315.07	-3.37	91.8
10	10	364.57	10	356.50	2.27	97.0
11	11	389.14	11	382.99	1.60	95.5
12	12	439.18	12	442.79	-0.81	96.2
13	13	442.02	13	449.90	-1.75	91.7
14	15	502.90	14	494.46	1.71	88.2
15	16	537.50	15	539.65	-0.40	92.3
16	17	566.07	16	569.26	-0.56	96.2

Average Diff. = 0.64
Average MAC = 95.8
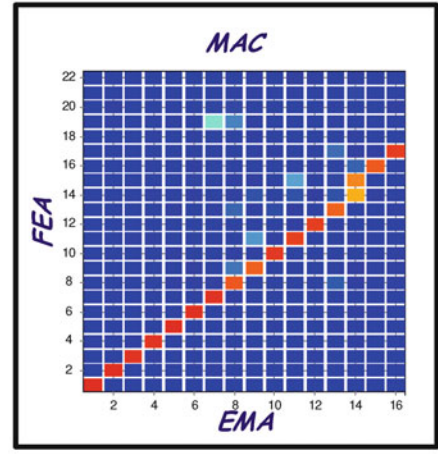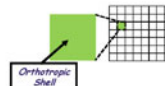
Fig. 24.14 Updated Model B correlated to configuration 1

#	FEA	Hz	EMA	Hz	% Diff.	MAC
1	1	13.72	1	12.69	8.10	99.4
2	2	30.36	2	29.54	2.77	99.7
3	3	84.19	3	84.57	-0.45	94.9
4	4	109.85	4	109.27	0.53	99.7
5	5	148.41	5	147.38	0.70	98.2
6	6	206.68	6	208.62	-0.93	98.0
7	8	239.08	7	229.9	3.99	97.7
8	9	239.25	8	240.41	-0.48	96.6
9	10	340.01	9	338.65	0.40	97.7
10	11	362.43	10	363.53	-0.3	95.9
11	12	405.75	11	409.32	-0.87	83.8
12	13	412.25	12	418.14	-1.41	93.9
13	14	430.91	13	430.84	0.02	84.9
14	15	503.28	14	508.87	-1.10	89.6
15	16	539.46	15	533.11	1.19	92.0
16	17	579.26	16	598.45	-3.21	85.5

Average Diff. = 0.56
Average MAC = 94.2
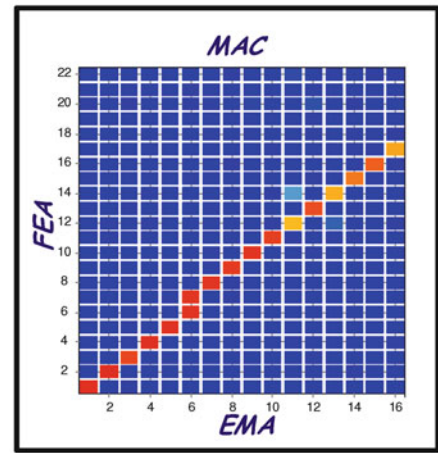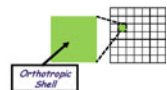
Fig. 24.15 Updated Model B correlated to configurations 2

24.5 Conclusion

Using modal tests and updating, an accurate finite element model is produced for use with the composite panel. Two models were produced using different techniques. Both Model A and Model B converge to the same mode shapes and frequencies using different parameters. The advantage of Model B is that the material properties can be used for calculation such as stress and strain. By only providing accurate displacements, Model A lacks that ability. Model A contains parameters that are sufficient to describe the response even though some of the material properties may not appear to reflect actual properties of the physical components; the accuracy of the model was confirmed by additionally correlating to two different perturbed boundary conditions.

#	Ortho	Hz	Unit Cell	Hz	% Diff.	MAC
1	1	49.40	1	49.64	-0.48	100
2	2	84.04	2	87.19	-3.62	98.7
3	3	129.50	3	131.23	-1.31	99.9
4	4	138.17	4	134.28	2.89	98.5
5	5	161.26	5	163.65	-1.46	99.1
6	6	238.70	6	229.83	3.86	98.7
7	7	249.37	7	249.63	-0.11	99.6
8	8	267.28	8	266.60	0.26	98.7
9	9	341.44	9	355.74	-4.02	98.9
10	10	367.40	10	381.52	-3.70	98.1
11	11	386.34	11	383.29	0.80	99.4
12	12	434.60	13	446.31	-2.62	79.8
13	13	445.39	12	420.79	5.85	98.6
14	14	481.59	14	466.30	3.28	79.5
15	15	565.50	16	581.73	-2.79	99.2
16	16	572.47	15	562.81	1.72	89.6
17	17	604.93	18	666.96	-9.30	90.1
18	18	613.38	20	687.99	-10.8	84.7
19	20	704.94	17	651.60	8.19	83.0

Fig. 24.16 Correlation between Model B (orthotropic plate) and Model A (unit cell)

Two modeling approaches were used to develop two separate models to identify the dynamic response of the composite panel structure. One model used orthotropic plate properties derived from the unit cell approach and the properties were updated and compared to the free-free test. The second model was developed from the unit cell approach and only the balsa material in the model was updated to correlate to the free-free test. In both cases, the models converged to an acceptable level of correlation and both models can be used for further response studies. In addition, both models were also subjected to two different sets of perturbed boundary conditions and both models correlated well to the measured data in those perturbed tests. While the updated models correlate well to test data in all perturbed boundary conditions, the models may not reflect the true material properties of the system needed for prediction of stress but are certainly suitable for use for dynamic response characterization studies.

References

1. FEMAP – Finite element modeling and postprocessing, Version 10.0.2, Siemens Product Lifecycle Management Software Inc
2. NX Nastran 6, Siemens Product Lifecycle Management Software Inc
3. Sherwood J, Fetfatsidis K, Winchester D, Jauffrès D, Avitabile P, Chen J (2010) Using modal analysis to investigate the validity of finite element models for simulating the thermostamping of woven-fabric reinforced composites. Int J Mater Form 3(1):687–690
4. LMS Test.Lab – Leuven measurement systems, Leuven
5. FEMtools 3 – Dynamic design solutions, Leuven

Chapter 25
Dynamic Stress-Strain Prediction from Limited Measurements in the Presence of Structural Defects

Eric Harvey, Peter Avitabile, and Christopher Niezrecki

Abstract Complex composite structures, that are subjected to appreciable externally induced loading, will fatigue and fail over time. For many structures, imminent failure and loss of structural integrity is not externally apparent. Typical failure occurs at the interfaces between the structure's surface and internal ribs or stiffening members. Conventional approaches for proper validation of full-scale exterior dynamic behavior of numerical models require a significant number of measurement points; unfortunately, interior dynamic response due to time-varying loads is not currently predictable from measured data.

The current research focuses on the global and local interior and exterior member dynamic interactions to understand the possible loss of structural integrity and fatigue failure of complex composite structures. Using some newly developed dynamic stress-strain modeling approaches from limited sets of measured locations, identification of stress-strain distributions will be used as a damage detection tool for structural health monitoring assessment.

25.1 Introduction

Structural systems need to withstand a wide variety of loading conditions during the life of the structure. Often times, periodic inspections are necessary or mandated through codes and standards or local ordinances. Whether or not these are mandatory, structures need to be evaluated over time to assure that the structural integrity of the system is guaranteed. These inspections can become extremely expensive over the life of the structure especially if there are periodic inspections based on calendar rather than based on the condition of the structure. In any event, there are many reasons to identify alternate or more efficient mechanisms for assuring the structural integrity of a system.

The field of structural health monitoring [1, 2] has blossomed for more than a decade and many researchers are studying alternate approaches for the identification of procedures to economically assure the integrity of these systems. There have been many approaches that have been suggested, proposed, evaluated and studied from a variety of researchers with completely different methodologies and approaches. Many approaches have merit in certain applications but most of the techniques have some shortcomings or are not appropriate for specific applications.

In this work, an alternate approach is proposed which is based on the recent work related to the identification of full field dynamic response and dynamic stress-strain prediction from limited sets of real time operating data. This approach has been recently reported in several papers and a brief summary of the development of the technique is discussed here.

In an effort to better understand complicated response from limited sets of data, Chipman [3] used a unique expansion process to provide improved visualization of missile firing systems from operating data. The main focus of that work was to provide a better overall visual description of the complicated response that is not easy to comprehend from a very limited set of measured data. While that work mainly focused on experimentally derived data and expansion functions, Chipman suggested that this could also be used in conjunction with a finite element model to provide full field response.

E. Harvey (✉) • P. Avitabile • C. Niezrecki
Structural Dynamics and Acoustic Systems Laboratory, University of Massachusetts Lowell,
One University Avenue, Lowell, MA 01854, USA
e-mail: Eric_Harvey@student.uml.edu
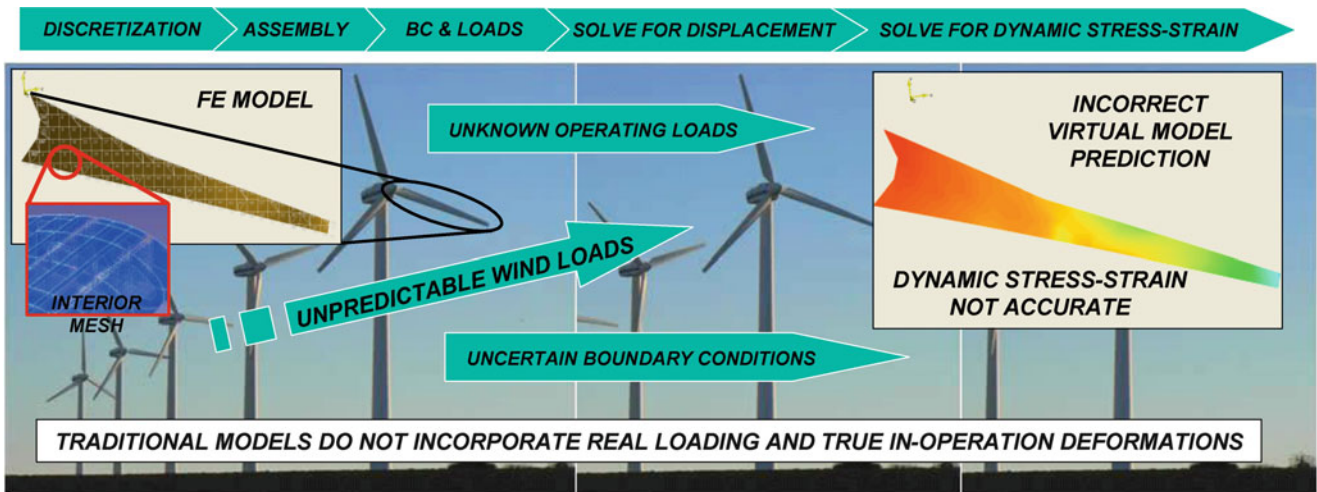
Fig. 25.1 Schematic showing normal finite element model development
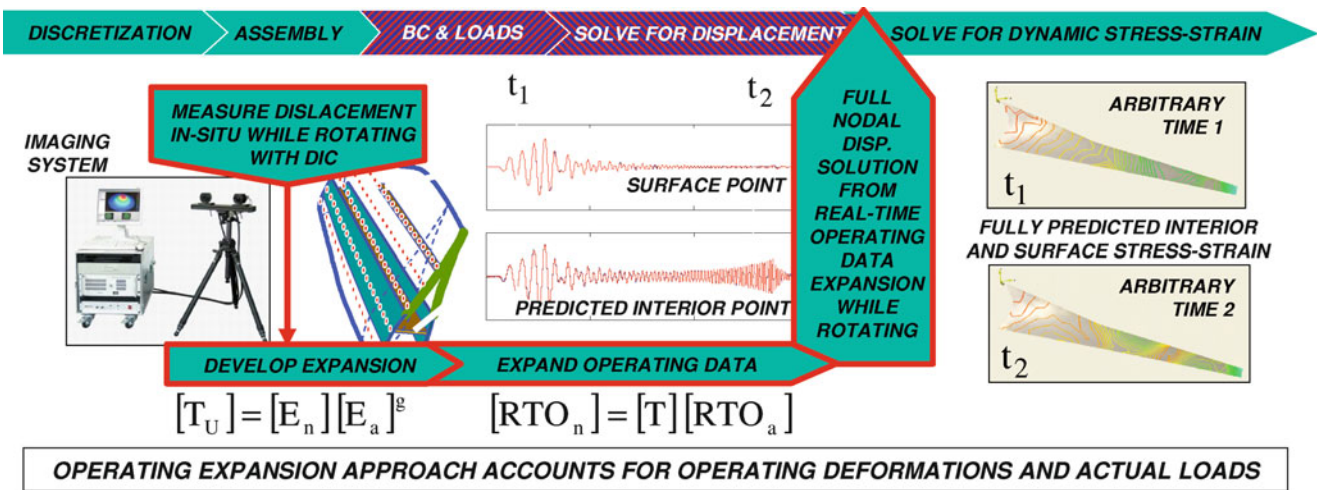
Fig. 25.2 Schematic showing alternate expansion/solution sequence

Following Chipman's work, Pingle [4] extended the expansion procedure to obtain full field displacements at the full set of finite element DOF. The expansion process was shown to provide acceptable results provided that a sufficient set of orthogonal projection vectors were used to formulate the expansion matrices. Pingle also showed that an over-specification of the set of projection vectors (using more modes in the process) did not unnecessarily smear the results or distort the information. Pingle further went on to use these full field displacement results in the back substitution process of the finite element model to obtain dynamic stress-strain due to real time transient data. Many analytical simulations were performed to study various effects that could possibly distort the results due to actual measurements. Pingle also used an academic structure to acquire actual measured transient impact data and was able to use the orthogonal expansion process to obtain full field displacements at all the finite element DOFs and dynamic stress-strain; these results were very favorably compared to measured data.

A simple schematic (Figs. 25.1, 25.2) is used in order to understand the approach. Generally, a finite element model is developed to study structural system characteristics and response. The steps in the development of the model can be stated as the general development of a finite element model, the assembly of the system matrices, the application of loads and boundary conditions followed by the solution of the set of equations and the recovery of the stress-strain solution. This procedure is shown schematically in Fig. 25.1 for a wind turbine blade where significant loadings may occur while the system is in normal operation (e.g. rotating). However, for many situations, the actual loading is not known and the actual boundary conditions are not well understood.

For the approach considered in Pingle's work, the difference is that the actual application of the loads and boundary conditions and the solution of the system set of equations are not specifically performed. Rather, the sparse set of displacements, measured from an actual operating event, are used with a set of orthogonal expansion functions to obtain the full field displacement solution. This displacement solution is then used with the normal recovery of the stress-strain solution in the finite element modeling process. This procedure is shown schematically in Fig. 25.2 where the limited set of measurement degrees of freedom are used with expansion processes to obtain the full field displacement for the system.

With this approach, the finite element modeling solution process is intercepted and replaced with the expansion of the limited set of measured degrees of freedom. In this current work, the expansion functions from the undamaged finite element model are used with limited sets of measured data to provide full field response as well as full field dynamic strain at many instances in time. These actual measured, expanded dynamic strain results are compared to the anticipated, undamaged finite element results to see what differences may exist. Obviously if there is damage to the structure, there will be a redistribution of load which will result in a different displacement pattern. The difference in the displacements will result in a change in the full field dynamic strain distribution that may be obvious to identify.

In order to understand the basic steps necessary to formulate the orthogonal projection matrices, the basic theoretical approach is summarized below and utilizes concepts from model reduction and model expansion as the underlying methodology for the expansion approach used for this work.

25.2 Model Reduction and Expansion Theory

Model reduction is necessary in order to develop expansion approaches for modal data for the unmeasured translational DOF (degree of freedom) as well as for rotational DOF. For this work the expansion is needed for augmenting the limited set of real-time operating data to provide a full field displacement solution. The reduction techniques are the basis of the expansion discussed in this work. These techniques have been presented in earlier work cited in the references; only summarizing equations are presented below. Several model reduction methods have commonly been used for expansion of measured data. Four common methods are Guyan [5], Dynamic Condensation [6], SEREP (System Equivalent Reduction-Expansion Process) [7], and a Hybrid method [8]. In these methods, the relationship between the full set of degrees of freedom and a reduced set of degrees of freedom can be written as

$$\{X_n\} = [T]\{X_a\} \tag{25.1}$$

All of these methods require the formation of a transformation matrix that can project the full mass and stiffness matrices to a smaller size. The reduced matrices can be formulated as

$$[M_a] = [T]^T [M_n][T] \tag{25.2}$$

$$[K_a] = [T]^T [K_n][T] \tag{25.3}$$

For the specific work in this paper, only the SEREP method has been used for the expansion of mode shapes. The System Equivalent Reduction Expansion Process (SEREP) produces reduced matrices for mass and stiffness that yield the exact frequencies and mode shapes as those obtained from the eigensolution of the full size matrix. The SEREP transformation is formed as

$$[T_U] = [U_n]\,[U_a]^g \tag{25.4}$$

The SEREP transformation is developed with analytical mode shapes for the structure (but can also be evaluated using measured modal vectors as done in Chipman's work [3]). Equation 25.1 is used for expansion of real-time operating data and is written as

$$[ERTO_n] = [T]\,[RTO_a] \tag{25.5}$$
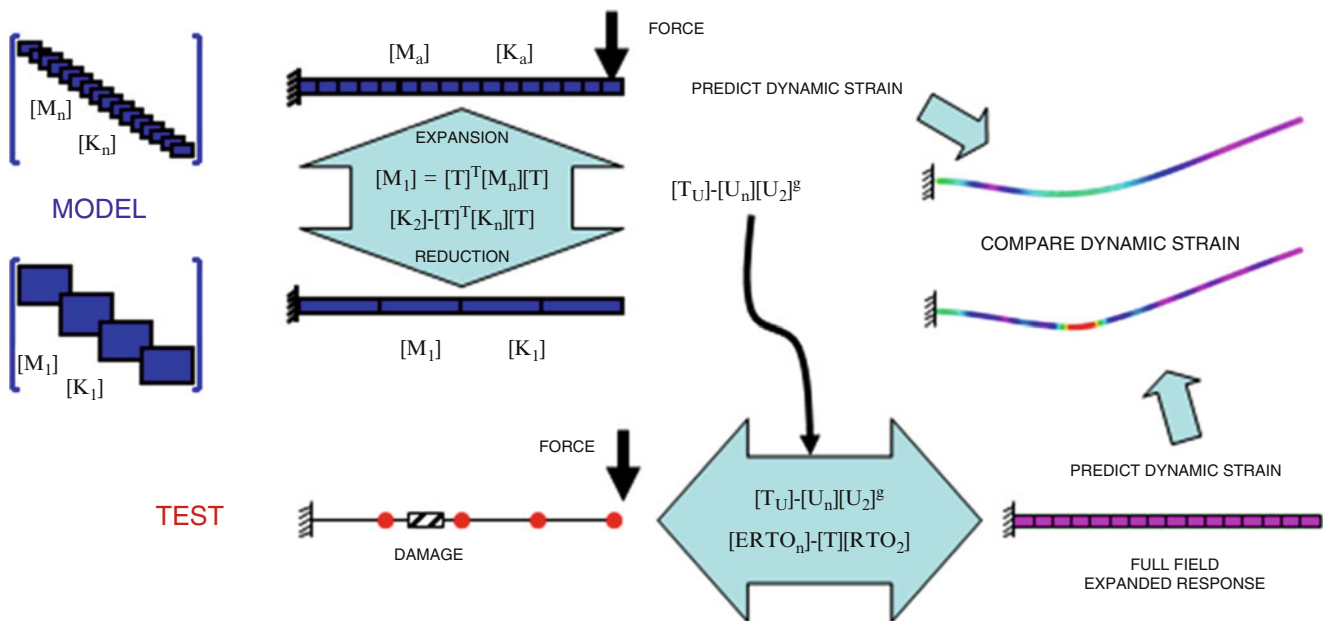
Fig. 25.3 Schematic of procedural overview of process

The transformation matrix, [T], can be one of the matrices used for reduction described above but SEREP is used in all work presented herein.

25.3 Procedure

The procedural mechanics of the process are described in this section as schematically shown in Fig. 25.3.

- The finite element model is developed as is typically done in any design sequence. An eigensolution is performed to obtain the mode shapes to be used as the orthogonal projector matrix.
- Next the selection of the test DOF (ADOF) is identified and the finite element model mapping matrix [Tu] (4) is formulated; note that the reduced mass (2) and stiffness (3) are not necessary for the processing of this procedure but may be useful for other processing.
- Measured data at the test measurement points is obtained (from either operating data or prescribed input).
- The measured data at ADOF is expanded to NDOF using [Tu] (4).
- The same forcing function is applied to the undamaged finite element model.
- The dynamic strain is computed from both the damaged and undamaged models. This strain is compared at several time steps to identify hot spots.

25.4 Finite Element Model Description

A simple beam type model was developed using quadrilateral plate elements. The cantilevered beam was modeled using aluminum and had a cross section of $2'' \times 1''$ and was $72''$ long; only bending response about the weaker axis was considered in this analysis and all loads were applied normal to the surface of the beam. The model consisted of 725 nodes and 576 elements with a total of 2160 degrees of freedom (DOF) and was modeled using FEMAP [9]. An eigensolution was performed to find the lower order modes of the system [10]. The first several modes are shown in Fig. 25.4.

Undamaged	Damaged
6.16 Hz	5.73 Hz
38.58 Hz	35.35 Hz
107.89 Hz	103.15 Hz
211.07 Hz	205.73 Hz
348.17 Hz	321.70 Hz
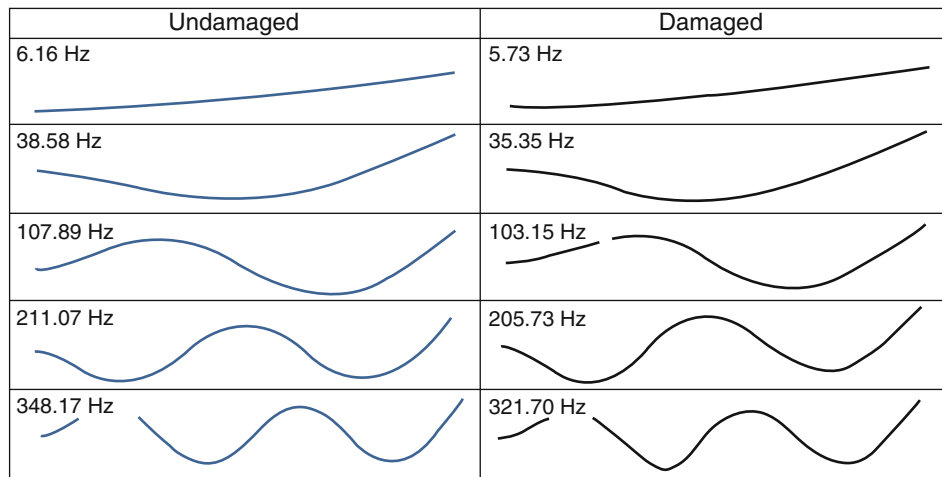
Fig. 25.4 Frequencies and mode shapes of the undamaged (*left*) and damaged (*right*) beam

Table 25.1 Mode shape pairs with frequency difference and MAC

Mode #	Undamaged freq (Hz)	Damaged freq (Hz)	Frequency % difference	N-space MAC
1	6.16	5.73	7.47	99.9
2	38.58	35.35	9.14	99.4
3	107.89	103.15	4.60	99.4
4	211.07	205.73	2.60	96.8
5	348.17	321.70	8.23	96.0
6	518.74	516.56	0.42	99.9
7	722.28	682.54	5.82	96.9
8	958.19	933.45	2.65	97.7

25.5 Damage Model Simulation Description

In order to provide a structure with damaged data for the simulations presented in this paper, the finite element model was modified to include a reduction of stiffness via a thickness change of 50% to 3% of the elements approximately one third of the distance from the clamped end. For reference, another eigensolution was performed to find the lower order modes of the system. The first several modes are shown in Fig. 25.4.

25.6 Comparison of Finite Element Model and Simulated Damaged Model

A correlation was performed for the finite element model and the simulated damaged test data for reference [11]. The frequency correlation along with the MAC for the correlated modes is shown in Table 25.1. In general, the damaged model is not significantly different in frequency from the undamaged model for the lower order modes and the mode shapes show a good deal of similarity; but there is not enough difference in the mode shapes to make any concrete evaluation as to the location of the damage. The mode shape correlation is shown in Fig. 25.5 where the right column contains the comparison of the test to finite element DOF at the limited set of measurement points (ADOF); the left column shows the same information but at the full set of finite element DOF (NDOF).
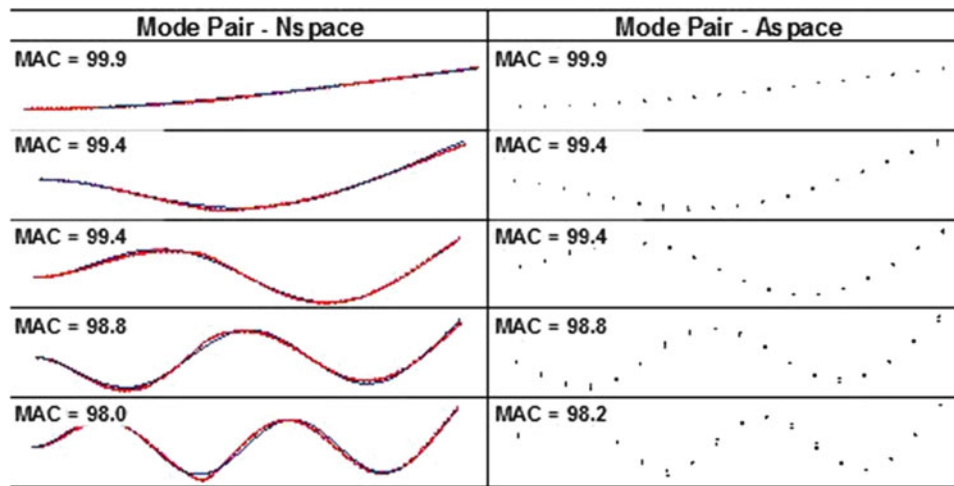
Fig. 25.5 Mode pairs for the damaged and undamaged beam at NDOF and ADOF

25.7 Forced Response of the Structure

In order to provide time response data, the structure was subjected to a force pulse that is comprised of a positive and negative pulse acting over a time span that excited approximately the first ten modes of the beam system. This is important to understand the mode contribution to the structure response to assure that an appropriate set of modes are used for the development of the expansion matrices used for the process. For this particular force pulse, the first ten modes are needed to characterize the response. Because adding more modes will not adversely affect the expansion process, 15 modes were utilized for the expansion process.

It is very important to note that because both the finite element model and the damaged model are available as analytical representations, the simulation of the response can be obtained for both configurations. This is useful for later comparison to the predicted expanded response results.

25.8 Cases Studied

For this preliminary evaluation, only one case was studied. The applied force was used to determine the response from the simulated, damaged model to obtain response at the measured ADOF. These were selected to 18 ADOF that were fairly uniformly distributed along the length of the beam along the center axis. For this preliminary work only bending modes were used in the studies presented here; future work will address more general cases of force and response due to a more general structure with general 3D response characteristics. This force was also applied to the undamaged finite element model to show the response of the system if no damage were to have occurred.

The time response for several points along the damaged beam are shown in Fig. 25.6 to illustrate the time response data that would be measured if an actual damaged structure were subjected to this force. And as a comparison for reference only, the same response points are also shown for the undamaged finite element model in Fig. 25.6.

Now the expansion process can be used to take the limited set of measured ADOF on the damaged structure and obtain an estimate of the response for the entire structure over the full set of all finite element DOF (NDOF). (NOTE: While all DOF could potentially be measured for the entire surface, the important item to note is that the expansion process provides all the finite element DOF which includes translation and rotation and would be able to identify interior DOF if they were available. In this simple structure, there are no interior DOF but this procedure is applicable to any general 3D finite element model that may be generated).

The expanded set of finite element DOF are used as a displacement pattern for the back substitution process in the finite element model to obtain dynamic stress-strain for the entire structure. The resulting strain from the expanded response displacements are viewed for several of the time steps resulting from the transient dynamic solution for the model. In order to properly understand the results, Fig. 25.7 shows three separate columns of data from the selected stages of the time response. The first column shows the anticipated strain that the finite element analyst would obtain from the model developed. The last
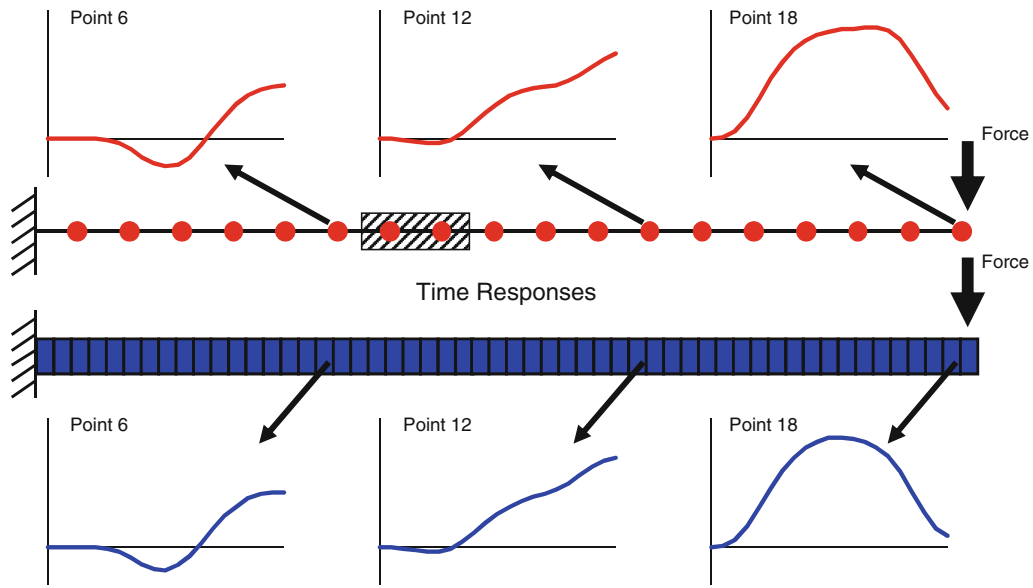
Fig. 25.6 Time response of beam (damaged and undamaged) due to applied force
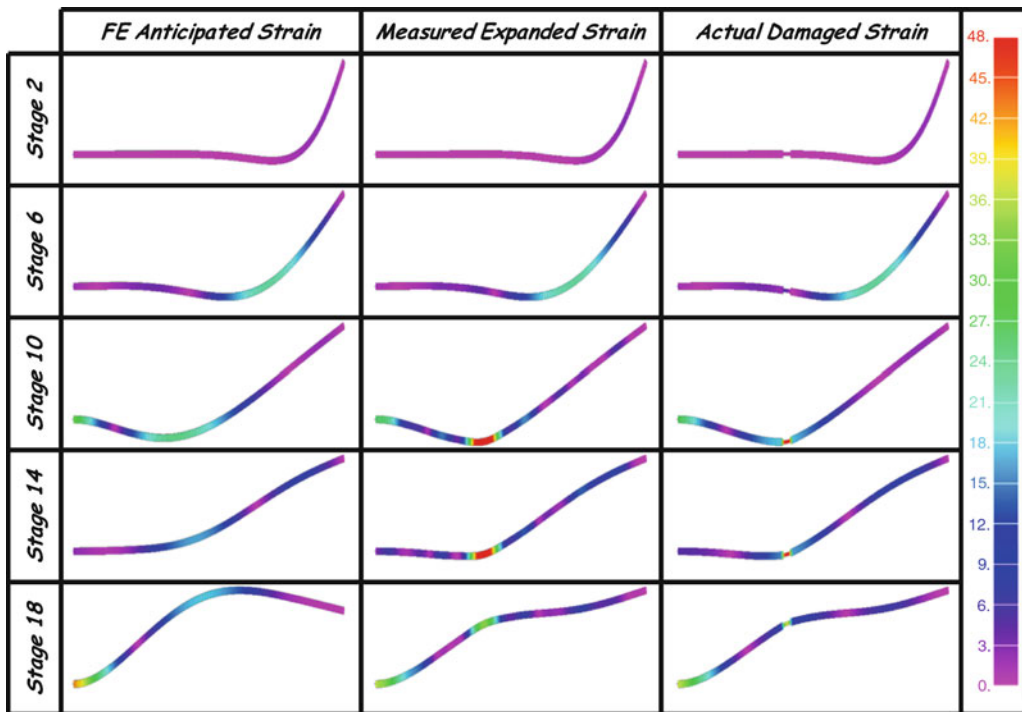
Fig. 25.7 Strain response of beam (damaged and undamaged) due to applied force for the anticipated finite element design model (*left*), for the expanded displacement solution (*middle*) and for the actual damaged beam (*right*) for several time stages analyzed

column shows the actual strain computed from the actual damaged beam to serve as a reference to compare the results of the dynamic expansion process. The middle column contains the dynamic strain resulting from the expansion of the limited set of measured displacements from the damaged beam using the dynamic expansion process.

In viewing these results, stage 10 and 14 in column 2 appear to have a high strain at the mid span of the beam that is higher than expected from the anticipated strain from the finite element design model. Note that the strain in this region is exactly where the damage occurs as seen in column 3. This is not seen at all in the finite element design model results in column 1.
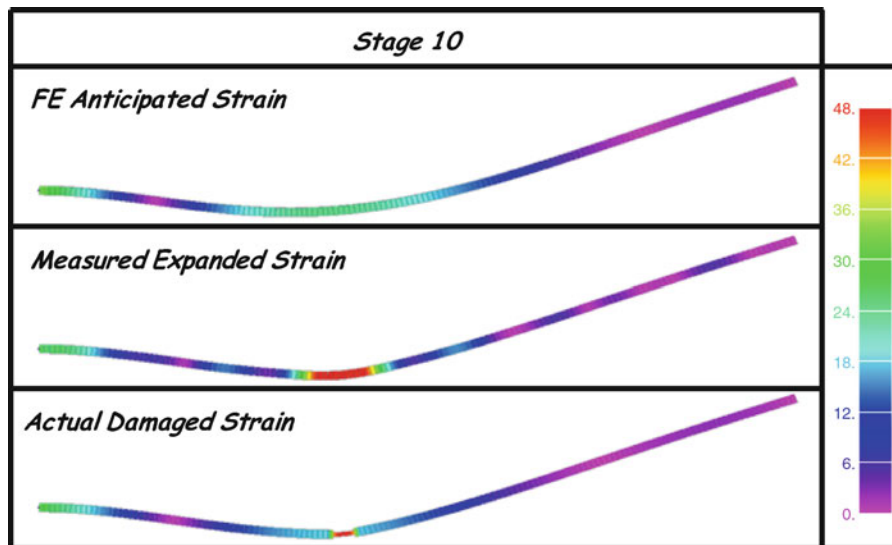
Fig. 25.8 Strain response of beam (damaged and undamaged) due to applied force for the anticipated finite element design model (*upper*), for the expanded displacement solution (*middle*) and for the actual damaged beam (*lower*) for stage 10

To further show this, stage 10 is presented separately in Fig. 25.8; this clearly shows that there is a significant change in the overall load distribution resulting in a different strain that clearly highlights the region where the actual damage was applied to the structure. These results are extremely encouraging and will be studied in more depth in future efforts related to this work.

The important characteristic that enables the clear depiction of the strain damaged area is due to the fact that transient response is used to interrogate the structure rather than mode shapes. The mode shapes may not be as revealing especially if the damage is in an area of little curvature. However, using transient response, which is comprised of the linear combination of all the modes that participate, there is a higher possibility to see the strain changes at various points in time due to the response of the structure. At this time there are no clear guidelines as to how many time steps may be needed or types of excitation that will be sufficient to excite the structure in such a manner as to efficiently capture the necessary response to clearly see the damage regions. However, these initial results are very promising and additional work is needed to address many of these issues.

25.9 Conclusion

Recent efforts on the identification of full field dynamic stress-strain using limited sets of measured data have produced very good results for the prediction of both dynamic displacements and dynamic stress-strain. Extensions of this work have been presented here in this paper to identify full field dynamic stress-strain from damaged structures using this approach. These predictions are compared to the anticipated results from the design finite element model. Differences in the strain patterns show possible locations where damage may exist. The test cases studied clearly showed the damage area. The main advantage of this technique over other modal based and contour based approaches is that the transient response used in the prediction has the effect of using multiple modes simultaneously and therefore appears to have better detection capability. While only limited cases have been studied, these results are very promising and will be the subject of future work.

References

1. Farrar CR, Sohn H, Hemez FM, Anderson MC, Bement MT, Cornwell PJ, Doebling SW, Schultze JF, Lieven N, Robertson AN (2004) Damage prognosis: current status and future Needs. Los Alamos National Laboratory report, LA-14051-MS, Los Alamos
2. Sohn H, Farrar CR, Hemez FM, Shunk DD, Stinemates SW, Nadler BR, Czarnecki JJ (2004) A review of structural health monitoring literature form 1996–2001. Los Alamos National Laboratory report LA-13976-MS, Los Alamos
3. Chipman C (2009) Expansion of real time operating data. Master's thesis, University of Massachusetts Lowell
4. Pingle P (2010) Prediction of full-field dynamic stress-strain from limited sets of measured displacement data. Doctoral thesis, University of Massachusetts Lowell
5. Guyan RJ (1965) Reduction of stiffness and mass matrices. AIAA J 3(2):380
6. Paz M (1984) Dynamic condensation. AIAA J 22(5):724–727
7. O'Callahan JC, Avitabile P, Riemer R (1989) System equivalent reduction expansion process. In: Seventh international modal analysis conference, Las Vegas
8. Kammer DC (1991) A hybrid approach to test analysis model development for large space structures. J Vib Acoust 113:325–332
9. FEMAP – finite element modeling and postprocessing, Version 10.0.2, Siemens Product Lifecycle Management Software Inc
10. NX Nastran 6, Siemens Product Lifecycle Management Software Inc
11. FEMtools 3 – Dynamic Design Solutions, Leuven, Belgium

Chapter 26
On the Mode Based Simulation of Dry Friction inside Lap Joints

Markus Breitfuss, Wolfgang Witteveen, and Gerhard Prechtl

Abstract   Recently proposed joint interface modes (JIM), which have been presented at the IMAC 25th, consider Newton's third law across a joint already at the stage of mode generation. This approach leads to significant improvements in the subsequent mode based simulation, where nonlinear contact and frictional forces are applied. This contribution is focusing on the efficient computation of forces according to dry friction. The first part covers the friction model itself. A lot of literature points out that the discontinuity of the well known Coulomb friction is a major drawback in terms of efficient time integration. Therefore alternative friction models are investigated and a comparison with the Coulomb model is performed. The second part deals with the relevance of trial functions in tangential direction of the contact surface. The latter mentioned JIM can be subdivided into Ritz vectors, which are required to approximate the joint deformation in joint normal direction where the contact forces are acting, and such, which are required to approximate the joint deformation in joint tangential direction where the friction forces are acting. Theoretical considerations and a numerical example are presented which reveal, that the number of JIM in tangential direction is significantly smaller as the one in contact direction without losing remarkable quality of the result.

Nomenclature

$\tilde{\mathbf{M}}$	Mass matrix of FE model
$\tilde{\mathbf{M}}_{\text{red}}$	Mass matrix of reduced model
$\tilde{\mathbf{D}}$	Damping matrix of FE model
$\tilde{\mathbf{D}}_{\text{red}}$	Damping matrix of reduced model
$\tilde{\mathbf{K}}$	Stiffness matrix of FE model
$\tilde{\mathbf{K}}_{\text{red}}$	Stiffness matrix of reduced model
$\tilde{\mathbf{T}}$	Transformation matrix
$\tilde{\mathbf{\Phi}}$	Mode matrix
$\vec{\mathbf{f}}_{\text{ext}}$	Vector of external nodal forces of FE model
$\vec{\mathbf{f}}_{\text{fric}}$	Vector of frictional nodal forces of FE model
$\vec{\mathbf{f}}_{\text{red}}$	Vector of projected nodal forces
$\vec{\mathbf{x}}$	Vector of nodal DOF of FE model
$\vec{\mathbf{x}}_{\text{B}}$	Boundary nodal DOF
$\vec{\mathbf{x}}_{\text{I}}$	Internal nodal DOF
$\vec{\mathbf{x}}_{\text{IJ}}$	Contact area nodal DOF
$\dot{\vec{\mathbf{x}}}$	First derivative of $\vec{\mathbf{x}}$ with respect to time

M. Breitfuss (✉)
Johannes Kepler University Linz, Altenbergerstraße 69, Linz 4040, Austria
e-mail: markus.breitfuss@jku.at

W. Witteveen • G. Prechtl
University of Applied Sciences Upper Austria, Stelzhamerstraße 23, Wels 4600, Austria
e-mail: wolfgang.witteveen@fh-wels.at; gerhard.prechtl@students.fh-wels.at

$\ddot{\vec{x}}$	Second derivative of $\vec{x}$ with respect to time
$\vec{q}$	Generalized coordinates of reduced model
$\dot{\vec{q}}$	First derivative of $\vec{q}$ with respect to time
$\ddot{\vec{q}}$	Second derivative of $\vec{q}$ with respect to time
n	Number of degrees of freedom of FE model
n_q	Number of generalized coordinates

26.1   Introduction

Nowadays simulation has become an integral part of modern product development processes. Belonging to one of the more challenging disciplines, the evaluation of a mechanical systems dynamic behavior requires complex models and reliable results are determined by several factors, realistic consideration of dissipation within lap joints being one of them.

The finite element (FE) method is a widely used technique for the numerical analysis of mechanical structures. It is capable to deliver very accurate results but lacks computational efficiency due to the high number of physical or nodal degrees of freedom (DOF) to be considered during a simulation. To overcome this drawback, model order reduction methods have been developed during the last decades, see [1] for a comprehensive overview. These methods reduce the number of DOF significantly by introducing Ritz trial functions, often referred to as mode base, and projecting the physical coordinates onto generalized coordinates.

As this approach usually involves the linearization of the mechanical system at a certain point of operation, these methods are not well suited for reducing systems involving nonlinearities as it is the case for built up structures containing contact regions within the joint areas. An extension to classic mode bases for handling such areas properly, even in reduced systems, was proposed at the IMAC 25th [2], 26th [3] and 27th [4]. By using additional trial functions within the reduction process, contact forces inside lap joints can be computed quite accurately during the simulation.

A short review on the idea behind and a possible method for the computation of these trial functions is given in the following section. The next section shortly recapitulates the influence of friction on the system behaviour within lap joints and summarizes some potentially interesting numerical models for friction found in literature. After this the necessity of additional trial functions in tangential direction of the contact surface is discussed. A numerical example and a conclusion complete this contribution.

26.2   Quick Review on Joint Interface Modes

As mentioned in the introduction, contact phenomena within joints represent local nonlinearities. Common modal reduction methods, like the well known component mode synthesis (CMS) according to [1], use a clever mixture of local and global mode shapes as approximation for the flexible structure deformation. These so called constraint modes (CM) for particular nodal FE DOF and boundary fixed normal modes (BFNM) for the remaining internal nodal FE DOF do not explicitly consider the local deformation within the joint area.

Theoretically it is possible to define CM for all nodal FE DOF located on contact surfaces. But this would not be a very efficient approach in case of automatically meshed structures containing large interface areas. The idea of the proposed joint interface modes (JIM) is exemplarily demonstrated on the generic structure outlined in Fig. 26.1. The FE Model consists of two substructures which are connected via a beam. The contact surfaces are outlined by black dots and the whole structure is supported on both sides. If all available nodal FE DOF would be retained via constrained modes, a joint deformation like the one in Fig. 26.2 could be represented by the resulting mode base.

To consider the nonlinear contact behavior in an adequate manner for industrial applications, the possible surface deformation, as pointed out in Fig. 26.2, is not relevant. Moreover the deformation shapes are likely to be much smoother. Therefore, the consideration of all nodal FE DOF preserves more information than needed to compute results with acceptable accuracy. The main idea is to provide an efficient extension to a classic mode base (e.g. computed according to Craig and Bampton, see [1] for more details) by particular modes, which are outlined in Fig. 26.3. Beside the deformation shapes of classical mode bases these additional trial vectors represent the local joint deformation of the joint contact surfaces for small relative movement of the involved contact surfaces.

In order to achieve a quickly converging set of modes, a fundamental mechanical characteristic is utilized during the process of mode generation: the local continuity of forces acting on the two contact surfaces of the joint is explicitly accounted for. This leads to a convergence of the solution which is almost twice as fast as the interface mode method. In order to provide

Fig. 26.1 Generic FE model
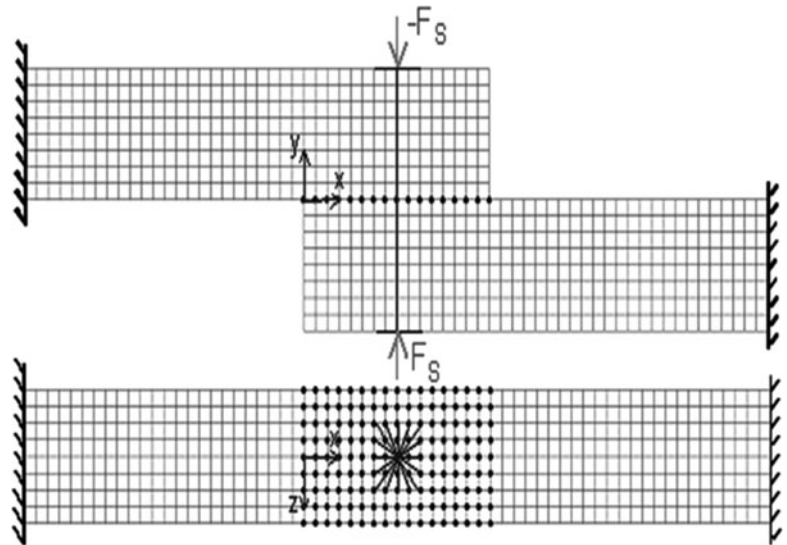
Fig. 26.2 Hypothetical
deformation of the joint area
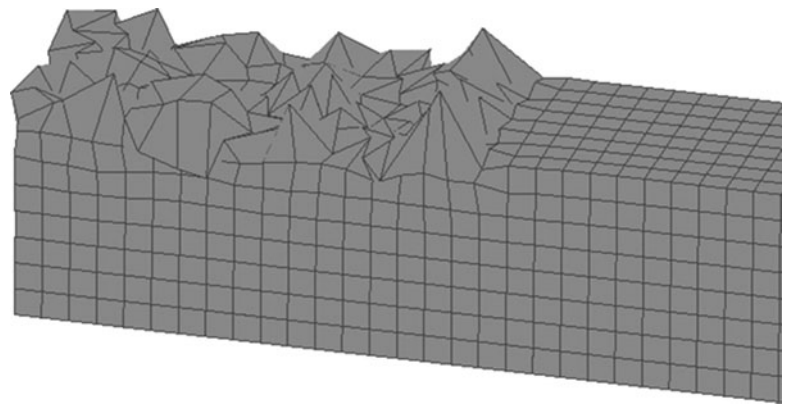
Fig. 26.3 Sample of contact
modes
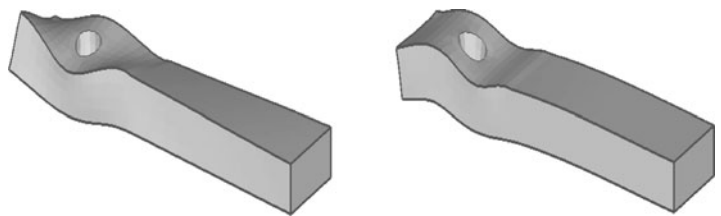
this extension in a very easy and convenient way, the software package called MAMBA [5] has been developed. One possible method for the computation of the proposed JIM is shortly outlined within this section, for more details refer to [2–4].

An example for a jointed FE structure is shown in Fig. 26.4. The letter B denotes nodal FE DOF loaded by external, concentrated forces. Nodal FE DOF of the joint contact surfaces are denoted by IJ1 and IJ2 respectively, depending on the surface number. The remaining nodes are denoted by NJ. Compatible meshes are assumed for the whole contact surface region. It should be noted that the theory of joint interface modes can be extended to the case of non matching meshes within the contact surface area as well. The software package MAMBA already provides this extension.

The equations of motion for a linear FE structure with n degrees of freedom can be given in the form

$$\tilde{\mathbf{M}}\,\ddot{\vec{x}} + \tilde{\mathbf{D}}\,\dot{\vec{x}} + \tilde{\mathbf{K}}\,\vec{x} = \vec{f}_{\text{ext}}. \tag{26.1}$$

Fig. 26.4 Exemplary jointed
FEM structure
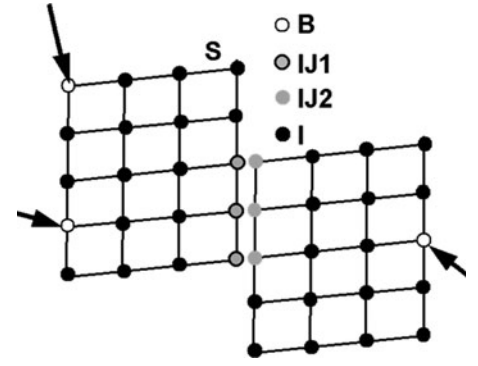
The vector of nodal DOFs

$$\vec{\mathbf{x}} = \left\{ \begin{array}{c} \vec{\mathbf{x}}_B \\ \vec{\mathbf{x}}_I \end{array} \right\} = \left\{ \begin{array}{c} \vec{\mathbf{x}}_B \\ \vec{\mathbf{x}}_{IJ} \\ \vec{\mathbf{x}}_{I\setminus IJ} \end{array} \right\} = \left[\begin{array}{cccc} \vec{\mathbf{x}}_B{}^T & \vec{\mathbf{x}}_{IJ1}{}^T & \vec{\mathbf{x}}_{IJ2}{}^T & \vec{\mathbf{x}}_{I\setminus IJ}{}^T \end{array} \right]^T \tag{26.2}$$

is assumed to be partitioned into a boundary part, which is loaded by concentrated forces and an internal part containing the remaining nodes. Considering only the static part of (26.1) leads to

$$\begin{bmatrix} \tilde{\mathbf{K}}_{B,B} & \tilde{\mathbf{K}}_{B,IJ1} & \tilde{\mathbf{K}}_{B,IJ2} & \tilde{\mathbf{K}}_{B,I\setminus IJ} \\ \tilde{\mathbf{K}}_{IJ1,B} & \tilde{\mathbf{K}}_{IJ1,IJ1} & \tilde{\mathbf{K}}_{IJ1,IJ2} & \tilde{\mathbf{K}}_{IJ1,I\setminus IJ} \\ \tilde{\mathbf{K}}_{IJ2,B} & \tilde{\mathbf{K}}_{IJ2,IJ1} & \tilde{\mathbf{K}}_{IJ2,IJ2} & \tilde{\mathbf{K}}_{IJ2,I\setminus IJ} \\ \tilde{\mathbf{K}}_{I\setminus IJ,B} & \tilde{\mathbf{K}}_{I\setminus IJ,IJ1} & \tilde{\mathbf{K}}_{I\setminus IJ,IJ2} & \tilde{\mathbf{K}}_{I\setminus IJ,I\setminus IJ} \end{bmatrix} \left\{ \begin{array}{c} \vec{\mathbf{0}} \\ \vec{\mathbf{x}}_{IJ1} \\ \vec{\mathbf{x}}_{IJ2} \\ \vec{\mathbf{x}}_{I\setminus IJ} \end{array} \right\} = \left\{ \begin{array}{c} \vec{\mathbf{f}}_B \\ \vec{\mathbf{f}}_{IJ1} \\ \vec{\mathbf{f}}_{IJ2} \\ \vec{\mathbf{0}} \end{array} \right\}. \tag{26.3}$$

Due to the explicit consideration of Newton's third law and the substitution of $\vec{\mathbf{x}}_{I\setminus IJ}$ by an identity obtained from the fourth row of (26.3) one obtains a relationship between the nodal degrees of freedom of both contact surfaces

$$\vec{\mathbf{x}}_{IJ1} = \underline{\tilde{\mathbf{G}}}\vec{\mathbf{x}}_{IJ2} \tag{26.4}$$

where $\quad \underline{\tilde{\mathbf{G}}} = \left[\tilde{\mathbf{K}}_{IJ1,IJ1} + \tilde{\mathbf{K}}_{IJ2,IJ1} - \left[\tilde{\mathbf{K}}_{IJ1,I\setminus IJ} + \tilde{\mathbf{K}}_{IJ2,I\setminus IJ} \right] \tilde{\mathbf{K}}^{-1}{}_{I\setminus IJ,I\setminus IJ} \tilde{\mathbf{K}}_{I\setminus IJ,IJ1} \right]^{-1} \left[\left[\tilde{\mathbf{K}}_{IJ1,I\setminus IJ} + \tilde{\mathbf{K}}_{IJ2,I\setminus IJ} \right] \tilde{\mathbf{K}}^{-1}{}_{I\setminus IJ,I\setminus IJ} \tilde{\mathbf{K}}_{I\setminus IJ,IJ2} - \tilde{\mathbf{K}}_{IJ1,IJ2} - \tilde{\mathbf{K}}_{IJ2,IJ2} \right]$. Using this relationship the static reduction rule

$$\left[\begin{array}{cccc} \vec{\mathbf{x}}_B{}^T & \vec{\mathbf{x}}_{IJ1}{}^T & \vec{\mathbf{x}}_{IJ2}{}^T & \vec{\mathbf{x}}_{I\setminus IJ}{}^T \end{array} \right]^T = \underline{\tilde{\mathbf{H}}}\vec{\mathbf{x}}_{IJ2} \tag{26.5}$$

is fully defined. Applying this reduction rule to the equations of motion (26.1) and neglecting the damping matrix $\tilde{\mathbf{D}}$ and the force vector $\vec{\mathbf{f}}_{ext}$ as well leads to the intermediate result

$$\underline{\tilde{\mathbf{M}}}_{red,IJ2}\ddot{\vec{\mathbf{x}}}_{IJ2} + \underline{\tilde{\mathbf{K}}}_{red,IJ2}\vec{\mathbf{x}}_{IJ2} = \tilde{\mathbf{0}} \tag{26.6}$$

where $\underline{\tilde{\mathbf{M}}}_{red,IJ2} = \underline{\tilde{\mathbf{H}}}^T \tilde{\mathbf{M}}\underline{\tilde{\mathbf{H}}}$ holds the reduced mass matrix and $\underline{\tilde{\mathbf{K}}}_{red,IJ2} = \underline{\tilde{\mathbf{H}}}^T \tilde{\mathbf{K}}\underline{\tilde{\mathbf{H}}}$ holds the reduced stiffness matrix. Solving a generalized eigenvalue problem with these matrices finally leads to the proposed JIM. The transformation matrix

$$\tilde{\mathbf{T}} = \left[\begin{array}{cc} \tilde{\mathbf{\Phi}}_{classic} & \tilde{\mathbf{\Phi}}_{JIM} \end{array} \right] \tag{26.7}$$

contains the classic mode base $\tilde{\mathbf{\Phi}}_{classic}$ and the proposed additional trial functions $\tilde{\mathbf{\Phi}}_{JIM}$ respectively and is used during the final model order reduction process using the approximation

$$\vec{\mathbf{x}} \approx \tilde{\mathbf{T}}\vec{\mathbf{q}} \tag{26.8}$$

which introduces the vector $\vec{q}$ containing $n_q = n_{classic} + n_{JIM}$ generalized coordinates. Finally the equations of motion for the reduced system can be written as

$$\tilde{\mathbf{M}}_{red}\ddot{\vec{q}} + \tilde{\mathbf{D}}_{red}\dot{\vec{q}} + \tilde{\mathbf{K}}_{red}\vec{q} = \vec{f}_{red}. \tag{26.9}$$

referencing

$$\tilde{\mathbf{M}}_{red} = \tilde{\mathbf{T}}^{T}\tilde{\mathbf{M}}\tilde{\mathbf{T}}, \tilde{\mathbf{D}}_{red} = \tilde{\mathbf{T}}^{T}\tilde{\mathbf{D}}\tilde{\mathbf{T}}, \tilde{\mathbf{K}}_{red} = \tilde{\mathbf{T}}^{T}\tilde{\mathbf{K}}\tilde{\mathbf{T}} \text{ and } \vec{f}_{red} = \tilde{\mathbf{T}}^{T}\vec{f}_{ext} \tag{26.10}$$

26.3   Numerical Models for Dry Friction

The quality and therefore reliability of result data obtained from the dynamic analyses of mechanical systems highly depends on the stiffness distribution, the mass distribution and the dissipative behavior of the model under investigation. In contrast to the stiffness and mass distributions, which are typically known quite well from geometry and material data of the system, the determination of damping values is usually quite inaccurate due to the load dependent and nonlinear characteristic of the governing effects.

One major source of dissipation within metallic structures is the friction inside jointed areas, which can be one order of magnitude higher than material damping. Detailed investigations of a simple structure containing a bolted joint are reported in [6] and [7]. Usually a characteristic hysteresis similar to the idealized one shown in Fig. 26.5 is used to describe the dissipative behavior of a joint. It is interesting to note that, according to [8], for excitation frequencies up to 1 kHz the hysteresis loop remains almost unchanged in shape and size.

Several states can be distinguished. Between 1 and 2 (4 and 5) the contact surfaces stick together. The slope is determined by a surface roughness dependent sticking stiffness. As a result the frictional forces can be considered as imposed forces without need to activate constraints to resemble sticking. Between 3 and 4 (6 and 1) the contact surfaces slide relative to each other. The slope is determined by a material and contact pressure dependent sliding stiffness. The transition from sticking to sliding takes place between 2 and 3 (5 and 6).

As friction is a highly nonlinear phenomenon, the according forces are typically applied as a state dependent force vector $\vec{f}_{fric}$ at the right hand side of the governing (26.1) of the unreduced system

$$\tilde{\mathbf{M}}\ddot{\vec{x}} + \tilde{\mathbf{D}}\dot{\vec{x}} + \tilde{\mathbf{K}}\vec{x} = \vec{f}_{ext} + \vec{f}_{fric}. \tag{26.11}$$

The damping matrix $\tilde{\mathbf{D}}$, if needed at all in this case, is often used to consider only the material damping. In terms of reduced order models $\tilde{\mathbf{M}}_{red}\ddot{\vec{q}} + \tilde{\mathbf{D}}_{red}\dot{\vec{q}} + \tilde{\mathbf{K}}_{red}\vec{q} = \vec{f}_{red}$, the so called modal damping approach is a common way to model dissipation. In contrast to a general reduced damping matrix according to (26.10), which may become a fully populated matrix, this approach uses a generic diagonal matrix

$$\tilde{\mathbf{D}}_{red} = \text{diag}(\delta_1, \delta_2, \cdots, \delta_n) \tag{26.12}$$
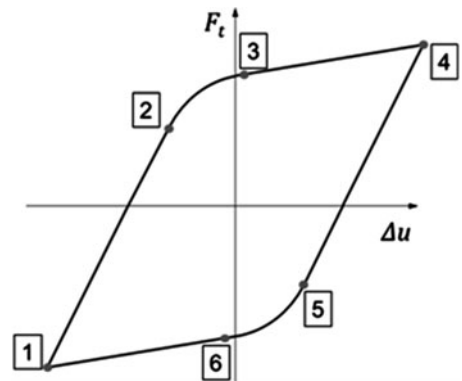
Fig. 26.5 Characteristic hysteresis of a bolted joint
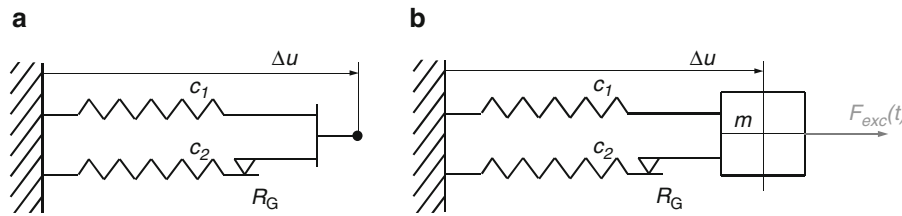
Fig. 26.6 Coulomb friction reference model: (**a**) enforced motion, (**b**) single DOF model
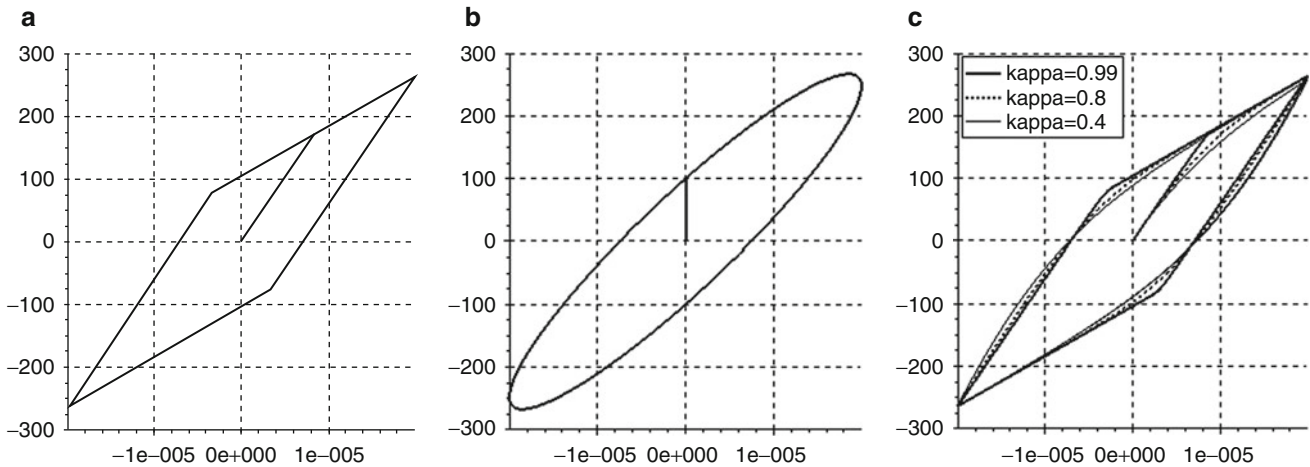
Fig. 26.7 Exemplary hysteresis loops (the x-coordinate represents the displacement in meter and the y-coordinate the tangential force in newton): (**a**) reference model, (**b**) Kelvin-Voigt element, (**c**) Valanis model

referencing n_q modal damping values δ_i. This fact is responsible for the very good performance in terms of computational efficiency as the equations of the reduced system remain uncoupled.

Though the concept of modal damping hardly fits for dissipative effects due to friction, making it very troublesome to estimate good damping values for a complex structure, it is common practice to utilize this approach for industrial applications and accept the possible negative impact on result quality. As the above mentioned method of using additional trial functions to account for the local deformation within the joint area facilitates a realistic computation of contact pressure distributions, the resulting surface normal stresses can be utilized for an up following computation of forces due to friction. This in turn enables a realistic consideration of such effects, even for reduced order models.

To compute frictional forces an efficient and robust mathematical model is needed. Beside the well known Coulomb friction many numerical models can be found in literature, each of them valuable for a certain reason. A good starting point for investigations is given by [9] and [10]. To select promising ones among these models, some criterions for evaluation need to be defined. Within this contribution the shape of the characteristic hysteresis loop and the efficiency in terms of computational effort are used as criteria.

The evaluation is carried out using two steps. In the first step the shape of the hysteresis loop of each model is evaluated using an enforced displacement setup. If the shape of the hysteresis loop is satisfactory, the computational effort during a dynamic simulation is evaluated. In Fig. 26.6 both setups are exemplarily depicted for the Coulomb friction reference model. This evaluation is without loss of generality as the enforced displacement setup can also represent the connection between two mating nodes of a complex contact area.

Beside the Coulomb friction two approaches for numerical friction models can be found in literature. One approach is to utilize springs and damper elements, as it is the case within the Maxwell element or the Kelvin-Voigt element. The other class of models relies on functional equations, like the Bouce-Wen model (refer to [7]), the Lu-Gre model (refer to [9]) or the Valanis model (refer to [6] or [7]). Some examples of the resulting hysteresis loops are shown in Fig. 26.7.

The evaluation reveals that models based on properly connected spring and damper elements are very easy to implement but deliver an unsatisfying approximation of the hysteresis loop. Furthermore, the size of the hysteresis loop depends on the

frequency. In contrast the models based on functional equations approximate the hysteresis loop very well. The drawback of these models is the necessity to solve an additional differential equation, which leads to additional computational effort. Consequently, the implementations of the Coulomb friction and the Valanis model used in this evaluation perform quite similar in terms of computational effort.

26.4   Additional Trial Functions in Tangential Direction

Depending on the system state the joint contact surfaces get divided into areas without relative movement and areas with significant relative movement. For all cases where the boundaries of these areas are approximated in a sufficient way by the trial functions within the transformation matrix $\tilde{\mathbf{T}} = \begin{bmatrix} \tilde{\boldsymbol{\Phi}}_{\text{classic}} & \tilde{\boldsymbol{\Phi}}_{\text{JIM}} \end{bmatrix}$ utilized during the model order reduction process, no additional trial functions in tangential direction are needed at all. As size and boundaries of these areas might change during a simulation, two cases can be distinguished:

- If the regions without relative movement were considered at the wrong location or estimated too large during the reduction process, the damping within the reduced system typically gets underestimated compared to the unreduced system as the trial functions represent less relative movement within the joint area.
- If the regions without relative movement were considered to small during the reduction process, the damping within the reduced systems typically gets overestimated compared to the unreduced system as the trial functions represent more relative movement within the joint area.

The authors propose to differ between $\tilde{\boldsymbol{\Phi}}_{\text{JIM,n}}$ holding $n_{\text{JIM,n}}$ trial functions in surface normal direction and $\tilde{\boldsymbol{\Phi}}_{\text{JIM,t}}$ referencing $n_{\text{JIM,t}}$ trial functions in surface tangential direction. This allows for separate computation of both types of additional trial functions using the above mentioned algorithm in a slightly extended way. Using a further partitioned vector of nodal DOF

$$\vec{\mathbf{x}} = \left\{ \begin{matrix} \vec{\mathbf{x}}_{\text{B}} \\ \vec{\mathbf{x}}_{\text{I}} \end{matrix} \right\} = \left\{ \begin{matrix} \vec{\mathbf{x}}_{\text{B}} \\ \vec{\mathbf{x}}_{\text{IJ}} \\ \vec{\mathbf{x}}_{\text{I}\backslash\text{IJ}} \end{matrix} \right\} = \begin{bmatrix} \vec{\mathbf{x}}_{\text{B}}{}^{\text{T}} & \vec{\mathbf{x}}_{\text{IJ1}}{}^{\text{T}} & \vec{\mathbf{x}}_{\text{IJ2}}{}^{\text{T}} & \vec{\mathbf{x}}_{\text{I}\backslash\text{IJ}}{}^{\text{T}} \end{bmatrix}^{\text{T}} = \begin{bmatrix} \vec{\mathbf{x}}_{\text{B}}{}^{\text{T}} & \vec{\mathbf{x}}_{\text{IJ1,n}}{}^{\text{T}} & \vec{\mathbf{x}}_{\text{IJ1,t}}{}^{\text{T}} & \vec{\mathbf{x}}_{\text{IJ2,n}}{}^{\text{T}} & \vec{\mathbf{x}}_{\text{IJ2,t}}{}^{\text{T}} & \vec{\mathbf{x}}_{\text{I}\backslash\text{IJ}}{}^{\text{T}} \end{bmatrix}^{\text{T}} \quad (26.13)$$

the contact area nodal DOF $\vec{\mathbf{x}}_{\text{IJ1}}$ and $\vec{\mathbf{x}}_{\text{IJ2}}$ are subdivided into normal and tangential direction. This can be done without loosing generality as for arbitrary oriented contact surfaces only an additional transformation into proper aligned local coordinate systems has to be considered. Considering only the static part of (26.1) leads to

$$\begin{bmatrix} \tilde{\mathbf{K}}_{\text{B,B}} & \tilde{\mathbf{K}}_{\text{B,IJ1n}} & \tilde{\mathbf{K}}_{\text{B,IJ1t}} & \tilde{\mathbf{K}}_{\text{B,IJ2n}} & \tilde{\mathbf{K}}_{\text{B,IJ2t}} & \tilde{\mathbf{K}}_{\text{B,I}\backslash\text{IJ}} \\ \tilde{\mathbf{K}}_{\text{IJ1n,B}} & \tilde{\mathbf{K}}_{\text{IJ1n,IJ1n}} & \tilde{\mathbf{K}}_{\text{IJ1n,IJ1t}} & \tilde{\mathbf{K}}_{\text{IJ1n,IJ2n}} & \tilde{\mathbf{K}}_{\text{IJ1n,IJ2t}} & \tilde{\mathbf{K}}_{\text{IJ1n,I}\backslash\text{IJ}} \\ \tilde{\mathbf{K}}_{\text{IJ1t,B}} & \tilde{\mathbf{K}}_{\text{IJ1t,IJ1n}} & \tilde{\mathbf{K}}_{\text{IJ1t,IJ1t}} & \tilde{\mathbf{K}}_{\text{IJ1t,IJ2n}} & \tilde{\mathbf{K}}_{\text{IJ1t,IJ2t}} & \tilde{\mathbf{K}}_{\text{IJ1t,I}\backslash\text{IJ}} \\ \tilde{\mathbf{K}}_{\text{IJ2n,B}} & \tilde{\mathbf{K}}_{\text{IJ2n,IJ1n}} & \tilde{\mathbf{K}}_{\text{IJ2n,IJ1t}} & \tilde{\mathbf{K}}_{\text{IJ2n,IJ2n}} & \tilde{\mathbf{K}}_{\text{IJ2n,IJ2t}} & \tilde{\mathbf{K}}_{\text{IJ2n,I}\backslash\text{IJ}} \\ \tilde{\mathbf{K}}_{\text{IJ2t,B}} & \tilde{\mathbf{K}}_{\text{IJ2t,IJ1n}} & \tilde{\mathbf{K}}_{\text{IJ2t,IJ1t}} & \tilde{\mathbf{K}}_{\text{IJ2t,IJ2n}} & \tilde{\mathbf{K}}_{\text{IJ2t,IJ2t}} & \tilde{\mathbf{K}}_{\text{IJ2t,I}\backslash\text{IJ}} \\ \tilde{\mathbf{K}}_{\text{I}\backslash\text{IJ,B}} & \tilde{\mathbf{K}}_{\text{I}\backslash\text{IJ,IJ1n}} & \tilde{\mathbf{K}}_{\text{I}\backslash\text{IJ,IJ1t}} & \tilde{\mathbf{K}}_{\text{I}\backslash\text{IJ,IJ2n}} & \tilde{\mathbf{K}}_{\text{I}\backslash\text{IJ,IJ2t}} & \tilde{\mathbf{K}}_{\text{I}\backslash\text{IJ,I}\backslash\text{IJ}} \end{bmatrix} \left\{ \begin{matrix} \vec{\mathbf{0}} \\ \vec{\mathbf{x}}_{\text{IJ1n}} \\ \vec{\mathbf{x}}_{\text{IJ1t}} \\ \vec{\mathbf{x}}_{\text{IJ2n}} \\ \vec{\mathbf{x}}_{\text{IJ2t}} \\ \vec{\mathbf{x}}_{\text{I}\backslash\text{IJ}} \end{matrix} \right\} = \left\{ \begin{matrix} \vec{\mathbf{f}}_{\text{B}} \\ \vec{\mathbf{f}}_{\text{IJ1n}} \\ \vec{\mathbf{f}}_{\text{IJ1t}} \\ \vec{\mathbf{f}}_{\text{IJ2n}} \\ \vec{\mathbf{f}}_{\text{IJ2t}} \\ \vec{\mathbf{0}} \end{matrix} \right\}. \quad (26.14)$$

The explicit consideration of Newton's third law and the separate treatment of normal and tangential direction lead to a relationship between the nodal degrees of freedom of both contact surfaces in normal direction

$$\vec{\mathbf{x}}_{\text{IJ1,n}} = \underline{\tilde{\mathbf{G}}}_{\text{IJ,n}} \vec{\mathbf{x}}_{\text{IJ2,n}} \quad (26.15)$$

and tangential direction respectively

$$\vec{\mathbf{x}}_{\text{IJ1,t}} = \underline{\tilde{\mathbf{G}}}_{\text{IJ,t}} \vec{\mathbf{x}}_{\text{IJ2,t}}. \quad (26.16)$$

Using these equations the static reduction rules

$$\begin{bmatrix} \vec{\mathbf{x}}_B^T & \vec{\mathbf{x}}_{IJ1,n}^T & \vec{\mathbf{x}}_{IJ1,t}^T & \vec{\mathbf{x}}_{IJ2,n}^T & \vec{\mathbf{x}}_{IJ2,t}^T & \vec{\mathbf{x}}_{I \setminus IJ}^T \end{bmatrix}^T = \underline{\tilde{\mathbf{H}}}_{IJ,n} \vec{\mathbf{x}}_{IJ2,n} \tag{26.17}$$

and

$$\begin{bmatrix} \vec{\mathbf{x}}_B^T & \vec{\mathbf{x}}_{IJ1,n}^T & \vec{\mathbf{x}}_{IJ1,t}^T & \vec{\mathbf{x}}_{IJ2,n}^T & \vec{\mathbf{x}}_{IJ2,t}^T & \vec{\mathbf{x}}_{I \setminus IJ}^T \end{bmatrix}^T = \underline{\tilde{\mathbf{H}}}_{IJ,t} \vec{\mathbf{x}}_{IJ2,t} \tag{26.18}$$

are fully defined. Applying these reduction rules to the equations of motion (26.1) and neglecting the damping matrix $\tilde{\mathbf{D}}$ and the force vector $\vec{\mathbf{f}}_{ext}$ as well leads to the intermediate result for the contact surface normal direction

$$\underline{\tilde{\mathbf{M}}}_{red,IJ2n} \ddot{\vec{\mathbf{x}}}_{IJ2,n} + \underline{\tilde{\mathbf{K}}}_{red,IJ2n} \vec{\mathbf{x}}_{IJ2,n} = \tilde{\mathbf{0}} \tag{26.19}$$

where $\underline{\tilde{\mathbf{M}}}_{red,IJ2n} = \underline{\tilde{\mathbf{H}}}_{IJ,n}^T \tilde{\mathbf{M}} \underline{\tilde{\mathbf{H}}}_{IJ,n}$ and $\underline{\tilde{\mathbf{K}}}_{red,IJ2n} = \tilde{\mathbf{H}}_{IJ,n}^T \tilde{\mathbf{K}} \underline{\tilde{\mathbf{H}}}_{IJ,n}$ and for the contact surface tangential direction respectively

$$\underline{\tilde{\mathbf{M}}}_{red,IJ2t} \ddot{\vec{\mathbf{x}}}_{IJ2,t} + \underline{\tilde{\mathbf{K}}}_{red,IJ2t} \vec{\mathbf{x}}_{IJ2,t} = \tilde{\mathbf{0}} \tag{26.20}$$

where $\underline{\tilde{\mathbf{M}}}_{red,IJ2t} = \underline{\tilde{\mathbf{H}}}_{IJ,t}^T \tilde{\mathbf{M}} \underline{\tilde{\mathbf{H}}}_{IJ,t}$ and $\tilde{\mathbf{K}}_{red,IJ2t} = \underline{\tilde{\mathbf{H}}}_{IJ,t}^T \tilde{\mathbf{K}} \underline{\tilde{\mathbf{H}}}_{IJ,t}$. Solving two generalized eigenvalue problems with these matrices finally leads to the proposed JIM for each direction.

In many technical structures the stiffness associated with $\vec{\mathbf{x}}_{IJ1,t}$ and $\vec{\mathbf{x}}_{IJ2,t}$ is significantly higher than the stiffness associated with $\vec{\mathbf{x}}_{IJ1,n}$ and $\vec{\mathbf{x}}_{IJ2,n}$. As a consequence the eigenvalues associated with the joint interface modes in contact surface tangential direction are higher than those associated with the joint interface modes in contact surface normal direction. This indicates that, compared to trial functions in normal direction, only a small amount of trial functions in tangential direction is needed, if necessary at all.

26.5 Numerical Example

The potential of the introduced approach is demonstrated using the FE model of a spare wheel carrier shown in Fig. 26.8. This model consists of three main components: the frame, the bracket and the wheel itself. Important to note are the two bolted joints between bracket and frame which are expected to have significant influence on the dissipative behavior of the structure.

The wheel is modeled as idealized rigid body parameterized by mass and moments of inertia. The remaining structure except the four bolts of the joint, which are modeled using beam elements, is built up using solid elements. All elements reference the material properties of iron. To clearly denote the involved nodal DOF the partitioning scheme of (26.13) is
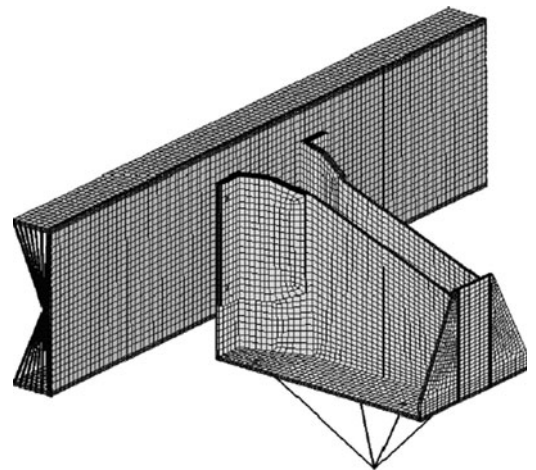
Fig. 26.8 FE model of a spare wheel carrier consisting of frame, bracket and idealized wheel

a

b
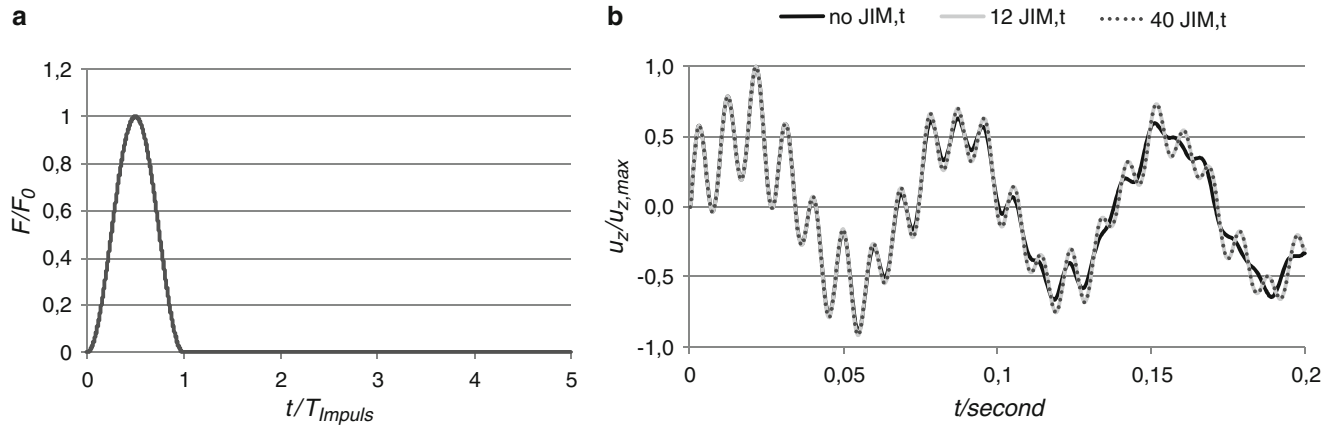
Fig. 26.9 Dynamic simulation: (**a**) force impulse, (**b**) vertical deflection measured at the wheel center

used. Interface nodes are located at the wheel center and in the middle of two rigid planes at both ends of the frame. The DOF of these nodes are collected within the boundary part $\vec{x}_B$, the remaining nodal DOF are referenced as the internal part $\vec{x}_I$ of the vector $\vec{x}$.

Before starting the dynamic simulation a convergence study is performed to verify whether the number of additional trial functions $\tilde{\boldsymbol{\Phi}}_{JIM}$ is sufficient or not. As the influence on the result quality within the joint region is of main interest the Euclidean norm of the relative displacement within this area is a good criterion for such a study. Although static load cases are used the informative value is not lowered as the dynamic behavior of the reduced system is mainly determined by the classic mode base $\tilde{\boldsymbol{\Phi}}_{classic}$. In return the computational effort for such a study is diminished significantly.

For the final reduced order model 24 JIM in contact surface normal direction are considered together with 18 CM due to $\vec{x}_B$, 10 FBNM and 4 pretension modes caused by the bolted joints. The investigated load case is the pretension of the bolts connecting the bracket to the frame combined with a force impulse applied at the center of the wheel. The structure is allowed to vibrate freely until amplitudes fade out. This results in growing regions of sticking friction within the joint contact area. The shape of the force impulse and the resulting vertical deformation of the wheel center are shown in Fig. 26.9. Both quantities are normalized to their respective maximum values.

The simulation results confirm the theoretical considerations regarding additional trial functions in contact surface tangential direction:

- Without consideration of $\tilde{\boldsymbol{\Phi}}_{JIM,t}$ damping gets overestimated and the "high frequency" displacement component fades out earlier.
- With consideration of $\tilde{\boldsymbol{\Phi}}_{JIM,t}$ holding less trial functions than $\tilde{\boldsymbol{\Phi}}_{JIM,n}$, the "high frequency" displacement component is damped less compared to the first case.
- With consideration of $\tilde{\boldsymbol{\Phi}}_{JIM,t}$ holding almost as much entries as $\tilde{\boldsymbol{\Phi}}_{JIM,n}$, no significant changes are observed compared to the second case.
- The consideration of $\tilde{\boldsymbol{\Phi}}_{JIM,t}$ is only necessary for problems with varying regions of sticking friction. During the first period of the displacement signal, no differences occur at all.

26.6 Conclusion

The presented investigations reveal that the consideration of forces due to friction within reduced order models is possible in a quite accurate way. Furthermore, this approach enables the consideration of dissipation due to friction in a more realistic way compared to the modal damping approach.

Several numerical models for the computation of forces due to friction in dynamic systems are available. A closer look on the Coulomb friction reveals that, if proper implemented, the drawback of the discontinuity in terms of efficient time integration can be avoided and simulations with reasonable computational effort are possible using this formulation.

The application of forces in contact surface tangential direction raises the question, if additional trial functions in this direction are necessary to capture energy dissipation correctly. Both, theoretical considerations and numerical examples clearly show that less additional JIMs in tangential direction than JIMs in normal direction are needed, if necessary at all.

Bibliography

1. Craig RR, Bampton MCC (1968) Coupling of substructures for dynamic analysis. AIAA J 6(7):1313–1319
2. Witteveen W, Irschik H (2007) Efficient modal formulation for vibration analysis of solid structures with bolted joints. In: Proceedings of IMAC 25th, Society of Experimental Mechanics Inc, Paper Nr. 385, Bethel
3. Witteveen W, Irschik H (2008) Joint interface modes: numerical 3D-Benchmark studies. In: Proceedings of IMAC 26th, Society of Experimental Mechanics Inc, Paper Nr. 318, Bethel
4. Witteveen W, Irschik H (2009) Efficient computation of joint interface modes. In: Proceedings of IMAC 27th, Society of Experimental Mechanics Inc, Paper Nr. 16, Bethel
5. MAMBA homepage, (2011) mamba.ecs.steyr.com
6. Gaul L, Lenz J (1997) Nonlinear dynamics of structures assembled by bolted joints. Acta Mech 125:169–181
7. Lenz J (1997) Strukturdynamik unter dem Einfluss von Mikro- und Makroschlupf in Fügestellen. Ph.D. thesis, University of the Federal Armed Forces Hamburg
8. Nitsche R (2001) Semi-active control of friction damped systems, Fortschritt-Berichte VDI Reihe 8, No. 907, Düsseldorf
9. Olsson H, Åström KJ, Canudas de Wit C, Gäfvert M, Lischinsky P (1998) Friction models and friction compensation. Euro J Control 4 (3):176–195
10. Gaul L, Nitsche R (2001) The role of friction in mechanical joints. Appl Mech Rev 54(2):93–105

Chapter 27
Efficient Updating of Static Modes in the Craig-Bampton Reduction Basis

S.N. Voormeeren and D.J. Rixen

Abstract Although component mode synthesis (CMS) methods for structural dynamic analysis were introduced in the 1960s, it is still an active field of research. One of the current challenges is to apply CMS in a design process in which some component(s) of the system are (parametrically) modified. For every design change, the component reduction basis needs to be recomputed, thereby seriously hindering the effectiveness of the CMS approach.In this work we address the static modes, which are an essential part of every component reduction basis. For the popular Craig-Bampton CMS method, we present an efficient yet accurate method for updating the static modes based on the iterative conjugate gradient solver. This way, no factorization of the modified stiffness matrix is needed and optimal use is made of the available information. The effectiveness of the proposed strategy will be illustrated by a case study.

27.1 Introduction

27.1.1 *Updating of Component Reduction Bases*

With ever shorter design cycles and increasingly complex products, the need for faster structural dynamic analysis never seizes to exist. One way of decreasing the computational burden of dynamic analysis is by applying the *dynamic substructuring* methodology. This paradigm combines the concepts of a componentwise approach and model reduction techniques, as follows:

1. The complete system is decomposed into components or substructures.
2. Each component is modeled and reduced separately, using a suitable reduction basis. This basis consists of a set of static modes describing the interaction with neighboring components, and some vibration modes to account for the dynamics.
3. The reduced component models are assembled to form the model of the complete system.

This approach is often also referred to as *component mode synthesis* (CMS) and was first introduced in the 1960s [10, 11]. One very popular CMS method often used today is the Craig-Bampton method [4]; this is the method considered in this work.

The main computational cost in the CMS process lies in the computation of the component reduction bases. This involves solving both a linear system of equations for the static modes and an eigenproblem to obtain the vibration modes. This investment pays off when the assembled system is analyzed, since it is very compact and can be analyzed efficiently. However, in the setting of a practical design process, some of the component models may be subject to successive (parametric) modifications. Hence for every design change their reduction bases need to be recomputed, which undermines the efficiency of the CMS approach.

However, the design changes made to the components are in practice often rather small. It is therefore unlikely that the modified component will start exhibiting completely different behavior in terms of eigenfrequencies and mode shapes. The question thus arises whether we actually need to recalculate the complete component reduction basis or if we could maybe

S.N. Voormeeren (✉) • D.J. Rixen
Section Engineering Dynamics, Delft University of Technology, Mekelweg 2, 2628CD Delft, The Netherlands
e-mail: s.n.voormeeren@tudelft.nl

use the knowledge of the nominal system to efficiently update its basis to suit the modified component. In the literature, different approaches have been proposed to achieve this.

For the static modes, one approach is to simply assume that the nominal static modes can also be used to reduce the modified component [13]. Another approach is to recompute them based on the new model [3]. Finally, the static modes can be updated using the Combined Approximations (CA) technique [12], as proposed in [1].

The vibration modes can also be updated using the Combined Approximations method, as proposed in [3]. Another approach is to enrich the reduction basis using sensitivity modes as described in [13, 1]. Such sensitivity modes represent the change of the vibration mode shapes around the nominal design point with respect to the design change.

In this work, we propose yet another approach. Given the importance of the static modes in predicting the low frequency behavior (including the rigid body modes), we wish to recompute them with sufficient accuracy. Since the accuracy of the CA updating procedure cannot be guaranteed [1], here it is proposed to use an iterative conjugate gradient (CG) based solver. Especially for small design changes such an iterative approach is expected to give the desired accuracy at low computational cost compared to recomputation using a direct solver. For the vibration modes we adopt the enrichment strategy from [13, 1], although iterative approaches similar to the CG method can also be devised for the vibration modes. This is however out of the scope of this paper.

27.1.2   Paper Outline

The starting points for the work presented in this paper are as follows:

- In line with the work referred to earlier [1, 13, 3], we assume that the component FE mesh topology and connectivity are not altered. Nodal positions may be changed (e.g. elongation or thickness changes) as long as this does not result in element shape violations.
- The goal of the methodology presented here is to update the static part of the reduction basis, such that it is suited to the modified component model and allows to accurately predict the static/rigid body behavior.
- The (quasi-)stiffness matrix of the nominal system is factorized when setting up the reduced model of the nominal system. This factorization is a significant part of the computational cost of the reduction. We assume that the factorized stiffness matrix of the nominal system is stored for further use.

As a result, the paper is organized as follows. In the next section we will briefly recapitulate the theory of the Craig-Bampton method. Thereafter, Sect. 27.3 will present the procedure for updating the static modes, based on the *Preconditioned Conjugate Gradient* method. Thereafter, the enrichment method for the vibration modes and the resulting modified reduction basis are briefly explained in Sect. 27.4. In order to assess the performance of the proposed updating strategy, Sect. 27.5 presents a case study where the methods are applied to an industrial sized FE problem. Conclusions are drawn in Sect. 27.6.

Regarding the notations in this paper: a superscript $\star^{(0)}$ refers to the nominal system, while $\star^{(1)}$ designates the modified component. The symbol $\Delta\star$ is used to indicate the difference between the nominal and modified system.

27.2   The Craig-Bampton Method

In order to derive the Craig-Bampton CMS method, we start from the component discretized equations of motion:

$$\mathbf{M}^{(s)}\ddot{\mathbf{u}}^{(s)}(t) + \mathbf{K}^{(s)}\mathbf{u}^{(s)}(t) = \mathbf{f}^{(s)}(t) \tag{27.1}$$

Here s is denoting the substructure at hand, M is its mass matrix, K is the stiffness matrix, u the vector of degrees of freedom (DoF) and f the external excitation vector. Next, the DoF vector is split into some set of internal DoF u_i and a set of boundary (or interface) DoF u_b, leading to the partitioned equations of motion:

$$\begin{bmatrix} M_{bb} & M_{bi} \\ M_{ib} & M_{ii} \end{bmatrix} \begin{bmatrix} \ddot{u}_b \\ \ddot{u}_i \end{bmatrix} + \begin{bmatrix} K_{bb} & K_{bi} \\ K_{ib} & K_{ii} \end{bmatrix} \begin{bmatrix} u_b \\ u_i \end{bmatrix} = \begin{bmatrix} f_b \\ 0 \end{bmatrix} \tag{27.2}$$

Here the explicit time dependence and substructure identifier ^{s} have been omitted for clarity. The Craig-Bampton method now consists in retaining the boundary and finding a good approximation for the internal DoF. This is done by splitting the response of the internal DoF into a static and a dynamic part:

$$u_i = u_{i,stat} + u_{i,dyn} \tag{27.3}$$

To obtain an approximation for the static part of the response, it is assumed that there is no external excitation on the internal DoF, i.e. $f_i = 0$. Now u_i can be condensed into u_b to find the so-called static constraint modes Ψ_C as:

$$u_{i,stat} = -K_{ii}^{-1}K_{ib}u_b = \Psi_C u_b \tag{27.4}$$

Note that using the static modes, the static response can be described exactly when the force is applied at the boundary DoF. The static modes are essential in a component reduction basis as they describe the static response of the component model to excitations coming from neighboring substructures through the boundary DoF. By taking only the static modes in the reduction basis one finds the classic Guyan method [8].

Next, to find an approximation for the dynamic part of the response the modal superposition principle is used. Hence, we describe the dynamic response of the internal DoF using internal vibration modes (often referred to as fixed interface vibration modes), which are computed by setting $u_b = 0$ and solving the following eigenproblem:

$$\left(K_{ii} - \omega_i^2 M_{ii}\right)\phi_i = 0 \tag{27.5}$$

In order to achieve the actual reduction, we only retain the first $m << n_i$ mode shapes ϕ_i which are mass normalized, such that:

$$\Phi_i = \begin{bmatrix} \phi_{i,1} & \phi_{i,2} & \cdots & \phi_{i,m} \end{bmatrix}$$

$$\Phi_i^T M_{ii} \Phi_i = I$$

$$\Phi_i^T K_{ii} \Phi_i = diag(\omega_{i,1}^2 \ldots \omega_{i,m}^2) = \Omega_i^2$$

The total set of internal degrees of freedom is therefore approximated by:

$$u_i \approx \Psi_C u_b + \Phi_i \eta_i \tag{27.6}$$

Where η_i are the modal amplitudes of the internal modes. This transformation can be put into matrix format in order to obtain the Craig-Bampton reduction matrix:

$$\begin{bmatrix} u_b \\ u_i \end{bmatrix} = \begin{bmatrix} u_b \\ \Psi_C u_b + \Phi_i \eta_i \end{bmatrix} = \begin{bmatrix} I & 0 \\ \Psi_C & \Phi_i \end{bmatrix} \begin{bmatrix} u_b \\ \eta_i \end{bmatrix} = R\,q \tag{27.7}$$

So, the original set of component DoF are reduced to a new set of DoF using the static constraint modes and fixed interface vibration modes. Substituting the reduction in the original set of equations then gives the following:

$$M\,R\ddot{q} + K\,R\,q = f + r \tag{27.8}$$

Here we have introduced a residual force r since the accuracy of the reduced model is always less then the full model and hence an equilibrium error will exist. By definition, this error is orthogonal to the space of the modes used in the reduction matrix and hence can be eliminated by pre-multiplication:

$$R^T M\,R\ddot{q} + R^T K\,R\,q = \tilde{M}\ddot{q} + \tilde{K}q = R^T f = \tilde{f} \tag{27.9}$$

Since the interface DoF are retained, this reduced component model can be easily assembled to other components, hence this type of model is often referred to as a *superelement*.

27.3 Updating of Static Modes

27.3.1 Approach: Direct vs. Iterative Methods

As outlined above, for the computation of the static modes one has to solve a static problem of the form:

$$K\boldsymbol{\Psi}_j = \boldsymbol{f}_j, \tag{27.10}$$

Here a more compact notation has been used, such that for the Craig-Bampton method it holds that:

$$\begin{cases} \mathbf{K} \rightarrow \mathbf{K}_{ii} \\ \boldsymbol{\Psi}_j \rightarrow \boldsymbol{\Psi}_{C,j} \\ \mathbf{f}_j \rightarrow \mathbf{K}_{ib,j} \end{cases}$$

where the index $_j$ refers to some static mode contained in the set of p static modes $\boldsymbol{\Psi}_C = [\boldsymbol{\Psi}_{C,\,1}\cdots\boldsymbol{\Psi}_{C,\,p}]$.

The most time consuming step in the process of computing the static modes is the factorization of the stiffness matrix, performed by so-called direct solvers. Such solvers are basically variants of the factorization techniques by Gauss, such as LDLT decomposition for symmetric matrices or Cholesky decomposition for symmetric positive matrices. Hence, when a component is modified one would ideally like to avoid refactorizing the stiffness matrix.

Indeed, it was noted earlier that when the modified system is "close" to the nominal one, its structural behavior will probably not change dramatically. Therefore, we propose not to start the calculations for the modified component from scratch but instead use iterative methods. The aim is to start from the solutions of the nominal system, reuse as much as possible from the available information and quickly converge to the solutions for the modified system. In this section we therefore present an approach for updating the static modes, based on the iterative conjugate gradient (CG) method. The starting point for this updating problem is as follows. For the nominal component, we have solved the static problem

$$\boldsymbol{\Psi}^{(0)} = \boldsymbol{K}^{(0)^{-1}}\boldsymbol{F}^{(0)}, \tag{27.11}$$

Subsequently we make a design modification to the component, which leads to the new static problem:

$$\boldsymbol{K}^{(1)}\boldsymbol{\Psi}^{(1)} = \boldsymbol{F}^{(1)} \tag{27.12}$$

The goal is now to efficiently find $\boldsymbol{\Psi}^{(1)}$ by reusing $\boldsymbol{\Psi}^{(0)}$ and $K^{(0)^{-1}}$, while avoiding the factorization of $\boldsymbol{K}^{(1)}$. This section is therefore organized as follows. First the general concept of the CG method is outlined, thereafter we discuss its convergence and how to improve it using preconditioning in Sect. 27.3.3. The issue of solving for multiple right hand sides is addressed in Sect. 27.3.4 while in Sect. 27.3.5 we finally return to the updating problem and show why the approach might be useful.

27.3.2 The Conjugate Gradient Method

Most iterative methods for static problems are based on the *conjugate gradient* algorithm proposed by Hestenes and Stiefel [9] in 1952. The conjugate gradient method is an iterative algorithm for solving systems of linear equations with symmetric and positive-definite operators, such as the problem for a static mode:

$$K\boldsymbol{\Psi} = \boldsymbol{f}$$

Solving this linear system is equal to minimization of the quadratic problem:

$$\mathcal{L}(\boldsymbol{\Psi}) = \frac{1}{2}\boldsymbol{\Psi}^T K\boldsymbol{\Psi} - \boldsymbol{\Psi}^T\boldsymbol{f} \tag{27.13}$$

Suppose that we have some initial guess $\boldsymbol{\Psi}_0$ of the solution ($\boldsymbol{\Psi}_0$ can be equal to $\boldsymbol{0}$) and we wish to iteratively refine it by adding some improvement: $\boldsymbol{\Psi}_1 = \boldsymbol{\Psi}_0 + \Delta\boldsymbol{\Psi}$. The question now is how to choose $\Delta\boldsymbol{\Psi}$. If we take the negative gradient of the quadratic problem around the initial guess, we find:

$$-\left.\frac{\partial\mathcal{L}}{\partial\boldsymbol{\Psi}}\right|_{\boldsymbol{\Psi}_0} = \boldsymbol{f} - K\boldsymbol{\Psi}_0 = \boldsymbol{r}_0 \tag{27.14}$$

In fact, r_0 is the residual force vector for the initial guess u_0 and corresponds to the steepest descent direction around Ψ_0, that is, the direction in which $\mathcal{L}$ is reduced quickest. Hence we write the new approximation Ψ_1 as

$$\Psi_1 = \Psi_0 + \eta_0 \mathbf{r}_0, \tag{27.15}$$

where η_0 is the unknown amplitude in the direction of the residual r_0. Inserting this in the linear problem yields

$$\mathbf{K}\Psi_1 = \mathbf{K}(\Psi_0 + \eta_0 \mathbf{r}_0) = \mathbf{f} - \mathbf{r}_1 \tag{27.16}$$

To find the "optimal" value for η, we require the new residual to be zero in the space of the current approximation, i.e. $r_0^T r_1 = 0$. This gives

$$\mathbf{r}_0^T \mathbf{K}(\Psi_0 + \eta_0 \mathbf{r}_0) = \mathbf{r}_0^T \mathbf{f}, \tag{27.17}$$

and using the expression for r_0 then allows us to find η_0:

$$\eta_0 = \frac{\mathbf{r}_0^T \mathbf{r}_0}{\mathbf{r}_0^T \mathbf{K} \mathbf{r}_0} \tag{27.18}$$

Note that this corresponds to a "line search" minimization step. Subsequently one can calculate Ψ_1 and the associated residual r_1, compute the next correction for η_1, and so on. In order to avoid that the same direction appears several times in the residual, such that the solution is not guaranteed to be found in a finite number of steps, an orthogonalization step should be included in this process. In this way, the search direction at iteration k is no longer directly the residual r_k, but is first $\mathbf{K}$-orthogonalized to all the previous search directions. In theory, the new search direction needs to be orthogonalized only with respect to the previous one, but due to numerical round-off errors the preceding directions will progressively reappear. Hence a full orthogonalization is needed, as follows:

$$\mathbf{p}_k = \mathbf{r}_k - \sum_{i=0}^{k-1} \mathbf{p}_i \beta_i \tag{27.19}$$

where k is the index of the current iteration and i the index of the previous directions. We use p to denote the search direction (i.e. orthogonalized residual) as opposed to the true residual r. Realizing that after orthogonalization it should hold that $p_i^T \mathbf{K} p_k = 0$, and after scaling the search directions such that $p_i^T \mathbf{K} p_i = 1$, the factor β_i is found as:

$$\beta_i = \mathbf{r}_k^T \mathbf{K} \mathbf{p}_i \tag{27.20}$$

Since the search directions obtained in this way span a $\mathbf{K}$-orthogonal space, the algorithm is guaranteed to converge in n iterations, where n is the size of the problem. We have now treated the basic ingredients of the CG method, which can be expressed in the form of Algorithm 1.

Algorithm 1 Basic Conjugate Gradient method

Input: $\mathbf{K}$, $\mathbf{f}$, ψ_0
$k = 0$
$\mathbf{r}_0 = \mathbf{f} - \mathbf{K}\psi_0$
while $\|\mathbf{r}_k\| > \varepsilon\|\mathbf{f}\|$ **do**
  $\mathbf{p}_k = \mathbf{r}_k$
  – Orthogonalization with previous directions –
  for $i = 0\ldots k-1$ **do**
    $\beta_i = \mathbf{r}_k^T \mathbf{K} \mathbf{p}_i$
    $\mathbf{p}_k = \mathbf{p}_k - \mathbf{p}_i \beta_i$
  end for
  $\mathbf{p}_k = \frac{\mathbf{p}_k}{\sqrt{\mathbf{p}_k^T \mathbf{K} \mathbf{p}_k}}$
  – Minimization and updating –
  $\eta_k = \mathbf{p}_k^T \mathbf{r}_k$
  $\psi_{k+1} = \psi_k + \eta_k \mathbf{p}_k$
  $\mathbf{r}_{k+1} = \mathbf{r}_k - \eta_k \mathbf{K} \mathbf{p}_k = \mathbf{f} - \mathbf{K}\psi_{k+1}$
  $k = k+1$
end while

Some remarks are in place regarding the Algorithm 1 and the CG method in general:

- The main cost of the algorithm is in the matrix-vector multiplication Kp_k. Hence one can optimize the algorithm by storing this product as w_k, so that it needs to be calculated only once per iteration.
- The calculation of the new residual can be done recursively or directly. For numerical stability it is advisable to explicitly evaluate the residual once every few iterations (for instance $\sqrt{n}$); see [23] for a discussion.
- The convergence criterion is to compare the norm of the residual with the norm of the force (right hand side) and define an iteration tolerance ε for their ratio.
- The normal CG method makes use of the symmetry of the operator K in the conjugation step. However, for non-symmetric operators similar algorithms can be devised such as the bi-CG or GMRES methods [22, 21].

27.3.3 Convergence and Preconditioning

In the original version of the CG method outlined above, the convergence of the algorithm is usually very slow. To illustrate this, let us first define the K-norm of some vector x as follows:

$$\|x\|_K = \sqrt{x^T K\, x} \tag{27.21}$$

Using this norm, a lower bound for the convergence rate of the conjugate gradient method can be expressed as a function of the condition number κ of the operator K [6]:

$$\|\boldsymbol{\Psi} - \boldsymbol{\Psi}_k\|_K \le 2\|\boldsymbol{\Psi} - \boldsymbol{\Psi}_0\|_K \left(\frac{\sqrt{\kappa} - 1}{\sqrt{\kappa} + 1}\right)^k \tag{27.22}$$

This indicates that when $\kappa(K) \approx 1$ the convergence of the CG algorithm is very fast. Most structural problems however, suffer from bad mathematical conditioning for instance arising from stiffness changes in the structure, mixing of translation and rotational DoF, etc. In those cases $\kappa(K) \gg 1$ and the convergence rate is very slow. An important way to increase the convergence rate is thus to improve the condition number of the operator. This can be done by the transformation

$$\hat{\mathbf{K}} = S^{-1}\mathbf{K}, \tag{27.23}$$

with S chosen such that the condition number of $\hat{K}$ is lower than that of K, a concept known as *preconditioning*. Note that S must be a full rank matrix in order to retain the full possible solution space. In the iterative scheme of the CG method the preconditioning step can be implemented by taking

$$\mathbf{p}_k = \mathbf{S}^{-1}\mathbf{r}_k, \tag{27.24}$$

In the ideal case one would take $\mathbf{S}^{-1} = \mathbf{K}^{-1}$, so that $\kappa(\hat{K}) = 1$. In that case the search direction becomes $\mathbf{p}_k = \mathbf{K}^{-1}\mathbf{r}_k$ and the exact solution would be found in one iteration. This is of course the paradox of the method: to achieve this we need the inverse of K from a factorization. The updating step is then nothing more than a forward/backward substitution and the CG method has in fact become a direct solver. The trick is therefore to come up with some approximation $\hat{K}^{-1}$ for K^{-1} which is good enough to seriously speed up the calculations but is not too costly in its construction.

A physical interpretation of the slow convergence without preconditioning is that the displacement solution we seek is iteratively updated using forces (the orthogonalized residual vectors). This seems inconsistent from a mechanical point of view and one should in fact translate the force errors to a displacement correction, using preconditioning. The better the preconditioner approximates the inverse of K, the closer the correction is to a true displacement correction.The issue of choosing an optimal preconditioner has been studied intensively over the years and as a result, many other preconditioners exist. This is however not of interest here, as we will show in Sect. 27.3.5.

27.3.4 Multiple Right Hand Sides

In the above discussion the CG method was considered for solving a static problem with a single right hand side:

$$K\boldsymbol{\Psi}_j = f_j$$

In practice however, a component very rarely has a single interface DoF and hence multiple static modes need to be calculated:

$$K\boldsymbol{\Psi} = \boldsymbol{F}, \tag{27.25}$$

where $\boldsymbol{\Psi} = [\boldsymbol{\Psi}_1 \cdots \boldsymbol{\Psi}_p]$ and $\boldsymbol{F} = [f_1 \cdots f_p]$. Using a direct solver this is very easy; since the factorization is already available only a forward/backward substitution is needed to solve for the new right hand sides.

The question thus arises if something similar can be done for the CG method. In fact, two ways exist to handle multiple right hand sides in the CG method, namely (1) performing subsequent iterations making use of the previous results through projection and reconjugation, and (2) simultaneous iteration on a block of vectors. Both will be treated next.

27.3.4.1 Projection and Reconjugation

Suppose that we have computed the first static mode with a (preconditioned) CG solver:

$$K\boldsymbol{\Psi}_1 = f_1$$

In the process the following sequences were generated $\boldsymbol{P}_1 = \boldsymbol{p}_1, \boldsymbol{p}_2, \cdots$ and $\boldsymbol{W}_1 = \boldsymbol{K}\boldsymbol{p}_1, \boldsymbol{K}\boldsymbol{p}_2, \cdots$, such that by construction we have a $\boldsymbol{K}$-orthonormal basis:

$$\boldsymbol{P}_1^T \boldsymbol{K}\boldsymbol{P}_1 = \boldsymbol{P}_1^T \boldsymbol{W}_1 = \boldsymbol{I} \tag{27.26}$$

Hence, if we consider a new right hand side to find the next static mode we can first search for (an estimate of) the solution in the existing space. So suppose we wish to solve

$$K\boldsymbol{\Psi}_2 = f_2 \tag{27.27}$$

and already have an initial guess $\boldsymbol{\Psi}_{2,0}$ for the solution (the following also holds if $\boldsymbol{\Psi}_{2,0} = \boldsymbol{0}$). Instead of directly starting the CG iterations, we first try to improve the solution by searching for a correction in the existing space:

$$\boldsymbol{\Psi}_2 \approx \boldsymbol{\Psi}_{2,0} + \boldsymbol{P}_1 \boldsymbol{\alpha}_1 \tag{27.28}$$

Inserting this in the static mode problem, premultiplying with $\boldsymbol{P}_1^T$ and solving for α_1 gives:

$$\boldsymbol{\alpha}_1 = \boldsymbol{P}_1^T \left(f_2 - \boldsymbol{K}\boldsymbol{\Psi}_{2,0} \right) \tag{27.29}$$

The improved solution for the second static mode is thus found as

$$\boldsymbol{\Psi}_2 = \boldsymbol{\Psi}_{2,0} + \boldsymbol{P}_1 \boldsymbol{P}_1^T \left(f_2 - \boldsymbol{K}\boldsymbol{\Psi}_{2,0} \right) = \boldsymbol{\Psi}_{2,0} + \boldsymbol{P}_1 \boldsymbol{P}_1^T f_2 - \boldsymbol{P}_1 \boldsymbol{P}_1^T \boldsymbol{K}\boldsymbol{\Psi}_{2,0}, \tag{27.30}$$

where the last term can be recognized as projection of the $\boldsymbol{\Psi}_{2,0}$ on the space $\boldsymbol{K}$-orthogonal to the existing space $\boldsymbol{P}_1$. By doing this we already have the solution in the space $\boldsymbol{P}_1$ and will improve the solution by CG iterations. To that end, we can calculate the associated residual:

$$\begin{aligned} \boldsymbol{r} &= f_2 - \boldsymbol{K}\boldsymbol{\Psi}_2 \\ &= f_2 - \boldsymbol{K}\boldsymbol{\Psi}_{2,0} - \boldsymbol{K}\boldsymbol{P}_1 \boldsymbol{P}_1^T f_2 + \boldsymbol{K}\boldsymbol{P}_1 \boldsymbol{P}_1^T \boldsymbol{K}\boldsymbol{\Psi}_{2,0} \\ &= \left(\boldsymbol{I} - \boldsymbol{W}_1 \boldsymbol{P}_1^T \right) f_2 - \left(\boldsymbol{K} - \boldsymbol{W}_1 \boldsymbol{W}_1^T \right) \boldsymbol{\Psi}_{2,0} \end{aligned} \tag{27.31}$$

This forms the starting point for the CG iterations for the new static mode. To avoid searching in the existing subspace, the new search directions should not only be mutually orthogonalized but should also be orthogonalized with respect to P_1 (this is sometimes called *reconjugation*). This process can be repeated for all right hand sides and the search space P is continuously enriched. When this space is rich enough, the solution for a new right hand side may be found with very few iterations. For more details see for instance [20].

27.3.4.2 Block Conjugate Gradient

Another way to treat multiple right hand sides in a CG solver is by solving them all simultaneously (i.e. solving directly (27.26)). This can be achieved by iterating on a block of vectors [14]. In order to adapt the CG algorithm to block computations, the only notable difference with the single vector algorithm is instead of simple scaling one needs to perform a K-orthonormalization of the vectors in the block of search directions P, such that $P^T K P = P^T W = I$. This can be accomplished for example through a modified Gram-Schmidt process [6]. Using this orthonormality, the orthogonalization step of the block of vectors with respect to the previous directions is straightforward:

$$P_k = R_k - \sum_{i=1}^{k-1} P_i \beta_i \quad \text{with} \quad \beta_i = W_i^T R_k. \tag{27.32}$$

Similarly, the minimization step in the block algorithm is also easily solved as:

$$\Psi_{k+1} = \Psi_k + P_k \eta_k \quad \text{with} \quad \eta_k = P_k^T R_k. \tag{27.33}$$

Since in the block implementation the residuals are minimized simultaneously in all search directions, the convergence of the method is very fast in terms of number of iterations. However, the total number of search directions needed for convergence (i.e. block size times number of iterations) is approximately equal for the block and the single vector algorithms. Still the block CG method is an interesting option since modern CPUs can run more efficiently when iterations are performed on a number of vectors instead of a single vector.

Algorithm 2 Block Conjugate Gradient with Preconditioning and multiple r.h.s.

Input: K, F, Ψ_0, S^{-1}
$k = 0$, $j = 1$
$R_0 = F_1 - K\Psi_{1,0}$
for $j = 1 \ldots p$ **do**
    – Initial guess for new r.h.s. –
    if $j > 1$ **then**
        $Q = K\Psi_{j,0}$
        $\alpha = P^T (F_j - Q)$
        $R_k = F_j - W\alpha - Q$
        $\Psi_{j,0} = \Psi_{j,0} + P\alpha$
    end if
    while $||r_{m,k}|| > \varepsilon ||f_{m,j}||$ **do**
        $P_k = S^{-1} R_k$
        – Orthogonalization with previous directions –
        for $i = 1 \ldots k - 1$ **do**
            $\beta_i = W_i^T P_k$
            $P_k = P_k - P_i \beta_i$
        end for
        $W_k = K P_k$
        Orthonormalize P_k : $P_k^T W_k = I$
        – Minimization and updating –
        $\eta_k = P_k^T R_k$
        $\Psi_{j,k+1} = \Psi_{j,k} + P_k \eta_k$
        $R_{k+1} = F_j - K\Psi_{j,k+1} = R_k - W_k \eta_k$
        $k = k + 1$
    end while
end for

However, the efficiency of the block approach is lost when a large number of static modes is sought (i.e. when the component has many interface DoF) due to the memory requirements and the need to orthonormalize P_k. To overcome this,

the projection and reconjugation approach for multiple right hand sides can be combined with the block CG algorithm. This allows one to choose the block size such that the processor is optimally used while at the same time using the previous iterates for finding the solutions for the other block right hand sides. So, the static problem of (27.26) is split in a number of block equations

$$K\Psi_j = F_j, \tag{27.34}$$

and subsequently solved using a combination of the projection/reconjugation and block approaches. This variation of the CG method is outlined in Algorithm 2.

27.3.5 Application to Updating of Static Modes

27.3.5.1 Preconditioning

In the previous subsections the basics of the CG method were outlined and it became clear that the convergence rate of the algorithm is highly dependent on the effectiveness of the preconditioner. In this section we will show why the CG algorithm is potentially very attractive for updating the static modes in a component reduction basis.

Suppose that we have calculated the static modes $\Psi^{(0)}$ of the nominal component and stored the factorization of $K^{(0)}$. Next we wish to solve the static modes problem for the modified component using the CG method from Algorithm 2. As initial guess for the solution we use the static modes of the nominal system and, more importantly, the factorization of the nominal stiffness matrix is used for preconditioning. Note that we can write the static problem for the modified system as:

$$\left(K^{(0)} + \Delta K\right)\Psi^{(1)} = \left(F^{(0)} + \Delta F\right), \tag{27.35}$$

Hence, taking the nominal static modes $\Psi^{(0)}$ as initial guess for $\Psi^{(1)}$, the initial (block) residual for the CG method can be calculated as:

$$R_0 = \left(F^{(0)} + \Delta F\right) - \left(K^{(0)} + \Delta K\right)\Psi^{(0)} = \Delta F - \Delta K\Psi^{(0)} \tag{27.36}$$

After preconditioning, minimization and updating, the new estimate for the updated static modes is found: $\Psi_1^{(1)}$. This approximation can be written as the nominal solution plus some correction $\Psi_1^{(1)} = \Psi^{(0)} + \Delta\Psi_0$. We can therefore calculate the next residual as:

$$R_1 = \left(F^{(0)} + \Delta F\right) - \left(K^{(0)} + \Delta K\right)\left(\Psi^{(0)} + \Delta\Psi_0\right) = R_0 - \left(K^{(0)} + \Delta K\right)\Delta\Psi_0 \tag{27.37}$$

Now we note that in case the correction would be exact, this residual R_1 would be equal to zero. Hence, for the exact correction we can write:

$$R_0 = \left(K^{(0)} + \Delta K\right)\Delta\Psi \tag{27.38}$$

The corresponding search directions are found after preconditioning:

$$P_0 = K^{(0)^{-1}}R_0 = \left(I + K^{(0)^{-1}}\Delta K\right)\Delta\Psi \tag{27.39}$$

This shows that the closer $K^{(0)^{-1}}\Delta K$ is to some factor times identity, the closer the search direction will be to the direction of the exact correction. Indeed, in case $\Delta K = \alpha K^{(0)}$, then the search direction would be $\Delta\Psi$, the minimization step scales this direction by the factor $(1 + \alpha)$ and the solution is obtained in one iteration. Hence, a very good preconditioner is available "for free" if $K^{(0)}$ was factorized for the nominal system. The closer the modified component is to the nominal one (i.e. the smaller the design change), the better this preconditioner becomes and the faster the CG algorithm will converge.

Note that in practice a component often undergoes a series of design modifications from the nominal to the final design. In that case, not only the factorization of the nominal component's stiffness matrix might be useful for preconditioning, but also the CG iterates obtained from updating computations of previous modifications. One important issue then becomes selecting from all this available information the most relevant content for approximating the inverse of the current stiffness matrix. This will not be addressed here.

27.3.5.2   Practical Issues Block Implementation

As outlined in the introduction, a component's static modes correspond physically to the static deformation shapes in response to an excitation (either displacement or force) at one of its boundary DoF. In practice, where the boundary DoF may be located close to each other, this means that some of the static modes may be very similar in shape. Mathematically speaking, such vectors are (nearly) linearly dependent. Indeed, when starting the CG iterations with $\boldsymbol{\Psi}_0^{(1)} = \boldsymbol{\Psi}^{(0)}$ and $\boldsymbol{\Psi}^{(0)}$ having linearly dependent columns, the initial residual will not have full rank. As a result, the orthonormalization process of the vectors in $\boldsymbol{P}_0$ will break down and the CG algorithm is no longer guaranteed to converge. To overcome this, a check on the rank of the initial residual needs to be performed when initializing the block CG algorithm [5]. If the block of vectors is rank deficient, they need to be orthogonalized such that:

$$\boldsymbol{R}_0 = \boldsymbol{F}^{(1)} - \boldsymbol{K}^{(1)}\boldsymbol{\Psi}^{(0)} = \bar{\boldsymbol{R}}_0\boldsymbol{G} \tag{27.40}$$

Here $\bar{\boldsymbol{R}}_0$ has size $n \times r$ and $\boldsymbol{G}$ has size $r \times p$, with r the rank of $\boldsymbol{R}_0$ and p the original number of vectors in the block. The original problem is then transformed to:

$$\boldsymbol{K}^{(1)}\bar{\boldsymbol{\Psi}}^{(1)} = \bar{\boldsymbol{R}}_0 \tag{27.41}$$

After solving the transformed problem, the solutions to the original updating problem can be recovered by:

$$\boldsymbol{\Psi}^{(1)} = \boldsymbol{\Psi}^{(0)} + \bar{\boldsymbol{\Psi}}^{(1)}\boldsymbol{G} \tag{27.42}$$

Another issue encountered in practice is that not all vectors in the block converge at the same rate. Some vectors may thus meet the convergence criterion much sooner than others. In order to minimize the computational effort and, more importantly, to avoid numerical instabilities in the minimization step it is therefore advisable to remove converged vectors from the block.

27.4   Modified Component Reduction Basis

In the previous section it was explained how the static modes of the modified component can be found by updating the nominal modes using the preconditioned conjugate gradient method. Here we will treat enrichment of the dynamic part of the reduction basis using vibration mode sensitivities. Thereafter we will show the complete reduction basis of the modified component and finally the reduction basis updating method will be briefly summarized.

27.4.1   Enrichment of Vibration Modes

As explained in the introduction, we choose not to recompute or update the (fixed interface) vibration modes but instead to enrich the basis using modal sensitivity vectors. This method was first described in [13] and also applied in [1]; its derivation will be treated below.

Based on the eigensolutions of the nominal component and the design modification, one can easily and fairly cheaply calculate so called modal sensitivities. These modal sensitivities contain information on the extent and direction in which the eigensolutions have changed due to the design modification. In order to obtain these sensitivity modes, suppose that we have solved the eigenproblem of the nominal system:

$$\boldsymbol{K}^{(0)}\boldsymbol{\Phi}^{(0)} - \boldsymbol{M}^{(0)}\boldsymbol{\Phi}^{(0)}\boldsymbol{\Omega}^{{(0)}^2} = \boldsymbol{0} \tag{27.43}$$

Here we have again used compact notation, such that for the Craig-Bampton (i.e. fixed interface vibration modes) case we have:

$$\begin{cases} \boldsymbol{K} \to \boldsymbol{K}_{ii} \\ \boldsymbol{M} \to \boldsymbol{M}_{ii} \\ \boldsymbol{\Phi} \to \boldsymbol{\Phi}_i \\ \Omega \to \Omega_i \end{cases}$$

Next, we wish to solve the eigenproblem for the modified component:

$$\boldsymbol{K}^{(1)}\boldsymbol{\Phi}^{(1)} - \boldsymbol{M}^{(1)}\boldsymbol{\Phi}^{(1)}\Omega^{(1)^2} = \left(\boldsymbol{K}^{(0)} + \Delta\boldsymbol{K}\right)\boldsymbol{\Phi}^{(1)} - \left(\boldsymbol{M}^{(0)} + \Delta\boldsymbol{M}\right)\boldsymbol{\Phi}^{(1)}\Omega^{(1)^2} = \boldsymbol{0} \quad (27.44)$$

This problem we can write as:

$$\boldsymbol{K}^{(0)}\boldsymbol{\Phi}^{(1)} - \boldsymbol{M}^{(0)}\boldsymbol{\Phi}^{(1)}\Omega^{(1)^2} = -\Delta\boldsymbol{K}\boldsymbol{\Phi}^{(1)} + \Delta\boldsymbol{M}\boldsymbol{\Phi}^{(1)}\Omega^{(1)^2} \quad (27.45)$$

Since we are interested in the lowest eigenmodes, assume now that the elastic forces are dominating over the inertia forces. This gives not the true modes, but some correction or sensitivity $\bar{\boldsymbol{\Phi}}^{(1)}$:

$$\boldsymbol{K}^{(0)}\bar{\boldsymbol{\Phi}}^{(1)} = -\Delta\boldsymbol{K}\boldsymbol{\Phi}^{(1)} + \Delta\boldsymbol{M}\boldsymbol{\Phi}^{(1)}\Omega^{(1)^2} \quad (27.46)$$

However, the eigenmodes and frequencies of the modified system are unknown. Still we can assume that

$$\boldsymbol{\Phi}^{(1)} = \boldsymbol{\Phi}^{(0)} + \Delta\boldsymbol{\Phi} \quad \text{and} \quad \Omega^{(1)^2} = \Omega^{(0)^2} + \Delta\Omega^2. \quad (27.47)$$

Inserting in (27.46) and neglecting higher order terms gives a set of first order correction/sensitivity modes as:

$$\boldsymbol{\Phi}^{(1)} = -\boldsymbol{K}^{(0)^{-1}}\left(\Delta\boldsymbol{K}\boldsymbol{\Phi}^{(0)} - \Delta\boldsymbol{M}\boldsymbol{\Phi}^{(0)}\Omega^{(0)^2}\right) \quad (27.48)$$

Since the factorization of $\boldsymbol{K}^{(0)}$ is already computed and the design changes may be only local, this is not very expensive to compute. These "modal sensitivities" or corrections are directly used to enrich the reduction basis, which is sometimes called the Enriched Craig-Bampton method (ECB) [1]. Physically, these modal corrections can be interpreted as the deformation shapes due to the force residual resulting from the applying the nominal eigensolutions to the modified structure.

In order to retain the sparsity of the reduced matrices, one can decide to orthogonalize the sensitivity modes. This involves both orthogonalization with respect to the nominal vibration modes and mutual orthogonalization by solving the so-called interaction problem. See for instance [18].

27.4.2 Modified Component Reduction Basis

In summary, the Craig-Bampton reduction basis for the modified component consists of:

- Modified static constraint modes $\boldsymbol{\Psi}_C^{(1)}$, obtained from updating the nominal static constraint modes using the PCG method.
- Original fixed interface vibration modes $\boldsymbol{\Phi}_i^{(0)}$, obtained from solving the nominal fixed interface eigenproblem.
- Modal sensitivity vectors $\bar{\boldsymbol{\Phi}}_i^{(1)}$, obtained from the first order perturbation analysis.

Hence, the internal DoF $\boldsymbol{u}_i$ of the modified structure are approximated by:

$$\boldsymbol{u}_i \approx \boldsymbol{\Psi}_C^{(1)}\boldsymbol{u}_b + \boldsymbol{\Phi}_i^{(0)}\boldsymbol{\eta}_i + \bar{\boldsymbol{\Phi}}_i^{(1)}\boldsymbol{\alpha} \quad (27.49)$$
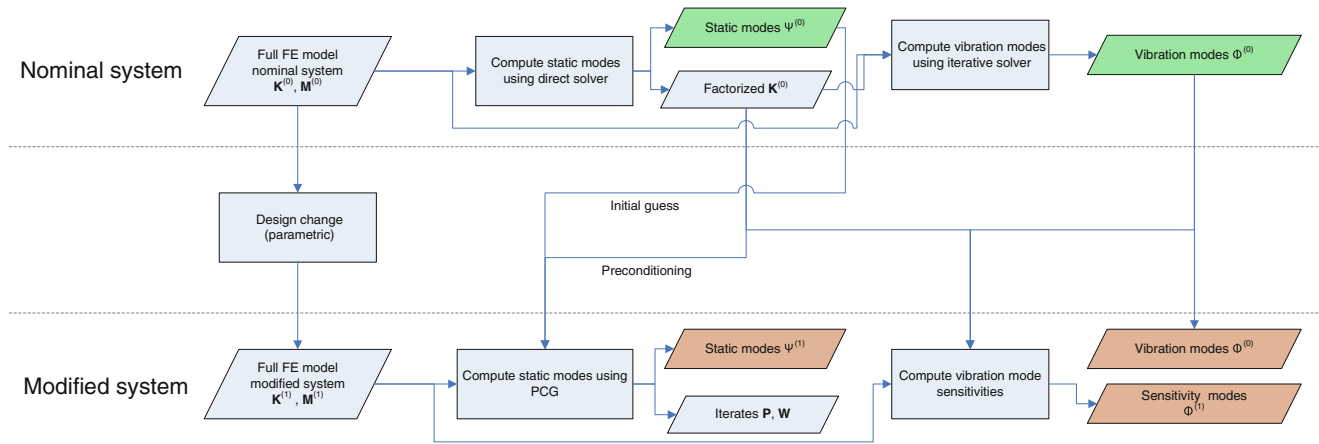
Fig. 27.1 Flowchart for updating of component reduction bases

Where α are the modal amplitudes of the sensitivity modes. As in the nominal Criag-Bampton basis the interface DoF are retained. This transformation can be put into matrix format in order to obtain the updated and enriched Craig-Bampton reduction matrix for the modified component:

$$\begin{bmatrix} u_b \\ u_i \end{bmatrix} = \begin{bmatrix} u_b \\ \Psi_C^{(1)} u_b + \Phi_i^{(0)} \eta_i + \Phi_i^{(1)} \alpha \end{bmatrix} = \begin{bmatrix} I & 0 & 0 \\ \Psi_C^{(1)} & \Phi_i^{(0)} & \Phi_i^{(1)} \end{bmatrix} \begin{bmatrix} u_b \\ \eta_i \\ \alpha \end{bmatrix} = R^{(1)} q \qquad (27.50)$$

The updating method is summarized in Fig. 27.1, where the blocks shown in green are the ingredients used in the original component reduction basis while the orange blocks form the reduction basis for modified component.

27.5 Case Study

27.5.1 Structure and Design Modifications

The structure taken for the case study is a so called bedframe from a modern multi-megawatt wind turbine. The bedframe is the central part of the nacelle and supports the wind turbine drive train. Common practice among wind turbine manufacturers is to base new wind turbine models on existing designs by changing the rotor diameter and/or rated generator power. In the design process, the nominal components from the original turbine are subjected to small design modifications such that they have sufficient capacity to withstand the loads associated with the new rotor and/or generator. This design approach also holds for the bedframe considered here.

Three finite element models have been created for the bedframe structure, only differing in their mesh size. These models will be referred to as the "coarse", "normal" and "fine" models, respectively, and their properties are listed in Table 27.1. Considering three FE models allows to study the influence of the model size on the effectiveness of the iterative CG method.

All three finite element models are meshed using quadratic (i.e. ten-node) tetrahedral elements with only translational nodal DoF. Note that this somewhat simplifies the analysis, as difficulties with scaling of rotational DoF are avoided. The normal finite element model of the nominal bedframe structure is shown in Fig. 27.2. The interfaces of the bedframe considered here are the red areas shown in the topview plot. At these locations, the so-called yaw system is connected. Each interface consists of multiple nodes which for simplicity have been replaced by a single 6 DoF master node by assuming the interface region behaves rigidly. In total, this leads to 24 interface DoF, regardless of the mesh size.

To resemble realistic situations, the bedplate structure is subjected to the following design modifications:

Case 1 – Global geometric change in *x*, *z* directions The complete bedframe geometry is modified to grow in the global *x* (width) and *z* (thickness) directions; both directions are scaled by the same factor. The length of the bedframe as well as its structural properties, such as the Young's modulus, Poisson ratio and density, remain constant. In order to study the effect of

Table 27.1 Bedplate FE model properties

	Coarse	Normal	Fine
# DoF	123.459	246.762	511.953
# Elements	23.651	49.882	107.681
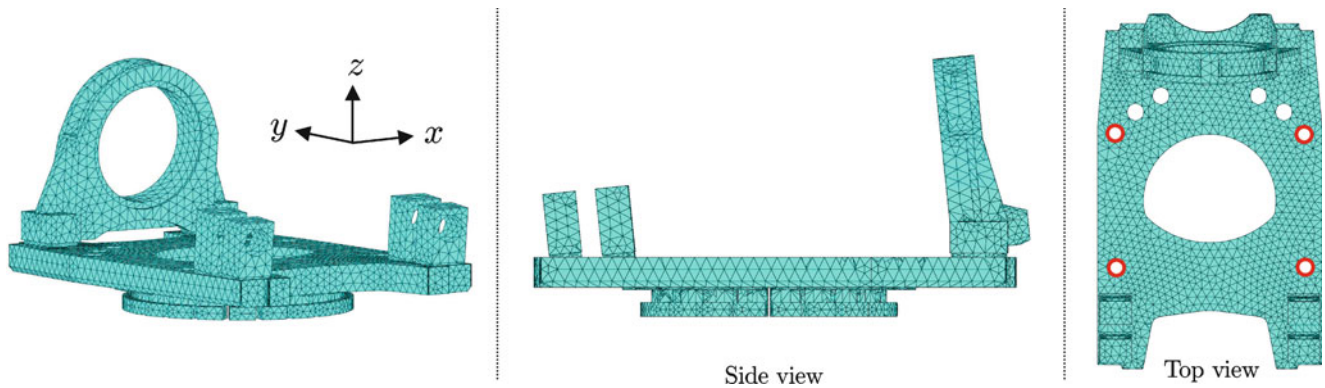
Fig. 27.2 Finite element model of bedframe structure
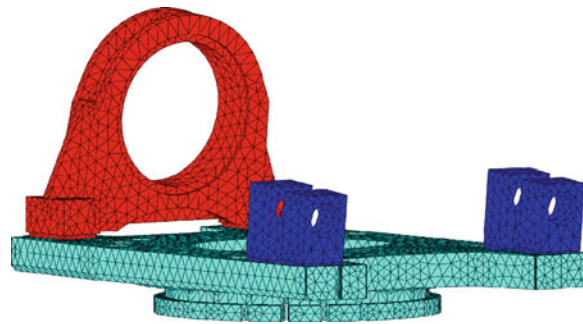
Fig. 27.3 Division of the bedframe finite element model into three parts

the magnitude of the design change, the following series of 15 scaling factors is used: [1.005, 1.01, 1.02, 1.03, 1.04, 1.05, 1.075, 1.10, 1.125, 1.15, 1.20, 1.25, 1.30, 1.40, 1.50]. This means that for each FE model 15 modified variants will be created.

Case 2 – Local material property change For this case the structure is divided into three parts as shown in Fig. 27.3: the bedplate (green), bearing housing (red, designated by "mb") and gearbox supports (blue, designated by "gs"). Two variants are considered for each FE model, namely where the material properties of the bearing housing and gearbox supports are individually changed from steel to aluminium. The material properties used for both materials are listed in Table 27.2.

In order to quantify the effect of the set of design changes described above, we define the following metrics based on the Frobenius norm of the structural matrices:

$$\boldsymbol{\delta}_K = \frac{\|\Delta \boldsymbol{K}\|}{\|\boldsymbol{K}^{(0)}\|} \quad \text{and} \quad \boldsymbol{\delta}_{\mathrm{M}} = \frac{\|\Delta \boldsymbol{M}\|}{\|\boldsymbol{M}^{(0)}\|} \tag{27.51}$$

Since the models at hand only consist of translational DoF, these numbers can be roughly interpreted as the factor by which the global stiffness and mass properties have changed by the design modification.

Table 27.2 Material properties

	Density [kg/m³]	Young's modulus [*GPa*]	Poisson ration [−]
Steel	7,850	210	0.30
Aluminium	2,700	70	0.35
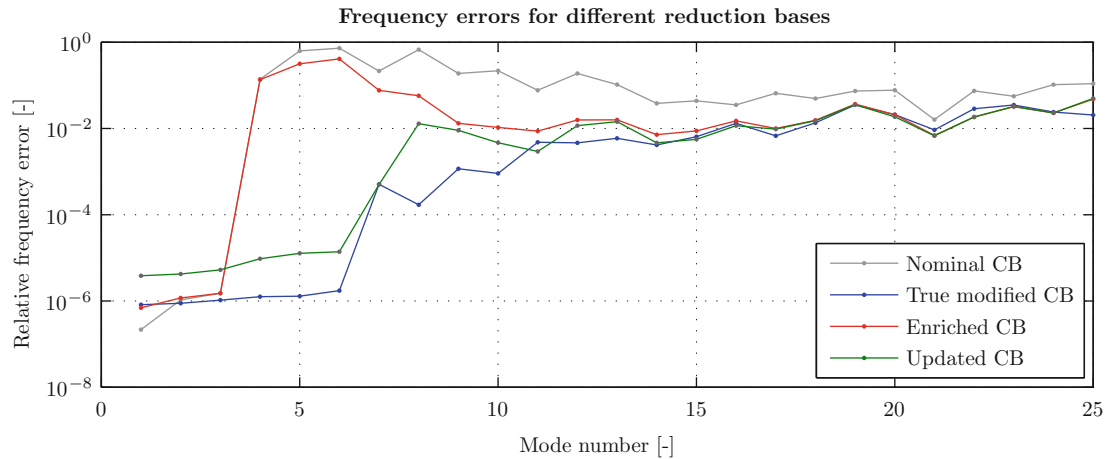
Fig. 27.4 Frequency errors for different reduction bases for normal FE model, case 1 – (*x*, *z*) scaling by 10%

In the remainder of this section we first illustrate the need for accurate updating of the static modes through a comparison with the ECB method [13]. Thereafter we present in Sect. 27.5.3 the results for the updating of the static modes, where we will address how the block size, design modification and model size affect the results. Finally, we note that all calculations are performed in MATLAB R2009b on a quad-core Intel Xeon machine running Windows XP64.

27.5.2 Importance of Accuracy of Static Modes

In order to illustrate the need for an accurate and efficient updating method for the static modes, we first show the difference between a modified component reduced using the ECB method and the updated/enriched basis proposed in (27.51). As explained before, the only difference between these reduction bases is that in the ECB method the static modes of the nominal component are applied to the modified component, whereas in our approach the static modes are updated to suit the modified component. The vibrational information is the same in both bases.

For this comparison the normal FE model (250k DoF) is taken and subjected to design modification case 1, variant 8 (i.e. 10% scaling in global *x* and *z* directions), which was considered a realistic testcase. This model is reduced using the nominal CB reduction basis, the true modified reduction basis, the ECB basis and the updated CB basis. This creates four reduced models of which the eigenfrequencies are computed and compared. The results are shown in Fig. 27.4.

Since the model is free-floating, the first six eigensolutions should be rigid body modes at (approximately) 0 Hz. However, as mentioned before, inaccuracies in the static modes can cause the rigid body modes to shift to higher frequencies. Therefore, the frequencies of the first six modes in Fig. 27.4 are normalized by the first true flexible frequency. For modes 7 and higher the difference between the full and reduced model frequency is plotted, normalized by the corresponding full model frequency. From Fig. 27.4 a number of observations can be made:

- Both the nominal CB and ECB bases are unable to properly describe the rotational rigid body modes of the modified reduced model. This severely handicaps the use of these models in an assembled model, as rigid motions already cause reaction forces to neighboring components.
- Sufficient accuracy of the static modes is also important to properly represent the first few flexible modes.
- Adding sensitivity modes to the basis helps the accuracy of the higher eigenfrequencies, as can be seen from the difference between the ECB method and applying the nominal CB basis to the modified component.

Table 27.3 CPU times for direct calculation of static modes

	Coarse	Normal	Fine
Factorization [s]	11	50	260
Backsubstitution [s]	2	5	16
Total direct [s]	**13**	**55**	**276**
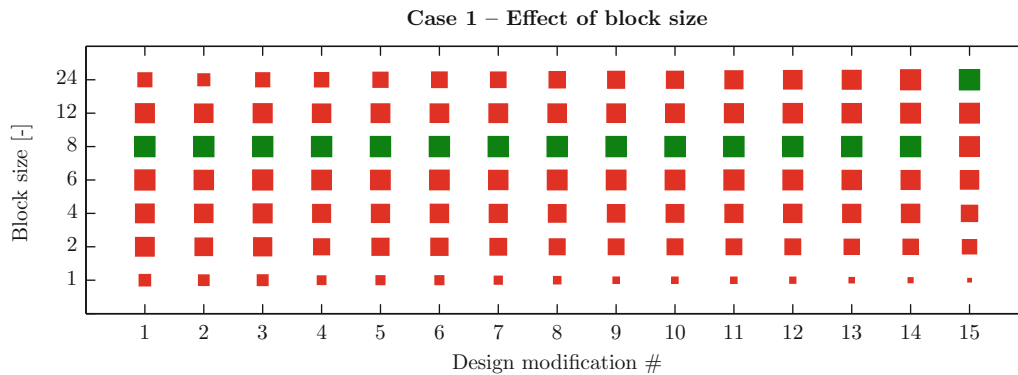
Fig. 27.5 Relative CPU time versus block size

- The updated basis presented here gives only slightly less accurate results than the true recomputed CB basis. Depending on its computational efficiency, the method could be very promising.

This comparison emphasizes the need to accurately represent the static modes in the component reduction basis. As mentioned earlier, this can be done by direct computation (requiring refactorization of the stiffness matrix) or using the iterative CG method proposed here. In order for the latter method to be successful, its computational cost must be lower. This will be investigated next, where the main comparison criterion will be CPU time.

27.5.3 Efficiency of Updating of Static Modes

The test structure has 24 interface DoF, hence we need to compute 24 static constraint modes. In order to obtain the static modes for the nominal component we apply a compiled direct solver based on sparse LDLt-type decomposition. This solver is part of the SD Toolbox [2]. For the three FE models, Table 27.3 lists the solver's computation times for the factorization of the stiffness matrix and backsubstitution to obtain the 24 static modes.

After performing the design modifications as outlined before and rebuilding the finite element matrices, we wish to compute the static modes of the modified structures using an implementation of Algorithm 2. In all subsequent calculations the relative iteration tolerance is set to $\varepsilon = 10^{-6}$.

27.5.3.1 Effect of Algorithm Settings

In the block CG algorithm shown in Algorithm 2 the block size used in the iterations can be freely chosen. In order to assess the influence of the block size on the efficiency of the CG solver, the normal FE model is taken and analyzed for all design modifications in case 1 and different block sizes ranging from 1 to 24. Figure 27.5 shows the results for the relative CPU time for each design modification, i.e. the CPU time for a specific block size divided by the lowest CPU time for that design modification. The size of the markers is inversely proportional to the relative CPU time, while the green markers indicate lowest CPU time.

Furthermore, taking case 1, design modification 8 (i.e. 10% scaling in global x and z directions) the effect of varying the block size is listed in Table 27.4.

Table 27.4 Effect of block size for normal FE model, case 1 – (x, z) scaling by 10%

Block size	CPU time [s]	# iterations	# vectors
1	105	141	141
2	69	77	144
4	63	43	149
6	54	28	148
8	51	22	150
12	59	15	175
24	68	11	195

From these results we observe the following:

- For the current implementation and calculation setup, in the majority of cases a block size of 8 is the most efficient choice. This seems to be independent of design modification and model size, as similar results are found for the coarse and fine FE model (not shown here).
- As speculated in Sect. 27.3.4.2, the block algorithm is always more CPU efficient than its single vector equivalent, even for a block size of 2.
- From a memory usage perspective the single vector algorithm is least demanding, as it finds the solution using the lowest number of search directions. However, these differences are rather small compared to the differences in CPU time.
- The block size times the number of iterations is in general not equal to the total number of vectors used in the approximation space, due to the fact that converged vectors have been removed from the iteration blocks.

Following these results, all subsequent calculations using the block CG method are performed with a block size of 8.

27.5.3.2 Effect of Design Modification and Model Size

As mentioned before, the most important criterion for the practical applicability of the updating strategy is its computational cost compared to that of direct methods for realistic design modifications. In order to assess this, the three finite element models are subjected to the design changes described in Sect. 27.5.1. The results are presented in Fig. 27.6 where the relative CPU time is plotted as a function of the intensity of the design change, expressed by δ_K as defined in (27.52). The relative CPU time is defined as the actual CPU time divided by the CPU time needed for the direct solver (see Table 27.3).

Furthermore, for each of the two design change cases we have chose one representative variant and provided detailed results in Table 27.5. For case 1 a global scaling of 10% was deemed realistic, while for case 2 the material change of the bearing housing is considered.

Based on Fig. 27.6 and Table 27.5, a number of observations and remarks can be made:

- From the results of case 1 it appears that a somewhat linear relation seems to exist between δ_K and the CPU time, regardless of the model size.
- With increasing model size the updating approach becomes relatively more efficient. This is due to the fact that factorization of the sparse stiffness matrix takes in the order of nb^2 floating point operations, where n is the model size and b the matrix' diagonal bandwidth [6]. Backsubstitution requires an additional nb operations, leading to a total of the order of $nb^2 + nb$ operations for the direct solver. From Table 27.5 we see that the number of CG iterations needed for convergence is not dependent on the model size. Hence the number of matrix-vector multiplications, each requiring of the order of nb operations, is constant and the total number of operations is of the order of nbm, where m is the number of iterations. In both cases the number of operations, and hence the computation time, scales linearly with the model size n. However, the matrix bandwidth b also increases with a smaller mesh size. Since the computational cost of the direct solver depends quadratically on b while the CG solver's cost depends only linearly, it is clear that for larger models the iterative method becomes more and more attractive.
- For the global modifications, the top plot in Fig. 27.6 can be used to determine the "break-even" point, i.e. the δ_K values and scaling factors for which the CPU time of the CG solver is equal to that of the direct solver (relative CPU time equal to 1) (Table 27.6).
- Local modifications can be handled much more efficiently then global changes even though the corresponding δ_K values are larger. In fact, for the two local modifications tested here, the updating approach is always more efficient then the direct method.
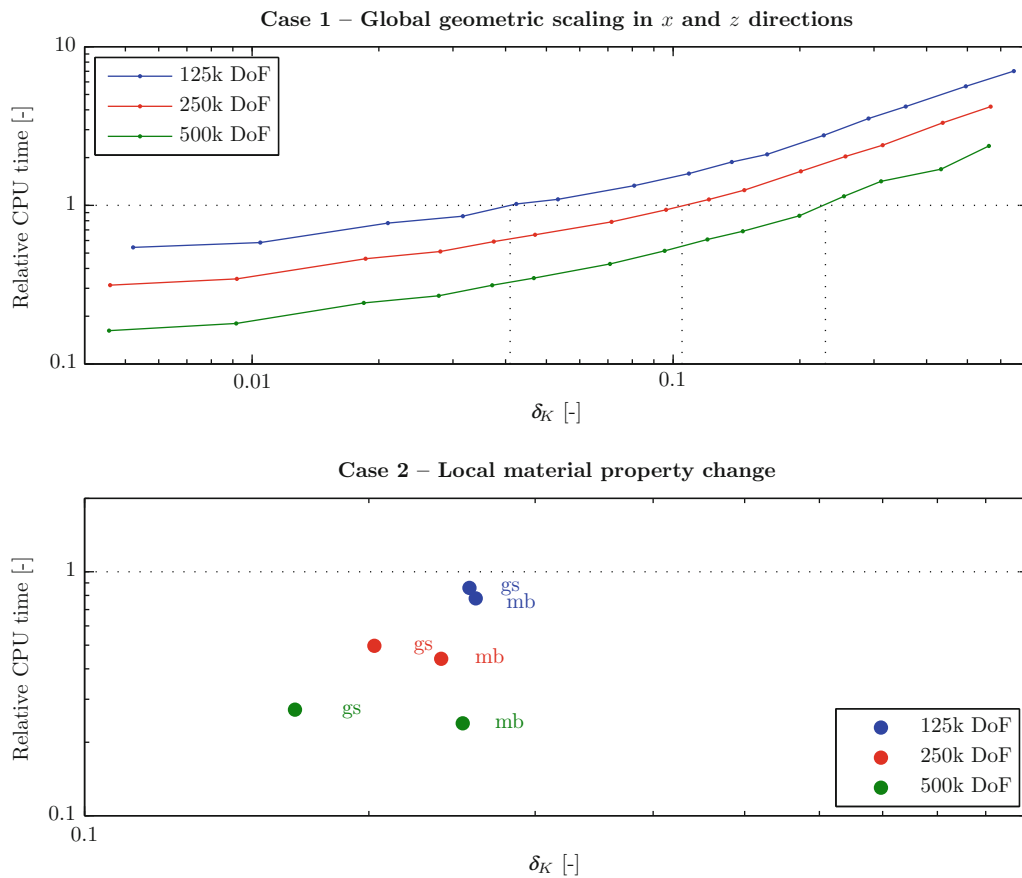
Fig. 27.6 Relative CPU time versus intensity of design modification

Table 27.5 Static modes updating results for three realistic cases

Design change		δ_K	CPU [s]	# iterations	# vectors	Rel. CPU [−]
Case 1 – 10%	Coarse	0.109	20	22	150	1.6
	Normal	0.096	51	22	150	0.9
	Fine	0.096	142	23	152	0.5
Case 2 – mb	Coarse	0.260	10	13	77	0.8
	Normal	0.239	24	12	76	0.4
	Fine	0.252	66	12	76	0.2

Table 27.6 Break even points for updating of static modes

Coarse		Normal		Fine	
δ_K	scale %	δ_K	scale %	δ_K	scale %
0.041	4	0.105	11	0.230	23

- In practice a design modification where the structure's dimensions are scaled by 50% is not realistic. In that case one either creates a new model or sequentially applies smaller design changes of for instance 10% scaling. In the latter case, one can use the updating approach combined with previous CG iterates to enhance the preconditioning. Although out of the scope of this work, an important aspect is then the selection of the most relevant parts of the old iterates for the current problem. See for instance [19, 16, 17, 7, 15].

27.6 Conclusions and Recommendations

Application of component model reduction techniques such as the Craig-Bampton method can be troublesome in practical design settings due to the need to recompute the component reduction basis when the model is subject to design modifications. Especially the static modes in this basis need to be adapted to the modified model in order to represent the rigid body modes and interaction with neighboring components.

In this paper a method was proposed for updating the static modes in the Craig-Bampton component model reduction method. The method is based on a preconditioned conjugate gradient method and reuses the factorization of the nominal stiffness matrix and nominal static modes. Furthermore, the enrichment strategy from the Enriched Craig-Bampton method was adopted to account for the modified component's dynamics by adding modal sensitivity vectors to the reduction basis. A case study was performed to test the proposed methodology.

From the results it can be concluded that proper description of the modified static modes is crucial to the reduced model accuracy, confirming the need for the proposed updating method. In many realistic cases the updating method also proved to be more computationally efficient than direct recomputation of the static modes. Depending on the intensity of the design change and the size of the model, the updating method is up to five times faster than recomputation. In addition, the enrichment method proved to give sufficient accuracy on the higher vibration modes for a realistic design change. It can therefore be concluded that the proposed method is an attractive alternative to both recomputation of the basis and existing reanalysis methods.

However, the method loses its strength for larger design changes and/or multiple parametric variations. In that case, the modal sensitivity vectors are not sufficient to describe the modified dynamics and/or the reduction basis needs to be enriched by so many modes that it loses its compactness. In that case an iterative updating strategy, similar to that devised here for the static modes, might be more efficient. Research on this topic is ongoing.

References

1. Akcay Perdahcioglu D, Ellenbroek M, Geijselaers H, de Boer A (2010) Updating the craig-bampton reduction basis for efficient structural reanalysis. Int J Numer Method Eng 85(5):607–624
2. Balmès E, Bianchi J, Leclère J (2011) Structural dynamics toolbox & FEMLink – user's guide. France
3. Cerulli C, van Keulen F, Rixen D (2007) Dynamic reanalysis and component mode synthesis to improve aircraft modeling for loads calculation. In: Structures, structural dynamics and material conference and exhibit. 15th AIAA/ASME/AHS adaptive structures conference, Waikiki, Hawaii
4. Craig R, Bampton M (1968) Coupling of substructures for dynamic analysis. AIAA J 6(7):1313–1319
5. Feng Y, Owen D, Peric D (1995) A block conjugate gradient method applied to linear systems with multiple right-hand sides. Comput Method Appl Mech Eng 127:203–215
6. Golub G, van Loan C (1996) Matrix computations, 3rd edn. John Hopkins, London
7. Gosselet P, Rey C (2002) On a selective reuse of Krylov subspaces in Newton-Krylov approaches for nonlinear elasticity. In: Fourteenth conference on domain decomposition methods. National Autonomous University of Mexico (UNAM), Mexico, pp 419–426
8. Guyan R (1965) Reduction of stiffness and mass matrices. AIAA J 3:380
9. Hestnes MR, Stiefel E (1952) Method of conjugate gradients for solving linear systems. J Res Nat Bur Stand 49:409–438
10. Hurty WC (1960) Vibrations of structural systems by component mode synthesis. J Eng Mech Div Am Soc Civ Eng 86(4):51–69
11. Hurty W (1965) Dynamic analysis of structural systems using component modes. AIAA J 3(4):678–685
12. Kirsch U (2008) Reanalysis of structures. A unified approach for linear, nonlinear, static and dynamic systems. Solid mechanics and its applications, vol 151. Springer, The Netherlands. doi:10.1007/978-1-4020-8198-9
13. Masson G, Brik BA, Cogan S, Bouhaddi N (2006) Component mode synthesis (CMS) based on an enriched ritz approach for efficient structural optimization. J Sound Vib 296(4–5):845–860
14. O'Leary DP (1980) The block conjugate gradient algorithm and related methods. Linear Algebra Appl 29:293–322. doi:10.1016/0024-3795 (80)90247-5
15. Parks ML, Sturler ED, Mackey G, Johnson DD, Maiti S (2004) Recycling Krylov subspaces for sequences of linear systems. Tech rep, SIAM J Sci Comput
16. Rey C, Devries F, Lene F (1995) Parallelism in non linear computation of heterogeneous structures. Calc Parallèles 7(3)
17. Risler F, Rey C (1998) On the reuse of Ritz vectors for the solution to nonlinear elasticity problems by domain decomposition methods. In: Tenth international conference on domain decomposition methods, contemporary mathematics. American Mathematical Society, Providence
18. Rixen D (2001) Generalized mode acceleration methods and modal truncation augmentation. In: Structures, structural dynamics and material conference and exhibit. 42st AIAA/ASME/ASCE/AHS/ASC, Seattle. AIAA 2001-1300
19. Roux FX (1995) Parallel implementation of a domain decomposition method for non-linear elasticity problems. In: Keyes D, Saad Y, Truhlar (eds) Domain-based parallelism and problem decomposition methods in computational science and engineering. SIAM, Philadelphia, pp 161–175

20. Saad Y (1987) On the Lanczos method for solving symmetric linear systems with several right-hand sides. Math Comput 48:651–662
21. Saad Y (2003) Iterative methods for sparse linear systems, 2nd edn. Society for Industrial and Applied Mathematics, Philadelphia
22. Saad Y, Schultz M (1986) GMRES: a generalized minimal residual algorithm for solving nonsymmetric linear systems. SIAM J Sci Stat Comput 7(3):856–869
23. Sleijpen GL, van der Vorst HA (1995) An overview of approaches for the stable computation of hybrid BiCG methods. Appl Numer Math 19(3):235–254. Special issue on iterative methods for linear equations

Chapter 28
Comparison of CMS, Krylov and Balanced Truncation Based Model Reduction from a Mechanical Application Engineer's Perspective

Wolfgang Witteveen

Abstract Component Mode Synthesis (CMS) is a well known and established method for order reduction of Finite Element (FE) models. One advantage of CMS is a clear physical interpretability and another, more practical one, is the availability in common FE packages. In the last years a lot of research has been done, in order to adapt reduction methods, which are based on Krylov subspaces and balanced truncation for FE models. Several recent publications denote mode based reduction methods, like CMS, as out-dated while the latter ones are so called 'modern methods'. For a mechanical application engineer the question arises, whether these methods are really so advantageous, that the reliable CMS should be exchanged against one of the two other methods.

This paper is devoted to a numerical and qualitative comparison of these three methods with respect to each other. The contribution starts with an introduction, where the 'mechanical application engineer's perspective' is explained in terms of requirements and boundary conditions of the reduction process. Next, all three approaches will be briefly outlined and representative literature will be cited. In the next chapter, all three methods will be demonstrated by a simple three mass example, so that some basic characteristics can easily be seen and first conclusions can be drawn. In the subsequent section the different methods will be applied to simple FE structures and the quality of the reduced models will be examined. Finally a conclusion will be drawn whether one of the three methods is clear better (or worse) with respect to the other ones.

Nomenclature

$\mathbf{M}$	Stiffness matrix
$\mathbf{K}$	Stiffness matrix
$\mathbf{B}, \mathbf{B}_1$	Input matrix
$\mathbf{C}, \mathbf{C}_1$	Output matrix
$\mathbf{E}, \mathbf{A}$	System matrices for LTI system
$\mathbf{q}$	State space vector
$\tilde{\mathbf{M}}$	Quantity M in reduced model
$\mathbf{u}$	Force vector
$\mathbf{x}$	Nodal DOF vector of FE model
$\mathbf{y}$	Output vector
n	Number of DOF of FE model
u	Number of external forces
y	Number of outputs
m	Number of DOF in reduced model

W. Witteveen (✉)

University of Applied Sciences Upper Austria – Wels Campus, Stelzhammer str. 69, Wels 4600, Austria

e-mail: wolfgang.witteveen@fh-wels.at

p	Number of considered modes
s	Number of static trial vectors
V, W	Subspace for reduction
$\mathbf{V}_D$	Modes gained by an eigenvalue problem
$\mathbf{V}_S$	Static deformation shapes
x_B	Boundary DOF
x_I	Inner DOF
b	Number of boundary DOF
s	Complex laplace variable
$\mathbf{H}(s)$	Transfer function matrix
f	Frequency
ω_i	Eigenfrequency of the i-th mode
ω^*	Eigenfrequency limit
$\mathbf{T}_j^{s_0}$	j-th moment around s_0
$\mathbf{W}_C$	Controllability Gramian matrix
$\mathbf{W}_O$	Observability Gramian matrix
t	Time
T	Particular time instant
σ_i	Hankel Singular Value
r	Number of considered trial vectors

28.1 Introduction and Motivation

Model order reduction is a key issue when the dynamics of Finite Element models is investigated. During the last decades a lot of reduction methods have been proposed. For linear elastic structures with a moderate number of input degrees of freedom (DOF), mode based reductions methods, like Component Mode Synthesis (CMS) have been developed to very reliable standard tools. In the last years a lot of effort has been made in order to adapt model reduction methods for mechanical structures which come from control engineering, namely Krylov subspace and balanced truncation based methods. In some newer publications the latter methods are named as 'modern methods' while the mode based methods are characterized as 'out dated'. For an application engineer the question arises whether the well established and very reliable CMS should be replaced by other methods. This work is devoted to a critical qualitative and numerical comparison of the three methods in the context of industrial use together with solid and lightly damped structures.

Key issues off this comparison are:

- Restriction to conservative systems.
- Sensitivity of the reduced system with respect to boundary conditions at the input/output DOF (multi body dynamics)
- Static response
- Structure and stability preserving model order reduction
- Full system response (for stress recovery)
- Number of required modes for convergence and parameters in order to select them

28.1.1 Restriction to Conservative Systems

For a wide range of applications in solid mechanics with iron like materials it is sufficient to regard the conservative system for model reduction only. This is because of the nature of the two most frequently involved damping mechanisms, namely joint damping (micro slip) and material damping. Both of them are mainly frequency independed energy dissipation mechanisms, see exemplarily [1] and [2]. Consequently a viscous model does not meet reality, see [3] for joint damping. Consequently, a viscous damping is always a rough approximation in such cases and it does not matter if it is introduced in the full system or in the reduced system. The latter statements are not valid for structures which consists entirely or partially of rubber or other visco-elastic materials. This publication deals with iron like materials where visco-elastic effects do not play an important role.

28.1.2 Sensitivity of the Reduced System with Respect to Boundary Conditions at the Input/Output DOF

One of the most frequent situations when model order reduction of Finite Element models has to be applied is when such structures are implemented in Multi Body Dynamics (MBD). In this particular case an arbitrary interaction of the input/ output DOF with the surrounding rigid or flexible bodies should be possible. In other words, the response of the reduced system has to be sufficient accurate if no stiffness or if infinite stiffness acts on the input/output DOF. Therefore, the response of the reduced system will be investigated in this paper when no stiffness acts on the input/output DOF and when a subset of the input/output DOF are mounted.

28.1.3 Static Response

In mechanics the static response of a system is of special interest. It is not just a theoretical issue as may be in other disciplines. Statics has a special physical meaning and an exact reproduction of the static system behavior is definitely an advantage of a certain reduction method.

28.1.4 Structure and Stability Preserving Model Order Reduction

If a reduced model is used for time integration it is of significant importance, that no instability will be introduced due to the model order reduction. In this particular case, when no damping is regarded the eigenvalues of the reduced model are required to be real such as they are in the original system. For the sake of physical interpretability it is furthermore required that the reduced mass and stiffness matrixes are symmetric such as they are in the full system. This requires, that the input DOF are the same as the output DOF which can be seen in the literature cited below. The investigations here are restricted to such systems.

28.1.5 Full System Response (for Stress Recovery)

Krylov subspace methods and in particular balanced truncation guarantee a defined behavior between the input and output DOF. This is of special interest in control but this is not sufficient in structural mechanics where the place of the highest stress is not known a priory and in general it is not at the location of an input or output DOF. For this reason this publication is not concerned about the input/output transfer behavior. The focus is on the response of the entire structure. As it can be seen in the theory, outlined below, the entire structure cannot be defined as input/output DOF because that would lead to a huge number of trial vectors.

28.1.6 Number of Required Modes for Convergence and Parameters in Order to Select Them

A key quality feature of a reduction method is the number of necessary trial vectors in order to obtain a sufficient accurate result. This issue has to be seen in the context of stress recovery where this convergence issue is more critical as when just displacements will be regarded. That means, error estimation for displacements is not sufficient. Stress and displacement are not necessarily directly connected. Locations with high displacements may have low stresses and vice versa.

Note, that the applicability of the methods for huge FE structures is not part of this publication. Furthermore it is not the meaning of this work to question the importance of the Krylov subspace or balanced truncation based methods for other fields like control engineering. The focus of this work is model reduction for solid mechanics.

There is already a considerable amount of comparative literature available, see exemplarily [4–8]. The latter publications do not have the particular focus on the issues mentioned above.

The paper is organized as follows: In the subsequent section all three approaches will be briefly outlined and representative literature will be cited. In the next chapter, all three methods will be demonstrated by a simple three mass example, so that some basic characteristics can easily be seen and first conclusions can be drawn. In the subsequent section the different methods will be applied to a simple FE structures and the quality of the reduced models will be examined. Finally a conclusion will be drawn whether one of the three methods is clear better (or worse) with respect to the other ones.

28.2 Short Review of Mode Based, Krylov Subspace Based and Balanced Truncation Based Model Order Reduction Methods

The Finite Element Method (FEM) leads to an equation of motion in the form of

$$
\begin{aligned}
\mathbf{M}\ddot{\mathbf{x}} + \mathbf{K}\mathbf{x} &= \mathbf{B}_1\mathbf{u} \\
\mathbf{y} &= \mathbf{C}_1\mathbf{x}
\end{aligned}
\tag{28.1}
$$

where the (n × n) matrixes $\mathbf{M}$ and $\mathbf{K}$ are the mass and stiffness matrix, the (n × 1) vector $\mathbf{x}$ contains the bodies degrees of freedom, the (u × 1) vector holds the time varying loads, the (n × u) matrix $\mathbf{B}_1$ maps the loads to the corresponding degrees of freedom, the (y × 1) vector $\mathbf{y}$ holds the output of interest and $\mathbf{C}_1$ maps the state variables to the output. In the following a symmetric system is considered with $\mathbf{M} = \mathbf{M}^T$ and $\mathbf{K} = \mathbf{K}^T$.

The corresponding reduced system can be given as

$$
\begin{aligned}
\tilde{\mathbf{M}}\ddot{\mathbf{z}} + \tilde{\mathbf{K}}\mathbf{z} &= \tilde{\mathbf{B}}_1\mathbf{u} \\
\mathbf{y} &= \tilde{\mathbf{C}}_1\mathbf{z}
\end{aligned}
\tag{28.2}
$$

$$
\mathbf{x} = \mathbf{V}\mathbf{z}, \quad \tilde{\mathbf{M}} = \mathbf{W}^T\mathbf{M}\mathbf{V}, \quad \tilde{\mathbf{K}} = \mathbf{W}^T\mathbf{K}\mathbf{V}, \quad \tilde{\mathbf{B}}_1 = \mathbf{W}^T\mathbf{B}_1, \quad \tilde{\mathbf{C}}_1 = \mathbf{C}_1\mathbf{V}
\tag{28.3}
$$

with the n × m matrixes $\mathbf{V}$ and $\mathbf{W}$. Model order reduction deals with the question of determining the matrixes $\mathbf{V}$ and $\mathbf{W}$ so that the reduced system captures somehow the important characteristics of the unreduced system.

System (28.1) can be transformed into a LTI system in standard state space representation:

$$
\begin{aligned}
\mathbf{E}\dot{\mathbf{q}} &= \mathbf{A}\mathbf{q} + \mathbf{B}\mathbf{u} \\
\mathbf{y} &= \mathbf{C}\mathbf{q}
\end{aligned}
\tag{28.4}
$$

$$
\mathbf{q}^T = \begin{bmatrix} \mathbf{x}^T & \dot{\mathbf{x}}^T \end{bmatrix}, \quad \mathbf{B} = \begin{bmatrix} \mathbf{0} \\ \mathbf{B}_1 \end{bmatrix}, \quad \mathbf{C} = \begin{bmatrix} \mathbf{C}_1 & \mathbf{0} \end{bmatrix}, \quad \mathbf{E} = \begin{bmatrix} \mathbf{I} & \mathbf{0} \\ \mathbf{0} & \mathbf{M} \end{bmatrix}, \mathbf{A} = \begin{bmatrix} \mathbf{0} & \mathbf{I} \\ -\mathbf{K} & \mathbf{0} \end{bmatrix}
\tag{28.5}
$$

In [9] a little modification of (28.4) is suggested, so that symmetric system matrixes are obtained in case of a symmetric system (28.1).

$$
\begin{aligned}
\mathbf{E}^*\dot{\mathbf{q}} &= \mathbf{A}^*\mathbf{q} + \mathbf{B}\mathbf{u} \\
\mathbf{y} &= \mathbf{C}\mathbf{q}
\end{aligned}
\tag{28.6}
$$

$$
\mathbf{E}^* = \begin{bmatrix} -\mathbf{K} & \mathbf{0} \\ \mathbf{0} & \mathbf{M} \end{bmatrix}, \quad \mathbf{A}^* = \begin{bmatrix} \mathbf{0} & -\mathbf{K} \\ -\mathbf{K} & \mathbf{0} \end{bmatrix}
\tag{28.7}
$$

The according reduced system is

$$
\begin{aligned}
\tilde{\mathbf{E}}\dot{\tilde{\mathbf{q}}} &= \tilde{\mathbf{A}}\tilde{\mathbf{q}} + \tilde{\mathbf{B}}u \\
\mathbf{y} &= \tilde{\mathbf{C}}\tilde{\mathbf{q}}
\end{aligned}
\tag{28.8}
$$

$$
\tilde{\mathbf{q}} = \mathbf{V}\mathbf{q}, \quad \tilde{\mathbf{E}} = \mathbf{W}^T\mathbf{E}\mathbf{V}, \quad \tilde{\mathbf{A}} = \mathbf{W}^T\mathbf{A}\mathbf{V}, \quad \tilde{\mathbf{B}} = \mathbf{W}^T\mathbf{B}, \quad \tilde{\mathbf{C}} = \mathbf{C}\mathbf{V}
\tag{28.9}
$$

28.2.1   Mode Based Approach

A mode based reduction procedure is typically directly applied to the second order system (28.1). In order to preserve the symmetric structure and the stability characteristics a so called symmetric or 'one sided' projection $\mathbf{W} = \mathbf{V}$ has to be applied. Commonly, the reduction matrixes are of the form

$$\mathbf{V} = \begin{bmatrix} \mathbf{V}_S & \mathbf{V}_D \end{bmatrix} \tag{28.10}$$

where the trial vectors in the (n × p) matrix $\mathbf{V}_D$ are vibration modes which capture the systems dynamics. These modes are obtained by a proper eigenvalue problem which delivers an additional eigenfrequency for each mode. For the reduction process just these p modes (p ≪ n) are regarded having an eigenfrequency which is in the range of the frequency spectra of external excitation forces, see [10–12].

In order to improve the convergence, some static trial vectors are added to the vibration modes. This is of particular importance in case of stress recovery, see [13]. The latter modes are collected in the columns of the (n × s) matrix $\mathbf{V}_S$.

During the last decades a lot of methods for the computation of $\mathbf{V}$ have been suggested, see [10–12]. One of the best known and a widely used approach is the one of Craig (and Bampton), see [14]. For this publication the latter method is chosen to represent the family of 'mode based' reduction methods.

The vector of nodal DOF of the FE model (28.1) is subdivided into

$$\mathbf{x}^T = \begin{bmatrix} \mathbf{x}_B{}^T & \mathbf{x}_I{}^T \end{bmatrix} \tag{28.11}$$

where the (b × 1) Vector $\mathbf{x}_B$ represents the ‚boundary'DOF and the ((n−b) × 1) vector $\mathbf{x}_I$ holds the emaining ‚inner'DOF. The boundary DOF are defined, as those DOF on which external forces may be applied. In terms of the system (28.1), the input matrix B_1 contains non zero entries at these DOF.

According to the subdivision (28.11), an eigenvalue problem in the form of

$$\left[\mathbf{K}_{I,I} - \omega_i{}^2 \mathbf{M}_{I,I} \right] \mathbf{v}_{D,i} = \mathbf{0} \tag{28.12}$$

can be solved. Because the boundary DOF are fixed, the obtained modes $\mathbf{v}_{D,i}$ are named as ‚Fixed Boundary Normal Modes'. The matrix of vibration modes can be given as

$$\mathbf{V}_D = \begin{bmatrix} \mathbf{0} & \mathbf{0} & \mathbf{0} & \mathbf{0} \\ \mathbf{v}_{D,1} & \mathbf{v}_{D,2} & \cdots & \mathbf{v}_{D,p} \end{bmatrix} \tag{28.13}$$

with an user defined eigenfrequency limit ω^* so that

$$\omega_p < \omega^* \tag{28.14}$$

The latter limit is usually connected to the highest relevant frequency content of the excitation. Die Matrix $\mathbf{V}_S$ is obtained according to a Guyan reduction

$$\mathbf{V}_S = \begin{bmatrix} \mathbf{I} \\ -\mathbf{K}_{I,I}{}^{-1}\mathbf{K}_{I,B} \end{bmatrix} \tag{28.15}$$

with the identity matrix $\mathbf{I}$. Obviously, each boundary DOF introduces a trial vector in $\mathbf{V}_S$. These strategy leads to difficulties in case of distributed loads when the number of b is very high. In such a case the space spanned by $\mathbf{V}_S$ can be approximated by a space with a lower dimension as b, see exemplarily [15] and [16].

Due to the clear physical meaning of the displacement fields and eigenvalues it is a nice and important feature of CMS, that measurements and experience can be directly used to evaluate the quality of the model and the projection base.

28.2.2 Krylov Subspace Based Approach

With the Laplace transformation the transfer function of the system (28.4) can be given as

$$\mathbf{H}(s) = \mathbf{C}(s\mathbf{E} - \mathbf{A})^{-1}\mathbf{B} \tag{28.16}$$

where s holds the complex Laplace variable, see [17–21]. An approximation of (28.16) with a Power Series around s_0 gives

$$H(s) = \sum_{j=0}^{\infty} \mathbf{T}_j^{s_0}(s_0 - s)^j \tag{28.17}$$

with the so called j-th moment $\mathbf{T}_j^{s_0}$ ([20]).

$$\mathbf{T}_j^{s_0} = \mathbf{C}\left((s_0\mathbf{E} - \mathbf{A})^{-1}\mathbf{E}\right)^j (s_0\mathbf{E} - \mathbf{A})^{-1}\mathbf{B} \tag{28.18}$$

If $\mathbf{W}$ and $\mathbf{V}$ are chosen in such a way, that the spanned space is equal to

$$\begin{aligned}
\mathbf{V} &= \begin{bmatrix} \mathbf{P}_v^{J-1}\mathbf{R}_v & \cdots & \mathbf{P}_v^{1}\mathbf{R}_v & \mathbf{R}_v \end{bmatrix} \\
\mathbf{W} &= \begin{bmatrix} \mathbf{P}_W^{J-1}\mathbf{R}_W & \cdots & \mathbf{P}_W^{1}\mathbf{R}_W & \mathbf{R}_W \end{bmatrix}
\end{aligned} \tag{28.19}$$

with

$$\begin{aligned}
\mathbf{R}_v &= (s_0\mathbf{E} - \mathbf{A})^{-1}\mathbf{B}, & \mathbf{P}_v &= (s_0\mathbf{E} - \mathbf{A})^{-1}\mathbf{E} \\
\mathbf{R}_W &= (s_0\mathbf{E} - \mathbf{A})^{-T}\mathbf{C}^T, & \mathbf{P}_v &= (s_0\mathbf{E} - \mathbf{A})^{-T}\mathbf{E}^T
\end{aligned} \tag{28.20}$$

it can be shown, that the first 2 J moments of the reduced system around s_0 are equal to the ones in the full system.

$$\mathbf{T}_j^{s_0} = \tilde{\mathbf{T}}_j^{s_0} \quad j = 1..2J \tag{28.21}$$

Note, that a direct implementation of (28.19) for the construction of $\mathbf{W}$ and $\mathbf{V}$ is numerically disadvantageous. The literature offers better choices, see exemplarily [19].

If model reduction is performed in order to enable efficient time integration, structure and stability preserving reduction schemes are required. For that reason a symmetric (or one sided) projection with $\mathbf{W} = \mathbf{V}$ is used. In such a case just J moments of the reduced and full model matches [19]. For system (28.6) and the special case that $\mathbf{M} = \mathbf{M}^T$, $\mathbf{K} = \mathbf{K}^T$ and $\mathbf{C}_1^T = \mathbf{B}_1$ it easily can be seen that $\mathbf{W}$ evaluates exactly to $\mathbf{V}$, see (28.20). Note, that in structural mechanics this case is very common.

The transfer function of the second order system (28.1) is

$$\mathbf{H}(s) = \mathbf{C}_1\left(s^2\mathbf{M} - (-\mathbf{K})\right)^{-1}\mathbf{B}_1 \tag{28.22}$$

The formal similarity of (28.22) and (28.16) can be used to obtain the desired quantities in a similar matter. Again $\mathbf{W}$ evaluates to $\mathbf{V}$ in case of a symmetric system ($\mathbf{M} = \mathbf{M}^T$, $\mathbf{K} = \mathbf{K}^T$) where the input is equal to the output ($\mathbf{C}_1^T = \mathbf{B}_1$), see [20].

$$\begin{aligned}
\mathbf{V} &= \begin{bmatrix} \mathbf{P}^{J-1}\mathbf{R} & \cdots & \mathbf{P}^{1}\mathbf{R} & \mathbf{R} \end{bmatrix} \\
\mathbf{R} &= \left(s_0^2\mathbf{M} + \mathbf{K}\right)^{-1}\mathbf{B}_1, \quad \mathbf{P} = \left(s_0^2\mathbf{M} + \mathbf{K}\right)^{-1}\mathbf{M}
\end{aligned} \tag{28.23}$$

The computation of $\mathbf{V}$ in the presence of a damping matrix can be found in [20].

A more mechanical interpretation of the Krylov sequences around $s_0 = 0$ can be found in [22] and [23]. There, each additional Krylov sequence regards the dynamic residua of the already existing Krylov subspace in a quasi-static matter. Note, that in [22] an estimation for the maximum error in the difference of the eigenfrequencies and eigenvectors can be found. This is of particular interest, because no direct error estimation is available, like it is, in the case of balanced truncation.

28.2.3 Balanced Truncation Based Approach

For the introduction of the Gramian matrixes the system (28.4) is considered with $\mathbf{E} = \mathbf{I}$. The conversion into such a system is trivial in case of a non singular $\mathbf{E}$. For a system (28.4) a matrix $\mathbf{W_C}(T)$ can be given, so that, based on this matrix an input signal $\mathbf{u}(t)$ can be computed, in order to reach an arbitrary state $\mathbf{q}(T)$ within the time T starting at $\mathbf{q}_0 = \mathbf{0}$, see [17, 18] and [9, 24–26].

The latter input signal can be given as

$$\mathbf{u}(t) = \mathbf{B}^T e^{-\mathbf{A}^T t} [\mathbf{W_C}(T)]^{-1} e^{-\mathbf{A}T} \mathbf{q}(T) \tag{28.24}$$

with the so called Gramian controllability matrix $\mathbf{W_C}(T)$

$$\mathbf{W_C}(T) = \int_0^T e^{-\mathbf{A}t} \mathbf{B}\mathbf{B}^T e^{-\mathbf{A}^T t} dt \tag{28.25}$$

Further one the L_2-norm for $\mathbf{u}(t)$ according to (28.24) can be given as

$$\|\mathbf{u}(t)\|_2^2 = \mathbf{q}(T)^T [\mathbf{W_C}(T)]^{-1} \mathbf{q}(T) \tag{28.26}$$

Very similar, the Gramian observability matrix $\mathbf{W_O}(T)$ can be given. The matrix $\mathbf{W_O}(T)$ can be used to reconstruct the initial condition $\mathbf{q}_0$ based on an arbitrary output $\mathbf{y}(t)$. This reconstruction can be given as ($\mathbf{u}(t) = 0$):

$$\mathbf{q}_0 = [\mathbf{W_O}(T)]^{-1} \int_0^T e^{\mathbf{A}^T t} \mathbf{C}^T \mathbf{y}(t) dt \tag{28.27}$$

with the Gramian observability matrix

$$\mathbf{W_O}(T) = \int_0^T e^{\mathbf{A}^T t} \mathbf{C}^T \mathbf{C} e^{\mathbf{A}t} dt \tag{28.28}$$

and for the time history of $\mathbf{y}(t)$ the L_2-norm can be given as:

$$\|\mathbf{y}(t)\|_2^2 = \mathbf{q}_0{}^T \mathbf{W_O}(T) \, \mathbf{q}_0 \tag{28.29}$$

Note, that controllability and observability have been assumed for the latter considerations. The particular Gramians $\mathbf{W_C}(\infty)$ und $\mathbf{W_O}(\infty)$ fulfill the Lyapunov equation:

$$\begin{aligned} \mathbf{A}\mathbf{W_C} + \mathbf{W_C}\mathbf{A}^T + \mathbf{B}\mathbf{B}^T &= \mathbf{0} \\ \mathbf{A}^T \mathbf{W_O} + \mathbf{W_O}\mathbf{A} + \mathbf{C}^T \mathbf{C} &= \mathbf{0} \end{aligned} \tag{28.30}$$

In case of $\mathbf{B} = \mathbf{C}^T$ and a symmetric system of the form (28.6), the matrixes $\mathbf{W_C}(\infty)$ and $\mathbf{W_O}(\infty)$ are identical and can be computed by the generalized Lyapunov equation, see [9].

$$\mathbf{E}^* \mathbf{W_C}[\mathbf{A}^*]^T + \mathbf{A}\mathbf{W_C}[\mathbf{E}^*]^T + \mathbf{B}\mathbf{B}^T = \mathbf{0} \tag{28.31}$$

At this point it is important to note, that the systems (28.4) and (28.6) und their Gramians are not unique. With each non singular $(2n \times 2n)$ transformation matrix $\mathbf{T}$ an equivalent but different system in the form of

$$\begin{aligned} \tilde{\mathbf{E}}\dot{\tilde{\mathbf{q}}} &= \tilde{\mathbf{A}}\tilde{\mathbf{q}} + \tilde{\mathbf{B}}\mathbf{u} \\ \mathbf{y} &= \tilde{\mathbf{C}}\tilde{\mathbf{q}} \end{aligned} \tag{28.32}$$

$$\tilde{\mathbf{q}} = \mathbf{T}\mathbf{q}, \;\; \tilde{\mathbf{E}} = \mathbf{T}\mathbf{E}\mathbf{T}^{-1}, \;\; \tilde{\mathbf{A}} = \mathbf{T}\mathbf{A}\mathbf{T}^{-1}, \;\; \tilde{\mathbf{B}} = \mathbf{T}\mathbf{B}, \;\; \tilde{\mathbf{C}} = \mathbf{C}\mathbf{T}^{-1} \tag{28.33}$$

can be constructed. A system is called 'balanced' when the Gramians are diagonal matrixes and $\mathbf{W}_C = \mathbf{W}_O$. This 'balanced' realization and the corresponding transformation is unique. For the balanced system, equation (28.26) evaluates to

$$\|\mathbf{u}(t)\|_2^2 = \tilde{\mathbf{q}}(T)^T \begin{bmatrix} \frac{1}{\sigma_1} & & \\ & \ddots & \\ & & \frac{1}{\sigma_{2n}} \end{bmatrix} \tilde{\mathbf{q}}(T) = \tilde{\mathbf{q}}_1(T)\frac{1}{\sigma_1}\tilde{\mathbf{q}}_1(T) + \dots\dots + \tilde{\mathbf{q}}_{2n}(T)\frac{1}{\sigma_{2n}}\tilde{\mathbf{q}}_{2n}(T) \tag{28.34}$$

with $\sigma_1 > \sigma_2 > \dots > \sigma_{2n}$. Equation (28.34) gives insight how the energy of the input signal (force) is distributed among the states which corresponds to the vectors of $\mathbf{T}^{-1}$. A small σ_j leads to a large σ_j^{-1} and that means, that the vector i needs a lot of energy from the input signal to be controlled. Equation (28.29) can be given as

$$\|\mathbf{y}(t)\|_2^2 = \tilde{\mathbf{q}}_0^T \begin{bmatrix} \sigma_1 & & \\ & \ddots & \\ & & \sigma_{2n} \end{bmatrix} \tilde{\mathbf{q}}_0 = \tilde{\mathbf{q}}_{0,1}\sigma_1\tilde{\mathbf{q}}_{0,1} + \dots\dots + \tilde{\mathbf{q}}_{0,2n}\sigma_{2n}\tilde{\mathbf{q}}_{0,2n} \tag{28.35}$$

and shows how the energy of the output signal depends from the states which corresponds to the vectors of $\mathbf{T}^{-1}$. A large value of σ_j means, that the energy of the output signal is strongly influenced by this particular state. The idea of balanced truncation is, to use just these states which need low energy to be controlled from the input and which give a lot of energy to the output. Note, that the so called Hankel singular values σ_1 to σ_{2n} decrease quickly for common mechanical structures so that just a view columns of the transformation matrix needs to be considered as trial vectors for the model reduction. A special feature of this approach is an a-priori error bound in the form of

$$\|\mathbf{y} - \tilde{\mathbf{y}}\|_2 \leqslant \delta_{BT}\|u\|_2 \tag{28.36}$$

with

$$\delta_{BT} = 2\sum_{j=r+1}^{2n} \sigma_j \tag{28.37}$$

and r as the number of the last considered trial vector, see [18].

For the implementation of balanced truncation several methods have been proposed, even for large structures, and directly to second order systems see [17, 18] and [9, 24–26]. Note that balanced truncation for systems with a large number of inputs and outputs still an active field of research. A more recent publication on that issue can be found in [27].

It is important to note, that there is a relation between balanced truncation and the vibration modes in case of an undamped system. In [28] and [17] it can be seen that the balanced controllability and observability Gamian can be computed (or low rank approximated) by the POD snapshot technique and in [29] it is shown, that the POD snapshot modes are identical with the vibration modes of a conservative and symmetric system like (28.1). Of course, just 'sufficient controllable' and 'sufficient observable' modes will form the base of Ritz vectors. This can be observed in the numerical examples below.

Note furthermore, that the Gramians obtained by the Lyaponov equations consider all frequencies. It is possible to compute or approximate the Gramians just for the frequencies of interest, see [17] or [28].

In some publications the connection of the Krylov subspace method together with balanced truncation has been suggested. In [30] it is suggested that the Krylov subspace method should be used to transform a huge system into a system of moderate size. In a second step balanced truncation will be applied in order to transform the moderate system into a system of small size.

28.2.4   Error Quantities

Three very simple error quantities will be used in this presentation, namely:

- The modal assurance criterion (MAC)
- The relative difference of the eigenvalues of the reduced and full system
- The difference of the according normalized eigenvectors

Due to these simple error norms, a very high accuracy is demanded for a satisfying performance. The modal assurance criterion (MAC) between an vector $\mathbf{v}_i$ and $\mathbf{w}_j$ is defined as

$$\text{MAC}(\mathbf{v}_i, \mathbf{w}_j) = \frac{\left(\mathbf{v}_i^T \ \mathbf{w}_j\right)^2}{\left(\mathbf{v}_i^T \ \mathbf{v}_i\right)\left(\mathbf{w}_j^T \ \mathbf{w}_j\right)} \tag{28.38}$$

The relative difference of the eigenfrequencies between the full and the reduced system is defined as

$$\varepsilon_i = \frac{\tilde{\omega} - \omega_i}{\omega_i} \tag{28.39}$$

Finally, the difference between the eigenvectors of the full and reduced systems is given by the Euclidian norm

$$\beta_i = \|\tilde{\boldsymbol{\varphi}}_i - \boldsymbol{\varphi}_i\|_2 \tag{28.40}$$

where $\boldsymbol{\varphi}_i$ holds the normalized i-th eigenvector of the full or the reduced system. This quantity will be used to measure the difference of static deflection shapes as well. In that case $\boldsymbol{\varphi}_i$ stands for a deflection due to a static load and the quantity is denoted as $\boldsymbol{\beta}_S$.

28.3 Simple 3 Mass Example

For qualitative considerations of the three reduction methods a system of three masses (DOF) will be investigated, see Fig. 28.1.

As output and input DOF, mass 1 is selected. All computations have been performed with the software package Scilab [31]. The system parameters are given as $c = 1$, $m_i = 1$ and $c^* = 1$. Three eigenfrequencies can be computed to $f_1 = 0.082$ Hz, $f_2 = 0.159$ Hz and $f_3 = 0.307$ Hz with the according eigenvectors $\boldsymbol{\varphi}_1^T = [-0.628 \ -0.46 \ -0.628]$, $\boldsymbol{\varphi}_2^T = [-0.707 \ 0 \ 0.707]$ and $\boldsymbol{\varphi}_3^T = [0.325 \ -0.888 \ 0.325]$. The static response due to a unit force acting on DOF 1 is $\boldsymbol{\varphi}_s^T = [2 \ 1 \ 1]$.

As frequency limit of the reduced system $f^* = 0.125$ Hz is chosen. Consequently, the accuracy of the first mode will be observed.

In a second step the error of an off tuned system will be observed. The idea is, that the reduction process should be independed of the finally applied loads. Consequently it should be possible to connect a spring with the input/output DOF. The properties of the off tuned full and reduced system should be similar even the reduction base of the original system has been used. For the off tuned system, the first DOF is connected via a spring to ground. The according spring parameter has been chosen to $c = 5$. The first eigenfrequency of the full system in off tuned condition is $f_1 = 0.119$ Hz and the according eigenvector has the form of $\boldsymbol{\varphi}^T = [-0.628 \ -0.46 \ -0.628]$. Note, that the second eigenfrequency is higher as f^* and therefore not of interest.
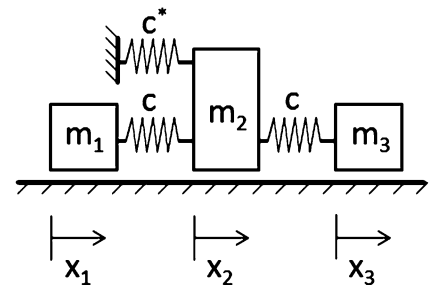

Fig. 28.1 One dimensional three mass example

28.3.1 Mode Based Approach

The first two eigenfrequencies of the Fixed Interface Normal Modes are 0.12 and 0.29 Hz. It is common to regard each eigenfrequency below $2f^*$ and this leads to one Fixed Interface Normal Mode. The second mode is obtained by the static deflection of the structure due to a unit displacement and DOF 1, see (28.41).

$$\mathbf{V}_{\mathrm{CMS}} = [\,\mathbf{v}_{\mathrm{S}} \quad \mathbf{v}_{\mathrm{D}}\,] = \begin{bmatrix} 1 & 0 \\ 0.5 & 0.937 \\ 0.5 & 2.263 \end{bmatrix} \tag{28.41}$$

Note, that the vectors in (28.41) are not normalized. It is obvious, that the static deflection can be exactly reproduced in the reduced systems. The relative error of the first eigenfrequencies is $\varepsilon_1 = 1.2e\text{-}3$ and $\varepsilon_2 = 8e\text{-}3$. Note, that just the first eigenfrequency is actually in the range of validity. The main diagonal entities in the MAC matrix are 1 and 0.997 and the off diagonal entity is 0.004.

For the off tuned system a relative eigenfrequency error of $\varepsilon_1 = 3.9e\text{-}5$ and a MAC value of 1 is obtained.

28.3.2 Krylov Subspace Based Approach

The Krylov vectors are computed by an algorithm which can be seen in [19]. The Krylov vectors are computed around $s_0 = 0$. For comparability with the CMS method, two vectors will be considered, see (28.42).

$$\mathbf{V}_{\mathrm{K}} = [\,\mathbf{v}_{\mathrm{K},1} \quad \mathbf{v}_{\mathrm{K},2}\,] = \begin{bmatrix} 1 & -1.31 \\ 0.5 & 0.655 \\ 0.5 & 1.964 \end{bmatrix} \tag{28.42}$$

Note again, that the vectors are not normalized. The first column contains the exact static solution as it has to be expected. It can be stated that the exact static solution cannot be guaranteed if s_0 is not equal to 0. The relative error of the first both eigenfrequencies are $\varepsilon_1 = 5.7e\text{-}4$ und $\varepsilon_2 = 3.2e\text{-}2$. The main diagonal entities in the MAC matrix are 1 and 0.988 and the off diagonal entity is 0.01.

For the off tuned system a relative eigenfrequency error of $\varepsilon_1 = 1e\text{-}2$ and a MAC value of 0.998 is obtained.

28.3.3 Balanced Truncation Based Approach

The application of the SBPOR algorithm of [9] delivers the following reduction base

$$\mathbf{V}_{\mathrm{BT}} = [\,\mathbf{v}_{\mathrm{BT},1} \quad \mathbf{v}_{\mathrm{BT},2}\,] = \begin{bmatrix} -0.628 & -0.707 \\ -0.46 & 0 \\ -0.628 & 0.707 \end{bmatrix} \tag{28.43}$$

The corresponding singular values are: 2746.2, 250 and 3.79. Again two modes have been selected in order to enable a 'fair' comparability with all other methods. Note, that the reduction base is formed by the first two vibration modes of the system. According to literature, this has to be expected, see Chap. 5. Consequently, there is no error in the reduced system concerning the eigenfrequencies and the modes. The static response $\boldsymbol{\varphi}_{\mathrm{BT,s}}^{\mathrm{T}} = [2\ 1.092\ 0.986]$ on the other hand is not exact. Furthermore it can be stated, that the singular values are of less physical meaning as frequencies even they can be used to compute an error bound. Note that the selection of just one mode (the first one) would lead to an exact representation of the first vibration mode, but would lead to a really bad solution for the static deformation.

Note furthermore, that the static error depends on the local mass distribution, which is not very physical, even it remains small in terms of an a-priory error estimation. In order to illustrate that, the mass m_3 is set to ten. The first two eigenfrequencies and eigenvectors of the reduced model fit exactly with the ones of the full model. Physically, the static deformation should not be influenced by changing the mass properties but evaluates to $\boldsymbol{\varphi}_{\mathrm{BT,s}}^{\mathrm{T}} = [2\ 1.13\ 1.02]$.

For the off tuned system a relative eigenfrequency error of $\varepsilon_1 = 4e\text{-}3$ and a MAC value of 0.999 is obtained.

Table 28.1 Comparison of the three methods

	β_S	ε_1	ε_2	β_1	β_2	Off tuned system with additional stiffness acting on m_1	
						ε_1	β_1
CMS	0	1.2e-3	8.0e-3	0.015	0.077	3.9e-5	0.004
K	0	5.7e-4	3.2e-2	0.011	0.15	1e-2	0.064
BT	0.087	0	0	0	0	4e-3	0.04
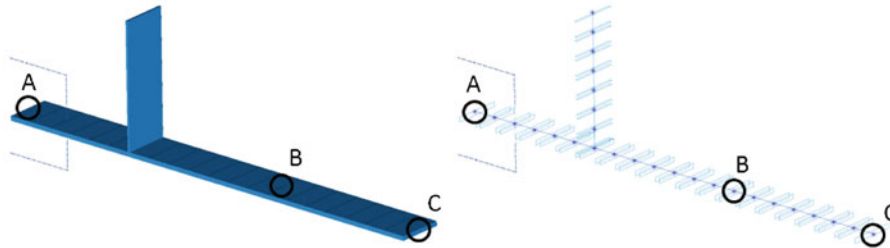
Fig. 28.2 Cantilever beam example – solid and wireframe representation

28.3.4 Comparison

All results have been collected in Table 28.1. As conclusion of the latter considerations and numerical results it can be said that:

- The CMS method delivers acceptable results for all test cases
- BT delivers the best results for the dynamics of the original undamped system because the vibration modes themselves are used.
- The CMS and Krylov subspace based reduction deliver exact results for the static case while BT does not.
- CMS delivers the best results for the off tuned system.
- The characteristic of BT that the vibration modes are used should lead to a bad convergence in case of off tuned system. However this cannot be observed in this example but will be clearly observed in the next one.

28.4 Cantilever Beam Example (Finite Element Model)

A beam modeled with the FEM is considered in this section. An image of the structure can be seen in Fig. 28.2. The structure is mounted at point A, where all translational and all rotational stiffness's where set to 1e + 10 and they are acting between the structure and ground. At point B a force is acting with two unit components in both lateral directions. The static deformation will be computed based on this force. The off tuned system is characterized by an additional mounting at point C. The parameters of this mount are the same as the ones of point A. Consequently there are 8 input/output DOF (2 at point B and 6 at point C).

The number of considered trial vectors is determined by the Krylov subspace based approach. This approach leads to 8, 16, 32 . . . . . . modes. For this example 16 modes will be used.

28.4.1 Mode Based Approach

As explained before, 16 modes will be used for this comparison. This leads to eight constraint interface modes and eight fixed constrained normal modes. This covers a frequency range from approximately $f^* = 250$ Hz and Fixed Constrained Normal Modes up to 400 Hz have been regarded.

Table 28.2 Comparison of the three methods

Mode	Freq. [Hz]	CMS		K		BT		With additional stiffness acting between Point C and Ground							
								Freq. [Hz]	CMS		K		BT		
		ε_i	β_i	ε_i	β_i	ε_i	β_i		ε_i	β_i	ε_i	β_i	ε_i	β_i	
1	8.28	5.6e-6	2.5e-5	8.0e-7	2.8e-6	8.0e-7	1.4e-8	44.4	2.3e-4	1.4e-3	1.5e-3	1.6e-2	1.7e-2	5.1e-2	
2	44.7	4.8e-4	2.4e-3	1.4e-3	1.7e-2	3.7e-9	1.0e-7	56.9	3.0e-4	1.6e-3	9.8e-3	2.1e-2	1.1e-2	5.2e-2	
3	56.3	4.7e-4	2.5e-3	9.7e-3	2.1e-2	-5.4e-10	2.0e-7	98.8	2.0e-7	2.6e-5	2.7e-3	2.5e-3	--	--	
4	76.0	2.9e-4	3.5e-3	3.3e-4	3.7e-3	9.0e-9	4.9e-6	130.0	2.8e-4	4.6e-3	3.3e-3	1.5e-2	3.4e-2	5.3e-2	
5	83.0	6.1e-4	4.7e-3	3.0e-4	2.9e-3	5.4e-8	3.5e-5								
6	129.9	1.7e-3	9.9e-3	3.3e-3	1.5e-2	6.2e-9	4.1e-7								
7	235.8	4.4e-3	1.6e-3	5.0e-2	8.9e-2	--	--								
Static			1.5e-9		1.7e-9		5.4e-5			1.6e-10		3.1e-10		5.7e-3	

28.4.2 Krylov Subspace Based Approach

As mentioned 16 trial vectors have been regarded. The first eight trial vectors contain the static solution due to unit forces at the input/output DOF.

28.4.3 Balanced Truncation Based Approach

As before it can be observed, that the trial vectors are indent with the vibration modes of the cantilever beam.

28.4.4 Comparison

A summary of all computations is given in Table 28.2.

Note, that the color of the cells have been chosen according to the error quantity:

- Green – Error below 1e-3
- Cyan – Error below 1e-2
- Yellow – Error below 1e-1
- Red – Error higher as 1e-1 or mode could not be found in the reduced system

It can be seen, that one mode could not be found in the reduced system in case of BT. For the original and the off tuned system, the first torsion mode could not be found. However, in case of BT 22 trial vectors have to be used in order to obtain this torsion mode.

The CMS method is the one with the best results for the original and off tuned system. Both, the static response and the vibration modes are of excellent accuracy.

It can be seen, that BT does not deliver that good results in case of the off tuned system. This is because the projection base is formed by the modes of the original system. It is well known, that projection bases where no trial vectors fulfill the boundary conditions of the reduced system have bad convergence. This is the case in the off tuned system. On the other hand, the construction of the CMS projection base ensures that for both systems some trial vectors fulfill the boundary conditions.

However, the Krylov subspace based approach delivers a better result in the off tuned case as BT but not that good result as the CMS method.

28.5 Conclusion

As conclusion with respect to the investigated issues it can be said that the CMS method is the best choice for model reduction of solid structures. The CMS method has clearly the best performance in terms of sensitivity of the reduced model with respect to varying boundary conditions. Balanced truncation has the worst one because of its characteristic, that just

vibration modes will be used for the projection base. The CMS method and Krylov subspace based (around frequency zero) method give exact static solutions while balanced truncation does not. For the investigated examples it could not be observed, that one of the three methods will lead in general to significant less trial vectors. However, balanced truncation needed a lot of more trial vectors in order to catch a torsion mode in the reduced model. If some input DOF in the reduced model are fixed it can be expected, that balanced truncation delivers bad convergence with respect to stress recovery. This is because no trial vectors of the projection base fulfil the boundary conditions of the fixed DOF. Another nice feature of CMS is that the mode selection criterion is the frequency of a particular mode. The Hankel singular values of balanced truncation on the other hand are difficult to interpret and for the advantage of a defined error limit in the L_2 norm the penalty of bad convergence in terms of stresses has to be paid. Finally it is worth to mention that the direct application of modal and static measurements complete the superior performance of CMS methods.

Bibliography

1. Gaul L, Nitsche R (2001) The role of friction in mechanical joints. Appl Mech Rev 54(2):93–105
2. Bogard S, Schmidt A, Gaul L (2007) Modeling of damping in bolted joints. VDI – Berichte Nr. 2003, pp 97–110
3. Witteveen W, Irschik H, Riener H, Engelbrechtsmüller M, Plank A (2008) An efficient mode based approach for the dynamic analysis of jointed and local damped structures: joint interface modes. In: Proceedings of ISMA 2008, Leuven, pp 1815–1824
4. Nowakowski C, Fehr J, Eberhard P (2011) Model reduction for a crankshaft used in coupled simulations of engines. In: Samin JC, Fisette P (eds) multibody dynamics 2011, ECCOMAS thematic conference, Brussels, ISBN 978-2-8052-0116-5
5. Koutsovasilis P, Beitelschmidt M (2008) Comparision of model reduction techniques for large mechanical systems. Multibody Sys Dyn 20:111–128
6. Tobias C, Eberhard P (2011) Stress recovery with krylov subspaces in reduced elastic multibody systems. Multibody Sys Dyn 25:377–393
7. Fehr J, Eberhard P (2009) Improving the simulation process in flexible multibody dynamics by enhanced model order reduction techniques. In: Arczewski L, Fraczek J, Wojtyra M (eds) multibody dynamics 2009, ECCOMAS thematic conference, Warsaw
8. Fehr J, Eberhard P (2011) Simulation process of flexible multibody systems with non-modal model order reduction techniques. Multibody Sys Dyn 25:313–334
9. Yan B, Tan SXD, McGaugy B (2008) Second-order balanced truncation for passive-order reduction of RLCK circuits. IEEE Trans Circuit Syst II 55(9):942–946
10. Craig RJ (1987) A review of time-domain and frequency-domain component mode synthesis methods. Int J Anal Exp Modal Anal 2(2):59–72
11. Noor AK (1994) Recent advances and applications of reduction methods. Appl Mech Rev 47(5):125–146
12. Zu QQ (2004) Model order reduction techniques. Springer, London. ISBN 1852338075
13. Schwertassek R, Dombrowski SV, Wallrapp O (1999) Modal representation of stress in flexible multibody simulation. Nonlinear Dyn 20:381–399
14. Craig RR, Bampton MCC (1968) Coupling of substructures for dynamic analysis. AIAA J 6(7):1313–1319
15. Tran DM (2001) Component mode synthesis methods using interface modes. Application to structures with cyclic symmetry. Comput Struct 79:209–222
16. Witteveen W, Irschik H (2009) Efficient mode-based computational approach for jointed structures: joint interface modes. AIAA J 47 (1):252–263
17. Lehner M (2007) Modellreduktion in elastischen Systemen. Shaker Verlag, Achen, ISBN 978-3-8322-6783-4
18. Benner P (2011) Numerical linear algebra for model reduction in control and simulation. http://www.tu-chemnitz.de/mathematik/preprint/2005/PREPRINT_18.pdf. Accessed 12 Aug 2011
19. Lohmann B, Salimbarhrami B (2004) Ordnungsreduktion mittels Krylov-Unterraummethoden. Automatisierungstechnik 52:30–38
20. Lehner M, Eberhard P (2006) On the use of moment-matching to build reduced order models in flexible multibody dynamics. Multibody Sys Dyn 16:191–211
21. Lehner M, Eberhard P (2006) Modellreduktion in elastischen Mehrkörpersystemen. Automatisierungstechnik 54:170–177
22. Hägblad B, Eriksson L (1993) Model reduction methods for dynamic analysis of large structures. Comput Struct 47(4/5):735–749
23. Rixon DJ (2009) Dual Craig-Bampton with enrichment to avoid spurious modes. In: Proceedings of IMAC-XXVII, © 2009 Society of Experimental Mechanics Inc., Orlando
24. Meyer DG, Srinivasan S (1996) Balancing and model reduction for second-order form linear systems. IEEE Trans Autom Control 41 (11):1632–1644
25. Reis T, Stykel T (2008) Balanced truncation model reduction of second-order systems. Math Comput Model Dyn Syst 14(5):391–406
26. Benner P, Saak J (2011) Efficient balancing based MOR for large scale second order systems. Math Comput Model Dyn Syst 17(2):123–143
27. Benner P, Schneider A (2010) Balanced truncation model order reduction for LTI systems with many inputs or outputs. In: Proceedings of the 19th international symposium on mathematical theory of networks and systems – MTNS 2010, Budapest, ISBN 978-963-311-370-7
28. Willox K, Peraire J (2002) Balanced model reduction via the proper orthogonal decomposition. AIAA J 40(11):2323–2330
29. Feeny BF, Kappagantu R (1998) On the physical interpretation of proper orthogonal modes in vibration. J Sound Vib 211(4):607–616
30. Lehner M, Eberhard P (2007) A two step approach for modal reduction in flexible multibody dynamics. Multibody Syst Dyn 17:157–176
31. www.scilab.org, Version 5.3

Chapter 29
Vertical Axis Wind Turbine Operational Modal Analysis in Sheared Wind Flow

J.F. Kusnick and D.E. Adams

Abstract There has been increased interest in implementing co-located renewable energy generation systems in urban areas, and vertical axis wind turbines (VAWTs) are a candidate technology for capturing the unsteady, omnidirectional winds that are typical of an urban environment. Before the technology can be widely deployed, the issues of reliability and environmental noise must be addressed. Knowledge of the structural dynamic response of the rotor blades as a function of the wind state that enters the rotor will facilitate a better understanding of both reliability (of the blades and driveline bearings) and noise (frequency content of the blade motions that causes structure-borne noise). An experimental modal model was developed to relate the forces introduced by wind loads to the response of the structure. Experimental modal analysis was performed on a 600 W lift-type (Darrieus) VAWT for a range of azimuth angles and tower heights. Additionally, operational modal analysis was conducted in an indoor simulated wind environment test bed. A modal filtering technique was applied and verified using an electro-dynamic shaker and was then used to analyze the operational data. The effects of wind speed and shear on the modal response were investigated. The key results were a shift down in resonance frequencies with increasing height of the turbine tower for rotor modes coupled to the tower response and significant changes in operational modal response for non-uniform (sheared) wind conditions, especially from the 5 Hz mode of vibration. Future work will involve operational testing of vibration and acoustic emissions of the VAWT on a building rooftop.

29.1 Introduction

VAWTs have been receiving renewed attention, especially for applications in urban environments since their low tip speeds translate to lower aeroacoustic noise emissions than traditional horizontal axis wind turbines [1]. Previous structural dynamic work was performed by Sandia National Laboratories on large (17 m and 34 m) experimental turbines, which were of a 2-blade parabolic design and had fairly high rotation speeds [2]. Most new designs are 3-bladed, are generally small (<5 kW), and some incorporate twisted, helical blades, which are meant to reduce torsional oscillations by maintaining a relatively constant solidity as they rotate [3]. VAWTs are being installed in urban locations and on building rooftops because of their ability to accept wind from all directions, making them impervious to yaw error, as well as their lower aero-acoustic emissions. The close proximity to people makes vibration and structure borne noise transmission important considerations. It is also important to classify how the turbine responds structurally to the dynamic wind environment, and to determine how to place urban wind turbine systems to maximize power output and component lifetime.

29.2 Experimental Modal Analysis

Two separate modal impact tests were performed. The first test focused solely on analyzing the turbine modes, as well as determining sensor placement and impact locations for subsequent modal tests. The second test took place with the turbine installed on a telescopic tower inside the laboratory, and included the tower response and its coupling effects with the rotor response.

J.F. Kusnick (✉) • D.E. Adams
Center for Systems Integrity, School of Mechanical Engineering, Purdue University, West Lafayette, IN, USA
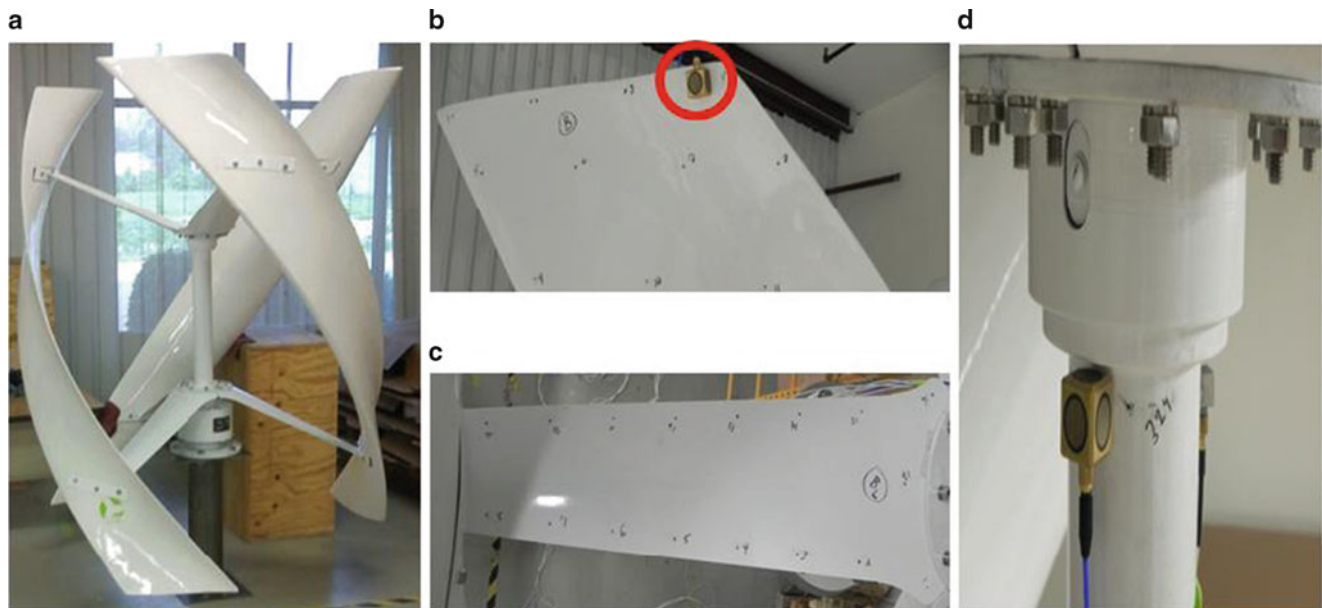e-mail: josh.kusnick@gmail.com

Fig. 29.1 First modal test setup. (**a**) turbine on base, (**b**) blade accelerometer location, (**c**) strut impact points, (**d**) tower accelerometer

29.2.1 VAWT Modal Impact Test No. 1

Experimental modal analysis was conducted to classify the free response characteristics of the turbine system. The first modal impact test on the wind turbine was conducted on a small test stand bolted to the concrete floor. The test stand was constructed from 1/8″ thick drawn-over-mandrel steel tubing, and had an overall height of 31″, which provided a rigid base on which to test the modes of vibration of the turbine. A FARO Arm® three dimensional coordinate measurement machine was used to consistently place the impact locations on each blade as well as to record their locations in space and the surface normal vectors for accurate mode shape animation. Four points were spaced 5 in. apart from the leading edge to the trailing edge of each blade on the low-pressure, outer surface of the blade, in 18 planes separated by 4 in. vertically, for a total of 72 impact points per blade. Each of the six struts supporting the blades had 17 impact points along the top edges, and there were 12 points on the rotor shaft:6 evenly spaced along the axis of the shaft, and another six rotated 120° from the first group. One triaxial, AC-coupled accelerometer was placed on the top, trailing edge of each blade using adhesive, and one was placed near the top of the rotor shaft. Figure 29.1 shows impact locations and accelerometer placement.

29.2.2 Modal Impact Test No. 2: VAWT on Telescopic Roof Fixture

VAWTs installed on or near buildings are subjected to a much different wind environment than in open areas, high off the ground where wind turbines are usually located. Wind flow accelerates over and around buildings, which can be advantageous in terms of energy capture, but also subjects the turbines to a high level of wind shear and turbulence. Figure 29.2 demonstrates this effect in a velocity vector field around a rectangular building using a k-epsilon turbulence computational fluid dynamics model [4], as well as a preliminary CFD model of the lab building on which the turbine will be installed.

A telescopic roof fixture was designed and fabricated to facilitate the observation of different intensities of wind shear over the building, as the wind field varies with height above the roofline. The fixture is constructed from two sleeved, drawn-over-mandrel steel tubes separated by Delron plastic bushings. A hand-winch and pulley system is used to raise and lower the inner tube, and 3/4″ through-holes in the outer tube allow a locking pin to be inserted through the inner tube in 6″ increments. The total vertical travel is limited to 5.5 ft, or about one turbine height. Figure 29.3 shows the roof fixture with the turbine installed in the lab, the pulley mechanism, and a dimensioned drawing of how the turbine will be installed on the lab roof in future operational testing.
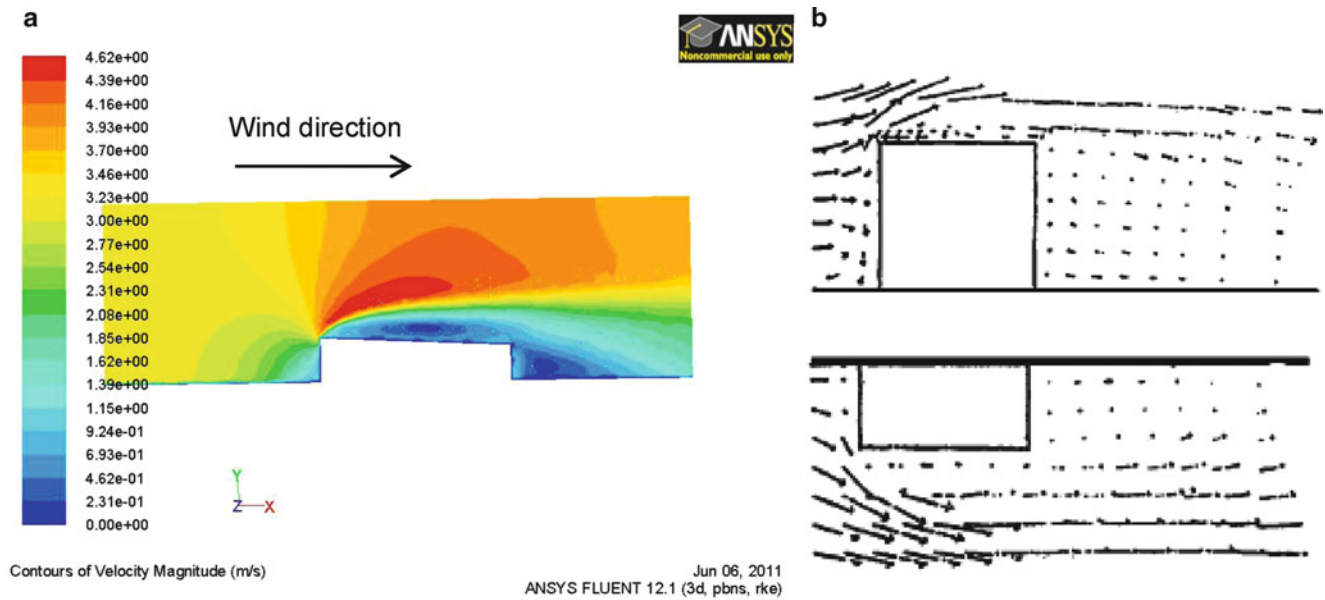
Fig. 29.2 (**a**) Velocity contours of wind flow over lab building from turbulent CFD simulation; (**b**) velocity vectors from CFD of wind flow over rectangular building (*top*), and around side of building (*bottom*) [4]
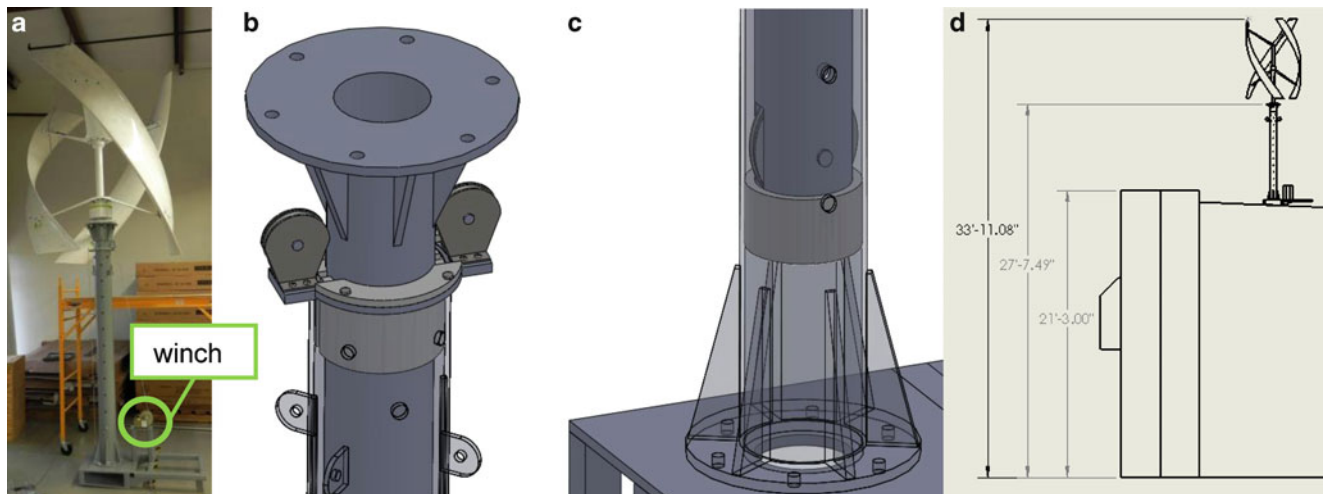
Fig. 29.3 (**a**) Turbine on telescopic fixture in lab; (**b**) CAD drawing with transparent outer tube showing pulleys, white plastic bushing, guy-cable tabs, and turbine mounting flange; (**c**) bottom of Inner tube with bushing and pulley; (**d**) Roof installation

In order to build a modal model that can be used for spatial modal filtering when the turbine is on the roof (see Sect. 29.3.3) several modal impact tests were conducted with the turbine installed on this roof fixture inside the lab to account for the change in boundary conditions associated with the tower. The bolted connections to the tower, the tower's varying stiffness as its height is adjusted, and the plastic bushings between the sleeved poles can affect the vibration response of the structure.

Because the twisted, composite blades may exhibit different directional stiffness, such as a higher stiffness in the lead-lag (edgewise) direction as compared to the flap direction, modal impact tests were conducted for seven equally spaced azimuth positions from 0 to 120°; after 120°, the orientation of the blades repeats due to the radial symmetry of the design. The blade geometry prevented a roving impact test since all points on the blades were not accessible by a modal hammer for one single impact direction; furthermore, the small edgewise area of the blades prevented impacting them in the lead-lag direction. Therefore, a roving accelerometer test was conducted, and all impact locations were on a single face of the tower in one direction – perpendicular to the plane of the winch cable. Five triaxial accelerometers were placed on the leading edge of the

blade to capture flap, edgewise, and vertical motion. Five additional single axis accelerometers were placed on the trailing edge of the blade measuring the flap degree of freedom; six single axis accelerometers were on each strut, six were on the rotor shaft, and 12 single-axis accelerometers were fastened to the telescopic mast. The modal tests for each azimuth position were repeated for three different extended heights of the mast – the retracted, lowest position; a middle height with the tower extended 2.5 ft, and at the fully extended position. The height of the turbine above the base of the tower in each position is 7, 9.5, and 12.5 ft, respectively.

29.2.3 Modal Analysis Results

The first modal test (Sect. 29.2.1) was conducted with high spatial resolution: 330 total impact locations. After observing the mode shapes, subsequent tests were completed with fewer inputs. The complex mode indicator function (CMIF) was used to determine the modal frequencies from the experimentally measured frequency response functions (FRFs), and the modal vectors were extracted from the left singular vectors corresponding to the peaks in the CMIF. Some of the resulting mode shapes are represented in Fig. 29.4 and are described in Table 29.1. For clarity in the images, the blades are not displayed, but in general they moved in a motion similar to that of their supporting struts.

For the testing conducted on the telescopic mast (Sect. 29.2.2), the complex mode indicator function was used to observe changes in the modal response among the three extended heights for one azimuth position. The bandwidth of interest in the tests was 0–100 Hz, and many of the resonant frequencies in this range exhibited a significant decrease in modal frequency as the height of the tower increased. This effect was especially evident in the 3.8 Hz mode indicated in Table 29.2, which was predominantly a mode of vibration of the tower. The mode shape of the turbine around 18 Hz appeared to be coupled to the tower motion, and also exhibited a significant shift down in frequency with increased tower height, as is expected due to the reduced stiffness. There were also several modes of vibration that involved little tower response, such as those near 30.6 Hz and 100.3 Hz, and these frequencies had a much smaller change in relation to the height of the tower. The effects are evidenced in the plot of the top line of the CMIF for each of the tower heights at one azimuth position in Fig. 29.5, and the frequency changes for the aforementioned modes are detailed in Table 29.2.

The results of the tests indicated that there was little change in modal response with respect to azimuth position. This may be due to the excitation being applied to the tower rather than to the blades and struts directly, which is likely less effective in exciting the blades and struts in the prescribed direction as compared to a direct impact. Figure 29.6 displays the top line of the CMIF for each of the azimuth angles on a single plot that reveals the similarity in the results. Notably, the 3.8 Hz tower mode had nearly the identical result in the CMIF for each azimuth angle, verifying that that particular resonant frequency is
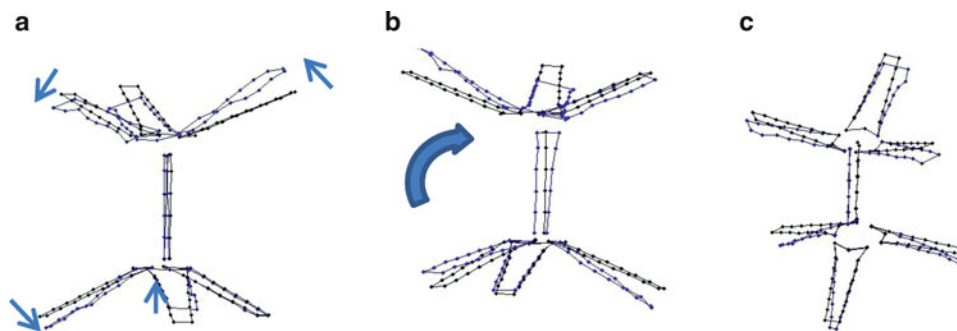
Fig. 29.4 (**a**) Mode 1; (**b**) Mode 2; (**c**) Mode 3. Undeformed shape in *black*, deformed shape in *blue* (color figure online)

Table 29.1 Mode shape descriptions

Mode	Frequency (Hz)	Description
1	7.8	Shaft: first vibrational mode of hollow cylinder
		Struts: top three first-bending coupled with torsion, two struts in-phase; two lower struts first bending, 180° out of phase
2	9.4	All struts and shaft rock side-to-side in phase
3	10.9	All struts first-bending in-phase

Table 29.2 Modal frequencies versus extended tower height

Retracted	Mid-height		Fully extended	
Frequency (Hz)	Frequency (Hz)	% Change	Frequency (Hz)	% Change
3.8	2.8	−26.3	2.2	−42.1
18.1	17.5	−3.3	15.6	−13.8
30.6	30.6	0.0	30.6	0.0
100.3	99.7	−0.6	99.7	−0.6
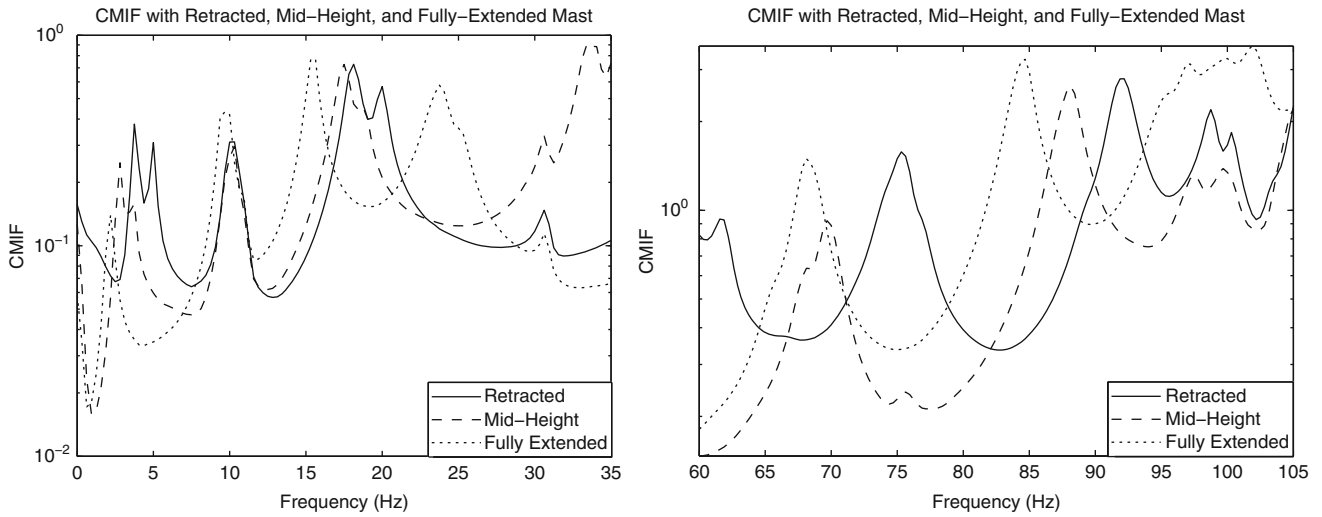
Fig. 29.5 Top line of CMIF for three extended heights of roof fixture at the 0° azimuth position
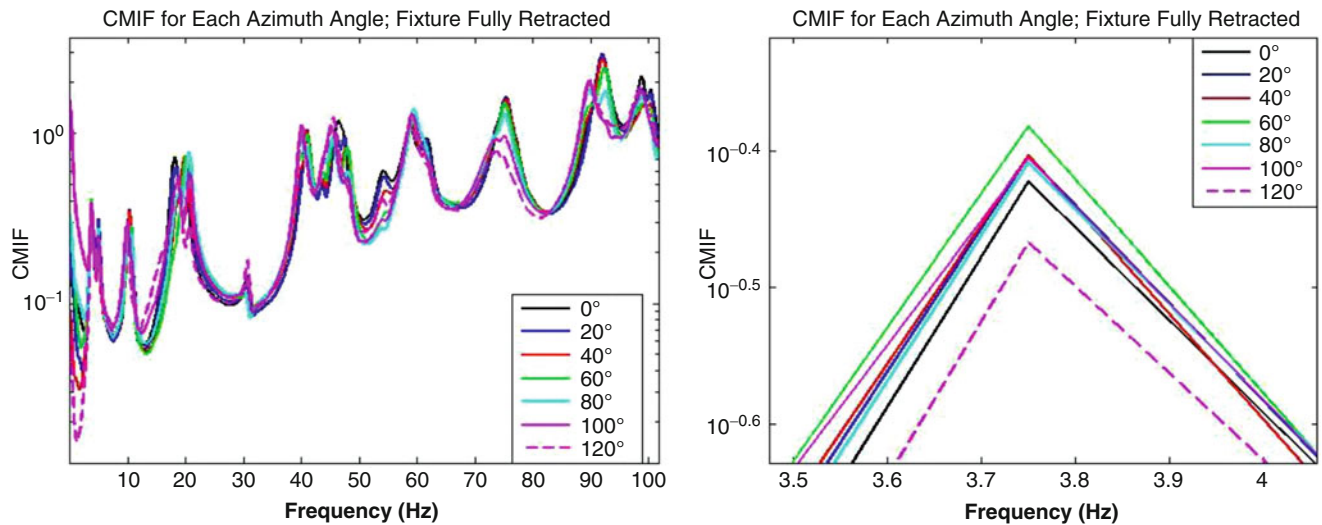
Fig. 29.6 Top line of CMIF for each azimuth position at lowest height setting

largely dependent on the tower height and not the rotor azimuth position. There were some subtle changes in rotor modes, such as a resonance around 138 Hz, which was present for azimuth positions 60 through 120°, but not 0, 20, and 40°. The mode shape involved the second bending mode of the struts attached to the two blades closest to the impact location when rotated from 60 through 120°, which may not have been well-excited in the first three blade orientations.

29.3 Operational Testing

With the modal frequencies and vectors determined, the next step was to use that information to gain insight into the structural response of the turbine in operation. This study used an in-house wind dynamics test bed to gather baseline data in a controlled airflow environment prior to future testing of the turbine in real rooftop operating conditions. Separate tests were conducted for a range of wind speeds from 3.4 to 5.4 m/s (7.6–12.1 miles per hour), which starts near the idle speed of the turbine and increases into the power-generating region. Additionally, four separate wind shear conditions were tested to explore the effect of wind shear on operational response: (1) a uniform flow with no wind shear; (2) a vertically sheared flow like that present in the atmospheric boundary layer or seen in the profile of wind flow over a building; and (3, 4) left and right side-shear, which may be due to obstructions, wind flow around the sides of a building, or upstream wind turbines.

29.3.1 Experimental Setup

The experimental test bed consists of an enclosed test section which generates a simulated wind flow using four large axial exhaust fans to pull air through a honeycomb, laminarizing core (see Fig. 29.7 below). Accelerometers were placed in the same locations on the rotor as during the first modal test (Sect. 29.2.1); however, unlike the modal impact tests, DC-coupled sensors were used to better capture the low frequency, per-revolution harmonics. A data acquisition device and wireless transmitter were statically balanced and fastened to the base of the rotor shaft. Because of the added mass and the change in boundary conditions inside the test bed, another modal impact test was conducted to obtain the modal parameters.

Wind shear was generated by placing window screening material on the inlet of the test bed. The resulting inlet wind plane was measured using an ultrasonic anemometer at 100 measurement points, 2 ft inward from the honeycomb core face, and the results were interpolated to generate the images in Fig. 29.8. Leading edge shear (hereafter denoted LS) indicates that the wind was slowed on the side of the leading, advancing edge of the blade. Trailing edge shear (TS) indicates the wind was slowed on the trailing, retreating edge of the blade.

29.3.2 Operational Modal Analysis

The wind velocity fields were experimentally measured, but because the force input on the turbine is unknown, operational modal analysis (OMA) was applied to relate the operational response of the turbine to the free response dynamics measured in the experimental modal analysis. The two primary assumptions in OMA are: (1) the power spectrum of the input force is
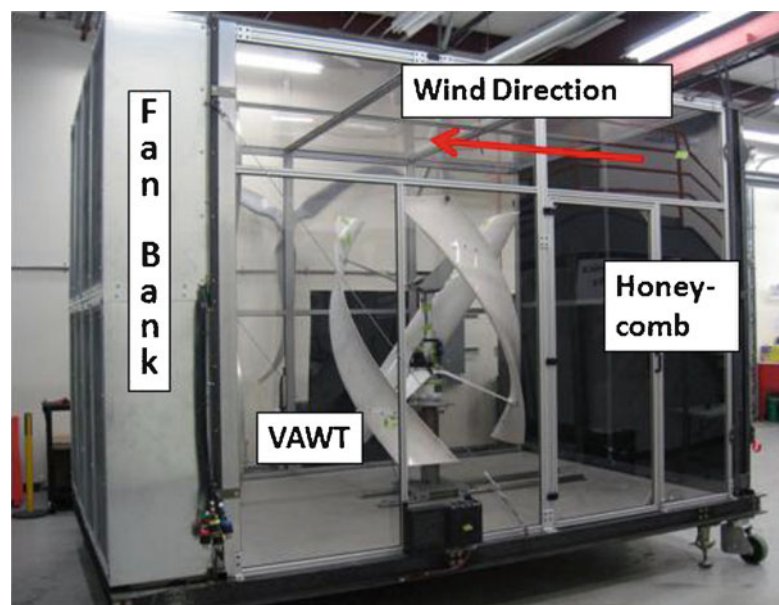
Fig. 29.7 Experimental test bed
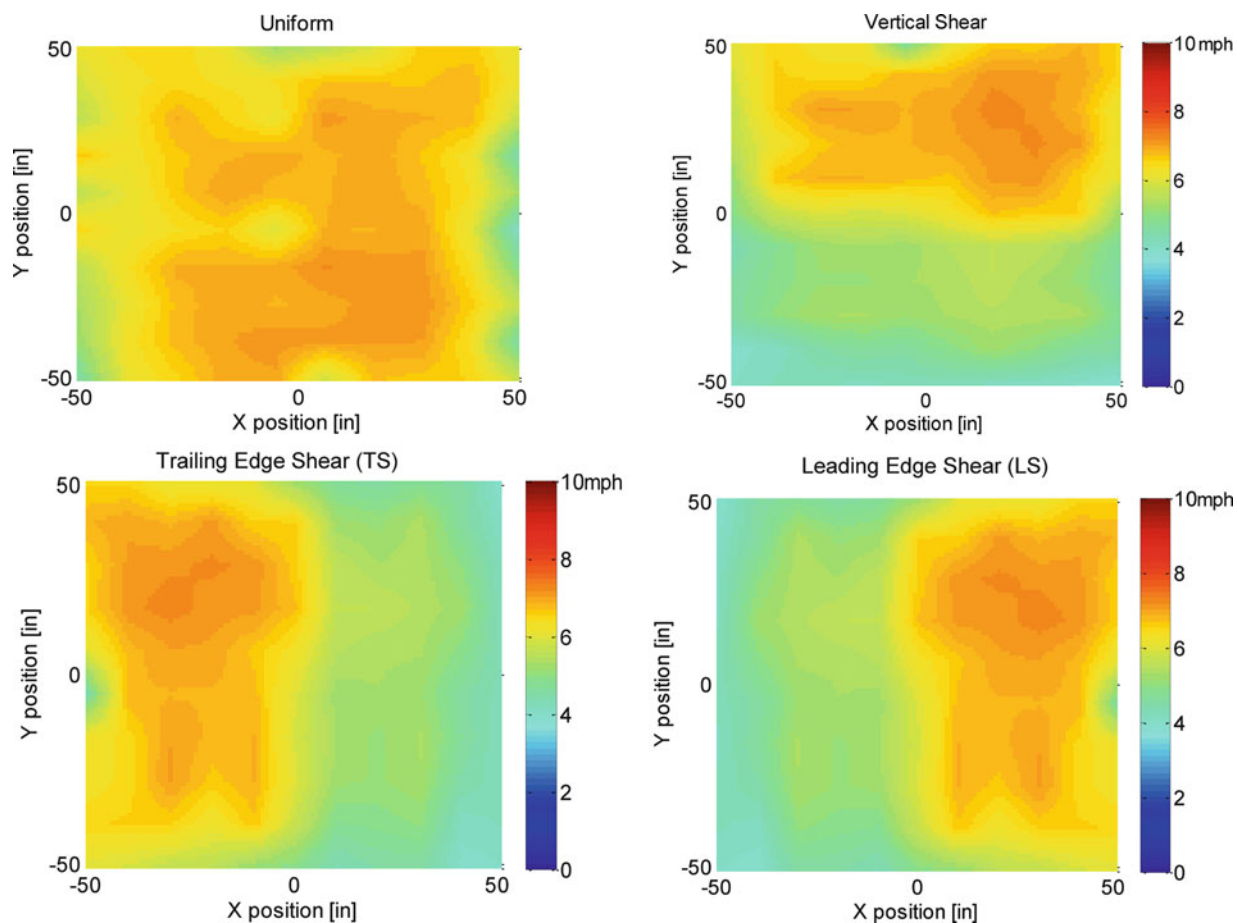
Fig. 29.8 Inlet wind velocity planes

broadband and smooth (i.e. has no poles or zeroes in the frequency range of interest), and (2) the forcing function is spatially distributed in a uniform manner [5]. Assumption (1) is not particularly well-fulfilled for wind-excited structures since the power spectrum of wind is generally dominated by low-frequency components [6]. In general, however, rotating machinery is self-excited at harmonics of the operating speed [7], and this was evident in the OMA frequency response functions measured on the VAWT. Assumption (2) is reasonable for the rotating wind turbine, and the measured wind planes in Fig. 29.8 demonstrate the spatial uniformity.

The data processing involved time-synchronously averaging the accelerometer responses, then performing OMA by first computing the autocorrelation of the time response, which is the time-domain equivalent of the auto power spectrum. The result is two-sided, containing a positive exponential portion corresponding to the negative poles of the power spectrum, and a decaying exponential portion corresponding to the positive poles [5]. Since both parts of the result contain the same information, the positive exponential part is set to zero, essentially zero-padding the time signal. The resulting function is treated as an impulse response function, the discrete Fourier transform of which is the OMA FRF. Figure 29.9 schematically describes the process.

29.3.3 Modal Filtering

The physical response spectrum is the result of a summation of individual modal responses. Spatial modal filtering can be applied to determine the values of the modal coordinates, or contribution from a subset of individual modes, at areas of interest in the operational response spectrum. In order to predict the fatigue and wear in components, modal filtering can be
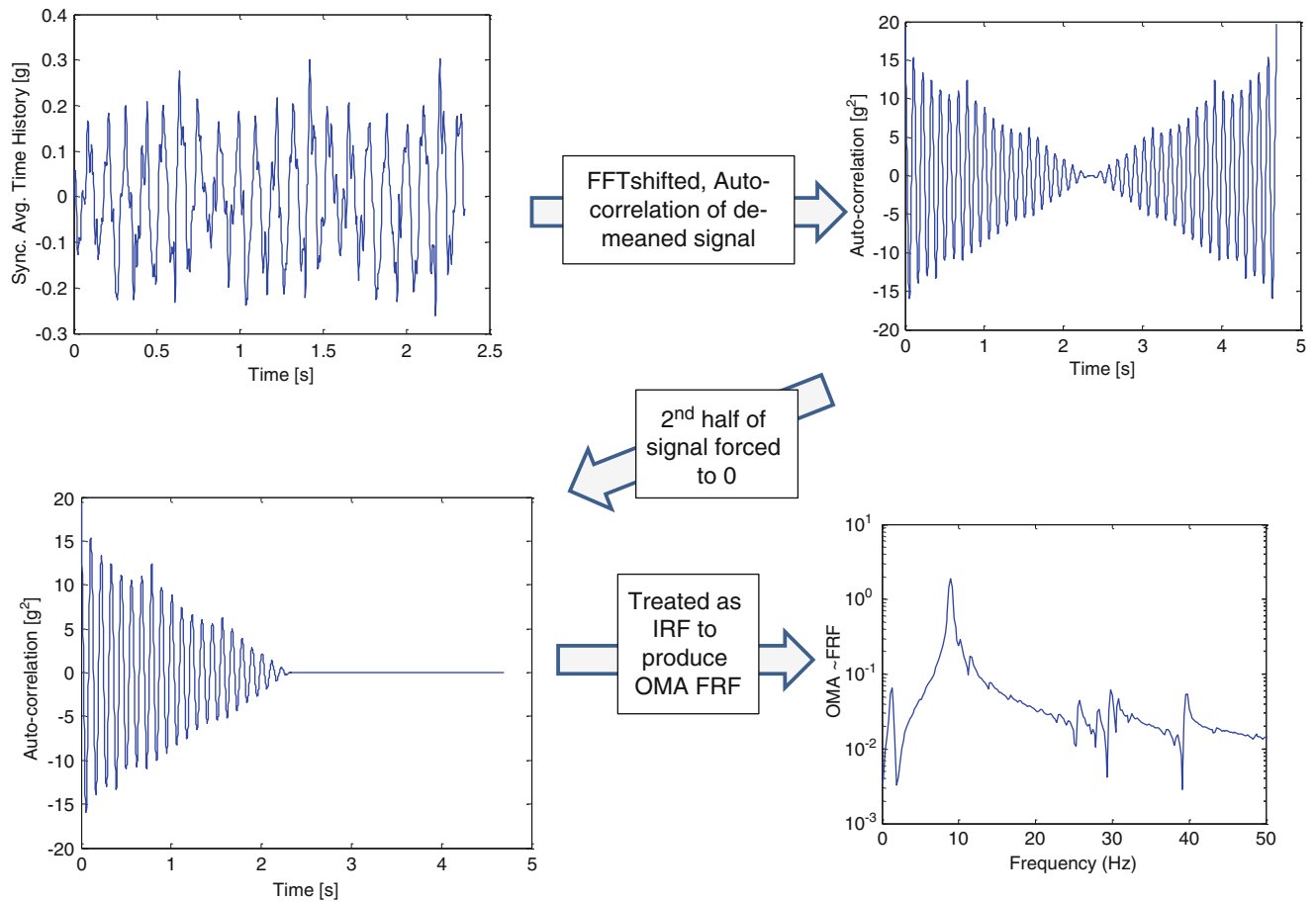
Fig. 29.9 OMA data processing flow chart, [8]

used to calculate the number of loading cycles and the magnitude of response each mode has undergone in operation. This has applications in cycle-based, predictive maintenance as well [9].

A modal filter transforms the physical coordinates of a system to modal coordinates, as shown in (29.1),

$$\{p(t)\} = [C]\{x(t)\} \tag{29.1}$$

where $\{x(t)\}$ is a column vector of physical coordinates – the outputs from each of the sensor channels, $\{p(t)\}$ is a column vector of modal coordinates, and $[C]$ is the transformation matrix, which is called the modal filter. The response, $\{x(t)\}$, can be expressed as a sum of modal coordinates spatially weighted by the modal vectors, which is written in matrix form in (29.2),

$$
\begin{Bmatrix} x_1(t) \\ x_2(t) \\ \vdots \\ x_m(t) \end{Bmatrix}
=
\begin{bmatrix}
\psi_{1,1} & \psi_{1,2} & \cdots & \psi_{1,N} \\
\psi_{2,1} & \ddots & & \vdots \\
\vdots & & \ddots & \vdots \\
\psi_{m,1} & \cdots & \cdots & \psi_{mN}
\end{bmatrix}
\begin{Bmatrix} p_1(t) \\ p_2(t) \\ \vdots \\ p_N(t) \end{Bmatrix}
\tag{29.2}
$$

where $[\Psi]$ is the modal matrix, which is experimentally measured in this case; m is the number of measurement channels; N is the number of modes; $p_N(t)$ is the response of mode N at time t; and $x_m(t)$ is the response of physical coordinate m at time t. To calculate the modal coordinates, the response vector $\{x(t)\}$ is left-multiplied by the pseudo inverse of the modal matrix for every time t.

a

b
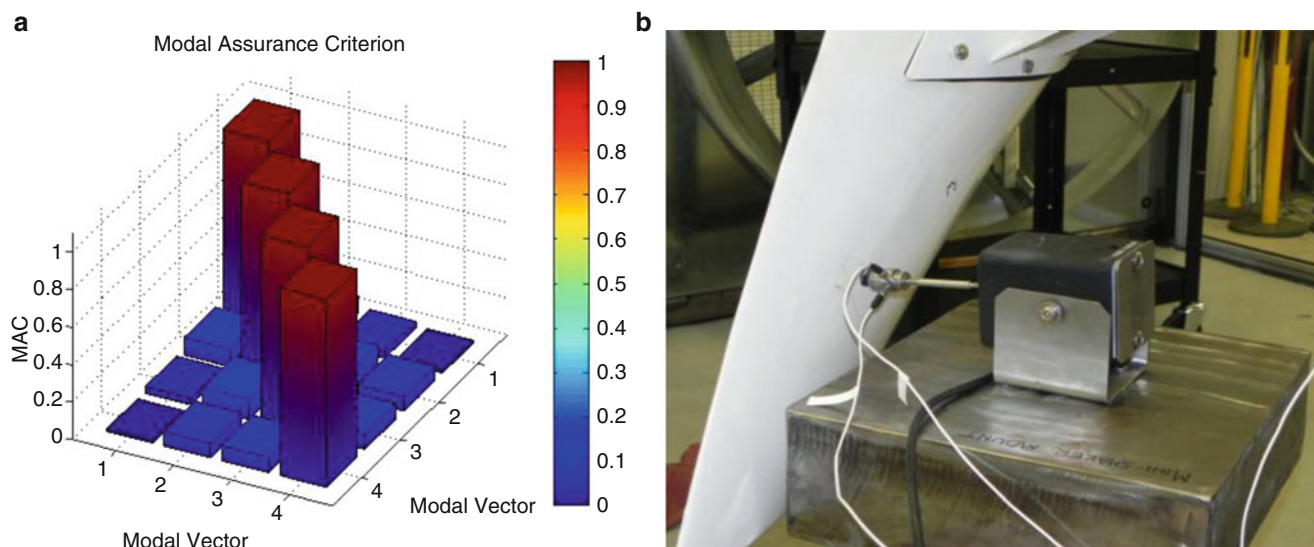
Fig. 29.10 (**a**) Modal assurance criterion for modal filter vectors, (**b**) Shaker test setup

29.3.4 Modal Vector Selection and Modal Filter Verification

In order to improve the numerics of the calculation by having an overdetermined system, the number of modal vectors chosen for the filter should be less than the number of measurement channels, typically by a factor of two or more. Furthermore, the modal vectors should be linearly independent so that they can be distinguished spatially [9]. The polyreference time domain (PTD) algorithm along with a consistency diagram approach was employed to identify physical, stable poles and vectors in the modal impact data. A modal assurance criterion (MAC) test was then performed to check the modal vectors for linear independence. There were 12 response channels, and four modes were chosen, corresponding to frequencies of 5.0, 42.7, 47.0, and 54.3 Hz. The low off-diagonal values of the MAC in Fig. 29.10a demonstrate the independence of the modal vectors.

Next, to verify the operation of the modal filter, a shaker test was performed. A small, seven-pound electro-dynamic shaker excited one of the rotor blades in the flap-direction shown in Fig. 29.10b with a sinusoidal input at each of the resonant frequencies used in the modal filter. The modal filter was then applied to the time response data from the accelerometers, and was able to extract the modal coordinate of the mode being excited. The modal coordinates for each test were summed and plotted in Fig. 29.11 below.

The filter was then applied to the operational data. The matrix representation of the modal filter in (29.2) can also be formulated in the frequency domain and evaluated at every frequency in the response spectra. The wind turbine operational data was analyzed in this way. In particular, the modal coordinates were computed at the peaks in the summed OMA FRF response spectrum of all 12 measurement channels for each wind speed and shear condition. A sample result is shown in Fig. 29.12 below, which shows the magnitude of the modal coordinates at each of those peaks.

To view the average value of the modal coordinates as a function of shear condition, the magnitude of each modal coordinate was summed at each of the peaks in the OMA response spectrum, then normalized for each wind shear. The results for the 35 Hz fan speed (3.4 m/s wind speed at no-shear) are shown in Fig. 29.13 below.

Clearly, the 47 Hz mode is dominant regardless of wind shear; however, the response of the remaining three modes does appear to depend on shear condition. The 5 Hz mode is of particular interest since it represents some considerable shaft vibration, which may introduce dynamic fatigue loads on the rotor bearings. The vertical shear condition, which will be predominant on the building rooftop, contains the highest contribution from the 5 Hz mode. Additionally, each shear condition has a higher normalized 5 Hz modal coordinate response than the baseline no-shear condition.
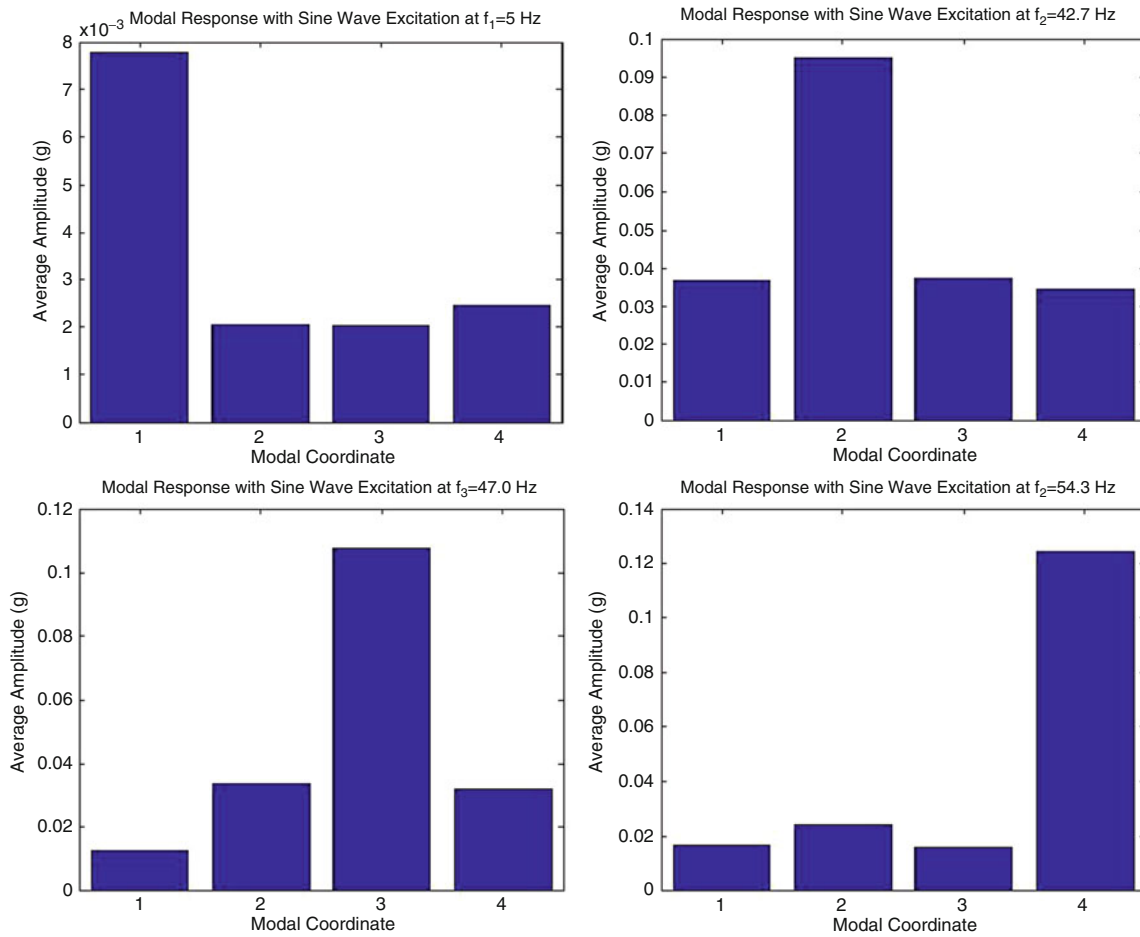
Fig. 29.11 Modal filter results from shaker test
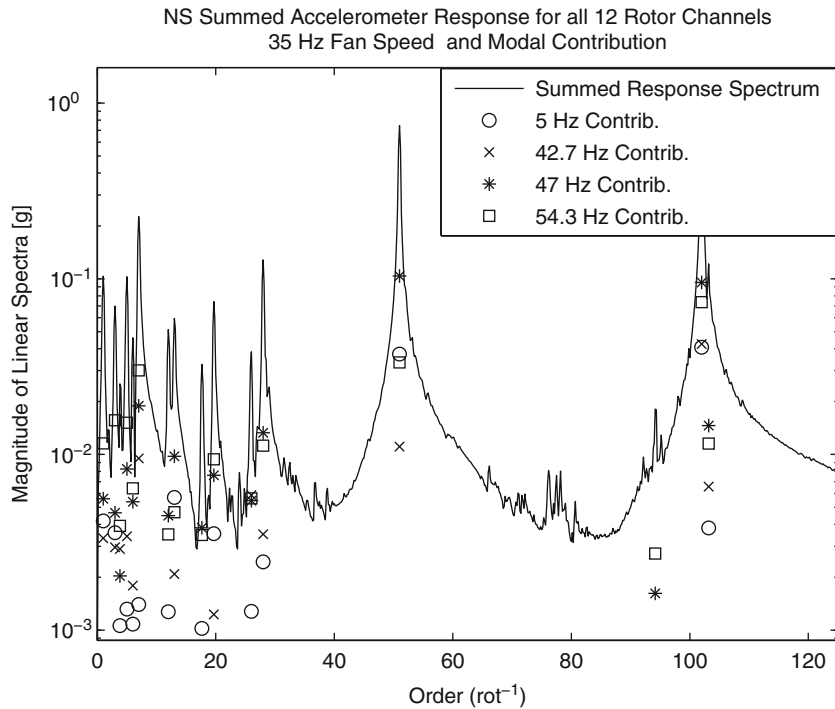
Fig. 29.12 Summed linear response spectrum for no-shear condition at 35 Hz fan speed and modal coordinate response

Fig. 29.13 Normalized modal coordinate response versus shear condition for 35 Hz fan speed
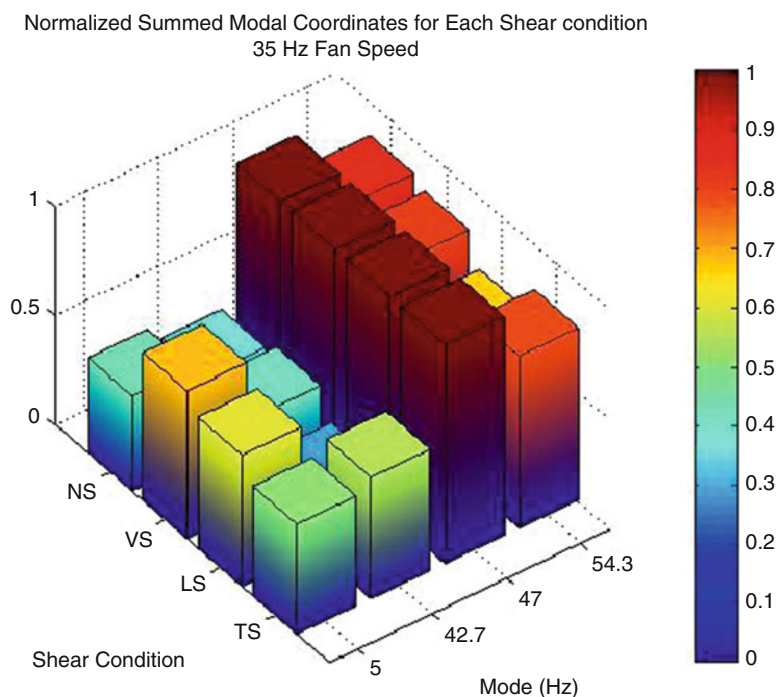
29.4 Conclusion

Several modal impact tests were performed on a small vertical axis wind turbine (VAWT). A telescopic roof-fixture was designed and built for future operational testing to explore the effects on the structural dynamic response of the wind turbine in sheared and turbulent wind flow in urban locations. Modal tests of the turbine were conducted for a range of azimuth angles and three different extended heights of the tower, resulting in a considerable shift downward in resonant frequencies for tower-coupled modes at extended heights, and relatively little change depending on azimuth position. The azimuth tests may have been less successful than anticipated in exciting the blades and struts in the directions intended: perpendicular to the tower base in six different orientations from 0 to 120° of rotation. The roving accelerometer test, as opposed to roving input, may also have decreased the quality of the results.

Operational data was recorded for a range of wind speeds and wind shear conditions with the VAWT installed in a wind-dynamics test bed under controlled wind-input conditions. A modal filtering technique was applied and verified using a shaker-test. The modal filtering results indicated significant changes in modal response among the different wind shear conditions. Future work will apply modal filtering to the operational response of the turbine installed on the laboratory roof. Loading cycles and magnitudes will be counted, and any changes in the performance of the turbine will be documented. Additionally, noise measurements will be taken to correlate modal response to structural noise emissions.

References

1. Iida A, Mizuno A, Fukudome K (2004) Numerical simulation of aerodynamic noise radiated from vertical axis wind turbines. In: 8th international congress on acoustics, Kyoto
2. Carne TG, Nord AR (1982) Modal testing of a rotating wind turbine. Sandia National Laboratories, Albuquerque
3. Sheurich F, Fletcher TM, Brown RE (2010) The influence of blade curvature and helical blade twist on the performance of a vertical-axis wind turbine. In: 29th ASME wind energy symposium, Orlando
4. Sun H, Huang S (2001) Simulation of wind flow around a building with a k-ε model. Theor Comp Fluid Dyn 14:283–292

5. Chauhan S, Martell R, Allemang RJ, Brown DL (2007) Unified matrix polynomial approach for operational modal analysis. In: IMAC-XXV, Orlando
6. Burton T, Sharpe D, Jenkins N, Bossanyi E (2001) Wind energy handbook. Wiley, New York
7. Rao SS (1995) Mechanical vibrations. Addison-Wesley, Reading
8. Yutzy J (2011) Characterizing the structural dynamic response of a horizontal axis wind turbine in a yawed flow field using rotor and nacelle-mounted inertial sensors. Master's thesis, Purdue University, West Lafayette
9. Garcia M, Reich A, ZhuY, White (2009) Real-time dynamic measurements of a wind turbine rotor blade using modal filtering. In: IMAC-XXVII, Orlando

Chapter 30
Output-Only Estimation of Wind Induced Stresses in Structures

Eric M. Hernandez, Dionisio Bernal, and Luca Caracologlia

Abstract The use of output feedback as a means to monitor stresses and fatigue in metal structures has been the subject of recent work by researchers in the field of vibration based structural health monitoring. The methodologies that have been proposed in the literature employ the Kalman filter as an estimator and operate under the premise that excitations are realizations of Gaussian white noise. In practice two issues arise, excitations cannot always be approximated by realizations of Gaussian white noise and performance requirements are such that engineers require the use of large finite element models to accurately estimate structural response. This is especially true in the case of wind excited structures, such as tall wind turbines and complex buildings. In the present paper we propose a model based state estimator that can be implemented as a modified finite element model of the system subjected to corrective forces proportional to the measurements. This allows for direct implementation within the context of an arbitrarily large finite element model (FEM) and is of significant importance for implementation purposes given the difficulties typically encountered when implementing the standard Kalman filter in large FEM. Additionally, the proposed estimator is able to explicitly account for the non-white nature of wind loads by using knowledge of the power spectral density of the process. The proposed methodology is successfully applied to estimate the time history of bending moments throughout the height of a simulated tall vertical structure subject to stationary turbulent wind using only sparse measurements of dynamic response and a FEM.

30.1   Introduction

The use of output feedback as a means to monitor stresses and fatigue in metal structures has been the subject of recent work by researchers in the field of vibration based structural health monitoring [1]. The methodologies that have been proposed in the literature employ the Kalman filter as an estimator and operate under the premise that excitations are realizations of Gaussian white noise. In practice two issues arise, excitations cannot always be approximated by realizations of Gaussian white noise and performance requirements are such that engineers require the use of large finite element models to accurately estimate structural response. This is especially true in the case of wind excited structures, such as tall wind turbines and complex buildings.

In this paper we present a model based state estimator that can be implemented as a modified finite element model of the system subjected to corrective forces proportional to the noise contaminated measurements. This allows for direct implementation within the context of an arbitrarily large finite element model (FEM). In addition the proposed estimator allows for explicit consideration of unmeasured turbulent stationary wind loads modelled as a realization of random fields with specified spectral density and spatial correlation.

E.M. Hernandez (✉)
College of Engineering and Mathematical Sciences, University of Vermont, Burlignton, VT 05405, USA
e-mail: eric.hernandez@uvm.edu

D. Bernal
Civil and Environmental Engineering Department-Center for Digital Signal Processing, Northeastern University,
Boston, MA 02115, USA

L. Caracologlia
Civil and Environmental Engineering Department, Northeastern University, Boston, MA 02115, USA

Throughout the paper we shall restrict our attention to symmetric finite n-dimensional linear structural systems satisfying Newton's equation of motion with velocity proportional damping. These systems can be described by the following matrix ordinary differential equation

$$M\ddot{q}(t) + C_D\dot{q}(t) + Kq(t) = b_2f(t) \tag{30.1}$$

where $q(t) \in R^{nx1}$ is the displacement vector at time t, $M = M^T > 0$ is the mass matrix, $C_D = C_D^T \geq 0$ is the damping matrix, and $K = K^T \geq 0$ is the stiffness matrix. The forcing function vector is $f(t) \in R^{mx1}$ and $b_2 \in R^{nxn}$ is the force distribution matrix, which indicates the degrees of freedom on which the forcing function is applied.

In addition m measurements of the system's response are available in the form

$$y(t) = Cx(t) + Df(t) + n(t) \tag{30.2}$$

where $C \in R^{mx2n}$ is the measurement matrix and $n(t) \in R^{mx1}$ is the measurement noise. For displacement or velocity measurements the Dmatrix is zero and C has the following form

$$C_{dis} = \begin{bmatrix} c_2 & 0 \end{bmatrix} \quad C_{vel} = \begin{bmatrix} 0 & c_2 \end{bmatrix} \tag{30.3}$$

where $c_2 \in R^{mxn}$ maps the degrees of freedom to the measurements. If the measurements consist of accelerations the C matrix is given by

$$C = \begin{bmatrix} -c_2M^{-1}K & -c_2M^{-1}C_D \end{bmatrix} \tag{30.4}$$

and the D matrix is given by

$$D = c_2M^{-1}b_2 \tag{30.5}$$

30.2 Wind Load Model

The main focus of this paper is to examine the problem of reconstructing internal stress fields in a structure induced by stationary turbulent wind excitation. In this section we describe the mathematical model to represent the unmeasured wind induced forces. The total wind induced force at height z is given by

$$F(z,t) = \frac{1}{2}\rho C_D(z)A_t(z)V(z,t)^2 = \frac{1}{2}\rho C_D(z)A_t(z)(U(z) + u(z,t))^2 \tag{30.6}$$

where $u(z,t)$ is the time varying component of the wind velocity at height z and at time t, and $U(z)$ is the mean wind speed at height z. The constants ρ, C_D and A_t are the air density, drag coefficient and reference area of contact respectively. The time varying component $u(z,t)$ may be simulated as a realization of a stationary random process with spectral density given by the single-sided Kaimal spectrum [2]

$$\frac{nS(z,n)}{u_*^2} = \frac{200f}{(1 + 50f)^{5/3}} \tag{30.7}$$

where $S(z,n)$ is the value of the spectrum measured at height z, u_* is the friction velocity and n is the frequency (in Hz). The Monin coordinate f is dimensionless and given by

$$f = \frac{nz}{U(z)} \tag{30.8}$$

where $U(z)$ is the mean wind speed at the height z. For any two points j and k, separated by distances Δ_y and Δ_z in the two orthogonal directions to the wind flow, the cross-spectral density between the two stochastic processes V_j and V_k is real and given by

$$S_{V_j,V_k} = \sqrt{S_{V_j,V_j}(\omega)S_{V_k,V_k}(\omega)}e^{-C_{j,k}(\omega)} \tag{30.9}$$

where the turbulence auto-spectra at j and k, $S_{V_j,V_j}(\omega)$ and $S_{V_k,V_k}(\omega)$, can be derived from (30.7) and the $C_{j,k}(\omega)$ is a function given by

$$C_{j,k}(\omega) = \frac{|\omega|\sqrt{C_y^2 \Delta_y^2 + C_z^2 \Delta_z^2}}{\pi(U_j + U_k)} \tag{30.10}$$

where ω is the circular frequency, C_y and C_z are appropriate decay constants and U_j and U_k are the mean wind speed at points j and k. For the case of interest in this paper, i.e. tall vertical structures, such as wind turbines, all points of interest can be assumed to lie in a vertical line and thus $\Delta_y = 0$.

Finally, in order to realize the Kaimal spectra as a digital time signal at various heights of the structure we employed the algorithm proposed in [3]. The algorithm is based on a spectral decomposition of the power spectral density matrix of the wind turbulence.

30.3 The Proposed Estimator

The proposed estimator that we present in this paper was originally derived in [4] and it is written in second order form as

$$M\ddot{\hat{q}}(t) + \left(C_D + c_2^T E c_2\right)\dot{\hat{q}}(t) + K\hat{q}(t) = c_2^T E y(t) \tag{30.11}$$

As can be seen from (30.11) and Fig. 30.1, under premise of velocity measurements, the proposed observer is a modified version of the system with added dampers and excited by forces which are linear combinations of the measurements proportional to the added dampers. This interpretation makes the application of the state estimation more direct, transparent and computationally efficient. The basic component of the proposed estimator is the matrix E which must be selected to minimize (with the constraints of the problem) the trace of the state error covariance, that is, the 2-norm of the state error vector.

Defining the state error as $e = q - \hat{q}$, one can find that the expression for the state error is given by

$$M\ddot{e}(t) + \left(C_D + c_2^T E c_2\right)\dot{e}(t) + Ke(t) = b_2 f(t) - c_2^T E n(t) \tag{30.12}$$

where E is still free to be selected. Before carrying out any further computations, one can see that as the matrix E increases the effective damping of the estimator increases and consequently reduces the estimation error. However, it also increases the term driving the estimation error on the right hand side of (30.12), which is proportional to the measurement noise. Therefore, intuitively a certain optimal balance should be reached in order to make the optimal choice for E. In addition it is important to note that the mathematical problem at hand is not a problem of pole placement. Selecting E solely based on a desired location of poles without accounting for the measurement noise will not yield accurate results in general.

In order to derive the exact expression for the state error covariance consider taking Fourier transforms of both sides of (30.12)

$$\left(-M\omega^2 + \left(C_D + c_2^T E c_2\right)i\omega + K\right)e(\omega) = b_2 f(\omega) - c_2^T E n(\omega) \tag{30.13}$$
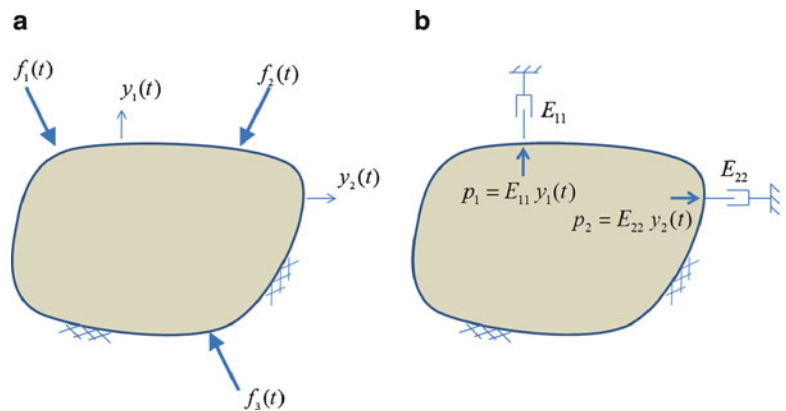

Fig. 30.1 (a) Generic system subject to disturbances $f(t)$ and measurements $y(t)$ (b) proposed observer, a modified model of the system with applied forces $p(t)$ proportional to the measurements and added dampers

Defining

$$G(\omega) = -M\omega^2 + C_D i\omega + K \tag{30.14}$$

and

$$H_o(\omega) = \left(G(\omega) + c_2^T E c_2 i\omega\right)^{-1} \tag{30.15}$$

we obtain the expression for the state error estimate in the frequency domain

$$e(\omega) = H_o(\omega)\left(b_2 f(\omega) - c_2^T E n(\omega)\right) \tag{30.16}$$

The spectral density matrix of the state error $S_{ee}(\omega)$ is given by

$$S_{ee}(\omega) = H_o(\omega)b_2 S_{ff}(\omega)b_2^T H_o^*(\omega) + H_o(\omega)c_2^T E S_{nn}(\omega)E c_2 H_o^*(\omega) \tag{30.17}$$

Where S_{ff} is the spectral density matrix of the wind load, described in the previous section and S_{nn} is the noise spectral density. This last equation assumes that the noise and excitation are uncorrelated and it takes advantage of the internal symmetry of E. Finally, the covariance matrix of the state error is given by

$$P = \int_{-\infty}^{+\infty} S_{ee}d\omega = \int_{-\infty}^{+\infty}\left(H_o(\omega)b_2 S_{ff}(\omega)b_2^T H_o^*(\omega) + H_o(\omega)c_2^T E S_{nn}(\omega)E c_2 H_o^*(\omega)\right)d\omega \tag{30.18}$$

The objective here is to select the matrix E in order to minimize the trace of P. Notice that this is the same objective function that is used in the Kalman filter, i.e. minimization of the trace of the state error covariance.

30.3.1 Selection of E

As explained in the previous section, the optimal selection of E depends on the minimization of the integral in (30.18). For a general multivariable case a close form solution for the optimal matrix E has not been found, therefore numerical optimization is required. However, as it will be shown in the examples to follow, such minimization is not numerically expensive because although in theory $(m^2 + m)/2$ independent values are required; using only m (the diagonal of E) can yield excellent results. Physically this means that the estimator (modified model) would only have added grounded dashpots at the location of the corrective forces which coincide with the measurements and no dashpots interconnecting the output location. In the specific case of Fig. 30.1, this results in an E matrix with the following form

$$E = \begin{bmatrix} E_{11} & 0 \\ 0 & E_{22} \end{bmatrix} \tag{30.19}$$

30.4 Simulation Results

In this section we present the results corresponding to the simulation of the proposed estimator within the wind load environment presented in a previous section.

The simulated system to be modeled is a cantilever with a height of 100 m and a tapered hollow circular cross section that varies from 5.00 m at the base (considered perfectly fixed) to 2.50 m. at the top (Fig. 30.2). The cantilever is modeled as having wall thickness of 0.305 m. The model is discretized every 5.00 m with 20 elements across the height. The structure is modeled as steel (E = 210,000 MPa) with 1% classical damping in every mode.

The wind is modeled as one-directional and for every point in the finite element model a wind load time history is assigned in accordance with the mathematical model described in a previous section based on the Kaimal power spectrum.
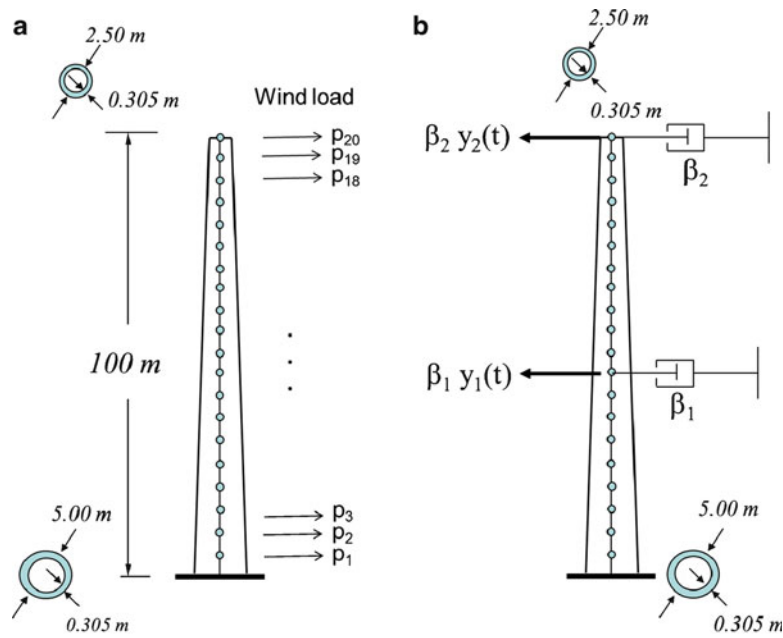
Fig. 30.2 (**a**) The original structure and (**b**) the propose finite element observer
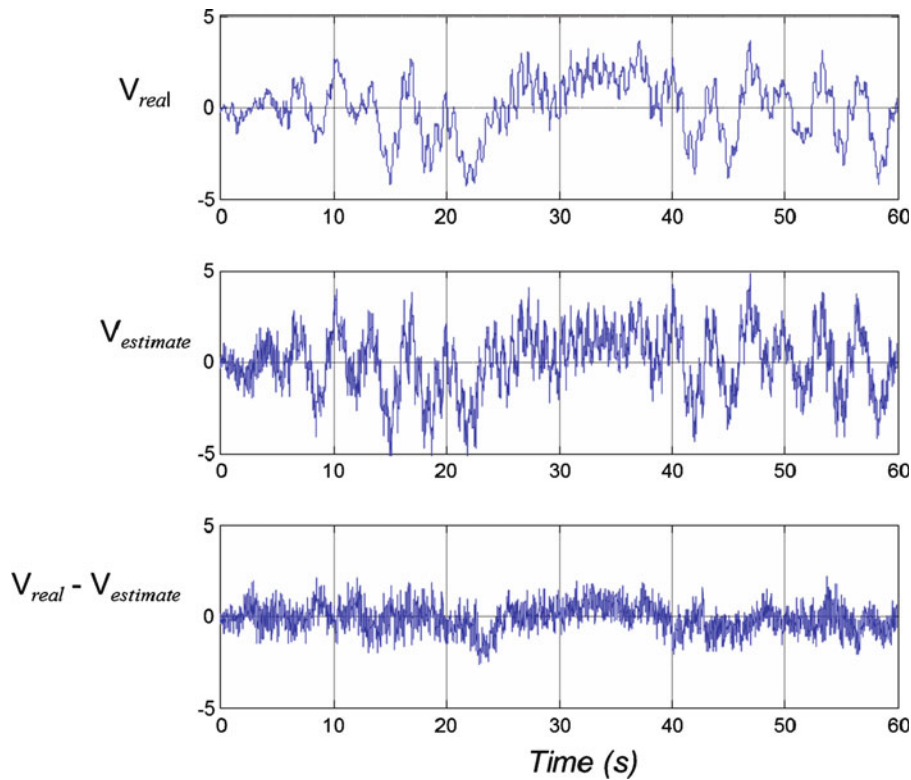
Fig. 30.3 Comparison of estimated base shear force with the true shear force at the base of the structure

For the wind simulations a density of 1.20 kg/m^3 and a drag coefficient of 1.20 were used. The wind parameters that define the Kaimal spectra are given by $z_o = 0.1$, $U = 30 \text{ m/s}$ and $C_z = 10$.

The objective in these simulations is to reconstruct the integral of the shear and normal stresses at the base of the cantilever, namely, the shear force and bending moment time history at the base of the structure. Implementing
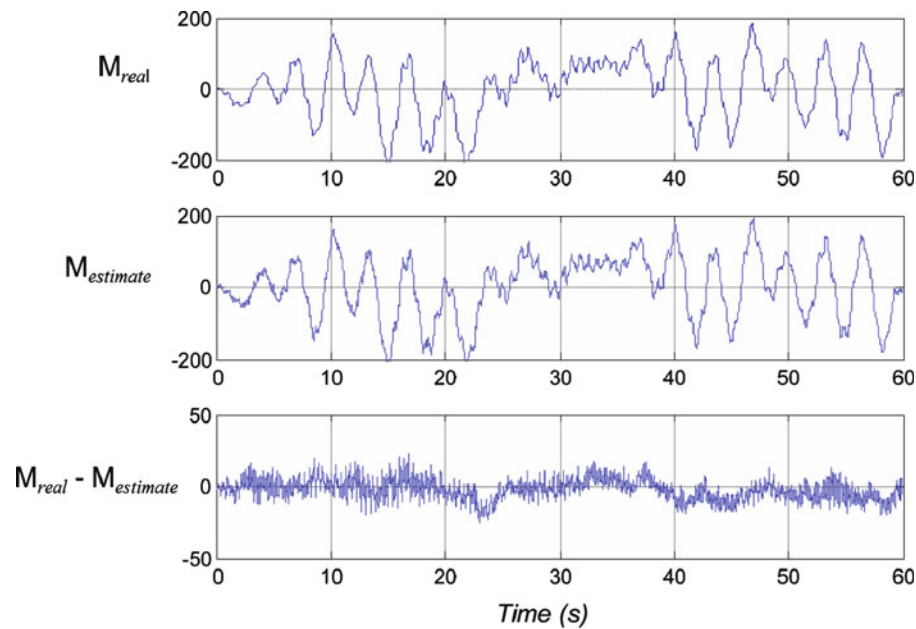
Fig. 30.4 Comparison of estimated bending moment with the true bending moment at the base of the structure

the minimization in (30.18) we find that the added dampers in order to implement the observers (see Fig. 30.2) we find that $\beta_1 = \beta_2 = 83.7 \times 10^6 \, \text{kNs}^2/\text{m}$. In Fig. 30.3 we show the estimated transverse shear in comparison with the real shear at the base of the structure. Similarly in Fig. 30.4 the estimated bending moment and the real bending moment at the base of the structure are compared.

30.5   Conclusions

The paper has shown that it is possible to use the model-based observer proposed in [4] in order to accurately reconstruct the internal forces in an instrumented tall vertical structure subject to transverse stationary wind. The estimation quality of the proposed observer, even with a very limited number of sensors, is adequate (see Figs. 30.3, 30.4). This shows that the proposed observer is a practical option for real-time monitoring of tall vertical structures subject to transverse wind. The estimates can be used as input for fatigue damage functions within the context of an on-line monitoring system. Further studies using non-stationary wind loads in the simulations will be carried out in order to verify the adequacy of the proposed estimator under these conditions.

References

1. Papadimitriou C, Fritzen C-P, Kraemer P, Ntotsios E (2011) Fatigue predictions in entire body of metallic structures from a limited number of vibration sensors using kalman filtering. J Struct Control Health Monitor 18(5):554–573
2. Simiu E, Scalan R (1996) Wind effects on structures. Wiley, New York
3. Di Paola M (1998) Digital simulation of wind field velocity. J Wind Eng Ind Aerodyn 74–76:91–109
4. Hernandez EM (2011) A natural observer for optimal state estimation in second order linear structural systems. J Mech Syst Signal Process 25:2938–2947

Chapter 31
Modal Testing of 9 m CX-100 Turbine Blades

Tim Marinone, Bruce LeBlanc, Julie Harvie, Christopher Niezrecki, and Peter Avitabile

Abstract Several modal tests were conducted on several CX-100 9-meter wind turbine blades (manufactured by TPI Composites Inc.) as part of an evaluation to identify their structural dynamic characteristics. Experiments were made with the blades using different boundary conditions including free-free and clamped. The data for the different tests was processed and compared for the different configurations. This paper presents the results of those studies to provide a database for future use.

31.1 Introduction

Wind energy in the United States is one of the fastest growing sources of clean and renewable domestic energy. A recent DOE technical report [1] prescribed a path for meeting 20% of the nation's energy needs through wind power by 2030. Because of this increased investment into wind energy, significant effort is being expended into the design and manufacturing of wind turbine blades. As part of this work, considerable testing is being conducted in order to provide empirical measurements that can be used to validate numerical blade models and give blade designers a better understanding of the structural and dynamic stiffness of the various designs.

The CX-100 is a 9-meter experimental blade designed by Sandia National Laboratories as part of a long-term effort into the research of innovative approaches to the design and manufacture of blades. The CX-100 contains a unidirectional carbon-fiber laminate spar cap, which provides increased stiffness while reducing the overall weight of the blade.

There have been several modal tests of the CX-100 blade reported with free-free and cantilevered results [2–6]. Of particular note was the free-free modal test by White et al. [2] and the multiple configurations tested by Deines et al. [3], both which will be used for comparison in this paper.

The first part of this paper contains a comparison of results for three blades tested in free-free configuration. Discrepancies between tests are noted and explained. The second part of this paper contains a re-evaluation of a series of tests described at IMAC 29 [3] based on additional testing (more recently performed) and analysis performed using more advanced data reduction techniques. In addition, a simplified analytical model was developed to substantiate the results.

31.2 Project Overview

As part of a project investigating the design of wind turbine blades (U.S. Department of Energy, Award No DE-EE001374 ARRA Funding- "Effect of Manufacturing-Induced Defects on Wind Turbine Blades"), the University of Massachusetts Lowell Structural Dynamics and Acoustics Laboratory (UML SDASL) collaborated with Sandia National Laboratories

T. Marinone (✉) • B. LeBlanc • J. Harvie • C. Niezrecki • P. Avitabile
Structural Dynamics and Acoustic Systems Laboratory, University of Massachusetts Lowell,
One University Avenue, Lowell, MA 01854, USA
e-mail: timothy.marinone@gmail.com

(SNL), the National Renewable Energy Laboratories (NREL), and TPI Composites Inc. (TPI) to manufacture two CX-100 wind turbine blades in early 2011. The first blade, hereafter known as "SDASL 1", was designed with known defects embedded into the blade. Fiber optic and structural health monitoring sensors were also inserted during layup in order to attempt to detect these known defects. The second blade ("SDASL 2") was also designed with known defects but was cut into sections for further static and fatigue testing as well as modeling efforts. In addition, in 2010 the Los Alamos National Laboratory (LANL) also obtained a CX-100 blade as a test bed to validate several structural health monitoring approaches. Previous test results conducted at SNL [2] are used in this paper for frequency comparison.

As part of the initial grant, there was no plan to conduct modal tests on the two SDASL blades. During the manufacturing and assembly process of the two blades, however, a short period of time was available in between the manufacturing and shipping of the blades. Therefore, a brief modal test was conducted on both blades, where the blade was only excited in the flapwise axis due to time constraints. Although both the flapwise and edgewise modes are listed, the focus of this paper is on the flapwise modes, as they were the modes primarily excited.

31.3 Cases Studied

The first set of cases studied presents a comparison of the results obtained for the three blades considered. The second set of cases studied shows some of the results obtained from perturbed boundary conditions tested along with some simple analytical models to substantiate the results.

31.3.1 Part 1: Comparison of Three Blades in a Free-Free Configuration

As described previously, modal testing was performed on three CX-100 blades listed above. In all cases, traditional modal testing methodologies and modal parameter estimation techniques were used for the extraction of modal parameters. However, each of the different groups utilized different data acquisition systems, different test setups, and different data reduction techniques for the identification of the frequencies and mode shapes for the blade characteristics. Sandia Labs used a VXI Technologies HPE 1432a data acquisition system and reduced data using X-Modal2. The work at Los Alamos National Labs used a LabVIEW/National Instruments acquisition system with ME'scope as the modal parameter estimation software. UMASS Lowell tests were performed using LMS DIFA SCADAS data acquisition with LMS TEST.LAB as the data reduction software.

One important consideration concerns the support mechanism for the so-called free-free testing. Sandia Lab utilized a soft bungee attachment for the vertical free-free support mechanism and had slightly different support locations for the testing performed. LANL and UML utilized a slightly stiffer vertical attachment for the free-free testing and similar support location (but different from those used by Sandia Labs); measurement and identification of flapwise modes were the major objective of the LANL and UML teams, so the vertical stiffness for the edgewise modes was not of particular interest in those tests. Care should be exercised when evaluating the reported frequencies due to these differences which can have a more serious effect for the edgewise modes of the blade.

A comparison of the results for the three blades with the Sandia reference mode set is shown in Table 31.1; note that the un-highlighted modes are the flapwise related modes which are most reasonable to compare, and are less affected by the differences in the vertical free-free support mechanism. The modes highlighted in grey are the edgewise and torsion modes, which are more significantly affected by the vertical free-free support mechanism.

Table 31.1 Comparison of frequency results of three tested blades with reference blade

Mode #	SDASL1 (Hz)	SDASL2 (Hz)	LANL (Hz)	Sandia (Hz)	Mode description
1	7.9	7.8	7.6	8.2	First flapwise bending
2[a]	16.0	15.7	18.1	16.8	First edgewise bending
3	20.8	21.3	20.2	20.3	Second flapwise bending
4	32.5	31.3	32.2	33.8	Third flapwise bending
5[a]	43.2	43.6	45.1	42.2	Second edgewise bending
6	50.9	49.7	50.5	52.2	Fourth flapwise bending
7[a]	65.6	63.1	63.9	60.6	First torsion
8[a]	70.5	68.2	70.1	69.9	Third edgewise bending

[a]Care should be taken when examining the edgewise and torsion modes, as the structure was only excited in the flapwise direction due to the significant stiffness of the supports in the edgewise axis
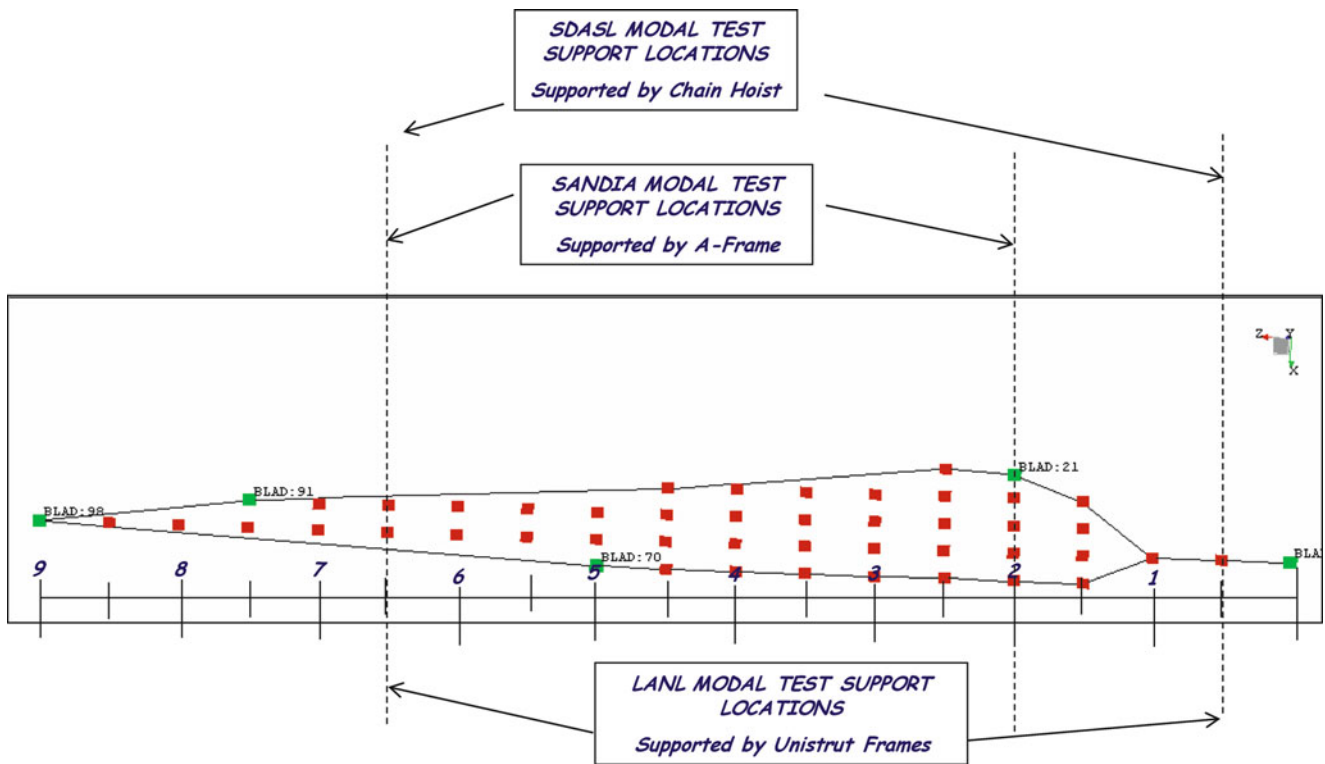
Fig. 31.1 Comparison of support locations for free-free test between tests

Fig. 31.2 (**a**) Supports used at Sandia [2]. (**b**) supports used at LANL [3]. (**c**) supports used by SDASL at TPI [6]

The frequency results are generally consistent between tests, although there is some discrepancy. In order to examine this frequency discrepancy, the boundary conditions were studied. Figure 31.1 shows the schematic for the support locations for the different tests, while Fig. 31.2 shows the various support conditions.

Fig. 31.3 Characteristic mode shapes – (**a**) first flapwise. (**b**) second flapwise. (**c**) third flapwise. (**d**) fourth flapwise
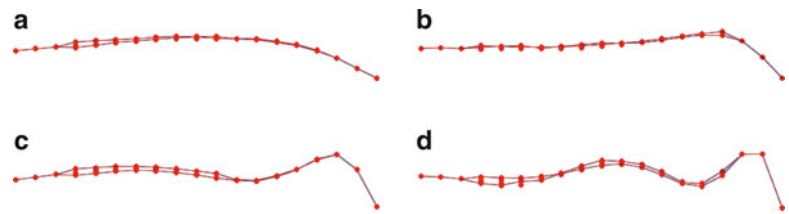
As seen in Figs. 31.1 and 31.2, all of the tests were conducted using different supports. Although there was an effort to replicate the support conditions as closely as possible, limitations in equipment and safety concerns governed the final support set up for each test configuration. Care was taken, however, in locating the support closer to the blade tip at the node of the first mode (6.5 m) in order to minimize the effect of the supports.

In addition to examining the frequencies, a Modal Assurance Criterion (MAC) was performed on the mode shapes of each blade to determine their level of correlation. Figure 31.3 shows the characteristic mode shapes for the first four flapwise modes. (The edgewise and torsion mode shapes are not shown as they were not primarily excited nor were of interest for the tests conducted). Table 31.2 lists the MAC for all three blades compared to each other. (The mode shapes from Sandia [2] were not available and thus were not compared). Note that the modes not highlighted in grey are the flapwise modes that were primarily excited. The grey highlighted modes are the edgewise modes which were not primarily excited and are only shown for completeness.

The sub-diagonals indicating the high level of correlation between the blades are evident in the MAC matrix. In addition, the two SDASL blades correlate well as seen in Table 31.3. The LANL blade did not correlate as well and is not shown. Again, note the high frequency and MAC correlation for the flapwise modes in white. The modes highlighted in grey are not the modes of interest, and do not correlate as well.

31.3.2 Part 2: Blade Boundary Condition Study

Previous work in the summer of 2010 at LANL [3] provided results of a modal test of the blade with three different boundary conditions. "Free # 1" involved suspending the blade with straps at both ends. "Free # 2" consisted of a 500 lb mass attached to the root end of the blade, while still being hung in a free-free configuration; although the mass rested on top of the 300 lb 80–20 aluminum fixture which was designed to represent a cantilever condition, the mass was not bolted down. "Clamped" consisted of bolting the 500 lb mass at the end of the blade to the 300 lb 80–20 fixture while the rest of the blade was suspended from the fixture with no other support for the structure. Figure 31.4 shows the various BCs studied.

The results reported are shown in Table 31.4; however, some of these frequencies will be further evaluated in the paper and the specific mode characteristics of the specific shape will be further re-identified and discussed

The LANL blade was eventually brought to NREL, where a modal test was conducted with the blade in a large massive fixture for fatigue and static loading. The results obtained at NREL using a much more substantial fixture were higher in frequency than the results reported from LANL. As a result, some frequencies were questionable; the data was re-examined and re-evaluated to confirm the original data results obtained.

Examination of the 3.2 Hz mode previously reported showed there was substantial motion in the fixture, and that the blade had minimal bending in contrast to the shearing of the 80–20 frame. Accordingly, the modal data was re-processed in order to better identify the flapwise modes. In addition, vector correlations were also performed rather than just relying on the frequency comparisons. The new mode shapes show that a high degree of correlation exists when compared to the free-free test as shown in Table 31.5. As a result, there appears to be a minimal frequency and mode shape change due to the addition of the 800 lb mass and attachment to the 80–20 frame structure in the LANL lab set up.

The updated frequency comparisons are shown in Table 31.6; these are different than those previously reported in Table 31.4

Examining Tables 31.5 and 31.6 show that the addition of the 800 lb mass and bolting to the 80–20 fixture was not sufficient to accurately represent a built in condition. Both the mode shapes and frequencies correlate well between the free-free and clamped condition, indicating the minimal effect due to the mass of the fixture and attachment to the 80–20 fixture at the LANL lab.

Table 31.2 MAC of all three blades for the first eight modes of each test (*F* flapwise, *E* edgewise, *T* torsional)

		SDASL 1								SDASL 2								LANL							
		7.9 (F)	16.0 (E)	20.8 (F)	32.5 (F)	43.2 (E)	50.9 (F)	65.6 (T)	70.5 (E)	7.8 (F)	15.7 (E)	21.3 (F)	31.3 (F)	43.6 (E)	49.7 (F)	63.1 (T)	68.2 (E)	7.6 (F)	18.1 (E)	20.2 (F)	32.2 (F)	45.1 (E)	50.5 (F)	63.9 (T)	70.1 (E)
SDASL 1	7.9 (F)	**100**	1.8	15.5	1.5	10.4	4.9	9.4	3.5	**98.3**	4.1	19.6	4.8	9.2	5.3	5	2.2	**99.6**	25.9	5.3	0.9	0.1	0.1	1.6	0
	16.0 (E)	1.8	100	76.5	3.7	29.8	1.6	1.9	9.1	4.4	96.2	68.8	5.5	15.7	1	0.1	2.6	21.9	84.9	81.2	4.9	2.8	0.1	5.2	0.2
	20.8 (F)	15.5	76.5	**100**	15.4	50.2	4.6	3.5	13.6	22.1	72	**97.6**	19.6	26.4	3.1	0.1	5.7	41.6	96.8	79	13.1	0.1	0	7.9	0.2
	32.5 (F)	1.5	3.7	15.4	**100**	49.3	3.8	14.6	9	4.3	6.2	20.5	**95.9**	23.5	2.1	1.4	6	16.5	38.4	27	**88.4**	20.3	0.3	0.2	3.7
	43.2 (E)	10.4	29.8	50.2	49.3	100	30.5	3.4	5.5	16.6	34.1	57.7	53.8	73.3	20.1	0.8	0.4	33.5	60.3	42.4	49.9	13.9	6.2	4.8	0.6
	50.9 (F)	4.9	1.6	4.6	3.8	30.5	**100**	7.5	8	7.3	4.4	9.2	11	73.6	**96**	1.4	3.9	22.8	20.9	9.9	19.2	50.6	62.5	0	0.2
	65.6 (T)	9.4	1.9	3.5	14.6	3.4	7.5	100	30	12	5.8	6.6	22	12	15.2	80.8	30.7	28	14.9	5.5	20.4	15.5	7.3	32.7	0.7
	70.5 (E)	3.5	9.1	13.6	9	5.5	8	30	100	5.6	14	18.7	15.9	15.6	15.3	27.4	90.2	38.4	44.4	28.6	15.2	1.7	5.9	3.8	19.2
SDASL 2	7.8 (F)	98.3	4.4	22.1	4.3	16.6	7.3	12	5.6	**100**	7.9	27.1	9.5	14.2	7.7	5.2	3.8	**98.9**	33.9	9.7	3.1	0.4	0.2	2.3	0
	15.7 (E)	4.1	96.2	72	6.2	34.1	4.4	5.8	14	7.9	100	67.7	9.7	23.4	3.8	1.6	5.6	28.3	81.6	73.8	8.7	0.8	0.9	2.7	0
	21.3 (F)	19.6	68.8	**97.6**	20.5	57.7	9.2	6.6	18.7	27.1	67.7	**100**	26.7	36.6	7.3	0.8	9.3	47.8	93.5	72.2	17.4	0.2	0.2	5.1	0.2
	31.3 (F)	4.8	5.5	19.6	**95.9**	53.8	11	22	15.9	9.5	9.7	26.7	**100**	35	9	4.4	12.2	24.5	42.9	28.2	**80.1**	24.2	2.2	0.1	3.8
	43.6 (E)	9.2	15.7	26.4	23.5	73.3	73.6	12	15.6	14.2	23.4	36.6	35	100	65.2	2	6.6	34.7	44.8	27.2	39	27.2	24.6	0	0.1
	49.7 (F)	5.3	1	3.1	2.1	20.1	**96**	15.2	15.3	7.7	3.8	7.3	9	65.2	**100**	6.9	10.9	26.8	20.1	8.7	15.1	46.9	61.6	1.2	0
	63.1 (T)	5	0.1	0.1	1.4	0.8	1.4	80.8	27.4	5.2	1.6	0.8	4.4	2	6.9	100	33.5	15.3	5.6	1.5	9.6	8.5	4.1	61.2	0.4
	68.2 (E)	2.2	2.6	5.7	6	0.4	3.9	30.7	90.2	3.8	5.6	9.3	12.2	6.6	10.9	33.5	100	39.5	40.4	25	16.3	0.8	1.6	5.9	17.4
LANL	7.6 (F)	99.6	25.9	5.3	0.9	0.1	0.1	1.6	0	98.9	33.9	9.7	3.1	0.4	0.2	2.3	0	**100**	27.9	6.4	1.2	0	0	2	0
	18.1 (E)	21.9	84.9	81.2	4.9	2.8	0.1	5.2	0.2	28.3	81.6	73.8	8.7	0.8	0.9	2.7	0	27.9	100	89.7	14.9	0.5	0.2	9.7	0.4
	20.2 (F)	41.6	96.8	79	13.1	0.1	0	7.9	0.2	47.8	93.5	72.2	17.4	0.2	0.2	5.1	0.2	6.4	89.7	**100**	12.1	2.4	0.6	9.2	0.6
	32.2 (F)	16.5	38.4	27	**88.4**	20.3	0.3	0.2	3.7	24.5	42.9	28.2	**80.1**	24.2	2.2	0.1	3.8	1.2	14.9	12.1	**100**	29.8	0.5	0.1	5.8
	45.1 (E)	33.5	60.3	42.4	49.9	13.9	6.2	4.8	0.6	34.7	44.8	27.2	39	27.2	24.6	0	0.1	0	0.5	2.4	29.8	100	52.9	3.8	14.4
	50.5 (F)	22.8	20.9	9.9	19.2	50.6	62.5	0	0.2	26.8	20.1	8.7	15.1	46.9	61.6	1.2	0	0	0.2	0.6	0.5	52.9	**100**	3.9	0
	63.9 (T)	28	14.9	5.5	20.4	15.5	7.3	32.7	0.7	15.3	5.6	1.5	9.6	8.5	4.1	61.2	0.4	2	9.7	9.2	0.1	3.8	3.9	100	0
	70.1 (E)	38.4	44.4	28.6	15.2	1.7	5.9	3.8	19.2	39.5	40.4	25	16.3	0.8	1.6	5.9	17.4	0	0.4	0.6	5.8	14.4	0	0	100

31.3.3 Analytical Model Approximations

In order to further substantiate these updated results, a very simple planar beam model approximation for the blade was developed. The model was not intended to be a super, high fidelity model but rather just a coarse approximation of the blade cross sections with a reasonable distribution of mass in the model to represent the generic free-free and mass loaded conditions.

Three sections of the blade "SDASL 2" were cut for further study at the University of Massachusetts Lowell. Based on these three sections and other dimensions given [7], the physical characteristics of the model were compared to the various known values shown in Table 31.7.

In addition, the first three flapwise modes along the centerline were compared between SDASL 2 and the model where Table 31.8 lists the frequency and MAC values. While the simple beam model is not perfect, the model allows for the investigation of different boundary conditions on the blade frequency.

With a reasonable degree of confidence in the model, a study was done to determine the effect of the 800 lb mass on the blade. Table 31.9 lists the results for adding various masses to the analytical model as well as the test results.

Table 31.3 Comparison of results between SDASL 1 and SDASL 2 blades

Pair #	SDASL 1 (Hz)	SDASL 2 (Hz)	%Frequency Difference	MAC	Mode Description
1	7.90	7.76	1.80	98.3	1st Flapwise Bending
2	15.97	15.67	1.89	96.2	1st Edgewise Bending
3	20.84	21.26	-1.94	97.6	2nd Flapwise Bending
4	32.45	31.34	3.55	95.9	3rd Flapwise Bending
5	43.20	43.60	-0.90	73.3	2nd Edgewise Bending
6	50.87	49.68	2.40	96.0	4th Flapwise Bending
7	65.55	63.09	3.90	80.8	1st Torsion
8	70.45	68.23	3.26	90.2	3rd Edgewise Bending

Fig. 31.4 Boundary condition setup for three tests conducted

Table 31.4 Original frequency results reported for three conditions[a]

Test:	First flap (Hz)	Second flap (Hz)	Third flap (Hz)	Fourth flap (Hz)
Free-free # 1 (straps only)	7.6	17.9	32.1	50.4
Free-free #2 (fixture + strap)[b]	3.3	8.7	17.6	30.7
Clamped-free (bolted to fixture + frame)[b]	3.2	8.8	19.2	30.8

[a]Note that these results were obtained by just considering frequency comparisons without mathematical comparisons of the actual shape correlations

[b]Note that the frequencies are of the combined system, where the fixture and frame have a significant contribution to the frequencies and mode shapes

Table 31.5 MAC comparing blade in all three configurations for first three flapwise modes

MAC		Free # 1			Free # 2			Clamped		
		1 – 7.61	2 – 20.11	3 – 32.23	1 – 7.15	2 – 17.5	3 – 30.66	1 – 7.11	2 – 16.84	3 – 30.85
Free # 1	1 – 7.61	**100**	7.3	1	**75.8**	24.2	2.5	**97.4**	32.3	8.2
	2 – 20.11	7.3	**100**	11.3	0.2	**87.9**	22.9	8.6	**82.9**	28.6
	3 – 32.23	1	11.3	**100**	0.9	9.4	**96.1**	2.6	10.4	**92**
Free # 2	1 – 7.15	**75.8**	0.2	0.9	**100**	6.8	1.6	**80.9**	9.3	5.2
	2 – 17.5	24.2	**87.9**	9.4	6.8	**100**	18.5	24.1	**97.5**	27.5
	3 – 30.66	2.5	22.9	**96.1**	1.6	18.5	**100**	5.3	19.9	**97.5**
Clamped	1 – 7.11	**97.4**	8.6	2.6	**80.9**	24.1	5.3	**100**	31.6	12.2
	2 – 16.84	32.3	**82.9**	10.4	9.3	**97.5**	19.9	31.6	**100**	30.1
	3 – 30.85	8.2	28.6	**92**	5.2	27.5	**97.5**	12.2	30.1	**100**

Table 31.6 Updated comparison of frequencies between boundary conditions

Test:	First flap (Hz)	Second flap (Hz)	Third flap (Hz)
Free-free # 1 (straps only)	7.61	20.11	32.23
Free-free #2 (fixture + strap)	7.15	17.5	30.66
Clamped-free (bolted to fixture, frame)	7.11	16.84	30.85
NREL test	4.35	11.51	20.54

Table 31.7 Comparison of calculated and actual physical characteristics

	Actual	Model	% Difference
Total length [m]	9.0 [7]	9.0	0.00
Total weight [lb]	382.9 [7]	382.6	0.08
Weight of 23″ section [lb]	16.7	17.1	−2.40
Weight of 21″ section [lb]	12.3	12.3	0.00
Weight of tip section [lb]	33.9	30.2	10.91

Table 31.8 Frequency and MAC values between model and test for free-free condition

Mode #	SDASL 2 (Hz)	Model (Hz)	MAC	Mode description
1	7.76	7.84	99.85	First flapwise bending
2	21.26	18.50	98.28	Second flapwise bending
3	31.34	34.52	98.85	Third flapwise bending

Table 31.9 Frequency values for model as various masses added at root section

	MATLAB results						Test results	
	Free-free (Hz)	250 lb mass (Hz)	500 lb mass (Hz)	1,000 lb mass (Hz)	1,000 lb mass w/inertia (Hz)	Built-in (Hz)	LADSS 2010 – 800 lb mass added (Hz)	LANL blade w/NREL fixture (Hz)
Mode 1	7.84	7.45	7.35	7.28	4.60	4.36	7.11	4.35
Mode 2	18.50	17.67	17.48	17.36	12.05	11.76	16.84	11.51
Mode 3	34.52	33.21	32.95	32.77	24.63	24.25	30.85	20.54

In order to replicate a built-in condition, a significant amount of mass would be required (much more than the weight of the 800 lb fixture) to be added to the root end of the blade. (Further modeling studies are provided in Reference [8]). The results of the model above substantiate the findings from the test results presented in the second part of the paper.

31.4 Conclusion

Two separate CX-100 wind turbine blades were tested in April 2011 and the results of these tests were correlated. Previous testing performed at Los Alamos National Laboratories (LANL) during the summer of 2010 on another CX-100 blade was re-evaluated and compared to these latest results. The LANL blade was also subjected to several different perturbed boundary conditions. All of the results from these three blades were compared and resulting flapwise modes correlated well following re-examination of previously collected data. In addition, a very simple analytical model of the blade was developed to further substantiate the result observed.

References

1. U.S. Department of Energy (2008) 20% wind energy by 2030. Report # DOE/GO-102008-2567, U.S. Department of Energy, Energy Efficiency and Renewable Energy, Washington, DC
2. White JR, Adams DE, Rumsey MA (2010) Modal analysis of CX-100 rotor blade and micon 65/13 wind turbine. In: Proceedings of the IMAC-XXVIII, Jacksonville, 1–4 Feb 2010
3. Deines K, Marinone T, Schultz R, Farinholt K, Park G (2011) Modal analysis and SHM investigation of CX-100 wind turbine blade. In: Proceedings of the IMAC-XXIX, Jacksonville, 31 Jan –3 Feb 2011
4. Casisas M, Smith G (2008) Two independent modal tests of two identical wind turbine blades. Sandia National Laboratories Report, 6 Feb 2008
5. Sandia National Laboratory (2008) CX-100 blade modal survey- cantilever and free-free test results. Test report
6. Marinone T, LeBlanc B, Carr J, Harvey E, Avitabile P (2011) Impact testing of CX-100 wind turbine blades (modal data). University of Massachusetts Lowell – SDASLrReport # L111966-1. Test report
7. Berry DS (2007) CX-100 manufacturing final project report. TPI composites Inc
8. Harvie J, Avitabile P (2012) Some considerations of boundary conditions in dynamic testing. In: Proceedings of the IMAC-XXX, Jacksonville, 30 Jan–2 Feb 2012